

PLASMA SOURCES SCIENCE & TECHNOLOGY

PLASMA SOURCES

SCIENCE & TECHNOLOGY

AD-A285 850



Institute of Physics Publishing

REPORT DOCUMENTATION PAGE

Form Approved
OMB No. 0704-0188

Public reporting burden for this collection of information is estimated to average 1 hour per response, including the time for reviewing instructions, searching existing data sources, gathering and maintaining the data needed, and completing and reviewing the collection of information. Send comments regarding this burden estimate or any other aspect of this collection of information, including suggestions for reducing this burden, to Washington Headquarters Services, Directorate for Information Operations and Reports, 1215 Jefferson Davis Highway, Suite 1204, Arlington, VA 22202-4302, and to the Office of Management and Budget, Paperwork Reduction Project (0704-0188), Washington, DC 20503.

1. AGENCY USE ONLY (Leave blank)

2. REPORT DATE

30 Aug--3 Sep 93

3. REPORT TYPE AND DATES COVERED

Final Proceedings 30 Aug--3 Sep 93

4. TITLE AND SUBTITLE

Final Proceedings: Formation, Transport and Consequences of Particles in Plasmas

5. FUNDING NUMBERS

CSP-93-1024

6. AUTHOR(S)

Dr Jean-Pierre Boeuf

7. PERFORMING ORGANIZATION NAME(S) AND ADDRESS(ES)

Universite Paul Sabatier
CNRS CENTRE DE Physique Atomique
118 Route de Narbonne
31062 Toulouse Cedex
France

8. PERFORMING ORGANIZATION
REPORT NUMBER

9. SPONSORING MONITORING AGENCY NAME(S) AND ADDRESS(ES)

Monitoring/Sponsoring Agency: European Office of Aerospace
Research and Development, PSC 802, Box 14, FPO AE 09499-
0200

10. SPONSORING MONITORING
AGENCY REPORT NUMBER

11. SUPPLEMENTARY NOTES

12a. DISTRIBUTION AVAILABILITY STATEMENT

Approved for public release, distribution unlimited.

12b. DISTRIBUTION CODE

13. ABSTRACT (Maximum 200 words)

This volume is the final proceedings of the conference.

94-31081
94 9

DTIC QUALITY INSPECTED 3

14. SUBJECT TERMS

15. NUMBER OF PAGES

451

16. PRICE CODE

17. SECURITY CLASSIFICATION
OF REPORT

UNCLASSIFIED

18. SECURITY CLASSIFICATION
OF THIS PAGE

UNCLASSIFIED

19. SECURITY CLASSIFICATION
OF ABSTRACT

UNCLASSIFIED

20. LIMITATION OF ABSTRACT

NSN 7540-01-280-5500

Standard Form 298 (Rev. 2/89)
Prescribed by ANSI Std. Z39-18
298-102

Reproduced From
Best Available Copy

GENERAL INSTRUCTIONS FOR COMPLETING SF 298

The Report Documentation Page (RDP) is used in announcing and cataloging reports. It is important that this information be consistent with the rest of the report, particularly the cover and title page. Instructions for filling in each block of the form follow. It is important to *stay within the lines* to meet optical scanning requirements.

Block 1. Agency Use Only (Leave blank)

Block 2. Report Date Full publication date including day, month, and year, if available (e.g., 1 Jan 88). Must cite at least the year.

Block 3. Type of Report and Dates Covered

State whether report is interim, final, etc. If applicable, enter inclusive report dates (e.g., 10 Jun 87 - 30 Jun 88).

Block 4. Title and Subtitle A title is taken from the part of the report that provides the most meaningful and complete information. When a report is prepared in more than one volume, repeat the primary title, add volume number, and include subtitle for the specific volume. On classified documents enter the title classification in parentheses.

Block 5. Funding Numbers Do not include contract and grant numbers, may include program element number(s), project number(s), task number(s), and work unit number(s). Use the following codes:

C	Contract	PR	Project
G	Grant	TA	Task
PE	Program Element	WU	Work Unit
			Accession

Block 6. Author(s) Name(s) of person(s) responsible for writing the report, performing the research, or credited with the content of the report. If editor or compiler, this should follow the name(s).

Block 7. Performing Organization Name(s) and Address(es) Self-explanatory.

Block 8. Performing Organization Report Number Enter the unique alphanumeric report number(s) assigned by the organization performing the report.

Block 9. Sponsoring/Monitoring Agency Name(s) and Address(es) Self-explanatory.

Block 10. Sponsoring/Monitoring Agency Report Number (If known)

Block 11. Supplementary Notes Enter information not included elsewhere such as: Prepared in cooperation with...; Trans. of...; To be published in... When a report is revised, include a statement whether the new report supersedes or supplements the older report.

Block 12a. Distribution/Availability Statement Denotes public availability or limitations. Cite any availability to the public. Enter additional limitations or special markings in all capitals (e.g., NOFORN, REL, ITAR).

DOD See DoDD 5230.24, "Distribution Statements on Technical Documents"
DOE See authorities
NASA See Handbook NHB 2200.2
NTIS Leave blank

Block 12b. Distribution Code

DOD Leave blank
DOE Enter DOE distribution category from the Standard Distribution for Uniformed Services for Health and Research Reports
NASA See authorities
NTIS Leave blank

Block 13. Abstract Include a brief (Maximum 200 words) factual summary of the most significant information contained in the report.

Block 14. Subject Terms Keywords or phrases identifying major subjects in the report.

Block 15. Number of Pages Enter the total number of pages.

Block 16. Price Code Enter appropriate price code (NTIS only).

Blocks 17. - 19. Security Classifications Self-explanatory. Enter U.S. Security Classification in accordance with U.S. Security Regulations (i.e., UNCLASSIFIED). If form contains classified information, stamp classification on the top and bottom of the page.

Block 20. Limitation of Abstract This block must be completed to assign a limitation to the abstract. Enter either UL (unlimited) or SAR (same as report). An entry in this block is necessary if the abstract is to be limited. If blank, the abstract is assumed to be unlimited.

Plasma Sources Science and Technology publishes papers on the generation and application of non-fusion plasma sources. It covers a wide range of cross-disciplinary research, catering for physicists, physical chemists and engineers.

Subscription information-1994 volume

Editor-in-chief

H. Hershkovitz, J. W. Wilson, Mark R. SA

Regional Editors

J. Keller, BMW - Regional Director SA (North America)

D C Schram, Entomology, University of Oxford, The Botanic Garden (Western Europe)

V. P. Ryzhov, Moscow Academy of Sciences, Moscow, U.S.S.R.

Editorial Board

16 APR 1964

4. APPROVED BY THE BOARD OF DIRECTORS

NO BUREAU. From Dayton through Dayton, Ohio

R W Dawkins, Australian Institute of Botany, Canberra, A.C.T.

10 Brown, 1970, 1971, 1972, 1973, 1974, 1975, 1976, 1977, 1978, 1979, 1980, 1981, 1982, 1983, 1984, 1985, 1986, 1987, 1988, 1989, 1990, 1991, 1992, 1993, 1994, 1995, 1996, 1997, 1998, 1999, 2000, 2001, 2002, 2003, 2004, 2005, 2006, 2007, 2008, 2009, 2010, 2011, 2012, 2013, 2014, 2015, 2016, 2017, 2018, 2019, 2020, 2021, 2022, 2023, 2024, 2025, 2026, 2027, 2028, 2029, 2030, 2031, 2032, 2033, 2034, 2035, 2036, 2037, 2038, 2039, 2040, 2041, 2042, 2043, 2044, 2045, 2046, 2047, 2048, 2049, 2050, 2051, 2052, 2053, 2054, 2055, 2056, 2057, 2058, 2059, 2060, 2061, 2062, 2063, 2064, 2065, 2066, 2067, 2068, 2069, 2070, 2071, 2072, 2073, 2074, 2075, 2076, 2077, 2078, 2079, 2080, 2081, 2082, 2083, 2084, 2085, 2086, 2087, 2088, 2089, 2090, 2091, 2092, 2093, 2094, 2095, 2096, 2097, 2098, 2099, 2100, 2101, 2102, 2103, 2104, 2105, 2106, 2107, 2108, 2109, 2110, 2111, 2112, 2113, 2114, 2115, 2116, 2117, 2118, 2119, 2120, 2121, 2122, 2123, 2124, 2125, 2126, 2127, 2128, 2129, 2130, 2131, 2132, 2133, 2134, 2135, 2136, 2137, 2138, 2139, 2140, 2141, 2142, 2143, 2144, 2145, 2146, 2147, 2148, 2149, 2150, 2151, 2152, 2153, 2154, 2155, 2156, 2157, 2158, 2159, 2160, 2161, 2162, 2163, 2164, 2165, 2166, 2167, 2168, 2169, 2170, 2171, 2172, 2173, 2174, 2175, 2176, 2177, 2178, 2179, 2180, 2181, 2182, 2183, 2184, 2185, 2186, 2187, 2188, 2189, 2190, 2191, 2192, 2193, 2194, 2195, 2196, 2197, 2198, 2199, 2200, 2201, 2202, 2203, 2204, 2205, 2206, 2207, 2208, 2209, 2210, 2211, 2212, 2213, 2214, 2215, 2216, 2217, 2218, 2219, 2220, 2221, 2222, 2223, 2224, 2225, 2226, 2227, 2228, 2229, 2230, 2231, 2232, 2233, 2234, 2235, 2236, 2237, 2238, 2239, 2240, 2241, 2242, 2243, 2244, 2245, 2246, 2247, 2248, 2249, 2250, 2251, 2252, 2253, 2254, 2255, 2256, 2257, 2258, 2259, 2260, 2261, 2262, 2263, 2264, 2265, 2266, 2267, 2268, 2269, 2270, 2271, 2272, 2273, 2274, 2275, 2276, 2277, 2278, 2279, 2280, 2281, 2282, 2283, 2284, 2285, 2286, 2287, 2288, 2289, 2290, 2291, 2292, 2293, 2294, 2295, 2296, 2297, 2298, 2299, 2300, 2301, 2302, 2303, 2304, 2305, 2306, 2307, 2308, 2309, 2310, 2311, 2312, 2313, 2314, 2315, 2316, 2317, 2318, 2319, 2320, 2321, 2322, 2323, 2324, 2325, 2326, 2327, 2328, 2329, 2330, 2331, 2332, 2333, 2334, 2335, 2336, 2337, 2338, 2339, 2340, 2341, 2342, 2343, 2344, 2345, 2346, 2347, 2348, 2349, 2350, 2351, 2352, 2353, 2354, 2355, 2356, 2357, 2358, 2359, 2360, 2361, 2362, 2363, 2364, 2365, 2366, 2367, 2368, 2369, 2370, 2371, 2372, 2373, 2374, 2375, 2376, 2377, 2378, 2379, 2380, 2381, 2382, 2383, 2384, 2385, 2386, 2387, 2388, 2389, 2390, 2391, 2392, 2393, 2394, 2395, 2396, 2397, 2398, 2399, 2400, 2401, 2402, 2403, 2404, 2405, 2406, 2407, 2408, 2409, 2410, 2411, 2412, 2413, 2414, 2415, 2416, 2417, 2418, 2419, 2420, 2421, 2422, 2423, 2424, 2425, 2426, 2427, 2428, 2429, 2430, 2431, 2432, 2433, 2434, 2435, 2436, 2437, 2438, 2439, 2440, 2441, 2442, 2443, 2444, 2445, 2446, 2447, 2448, 2449, 2450, 2451, 2452, 2453, 2454, 2455, 2456, 2457, 2458, 2459, 2460, 2461, 2462, 2463, 2464, 2465, 2466, 2467, 2468, 2469, 2470, 2471, 2472, 2473, 2474, 2475, 2476, 2477, 2478, 2479, 2480, 2481, 2482, 2483, 2484, 2485, 2486, 2487, 2488, 2489, 2490, 2491, 2492, 2493, 2494, 2495, 2496, 2497, 2498, 2499, 2500, 2501, 2502, 2503, 2504, 2505, 2506, 2507, 2508, 2509, 2510, 2511, 2512, 2513, 2514, 2515, 2516, 2517, 2518, 2519, 2520, 2521, 2522, 2523, 2524, 2525, 2526, 2527, 2528, 2529, 2530, 2531, 2532, 2533, 2534, 2535, 2536, 2537, 2538, 2539, 2540, 2541, 2542, 2543, 2544, 2545, 2546, 2547, 2548, 2549, 2550, 2551, 2552, 2553, 2554, 2555, 2556, 2557, 2558, 2559, 2560, 2561, 2562, 2563, 2564, 2565, 2566, 2567, 2568, 2569, 2570, 2571, 2572, 2573, 2574, 2575, 2576, 2577, 2578, 2579, 2580, 2581, 2582, 2583, 2584, 2585, 2586, 2587, 2588, 2589, 2590, 2591, 2592, 2593, 2594, 2595, 2596, 2597, 2598, 2599, 2600, 2601, 2602, 2603, 2604, 2605, 2606, 2607, 2608, 2609, 2610, 2611, 2612, 2613, 2614, 2615, 2616, 2617, 2618, 2619, 2620, 2621, 2622, 2623, 2624, 2625, 2626, 2627, 2628, 2629, 2630, 2631, 2632, 2633, 2634, 2635, 2636, 2637, 2638, 2639, 2640, 2641, 2642, 2643, 2644, 2645, 2646, 2647, 2648, 2649, 2650, 265

M. d. Agostino, 1970, 1971, 1972, 1973, 1974, 1975, 1976, 1977, 1978, 1979, 1980, 1981, 1982, 1983, 1984, 1985, 1986, 1987, 1988, 1989, 1990, 1991, 1992, 1993, 1994, 1995, 1996, 1997, 1998, 1999, 2000, 2001, 2002, 2003, 2004, 2005, 2006, 2007, 2008, 2009, 2010, 2011, 2012, 2013, 2014, 2015, 2016, 2017, 2018, 2019, 2020, 2021, 2022, 2023, 2024, 2025, 2026, 2027, 2028, 2029, 2030, 2031, 2032, 2033, 2034, 2035, 2036, 2037, 2038, 2039, 2040, 2041, 2042, 2043, 2044, 2045, 2046, 2047, 2048, 2049, 2050, 2051, 2052, 2053, 2054, 2055, 2056, 2057, 2058, 2059, 2060, 2061, 2062, 2063, 2064, 2065, 2066, 2067, 2068, 2069, 2070, 2071, 2072, 2073, 2074, 2075, 2076, 2077, 2078, 2079, 2080, 2081, 2082, 2083, 2084, 2085, 2086, 2087, 2088, 2089, 2090, 2091, 2092, 2093, 2094, 2095, 2096, 2097, 2098, 2099, 2100, 2101, 2102, 2103, 2104, 2105, 2106, 2107, 2108, 2109, 2110, 2111, 2112, 2113, 2114, 2115, 2116, 2117, 2118, 2119, 2120, 2121, 2122, 2123, 2124, 2125, 2126, 2127, 2128, 2129, 2130, 2131, 2132, 2133, 2134, 2135, 2136, 2137, 2138, 2139, 2140, 2141, 2142, 2143, 2144, 2145, 2146, 2147, 2148, 2149, 2150, 2151, 2152, 2153, 2154, 2155, 2156, 2157, 2158, 2159, 2160, 2161, 2162, 2163, 2164, 2165, 2166, 2167, 2168, 2169, 2170, 2171, 2172, 2173, 2174, 2175, 2176, 2177, 2178, 2179, 2180, 2181, 2182, 2183, 2184, 2185, 2186, 2187, 2188, 2189, 2190, 2191, 2192, 2193, 2194, 2195, 2196, 2197, 2198, 2199, 2200, 2201, 2202, 2203, 2204, 2205, 2206, 2207, 2208, 2209, 2210, 2211, 2212, 2213, 2214, 2215, 2216, 2217, 2218, 2219, 2220, 2221, 2222, 2223, 2224, 2225, 2226, 2227, 2228, 2229, 2230, 2231, 2232, 2233, 2234, 2235, 2236, 2237, 2238, 2239, 2240, 2241, 2242, 2243, 2244, 2245, 2246, 2247, 2248, 2249, 2250, 2251, 2252, 2253, 2254, 2255, 2256, 2257, 2258, 2259, 2260, 2261, 2262, 2263, 2264, 2265, 2266, 2267, 2268, 2269, 2270, 2271, 2272, 2273, 2274, 2275, 2276, 2277, 2278, 2279, 2280, 2281, 2282, 2283, 2284, 2285, 2286, 2287, 2288, 2289, 2290, 2291, 2292, 2293, 2294, 2295, 2296, 2297, 2298, 2299, 2300, 2301, 2302, 2303, 2304, 2305, 2306, 2307, 2308, 2309, 2310, 2311, 2312, 2313, 2314, 2315, 2316, 2317, 2318, 2319, 2320, 2321, 2322, 2323, 2324, 2325, 2326, 2327, 2328, 2329, 2330, 2331, 2332, 2333, 2334, 2335, 2336, 2337, 2338, 2339, 2340, 2341, 2342, 2343, 2344, 2345, 2346, 2347, 2348, 2349, 2350, 2351, 2352, 2353, 2354, 2355, 2356, 2357, 2358, 2359, 2360, 2361, 2362, 2363, 2364, 2365, 2366, 2367, 2368, 2369, 2370, 2371, 2372, 2373, 2374, 2375, 2376, 2377, 2378, 2379, 2380, 2381, 2382, 2383, 2384, 2385, 2386, 2387, 2388, 2389, 2390, 2391, 2392, 2393, 2394, 2395, 2396, 2397, 2398, 2399, 2400, 2401, 2402, 2403, 2404, 2405, 2406, 2407, 2408, 2409, 2410, 2411, 2412, 2413, 2414, 2415, 2416, 2417, 2418, 2419, 2420, 2421, 2422, 2423, 2424, 2425, 2426, 2427, 2428, 2429, 2430, 2431, 2432, 2433, 2434, 2435, 2436, 2437, 2438, 2439, 2440, 2441, 2442, 2443, 2444, 2445, 2446, 2447, 2448, 2449, 2450, 2451, 2452, 2453, 2454, 2455, 2456, 2457, 2458, 2459, 2460, 2461, 2462, 2463, 2464, 2465, 2466, 2467, 2468, 2469, 2470, 2471, 2472, 2473, 2474, 2475, 2476, 2477, 2478, 2479, 2480, 2481, 2482, 2483, 2484, 2485, 2486, 2487, 2488, 2489, 2490, 2491, 2492, 2493, 2494, 2495, 2496, 2497, 2498, 2499, 2500, 2501, 2502, 2503, 2504, 2505, 2506, 2507, 2508, 2509, 2510, 2511, 2512, 2513, 2514, 2515, 2516, 2517, 2518, 2519, 2520, 2521, 2522, 2523, 2524, 2525, 2526, 2527, 2528, 2529, 2530, 2531, 2532, 2533, 2534, 2535, 2536, 2537, 2538, 2539, 2540, 2541, 2542, 2543, 2544, 2545, 2546, 2547, 2548, 2549, 2550, 2551, 2552, 2553, 2554, 2555, 2556, 2557, 2558, 2559, 2560, 2561, 2562, 2563, 2564, 2565, 2566, 2567, 2568, 2569, 2570, 2571, 2572, 2573, 2574, 2575, 2576, 2577, 2578, 2579, 2580, 2581, 2582, 2583, 2584, 2585, 2586, 2587, 2588, 2589, 2590, 2591, 2592, 2593, 2594, 2595, 2596, 2597, 2598, 2599, 2600, 2601, 2602, 2603, 2604, 2605, 2606, 2607, 2608, 2609, 2610, 2611, 2612, 2613, 2614, 2615, 2616, 2617, 2618, 2619, 2620, 2621, 2622, 2623, 2624, 2625, 2626, 2627, 2628, 2629, 2630, 2631, 2632, 2633, 2634, 2635, 2636, 2637, 2638, 2639, 2640, 2641, 2642, 2643, 2644, 2645, 2646, 2647, 2648, 2649, 2650,

✓ Goodluck PLANT System SA

R A Gattochio, A A R Bar, Lexington, Mass., U.S.A.

J. Robertson, reverse, 1 March 68, p. 10.

H. J. Kung'u, H. J. Kung'u, H. J. Kung'u, H. J. Kung'u, H. J. Kung'u



Dr. J. E. Sweeney **Dr. J. E. Sweeney** **Dr. J. E. Sweeney**

1. *Chlorophyll a* (Chl *a*)

[illegible]

1. Introduction

1. *Chlorophyll a* (Chl a) is the primary photosynthetic pigment in most plants and algae. It is a green pigment that absorbs light energy in the blue and red regions of the visible spectrum. Chl a is essential for the light-dependent reactions of photosynthesis, where it converts light energy into chemical energy in the form of ATP and NADPH.

Accession No.	
<div style="text-align: right;">X</div>	
<div style="text-align: center;">  </div>	
<div style="text-align: center;">  </div>	
Dist	
A-1	

Publisher

J Haynes

Production

Production
T M Edmonds

**Editorial, Advertisement and
Marketing Office**

Institute of Physics Publishing
Techno House, Redcliffe Way

Bristol BS1 6NX, UK

Tel: 0272 297481

1.4 0.77, 2.90
1.18 1.19, 1.19

Fax (927) 291319

E-mail: within.JANETprod1@uk.co.jonppublishing

E-mail: within JANE1 prod1 : uk co toppublishing
from other networks prod1 : toppublishing.co.uk

$$x400 / s = prod1 / o = iopp / prmd \quad iopp / admd = 0 / c = qb$$

Plasma Sources Science & Technology

Journal scope

Plasma Sources Science and Technology will publish papers on non-fusion plasma sources which operate at all ranges of pressure and density, including: neutral and non-neutral plasma sources; positive and negative ion sources; free radical sources; microwave, RF, direct current and electron beam excited sources; resonant sources; plasmas for processes such as etching, deposition, polymerization, sintering; plasma sources for accelerators; lighting applications; plasma sources for medical physics; plasma sources for lasers; other applications, eg spacecraft thrusters, industrial arc melting, etc; plasmas as sources of uv and x-ray radiation; plasma source design, monitoring and control; source stability and reproducibility.

Low pressure plasma sources: distribution functions; excitation-radiation equilibria; vibrational excitation; mass, momentum and energy transport; ion implantation.

Low to medium pressure sources—plasma surface

Interactions: RF etching; microwave etching; magnetron etching; sputtering; reactive ion etching; ion plating; ion beam processing; materials modification; deposition processes; plasma enhanced chemical vapour deposition; techniques for plasma edge control.

High pressure sources, thermal plasmas: mass, momentum and energy transport; radiation and radiative losses, inductively coupled plasmas; plasma spraying techniques; high pressure light sources.

Plasma diagnostic techniques including: actinometry, beam probes, CARS, emission spectroscopy, holographic techniques, Langmuir probes, laser induced fluorescence, interferometry, line broadening, line shifts, line profile analysis, line radiation, magnetic probes, molecular radiation; microwave diagnostics, mass spectroscopy, optical galvanic spectroscopy, plasma induced emission, Thomson and collective scattering.

Plasma and plasma source modelling: charged particle species, neutral species; plasma monitoring and control.

A brief guide for authors

Contributions will be considered for publication in *Plasma Sources Science and Technology* if they have not been published previously and are not under consideration for publication elsewhere. Full length Papers and Brief Communications (two journal pages or less) will be considered. They must be in English. The following material should be submitted:

- (1) Four copies of the typescript, only one of which must be single-sided. Each should include:
 - (a) Title page with:
 - (i) title of article, name(s) of author(s) and address(es) of establishment(s) where work was carried out;
 - (ii) short title of not more than 50 characters (for papers only);
 - (b) Abstract;
 - (c) Text typed with double spacing on A4 (210 mm × 297 mm) or similar paper with a margin not less than 40 mm on the left-hand side of the page and of not less than 20 mm on the right-hand side;
 - (d) List of references given in either the numerical or the Harvard (alphabetical) system (on separate sheet);
 - (e) List of captions for illustrations (on separate sheet);
 - (f) Set of copies of illustrations.
- (2) One further copy of the title and abstract.
- (3) One set of fair copies of line diagrams, suitable for reproduction. These should be in Indian ink on tracing cloth, tracing paper, white card or plastic. Glossy photographs are also acceptable. The line thickness (ie pen 'size') used for a line drawing should be related to the width of the diagram and the reduction that is likely to be used (ie the percentage of the original size to which the diagram is reduced before printing). *Plasma Sources Science and Technology* uses four standard reductions: 70, 50, 35 and 25% and aims for a standard line thickness of 0.175 mm. The reduction used for a particular diagram will, of course, depend not only on the width of the original, but also on the complexity of the diagram. Authors should try to bear these points in mind when preparing fair copies.
- (4) One set of good-quality prints of photographs (not negatives). Three sets of good-quality prints should be provided where the content and detail of the photographs is needed for the refereeing process.
- (5) A completed Assignment of Copyright form. Authors unable to include this with their submissions will be sent a copy for signature.
- (6) No page charges. There are no page charges and 50 offprints of each article will be supplied free of charge to the principal author.
- (7) Colour reproduction. Colour reproduction of illustrations is available in four colour or spot colour, for which the author will be asked to pay the additional reproduction costs incurred.
- (8) Articles in TeX.

Plasma Sources Science and Technology is happy to receive articles on floppy disk media formatted with TeX code. Hard copy versions must be submitted for refereeing as normal and it must be made clear in the submission letter the form in which the TeX file is available.

For more details and specific guidelines on the preparation of articles in TeX, please contact the Editorial Services Manager, Institute of Physics Publishing, Techno House, Redcliffe Way, Bristol BS1 6NX, UK (Tel: 0272 297481 Fax: 0272 294318, E-mail: JANET.cox@iuk.co.ioppublishing).

(9) Address for submissions

The typescripts and figures should be sent to either the appropriate Regional Editor or the Editor-in-Chief.

Editor-in-Chief

Professor H. Hershkovitz
Department of Nuclear Engineering
and Engineering Physics
University of Wisconsin
Madison
WI 53706-1587, USA
Tel: (608) 608 263 2925
Fax: (608) 608 265 2364
E-Mail: hershkovitz@engr.wisc.edu

North America

Dr J Keller
IBM
300-48A Route 52
Hopewell Junction
NY 12533, USA
Tel: (914) 914 894 3582
Fax: (914) 914 892 6258

Western Europe

Professor D G Schram
Department of Physics
Eindhoven University of Technology
PO Box 513
5600 MB Eindhoven
The Netherlands
Tel: (31) 40 474369
Fax: (31) 40 456442

Russia

Professor Yun P. Raizer
The Institute for Problems in Mechanics
Russian Academy of Sciences
Vernadsky Str 101
117526 Moscow, Russia
Fax: (07) 095 9382048

Further details

Authors who are submitting to *Plasma Sources Science and Technology* for the first time, or who require more detail on presentation and style, should consult the booklet *Notes for Authors*, obtainable free of charge from Institute of Physics Publishing Ltd at the address given above.

Editorial

Plasmas, both in space and terrestrial, have historically been studied in their pristine state. By pristine we mean that the plasma is composed of only electrons and ions, and free atoms and molecules. In reality, the vast majority of space and terrestrial plasmas are not pristine, but are contaminated by particles, dust and aerosols. The ubiquitous presence of dust in plasmas was first recognized by astrophysicists. Reddening and polarization of light from distant galaxies and planet-forming HII regions have been attributed to dust grains in interstellar plasmas.

As terrestrial plasmas were applied to high technology tools and manufacturing, the ubiquitous presence of dust in plasmas was rediscovered, and its study expanded beyond astrophysics. Dust in high technology plasmas first came to the forefront in the context of high pressure excimer and CO₂ electric discharge lasers in which particles scattered light and caused plasma instabilities. Particles in low pressure plasmas in the context of pulse power switching were also recognized early on as a source of device failure and flashover. Premature breakdown and arcs in spark gaps, and the diode regions of accelerators and e-beam generators have been attributed to the presence of particles.

The main focus of the study of particles in plasmas during the past five years has been in the context of the manufacture of microelectronics components. Plasma etching and deposition are essential processes in the semiconductor industry for the fabrication of fine features for microprocessors, memory chips and other devices. The presence of particles (tens of nanometres to many micrometres in size) in the plasma not only contaminates the wafers, thereby reducing the manufacturing yield, but perturbs the plasma in presently unpredictable ways. The formation and nucleation of particles in plasma processing discharges, the transport of those particles and their effects on the properties of the discharge are at best poorly characterized. Remedying our lack of fundamental understanding of these issues is not only an intellectual challenge but has extreme economic implications. The cost of particle contamination through reduced yields in semiconductor manufacturing approaches US\$100 million per year.

To address these issues, the NATO Advanced Research Workshop on the Formation, Transport and Consequences of Particles in Plasmas was held at the Chateau de Bonas, Castéra-Verdun, France between 30 August and 3 September 1993. The purpose of the workshop was to gather together experts from diverse fields of plasma physics, plasma-based manufacturing, cluster physics and aerosol science to broaden the scientific knowledge base on contaminated plasmas. The intent of the workshop was to help accelerate improvements in contamination control of plasma processing of microelectronics by leveraging the expertise of researchers in closely aligned fields who may not be directly involved in plasma processing. The workshop was attended by 63 researchers over 5 days. 56 oral and poster papers were presented on particle detection, nucleation and growth, chemical and electrical diagnostics, clusters and aerosols, particles in astrophysical plasmas, and modelling particle behaviour in plasmas. This special issue contains the proceedings of the workshop.

We would like to thank the organizing committee (Professors David B Graves, Ove Havnes, Mark J Kushner and Yukio Watanabe) for their efforts in assembling a fine slate of speakers. We would also like

to acknowledge and thank the sponsors of the workshop. The workshop could not have been held without their generosity.

United States Air Force Office of Scientific Research

Air Liquide

Applied Materials Inc

CNRS

Drytek Inc

IBM Watson Research Center

Lam Research Inc

Novellus Inc

Region Midi Pyrénées

Tegal

Université Paul Sabatier

Sematech

North Atlantic Treaty Organization

Dr Jean-Pierre Boeuf Co-Director

CNRS, Université Paul Sabatier, Toulouse, France

Dr Gary S Selwyn Co-Director

IBM T J Watson Research Center, Yorktown Heights, NY, USA

Professor Mark J Kushner Proceedings Editor

University of Illinois Urbana, IL, USA

Overview of growth and behaviour of clusters and particles in plasmas

A Garscadden, B N Ganguly, P D Haaland and J Williams

Wright Laboratory, Wright-Patterson AFB, OH 45433, USA

Received 3 January 1994, in final form 25 January 1994

Abstract. A review is presented of the phenomena associated with particles in low pressure plasmas. Dust particles which are typically micrometers in diameter have been observed by laser light scattering in various low-pressure, radiofrequency-excited plasmas. Experiments have been designed so that the origin of the dust material is unambiguous and, to some extent, quantitative. The processes involved in the appearance of the mesoscopic dust particles are outlined and compared with our experimental observations. The source material and its required generation rate, nucleation, charging, growth mechanisms, growth rates, and saturation mechanisms are discussed. The mutual influences of dust and plasma, particularly the role of geometric and circuit boundary conditions in laboratory plasmas, are described.

1. Occurrence of particles in plasmas

Particles with sizes in the micrometer range have been observed in ionized media for many years. At the extremely low densities of interstellar space, Gould and Salpeter [1] invoked the presence of small charged grains to explain the synthesis of molecular species in diffuse nebulae. Hoyle and Wickramasinge [2] reviewed the insights into the weak galactic magnetic field and cosmic chemical synthesis on small, charged dust particles. At higher pressures, but still with distant spatial boundaries, the dust in planetary atmospheres and planetary ring structures has been studied extensively by Goertz [3], Whipple [4], Northrop [5] and others [6-7]. As early as 1924 the observation of dust in a plasma was noted by Langmuir *et al* [8]. Fifty years later the occurrence of dust in bounded positive column plasmas was studied in some detail by Feneis and Breslin [9].

Increasing use of low pressure plasma processing reactors and the easy availability of laser light scattering diagnostics showed that many of these discharges produced and trapped large quantities of microscopic dust. The extensive literature on dust in astrophysical plasmas, colloidal suspensions, nucleation theory, and charged aerosols is a terrific starting point for the understanding of dusty laboratory plasmas. However there are two distinctive features of laboratory plasmas which differ significantly from these classical areas. First, laboratory discharges have geometric boundaries whose structure, composition, temperature, history and conductivity influence the formation and transport of dust grains. Second, the external circuit which maintains the dusty plasma imposes spatiotemporally varying boundary conditions on the dusty discharge.

At early times dust provides a distributed recombination sink for electrons and ions, the impedance of the discharge increases, and there may be a local elevation of the electron temperature. At later times the combination of dust density and apparent dust floating potential (as derived and refined in many papers) [4, 5] appear to satisfy the condition to form a Coulomb solid [10]. However, the experiments do not exactly confirm this theory. After some time of running a confined discharge, the dusty volume is sharply delineated and its behaviour, while collective, appears to resemble a liquid droplet. This droplet is bounded by the self-consistent interactions between the dust and the plasma. There is a distinct interface between the dust volume and the remaining plasma which has a structure and charge distribution similar to a micelle.

Scanning electron micrographs (SEMs) of the dust using a low energy (0.5-2 keV) probe reveal narrow size distributions and a morphology reminiscent of microscopic sunflowers (figure 1). Low voltage SEMs are essential if one is to resolve the surface texture of low atomic number material. The low voltage, low current probe also permits one to examine uncoated samples without beam damage. Transmission electron micrographs (TEMs) of whole grains, and thin sections show radial columnar microstructure and a lack of crystallinity in domains as small as 200 Å. The fractal morphology and surface texture are similar to those encountered in sputtered coatings, where the surface temperature is less than half the melting temperature of the deposited material [11]. The particles' morphology permits insights into the nature of the fluxes from which homogeneously nucleated grains are built.



Figure 1. Low voltage high resolution scanning electron micrograph of a typical dust particle grown from a 1 Torr 15 kHz He plasma with graphite electrodes. The particle diameter is 650 nm. See also [17]

2. Dust in RF discharges

While dust is found in direct current (DC) discharges, it is usually observed in larger quantities for the same gases under conditions of radiofrequency (RF) excitation. We note that the dust appears most readily in electronegative gas mixtures and also when there is a substrate such as silicon or carbon present. Both silicon and carbon, when sputtered, yield electronegative free radicals. To satisfy ambipolarity the dust will be negatively charged. The RF discharge is a very efficient trap for negative ions and for microscopic, negatively charged particles. The electrodes acquire a negative DC bias due to the much higher mobility of the electrons compared to that of the positive ions. The ambipolar electric fields that occur in the radial direction because of the same effect also trap negative ions and particles. Thus even at low pressures, negative ion concentrations are limited by homogeneous processes such as ion-ion recombination and electron detachment, rather than diffusion and heterogeneous wall recombination. Homogeneous loss kinetics can, with a relatively small attachment rate, still result in negative ion densities which greatly exceed the electron density [12]. Using on-line mass spectrometry Howling *et al* [13] showed anticorrelations of negative ions and powder in silane RF discharges. Watanabe *et al* [14] demonstrated that square wave modulation of the RF voltage suppressed particle growth (or trapping) and that the modulation facilitates study of the growth kinetics. Low duty cycle modulation relaxed the electron temperature and allowed the nascent grains to diffuse to the boundaries, inhibiting growth to macroscopic sizes.

Table 1. Intertwined constraints on particles in plasmas.

1. Growth	Radicals and ion fluxes Bonds Temperature Desorption Surface Charge Sputtering
2. Charge	Floating potential Electron and ion fluxes Electron affinity and work function Electrostriction Field and thermionic emission Photoelectric charging
3. Position	Electrostatic-gravitational balance Collisional drag from ions and neutrals Ensemble polarizability Mass
4. Temperature	Surface radical recombination Surface electron-ion recombination Surface quenching of energetic species Thermionic emission Pyrolysis Radiation
5. Plasma perturbation effects	Knudsen or continuum cooling Neutral recombination Charged particle recombination Particle scattering Particle asymmetry

Dust particle concentrations as large as 10^{17} cm^{-3} have been reported [14]. The dust grains, once formed, have to satisfy many constraints at the same time (table 1). Among these the floating potential, which results from balancing the electron and ion fluxes to the particle, has received the greatest attention. Grain temperatures, while often equilibrated with the neutral gas, may be substantially elevated at higher power densities and lower pressures. Incandescence or particle melting as well as thermionic emission can fundamentally alter the grain morphology and plasma properties. Particles also respond to forces which vary in magnitude among diverse experiments. Gravitational, electrostatic, neutral and ion drag, thermophoretic, and pressure gradient forces all influence particle transport. These have been catalogued for small grains in a 1 Torr Argon plasma elsewhere in this issue [15].

3. Sources of dust

The dust can originate from plasma chemistry in the gas phase (e.g. carbon monoxide or silane containing discharges) or from sputtering of the electrodes (e.g. most metals, graphite). If the discharge is in a gas that can dissociate to produce carbon atoms, then atom concentrations approaching 10^{17} cm^{-3} are possible. The equilibrium vapour pressure of carbon at room temperature is essentially zero, so that electron

impact dissociation of the parent gas will produce a supersaturated vapour. Under such conditions the nucleation rate is very large and the onset of stable cluster size is driven to small clusters of just a few atoms [16]. This is important because the rate-limiting steps of cluster formation are those early steps to form molecules such as C_2 and C_3 if they are not provided as precursors. Whether the initial grain nuclei come from homogeneous or heterogeneous reactions is difficult to quantify. Carbon is exceptional because experiments indicate its condensation kinetics are much faster than for any other element. The clustering reactions of carbon have received a lot of attention with the fullerene synthesis of Kratschner *et al* [17] and the ensuing cyclone of literature. Recently Heath [18] has calculated the lifetime of the energized linear trimer C_3^* using RRKM theory. He predicts lifetimes in the nanosecond regime for this species, long-enough for collisional stabilization to form neutral C_3 at intermediate pressures. At the Torr pressures typical of our own experiments these stabilizing collisions would occur in each cubic centimeter of gas about once every thousand seconds. The lifetime of the C_n^* complex is expected to increase with the number of carbon atoms n due to the rising number of low frequency vibrational modes as clusters grow.

At $mA\ cm^{-1}$ current densities sputtering yields of 10^{-1} atoms per ion give atom densities in the $10^7\ cm^{-3}$ range, which are sufficient to account for the observed growth kinetics [19]. Dust formation in a freshly cleaned discharge tube takes tens of minutes. Once dust has been observed in a tube, however, the induction time is substantially less. The initial molecules may be precursor from the electrode sputtering. Whether initial nucleation arises from heterogeneous or homogeneous chemistry is at the moment an open question. Under our low pressure conditions it appears that negative ions must be invoked very early in the growth, or even nucleation, to explain the rapid growth and long trapping times observed in the bounded plasma.

4. Light scattering from dust in laboratory plasmas

Laser light scattering diagnostics fall into four categories: (1) spatially resolved detection of the dust from its Mie scattering using a broad area beam and CCD video cameras, (2) angular variation of scattered light intensity from a small focal volume, (3) scattering depolarization using a polarized laser (or white light) beam. The Mie scattering formalism permits straightforward inference of the particle size and concentration when the complex refractive index is known, the dust particles are spherical, and the size distribution is monodisperse. *Ex situ* examination of the dust using SEMs can be used to verify the latter two assumptions, making the analysis unambiguous.

A fourth method infers the concentration of the particles in-situ by examining the fluctuations of the

scattered optical signal. In a test using a helium discharge with graphite electrodes the light scattering intensity initially showed significant noise. After 30 min there was no detectable fluctuation of the signal within the ten bit resolution of the digitizer. The sampling volume for this measurement was approximately $0.1\ cm^3$. The ratio of the fluctuations to the total signal scales as $N^{-1/2}$ where N is the number of particles in the scattering volume [20]. This experiment implies particle concentrations in excess of $10^7\ cm^{-3}$.

5. Grain nucleation considerations

The growth rate at early times is very large—Watanabe *et al* [14] report 10^8 , 100 nm particles per cubic centimeter after only 1 s and we have obtained micron sized particles after seconds in CO/argon discharges. In rare gas plasmas where the grain material can only come from the electrodes such particles are observed after a few minutes. The similar sizes of the grains suggest the same starting conditions and time, while their spheroidal symmetry implies that growth is by homogeneous nucleation. Growth by interception of radicals is not adequate to give the measured early growth rates. The very rapid growth rate at early times is compatible with accumulation of mass by ion collection across the Debye sheath. Of course the growth is a dynamic process with deposition and sputtering of the growing particle as well as some rearrangement of the surface structure.

Some fundamental physics questions are raised for this early growth stage. When does a negative ion become a cluster and achieve macroscopic properties? Gibson [21] and Breslin and Emeleus [22] explored the criteria for the size and charge at which an ion is more accurately described as a particle. They derived the same transition size, about $10^{-7}\ cm$, by two routes. First they obtain $10^{-7}\ cm$ by requiring a small number for the surface charge on small particles with typical plasma conditions. The same size results by requiring a symmetric sheath; the grain must not move more than a Debye length in an ion period. Finally, the transition size corresponds to conditions where bulk properties of the material change. Low melting temperatures for small clusters are a result of most atoms being at the surface. This means that the surface mobility of adsorbed atoms is high.

How do the very small particles survive Coulomb explosion? In order to stay at the floating potential the dust must acquire negative charge, but not so much that the radial electric stress exceeds the tensile strength of the material. One way around this constraint is the homogeneous nucleation suggested above, which produces a high concentration, N , of clusters. These become negatively charged with surface charge Q . The product NQ becomes sufficient to perturb the local electron density and hence the space potential decreases while the floating potential becomes less negative [3, 4]. However, extreme reduction of the floating potential

destroys the ion-sheath accelerated growth mechanism. Particles may grow outside the main discharge region. If they are large enough they can survive the charging process. This mechanism is almost certainly at work in etching plasmas, where large, irregularly shaped particles from the reactor walls are an important source of dust.

The spatial distribution of the dust particles in the plasma depends on the several forces that act on them. These forces have been summarized by Barnes *et al* [23] and include gravitational, neutral and ion drag, electrostatic, thermophoretic and pressure gradient forces. Which of these forces is largest depends in detail on the plasma conditions. The repeated observation of dust clouds at sheath edges would seem to implicate electrostatic and ion-drag forces under many conditions. In our own plasmas whose geometrical boundaries are symmetric and whose vertical electrodes reduce the dominance of the electrode sheaths we see unambiguous evidence of asymmetry due to gravity.

Choi and Kushner [24], Daugherty *et al* [25] and Boeuf [26] have modelled the RF discharge with dust and generally concluded that the particles will be negatively charged and confined by the sheaths. Whipple *et al* [27], in describing dusty plasmas in planetary atmospheres, conclude that the vacuum capacitance and floating potentials for an isolated particle are not appropriate for the dust ensemble. Rather the capacitance must be that of a particle immersed in the plasma as modified by the ensemble of nearby charged dust. The floating potential will be less negative than computed when ignoring the ensemble, so that fewer surface charges are required. Electron depletion effects are significant not only in astrophysical environments but also in the estimation of plasma conditions inside dust regions.

The experimental results on RF discharges are not quite in agreement with all of the present theoretical papers. Most of the differences are probably attributable to the different boundary conditions imposed by the RF discharge or by the circuit. If the discharge geometry is constrained then the dust influences the electron energy distribution function and the discharge impedance increases. If constant current is the circuit constraint, then the electric field must increase and the local electron temperature increases as observed by Carlile and Geha [28]. In most laboratory plasma geometries the discharge current can flow around the dust cloud by choosing a lower impedance path. This effect seems to occur when the dust density is high or with low frequency discharges. Dramatic impedance changes, both resistive and capacitive, have been observed. At high dust concentrations the dusty region is sharply defined as seen in figure 2. The boundary is visually film-like. Igloo formations above wafers [29] and sacs of dust both within and outside the electrode region are easily observed [19].

6. Morphology of the dust

One of the obvious questions raised by the presence of geometrical boundaries is whether the dust particles

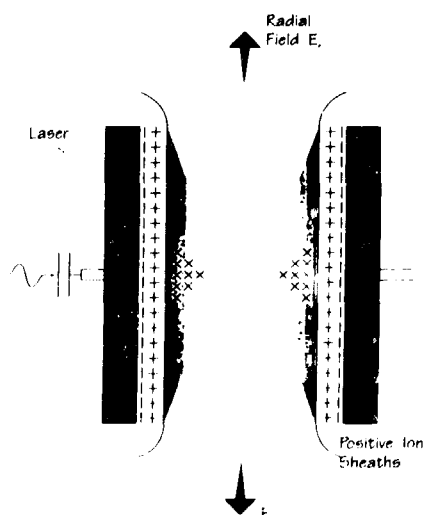


Figure 2. Schematic view of a dusty plasma showing crisp spatial boundaries at the sheath edge and also in the radial direction. Shaded regions indicate trapped dust.

or the nuclei from which they grow are generated at the reactor walls. Large, aspherical particles observed by Selwyn *et al* [29], Stoffels *et al* [30] and others in halogen mixtures are clearly derived from etched fragments. The micrograph in figure 3 shows the surface of a silicon wafer etched in an RF diode reactor using Selwyn's recipe of high powers in a $\text{CCl}_2\text{F}_2/\text{O}_2$ gas mixture. If formed on an insulating surface particles charge negatively when the discharge is initiated. The electrostatic repulsion between the wall and the particle and an electric field of the ion sheath can overcome the force binding the grain to the surface and inject the particle into the plasma. The negative ions and the larger negatively charged grains are precluded from wall contact by the sheath and ambipolar fields. It has been suggested [31] that positive ion-molecule reactions might be responsible for the rapid growth of grains in silane plasmas. However, the same fields that trap anions guarantee a short residence time for cations. Even with ion-molecule reactions at Langevin rates ($10^{-9} \text{ cm}^3 \text{ s}^{-1}$) one has time for only a few ion clustering reactions before the positively charged species are neutralized at a wall or electrode.

The size of the grains provides some clues about their origin. X-ray analysis of particles from the rare-gas discharges show that they are formed of carbon, which can only come from the graphite electrodes. The transit time of a sputtered carbon atom traversing the interelectrode gap is of the order of milliseconds for our conditions. The neutral deposition rate scales with the surface area of the growing grain, which is only about 10^{10} cm^2 for a 50 nm grain. The measured growth rate of 10^7 atoms per second would require unreasonably large partial pressures of carbon. However ionic growth rates scale with the surface area of the Debye sphere, proportional to $\lambda_D^2 \approx 10^{-4} \text{ cm}^2$, which is six orders of

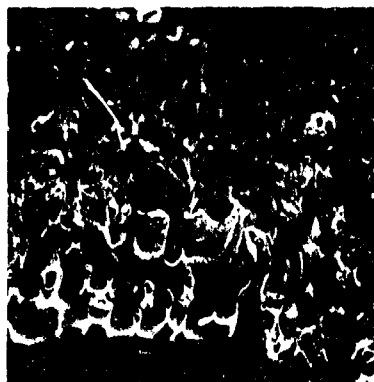


Figure 3. Silicon wafer etched in an RF diode using a $\text{CCl}_2\text{F}_2/\text{O}_2$ plasma. Undercut features have broken off and presumably led to dust in the plasma reactor. (Sample courtesy of Winfred and Eva Stoffels, Technische Universiteit, Eindhoven, The Netherlands).

magnitude larger than the geometrical area. An electron density of 10^{19} cm^{-3} and a ionization rate of $10^{-4} \text{ cm}^3 \text{ s}^{-1}$ imply an ionization probability of 10^{-4} as a sputtered atom moves from one electrode to another. A carbon atom concentration of 10^7 cm^{-3} is required to account for the early growth rate by an ionic mechanism. With discharge current densities of 1 mA cm^{-2} the required flux of $10^{12} \text{ cm}^{-2} \text{ s}^{-1}$ is obtained at a sputtering yield of only 2×10^{-4} atoms per ion.

Examination of particles extracted from the sputtered carbon plasma by SEMs and TEMs demonstrates monodisperse size distributions [19]. The particles have approximately spherical symmetry. However they are not compact material. The internal morphology revealed by TEM or in broken particles (figure 6 of ref [15]) shows fractal or cauliflower-like texture. The partial columnar structures are consistent with ballistic deposition [32] rather than diffusion limited aggregation [33]. Ballistic mechanisms invoking ions and the sheath field use the large C^+ ion mobility responding to the instantaneous local electric field near the surface of the spinning particle. Complicated textures, including self-affine surfaces, may result from isotropic, diffusive fluxes of neutral radicals to the grain. However the stark radial symmetry of the particles is more simply explained with an ionic deposition mechanism. The fractal characteristics of the growing grain may play an important role in limiting the surface charge. Surface features with a small radius of curvature have enhanced local electric fields, permitting the field emission of electrons to act as a limit on the equilibrium floating potential [34]. Field emission from whiskers may in this way prevent disruption of the grain by coulomb explosion.

7. Chemical kinetics modification by dust

Salpeter *et al* [1] have examined the enhanced recombination of atomic hydrogen on grains in space.

Similar effects are expected for other radicals derived from deposition and etching gases. The fractal structure of the small growing grains means that the total surface area of the dust often far exceeds the surface area of the electrodes. Thus dust will reduce the concentration of etching atoms such as chlorine and reduce the etch rate and uniformity. In the carbon dust discharges we have found that the process of dust growth is self-limiting.

In silane discharges at higher pressures and powers the dust grows very rapidly and to larger diameters. Calculations show that generally the dust temperature should be close to ambient for typical reactor conditions. There are some interesting thermal effects for very small grains. The radiation from small particles decreases rapidly with increasing wavelength once the wavelength is larger than the particle. This effect reduces radiative cooling more dramatically the smaller the particle. Many material clusters have melting temperature that decrease rapidly with decreasing size. Hence higher powers may remove dust since the stability of a liquid droplet to electrostatic disruption is much less than that of a solid grain. At higher powers and in reactive gases such as silane, the surface heating can cause pyrolysis of the parent gas.

8. Collective and non-ideal plasma effects

Ikezi [35] outlined the conditions for which small particles in plasmas could form a Coulomb lattice. The ratio between the Coulomb energy and the kinetic energy is

$$\Gamma = \frac{Z^2 e^2}{d T}$$

where Z , d and T are the grain charges, interparticle distance and kinetic temperature, respectively. This can be rewritten in terms of the dust concentration N

$$\Gamma = 2.7 \times 10^{-4} Z^2 \left(\frac{N}{10^{12}} \right)^{-1} \frac{10^6}{T}$$

so that when Γ is larger than 2, a Coulomb liquid is predicted, and when it exceeds 170, a Coulomb solid should result. As a result of the large Z in dusty plasmas, this ratio can be large even for relatively large d . Several authors [36, 37] have suggested that the particles trapped in RF discharges satisfy the conditions for phase transition of the dust ensemble to a liquid or perhaps even to a solid.

When examining the scattering of light from the interior region of a dust cloud we see no evidence of Brownian motion. The boundaries of the dust cloud respond to perturbations at very low frequencies. We have applied a chirped, one per cent amplitude modulation to our 15 kHz dusty helium plasma with graphite electrodes. The modulation frequencies were varied from 0.1 to 50 Hz over 2.5 s and the scattered light was imaged from an edge of the dusty volume onto a photomultiplier and recorded. Figure 4 shows both the amplitude modulation of the plasma voltage

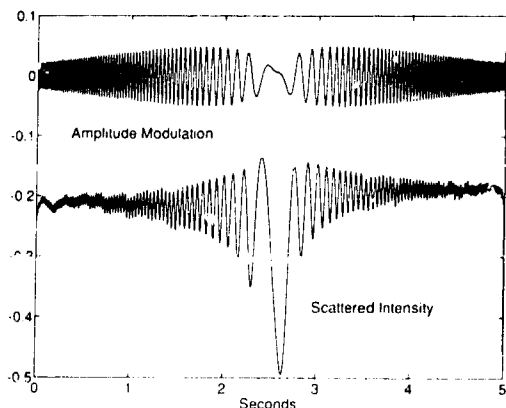


Figure 4. Amplitude modulation of the RF driving voltage applied to a 15 kHz Helium plasma and the resulting modulation from light scattered by dust near a radial cloud boundary (not the electrode sheath).

and the scattered light modulation. The scattering is most intensely modulated at low frequencies. This observation is quantified in figure 5, where the ratio of the Fourier transforms of the modulated signals shows a transfer function which is inversely proportional to frequency, as expected for a viscous damping force proportional to velocity. No evidence of resonance was observed, though the sub-Hertz responses seem incompatible with independent motion of individual dust grains. We suggest that collective motion of the boundary or double layer which envelopes the dusty region is constrained by surface tension and it is this force to which the lethargic motions correspond. Our own evidence for collective behaviour is given by a visual sheath which surrounds suspended dust clouds. This sheath is thicker on the side facing the powered electrode than it is on the side of the plasma region. Motion of dust following extinction of the plasma occurs over seconds, more slowly than classical diffusion and other transport processes in glow discharges. Recently Thomas [38] has obtained direct evidence of a phase change of the dust. He introduced larger particles into a plasma with an ultrasonic nebulizer and obtained micro-video recordings of the stabilized and reasonably crystalline particle positions.

9. Fractal texture

The cauliflower morphology has been reported in a wide range of reactive plasmas including our own 1 Torr noble gas plasmas with graphite electrodes [19], diamond synthesis plasmas in a kilowatt-class cascaded arc reactor [39], RF silane plasmas [40], and low power flowing afterglows used in synthesis of organic thin films [41]. We have developed a simple fractal recursion on which summarizes the texture of cauliflowers embedded in two and three dimensions. An outline of the 2D recursion, which is based on a variation

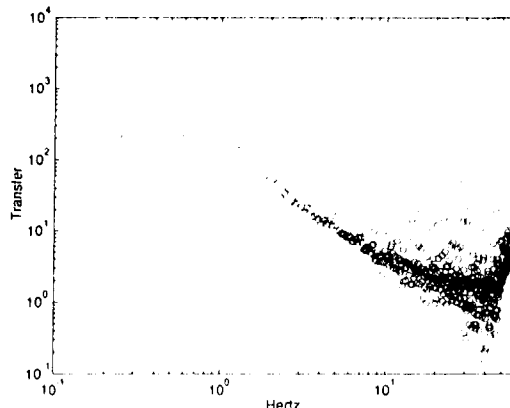


Figure 5. Ratio of the power spectra for the two traces shown in figure 4. The linear increase of damping with velocity indicates a viscous drag on the dust ensemble.

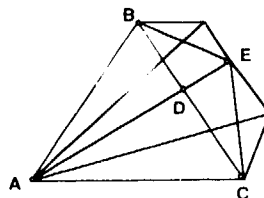


Figure 6. 2D fractal recursion for generating cauliflower textures.

of the modified midpoint method, is shown in figure 6. From vertex A construct any triangle. Next draw a line from A through the midpoint of the opposite side BC and continue for a distance DE. Repeat this construction using ABE and AEC as the initial triangles while scaling the distance by some fraction F times the length DE. An example of this recursion applied to a hexagon is shown in figure 7(a), which illustrates the extreme sensitivity of the surface texture to the fraction F . In figure 7(b) we see the influence of gaussian random fluctuations in F between steps in the recursion. The structure is less symmetrical but retains a texture which is still sensitive to the average value of F . We suggest that this F , or the fractal dimension derived from it, provides parsimonious descriptions of the surface texture. Generalization of this approach to solids embedded in three dimensions employs tetrahedra in place of triangles and constructions which intercept the center of opposing triangular faces. The fractal dimension is retained as a parameter whose subtle variation causes a dramatic change in the surface morphology. The growth mechanisms can be fruitfully compared with the observed fractal textures in a quantitative way through their fractal dimension.

10. Conclusions

Charged dust grains in laboratory plasmas share much with dust in planetary nebulae, the interstellar

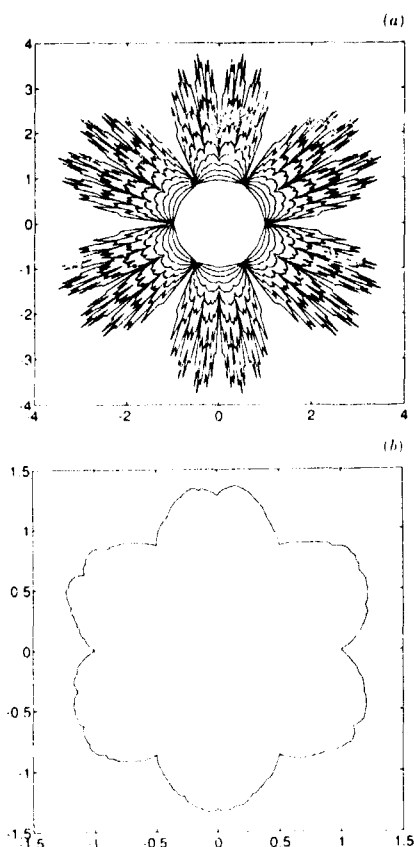


Figure 7. (a) Variation of texture with the scaling ratio F from 0.1 to 0.9 and (b) influence of gaussian variation of F about an average value of 0.3 on the resulting fractal texture.

media, rings in planetary atmospheres, colloids, and aerosols. Dust in laboratory plasmas is set apart by the potential importance of geometrical and circuit boundary conditions which make possible its trapping and observation. The ease with which different materials can be made and trapped for long times should permit interesting experiments on heterogeneous synthesis from unusual radicals, production of novel, monodisperse colloids, and new understanding of the mechanisms by which the non-equilibrium of reactive plasmas leads to solid materials.

References

- [1] Gould R J and Salpeter E E 1963 *Astrophys J.* **138** 393
- [2] Hoyle F and Wickramasinghe N C 1991 *The Theory of Cosmic Grains* (Dordrecht: Kluwer)
- [3] Goertz C K 1989 *Rev. Geophys.* **27** 271
- [4] Whipple E C 1981 *Rep. Prog. Phys.* **44** 1197
- [5] Northrop T G 1992 *Phys. Scr.* **45** 475
- [6] de Angelis U 1992 *Phys. Scr.* **45** 465
- [7] Houps H L F 1987 *J. Geophys. Res.* **92** 12057
- [8] Langmuir I, Foud G and Dittmer A F 1924 *Science* **60** 392
- [9] Emeleus K G and Breslin A C 1970 *Int. J. Electron.* **29** 1
- [10] Fortov V E and Yakubor I T 1999 *Physics of Nonideal Plasmas* (Moscow: Hemisphere Publications)
- [11] Pulker H 1988 *Coatings on Glass* (New York: Springer)
- [12] Garscadden A 1990 *Non Equilibrium Processes in Partially Ionized Gases* (NATO ASI Series 220) ed M Capitelli and J N Bardsley (New York: Plenum)
- [13] Howling A A, Sansonnens L, Dover J-L and Hollenstein Ch 1993 *J. Phys. D: Appl. Phys.* **26** 1003
- [14] Wantanabe Y, Shiritani M, and Yamashita M 1992 *Appl. Phys. Lett.* **61** 1510
- [15] Haaland P, Garscadden A, Ganguly B, Ibrani S and Williams J 1994 *Plasma Sources Sci. Technol.* **3** 381
- [16] Abraham A A *Homogeneous Nucleation Theory* (New York: Academic)
- [17] Kratschmer W, Lamb L D, Fostiropoulos K and Huffman D R 1990 *Nature* **347** 354
- [18] Heath J R 1992 *Fullerenes* (American Chemical Society Symp. Series 481) ed G S Hammond and V J Kuck (Chicago, IL: American Chemical Society)
- [19] Ganguly B N, Garscadden A, Williams J and Haaland P D 1993 *J. Vac. Sci. Technol.* **A11** 1119
- [20] Chandler D 1987 *Introduction to Modern Statistical Mechanics* (New York) p 84
- [21] Gibson E G 1966 *Phys. Fluids* **9** 2389
- [22] Breslin A C and Emeleus K G 1971 *Int. J. Electron.* **31** 189
- [23] Barnes M S, Keller J H, Forster J C, O'Neill J A and Coultas D K 1992 *Phys. Rev. Lett.* **68** 313
- [24] Choi S J, and Kushner M J 1993 *Appl. Phys. Lett.* **18** 2197
- [25] Daugherty J E, Porteous R K and Graves D B 1993 *J. Appl. Phys.* **73** 1617
- [26] Boeuf J-P 1992 *Phys. Rev. A* **46** 7910
- [27] Whipple E C, Northrop T G and Mendis D A 1985 *J. Geophys. Res.* **90** 7405
- [28] Carlisle R N and Geha S S 1993 *J. Appl. Phys.* **73** 4785
- [29] Selwyn G S, Singh J and Bennett R S 1989 *J. Vac. Sci. Technol. A* **7** 2758
- [30] Stoffeis W, Stoffels A and Kroessen G 1994 *Plasma Sources Sci. Technol.* **3** 320
- [31] Mandich M L, Reents W and Kolenbrander K D 1990 *J. Chem. Phys.* **92** 437
- [32] Ramanlal P and Sander L M 1985 *Phys. Rev. Lett.* **54** 1828
- [33] Weitz D A and Oliveriea M 1984 *Phys. Rev. Lett.* **52** 1433
- [34] Lafon J-P J and Miller J M 1983 *J. Astron. Astrophys.* **123** 73
- [35] Ikezi H 1986 *Phys. Fluids* **29** 1764
- [36] Boufendi L F, Bouchoule A, Porteous R K, Plain A and Laure C 1993 *J. Appl. Phys.* **73** 2160
- [37] Jeilum G M, Daugherty J E and Graves D E 1991 *J. Appl. Phys.* **69** 6923
- [38] Thomas J 1993 *Private communication*
- [39] Buuron A J M, Meeusen G J, Beulens J J, van de Sanden M C M and Schram D C 1993 *J. Nucl. Mater.* **200** 430
- [40] Spears K G, Robinson T J and Roth R M 1986 *IEEE Trans. Plasma Sci.* **14** 179
- [41] Haaland P, Ibrani S, Jiang H 1994 *Appl. Phys. Lett.* **64** 1629

Negative ions and particle formation in low-pressure halocarbon discharges

G M W Kroesen, W W Stoffels, E Stoffels, M Haverlag,
J H W G den Boer and F J de Hoog

Department of Physics, Eindhoven University of Technology, PO Box 513,
5600 MB Eindhoven, The Netherlands

Received 3 January 1994, in final form 14 January 1994

Abstract. The growth of particles in a radiofrequency (RF) (13.56 MHz) plasma at pressures from 25 to 200 mTorr in mixtures of CF_4 , CF_3Cl , and argon has been studied experimentally. A planar configuration was used, with a silicon wafer on the powered electrode. The electron density has been measured with microwave resonance spectroscopy using a cylindrical cavity surrounding the plasma. The same geometry has been used to measure the density of various species of negative ions by detecting the extra electrons created by laser-induced photo detachment. It appears that the negative ion density is much larger in the case of CF_3Cl than in the case of CF_4 . There seems to be hardly any dependence of the negative ion concentration on the CF_3Cl/Ar partial pressure ratio in the range where powder growth occurs. However, the attachment rate to chlorine is found to be much higher than to fluorine. Furthermore the gas phase discharge chemistry has been studied using infrared absorption spectroscopy. Both a tunable diode laser system, and a Fourier transform spectrometer have been applied. The CF_2 concentration appears to decrease strongly when powder growth occurs. The SiF_4 concentration then has a maximum. The results indicate that the presence of chlorine in the plasma feed gas is essential. In CF_4 no particle formation is detected. The wafer surface is blackened during powder formation. SEM inspection indicates that this is caused by micromasking. Considering all the information, we arrive at the conclusion that particle growth is initiated by micromasking at the Si surface combined with a highly directional etching process. Due to residual isotropic etching the particles are released from the surface and enter the plasma, where they start coalescing and growing under the influence of CF_2 polymerization.

1. Introduction

Powder formation in radiofrequency (RF) low-pressure plasmas is a research topic which has gained considerable attention over the last four years. Basically, there are three main chemistries under study: halocarbons mixed with noble gases like argon, usually with a silicon wafer placed inside the reactor [1]; silane/argon mixtures [2,3]; and noble gas plasmas struck between graphite electrodes [4]. The first (CF_3Cl/Ar) is related to the industrial problem of yield loss in semiconductor processing due to particle contamination inside the plasma processing (generally etching) reactor. It appears that nowadays, particle contamination which damages processed wafers takes place inside the plasma reactors,

not in the clean room. Plasmas have a tendency to charge small particles negatively due to the large mobility of the electrons in the plasma. They are then trapped in the glow by the surrounding space charge region (sheath). Typically, non-uniformities of the sheath geometry occur over silicon wafers which are placed on the electrode. As a result of this, the particles gather in regions above the wafer. In effect, the plasma acts as a very effective particle transporter: any particle present in the plasma will be trapped in the glow and transported towards the wafer. After plasma extinction the particles will be deposited on the wafer. The electrostatic force ensures good adhesion of the particles to the wafer surface. Recently, Selwyn and Patterson [5] introduced the concept of the self-cleaning plasma reactor: deliberately introduced non-uniformities of the sheath re-

move the particles from the water area. The second chemistry (SiH_4/Ar) has arisen from problems in the manufacturing of solar cells and flat panel displays using amorphous silicon. Typically, at discharge conditions which generate high deposition rates of good quality material, abundant particle generation also takes place. The aforementioned phenomena of particle trapping and electrostatic charging also complicate matters here. Recent investigations have shown that the particle precursors are negative ions, which grow into clusters by association with radicals in the plasma [6]. This mechanism is possible because of the trapping of negative ions in the plasma. The particles appear to be small crystallites with a monodisperse size distribution. After some time, the crystallites coalesce to form larger particles. The size distribution remains monodisperse [7]. The particles are thus generated in the gas phase on a timescale of seconds; the surface is not believed to play any role of importance. The third chemistry (Ar graphite) is used mainly for fundamental studies.

In this paper we will focus on the first chemistry: $\text{CF}_2\text{Cl}_2/\text{Ar}$ mixtures with a silicon wafer mounted on the RF powered electrode. This chemistry has been chosen for two reasons. CF_2Cl_2 is still used as a feed gas for plasma and reactive ion etching, although its use will be forbidden in the future by the Edict of Montreal. Furthermore, it offers a convenient vehicle for studying particle formation in low-pressure plasmas: particle growth appears to be very reproducible and comparatively slow (timescale of tens of minutes). The main aim of this paper is to find out whether the nucleation and growth of the particles in this chemistry can in any way be compared to the abovementioned case of SiH_4/Ar , i.e. what roles do the negative ions, the plasma chemistry and the surface play.

2. Experimental set-up and diagnostics

The experiments have been performed in a planar, parallel RF plasma reactor. The diameter of the water cooled electrode was 124 mm. RF power levels from 10 to 200 W have been used. The electrode separation was 4 cm. The gases were fed through mass flow controllers. The pressure was controlled by a throttle valve in the pumping line of a roots blower. Pressures of 25 to 200 mTorr were used. The reactor is equipped with exchangeable windows: for photodetachment quartz is used; for IR experiments BaF_2 or KRS-5 is used. The pressure is measured with an MKS Baratron pressure transducer.

For the measurements of the densities of electrons and negative ions, the grounded electrode is extended to enclose the plasma in a cylindrical cavity. Microwaves are fed into, and extracted from, the cavity with small pick-up loops. The resonance frequency of the cavity depends on the dielectric constant of the plasma for the used frequency. The dielectric constant in this frequency range is determined by the electron density. A laser beam is fired (Spectra Physics GCR11) through a hole in the sidewall of the cavity. In figure 1 a sketch of the

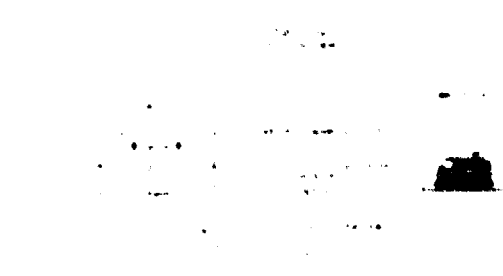


Figure 1. Outline of the experimental set-up used for the measurement of the electron density and the negative ion density using microwave resonance spectroscopy and the photodetachment effect.

set-up is given. The microwaves are generated by a Gigatronics Model 605 synthesizer. For each microwave frequency the response of the plasma is measured as a function of time with a Hewlett Packard 54111 D digitizing oscilloscope. The thus obtained matrix is then analysed in the perpendicular direction: for each time sample the resonance profile is reconstructed, and its shift from the undisturbed position is determined. In this way the temporary increase of the electron density due to the detached electrons is measured. At a quadrupled laser wavelength (266 nm) all negative ions will detach (Cl^- , F^- , CF_3Cl^- , etc.). At tripled wavelength (365 nm) Cl^- is excluded. At doubled wavelength (532 nm) F^- is also excluded. In this way one can obtain an impression of the distribution over several negative ions by changing the laser wavelength. The measurement principle and practical implementation is discussed in more detail elsewhere [8].

For the IR measurements BaF_2 or KRS-5 windows are used. The beam of a Laser Photonics tunable diode laser (TDL) system is directed through the plasma. One single pass has been used. A mercury cadmium telluride (MCT) detector converts the intensity to an electric signal. A 1 m monochromator is used to select one of the modes of the laser. The exact wavelength of the laser beam is measured with a combination of a gas reference cell filled with NH_3 , a germanium etalon, and a 0.5 m path length Michelson interferometer. One arm of the Michelson interferometer is scanned, and the number of fringes is counted and compared with the number of fringes from a stabilized HeNe laser interferometer with identical path lengths. This gives the absolute wavelength with a precision of about 10^{-2} m^{-1} . The absolute accuracy is increased further by interpolating the fringes of the Ge etalon between two peaks of the absorption spectrum of NH_3 . The wavelength of the TDL is modulated, and the first derivative of the absorption signal is measured with a lock-in amplifier. One measurement takes about 30 s. Details of the set-up will be published elsewhere [9]. Since the gas and rotational temperatures of the plasma do not change during plasma ignition [10], it is sufficient to study just one rotational line. If the temperature changes, more lines

would have to be analysed in order to correct for thermal effects.

Survey spectra were taken with a Bruker IFS 66 Fourier interferometer (FTIR). A parallel beam exiting the spectrometer was directed through the plasma and focused into a MCT detector with a BaF₂ lens. The wavelength range was 400–9000 cm⁻¹. Again, one single pass was used. The applied spectral resolution was 4 cm⁻¹. Spectra were taken at a rate of 15 Hz and usually a few hundred spectra were averaged to improve the signal to noise ratio (SNR).

In order to be able to measure axial profiles, the whole reactor is movable in a vertical direction. In this way the optical systems (YAG laser, TDL, FTIR) may remain in place.

The combined set-up for TDL and FTIR infrared measurements is depicted in figure 2.

3. Experiments and results

Discharge conditions similar to those reported by Selwyn *et al.* [1] were chosen—these are known to guarantee abundant particulate formation. A mixture of Ar and CF₂Cl₂ was fed to the plasma at a pressure of 200 mTorr. In order to change the CF₂Cl₂ admixture ratio, the CF₂Cl₂ flow and the Ar flow were varied while keeping the total flow (30 sccm) constant. Usually a power level of 100 W was applied.

At a CF₂Cl₂ admixture ratio of 10% when looking through the sheath boundary, the formation of a shallow cloud of particulates became visible by the eye after about 20 min, depending on the cleanliness of the silicon wafer (faster with a 'dirty' wafer, slower with a clean wafer). Given more time, the particles are observed to grow to sizes individually visible to the eye (order of a millimetre). After an even longer time the largest particles can no longer be levitated by the sheath and begin to drop onto the wafer. At the same time the sheath is observed to change shape: over the middle of the wafer

a dip is formed, with a larger depth for larger particulate concentrations. The sheath seems to behave like a mattress. The recently introduced technique of laser evaporation and subsequent detection using emission of thermal radiation [11] was used to determine where the particles were residing in the plasma. At 10% CF₂Cl₂ only a signal is obtained at the sheath boundary, indicating that the particles are present only there. At the same location scattering from a HeNe laser is also observed. At lower CF₂Cl₂ admixtures (e.g. 3%), a laser evaporation signal is obtained everywhere in the glow, although nothing can then be seen with the eye or with HeNe laser scattering. In the latter case abundant formation of small particles (diameter ≤ 100 nm) takes place.

If CF₂Cl₂ is replaced by CF₄ or CHF₃, no particle formation is found. Apparently the presence of chlorine in the feed gas molecules is necessary.

Scanning electron microscope (SEM) pictures of the surface of the silicon wafer show a lot of hollow, needle-like structures [12], which show a close resemblance to the structures created on silicon wafers by micromasking in chlorine or HBr discharges [13]. Micromasking is the phenomenon that a very anisotropic (and at the same time very selective) etching process can lead to needle-like structures if the surface is contaminated: the contaminated spots locally block the etching. This indicates that an anisotropic etching process (common to CCF₂Cl₂ plasmas) is combined with some local surface contamination (e.g. oxidation due to residual water or redeposition of sputtered Al electrode material), which initially locally inhibits etching and allows the creation of a needle-like structure. After a while the 'mask' is etched off by residual F atoms (they will be present even though the surface of Si subjected to CF₂Cl₂ plasmas mainly consists of a SiCl_x reaction layer [14]). The silicon inside the needle is then also etched away, and the side wall passivation material remains to form the hollow needle. Hollow structures like this have recently been prepared by a similar process: etching a patterned

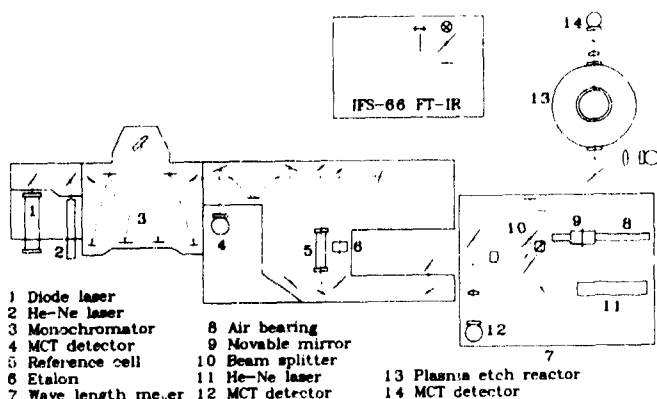


Figure 2. Schematic view of the experimental set-up used for *in situ* infrared absorption spectroscopy using TDL as well as FTIR.

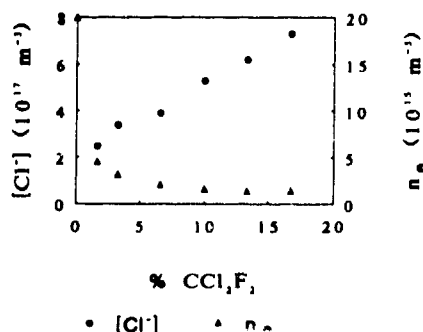


Figure 3. Density of negative chlorine ions as a function of CF₂Cl₂ admixture. Plasma conditions: 200 mTorr, 30 sccm total flow, 100 W RF power in 124 mm diameter electrode.

wafer, removing the mask, and etching the interior silicon away [15].

The electron density and the density of negative chlorine ions are given as a function of CF₂Cl₂ admixture in figure 3. The density of negative fluorine ions appeared to be of the order of the electron density. The density of the larger negative ions CF₂Cl₂⁻ appeared to be too low to be measurable (i.e. much smaller than the electron density). One can see that in the range where powder formation takes place (3–10%) the negative ion concentration is roughly constant. This is not surprising since a similar behaviour is seen for F⁻ ions in a CF₄/Ar plasma (see figure 4), although the negative ion density for CF₂Cl₂ is much higher than for CF₄. This leads us to the conclusion that an analogue of the abovementioned explanation for particle growth in SiH₄/Ar plasmas (increased attachment at higher electron temperatures in order to be able to create more negative ions at low CF₂Cl₂ admixture), is not valid for these discharge conditions.

In figures 5(a) and 5(b) the attachment of the electrons released by photodetachment is shown for chlorine and fluorine. It is obvious that the attachment to chlor-

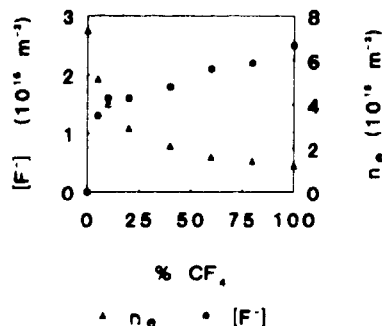


Figure 4. Density of negative fluorine ions as a function of CF₄ admixture. Plasma conditions: 200 mTorr, 30 sccm total flow, 100 W RF power in 124 mm diameter electrode.

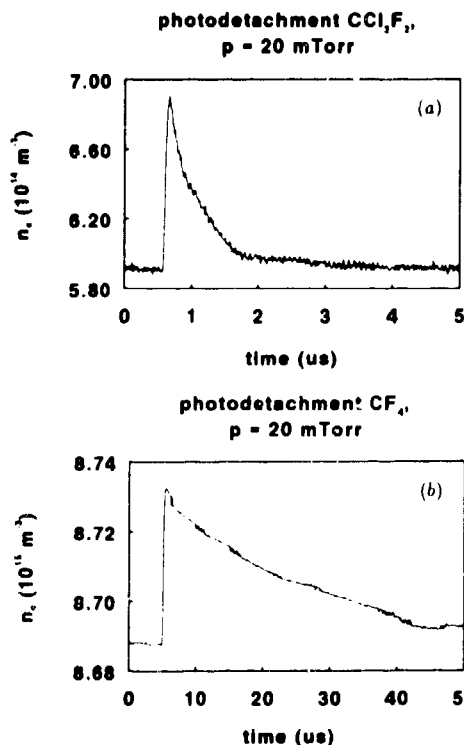


Figure 5. Decrease due to attachment of the density of the electrons created by photodetachment as a function of time for (a) Cl⁻ and (b) F⁻. Plasma conditions: 200 mTorr, 30 sccm total flow, 100 W RF power in 124 mm diameter electrode.

ine is much faster; the timescales differ by more than one order of magnitude. This difference is also expected to occur when chlorine or fluorine is incorporated at the surface of a small particulate, albeit less pronounced. Therefore it is probable that attachment of an electron to a particulate is more effective if the particulate contains chlorine. This may explain why abundant particu-

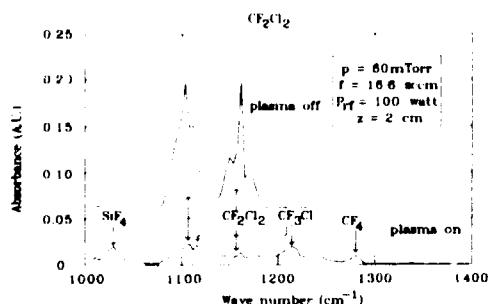


Figure 6. Infrared survey spectrum of the CF₂Cl₂/Ar plasma. The peaks associated with the several plasma species are indicated.

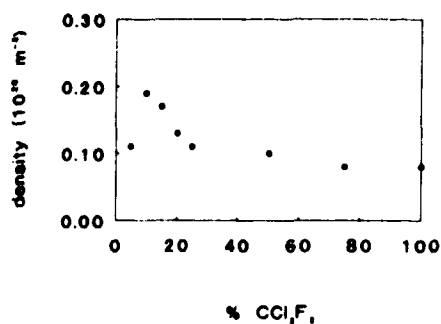


Figure 7. Intensity of the SiF₄ absorption as a function of the CF₂Cl₂ admixture ratio. The maximum occurs at the discharge conditions where generation of large size powders is most abundant.

late formation only occurs in chlorine containing plasmas.

Figure 6 shows an IR survey spectrum as measured with the FTIR. A measurement with 'plasma off' and 'plasma on' is shown. It is obvious that the CF₂Cl₂ absorption peak is reduced substantially when the plasma is switched on. This indicates that the gas is very effectively dissociated and converted to CF₄ and other products like CF₃Cl. Also one observes the extra peak of SiF₄, created from the etching of the silicon surface. Figure 7 shows the SiF₄ peak intensity as a function of the CF₂Cl₂ admixture. It is remarkable to observe that the SiF₄ density shows a maximum where also large particles are more abundantly generated. The SiF₄ density is proportional to the number of Si etch reactions which occur at the wafer surface. Apparently the etching of silicon plays an important role in the generation of powders.

Figure 8 shows a small part of the absorption spectrum of CF₂ radicals as measured with the TDL. The first derivative of the spectrum is shown. The distinctive peaks are clearly recognizable. Separate measurements have shown that there is hardly any change of the rotational temperature when the plasma is ignited, so the intensity of any of the peaks may be used to calculate the density. Figure 9 shows the CF₂ density as

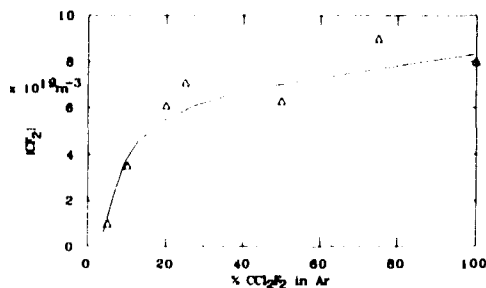


Figure 9. The CF₂ density as a function of CF₂Cl₂ admixture in argon. Plasma conditions: 200 mTorr, 30 sccm total flow, 100 W RF power in 124 mm diameter electrode.

a function of CF₂Cl₂ admixture. In the range where powder generation takes place (low percentages) the CF₂ density drops dramatically. The drop is steeper than one would expect from the measured dissociation degrees, which are obtained from IR spectra such as the one shown in figure 6, and which is reported elsewhere [16]. This could be related to removal of CF₂ by deposition on the particles suspended in the plasma.

4. Conclusions

Based on the information given in the previous section, we suggest the following sequence for the creation of particles in the CF₂Cl₂/Ar/Si system. Micromasking in combination with anisotropic etching creates needle-like structures with side wall passivation layers. After a while the mask is etched away and the needles become hollow. When they become too long, they break off, and electrons attach quickly to the Cl atoms at the surface of the needle. The needles are drawn into the glow by electrostatic forces. In the glow they are suspended and start to coalesce. Further growth may then occur due to deposition from (e.g. CF₂) radicals in the gas phase.

Acknowledgments

The research was supported by the Commission of the European Communities in the framework of the BRITE-EURAM programme under contract no. BREU-CT91-0411. Part of the research was supported by the Netherlands Technology Foundation (STW) in the programme of the Dutch Organisation for Fundamental Research on Matter (FOM).

References

- [1] Selwyn G S, Heidenreich J E and Haller K L 1991 *J. Vac. Sci. Technol. A* **9** 2817-24
- [2] Boufendi L, Plain A, Blondeau J P, Bouchoule A, Laure C and Toogood M 1992 *Appl. Phys. Lett.* **60** 169-71
- [3] Howling A A, Hollenstein Ch and Paris P-J 1991 *Appl. Phys. Lett.* **59** 1409-11

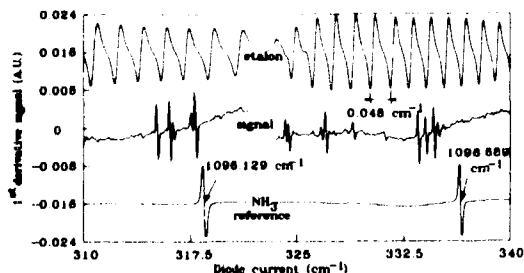


Figure 8. Detail of the first derivative IR absorption spectrum of CF₂ radicals as measured with the tunable diode laser system.

- [4] Garscadden A 1994 *12th Int. Conf. on Plasma Chemistry (Loughborough, UK) 1993 Pure Appl. Chem.* to be published
- [5] Selwyn G S and Patterson E F 1992 Plasma particulate contamination control: II Self-cleaning tool design *J. Vac. Sci. Technol. A* **10** 1053-9
- [6] Howling A A, Sansonnens L, Dorier J-L and Hollenstein Ch 1993 *J. Phys. D: Appl. Phys.* **26** 1003-6
- [7] Bouchoule A, Plain A, Boufendi L, Blondeau J Ph and Laure C 1991 *J. Appl. Phys.* **79** 1991
- [8] Haverlag M, Kono A, Passcier D, Kroesen G M W, Goedheer W J and de Hoog F J 1991 *J. Appl. Phys.* **70** 3472-80
- [9] Haverlag M, Kroesen G M W, Stoffels E, Stoffels W W and de Hoog F J 1994 Absolute wavenumber calibration of an infrared tunable diode laser to be published
- [10] Stoffels E, Stoffels W W, Verhamme L C T, van Wieringen E, Kroesen G M W and de Hoog F J 1992 *Europhys. Abstr.* **16 F** 455-6
- [11] Stoffels W W, Stoffels E, Appelman W W J, Kroesen G M W and de Hoog F J 1993 *Proc. 11th Int. Symp. on Plasma Chemistry (ISPC) (Loughborough, UK)* ed J Harry pp 1528-33
- [12] Stoffels W W, Stoffels E, Kroesen G M W, Haverlag M, den Boer J H W G and de Hoog F J 1994 *Plasma Sources Sci. Technol.* **3** 320-5
- [13] Bestwick T D, Oehrlein G S, Kroesen G M W, Cardone F and Scilla G J 1990 *Proc. Eighth Symp. on Plasma Processing* ed G S Mathad and D W Hess (Montréal: Electrochemical Society) p 285
- [14] Oehrlein G S, Kroesen G M W, de Fresart E, Zhang Y and Bestwick T D 1991 *J. Vac. Sci. Technol. A* **9** 768-74
- [15] Oehrlein G S, Rembetski J F and Payne E H 1990 *J. Vac. Sci. Technol. B* **8** 1199-211
- [16] Stoffels E, Stoffels W W, Haverlag M, Kroesen G M W and de Hoog F J 1994 to be published

Possible routes for cluster growth and particle formation in RF silane discharges

Jérôme Perrin, Christian Böhm, Roxana Etemadi and Antoni Lloret

Laboratoire de Physique des Interfaces et des Couches Minces, CNRS UPR A0258, Ecole Polytechnique, F91128 Palaiseau Cedex, France

Received 6 January 1994, in final form 3 February 1994

Abstract. After having distinguished five successive steps in the temporal evolution of a powder-forming SiH_4 radiofrequency glow discharge, we examine the initial mechanism by which silicon clusters start growing up to the point where they suddenly aggregate into multiply charged particles and modify the discharge regime. This 'induction' period can be much longer than the diffusion time of positive ions and neutral radicals, which implies that cluster growth involves negative ions (anions). We provide a review of basic data concerning anions in SiH_4 plasmas and analyse mass spectrometric data showing that anion–molecule reactions $\text{Si}_i\text{H}_{2i-1} + \text{SiH}_4 \rightarrow \text{Si}_{i+1}\text{H}_{2i+1} + \text{H}_2$ at relatively low rate (about $10^{-12} \text{ cm}^3 \text{ s}^{-1}$), and fast exothermic anion–radical reactions $\text{Si}_i\text{H}_{m-1} + \text{SiH}_m \rightarrow \text{Si}_{i+1}\text{H}_{m+m-2} + \alpha\text{H}_2$ at Langevin rates (about $10^{-9} \text{ cm}^3 \text{ s}^{-1}$), initiate clustering. The effective anion lifetime involves a succession of dissociative attachment to SiH_4 , detachment or recombination, and attachment to neutral radicals or clusters competing with diffusion out of the plasma. Anion–molecule and anion–radical cluster reactions at Langevin rates probably dominate the cluster growth kinetics below 100 Si atoms whereas anion–neutral and neutral–neutral condensation at size-scaling collision rates govern the subsequent homogeneous nucleation regime. At the end of the nucleation period (up to 10^4 Si atoms) the fraction of singly charged clusters can reach 50%. The reduction of powder formation upon gas heating is attributed to a decrease of the rate of non-dissociative attachment to radicals and neutral clusters.

List of symbols

d_i	diameter of a cluster of i atoms	k_0	effective bimolecular rate constant for the reaction between a monomer anion and a monomer neutral
A_e	electron affinity	k_{c11}	collision rate constant between neutral monomers
IP	ionization potential	k_{c1i}	Langevin collision rate between an anion monomer and a neutral monomer
k_a	effective attachment rate constant of electrons on neutral radicals or clusters	k_{ij}	rate constant for the reaction between neutral clusters of i and j atoms
k_{ai}	attachment rate constant of electrons on neutral radicals or clusters of i atoms	k_{ji}	rate constant for the reaction between an anion of i atoms and a neutral cluster of j atoms
k_{da}	dissociative attachment rate constant of electrons on silane molecules	k_m	mutual anion–cation neutralization rate constant
$k_{a\text{max}}$	maximum attachment rate constant of electrons on a neutral cluster of i atoms	k_{mi}	mutual anion–cation neutralization rate constant for an anion of i atoms
k_{ed}	electron impact detachment rate constant of anions	$k_{st(i+j)}$	bimolecular rate constant for the stabilization of a transient neutral or anion cluster of $(i+j)$ atoms by collisions with gas molecules
k_{edi}	electron impact detachment rate constant of anions of i atoms		
$k_{ed\text{max}}$	maximum electron impact detachment rate constant of an anion cluster of i atoms		
k_{ii}	effective bimolecular rate constant for the reaction between neutral monomers		

f_{ij}	size scaling factor for the reaction rate between neutral clusters of i and j atoms
f_{ij}^-	size scaling factor the reaction rate between an anion of i atoms and a neutral cluster of j atoms
J_e	time-averaged electron current on the electrode
J_+	positive ion current on the electrode
J_{RF}	amplitude of the RF current in the discharge
m_i	mass of a cluster of i atoms
m_e	reduced mass
n_e	electron density in the plasma bulk
n_+	positive ion density in the plasma bulk
n_i	density of neutral clusters of i atoms
n_i^-	density of anion clusters of i atoms
n_r	total density of neutral radicals
N	gas density
N_p	particle number density in the plasma bulk
N_{p0}	initial particle number density at the beginning of the aggregation phase
P	gas pressure
$p_{st}^{(i+j)}$	stabilization probability of a transient neutral or anion cluster of $(i+j)$ atoms
r_p	mean radius of a particle
V_{RF}	the RF voltage amplitude between parallel-plate electrodes
T	translational temperature of neutral molecules, radicals and clusters
T_e	electron temperature in the plasma bulk
T_i	ion temperature in the plasma bulk
Z_p	average negative charge number on a particle
α	symbol for the 'wave-riding' mechanism of electron acceleration by the sheath and corresponding discharge regime
α_i	polarizability of a neutral cluster of i atoms
β	ratio of positive ion to electron density in the plasma bulk, $\beta = n_+/n_e$
γ	symbol for the 'Joule heating' mechanism of electrons in the plasma bulk and corresponding discharge regime
θ_i^-	fraction of singly charged anion clusters of i atoms
τ_{ad}	autodetachment lifetime of an excited anion
$\tau_{st}^{(i+j)}$	redissociation time of a transient neutral or anion cluster of $(i+j)$ atoms

1. Introduction

Concern about particulate contamination in industrial plasma reactors used for material processing by etching, sputtering or PECVD has triggered active research on the phenomena associated with particle formation in low-pressure glow discharges. Up to now most of the experimental [1-7] and theoretical [8-10] effort has dealt with the detection and dynamics of medium and large size (>10 nm) particles, which are electrostatically suspended in the plasma bulk and affect the discharge behaviour. However, the initial mechanism by which

clusters start growing just after discharge ignition up to the point where they suddenly aggregate into multiply charged particles is still obscure.

The model of Choi and Kushner [11] offers a general framework of interpretation emphasizing the role of negative ions (anions) in enhancing the effective residence time of small clusters up to a critical size at which homogeneous nucleation develops. Nevertheless, there are significant variations in the detailed physico-chemistry of cluster growth between, for example, a sputtering discharge, in which particles grow from the atomic vapour sputtered from the walls, and a chemically reactive plasma. Fortunately, Hollenstein and co-workers [12, 13] have remarkably illustrated the role of molecular anions in powder forming SiH_4 discharges by combining anion mass spectrometry and laser Mie scattering.

Here we first present the evolution of a powder-forming SiH_4 discharge in five steps from a combination of experimental observations. Then, focusing on the initial steps, we analyse the anion plasma chemistry and propose some refinements in modelling of cluster formation. Next we discuss the effect of temperature on powder formation. We finally evaluate other nucleation schemes of Si clusters in reactive plasmas that have been proposed recently.

2. A five-step scenario for particle formation in SiH_4 discharges

If the RF voltage V_{RF} or the pressure P of a pure SiH_4 RF discharge are continuously increased at a given temperature T , then a sudden change in the power dissipation regime occurs above some critical values $V_{RF,c}(P, T)$ or $P^*(V_{RF}, T)$ [14, 15]. This transition from collisional 'wave-riding' at the sheath boundaries (α regime) to 'Joule heating' in the plasma bulk (referred to here as the γ regime) is associated with powder accumulation in the plasma enhancing by a factor of 10-15 the electron attachment rate [16]. However, if one ignites a discharge below these critical values, the transition may be delayed [13, 17]. In figure 1 we show the temporal evolution of V_{RF} and J_{RF} (RF current) and of the spatially resolved optical emission of SiH^* at 414 nm in a pure SiH_4 parallel-plate 13.56 MHz discharge ($P = 0.13$ mbar, $T = 200$ C, about 40 mW cm^{-2}). Figure 2 shows in detail the first millisecond, illustrating a perturbation ($\pm 30\%$) of the RF-averaged electron current J_e (measured using a grid probe at the wall), whereas V_{RF} , J_{RF} , the ion current J_+ (measured with the same grid probe) and the SiH^* intensity and profile remain steady within 5%.

These observations, together with measurements of the time evolution of particle density and size by Hollenstein *et al* [13] in very similar conditions (pure SiH_4 , 0.1 mbar, 150 C, 38 mW cm^{-2}) or Boufendi *et al* [6] ($\text{SiH}_4(4\%) \text{ Ar}$), reveal five successive steps:

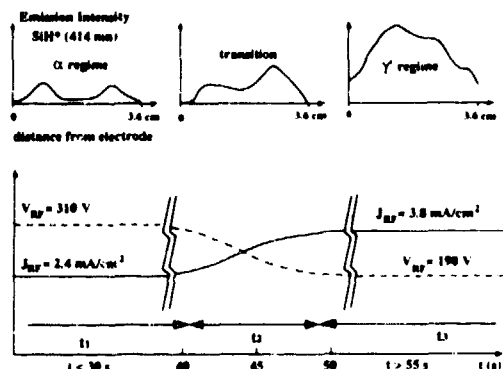


Figure 1. Development of the transition towards powder formation after plasma ignition in a SiH₄ 13.56 MHz radiofrequency discharge at 0.13 mbar and 200 °C characterized by the evolution of the spatially resolved optical emission of SiH* at 414 nm and of the electrical properties. The net radiofrequency power density fed to the discharge changes from 30 mW cm⁻² ($t < t_1$) to 50 mW cm⁻² ($t > t_1 + t_2$). Before the transition the ion density estimated from PIC modeling is $n_i \approx 10^{10}$ cm⁻³ and $\beta = n_e/n_i \approx 15$.

(i) During the first step t_0 (figure 2) the fast electron population is quickly established (in some 10 μ s) and does not evolve, as revealed by the constancy of the SiH* emission. However, the perturbation of J_e , although difficult to interpret, reveals that the cold plasma electron density n_e is affected within a few milliseconds. Verdeyen *et al* [18] made similar observations by recording SiH* emission and n_e in a SiH₄ He discharge and invoked enhanced attachment to the primary SiH₃

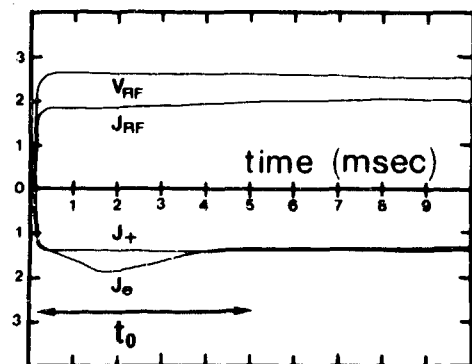


Figure 2. Initial evolution of V_{RF} , J_{RF} and radiofrequency-averaged ion and electron currents J_+ and J_- on the wall after plasma ignition (same discharge conditions as in figure 1). All quantities are in arbitrary units.

radicals during their diffusion to the walls. This enhanced attachment is, however, much smaller than that which occurs when powder appears and does not modify significantly the α regime of the discharge.

(ii) During the second step t_1 , from a fraction of a second [6] to several minutes (40's here, as in [13]) the discharge remains in the α regime and no particles are yet detected by the most sensitive techniques (Mie scattering, laser-induced fluorescence or transmission electron microscopy), but this is the stage at which Si cluster growth proceeds.

(iii) The critical step t_2 of a few seconds is the drastic $\alpha \rightarrow \gamma'$ transition in the discharge regime and the concomitant onset of monodispersed particles whose density N_p drops by two orders of magnitude (from 10^9 to 10^7 cm⁻³ in range) while their radius r_p increases by aggregation of primary clusters (2.5 nm) [6, 13]. Enhanced attachment to multiply charged particles makes the plasma more resistive (V_{RF} decreases and J_{RF} increases) [14, 16].

(iv) During the next long step t_3 after the $\alpha \rightarrow \gamma'$ transition the discharge power dissipation is dominated by attachment to particles of $r_p \geq 40$ nm [8, 16]. Particle aggregation has stopped, N_p is fixed and growth slowly continues by condensation of radicals.

(v) Eventually, for $r_p \geq 100$ nm, the increasing charge on particles makes the plasma unstable, which leads to partial expulsion of particles. Then new generations of particle generation take place with dispersed particle sizes.

3. Anion plasma chemistry

3.1. Enthalpies and electron affinities

Table 1 provides a review of measured or *ab initio* computed enthalpies of formation, ionization potentials (IP) and electron affinities (A_e) of Si_nH_m species. Notice the general trend that A_e increases with number of Si atoms towards the work function of Si at 4.85 eV even though some local maxima appear at 'magic' numbers.

3.2. Dissociative attachment on silane

From dissociative attachment cross sections for SiH₄ and Si₂H₆ [19, 20] we derived rate constants by integration over Maxwellian energy distributions. The total rates are shown in figure 3. For $T_e = 3$ eV, which is typical of bulk SiH₄ plasma, $k_{da}(\text{Si}_2\text{H}_6)$ is at most three times larger than $k_{da}(\text{SiH}_4)$. Since the Si₂H₆ concentration is only a few percent, the enhanced attachment after discharge ignition cannot be attributed to build-up of higher order silanes. The dominant primary anion is SiH₃⁻, with additional contribution of the fast H⁻ reaction [21]



Table 1. Enthalpies of formation, adiabatic electron affinities and ionization potentials.

Species Si_nH_m		$\Delta H_{f,298\text{K}}$ (eV)	A_e (eV)	IP (eV)
	H_2	0		15.427 ^a
	H	2.259 ^a	0.754 ^a	13.598 ^a
$\text{Si}_n\text{H}_{2n+2}$	$n=1$	SiH_4	0.355 ^{a,b}	<0
	$n=2$	Si_2H_6	0.828 ^b	<0
	$n=3$	Si_3H_8	1.281 ^b	<0
	$n=4$	Si_4H_{10}	1.746 ^b	<0
	$n=5$	Si_5H_{12}	2.21 ^b	<0
$\text{Si}_n\text{H}_{2n+1}$	$n=1$	SiH_3	2.071 ^b	1.406 ^a
	$n=2$	Si_2H_5	2.444 ^b	$\approx 1.45^f$
	$n=3$	$n\text{-Si}_3\text{H}_7$	2.841 ^b	$\geq 1.47^g$
		$i\text{-Si}_3\text{H}_7$	2.766 ^b	$\geq 1.39^g$
	$n=4$	Si_4H_9	3.222 ^b	$\geq 1.49^g$
$\text{Si}_n\text{H}_{2n}\text{-Si}_n\text{H}_2$	$n=1$	SiH_2	2.872 ^b	1.124 ^h
	$n=2$	H_3SiSiH	3.287 ^b	$\approx 1.30^f$
		$\text{H}_2\text{Si}=\text{SiH}_2$	2.911 ^b	$\approx 0.9^f$
		$\text{H}_2\text{Si}=\text{SiH}$	4.315	
		H_3SiSi	4.267 ^b	1.545 ⁱ
		$\text{H}_2\text{Si}=\text{Si}$	4.678 ^b	1.65 ^j
		$\text{Si}(\text{H}_2)\text{Si}$	4.146 ^c	8.20 ⁱ
	$n=3$	$(\text{SiH}_2)_3$	3.779 ^b	
		$\text{Si}_2\text{H}_5\text{SiH}$	3.717 ^b	
		$c\text{-Si}_3\text{H}_6$	2.638 ^b	
		$c\text{-SiH}(\text{SiH}_2)_2$	3.99 ^b	
		$\text{H}_3\text{SiSiSiH}$	4.987 ^b	
		$c\text{-Si}(\text{SiH}_2)_2$	4.617 ^b	
	$n=1$	SiH	3.904 ^b	1.277 ^h
	$n=2$	Si_2H	5.608 ^b	$\geq 1.75^k, \approx 2.0^l$
		$\text{Si}(\text{H})\text{Si}$	5.153 ^c	$\geq 1.285^k$
Si_n	$n=1$	Si	4.664 ^a	1.385 ^h
	$n=2$	Si_2	6.114 ^a	2.173 ^m
	$n=3$	Si_3	6.592 ^a	2.33 ⁿ
	$n=4$	Si_4	5.98 ^a	2.15 ^o
	$n=5$	Si_5	6.82 ^a	2.7 ^o
	$n=6$	Si_6	6.38 ^a	2.0 ^o
	$n=7$	Si_7	6.05 ^a	1.9 ^o
	$n=8$	Si_8	8.11 ^a	2.5 ^o
	$n=9$	Si_9	9.67 ^a	2.6 ^o
	$n=10$	Si_{10}	8.44 ^a	2.4 ^o
	$n=11$	Si_{11}		2.7 ^o
	$n=12$	Si_{12}		2.8 ^o
	$n=12$	c-Si		4.85 ^p

^aJANAF thermochemical tables.^bSax A F and Kalcher J 1991 *J. Phys. Chem.* **95** 1768.^cHo P and Melius C F 1990 *J. Phys. Chem.* **94** 5120.^dRaghavachari K and McMichael Rohlfing C 1988 *J. Chem. Phys.* **89** 2219.^eNimlos M R and Ellison G B 1986 *J. Am. Chem. Soc.* **108** 6522.^fThe *ab initio* computation by Kalcher J and Sax A F 1988 *Chem. Phys. Lett.* **150** 99 shows that $A_e(\text{H}_3\text{SiSi}) > A_e(\text{Si})$ by 0.16 eV. Since $A_e(\text{Si}) > A_e(\text{SiH})$ by 0.108 eV, substitution of H by SiH_2 stabilizes the electron by about 0.26 eV. We adopt the rule of thumb that $A_e(\text{H}_3\text{SiSiH}_m) \approx A_e(\text{SiH}_m) + [1 - (m-1)/3] \times 0.26$ eV.^gLower limits from the condition of exothermicity of the reactions $\text{Si}_n\text{H}_{2n} + \text{SiH}_4 \rightarrow \text{Si}_n\text{H}_{2n+1} + \text{H}_2$.^hKasdan A, Herbst E and Lineberger W C 1975 *J. Chem. Phys.* **62** 541.ⁱAssuming that H_2SiSiH_2 and H_3SiSiH have similar stabilities.^jKalcher J and Sax A F 1987 *Chem. Phys. Lett.* **133** 135.^kFrom the mean appearance potentials of anions in the Si_2H_6 dissociative attachment cross sections measured in [20].^lEstimated to be 0.2 eV smaller than $A_e(\text{Si}_2)$ due to the effect of H bonding. Indeed, single H bonding on a Si centre reduces A_e : $A_e(\text{SiH}) \approx A_e(\text{Si}) - 0.11$ eV, $A_e(\text{H}_2\text{SiSiH}) \approx A_e(\text{H}_2\text{SiSi}) - 0.25$ eV.^mKitsopoulos T N, Chick C J, Zhao Y and Neumark D M 1991 *J. Chem. Phys.* **95** 1441.ⁿKitsopoulos T N, Chick C J, Weaver A and Neumark D M 1990 *J. Chem. Phys.* **93** 6108.^o[42]. A correction of +0.2 eV is applied to photoelectron thresholds to derive adiabatic A_e as suggested in [43].^pWork function of bulk crystalline silicon.^qBerkowitz J, Greene J P, Cho H and Ruscic B 1987 *J. Chem. Phys.* **86** 1235.^rRuscic B and Berkowitz J 1991 *J. Chem. Phys.* **95** 2407.^sFrom thresholds of photoelectron spectra recorded by Bock H, Ensslin W, Feher F and Freund R 1976 *J. Am. Chem. Soc.* **98** 668. Applied to SiH_4 and Si_2H_6 *et al.* this gives ionization potentials in agreement with the values of Ruscic and Berkowitz.^tRuscic B and Berkowitz J 1991 *J. Chem. Phys.* **95** 2416.^uCurtiss L A, Raghavachari K, Deutsch P W and Pople J A 1991 *J. Chem. Phys.* **95** 2433.^vChailion C, Allibert M and Patoret A 1975 *C.R. Hebd. Seances Acad. Sci. Ser. C* **280** 1505.^wTrevor D J, Cox D M, Reichmann K C, Brickman R O and Kaldor A 1987 *J. Phys. Chem.* **91** 2598.

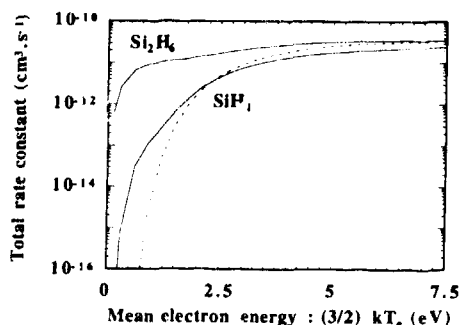
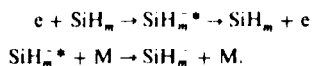


Figure 3. Dissociative attachment rate constants versus mean electron energy computed from cross sections for SiH_4 from Haaland [19] (broken line) and Srivastava *et al* [20] (full line) and for Si_2H_6 from Krishnakumar *et al* [20]. (Rates computed by Haaland were found to be too large by a factor π .)

3.3. Electron attachment and detachment on radicals and neutral clusters

The perturbation of n_e after plasma ignition (step t_0) suggests that electron attachment on radicals takes place in addition to dissociative attachment to SiH_4 . Moreover, electron attachment to neutral clusters is a key parameter governing evolution towards nucleation in the model of Choi and Kushner. Fledderman *et al* [22] have determined a lower bound of $2.65 \times 10^{-10} \text{ cm}^3 \text{ s}^{-1}$ for k_a of monosilicon radicals SiH_m in a SiH_4 (1–5%) He discharge afterglow at 0.4 mbar, $T = 300 \text{ K}$ and $T_e \approx 0.05$ – 0.1 eV . At such low T_e dissociative attachment to radicals is excluded and the only process is three-body attachment, requiring collisional stabilization of the transient excited anion state to compete with autodetachment:



At low pressures the effective bimolecular attachment rate k_a should be proportional to the gas density N and to the autodetachment lifetime τ_{ad}^+ of the excited anion. Abundant results on molecular anions [23, 24] show that k_a decreases as a function of both T_e and T , mostly due to the decrease of τ_{ad}^+ , as opposed to the dissociative attachment rate k_{da} , which increases with both T_e and T . Our SiH_4 discharge is at lower pressure, higher T and much higher T_e than the post-discharge of Fledderman *et al*, so we could expect a smaller k_a . However, SiH_4 is probably a more efficient stabilizer than He. To explain the perturbation of J_e in figure 2 the attachment frequency $k_a n_e$ to radicals of total density n_r should be at least 10% of the dissociative attachment frequency $k_{da} N$ on SiH_4 . Since $k_{da} \approx 8 \times 10^{-12} \text{ cm}^3 \text{ s}^{-1}$ and $n_r/N \approx 1.5 \times 10^{-3}$ in our conditions, $k_a \approx 5 \times 10^{-10} \text{ cm}^3 \text{ s}^{-1}$.

For larger Si_nH_m clusters τ_{ad}^+ is expected to increase with the number of multiple bonds [25], whence k_a

should increase with cluster size. However, the fast electron impact detachment rate k_{ed} above A_e also increases with anion size. Upper limits scaling with the number i of atoms in large clusters are given by the electron collision rates obtained by integrating a Maxwellian energy distribution up to A_e for k_a and above A_e for k_{ed} , assuming a stepwise cross section:

$$k_{a\text{max}}(\text{cm}^3 \text{ s}^{-1}) \approx 1.7 \times 10^{-8} T_e^{1/2} i^{2/3} \left[1 - \left(1 + \frac{A_e}{T_e} \right) \exp \left(-\frac{A_e}{T_e} \right) \right]$$

$$k_{e\text{dmax}}(\text{cm}^3 \text{ s}^{-1}) \approx 1.7$$

$$\times 10^{-8} T_e^{1/2} i^{2/3} \left(1 + \frac{A_e}{T_e} \right) \exp \left(-\frac{A_e}{T_e} \right).$$

3.4. Mutual anion–cation neutralization

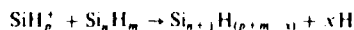
Hickman [26] proposed an approximate formula for the mutual anion–cation neutralization rate constant k_m as a function of the reduced mass m_i and A_e of the parent neutral species of the anion and the ion temperature T_i :

$$k_m(\text{cm}^3 \text{ s}^{-1}) = 5.34 \times 10^{-7} A_e^{-0.4} m_i^{-1/2} (T_i/300)^{-1/2}$$

with A_e in electron-volts, T_i in kelvins and m_i in atomic mass units.

Thus k_m should slightly decrease with the number i of Si atoms of the anion, typically from $k_{m1} \approx 9 \times 10^{-8} \text{ cm}^3 \text{ s}^{-1}$ to $k_{mi} \approx 4 \times 10^{-8} \text{ cm}^3 \text{ s}^{-1}$ for large anions ($A_e \rightarrow 4.85 \text{ eV}$, $m_i \rightarrow m_1$) for collisions with monomeric SiH_m^+ cations at $T_i \approx T = 500 \text{ K}$.

Instead of charge exchange, Haaland [19] invoked mutual anion–cation association



with H or H_2 elimination to release excess energy (about 5 eV considering the IP and A_e for Si_nH_m radicals in table 1). Association was also proposed for ion clusters involving polar molecules [27]. However, we calculated that mutual association could represent at most a quarter of the contribution of anion–radical and radical–radical reactions in our discharge conditions at the early stage of cluster growth.

3.5. Anion–molecule and anion–radical reactions

Mandich and Reents [28] have definitively excluded clustering by Si_nH_m^+ cation reactions on SiH_4 or Si_2H_6 above $n = 6$ or 7. Moreover radical molecule chain insertion reactions of SiH_2 in SiH_4 , Si_2H_6 , Si_3H_8 and so on cannot develop far enough in our discharge conditions. The mass spectrometry studies of Perrin *et al* [29] in a low-pressure (0.00013–0.013 mbar) dc multipole discharge and of Howling *et al* [12] in a 0.1 mbar rf discharge showing that Si_nH_m anions polymerize much faster than Si_nH_m^+ cations (figure 4) suggest that anions are responsible for powder formation, in agreement with the model of Choi and Kushner.

Little is known about anion reaction rates in SiH_4

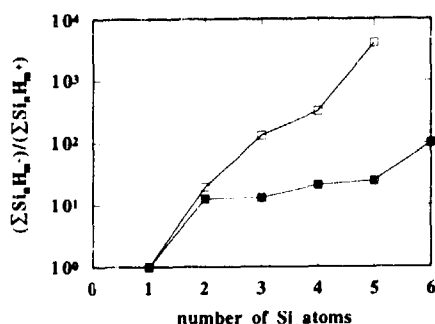
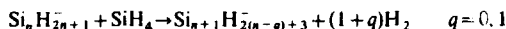
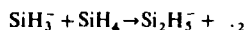


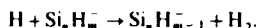
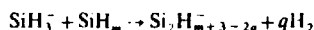
Figure 4. Ratio of negative to positive ions as a function of number of Si atoms (normalized at $n = 1$) measured by mass spectrometry in a 0.013 mbar multipole direct current discharge [29] (filled squares) and in a 0.1 mbar radiofrequency discharge [12] (open squares).

except upper limits of $10^{-11} \text{ cm}^3 \text{ s}^{-1}$ for SiH_3^- [19] and about $10^{-13} \text{ cm}^3 \text{ s}^{-1}$ for Si_n^- and Si_nH^- ($n \leq 7$) [29, 30], consistent with the fact that H-bare anions have the highest A_e (table 1) and have no exothermic channels by which to react with SiH_4 . The H atom

distribution in Si_nH_m^- mass spectra of figure 5 reveals different reaction pathways depending on discharge conditions, although SiH_3^- is the dominant primary anion in both cases. In the 0.1 mbar RF discharge the main pathway is obviously



with rate constants of the order of $10^{-12} \text{ cm}^3 \text{ s}^{-1}$ [13]. However, the dominance of Si_n^- and Si_nH^- in the 0.013 mbar multipole discharge can hardly be attributed to reactions with SiH_4 , as was proposed initially [29]. Instead, exothermic reactions at Langevin rates [31] of the order of $10^{-9} \text{ cm}^3 \text{ s}^{-1}$ with SiH_m radicals and H atoms can explain the anion dehydrogenation:



Reaction rates even greater than Langevin rates were measured for Si_n^- on the 'radical-like' polar NO_2 molecule [32].

4. Cluster growth kinetics

Choi and Kushner considered for simplicity that clustering proceeds via anion neutral and neutral neutral reactions involving only Si_n and Si_n^- clusters. They used a common rate constant for neutral-neutral and anion-neutral reactions scaling as a function of the numbers (i, j) of atoms of the partners

$$k_{ij} = k_0 f_{ij} \quad f_{ij} = \frac{1}{4\sqrt{\pi}} \frac{(i^{1/3} + j^{1/3})^2}{[ij/(i+j)]^{1/2}}$$

normalized to $f_{11} = 1$.

The effective bimolecular rate constant k_n is bounded by the (1,1) monomer collision rate $k_{111} (\text{cm}^3 \text{ s}^{-1}) = 2.8 \times 10^{-11} d_1^2 m_1^{-1/2} (T/300)^{-1/2}$ where T is in kelvins and d_1 (\AA) and m_1 (amu) are the monomer diameter and mass. k_0 may also involve termolecular collisional stabilization. f_{ij} is maximized for $j \ll i$ or $j \gg i$, which implies that large clusters preferentially grow by accretion of small ones, leading to the homogeneous nucleation phenomenon. The key parameters of the model are k_0 , the attachment rate k_a and a minimum cluster size at which attachment takes place.

For future refinement of the modelling we would like to make four remarks.

(i) Ion-neutral collisions are governed by Langevin dipole-induced interaction [31] so that anion-neutral and neutral-neutral reactions should be distinguished. Since the polarizability of the neutral partner is approximately proportional to its number of atoms, the rate constant for the (i, j) anion-neutral reaction should scale as

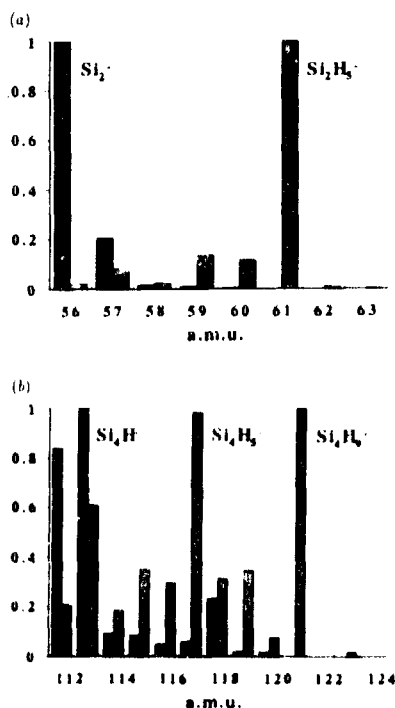


Figure 5. Mass spectra of Si_nH_m^- and Si_nH_m (corrected for isotopic scrambling) from a 0.013 mbar multipole direct current discharge [29] (black) and from a 0.1 mbar radiofrequency discharge [12] (grey).

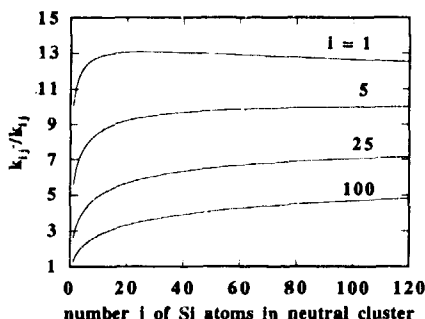


Figure 6. Ratio of the anion-neutral Langevin rate constant and the neutral-neutral rate constant as a function of the number j of Si atoms in the neutral species and for different values of the number i of Si atoms in the anion or neutral partner ($T = 500$ K).

$$k_{ij}^- = k_0^- f_{ij}^- \quad f_{ij}^- \approx \frac{1}{\sqrt{2}} \frac{j^{1/2}}{[ij/(i+j)]^{1/2}}.$$

Here k_0^- is bounded by the (1,1) Langevin rate k_{c11}^- ($\text{cm}^3 \text{s}^{-1}$) = $3.3 \times 10^{-9} (\alpha_1/m_1)^{1/2}$ where α_1 (\AA^3) is the single-atom polarizability. The ratio k_{ij}^-/k_{ij} is plotted in figure 6 as a function of j for different i , assuming no need for collisional stabilization, so that $k_0 = k_{c11} \approx 1.3 \times 10^{-10} \text{ cm}^3 \text{s}^{-1}$ ($T = 500$ K) and $k_0^- = k_{c11}^- \approx 1.3 \times 10^{-9} \text{ cm}^3 \text{s}^{-1}$ ($\alpha_1 \approx 5 \text{ \AA}^3$). Small anions react much faster than small neutrals and are scavenged by large neutrals. The limit of the Langevin model for a point charge [31] is attained when the Langevin cross section becomes smaller than the size-limited cross section of the collision partners. In such case a lower bound of k_{ij}^- is k_{ij} . This limit would be reached when $k_{c11} f_{ij} \geq k_{c11}^- f_{ij}^-$, namely when $i^{1/3} + j^{1/3} \geq 2j^{1/4} (k_{c11}/k_{c11}^-)^{1/2}$. Since $(k_{c11}/k_{c11}^-) \approx 10$ in our case, this condition shows that the Langevin cross section always dominates for a small anion on a large neutral ($i \ll j$) at least up to $j < 10^9$. For an anion and a neutral of the same size ($i \approx j$), the limit is only reached for $i \geq 10^6$. For a large anion and a small neutral ($i \gg j$) this would occur for $i > 250j^{3/4}$. This means that Langevin reaction rates govern the cluster growth at least up to a few hundred atoms.

(ii) If collision stabilization is needed k_0 and k_0^- should also be size-dependent. Since the gas (SiH_4) has roughly the same mass and polarizability as a single Si atom

$$k_0^{(+)} \approx k_{c11}^{(+)} \frac{\tau_{d(i+j)}^{(+)} k_{ai}^{(+)} k_{aj}^{(+)} N}{(1 + \tau_{d(i+j)}^{(+)} k_{ai}^{(+)} k_{aj}^{(+)} N)} \quad k_{ai}^{(+)} \approx p_{ai}^{(+)} k_{c11}^{(+)} f_{ii}^{(+)},$$

where $\tau_{d(i+j)}^{(+)}$ is the redissociation time and $p_{ai}^{(+)}$ the stabilization probability of the transient $(i+j)$ cluster. Since $\tau_{d(i+j)}^{(+)}$ and $p_{ai}^{(+)}$ usually increase with the number of vibrational degrees of freedom, k_0 and k_0^- would also be increasing functions of the cluster size.

(iii) As discussed above, k_a and k_{ad} should increase with cluster size. Hickman's formula for k_m can be safely

used for singly charged anions up to $i \approx 5000$ where the $(i, 1)$ collision-limited rate k_{i1} takes over. The maximum ratio of electron-impact detachment to mutual neutralization frequencies $k_{ed\text{max}} n_e / k_{m+} n_+ \approx k_{ed\text{max}} / k_{m+} \beta \propto 0.025 i^{2/3}$ under our conditions ($T_e \approx 3 \text{ eV}$, $\beta \approx 15$, $A_e \rightarrow 4.85 \text{ eV}$) exceeds 1 for $i > 250$, showing that electron impact detachment can be neglected at small sizes but probably not for $500 < i < 5000$, where the anion lifetime would be controlled by the balance between k_{ai} and k_{ed} .

(iv) To simulate the powder onset in a chemically reactive plasma ($\text{SiH}_4(90\%) \text{ N}_2$, $P = 0.26 \text{ mbar}$), Choi and Kushner [11] had to choose $k_0 = 5.7 \times 10^{-10} \text{ cm}^3 \text{s}^{-1}$ (corrected for the $4\sqrt{2}$ factor in f_{ij}), which exceeds k_{c11} . This reveals the fact that anion SiH_4 and fast anion-radical reactions play a leading role at the early stage of clustering, and that subsequent reactions between small hydrogenated radicals or molecular anions and large clusters do not need collisional stabilization thanks to H_2 elimination to release excess energy.

5. From singly to multiply charged particles

After the aggregation phase t_2 , big particles bear all the negative charge since β increases from about 15 to 100 during the $\alpha \rightarrow \gamma'$ transition [16] and molecular anions have disappeared [12, 13]. Their average charge number Z_p obtained from the plasma neutrality: $n_+ = n_e + Z_p N_p$ is of the order of 100 during step t_3 since N_p is a few times 10^7 cm^{-3} [13]. However, at the end of the clustering step t_1 before aggregation, particles contain less than 10^5 atoms ($r_p \leq 5 \text{ nm}$), and N_p is a few times 10^9 cm^{-3} [13]. Since $n_+ \approx 10^{10} \text{ cm}^{-3}$ and $\beta \approx 15$, at this stage $Z_p = 1$, which means either that all clusters are singly charged, or that most of the charge is still born by molecular negative ions, or that a small fraction of clusters is multiply charged. The latter hypothesis would explain the sudden triggering of aggregation but is unlikely during the preceding nucleation sequence in which only singly charged anions are stable enough to survive electron impact detachment.

A simple calculation can be made for the homogenous nucleation regime, which develops for clusters of more than several 100 atoms in which there remain only small anions and radicals and monodispersed anion or neutral clusters [11]. For simplicity we only consider a monomer anion density n_1^- and i -cluster densities $n_i^- + n_i = N_{p0}$ where N_{p0} is the initial particle density at the very beginning of the aggregation phase t_2 . Then the steady-state charged density of clusters at a given average size is given by the balance equation

$$\frac{\partial n_i^-}{\partial t} = (k_{ai} n_e + k_{i1}^- n_1^-) n_i - (k_{mi} n_+ + k_{ed i} n_e) n_i \approx 0$$

with the additional plasma neutrality condition $n_+ = n_e + n_1^- + n_i^- = \beta n_e$. From this equality we derive the cluster charged fraction $\theta_i = n_i^- / N_{p0}$ for $500 < i < 10^4$ ($r_p \leq 4 \text{ nm}$) under our SiH_4 discharge condition $P = 0.13 \text{ mbar}$, $T = 500 \text{ K}$, $n_e = 10^{10} \text{ cm}^{-3}$, $\beta \approx 15$,

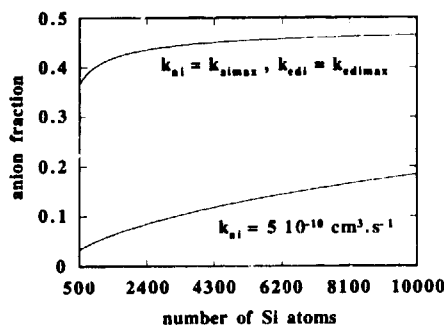


Figure 7. Charged fraction of large clusters in the homogeneous nucleation regime for two hypotheses concerning electron attachment and detachment rates (see text).

$N_{e0} \approx 5 \times 10^9 \text{ cm}^{-3}$, with $k_{mi} = 4 \times 10^{-8} \text{ cm}^3 \text{ s}^{-1}$ and $k_{1i} \approx k_{1i} \rightarrow k_0 i^{2/3} / 4\sqrt{2} = 2.3 \times 10^{-11} i^{2/3} \text{ cm}^3 \text{ s}^{-1}$. Two extreme hypotheses are made for k_{ai} and k_{edi} : (i) low attachment rate on clusters, $k_{ai} = k_{a1} = 5 \times 10^{-10} \text{ cm}^3 \text{ s}^{-1}$ and $k_{edi} = 0$ as in the model of Choi and Kushner; and (ii) maximum attachment and detachment rates, $k_{ai} = k_{aimax} \approx 1.4 \times 10^{-8} i^{2/3} \text{ cm}^3 \text{ s}^{-1}$ and $k_{edi} = k_{edimax} \approx 1.5 \times 10^{-8} i^{2/3} \text{ cm}^3 \text{ s}^{-1}$ for $T_e \approx 3 \text{ eV}$ and $E_e = 4.85 \text{ eV}$. Figure 7 shows that θ_i^- increases with average cluster size during nucleation, being larger when maximum attachment and detachment rates are assumed: $\theta_i^- \rightarrow k_{aimax} / (k_{aimax} + k_{edimax}) \approx 0.5$. The total fraction of negative charge of the plasma born by monomer anions remains larger than 60%.

6. The influence of gas temperature

Increasing the gas temperature reduces particle formation in SiH_4 discharges [5,6]. This cannot be simply attributed to thermophoresis [7], nor to a decrease in gas density when working at constant $P = Nk_B T$. Thus a close examination of the temperature-dependent rates of cluster growth kinetics at constant N is necessary.

Fast electron impact dissociation of SiH_4 into SiH_m radicals is not affected by T but the diffusion rates of these primary radicals and of all neutral clusters to the walls are proportional to $N^{-1} T^{1/2}$. Nevertheless, this should not affect the rate of condensation of SiH_m monomers on neutral i -clusters, $k_{1i}[\text{SiH}_m]$, since $k_{1i} \propto T^{1/2}$ whereas $[\text{SiH}_m] \propto T^{-1/2}$. However, radical SiH_4 reactions can be thermally activated. We have recently demonstrated [33] that the increase of the a-Si:H deposition rate between 100 and 250 °C in a powder-free low-pressure SiH_4 discharge at constant N and power density could be attributed to the thermally activated insertion reaction of H in SiH_4 enhancing the yield of SiH_3 radicals. On the other hand, we also observed by mass spectrometry a decrease in the yield of higher order silanes (Si_2H_6 and Si_3H_8), which suggests that the chain propagating sequence $\text{SiH}_2 + \text{Si}_n\text{H}_{2n+2} + \text{M} \rightarrow \text{Si}_{n+1}\text{H}_{2(n+1)+2} + \text{M}$ is hindered by

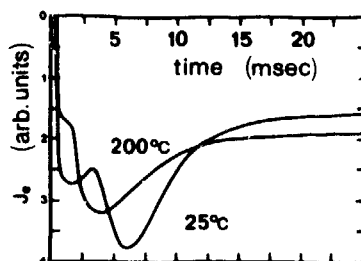


Figure 8. Perturbation of the radiofrequency-averaged electron current at the wall, J_e , after plasma ignition at two gas temperatures, keeping a constant gas density $N = 2 \times 10^{18} \text{ cm}^{-3}$ (0.13 mbar at 200 °C) and the same electrical parameters as in figure 1.

thermally activated reverse decomposition of large silanes. Nevertheless, these opposite trends cannot account for the temperature-dependence of cluster formation, which should be considered in terms of the anion physico-chemistry.

The decrease of the mutual neutralization rate as $k_m \propto T_i^{-1/2} \approx T^{-1/2}$ could reduce clustering via associative anion-cation reactions but we have shown that this contributes at most one quarter of small cluster growth. On the other hand, decreasing k_m increases the anion lifetime, which should favour nucleation, in contradiction with observation.

Temperature should enhance the dissociative attachment rate k_{da} to SiH_4 and thus the yield of primary SiH_3^- anions but strongly reduce the non-dissociative attachment k_a to radicals and small clusters due to decrease of the autodetachment lifetime τ_{ad} [23,24]. Howling *et al* [12] observed an increase of the flux of molecular anions when heating the electrode, which is compatible with an increase of k_{da} and a brake upon nucleation by a decrease of k_a . Since we attributed to attachment to radicals the perturbation of J_e at the first step t_0 after plasma ignition (figure 2), we repeated the experiment at two gas temperatures and the same SiH_4 density. Figure 8 shows that the amplitude of the perturbation is larger at 25 °C than at 200 °C, which tends to confirm that a decrease of k_a might cause a reduction of powder formation.

7. Evaluation of other cluster nucleation schemes

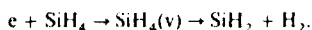
Three other cluster nucleation schemes not based on anion plasma chemistry have been proposed during the last few years.

Anderson *et al* [34] have studied the formation of silicon nitride particles from SiH_4 NH_3 discharges. They first analysed the possibility of gas-phase nucleation from radical molecule reactions or cation molecule reactions and argued that gas-phase mechanisms cannot account for their experimental observations. However, they have forgotten to examine nucleation

from anion plasma chemistry, which can apply to their case. Then they proposed a mechanism in which particle nucleation is induced by sputtering of silicon nitride clusters from the deposited film on the wall. Although this mechanism is likely to occur in high-power discharges, in which large sheath electric fields can develop on the cathode, it can be certainly rejected in our case and in the experiments by Hollenstein *et al* and Boufendi *et al* since we could obtain excellent reproducibility of temporal evolution of discharge properties and particle formation when igniting the discharge on clean reactor walls or after thin film deposition under various conditions.

Mandich and Reents [35] have shown that the addition of a few mole percent of water vapour to SiH_4 can lead to cluster growth of apparently unlimited size by cation-molecule reactions. However, the water contamination in our PECVD reactors has been checked by mass spectrometry and remains well below 0.1%.

Veprek *et al* [36] have recently argued that the mechanism of cluster formation cannot proceed from anion reactions but rather from SiH_2 radical insertion reactions leading to the building up of large polysilanes. We reject their conclusions for several reasons. First, the authors underline that the rate of primary anion production by dissociative attachment to SiH_4 is too low but they forget that anions are trapped in the plasma and therefore have a much longer residence time than cations or neutrals. Moreover, we have here emphasized the role of non-dissociative attachment to radicals or neutral clusters. Secondly, they have misunderstood the apparent anticorrelation between negative ion detection and powder accumulation in the plasma reported by Howling *et al* in square-wave modulated discharges [12, 13]. Thirdly, the SiH_2 -insertion reaction scheme proposed by Veprek *et al* starts from the hypothesis that the dominant SiH_4 dissociation pathway by electron impact is a plasma-induced pyrolysis of the molecule by vibrational excitation:



Unfortunately this dissociation mechanism has not received any theoretical justification, contrary to what the authors claim on the basis of their previous work. As a matter of fact, modelling and diagnostics of power dissipation in SiH_4 discharges [37] show that the rotational and vibrational temperatures attained by SiH_4 molecules remain much too low to induce significant gas-phase pyrolytic dissociation. Most research groups involved in SiH_4 plasma chemistry diagnostic and modelling studies now agree that the dominant SiH_4 electron-impact dissociation mechanism is dissociative electronic excitation leading to fragmentation into SiH_3 , SiH_2 , SiH and H atoms, and that a-Si:H deposition is mostly due to radical chemisorption, SiH_3 being the dominant species under moderate pressure conditions (about 0.1 mbar) [38–41]. Finally, the correlation between a drop in polysilane densities and onset of powder formation that is the basis of the argument of Veprek *et al* is not verified in experiments conducted at constant

pressure and constant power density under square-wave modulation in RF discharges. Moreover, only anion-assisted nucleation mechanism according to the model of Choi and Kushner complemented by the present analysis of anion cluster chemical kinetics can explain the temporal evolution of cluster formation over several tens of seconds.

Acknowledgments

We are grateful to A Howling and Ch Hollenstein for providing results of Mie scattering and anion mass spectrometry prior to publication. We also thank A Bouchoule, J P Boeuf and Ph Belenguer for fruitful collaborations and discussions. This work was supported by the BRITE-EURAM project BE-4529 of the European Community and by a grant from the Centre National d'Etude des Télécommunications (CNET) of France-Telecom.

References

- [1] Spears K, Robinson T M and Roth R 1986 *IEEE Trans. Plasma Sci.* **14** 179; Spears K G, Kampf R P and Robinson T J 1988 *J. Phys. Chem.* **92** 5297
- [2] Selwyn G S, Heidenreich J E and Haller K L 1990 *Appl. Phys. Lett.* **57** 1876; 1991 *J. Vac. Sci. Technol. A* **9** 2817
- [3] Watanabe Y, Shiratani M, Kubo Y, Ogawa I and Ogi S 1988 *Appl. Phys. Lett.* **53** 1263; Watanabe Y, Shiratani M and Yamashita M 1992 *Appl. Phys. Lett.* **61** 1510
- [4] Yoo W J and Steinbrüchel Ch 1992 *J. Vac. Sci. Technol. A* **10** 1041
- [5] Howling A A, Hollenstein Ch and Paris P J 1991 *Appl. Phys. Lett.* **59** 1409; Dorier J L, Hollenstein Ch, Howling A A and Kroll U 1992 *J. Vac. Sci. Technol. A* **10** 1048
- [6] Bouchoule A, Plain A, Boufendi L, Blondeau J Ph and Laure C 1991 *J. Appl. Phys.* **69** 1991; Boufendi L, Plain A, Blondeau J Ph, Bouchoule A, Laure C and Toogood M 1992 *Appl. Phys. Lett.* **60** 169; Boufendi L, Bouchoule A, Porteus R K, Blondeau J Ph, Plain A and Laure C 1993 *J. Appl. Phys.* **73** 2160
- [7] Jellum G M and Graves D B 1990 *J. Appl. Phys.* **67** 6490; 1990 *Appl. Phys. Lett.* **57** 2077; Jellum G M, Daugherty J E and Graves D B 1991 *J. Appl. Phys.* **69** 6923
- [8] Boeuf J P 1992 *Phys. Rev. A* **46** 7910; Belenguer Ph, Blondeau J Ph, Boufendi L, Toogood M, Plain A, Bouchoule A, Laure C and Boeuf J P 1992 *Phys. Rev. A* **46** 7923
- [9] Sommerer T J, Barnes M S, Keller J H, McCaughey M J and Kushner M J 1991 *Appl. Phys. Lett.* **59** 638; Barnes M S, Keller J H, Forster J C, O'Neill J A and Coultas D K 1992 *Phys. Rev. Lett.* **69** 313
- [10] Daugherty J E, Porteus R K, Kilgore M D and Graves D B 1992 *J. Appl. Phys.* **72** 3934; Daugherty J E, Porteus R K and Graves D B 1993 *J. Appl. Phys.* **73** 1617; Kilgore M D, Daugherty J E, Porteus R K and Graves D B 1993 *J. Appl. Phys.* **73** 7195
- [11] Choi S J and Kushner M J 1993 *J. Appl. Phys.* **74** 853
- [12] Howling A A, Dorier J L and Hollenstein Ch 1993 *Appl. Phys. Lett.* **62** 1341.

- Howling A A, Sansonnens L, Dorier J L and Hollenstein Ch 1993 *J. Phys. D: Appl. Phys.* **26** 1003
- [13] Hollenstein Ch, Dorier J L, Dutta J, Sansonnens L and Howling A A 1994 *Plasma Sources Sci. Technol.* **3** 278-85
- [14] Böhm C and Perrin J 1991 *J. Phys. D: Appl. Phys.* **24** 865
- [15] Perrin J 1991 *J. Non-Cryst. Solids* **137&138** 639
- [16] Boeuf J P and Belenguer Ph 1992 *J. Appl. Phys.* **71** 4751 and private communications
- [17] Perrin J and Schmitt J P M 1992 *Proc. 11th European Photovoltaic Solar Energy Conf.* ed L. Guimaraes et al (Coire, Switzerland: Harwood) p 80
- [18] Verdeyen J T, Beberman J and Overzet L 1990 *J. Vac. Sci. Technol. A* **8** 1851
- [19] Haaland P 1990 *J. Chem. Phys.* **93** 4066
- [20] Srivastava S K, Krishnakumar E and de Souza A C 1991 *Int. J. Mass Spectrom. Ion Proc.* **107** 83; Krishnakumar E, Srivastava S K and Iga I 1991 *Int. J. Mass Spectrom. Ion Proc.* **103** 107
- [21] Payzant J D, Tanaka K, Betowski L D and Bohme D K 1976 *J. Am. Chem. Soc.* **98** 894
- [22] Fledderman C, Beberman J and Verdeyen J T 1985 *J. Appl. Phys.* **58** 134
- [23] Christophorou L G 1980 *Environ. Health Perspect.* **36** 3
- [24] Christophorou L G, Hunter S R, Carter J G and Spyrou S M 1985 *Swarm Studies and Inelastic Electron-Molecule Collisions* ed L C Pitchford et al (Springer: New York) p 303
- [25] Christodoulides A A, Christophorou L G, Pai R Y and Tung C M 1979 *J. Chem. Phys.* **70** 1156; Pai R Y, Christophorou L G and Christodoulides A A 1979 *J. Chem. Phys.* **70** 1169
- [26] Hickman A P 1979 *J. Chem. Phys.* **70** 4872
- [27] Castelman A W and Keese R G 1986 *Chem. Rev.* **86** 589
- [28] Reents W D and Mandich M L 1992 *J. Chem. Phys.* **96** 4429;
- Mandich M L and Reents W D 1992 *J. Chem. Phys.* **96** 4233 and references therein
- [29] Perrin J, Lloret A, de Rosny G and Schmitt J P M 1984 *Int. J. Mass Spectrom. Ion Proc.* **57** 249
- [30] Mandich M L and Reents W D 1989 *J. Chem. Phys.* **90** 3121
- [31] Gioumousis G and Stevenson D P 1958 *J. Chem. Phys.* **29** 294
- [32] Mandich M L, Bondybyev V E and Reents W D 1987 *J. Chem. Phys.* **86** 4245
- [33] Böhm C, Perrin J and Roca i Cabarrocas P 1993 *J. Appl. Phys.* **73** 2578
- [34] Anderson H M, Jairath R and Mock J L 1990 *J. Appl. Phys.* **67** 3999
- [35] Mandich M L and Reents W D 1992 *J. Chem. Phys.* **96** 4245
- [36] Veprek S, Schopper K, Ambacher O, Rieger W and Veprek-Heijman M G J 1993 *J. Electrochem. Soc.* **140** 1935
- [37] Perrin J 1993 *J. Phys. D: Appl. Phys.* **26** 1662
- [38] Doyle J R, Doughty D A and Gallagher A 1990 *J. Appl. Phys.* **68** 4375; Doughty D A and Gallagher A 1990 *J. Appl. Phys.* **67** 139; 1990 *Phys. Rev. A* **42** 6166; Doughty D A, Doyle J R, Lin G H J R and Gallagher A 1990 *J. Appl. Phys.* **67** 6220
- [39] Itabashi N, Kato K, Nishiwaki N, Goto T, Yamada C and Hirota E 1989 *Japan. J. Appl. Phys.* **29** L505
- [40] Matsuda A, Nomoto K, Takeuchi Y, Suzuki A Yuuki A and Perrin J 1990 *Surf. Sci.* **227** 50
- [41] Kushner M J 1988 *J. Appl. Phys.* **63** 2532
- [42] Cheshnovsky O, Yang S H, Peltiette C L, Craycraft M J, Liu Y and Smalley R E 1987 *Chem. Phys. Lett.* **138** 119
- [43] Raghavachari K and McMichael Rohlffing C 1991 *J. Chem. Phys.* **94** 3670

Particle nucleation and growth in a low-pressure argon-silane discharge

L Boufendi and A Bouchoule

Groupe de Recherche sur l'Energétique des Milieux Ionisés, Unité de Recherche Associée au CNRS (URA 831), UFR Sciences, Université d'Orléans, BP 6759, 45067 Orléans Cedex 02, France

Received 3 January 1994, in final form 11 January 1994

Abstract. The growth of particle size has been measured in a low-pressure argon-silane plasma using high-resolution transmission electronic microscopy. The results show that formation and growth of dust particles is an homogeneous process; the first generation size distribution is monodispersed; and the growth kinetics reveals a three-step process from molecular ions to large particles. Together with measurements of particle concentration obtained by laser light scattering, these measurements give a clear indication that the growth proceeds through three successive steps: (i) 'rapid' formation of crystalline clusters (as shown by dark-field high-resolution transmission electron microscopy) with concentrations of up to 10^{10} cm^{-3} ; (ii) formation of aggregates, of diameters up to 50 nm, by coagulation (during coagulation the particle concentration decreases dramatically); and (iii) growth of the particles with a constant concentration by surface deposition of SiH_3 radicals, whilst the numerical density remains constant. Laser-induced particle explosive evaporation has been performed using a XeCl (308 nm) laser. This experiment allowed detection of nanocrystallites and also the beginning of their coagulation and gave clear evidence of the temperature effect on particle formation.

1. Introduction

Particles occurring in low-pressure discharges used in semiconductor manufacturing are considered as an important source of device contamination [1]. They have been observed in practically all plasmas used for etching [2, 3], deposition [1, 4, 5] and sputtering [6-8]. Furthermore, much effort has been devoted to production of materials based on plasma-synthesized nanoscale particles [9]. In this contribution we focus our interest on particle nucleation and growth. These two aspects are important, in terms of both fundamental knowledge and potential applications.

Many workers have measured particle sizes in the range 10-1000 nm [1, 6, 10, 11]. Two experimental techniques have been used: *in situ* laser light scattering (LLS) and *ex situ* transmission electron microscopy (TEM) [12]. However, for scattering measurements, when the particle radius is smaller than the wavelength of the incident light λ , the scattered intensity is proportional to (R^6/λ^4) ; hence this method is extremely sensitive to any large particles. Therefore care is required if a polydisperse distribution, as observed in this work, is present. In previous work particle sizes were estimated from photomicrographs of particles collected at surfaces placed in the discharge [13]. This method indicates the range of particle sizes but does not provide time-resolved information on formation and growth kinetics. In this report we present results on particle size and concentration kinetics in the preliminary step of formation.

The measurements were carried out on particles produced in a low-pressure argon-silane RF discharge and performed by time-resolved statistical TEM analysis.

The (R^6/λ^4) law (Rayleigh scattering), in the small particle size domain, leads to a size limitation of scattering as a diagnostic technique. For example, using the blue (488 nm) line of the Ar^+ laser, the scattered intensity becomes observable at about 2 s. At this time, as we shall see, the particle mean size (diameter) is about 20 nm. Clearly the LLS method is not sufficiently sensitive to detect 2 nm nanocrystals. We also present results obtained by laser-induced particle explosive evaporation (LIEPE) [15]. This technique can provide useful information on the first step of particle growth.

2. Experimental set-up

The experimental set-up has been described previously [4]. The RF discharge is produced in a earthed cylindrical box (13 cm inner diameter) equipped with a shower-type RF-powered electrode. A grid is used as the bottom of the chamber to allow vertical laminar flow in the discharge box. The discharge structure is surrounded by a cylindrical oven. The gas temperature can be varied from room temperature up to 200 °C and is measured in the gas flow below the discharge box by a thermocouple. Three vertical slits (2 mm width, 4 cm height) allow optical access to the plasma at 0°, 90° and 180° around

the chamber. The whole system is enclosed in a vacuum vessel of 30 cm height and inner diameter. Three optical viewports on the vacuum vessel (5 cm in diameter and 90° apart) are aligned with the observation slits.

For the TEM size measurements we use a particle collection device, which is a rotatable multigrid holder [14]. An aluminium conical tube with a 3 mm diameter hole (collection hole) on its upper surface covers the holder. The electron microscopy grid, in front of the collection hole, can collect particles swept down by the gas flow when the RF power is switched off. The grids are observed using JEOL 100 CX or Philips CM20 microscopes. Statistical analyses of the particle sizes are performed on these micrographs for given experimental conditions (gas flow, plasma duration and so on).

The LIPEE experiment is described in detail elsewhere [15]. It was performed using an XeCl laser (Lambda Physik EMG 100 MCS). The beam is focused in the discharge box through a window and the fluorescence signal is viewed at 90° to the laser beam through the access slits by either a photomultiplier tube (PMT RCA 7265 with a S1 photocathode) or an optical multichannel analyser (OMA) (EG&G OMA III model 1460) with a signal intensifier.

Throughout this work the experimental conditions were: argon flow 30 sccm, silane flow 1.2 sccm, total pressure 117 mTorr, RF power 10 W corresponding to 600 V (peak to peak) and ambient temperature.

3. Results and discussion

3.1. Size kinetics

Figure 1 shows the time evolution of the mean particle size for plasma durations in the range 0.5–300 s. In figure 1 we also present the standard deviation of the measured size distribution. Up to 30 s, a monodispersed distribution is obtained with small and constant dispersion as shown in figure 2. For long plasma durations (> 30 s) we can observe the occurrence of several well-defined particle sizes, corresponding to successive (in time) particle generations (figure 3). In the following, we

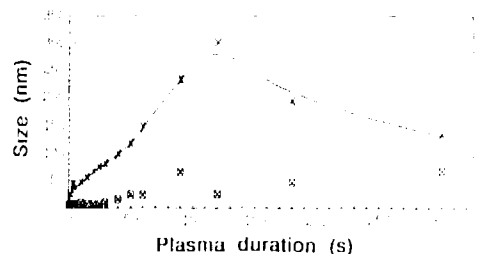


Figure 1. Time evolution of particle size over the time scale 0.5–300 s (x, mean size; [x], standard deviation).

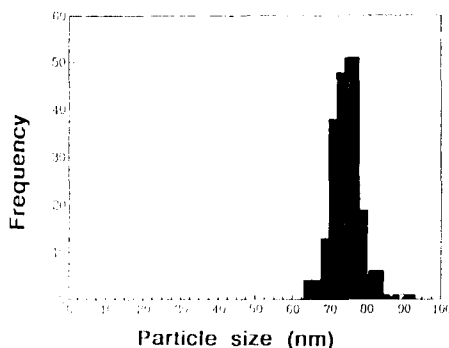


Figure 2. Histogram of the sizes of particles collected from plasmas of 25 s duration.

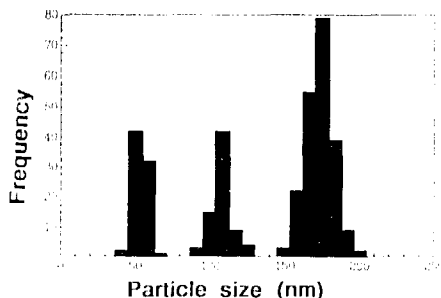


Figure 3. Histogram of the sizes of particles collected at 60 s.

will describe results obtained in the early initial part of these size kinetics ($t \leq 30$ s).

The evolution of particle sizes and concentration as generated for plasma durations from 1 to 30 s is illustrated in figure 4. The first result is the observation of two well-defined phases. The first phase corresponds to rapid increase in particle size (10 nm s^{-1}) and sharp decrease in concentration. In the second phase the concentration stays constant while the growth rate slows down to 2 nm s^{-1} . From these results we deduce the total mass $\frac{4}{3}\pi R^3 N_p \rho$ representing the particles present in the discharge for this period. As shown in figure 5, where we have assumed a constant specific mass ρ , this quan-

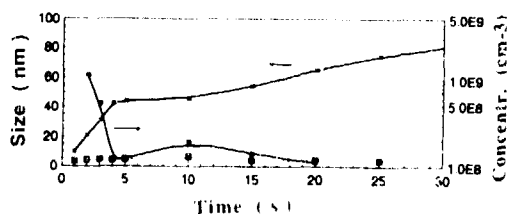


Figure 4. Time evolution of particle sizes (x), concentration (■) and standard deviation (x) up to 30 s.

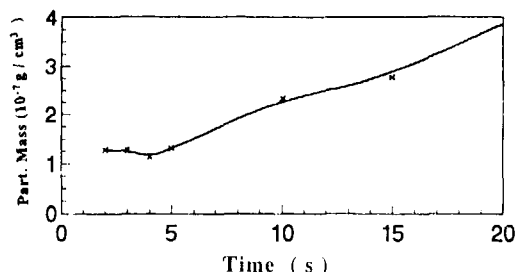


Figure 5. Time evolution of the total mass of particles present in the plasma.

tity is almost constant in the first phase and slowly increasing in the second one. This situation suggests that, in the first phase, the particle size growth is due to an agglomeration (coalescence) phenomenon, while in the second phase, it is due to a surface deposition (SiH_x species) process on independent particles.

These results are confirmed by the morphology of the particles, as observed by HRTEM [16]. The successive steps of agglomeration are clearly seen for the small

particles ($R < 25 \text{ nm}$) (figure 6(a)) while the 'big' ones ($R > 50 \text{ nm}$) have a spherical shape with moss surface (figure 6(b)).

Detailed inspection of the TEM micrographs of small particles (20–40 nm) reveals the presence of crystalline substructures of small size (2 nm). In order to investigate these structures they were examined using both electron diffraction (figure 7) and dark-field TEM micrography [16]. This confirmed that the particulate material, at this size scale, has a nanocrystalline structure, revealed by the diffraction patterns and dense distribution of bright points in the micrographs. These nanocrystallites have a well-defined size (2 nm) and must be formed in the few first milliseconds of the discharge, as will be explained below.

In the previous experiment, the TEM grids were always placed 2 cm from the axis of the reactor, while the LLS measurements were performed in the centre of the reactor. As previous work had shown the possibility of spatial segregation [10, 17] of particles as a function of their size, we studied the radial variations of particle size distribution, collecting particles coming from 19 different radial positions using a linear grid holder. Figure 8 presents the mean size of the three generations of particles as obtained for long plasma duration (60 s, see figure 3). A small radial segregation effect is only visible for the largest sized particles whose growth starts at $t = 0$ (first generation). This result shows that particle growth is radially uniform. The LLS measurements performed between the two electrodes along the reactor axis show that the particle distribution is almost uniform [4]. So under our conditions, the formation and growth of particles is a homogeneous process in the whole volume of the plasma.

(a)



(b)



Figure 6. (a) Transmission electron micrograph of particles formed in a plasma of 5 s duration. The particle mean diameter here is 45 nm. (b) Transmission electron micrograph of a particle formed after a plasma of 30 s duration. Its diameter is about 100 nm.

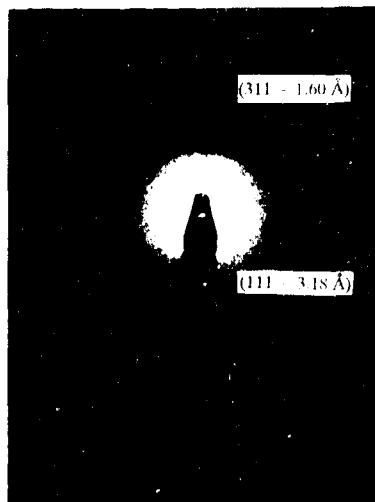


Figure 7. Electron diffraction pattern from particles of 40 nm size.

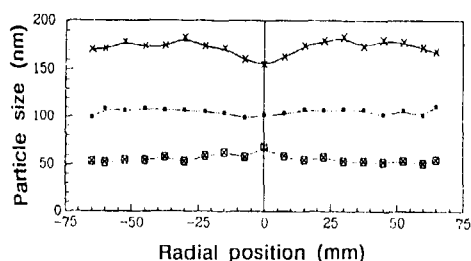


Figure 8. Radial distribution of the mean size of particles collected at 60 s (x, first generation; ■, second generation; and ⊠, third generation).

recorded, appears to be a powerful way to detect these very small entities.

To perform the LIPEE experiment we used the set-up represented in figure 9. The energy of the XeCl laser pulse ($\lambda = 308$ nm, 10 ns pulse) in the focal region is 25 mJ. The spot area has been evaluated to be about 1.25 mm^2 . The particles formed during a given plasma duration are irradiated 5 ms after the extinction of the plasma. All the particles localized in the focal region are completely evaporated.

The hot vapour produced by the high power of the pulsed XeCl laser is already ionized when ejected. This plasma is characterized by atomic and ion line emission and also by continuum emission due to recombination and the Bremsstrahlung effect. Electron-neutral species and electron-ion Bremsstrahlung is important during

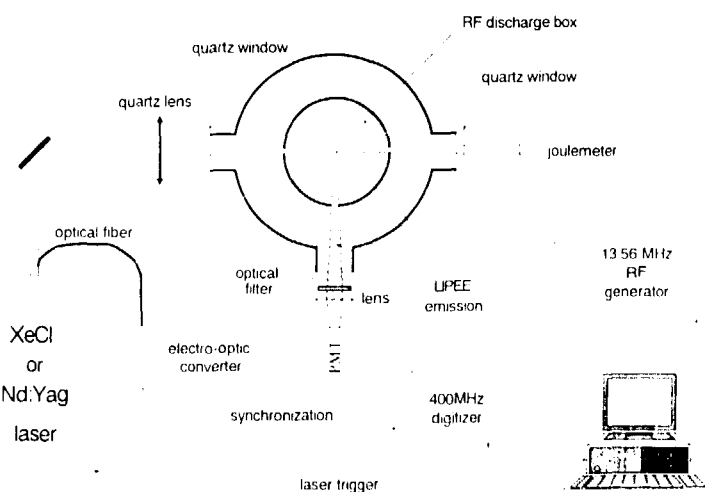


Figure 9. Schematic description of the laser-induced particle explosive evaporation experimental set-up.

It is interesting to point out that the growth phenomenon, as observed in this work in a three-dimensional system, exhibits the same statistical evolution as the 'breath figures' formed when water vapour condenses on a cold surface [18].

3.2. Particle detection

Particles appearing in plasma processing devices, or laboratory plasmas, are in general detected by light scattering. This method has clear limitations in terms of particle size. As reported above the smallest observable size, in our conditions, have diameter of about 20 nm for the Ar^+ line (488 nm) while for the 647 nm Kr^+ laser this limit is about 60 nm. The *in situ* detection of the primary crystallites of 2 nm diameter is not possible with these lasers.

The LIPEE experiment where the light emission induced by a XeCl excimer laser (power 200 MW cm^{-2}) is

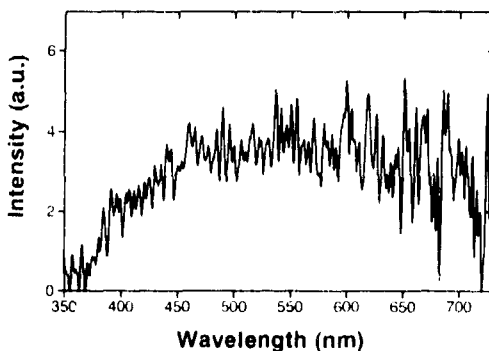


Figure 10. Laser-induced particle explosive evaporation spectrum obtained for particles formed in a 30 s duration plasma.

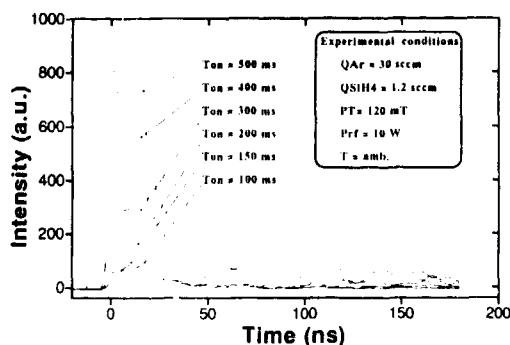


Figure 11. Typical laser-induced particle explosive evaporation signals.

the laser pulse, when the electronic density is high. Figure 10 shows the LIPEE spectrum obtained with particles formed after a plasma of 30 s duration, recorded using a spectrometer of 0.4 nm resolution (Jobin-Yvon UFS 200) and the OMA. The integration time is 100 ns.

Typical signals of light emission recorded with a PMT are shown in figure 11, for different plasma durations.

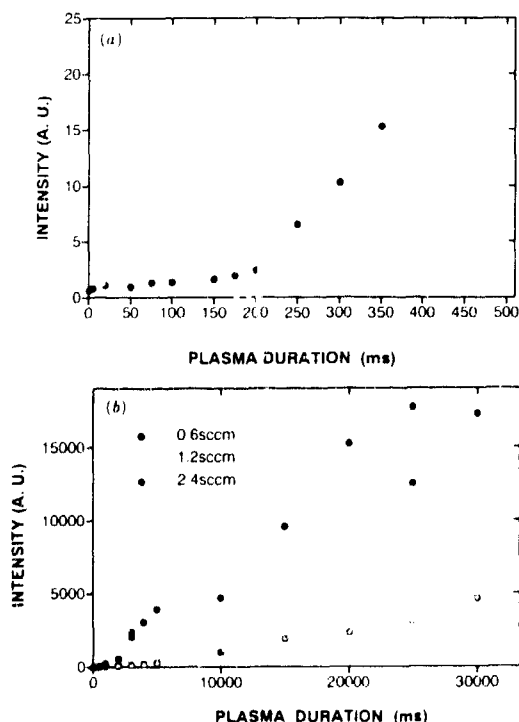


Figure 12. (a) Time evolution of signal intensity over short plasma durations. (b) Time evolution of signal intensity up to 30 s plasma duration.

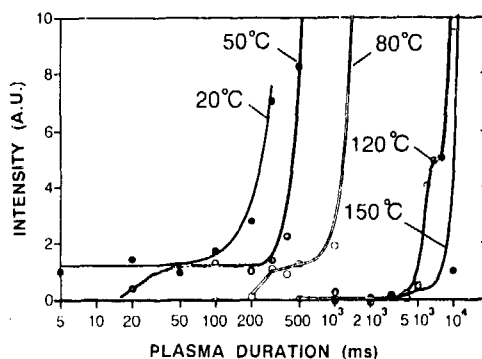


Figure 13. Temperature effects on particle formation.

The time evolutions of the intensity of these light pulses are shown in figure 12. Figure 12(a) shows the evolution of the signal corresponding to short plasma durations. Two well-defined phases are observable. The first corresponds to the crystallites, which occur rapidly (within a few milliseconds) when the discharge is switched on. The fast increase, observed here at about 150 ms, corresponds to the beginning of the coalescence step. Figure 12(b) shows this evolution up to 30 s.

To be trapped in the plasma, the crystallites must be negatively charged. This charge may come from hydrogenated silicon negative ions, which are suspected to be the precursors of these particles [19]. These nanocrystallite particles have no effect on the plasma properties [20]. Their effects begin at about 400 ms, when the particle size is about 5 nm.

The effect of temperature on particle formation has been studied. Figure 13 shows the time evolution of LIPEE signal intensity for different temperatures. The most important conclusion that we can formulate is that higher temperatures delay the appearance of crystallites; but when they do appear, they grow as explained above.

4. Conclusion

We have presented measurements of particle growth. Particle formation follows three well-defined steps. The initial step corresponds to formation of crystallites (2 nm) followed by coagulation leading to small particles (about 50 nm) that become increasingly negatively charged, which then grow by surface deposition processes on independent particles. The first step has been clearly seen by excimer laser-induced fluorescence performed on the particles. As yet the coalescence mechanisms are not understood.

It is well known that particles can strongly influence discharge properties but the most important information that we get through both spectroscopic investigations and LIPEE is that the beginning of these effects occurs only once the crystallites have aggregated to form particles whose sizes are ≥ 6 nm.

Acknowledgments

This work has been supported by the CNRS-PIRSEM under contract 89N80/0095 and BRITE-EURAM contract BREU-CT91-0411.

References

- [1] Selwyn G S, Singh J and Bennett R S 1989 *J. Vac. Sci. Technol. A* **7** 2758;
Donovan R P (ed) 1990 *Particle Control for Semiconductor Manufacturing* (New York: Marcel Dekker)
- [2] Spears K G, Robinson T J and Roth R M 1986 *IEEE Trans. Plasma Sci.* **14** 179
- [3] Watanabe Y, Shiratani M, Kubo Y, Ogawa I and Ogi S 1988 *Appl. Phys. Lett.* **53** 1263
- [4] Bouchoule A, Plain A, Boufendi L, Blondeau J Ph and Laure C 1991 *J. Appl. Phys.* **70** 1991
- [5] Stadler K R 1989 *Proc. SPIE* **1185** 164
- [6] Jellum G M and Graves D B 1990 *J. Appl. Phys.* **67** 6490
- [7] Selwyn G S, McKillop J S, Haller K H and Wu J J 1990 *J. Vac. Sci. Technol. A* **8** 1726
- [8] Selwyn G S, Heidenreich J E and Haller K L 1990 *Appl. Phys. Lett.* **57** 1876
- [9] Ho P, Buss R S and Loehman R E 1989 *J. Mater. Res.* **4** 873;
- Anderson H M, Kodas T T and Smith D M 1989 *Ceramic Bull.* **68** 996;
- Iahn H and Averback R S 1990 *J. Appl. Phys.* **67** 113;
- Chow G M, Holtz R L, Pattnaik A, Edelstein A S, Schlesinger T E and Cammarata R C 1990 *Appl. Phys. Lett.* **56** 1853
- [10] Spears K G, Kampf R P and Robinson T J 1988 *J. Phys. Chem.* **92** 5297
- [11] Hurd A J and Ho P 1989 *Phys. Rev. Lett.* **62** 3034
- [12] Ganguly B, Garscadden A, Williams J and Haaland P 1993 *J. Vac. Sci. Technol. A* **11** 1119
- [13] Shiratani M, Kubo Y, Ogawa I, Matsuo S, Makino H, Ogi S and Watanabe Y 1988 *Proc. Japan. Symp. Plasma Chem.* **1** 145
- [14] Boufendi L, Plain A, Blondeau J Ph, Bouchoule A, Laure C and Toogood M 1992 *Appl. Phys. Lett.* **60** 169
- [15] Boufendi L, Hermann J, Stoffels E, Stoffels W, De Giorgi M L and Bouchoule A *J. Appl. Phys.* submitted
- [16] Bouchoule A and Boufendi L 1993 *Plasma Sources Sci. Technol.* **2** 204
- [17] Jellum G M and Graves D B 1990 *Appl. Phys. Lett.* **57** 2079
- [18] Beysens D, Knobler C M and Schaffar H 1990 *Phys. Rev. B* **41** 9814;
Derrida B, Godrèche C and Yekutieli I 1991 *Phys. Rev. A* **44** 6241
- [19] Howling A A, Sansonnens L, Dorier J L and Hollenstein Ch 1993 *J. Phys. D: Appl. Phys.* **26** 1003
- [20] Bouchoule A and Boufendi L 1994 *Plasma Sources Sci. Technol.* **3** 292-301

Gas phase particulate formation in radiofrequency fluorocarbon plasmas

Richard J Buss and Willard A Hareland

Sandia National Laboratories, Albuquerque, New Mexico 87185, USA

Received 28 December 1993; in final form 18 January 1994

Abstract. The production, suspension and transport of fluorocarbon particulates in capacitively coupled radiofrequency discharges are studied using *in situ* laser light scattering and *ex situ* chemical analysis. The time evolution of the spatial distribution of suspended particles is obtained by two-dimensional imaging of the scattered light. The chemistry of the discharge is varied by use of a range of pure fluorocarbon gases and mixtures with argon, oxygen and hydrogen-containing molecules. Addition of hydrogen to a fluorocarbon discharge increases the rate of formation of particles although these powders are found by Fourier transform infrared measurements to contain negligible amounts of hydrogen. Particle formation rates correlate with polymer deposition rates and are independent of apparatus history. It is proposed that this is a clear example of gas phase rather than surface processes leading to particle nucleation and growth.

1. Introduction

Fluorocarbon plasmas find widespread application in industrial manufacturing, particularly in microelectronics. Many plasma etching formulae for silicon or its compounds call for use of CF_4 , C_2F_6 or CHF_3 alone or as a component of a gas mixture [1]. Unsaturated or aromatic fluorocarbons, such as C_2F_4 and $\text{C}_6\text{F}_4(\text{CF}_3)_2$, are used for thin film deposition in a range of applications such as chemically resistant barriers, mould release and dry lubricants [2]. Plasma-polymerized C_2F_4 is used to fabricate fibre-optic-based chemical sensors [3, 4]. For most of these applications, formation of particulates is undesirable or unacceptable.

The chemistry of plasma deposition of fluorocarbon films from C_2F_4 has been the subject of much study [5], although the details of the mechanism are not yet known at the molecular level. Much less has been reported on fluorocarbon particulate formation. In an early study by Liepins and Sakaoku [6], it was shown that particulates could be generated in a C_2F_4 inductively coupled plasma at elevated pressures (0.8 Torr). Buzzard *et al* [7] reported production of particulates from a capacitively coupled C_2F_4 plasma at reduced pressure and high power.

Several mechanisms for production of particulates in RF plasmas have been proposed, including gas-phase nucleation and growth and surface-mediated growth. Here we report a study of the formation of particles in fluorocarbon-containing plasmas. Laser light scattering is used to monitor the appearance and trapping of particles. Particles are collected and analysed by Fourier transform infrared absorption (FTIR) and transmission electron microscopy (TEM). A range of gas flow rates,

pressures and gas compositions are explored. It is argued that gas-phase nucleation and growth is the dominant mechanism leading to particle formation.

2. Experimental

The plasma apparatus is a modified version of a chamber used earlier for synthesis of silicon nitride particles [8]. It consists of a 46 cm cubic aluminium chamber equipped with 15 cm diameter parallel-plate electrodes with 3 cm separation. Gas is delivered to the chamber either through the upper, grounded electrode in shower-head configuration, or directly through a single orifice at the top of the apparatus. For most of the experiments, the electrode temperature is not controlled, but, to study the effect of thermophoresis, the powered electrode is water-cooled. 13.56 MHz power is delivered through an impedance-matching network to the lower electrode. A voltage probe monitors the RF voltage and self-bias on the lower electrode.

A 10 mW helium–neon laser is used to detect particles in the plasma. The laser beam is expanded into a plane by passing through a horizontal glass tube (diameter 1.66 cm). The resulting beam propagates 254 cm to the electrodes with apertures to give a divergence in the vertical plane of 6.5°, such that the laser fills almost the entire vertical space between the electrodes. Scattered laser light is observed in one of two geometries. A charge-coupled device (CCD) camera views the plasma through the quartz exit window and detects small-angle light scattering. Additionally, monochromatic images of the scattered 632 nm light are obtained with an intensified CCD camera viewing the 90° scattered light through

a monochromator. Imaging is achieved by equipping the monochromator with both entrance and exit slits and using a single lens to focus the output onto the camera [9]. The monochromator can also be tuned to specific emission lines to obtain two-dimensional images of plasma emission. Particle generation rates are determined by measuring the time from plasma initiation to first detection of particles by light scattering.

We obtain transmission FTIR spectra of powder samples removed from the apparatus and reflectance IR spectra of thin films deposited on copper substrates placed on the powered electrode. After long plasma operation times, the particles accumulate in thick deposits on the electrode assemblies outside the plasma region.

Particle appearance times are measured for a large number of plasma chemistries. Most experiments use C_2F_4 mixed with a second gas including argon, hydro-

gen, deuterium, oxygen, methane and *trans*-2-butene. Additionally, vinylidene fluoride ($1,1-C_2H_2F_2$) or CF_4 is used as the fluorocarbon. The deposition rate of fluorocarbon film is determined by placing partially masked silicon substrates on the lower electrode, and determining film thickness by post-plasma profilometry.

Particle samples for TEM are prepared by extinguishing the plasma immediately after first appearance and allowing the particles to cascade onto carbon TEM grids. In addition, samples of particles that accumulate as wall deposits are suspended in *n*-butanol and transferred to TEM grids.

3. Results and discussion

Formation of particles in the plasma is readily monitored by laser light scattering. Figure 1 shows a sequence of monochromatic images (false colour)

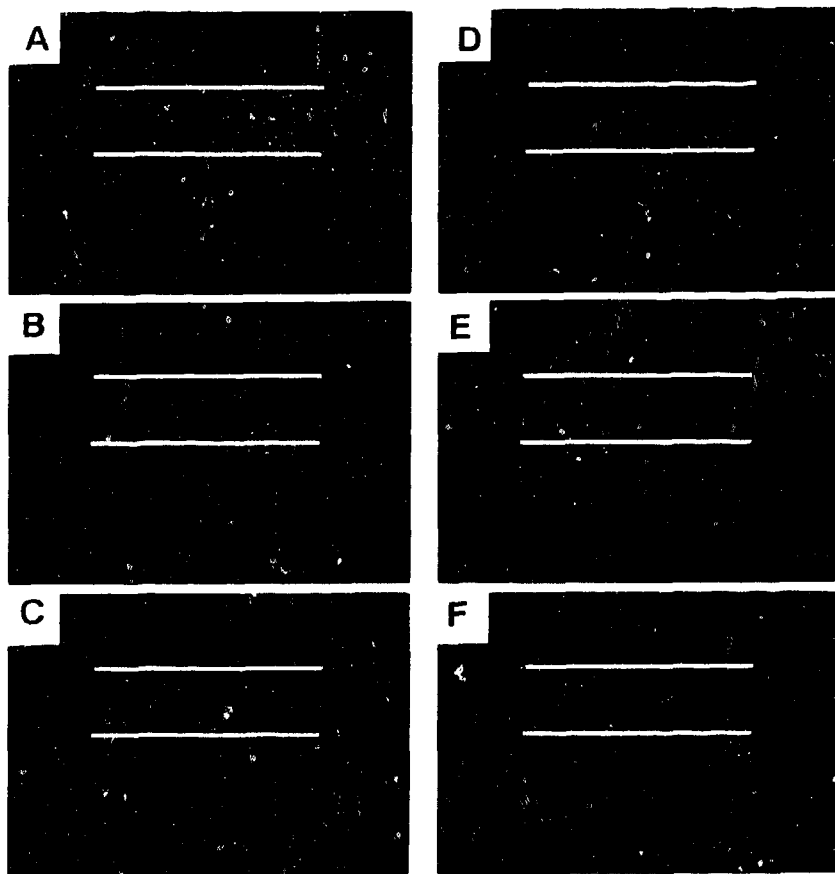


Figure 1. False-colour monochromatic images of particles in a $1,1-C_2H_2F_2$ plasma. A is at first appearance of particles at 11 s, B–F are sequential at 30 s intervals thereafter. Each image shows scattering from a continuous plane of 633 nm laser light.

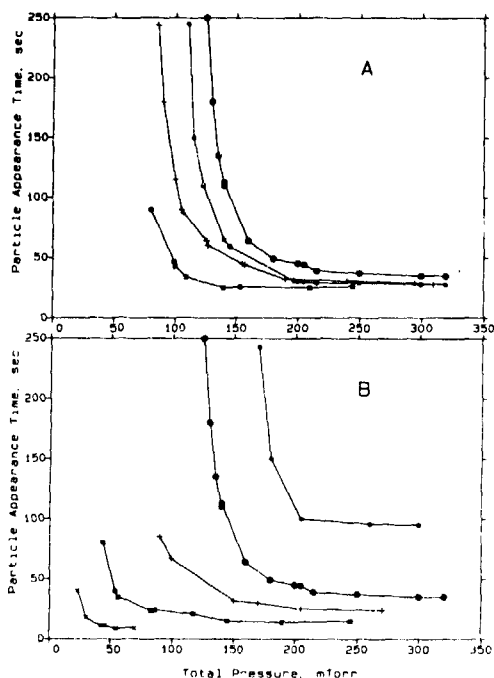


Figure 2. Particle appearance times for various gas mixtures (flow rates, f , in sccm). A: C_2F_4 ($f = 20$) (●), C_2F_4 and D_2 ($f = 20$ and 2.5) (○), C_2F_4 and D_2 ($f = 20$ and 5) (+), C_2F_4 and D_2 ($f = 20$ and 10) (□); B: C_2F_4 ($f = 20$) (●), C_2F_4 and O_2 ($f = 20$ and 5) (○), CF_4 and D_2 ($f = 20$ and 10) (+), C_2F_4 and CH_4 ($f = 20$ and 10) (□), 1,1- $C_2H_2F_2$ ($f = 20$) (X). Lines are drawn between points to guide the eye.

obtained from a vinylidene fluoride plasma (0.027 Torr, 15 sccm flow rate, 30 W RF power, gas introduced at top of chamber). The time to first detection of particles is 11 s. The particles develop in size and segregate into a pattern, which evolves in time. The spatial pattern of particles is sensitive to the electrode geometry, temperature and gas flow rates. For example, if the gas is delivered at high flow rates in shower-head configuration, then the particles in this apparatus are found in rings near the outer edge of the electrodes. Likewise, the post-plasma behaviour of the particles is strongly affected by details of fluid flow and electrode temperature. Images were recorded in which, at extinction of the plasma, the particles move rapidly (8 cm s^{-1}) upward under the influence of a small temperature gradient. This effect is reversed by cooling of the lower electrode.

The time to first appearance of particles is found to be relatively independent of the above conditions, but is quite sensitive to the total pressure for the chemistries studied here. In figure 2(a) is shown the first appearance time of particles as a function of total pressure for pure C_2F_4 gas (20 sccm, 30 W). Typically, there is a pressure below which particle formation is not observed. The

appearance time becomes independent of pressure at high pressures.

Also shown in figure 2(a) is the effect of added deuterium gas. The presence of D_2 in the plasma greatly accelerates formation of particulates at a given pressure, and lowers the pressure at which particles are first observed. Figure 2(b) shows the particle appearance time in mixtures of C_2F_4 with CH_4 and O_2 . The acceleration of particle formation is very dramatic for methane (and for *trans*-2-butene, not shown). In contrast, O_2 suppresses particle formation until much higher pressures are achieved. Also shown in figure 2(b) is the extreme behaviour of vinylidene fluoride, for which particle formation is very rapid even at low pressures. Particle appearance time is independent of gas flow rate. Mixtures of C_2F_4 with argon (20% Ar) give appearance times indistinguishable from those for pure C_2F_4 .

The FTIR spectra of particles formed from each of the plasma chemistries are generally very similar to spectra of thin films deposited on substrates placed in the plasma (compare figure 3 curves B and C). In all cases, the spectral features correspond to a fluorocarbon. The major absorption, the C—F stretch at $1170\text{--}1230 \text{ cm}^{-1}$, is broad with minor substructure. Surprisingly, addition of CH_4 , D_2 or H_2 to the plasma does not result in significant incorporation of hydrogen into the particles, as seen in figure 3 curves A and B (less than 1%). Only when high concentrations of butene are added does the CH absorption appear in the FTIR spectrum.

The TEM results show that the particles (figure 4(a)) are spherical and non-agglomerated with diameter in the range 110–270 nm. Particles that accumulate on the walls during extended plasma operation (figure 4(b)) have individual particle sizes also about 150 nm but are

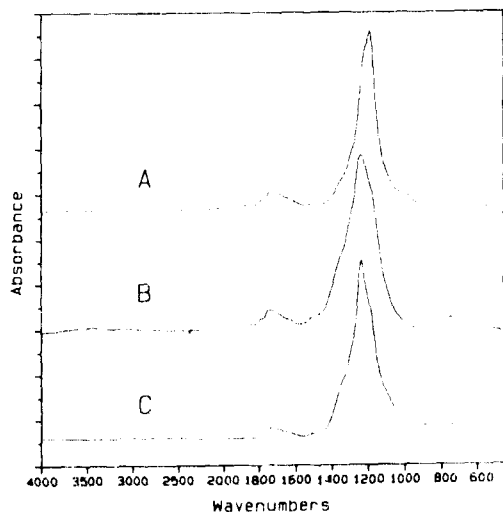


Figure 3. Fourier transform infrared absorption spectra. A powder formed in a pure C_2F_4 plasma; B, powder formed in a C_2F_4 , H_2 plasma; and C, thin film formed in a C_2F_4 , H_2 plasma.

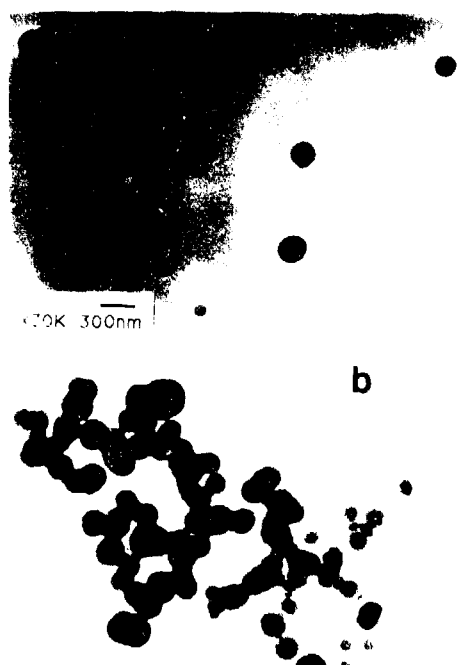


Figure 4. Transmission electron micrographs of fluorocarbon particles: (a) deposited directly on carbon grids, from a C_2F_4 plasma at 140 mTorr; and (b) particles collected from electrode assembly, suspended in *n*-butanol and dispensed onto grids.

fused into strongly agglomerated chains. The spherical shape suggests uniform radial growth in the plasma as opposed to spatially non-uniform growth on a surface.

The observations reported here are qualitatively consistent with a gas-phase nucleation model, which supposes growth of particles in the plasma by attachment of gas-phase reactants. Immediately upon plasma ignition, reactive radicals (such as CF , CF_2 and CF_3) are generated from the fluorocarbon. Although the chemistries of these species are not well known, it is probable, based on hydrocarbon analogues, that CF or CF_2 addition to C_2F_4 is facile. Such collision complexes will be readily stabilized by three-body collisions even at these reduced pressures (based on RRKM calculations). As the particle grows, it will acquire a negative charge and become trapped [10], precluding loss through the sheath. When the particle has grown to around 200 nm, it scatters sufficient light to be detectable (at high particle number densities).

The appearance time for particles in a C_2F_4 plasma at 140 mTorr is measured to be 110 s. Assuming a constant radial growth rate (and 100–300 nm diameter), this corresponds to $0.5\text{--}1.4\text{ nm s}^{-1}$. Initial thin film growth on a substrate placed on the lower electrode occurs at a similar rate of 2 nm s^{-1} for the same plasma conditions. The film deposition rate is not uniform in time. The initial rate of $>2\text{ nm s}^{-1}$ falls to 0.3 nm s^{-1}

steady state when the plasma is loaded with particulates. A likely explanation is that the plasma-generated reactive molecules are strongly scavenged by the particles in the plasma, reducing their flux to the substrate. When the plasma is operated at pressures below onset of particle formation, the film deposition rate is constant in time. At 40 mTorr C_2F_4 pressure, very thick film ($>8000\text{ nm}$) can be deposited without the appearance of particles. While particle shedding from electrodes or walls may lead to particulates under some plasma conditions, it is clear that gas-phase processes predominate here.

It has been reported that hydrogen enhances the rate of film deposition in fluorocarbon plasmas [11]. This effect has been attributed to enhanced production of free radicals by hydrogen atom abstraction of fluorine [12]. The presence of hydrogen-containing molecules in the plasma significantly shortens the appearance time for particles. If the major role is, indeed, to increase the density of CF or CF_2 , this would qualitatively explain the lack of hydrogen incorporation in particulates or films despite the enhanced growth rates. The suppression of particles by oxygen can be attributed to blocking of attachment sites by O_2 or scavenging of the gas-phase radicals needed for growth.

The formation of particles in these experiments is independent of the apparatus history. The first plasma run after cleaning of the walls and electrodes has a particle appearance time within seconds of those of later runs. The electrodes and walls become coated with a fluorocarbon film and subsequent repetitions yield reproducible times. It is difficult to reconcile these observations with any mechanism that attributes a large role to surface formation of particles. While emission of CF_n moieties from the electrodes by sputtering may contribute to particle growth, the strong pressure-dependence of particle formation points to gas-phase nucleation as the predominant mechanism.

In summary, the combination of formation of spherical particles at a repeatable, fixed time after plasma initiation, independent of thickness of pre-deposited film and exhibiting a strong pressure-dependence, all point to a gas-phase growth process. The actual molecular sequence leading to nucleation is not, however, inferable from these experiments.

Acknowledgments

The authors wish to express their appreciation for the valuable technical assistance of Pamela Ward and Alex Pimentel and for the expert TEM work by Chuck Hills. This work was performed at Sandia National Laboratories and was supported by the USA Department of Energy under Contract DE-AC0476DP00789.

References

- [1] Oehrlein G S 1990 *Handbook of Plasma Processing Technology* ed S M Rossnagel et al (New Jersey: Noyes) ch 8

- [2] Boenig H V 1988 *Fundamentals of Plasma Chemistry and Technology* (Lancaster, Pennsylvania: Technomic)
- [3] Butler M A, Ricco A J and Buss R J 1990 *J. Electrochem. Soc.* **137** 1325
- [4] Butler M A, Buss R J and Galuska A 1991 *J. Appl. Phys.* **70** 2326
- [5] Yasuda H 1985 *Plasma Polymerization* (Orlando, Florida: Academic) and references therein
- [6] Liepins R and Sakaoku K 1972 *J. Appl. Polym. Sci.* **16** 2533
- [7] Buzzard P D, Soong D S and Bell A T 1982 *J. Appl. Polym. Sci.* **27** 3965
- [8] Ho P, Buss R J and Loehman R E 1989 *J. Mater. Res.* **4** 873
- [9] Williamson R L, Hareland W A and Peebles H C 1989 *Appl. Opt.* **28** 2201
- [10] Choi S J and Kushner M J 1993 *J. Appl. Phys.* **74** 853
- [11] Kay E, Dilks A and Seybold D J 1980 *J. Appl. Phys.* **51** 5678
- [12] Golub M A, Wydeven T and Cormia R D 1992 *J. Polym. Sci. A* **30** 2683

Process-induced particle formation in the sputtering and reactive ion etching of silicon and silicon dioxide

Christoph Steinbrüchel and Won Jong Yoo

Materials Engineering Department and Center for Integrated Electronics, Rensselaer Polytechnic Institute, Troy, NY 12180, USA

Received 4 January 1994, in final form 17 January 1994

Abstract. Particle formation has been studied in Ar sputtering plasmas and CCl_2F_2 -Ar reactive ion etching plasmas from Si and SiO_2 substrates by laser light scattering, scanning and transmission electron microscopy and optical emission plasma diagnostics. Particles nucleate and grow continuously, and are swept out into the exhaust under a wide variety of plasma conditions. Within a more limited range of values for pressure and flow rate, particles grow large enough in the plasma so as to form a particle cloud suspended above the substrate. Stability and position of the cloud depend on the process conditions. When particles become visible by light scattering, at a diameter of about 200 nm, they are essentially spherical and monodisperse in size, but the size distribution becomes much wider as the average particle size increases with increasing discharge time. In sputtering, particles smaller than about 100 nm are quite porous, have a somewhat more irregular shape and exhibit a spherulitic (spherically columnar) mode of growth. Optical emission spectroscopy of the plasma and compositional analysis of the particles indicate that in all cases, Si atoms are responsible for particle nucleation and growth. These observations are discussed in terms of possible mechanisms for generation and transport of plasma species in the discharge, particle nucleation and growth, particle transport and particle cloud formation.

1. Introduction

Maximization of the yield achieved is a major concern in present day microelectronics manufacturing. One of the main factors limiting the yield is particle contamination. The traditional way of dealing with this problem has been to control wafer handling and the wafer ambient. However, if the process involves a plasma, it has become apparent that particle contamination may be a more or less unavoidable by-product of wafer processing itself [1].

Process-induced particle formation was first observed in plasma-enhanced chemical vapour deposition (PECVD) [2-10], and later also in sputtering [11-20] and reactive ion etching (RIE) [11, 12, 16-18, 20-24]. In all of this work, particle formation occurred in the plasma itself, due to some undesired chemical reactions between plasma species, and was not primarily a function of the cleanliness of the reactor or of wafer handling before and after the process.

In the present paper, we shall review recent work in the authors' laboratory, focusing on process-induced particle generation in the sputtering and RIE of silicon and silicon dioxide [11, 12, 16-18, 23]. Emphasis will be placed on the plasma conditions under which particles form, the mode of growth of these particles and the

plasma species responsible for nucleation and growth of particles. The results we shall report have been obtained mainly from laser light scattering, scanning (SEM) and transmission electron microscopy (TEM) and optical emission plasma diagnostics.

2. Experimental results

Details of our experimental set-up have been described previously [11, 12, 16]. The reactor is a conventional parallel plate 13.56 MHz reactor with 5 inch electrodes and Al guard rings to confine the discharge (figure 1). Process gases are fed in at the top plate on the right-hand side and pumped out through the exhaust at the left-hand side wall. Ar is used for sputtering and 10% CCl_2F_2 in Ar for RIE. Light scattering from particles is performed using a frequency-doubled Nd:YAG laser (beam diameter 16 mm, average pulse energy 17 mJ) and is observed visually in a direction approximately perpendicular to the beam. Particles large enough to settle onto the substrate are examined by SEM. Very small particles are collected downstream, between the substrate and the exhaust, on TEM grids. Optical emission from a region near the sheath edge is focused with a lens through a quartz window onto a fibre-optic cable connected to a monochromator.

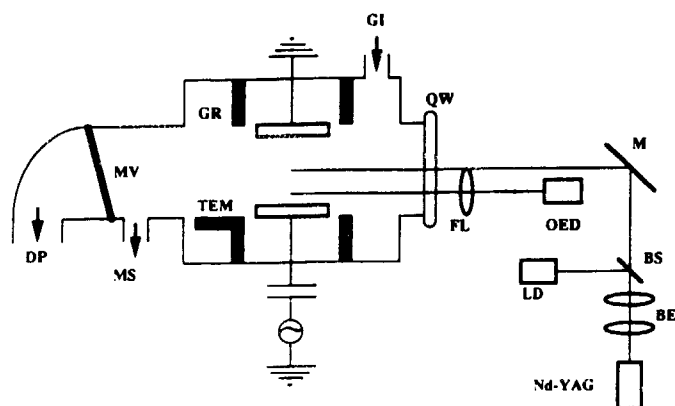


Figure 1. Experimental set-up. DP, diffusion pump; MV, manual throttle valve; MS, mass spectrometer; GR, guard ring; TEM, TEM grid holder; GI, gas inlet; QW, quartz window; FL, focusing lens; OED, optical emission detector; M, mirror; BS, beam splitter; BE, beam-enlarging lens; LD, laser power detector.

Our set-up differs from that of a number of other authors [13, 14, 21, 24] in that our substrate is of the same size as the electrode, so that only the substrate (plus the guard ring) is exposed to the plasma and thereby etched. This, however, causes a certain degree of non-uniformity of the discharge (and the etch rate) along the substrate edge. In the other cases, the substrate electrode is much larger than the substrate and also consists of a different material, so that the etch rate across the substrate is quite uniform, but species etched from the electrode are also introduced into the plasma.

Particles in the form of a particle cloud above the wafer near the sheath edge are observed under a variety of plasma conditions (figure 2) [16–18]. We use a quantity called the onset rate, which is defined as the inverse of the time at which the particle cloud begins to be observable by laser light scattering, as a convenient measure for comparing qualitatively different experimental situations. If two of the three discharge variables (pressure, gas flow rate and RF power) are held constant, then we observe threshold behaviour for the appearance of a particle cloud versus the third variable [16–18]. That is, no particle cloud is observed even after an extended period of time unless the third variable exceeds a certain value. An example of this is given in figure 3, where the RF power and flow rate are held constant and the pressure is varied.

With a particle cloud already formed, the shape and position of the cloud depend on the pressure and flow rate. For example, if the pressure is reduced gradually at a constant flow rate, the cloud moves to the left until it reaches the edge of the wafer, at which point it is swept out into the exhaust [18]. The pressure at which this occurs coincides with the threshold pressure for the cloud formation mentioned above (figure 3).

When particles become visible by light scattering they are about 200 nm in diameter and appear fairly

spherical and monodisperse in SEM (figure 2) [17, 18]. Upon growing further, they show an orange-peel-type surface texture, which is due to their being made up of numerous cone-shaped pieces. Such pieces are often observed as particle fragments in SEM samples (figure

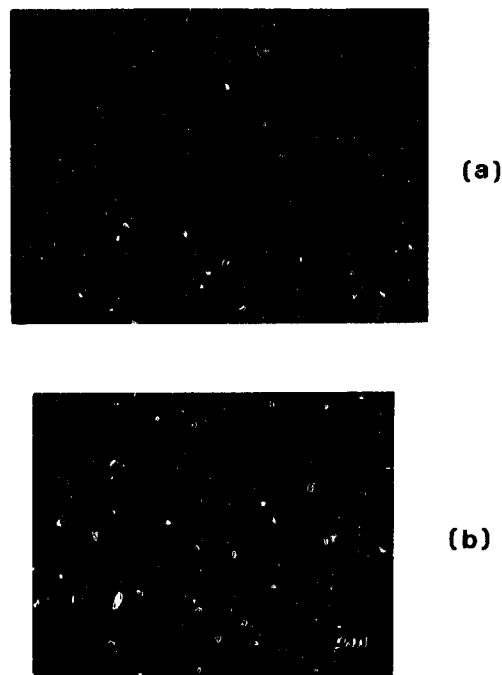


Figure 2. (a) Particle cloud scattering laser light (and reflection on wafer). Ar sputtering of Si at 120 mTorr. (b) Particles deposited on wafer at onset of light scattering.

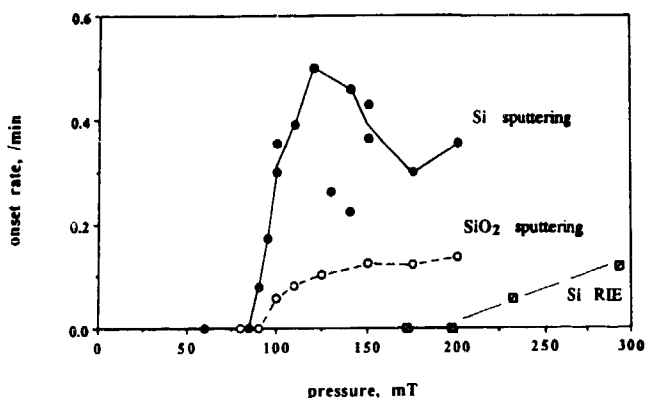
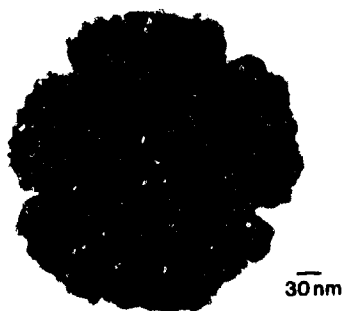


Figure 3. Onset rates versus pressure: Si sputtering in Ar (100W); SiO₂ sputtering in Ar (100W); Si RIE (200W, 10% CCl₂F₂/90% Ar).



(a)



(b)

Figure 4. (a) SEM of a large particle with fragments, deposited on the wafer, from sputtering of Si in Ar. (b) TEM of small particle collected downstream from sputtering of Si in Ar.

4(a)). The growth mode of these particles is elucidated further by TEM analysis. What appears as a spherical particle in SEM actually displays a somewhat irregular, porous, overall amorphous structure in TEM showing spherically columnar, or 'spherulitic', growth [25] for the case of sputtering (figure 4(b)) [18].



Figure 5. TEM of particles collected downstream from RIE of SiO₂ (200W, 100mTorr, 10% CCl₂F₂/90% Ar).

Very small particles can be collected downstream from the substrate on TEM grids either below or above threshold conditions, but before a particle cloud becomes visible in light scattering [18, 23]. An example of this is given in figure 5 (see also figure 4(b)).

It is also important to note that particle formation is much faster in sputtering than in RIE, although the etch rate is much larger in RIE at a fixed pressure (figure 3) [17, 23]. Furthermore, in sputtering the threshold for cloud formation is correlated with noticeable redeposition over the centre part of the wafer (at which point there still is net etching along the edge of the wafer) [17]. In RIE of Si, cloud formation occurs only at fairly high pressures, i.e. considerably above the point of maximum etch rate or, in other words, only when there is significant polymerization in the plasma and polymeric deposition on the wafer [17]. No cloud formation is observed in the RIE of SiO₂ up to a pressure of 600 mTorr in our system.

In sputtering, the size distribution of particles depends on time and on the location within the cloud. On the one hand, the average particle size increases and the

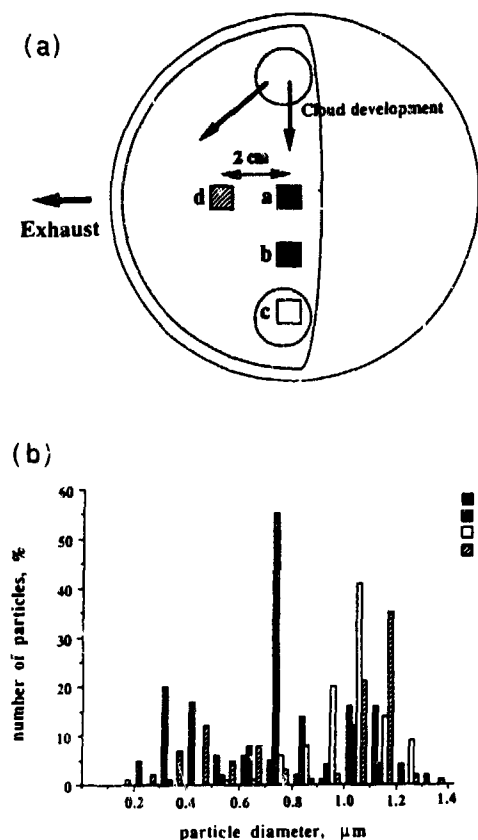


Figure 6. Particle size distributions versus location in a fully developed cloud. The cloud appears at location c at the onset of light scattering, then expands with time, and eventually covers about half of the wafer.

size distribution becomes wider with time [18]. On the other hand, the 'oldest' part of a cloud, i.e. the location where particles appear first, on average exhibits the largest particles (figure 6) [18].

The most important feature of the optical emission spectra is that Si atoms are detected only in sputtering, and not in RIE (figure 7) [23], although, as mentioned above, the etch rate is much higher in RIE. In addition, in comparing sputtering of Si and SiO_2 at a given pressure, the ratio of the emission intensities from Si atoms is about the same as the ratio of the sputter etch rates or the ratio of the onset rates [23].

EDX analysis reveals that the major constituent of particles produced in sputtering is Si. Particles collected in RIE contain less Si but more Al (from the guard ring), as well as Cl and F [23].

3. Discussion and conclusions

The most important conclusion suggested by our results is that, in the systems studied, sputtering and RIE of Si

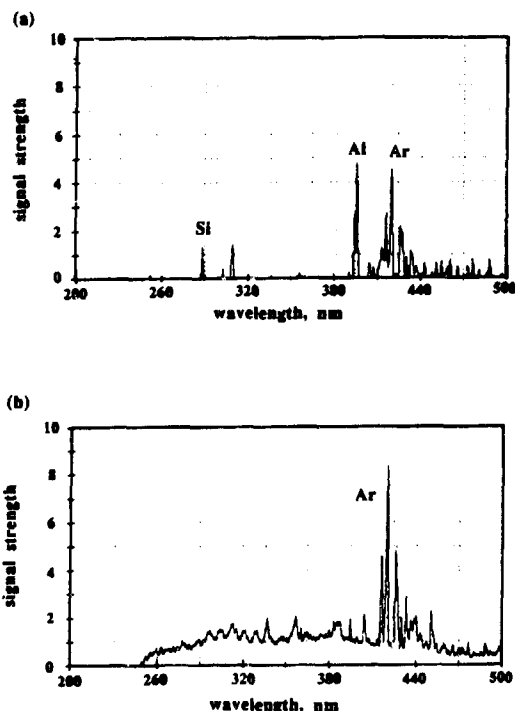


Figure 7. Optical emission spectra. (a) sputtering of Si (120 mTorr, 200 W); (b) RIE of Si (120 mTorr, 200 W).

and SiO_2 , the species responsible for particle nucleation and growth are probably Si atoms. This follows from a combination of several observations. First, in the sputtering of Si and SiO_2 the most important 'etch' products are clearly Si atoms. Hence it is notable that the onset rate for light scattering, the sputter etch rate (thus the flux of Si atoms into the plasma), and the optical emission intensity from Si atoms (thus the Si atom concentration in the plasma) are all higher in the same proportion for Si as compared to SiO_2 . Second, in the RIE of Si and SiO_2 , the overall removal rate of Si atoms is much larger than in sputter etching, yet particle formation is much slower. However in RIE most etch products are volatile species of the form SiCl_xF_y , whereas Si atoms are at most a minor etch product and are present at a much lower concentration than in sputtering, as is indicated by our optical emission results (figure 7).

As a second conclusion, we wish to emphasize that particle nucleation and growth evidently occur continuously under all experimental conditions, even when a stable particle cloud is never observed by light scattering. This follows from the fact that one can collect particles downstream either before the appearance of a particle cloud over the wafer (above threshold conditions), or even below threshold conditions where no particle cloud is ever detected. Furthermore, even in a

well-developed cloud some very small particles can always be found (figure 6).

The formation of a stable particle cloud thus requires that nuclei grow and become negatively charged fast enough so as not to be swept out directly into the exhaust. Confinement of the particle cloud in the direction perpendicular to the parallel plate discharge electrodes depends on a balance of electrical and ion drag forces on the particles [26–29]. The reversible changes in cloud shape and transverse cloud position which can be induced by changes in flow rate or pressure indicate that the neutral drag force on the particles is also very important. In fact, it is not clear yet what combination of effects gives rise to transverse confinement of a particle cloud, since clouds can form even over the centre of a wafer, where there are no nearby geometric, electrical discontinuities in the surfaces in contact with the plasma [30].

Our results also suggest some approaches toward minimizing particle contamination. The threshold observations for particle cloud formation indicate that there may be 'safe' regions for operating a certain process as far as deposition of particles on a wafer is concerned. Also, a soft shut-down of the discharge is advisable, whereby the pressure is reduced gradually before the RF power is turned off. This will move the particle cloud, if any, off the wafer into the exhaust. Furthermore, if operating a process in a 'safe' region is not possible, then it will be preferable to modulate or pulse the discharge power, the benefits of which have already been demonstrated [6–8].

References

- [1] Steinbrüchel Ch 1994 ed J Vossen *Physics of Thin Films* to be published
- [2] Roth R M, Spears K G and Wong G 1984 *Appl. Phys. Lett.* **45** 28
- [3] Roth R M, Spears K G, Stein G D and Wong G 1985 *Appl. Phys. Lett.* **46** 253
- [4] Spears K G, Robinson T J and Roth R M 1986 *IEEE Trans. Plasma Sci.* **14** 179
- [5] Watanabe Y, Shiratani M and Kubo Y 1988 *Appl. Phys. Lett.* **53** 1263
- [6] Watanabe Y, Shiratani M and Makino H 1990 *Appl. Phys. Lett.* **57** 1416
- [7] Watanabe Y, Shiratani M and Yamashita M 1992 *Appl. Phys. Lett.* **61** 1510
- [8] Bouchoule A, Plain A, Boufendi L, Blondeau J Ph and Laure C 1991 *J. Appl. Phys.* **70** 1991
- [9] Dorier J L, Hollenstein Ch, Howling A A and Kroll U 1992 *J. Vac. Sci. Technol.* **A10** 1048
- [10] Anderson H M, Jairath R and Mock J L 1990 *J. Appl. Phys.* **67** 3999
- [11] Durham J A and Steinbrüchel Ch 1990 *Proc. 8th Symp. Plasma Process* ed G S Mathad and D W Hess (Pennington, NJ: The Electrochemical Society) p 207
- [12] Petrucci J L Jr and Steinbrüchel Ch 1990 *Proc. 8th Symp. Plasma Process* ed G S Mathad and D W Hess (Pennington, NJ: The Electrochemical Society) p 219
- [13] Selwyn G S, Heidenreich J E and Haller K L 1991 *J. Vac. Sci. Technol.* **A9** 2817
- [14] Selwyn G S, McKillop J S and Haller K L 1990 *J. Vac. Sci. Technol.* **A8** 1726
- [15] Carlile R N, Geha S, O'Hanlon J F and Stewart J C 1991 *Appl. Phys. Lett.* **59** 1167
- [16] Yoo W J and Steinbrüchel Ch 1992 *Appl. Phys. Lett.* **60** 1073
- [17] Yoo W J and Steinbrüchel Ch 1992 *J. Vac. Sci. Technol.* **A10** 1041
- [18] Yoo W J and Steinbrüchel Ch 1993 *J. Vac. Sci. Technol.* **A11** 1258
- [19] Jellum G M and Graves D B 1990 *Appl. Phys. Lett.* **57** 2077
- [20] Daugherty J E and D B Graves 1991 *J. Appl. Phys.* **69** 6923
- [21] Selwyn G S, Singh J and Bennett R S 1989 *J. Vac. Sci. Technol.* **A7** 2758
- [22] O'Neill J A, Singh J and Gifford G G 1990 *J. Vac. Sci. Technol.* **A8** 1716
- [23] Yoo W J and Steinbrüchel Ch 1994 *J. Vac. Sci. Technol.* to be published
- [24] Smadi M M, Kong G Y, Carlile R N and Beck S F 1992 *J. Vac. Sci. Technol.* **B10** 30
- [25] Keith H D and Padden F J Jr 1963 *J. Appl. Phys.* **34** 2409
- [26] McCaughey M J and Kushner M J 1991 *J. Appl. Phys.* **69** 6952
- [27] Daugherty J E, Porteous R K, Kilgore M D and Graves D B 1992 *J. Appl. Phys.* **72** 3934
- [28] Sommerer T J, Barnes M S, Keller J H, McCaughey M J and Kushner M J 1991 *Appl. Phys. Lett.* **59** 638
- [29] Barnes M S, Keller J H, Forster J C, O'Neill J A and Coultas D K 1992 *Phys. Rev. Lett.* **68** 313
- [30] Selwyn G S 1992 *J. Vac. Sci. Technol.* **A10** 1053

Diagnostics of particle genesis and growth in RF silane plasmas by ion mass spectrometry and light scattering

Ch Hollenstein, J-L Dorier, J Dutta, L Sansonnens
and A A Howling

Centre de Recherches en Physique des Plasmas, Ecole Polytechnique Fédérale de
Lausanne, Avenue des Bains 21, CH-1007 Lausanne, Switzerland

Received 7 January 1994, in final form 12 January 1994

Abstract. Experimental identification of the precursors and processes leading to particles is essential for understanding particulate contamination in deposition plasmas. We have investigated particle formation in radiofrequency silane plasmas using light scattering (elastic and inelastic) and quadrupole ion mass spectrometry as complementary plasma diagnostics. Negative ions reach high masses (at least 500 amu) and are the only elementary species with a residence time on the scale of the powder formation time. Furthermore, a negative-ion polymerization scheme shows that the densities of high-mass anions are strongly diminished at kilohertz power modulation frequencies, at which reduced powder production is also observed. We conclude that negative ions are the particle precursors and that initial clusters grow by negative-ion polymerization in silane plasmas. *In situ* light scattering techniques are described to determine particle size, number density and refractive index self-consistently. Novel, visible photoluminescence measurements from particles suspended in the plasma are also reported. These diagnostics demonstrate that particle evolution proceeds by an agglomeration phase and that the particle properties are different from those of the bulk material early in particle development.

1. Introduction

Particulate contamination formed in plasmas for industrial applications presents a major problem by limiting manufacturing productivity and device reliability [1-3]. Suppression of particle formation in silane plasmas for amorphous silicon deposition presupposes a knowledge of the powder precursor identity and of the reactions leading from monosilicon process gas to particles containing millions of silicon atoms. In this paper we simultaneously use quadrupole ion mass spectrometry and light scattering to investigate precursor formation and particle growth in silane RF plasmas.

Various species could be involved in plasma polymerization leading to particle precursor formation. Polymerization could propagate by insertion of silane radicals into higher saturated molecules [4,5] or by silane addition to positive ions [4,6]. Negative ions are trapped in the plasma by the sheath potentials, which suggests that plasma polymerization could also proceed via negative-ion pathways even if the reaction

rates are slow [7-12]. Time-resolved mass spectrometric measurements of the diffusion of heavy polymerized negative ions from power-modulated RF silane plasmas are modelled by a simple polymerization scheme to demonstrate the effect of modulation on precursor formation.

Particle precursors are too small to be visible, although particles suspended in the plasma can be detected by light scattering [1,3,13-19]. The scattering is often monitored simply as a guide to the amount of powder and onset rate [20] because the intensity is a complex convolution of particle size, number density and refractive index [21,22]. Different methods have been applied to deconvolve the particle parameters using angular dissymmetry [23] and polarization-sensitive diagnostics. In general, additional *ex situ* measurements [15] or assumptions (such as using the refractive index of amorphous silicon [18]) are necessary. In this paper, we attempt to determine the particle size, number density and refractive index self-consistently from 90° polarization-sensitive scattering and extinction measurements. In addition, visible photoluminescence from the

suspended particles [24] is briefly described and proposed as a potential *in situ* diagnostic.

2. Experimental description

The conventional parallel-plate RF reactor comprises two symmetric 130 mm diameter electrodes with a 25 mm electrode gap, described in detail elsewhere [25]. Plasma parameters for good quality a-Si:H deposition were chosen: 30 sccm pure silane flow at 0.1 mbar pressure. The RF power of 4–10 W at an excitation frequency of 30 MHz was capacitively coupled to the RF electrode.

2.1 The experimental method for light scattering measurements

Light scattering by a spherical, homogeneous particle is described by the Lorentz-Mie theory [21, 22]. For a randomly distributed ensemble the total scattered intensity is the sum of the individual particle intensities provided that no multiple scattering occurs. For identical particles, the power at the detector is

$$W_{\perp}^{\perp} \propto N_p \Delta V \Delta \Omega |S_{\perp}|^2 I_0^{\perp} \quad (1)$$

and equivalently for $W_{\parallel}^{\parallel}$, where the polarizations are represented in figure 1. The terms S_{\perp} and S_{\parallel} are complex elements of the amplitude scattering matrix [26] and are a function of the complex refractive index n , the size parameter $x = 2\pi r/\lambda$ (r is the particle radius and λ the source wavelength) and the scattering angle θ (90° in our

case). N_p is the number density of particles present in the observation volume ΔV . Note that ΔV and the solid angle $\Delta \Omega$ must be sufficiently small for the scattering angle to be close to 90° and for the purity of polarization to be conserved. The incident intensities (I_0^{\perp} , I_0^{\parallel}) at the observation volume are corrected for any absorption and scattering losses from powder between the source and this volume. The experiment is also arranged to avoid scattering and absorption losses between the observed volume and the detector. The measured transmitted power fraction W_t/W_0 is independent of polarization and, for simple scattering, is given by

$$W_t/W_0 = \exp(-C_{\text{ext}} N_p d) \quad (2)$$

where d is the path length of the visible beam in the powder layer suspended in the plasma. C_{exp} is the extinction cross section (sum of scattering and absorption) and depends on x and n .

2.1.1. Experimental procedure. The scattered power is monitored during particle growth with both the source and detector polarized parallel or perpendicularly, giving W_{\perp}^{\perp} and $W_{\parallel}^{\parallel}$ in consecutive experiments. Since we arrange that $I_0^{\perp} = I_0^{\parallel}$, we can define

$$P = \frac{W_{\perp}^{\perp} - W_{\parallel}^{\parallel}}{W_{\perp}^{\perp} + W_{\parallel}^{\parallel}} = \frac{|S_{\perp}|^2 - |S_{\parallel}|^2}{|S_{\perp}|^2 + |S_{\parallel}|^2} \quad (3)$$

which would be equivalent to the degree of linear polarization for the case of unpolarized incident light. Note that P is a function of x and n only, and S_{\perp} and S_{\parallel} , which also determine C_{ext} , are calculated using the *BHME* algorithms [26]. The signal evolution has been demonstrated to be highly reproducible even down to the smallest features. P is a multi-valued function of the size parameter and therefore an estimation of particle size requires that the particle development be followed from the beginning. The technique therefore cannot be used for instantaneous measurements in an already-formed plasma particle system.

We find that there is no unique refractive index that can describe the time variation of P assuming particle growth with continuous, monotonically increasing radii. Therefore we must allow for a changing refractive index $n(t)$ during particle growth, and follow an iterative procedure to determine self-consistently the parameters $\{N_p, x, n\}$ as a function of time.

(i) Firstly, the P curve is reproduced using $S_{\perp}(t)$ and $S_{\parallel}(t)$ values calculated from an assumed step-by-step variation for the real and complex parts of $n(t)$ during the particle growth phase, along with the corresponding size parameter variation $x(t)$.

(ii) The value of $C_{\text{ext}}(t)$ is then calculated using these S_{\perp} and S_{\parallel} values, and the time-varying particle number density $N_p(t)$ is estimated from the W_t/W_0 measurement and equation (2).

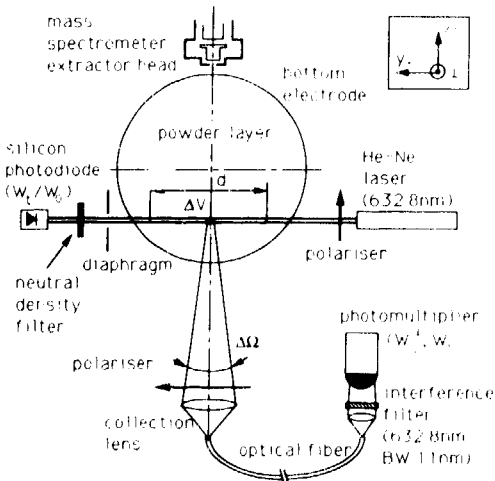


Figure 1. Schematic plan view of the diagnostic arrangement in the plane of a powder layer suspended in the plasma above the bottom electrode. The light source is a 10 mW He-Ne laser.

(iii) Using equation (1) values for W_s^+ and $W_s^||$ are calculated and compared with the experimentally measured W_s^+ and $W_s^||$ signals.

The procedure is iterated until a reasonably accurate self-consistent agreement is found for the measured values of $\{W_s^+, W_s^||, W_i\}$ in terms of the particle parameters $\{n, x, N_p\}$ over the whole time period investigated.

2.1.2. Limitations of the technique. The method described is non-perturbative, easy to install in a plasma reactor and gives self-consistent results without requiring any *ex situ* measurements. However, to follow the particle evolution, it is necessary to arrange for the observation volume to coincide with a position in the discharge region where the particles form and grow without drifting out of the zone under observation. Displacement of the particle cloud can be minimized by using an isothermal environment to eliminate thermophoretic forces [27] and by using conditions that avoid rapid production of high particle densities leading to instabilities, which can empty particles from the plasma, because light scattering diagnostics could wrongly interpret these effects as a real reduction in particle formation rates.

Boufendi *et al* [15] have demonstrated that particles are mono-sized during the early stage of development. Moreover, since the scattering cross section varies as r^6 for the smallest particles (Rayleigh scattering for $x < 0.1$ –0.3, depending on the refractive index [28]) and at least as r^2 for larger particles, our assumption of identical particles is justifiable by considering that light scattering from the initial class of particles will dominate the detected signal during the particle development investigated here.

The iterative data interpretation procedure is not automatic, but requires a degree of judgement and experience to aid in identifying the parameter trends most likely to yield self-consistent results.

2.2. Ion mass spectrometry

The differentially pumped mass spectrometer was a Hiden Analytical Limited Plasma Monitor type HAL-EQP 500 (Hiden Analytical Limited, Gemini Business Park, Warrington WA5 5TN, UK) for masses 1–500 amu. The ion extractor head in figure 1 was positioned with its axis in the electrode plane 10 mm beyond the earthed guard screen [12]. In this work, therefore, ions were not extracted at the earthed electrode but at the mass spectrometer head, which was at the same potential. Ions enter the monitor through a 100 μ m aperture in the extractor electrode. A +40 V bias gave a good negative-ion signal without creating a visible secondary plasma in the extraction orifice. For time-resolved measurements, the channeltron pulses triggered by ion events were registered by a gated counter [12]. The deposited film or powder can block the aperture [8] and the monitor extraction head had to be dismantled and

cleaned in acid after every few hours of exposure to the plasma.

3. Results

3.1. Negative ions

Figure 2 shows the time-resolved behaviour of mono- to hexasilicon hydride anions in an on-off power-modulated plasma [12]. The double peak in the mono-, di- and trisilicon hydride anion groups is predicted by the model of Overzet *et al* [29]: the first peak is due to attachment in the decaying sheath after plasma extinction and the second peak is due to negative ions diffusing from the plasma bulk when the sheath has collapsed [11, 12, 30, 31]. Figure 2 also shows that only the monosilicon hydride anions have enough time to disappear completely at 1 kHz modulation frequency. Because of the mass-dependent diffusion loss rates [12] the modulation frequency influences the composition of the plasma. This point will be demonstrated by a simple polymerization model below.

Negative polysilicon hydride ionic clusters have been observed up to the 500 amu mass limit of the mass spectrometer [32], corresponding to $[\text{Si}_n\text{H}_{n+2}]^-$, indicating that negative ions could be precursors to larger clusters and ultimately to powder particles. These negative molecular ions are singly charged by incorporation of an electron into a molecular orbital; the concepts of sheaths and floating potential only apply when the object is large enough for it to be statistically meaningful to speak of electron and positive ion fluxes to its surface [9, 33, 34]. The positive-ion masses are limited to a mere 150 amu, possibly because of the activation energy barriers described by Mandich *et al* [35]. The positive-ion size might also be limited because of ion-ion recombination losses, or because they are efficiently evacuated

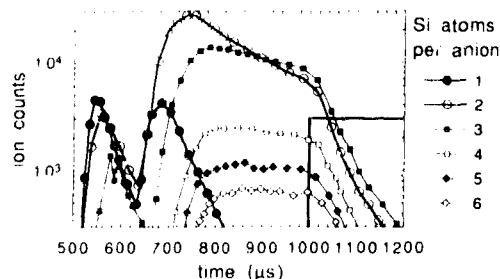


Figure 2. Time-resolved fluxes for mono- to hexasilicon hydride molecular anion groups measured at 1 kHz power modulation frequency. Time is referenced to the beginning of a plasma period and the afterglow is from 500 to 1000 μ s. The heavy line represents the following plasma duration. For each data point, the negative ions were counted with a 5 μ s time window over 10000 modulation cycles. Pure silane at 0.1 mbar and 4 W average power (50 mW/cm² during the plasma period) at 30 MHz excitation frequency, electrode temperature 150°C.

from the plasma across the sheaths.

3.1.1. Polymerization scheme for negative ions. Experimental results suggest that a polymerization pathway proceeds via negative ion clustering; they are not simply by-products formed by electron attachment to a neutral species pathway. Three reasons why the high-mass negative ions are not formed by attachment to heavy neutrals are the following [12].

(i) No neutrals with masses as high as those of the negative ions are detected in the mass spectra.

(ii) Negative ions and neutrals have very different abundance ratios.

(iii) No attachment peaks exist in the time-resolved measurements for negative ions heavier than trisilicon hydride anions (figure 2).

One possible polymerization pathway, which propagates via negative ions, is by silane addition [7], analogous to the condensation reactions proposed for positive ions [4, 6, 36]. Ion-ion recombination is the second possible pathway for polymerization [37, 38]. Since heavy neutral species are not observed, it must be supposed that they are re-attached and therefore ion-molecule and ion-ion reactions both eventually lead to stable higher-mass negative ions. The conditions for negative-ion formation are discussed in more detail in [12].

The qualitative behaviour of negative-ion polymerization in modulated silane plasmas can be described by a phenomenological model [12]. In the following, the term $S_n(t)$ designates the time-varying plasma density of all the polysilicon hydride anions containing n silicon atoms. The conservation equation for the monosilicon hydride anion density is

$$dS_1(t)/dt = f(t) - K_1 S_1(t) - g_1(t) \quad (4)$$

where $f(t)$ is the monomer source term due to electron attachment on silane, K_1 is the reaction rate for silane addition and $g_1(t)$ is the monomer loss rate due to detachment and modulation losses. In this model the aim is to study a simple clustering sequence. In what follows, the phenomenological polymerization rate constant K_n includes all possible reactions such as ion-molecule, ion-radical and ion-ion recombination (followed by re-attachment). The relative importance of these reactions is discussed further in [12]. For the remaining equations we ignore formation of higher-mass negative ions $S_n(n > 1)$ by any process other than by polymerization from the preceding S_{n-1} ion, to obtain

$$dS_n(t)/dt = K_{n-1} S_{n-1}(t) - K_n S_n(t) - g_n(t). \quad (5)$$

The function $g_n(t)$ represents modulation-induced loss rates due to sheath collapse, which are considered to be large relative to the weak transverse diffusion losses from between the electrodes. Time-averaging over a power modulation cycle under steady-state conditions

and adding the first N equations gives the mean polysilicon hydride anion density

$$\bar{S}_N = \left(\bar{f} - \sum_{i=1}^N \bar{g}_i \right) / K_N \quad (6)$$

where it is assumed that there is no break in the polymerization sequence since all K_n are taken to be non-zero. Equation (6) shows that the time-averaged plasma density of the polymerized negative ion S_N is determined by the monosilicon hydride anion production rate, the polymerization reaction rate K_N for the ion itself, and the total of the modulation-induced losses of

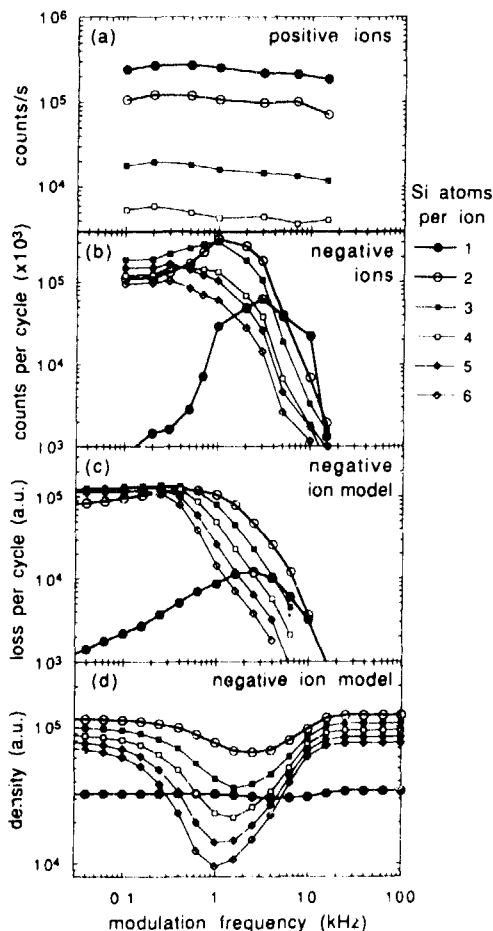


Figure 3. Dependence of (a) positive and (b) negative ion signals on modulation frequency. Each data point is averaged over 300 cycles. The negative-ion intensities are divided by the modulation frequency to give the loss counts per cycle. The plasma parameters are as in figure 2. The calculated frequency dependence of (c) the anion loss flux is shown for comparison, along with (d) the estimated anion densities in the plasma.

all the preceding negative ions. This emphasises the importance of power modulation for controlling the density of negative, highly polymerized species in the plasma. We estimate the time window for anion loss during afterglow by extrapolation from experimental data as a function of modulation frequency and anion mass [12]. Steady-state time-averaged negative ion densities for a given modulation frequency are determined by iterating equations (4) and (5) until the time-variation of each ion density is the same in successive cycles. Values for g_n and K_n were self-consistently chosen so that the calculated losses gave a reasonable fit to the experimental data [12].

Figures 3(a) and (b) show how the time-averaged negative- and positive-ion signals vary with modulation frequency. Above 15 kHz the sheath does not have time to collapse sufficiently for any negative ions to escape. Figure 3(c) shows the modelled losses for comparison with figure 3(b), and the corresponding calculated anion densities are shown in figure 3(d). The time-averaged negative-ion densities in the limits of high and low modulation frequency are equal and half of the continuous plasma values for a 50% duty cycle [12]. In the intermediate frequency range around 1 kHz the densities decrease strongly for the higher masses. The implications for powder formation are discussed in section 4.

3.2. Light scattering results

Figures 4(a) and (b) show the measured signals with the fitted points from the iteration procedure superposed. Figure 4(c) shows the concomitant particle radius, number density and refractive index. We can distinguish several stages of particle formation.

For the first 35 s after plasma ignition, no scattered signal is observable. The particle precursors and nucleation centres are below the detection limit.

From 35 to 50 s, only perpendicularly polarized light is measurable, corresponding to Rayleigh scattering; the particle radius is less than 15 nm.

From 50 to 80 s, the fitting procedure gives a reasonable fit to the raw data (see figure 4(a)) for which the corresponding $\{n, x, N_p\}$ values are shown in figure 4(c).

At least three different refractive index values are necessary to describe self-consistently the whole particle evolution. An initial rapid increase in particle radius is accompanied by a strong decrease in number density (50–53 s), and could be interpreted as an agglomeration of invisibly small particle precursors. These particles show a high refractive index [39]. A particle growth period ensues with moderate increase in radius at almost constant number density. This general trend of an early agglomeration phase followed by slow particle growth reproduces the observations of Bouchoule and Boulendi [40], and the final number density is comparable to that found in other work in silane-containing plasmas [15, 18].

As the particles grow further, the refractive index tends towards that of amorphous silicon bulk material. At 76 s, there is an additional change, whereby the radii

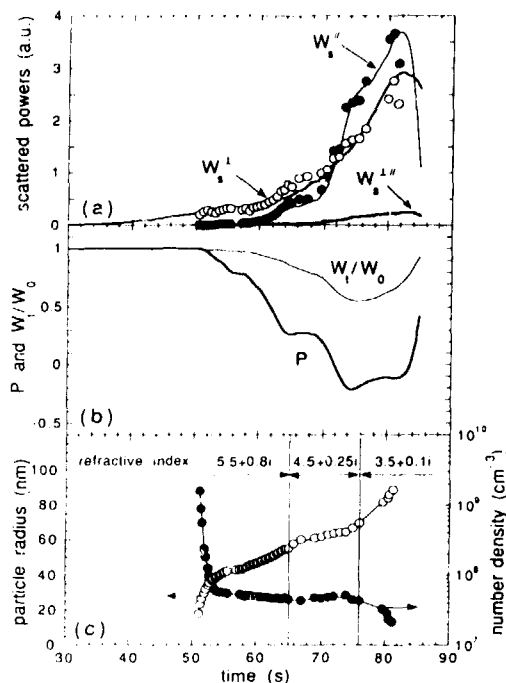


Figure 4. Results from light-scattering measurements during powder development in a continuous wave plasma. (a) The full lines are measured scattered intensities (corrected for extinction) and symbols represent self-consistent fitted data. (b) The measured transmitted power fraction W_{\parallel}/W_0 and polarization degree P . (c) The deduced particle radii, number density and refractive index values at 632.8 nm. Pure silane at 0.1 mbar and 30 MHz with 5 W continuous wave power and 100°C electrode temperature.

increase strongly concurrently with a fall in number density. The volume fraction of powder, defined as $N_p 4\pi r^3/3$, remains approximately constant up to this time and so this appears to be a second phase of particle aggregation. This is supported by transmission electron microscopy, which shows both single smooth spheres and aggregates of spheres; the latter having semblance of a blackberry. During this aggregation, the measured cross polarization intensity W_{\perp}^{II} becomes non negligible. Assuming that multiple scattering can be neglected, this indicates that the particles are no longer purely spherical [41]; the fit is less accurate in this region. Finally, the scattered intensities for both polarizations fail sharply, coinciding with a rise in transmitted intensity and accompanied by strong fluctuations in plasma light emission. This is due to instabilities of the plasma powder ensemble, which eject powder from the observation volume.

3.2.1. Photoluminescence measurements were carried out for the first time on particles suspended in the plasma by illuminating with a 488 nm argon ion laser and monitoring the spectrum at 90° via a 530 nm high-pass filter and

optical multichannel analyser [24] with an arrangement similar to figure 1. The visible photoluminescence in figure 5 is suggested to originate from quantum confinement effects in nano-crystallites [24] and as such is a probe for the particulate structure. The spectral shift with time as shown in figure 5 reveals an evolution in particle morphology during its formation.

3.2.2. Light scattering in power-modulated plasmas. Figure 6 shows the powder onset rate (defined as the inverse of the powder appearance time) and the volume of powder material in the horizontal layer at the position of the laser beam (estimated from the product of volume

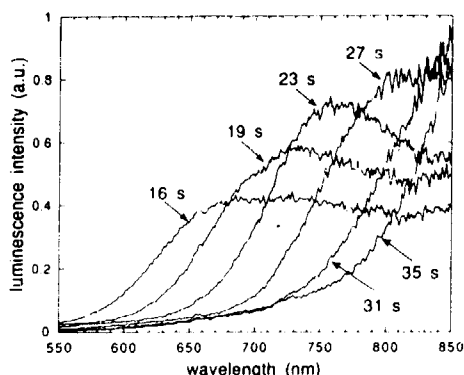


Figure 5. Photoluminescence spectra from particles suspended in a pure silane plasma for different times during powder development after plasma ignition. Incident light at 488 nm wavelength. The spectra are corrected for the spectral response of the detection system and for background plasma emission. Pure silane at 0.1 mbar, 20 kHz modulation at 5 W average radiofrequency power (30 MHz) and 20°C temperature.

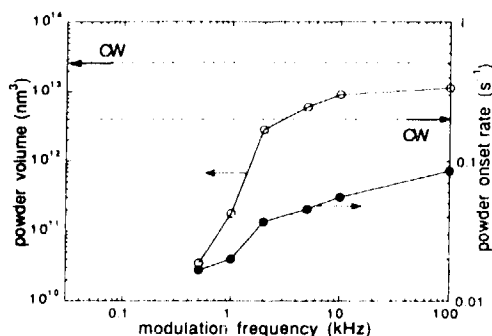


Figure 6. The powder onset rate and volume of powder material suspended in the plasma as a function of square-wave power modulation frequency, compared with values in the continuous wave plasma. The powder material volume is estimated from $(N_p 4\pi r^3/3) \times (\text{powder layer volume})$. Pure silane at 0.1 mbar, 4 W average power at 30 MHz and 100°C.

fraction and layer volume), for different modulation frequencies. Powder formation is strongly reduced for modulation frequencies below 1 kHz, in agreement with other work [8, 16–19].

The time-developments of ionic species and scattered light intensity are compared in figure 7(a) for a square-wave power-modulated plasma (50% duty cycle) at 2 kHz modulation frequency. Both positive- and negative-ion fluxes vary on a slow timescale similar to the powder appearance time of 16 s before reaching steady-state levels. Comparison with figure 7(b), for a 10% duty cycle in otherwise identical plasma conditions, shows that the negative-ion flux time-dependence is markedly different in the absence of powder formation although

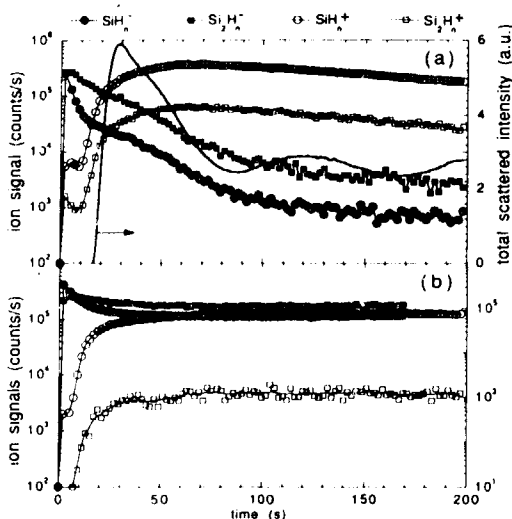


Figure 7. Simultaneous measurements of ion fluxes and powder development at 2 kHz modulation frequency for (a) 50% duty cycle and (b) 10% duty cycle. No powder is visible for the 10% duty cycle. Plasma parameters as for figure 6.

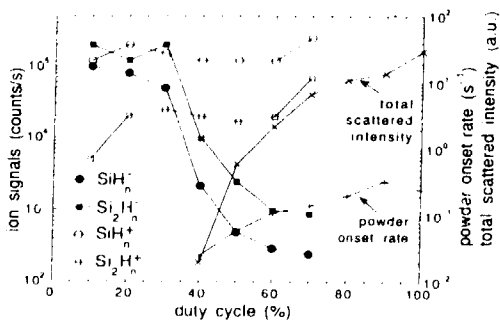


Figure 8. Powder onset rate, steady-state scattered intensity and ion fluxes for different duty cycles at 2 kHz modulation frequency. Pure silane at 0.1 mbar, 4 W average power at 30 MHz and 80°C.

the positive-ion flux behaviour is relatively unchanged. Figure 8 represents the steady-state ion fluxes, the total scattered intensity and the powder onset rate for a range of duty cycles at 2 kHz modulation frequency. The negative-ion loss flux is again anti-correlated with the scattered light intensity and powder onset rate, all of which vary strongly compared to the positive ion flux.

4. Discussion

Particles large enough to be visible by light scattering form in the RF silane plasma only after many seconds as shown in figure 4 and 7. This delay is much greater than the residence time for positive ions or neutrals in the discharge region. Negative species could, however, remain trapped by the plasma electric potential for this duration [9] and act as precursors for particle growth.

Figures 3 and 6, using a simple model to interpret the experimental measurements, demonstrate that the negative-ion density in the plasma is correlated with the onset rate and powder quantity above 1 kHz. Extrapolation to higher-mass negative ions in figure 9 indicates that the macro-molecular anion densities would fall to near zero for a wide range of modulation frequencies below 1 kHz. This is because the plasma periods are then too short for the polymerization chain to propagate from monosilicon hydride anions to highly polymerized species before almost all of the low-mass species are lost in the subsequent 'off' periods. Equilibrium between the diminished supply from preceding negative ions and the

polymerization of the polysilicon hydride anion itself results in a strongly diminished density of the highly-polymerized anions (see equation (6) and figure 9). Above 1 kHz, the sheaths do not fully collapse and high-mass negative ions reach significant densities. At very low modulation frequencies [10], the polymerization in a single plasma period propagates sufficiently far (to clusters containing perhaps 30 or 50 silicon atoms) to initiate particle growth. The onset rate in figure 6 is a measure of the growth rate from precursors to detectable particles and consequently is an indication of the precursor density. Therefore the identification of negative ions as the precursors to particle formation [12, 42] is consistent with experimental observations of powder reduction in plasmas modulated at kilohertz frequencies [8, 10, 12, 16, 17, 19, 42]. Similar considerations also account for the observations in figure 8. We can now speculate the following stages of particle formation.

(i) Dissociative electron attachment on silane creates the primary monosilicon hydride anions. Subsequent anion chemical reactions with silane, radicals or positive ions yield highly polymerized structured anionic clusters [12, 42], which are singly charged and are trapped in the discharge by the RF electrode sheath potentials during continuous plasma operation. These anions are the precursors to cluster formation and ultimately lead to particles; such processes are considered in the recent theoretical paper by Choi and Kushner [43].

(ii) These invisibly small negatively charged nano-particles remain trapped in the plasma and continue to grow by physico-chemical accretion. The nano-particles undergo an agglomeration phase and become large enough to be visible by light scattering (figure 4).

(iii) At some point during particle growth [9, 33, 34], equilibrium of electron and ion fluxes to its surface results in a multiple electronic surface charge and a sheath forms around the particle. Probably because the resultant micro-particles are composites of structured nano-particles, they exhibit properties different from those of the bulk material, such as a high refractive index [44, 45] and visible photoluminescence [24] (see figure 4(c) and 5). Particles continue to develop further by processes analogous to film growth leading to particles with a-Si:H properties.

For plasma processing applications, restriction of polymerization to low-mass anions could conceivably suppress particulate contamination and improve deposition efficiency. Alternatively to power modulation, this could perhaps be achieved by illuminating the plasma [32] with photodetaching radiation.

5. Conclusions

The genesis and growth of particles in a-Si:H plasmas has been investigated by a combination of light scattering (for a self-consistent determination of particle size, number density and refractive index) and ion mass

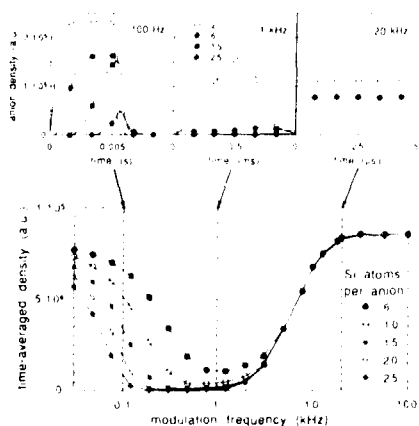


Figure 9. Estimation of time-averaged anion densities, as a function of modulation frequency, extrapolated to anions containing 25 silicon atoms (polymerization rates assumed independent of size for anions of six or more silicon atoms). Insets show the time-varying density during a modulation cycle for three frequencies: at 100 Hz, the polymerization chain has insufficient time to propagate to the highest masses; at 1 kHz, the elementary anions are lost before significant polymerization can occur; and at 20 kHz, all anions are trapped and high densities are reached.

spectrometry. Time-resolved measurements of negative ion fluxes are interpreted in terms of a polymerization scheme. Based on this, a simple model shows that anion cluster densities are depressed for the kilohertz range of power modulation frequencies corresponding to observed powder reduction. In addition, the observations that negative ions reach high masses and are the only species with a residence time on the scale of the powder growth time combine to show that negative ions are the precursors to particulate formation. Light-scattering diagnostics demonstrate that particle evolution proceeds by an agglomeration phase and that the particles exhibit properties different from those of the bulk material, such as a high refractive index and visible photoluminescence.

Acknowledgments

We thank Dr J Perrin for valuable comments and suggestions. We also thank Dr T Stoto of Department IGA at EPFL for electron microscopy, and Hiden Analytical Limited. This work was funded by Swiss Federal Research Grant BBW.EG(91)3 (for BRITE/EURAM contract BE-4529-90) and by the Swiss Department of Energy Grant EF-REN(91)31.

References

- [1] Selwyn G S, Singh J and Bennett R S 1989 *J. Vac. Sci. Technol.* **A7** 2758
- [2] Selwyn G S, McKillop J S, Haller K L and Wu J J 1990 *J. Vac. Sci. Technol.* **A8** 1726
- [3] Selwyn G S, Heidenreich J E and Haller K L 1991 *J. Vac. Sci. Technol.* **A9** 2817
- [4] Kushner M J 1988 *J. Appl. Phys.* **63** 2532
- [5] Veprek S, Schopper K, Ambacher O, Rieger W and Veprek-Heijman M G J 1993 *J. Electrochem. Soc.* **140** 1935
- [6] Haller I 1980 *Appl. Phys. Lett.* **37** 282
- [7] Perrin J, Lloret A, de Rosny G and Schmitt J P M 1984 *Int. J. Mass Spectrom. Ion Processes* **57** 249
- [8] Verderyn J T, Beherman J and Overzet L 1990 *J. Vac. Sci. Technol.* **A8** 1851
- [9] Garscadden A 1990 *Nonequilibrium Processes in Partially Ionised Gases* ed M Capitelli and J N Bardsley (New York: Plenum) p 541; Garscadden A 1991 *Proc. XXth Int. Conf. on Ionised Gases (Pisa)* (Pisa: Istituto di Fisica Atomica e Molecolare) Invited Paper 147
- [10] Lloret A, Bertran E, Andujar J L, Canillas A and Morenza J L 1991 *J. Appl. Phys.* **69** 632
- [11] Boswell R W and Vender D 1991 *IEEE Trans. Plasma Sci.* **19** 141
- [12] Howling A A, Sansonnens L, Dorier J-L and Hollenstein Ch 1994 *J. Appl. Phys.* **75** 1340
- [13] Spears K G, Robinson T J and Roth R M 1986 *IEEE Trans. Plasma Sci.* **14** 179; Spears K G, Kampf R P and Robinson T J 1988 *J. Phys. Chem.* **92** 5297
- [14] Bouchoule A, Plain A, Boufendi L, Blondeau J Ph and Laure C 1991 *J. Appl. Phys.* **70** 1991
- [15] Boufendi L, Plain A, Blondeau J Ph, Bouchoule A, Laure C and Toogood M 1992 *Appl. Phys. Lett.* **60** 169
- [16] Watanabe Y, Shiratani M, Kubo Y, Ogawa I and Ogi S 1988 *Appl. Phys. Lett.* **53** 1263
- [17] Watanabe Y, Shiratani M and Makino H 1990 *Appl. Phys. Lett.* **57** 1616
- [18] Watanabe Y, Shiratani M and Yamashita M 1992 *Appl. Phys. Lett.* **61** 1510
- [19] Howling A A, Hollenstein Ch and Paris P-J 1991 *Appl. Phys. Lett.* **59** 1409
- [20] Yoo W J and Steinbrüchel Ch 1992 *J. Vac. Sci. Technol.* **A10** 1041
- [21] Mie G 1908 *Ann. Physik* **25** 377
- [22] Kerker M 1969 *The Scattering of Light and Other Electromagnetic Radiation* (New York: Academic)
- [23] Jellum G M and Graves D B 1990 *Appl. Phys. Lett.* **57** 2077
- [24] Dutta J, Dorier J-L, Hollenstein Ch, Howling A A, Sansonnens L, Nieswand C, Fasoli A and Stoto T 1993 *Lausanne Research Paper LRP478/93*
- [25] Dorier J-L, Hollenstein Ch and Howling A A 1992 *J. Vac. Sci. Technol.* **A10** 1048
- [26] Bohren C F and Hauffman D R 1983 *Absorption and Scattering of Light by Small Particles* (New York: Wiley)
- [27] Jellum G M, Daugherty J E and Graves D B 1991 *J. Appl. Phys.* **69** 6923
- [28] Kerker M, Scheimer P and Cooke D D 1978 *J. Opt. Soc. Am.* **68** 135
- [29] Overzet L J, Lin Y and Luo L 1992 *J. Appl. Phys.* **72** 5579
- [30] Gottscho R A and Gaeb C E 1986 *IEEE Trans. Plasma Sci.* **14** 92
- [31] Gottscho R A 1987 *Phys. Rev. A* **36** 2233
- [32] Howling A A, Sansonnens L, Dorier J-L and Hollenstein Ch 1993 *J. Phys. D: Appl. Phys.* **26** 1003
- [33] McCaughey M J and Kushner M J 1991 *J. Appl. Phys.* **69** 6952
- [34] Daugherty J E, Porteous R K, Kilgore M D and Graves D B 1992 *J. Appl. Phys.* **72** 3934
- [35] Mandich M L, Reents W D and Kolenbrander K D 1990 *Pure Appl. Chem.* **62** 1653
- [36] Weakliem H A, Estes R D and Longeway P A 1987 *J. Vac. Sci. Technol.* **A5** 29
- [37] Haaland P 1990 *J. Chem. Phys.* **93** 4066
- [38] Perrin J and Schmitt J 1992 *Proc. 11th Eur. Photovoltaic Solar Energy Conf. (Montreux)* (Harwood Academic Publishers) p 80
- [39] Blondeau J-Ph 1992 *Thèse Université d'Orléans*
- [40] Bouchoule A and Boufendi L 1994 *Plasma Sources Sci. Technol.* **3** 292-301
- [41] Heller W and Nakagaki M 1974 *J. Chem. Phys.* **61** 3619
- [42] Howling A A, Dorier J-L and Hollenstein Ch 1993 *Appl. Phys. Lett.* **62** 1341
- [43] Choi S J and Kushner M J 1993 *J. Appl. Phys.* **74** 853
- [44] Brus L 1986 *J. Phys. Chem.* **90** 2555
- [45] Rossetti R, Elison J L, Gibson J M and Brus L F 1984 *J. Chem. Phys.* **80** 4464

Experimental investigation of particulate formation in He–SiH₄ modulated RF discharges

Yukio Watanabe and Masaharu Shiratani

Department of Electrical Engineering, Faculty of Engineering, Kyushu University, Hakozaki, Fukuoka 812, Japan

Received 10 January 1994, in final form 4 February 1994

Abstract. Formation processes of particulates in radiofrequency power-modulated SiH₄ discharges have been studied using two kinds of laser light scattering, a modified Langmuir probe and absorption methods. The results suggest that particulates are formed by three phases of nucleation, rapid growth and growth saturation. In the nucleation phase, the formation may be caused by short-lifetime radicals such as SiH₂, SiH, or Si. In the rapid growth phase, SiH_n⁺ ($n = 0–3$) ions and/or SiH₃ radicals seem to make an important contribution to particulate growth, if only direct influx of the particles onto a particulate is taken into account. In the growth saturation phase, the saturation may be explained by taking into account the decrease in enhancement factor of the ion-collecting areas of particulates and the increase in their loss due to the reduction of ambipolar field in the periphery of the discharge column. Power modulation in SiH₄ radiofrequency discharges is found to be practically very effective for decreasing the sizes of particulates.

1. Introduction

Since particulates in processing plasmas are serious obstacles to microelectronics fabrication, great attention has been placed on clarifying their formation kinetics and suppressing their growth [1–7]. We have shown that, concerning RF silane (SiH₄) plasmas, a power-modulation method is useful not only for suppressing the growth of particulates but also in studying their formation kinetics [3–7]. Our work has been carried out using two laser light scattering (LLS) methods cooperatively. They have given the interesting result that particulates grow rapidly in a short period after turning on the RF power and are localized around the sheath edge. The results have revealed some features concerning the growth processes of particulates and the forces exerted on them.

While the LLS methods are useful for observing the behaviour of particulates *in situ*, they give information only on those above a few tens of nanometres in size. Hence, another method is necessary to gain insight into their early formation processes. We have recently proposed a modified Langmuir probe method for this purpose, which detects cluster-like small particulates, formed during a RF power-on period, as negative ions in a subsequent RF power-off period [8,9]. Preliminary measurements using this method have given some re-

sults supporting our previous speculation that particle species contributing to particulate nucleation may be short-lifetime radicals such as SiH_n ($n = 0–2$). Motivated by these results, we have been interested in measuring spatial profiles of radical species, especially ones of short lifetime, in the power-modulated RF discharge. Recently, as the first step, an absorption method has been applied to Si radicals. The results have shown an interesting close correlation between their spatial density profiles and those of particulates [10].

We have also been interested in the formation processes of particulates after their rapid growth, because their sizes are in the submicrometre to micrometre range for conventional CW RF SiH₄ plasmas, which is not so large compared with those observed in our work. Thus, observation using the LLS methods has been performed by prolonging the RF power-on period. The results show saturation of particulate growth as expected.

We have pointed out that the LLS intensity in the RF silane discharge is suppressed by the RF power modulation, suggesting a decrease in particulate amount [3]. Size and density of particulates have recently been measured separately as parameters of the duty cycle [10]. The results show that particle sizes decrease with decreasing duty cycle as predicted.

In this paper, we present some results from a series of recent experiments carried out using RF power-

modulated SiH₄ discharges, and, based on these results, discuss formation processes of particulates.

2. Experimental

Experiments were carried out using two types of conventional parallel plate RF reactors, A and B, which have been described elsewhere in detail [6, 8]. For type A, stainless steel plane electrodes 10 cm in diameter were placed at a separation of 4.3 cm in a stainless steel reactor 30 cm in diameter. Reactor A was employed for both LLS measurements to observe particulate behaviour and density measurements of Si radicals. For the LLS measurements, 5% SiH₄-He gas was used and an RF power of 20, 30 or 40 W was supplied during an RF power-on period $T_{on} = 2-8$ s at intervals of RF power-off period $T_{off} = 30-60$ s. For the Si density measurements, 10% SiH₄-Ar gas was used and RF power 80 W was supplied during $T_{on} = 0.08$ s at intervals $T_{off} = 0.08$ s. For type B, a Pyrex glass tube 9.45 cm in inner diameter was employed as a discharge vessel and stainless steel plane electrodes 8.5 cm in diameter were placed at a distance of 6.5 cm. Reactor B was employed to study the growth process of small particulates in their early formation phase. The gas used was 0.5% SiH₄-He and it was fed from the RF electrode toward the grounded one at a flow rate of 10-170 sccm. A RF power of 60 W was supplied during $T_{on} = 0.02-1$ s at intervals $T_{off} > 60$ s. The Langmuir probe used was 0.6 mm in diameter and 3 mm in length and was movable between the electrodes. Two probe currents were detected at its bias potentials of ± 27 V to the plasma potential 1 ms after RF power was turned off. The square of the ratio between these currents is considered to give the ratio between the mass of small particulates, M_- , and that of positive ions, M_+ [8].

The particulate behaviour was observed using two LLS methods, as reported elsewhere in detail [6]. They give time evolutions of spatial profiles of two-dimensional LLS intensity and the size and density of particulates. Spatial Si density profiles were measured by the absorption method, using a spectral line (288.2 nm) from a Si hollow cathode lamp. Sheet-like light 20 mm in width chopped at 25 Hz was passed parallel to the electrode surfaces twice. Spatial resolution along the discharge axis was about 5 mm. Measurements were performed during a period in which the line absorption was not affected by particulates [10].

3 Results

We have already reported the particulate behavior for $T_{on} = 2$ s [6, 7]. Figure 1 shows a typical spatial profile of particulate size and density obtained. The main points are summarized as follows: particulates begin to be observed around the sheath edge near the RF electrode; particulate size and density amount to 60-180 nm and

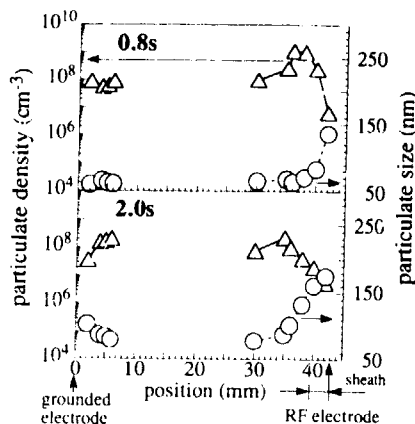


Figure 1. Spatial distributions of particle size and density between electrodes on discharge column axis at $t = 0.8$ and 2 s after discharge initiation. $T_{on} = 2$ s, 40 W, 5% SiH₄-He, 30 sccm, 80 Pa.

10^8-10^9 cm⁻³ during a short time of 1-2 s after the RF power being turned on; and particulates of a larger size reside in a higher DC field region near the electrodes. Based on these results, qualitative discussion has been given on the formation processes of particulates [6, 7].

To discuss the processes of interest in more detail, we need information on the growth of smaller particulates in their early nucleation phase. For this purpose, Langmuir probe and Si line absorption measurements have

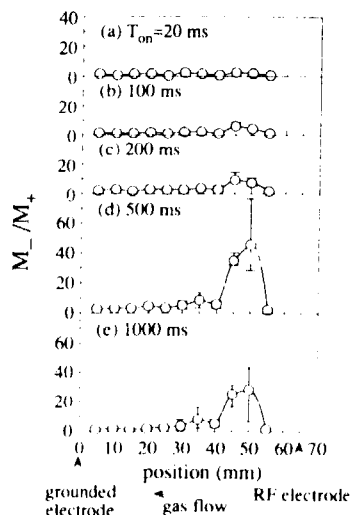


Figure 2. Spatial distributions of M_-/M_+ for $T_{on} = 20$ ms (a), 100 ms (b), 200 ms (c), 500 ms (d) and 1000 ms (e). 60 W, 0.5% SiH₄-He, 10 sccm, 80 Pa.

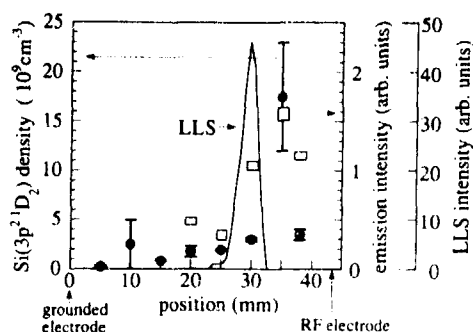


Figure 3. Spatial profiles of Si density, Si 288.2 nm intensity and laser light scattering intensity between electrodes.

$T_{on} = T_{off} = 80$ ms, 80 W, 10% SiH_4 -Ar, 20 sccm, 13 Pa.

been carried out [8,9]. Figures 2(a)–(e) show spatial distributions of M_-/M_+ deduced from the ratio between the negative and positive ion currents as a function of T_{on} . It can be seen that the ratio M_-/M_+ increases with T_{on} and becomes large in the sheath edge region 15–20 mm away from the RF electrode. This trend of localization becomes weak with increasing gas flow rate and, at a high flow rate over about 150 sccm, the region of large M_-/M_+ tends to shift downstream (not shown). Figure 3 shows spatial profiles of Si density

together with those of Si emission and LLS intensities. One can see that the Si density is high around the region where particulates are localized and its profile is also very similar to that of the Si emission.

To study the formation processes of particulates for RF power-on periods longer than $T_{on} = 2$ s, time evolutions of the particulate behaviour were observed using the LLS methods in the range $2 \text{ s} \leq T_{on} \leq 8 \text{ s}$ [10]. Figure 4 shows time evolutions of the spatial LLS intensity distribution (contours) between electrodes for $T_{on} = 4$ s. One can see that particulate amounts are predominantly rich around the sheath edges near the electrode, especially the RF electrode. Just after the RF power is turned off, a group of particulates move toward the grounded electrode and then downstream (right-hand side of figure 4) with the gas flow. Thus, spatial profiles of particulate amounts for $T_{on} = 4$ s are quite similar to those for $T_{on} = 2$ s reported previously, except that their intensity seems to saturate for $t \geq 2$ s. Figures 5(a) and (b) show LLS intensities and particulate sizes around the sheath edge of the RF electrode under the same conditions as in figure 4. It can be clearly seen that particulate growth tends to saturate after $t \approx 2$ s. In our experiment, on decreasing the RF power, the growth rate in the rapid growth phase decreased while the saturated sizes were almost constant (not shown).

The LLS intensity measurements were also carried out as a function of gas flow rate. It can be seen in figures 6(a) and (b) that the particulate amount becomes

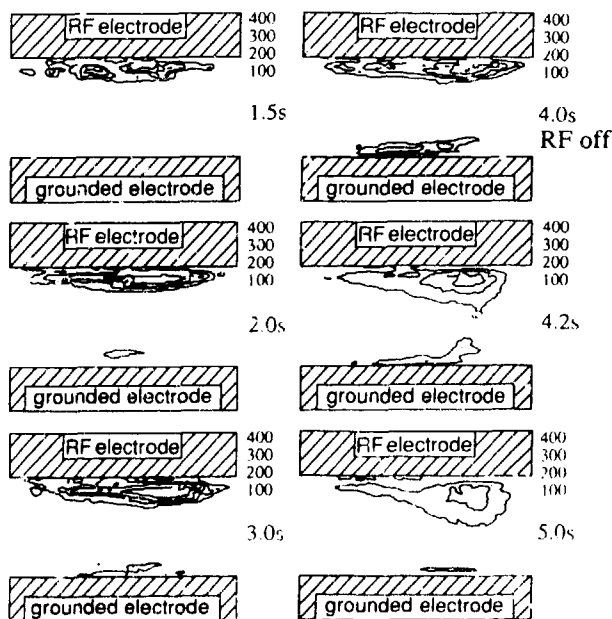


Figure 4. Time evolutions of laser light scattering intensity distribution (contours) for $T_{on} = 4$ s. Relative intensity of each contour is shown beside the radiofrequency electrode in each part. 40 W, 5% SiH_4 , He, 30 sccm, 80 Pa. The laser beam is passed from right to left at an angle of 135° to the gas flow.

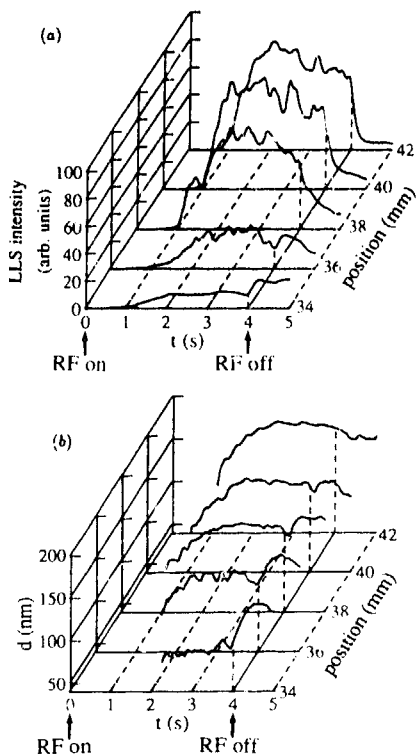


Figure 5. Time evolutions of laser light scattering intensity (a) and particulate size d (b) 34–42 mm above the grounded electrode after the radiofrequency power has been turned on for $T_{on} = 4$ s. 40 W, 5% SiH₄-He, 30 sccm, 80 Pa.

rich in the downstream region, increasing with gas flow rate, and further, that the sizes become large in the downstream region.

We have proposed the RF power-modulation method to suppress the particulate growth and shown that it brings about a drastic decrease in LLS intensity. To verify this effect more quantitatively, dependences of the spatial LLS intensity distribution and particulate size on duty cycle were investigated [10]. Figure 7 shows spatial LLS intensity profiles 1.4 s after the RF power has been turned on as a parameter of duty cycle D . For $D = 20\%$, the LLS intensity was too low to be observed. Decrease in D makes the high intensity region shift away from the RF electrode, and brings about a significant decrease in particulate amount. Figure 8 shows the dependence of the particulate size on D . It can be seen that the size becomes considerably decreased with decrease in D .

4. Discussion

As shown in figure 1, particulates are mainly observed around the sheath edge on the RF electrode side and those of a larger size reside in a higher DC field part of the region. This spatial size distribution can be ex-

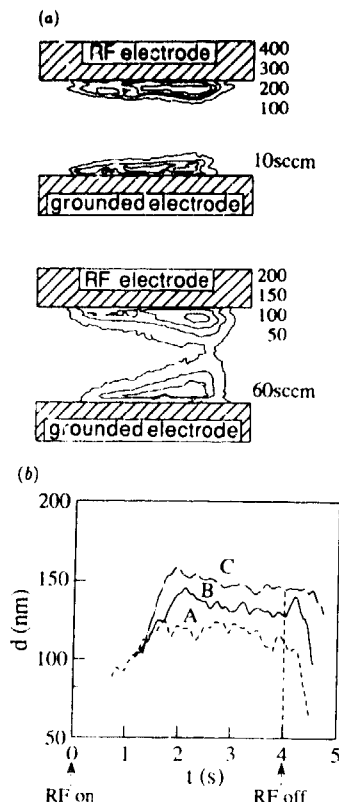


Figure 6. (a) Laser light scattering intensity distributions (contours) 4 s after the radiofrequency power has been turned on for $T_{on} = 8$ s. (b) Time evolutions of particulate size d at 1 mm below the radiofrequency electrode for positions 28 mm upstream (A), 0 mm (B) and 28 mm downstream (C) from the centre for $T_{on} = 4$ s; 40 W, 5% SiH₄-He, 60 sccm, 80 Pa.

plained by the balance between electrostatic and ion

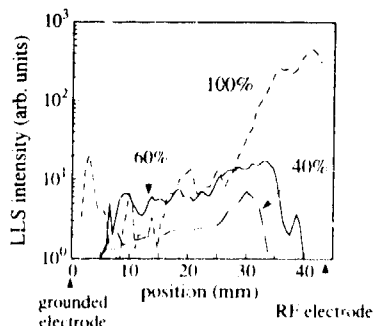


Figure 7. Laser light scattering intensity profiles between electrodes at 1.4 s after the radiofrequency power has been turned on for $D = 40, 60$ and 100% . 40 W, 5% SiH₄-He, 30 sccm, 80 Pa.

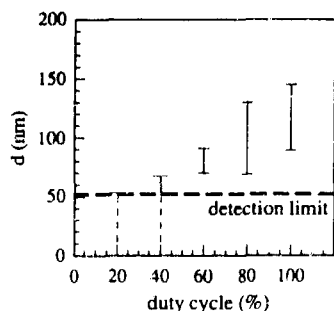


Figure 8. Duty-cycle-dependence of range of particulate size d in the discharge space at $t = 2$ s. $T_{on} = 2$ s, 40 W, 5% SiH_4 -He, 30 sccm, 80 Pa.

drag forces [11]. Further, it has been established that the relevant DC field becomes high with increasing particulate amount, that is, particulate growth [12]. These facts mean that information on the growth of particulates can be obtained *in situ* by observing their behaviour in the higher DC field part. From figures 1, 2, 4 and 5, on the basis of such a standpoint, it can be suggested that the formation processes of interest are composed of three phases, namely nucleation, rapid growth and growth saturation.

First, we shall discuss the nucleation phase based on the results shown in figures 2 and 3. Concerning small particulates detected as negative ions using the probe, those around the sheath edge are considered to be electrically neutral during the RF power-on period, because negatively charged ones would in this period be pushed toward the plasma bulk region by the DC field developed in front of the RF electrode, and, on the other hand, those in the plasma bulk region may be already charged up during this period. Hence, the result in figures 2(a)–(e) that small particulates grow while localized in the sheath edge region is interpreted as showing that they are nucleated and grow there without being charged. Further, in figure 3, the localized profiles are very similar not only to the Si density profile but also to that of Si emission, which is closely related to production of Si radicals. This means that the density of Si radicals becomes high only in their production region, because of their high reactivity. Actually, taking into account recent data on Si reaction rates [14], Si radicals are estimated to diffuse only about 0.01 mm at most before they react with SiH_4 . Figure 3 also shows that the high LLS intensity region is located around the high-density region for Si radicals. While our present radical density measurements are carried out only for Si atoms, the other short-lifetime radicals, SiH_2 and SiH , are also expected to have similar spatial profiles. From the examination above, it is strongly suggested that short-lifetime radicals SiH_n ($n = 0-2$) mainly contribute to formation in the nucleation phase, while it is not yet clear which one is more important among them. As

formation reactions related to such radicals in this phase, those between these species and SiH_4 may be promising.

Particle species contributing to formation in the rapid growth phase can be picked up, taking into account their influx to a particulate. A particulate over a few nanometres in size tends to be charged up negatively in a plasma and hence its positive-ion collection area is estimated to be enhanced by a factor of $(1 - V_f/T_+)$ using the orbital theory of a Langmuir probe [15], where $V_f (< 0)$ is the floating potential of the particulate and T_+ the positive-ion temperature in volts. In conventional RF plasmas, it is possible that this factor amounts to 200–300, which is large enough to account for the high growth rate of interest. Positive ions reaching the particulate surface may be changed to neutral radicals by recombining with electrons accompanying them and/or present on the surface. Neutral radicals can contribute to particulate growth by their thermal motion. The growth rates from these particle species are estimated assuming relevant parameter values, resulting in 140 nm s^{-1} for positive ions, $< 3 \text{ nm s}^{-1}$ for SiH_n ($n = 0-2$) and $< 20 \text{ nm s}^{-1}$ for SiH_3 . Such examination shows that densities of SiH_n^+ ($n = 0-3$) and/or SiH_3 are high enough to explain the growth rate in the rapid growth phase [11]. The RF power-dependence of the growth described in section 3 may be explained by the similar power-dependence of the ion and/or radical densities generated in RF discharges. In the above consideration, only direct influx of the particles onto a particulate is taken into account. It is necessary, for more precise argument, to get information on the number of charges on a particulate and on coagulation of particulates.

Next, we shall discuss the growth saturation phase. The growth of particulates depends on both the particle influx to them and their loss out of the discharge space. We have pointed out above that SiH_n^+ ($n = 0-3$) ions and/or SiH_3 radicals may play an important role in the rapid growth phase. If mainly the ions contribute, then enhancement of the collection area should decrease with particulate growth. Estimation of the enhancement factor gives that it decreases by about one order or more during growth of particulates in a range of density ratio between them and ions of 0.02–0.2 in our case [11]. For SiH_3 , on the other hand, there is no mechanism to suppress their influx.

Particulate loss may be closely related to balance between the drag force due to the gas flow and the electrostatic force due to the ambipolar field in the periphery of the discharge column. For reactor A, which has gas flow parallel to the electrodes, the two forces are opposite to each other in the downstream region of interest. Particulate loss is considered to increase with particulate growth for the following reason: for a plasma composed of positive ions, negative ions (or negatively charged particulates) and electrons, diffusion of electrons becomes very fast relative to that of negative and positive ions, when the density ratio between negative and positive ions is close to or larger than unity during

particulate growth [16]. As the diffusion of electrons becomes free from positive and negative ions, the ambipolar field tends to be dominated by diffusion of negative and positive ions, leading to the decrease in itself; the decrease in ambipolar field weakens the electrostatic force and hence brings about the increase in particulate loss due to gas flow. The results in figures 6(a) and (b) show that the gas flow drives particulates downstream. An overall particulate amount evaluated by integrating a spatial LLS intensity distribution at a particular time throughout the discharge space tends to decrease with increasing gas flow rate. The above loss mechanism also seems to be supported by the experimental result, described in the last section, that the size of particulates in the saturated phase is almost independent of RF power for a given flow rate.

Finally, the effect of RF power modulation is discussed. The results in figures 7 and 8 show that modulation is really effective in decreasing not only the amount of particulates throughout the discharge space but also their size. From the balance between the electrostatic and ion drag forces, particulates of smaller size should reside far away from the RF electrode. Further, as observed in figure 4, particulates tend to move toward the bulk plasma region just after the RF power is turned off. These phenomena are considered to be related to the shift of the high-LLS-intensity region toward the bulk plasma region with the decrease in duty cycle shown in figure 7.

5. Conclusions

From the experimental studies, formation processes of particulates in SiH₄ RF plasmas have been found to grow through nucleation, rapid growth and growth saturation phases. Initially, particulates are considered to be formed by short-lifetime radicals, SiH₂, SiH or Si. The subsequent rapid growth seems to be explained by the contribution of SiH_n⁺ ($n = 0-3$) and/or SiH₃, if only direct influx of the particles onto a particulate is taken into account. As particulates grow, the enhancement factor of their ion-collecting area decreases and also the ambipolar field in the periphery of the discharge column is weakened. These two factors related to the growth of

particulates may bring about their growth saturation. The RF power modulation has been found to be really effective in decreasing the size of particulates.

Acknowledgments

This work was supported principally by a Grant-in-Aid for Scientific Research on Science of Free Radicals in Priority Areas and a Grant-in-Aid for Cooperative Research (A) from the Ministry of Education, Science and Culture of Japan.

References

- [1] Bouchoule A, Plain A, Boufendi L, Blondeau J Ph and Laure C 1991 *J. Appl. Phys.* **70** 1991
- [2] Boufendi L, Plain A, Blondeau J Ph, Bouchoule A, Laure C and Toogood M 1992 *Appl. Phys. Lett.* **60** 169
- [3] Watanabe Y, Shiratani M, Kubo Y, Ogawa I and Ogi S 1988 *Appl. Phys. Lett.* **53** 1263
- [4] Shiratani M, Matsuo S and Watanabe Y 1991 *Japan. J. Appl. Phys.* **30** 1887
- [5] Watanabe Y, Shiratani M and Yamashita M 1992 *Appl. Phys. Lett.* **61** 1510
- [6] Watanabe Y and Shiratani M 1993 *Plasma Sources Sci. Technol.* **2** 35
- [7] Watanabe Y and Shiratani M 1993 *Japan. J. Appl. Phys.* **32** 63
- [8] Fukuzawa T, Shiratani M and Watanabe Y 1994 *Appl. Phys. Lett.* to be published
- [9] Fukuzawa T, Shiratani M and Watanabe Y 1993 *Proc. 11th ISPC* vol 3 (Loughborough) p 1125
- [10] Shiratani M, Tsuruoka H, Fukuzawa T, Kawasaki H and Watanabe Y 1993 *Proc. 11th ISPC* vol 4 (Loughborough) p 1469
- [11] Shiratani M, Fukuzawa T and Watanabe Y *IEEE Trans. Plasma Sci.* **22** 1
- [12] Sommerer T J, Barnes M S, Keller J H, McCaughey M J and Kushner M J 1991 *Appl. Phys. Lett.* **59** 638
- [13] Boeuf J P and Belenguer Ph 1992 *J. Appl. Phys.* **71** 4751
- [14] Tanaka T, Hiramatsu M, Nawata M and Goto T 1993 *Proc. 10th Symp. on Plasma Processing* (Osaka) p 207
- [15] Hershkovitz N 1989 *Plasma Diagnostics* vol 1 (San Diego: Academic) p 130
- [16] Rogoff G L 1985 *J. Phys. D: Appl. Phys.* **18** 1533

High concentration effects in dusty plasmas

André Bouchoule and Laïfa Boufendi

Groupe de Recherche sur l'Energétique des Milieux Ionisés, Unité de recherche associée au CNRS (URA 831), UFR Sciences, Université d'Orléans, BP 6759 45067, Orléans Cedex 02, France

Received 11 January 1994, in final form 14 January 1994

Abstract. Dust generation in plasma reactors used for PECVD is a general limiting effect which occurs when trying to obtain high deposition rates in the fabrication of thin films. In such dust-forming processes, for instance silane discharges, very high concentrations of submicrometre sized particulates are readily produced. The theoretical approach and the modelling of these dusty dense plasmas suggest that they have very peculiar properties with spectacular effects concerning the plasma equilibrium and the behaviour of the particulate cloud.

Well characterized dusty dense plasma situations have been obtained in argon-silane or in pure argon RF discharges and experimental data obtained in these situations are reported here, in connection with the theoretical predictions.

In terms of plasma properties the drastic modification of the free electron population, induced by the presence of the particles, is one of the most important results, with significant effects on the chemical equilibrium of the plasma.

In terms of the particle cloud behaviour the strong electrostatic interaction between the negatively charged particulates is shown to be an order of magnitude higher than their kinetic energy and this particle cloud has to be described as a 'Coulomb liquid'.

An overview of our experimental studies of these effects in a dusty dense plasma situation is given, including the most recent results.

1. Introduction

In a companion paper (Boufendi *et al*) [1] the growth kinetics of particles in a RF argon-silane plasma are described for particle sizes from 2 nm to a few 100 nm. The experimental set-up, as well as the diagnostics developed for particle characterization (size and concentration) are given in that paper.

This contribution will discuss the effects of this dusty situation on the plasma and discharge properties and the particle-particle interactions in the cloud. Dusty dense plasmas have already been observed and studied in various experimental situations [2-4], so a specific purpose of the present work was to take advantage of the well defined conditions obtained in our reactor (in terms of particulate cloud characterization) for a more precise evaluation of the dusty plasmas properties, in connection with theoretical predictions.

The results concerning the effects of the dust on the RF discharge properties and the particle-particle interactions will be summarized here as they have already been published elsewhere.

New results on the evolution of the plasma properties when the particles are growing in size will be described in more detail in this contribution. They have

been obtained by using time-resolved optical emission spectroscopy and mass spectrometry. The variation of the free electron concentration associated with the pristine dusty plasma transition is determined by a microwave diagnostic technique.

As the particle size kinetics are known, this study adds complementary knowledge to the connection between the particle size and the induced effect on the plasma properties.

These effects, in terms of plasma properties, are observed when the particle size is significantly larger than the initial clusters of a few nanometres and occurs in the coagulation step of the growth of the particles (as shown in the companion paper).

The dusty situation is characterized by a severe drop in free electron concentration and a strong enhancement of their mean energy, such that an important overall enhancement of the excitation and dissociation rates is observed in the plasma.

As our results will be compared with theoretical predictions of cloudy plasma behaviour some of the relevant theoretical works will be briefly reviewed in section 2 with a particular emphasis on the points where comparison with experimental data has been made.

In section 3 the transition of the plasma properties from a pristine to a dusty situation is studied experimentally and compared to model predictions.

Finally, in section 4 an overview of particle-particle interactions as observed experimentally and previously reported will be presented.

2. Theoretical considerations

Many theoretical studies of dusty plasma media have already been published, including analytical and statistical Monte Carlo simulations. These studies are connected to typical situations relevant to laboratory discharges and extraterrestrial plasmas and concern several physical problems such as:

- (i) the electrostatic equilibrium of a single particle with respect to the incident charge flux from a given plasma medium, and size dependent effects [5, 6];
- (ii) the effects of other processes (e.g. electron photo-emission) on this equilibrium [7];
- (iii) the effects of particle concentration on the plasma-particle equilibrium and particle-particle interactions [8, 9];
- (iv) the collective properties (fluctuations, wave propagation) which are of most recent interest [11] (see Tsyтовich [10]).

A brief review is given here, with particular emphasis on the plasma-particle equilibrium and particle-particle interactions in the situation of 'dusty dense plasmas'.

2.1. Electrostatic equilibrium of a single particle immersed in a plasma

This equilibrium has been studied in a broad range of situations. The problem is treated through the theory of a spherical Langmuir probe in the zero mean total current (floating potential) condition.

Illustrative examples are given by the study of the structure of the sheath surrounding a particle in a given, otherwise unaffected, plasma ambience [5] and by the study of the influence of the collision-induced trapping effects of ions around a negatively charged particle [6].

In the first study the effective screening radius around the particle was shown to be a sensitive function of the particle radius. It varies from the order of an ionic Debye length when the particle radius is much smaller than this characteristic length to the order of several times an electronic Debye length when the particle size becomes much larger. In typical low-pressure discharge plasmas of interest here (concentrations $n_e = n_i \sim 10^{10} \text{ cm}^{-3}$, electronic temperature $\sim 2 \text{ eV}$, ionic temperature $< 0.06 \text{ eV}$ (argon)) this critical radius is of the order of $50 \mu\text{m}$. This value is much larger than the particle sizes commonly present in plasma reactors, so the ionic Debye length gives the right order of magnitude of the extent r_s of the sheath surrounding a particle.

In the second study it is shown that the trapping effects could play an important role in laboratory discharge conditions and this would have an important consequence for the force exerted on a 'dressed particle' by a macroscopic electric field [12].

However one question remains to be addressed: for given plasma conditions a critical particle size must exist below which these studies are no longer valid to describe properly the actual time-varying charge of the particles. When the fluctuations of the charge supported by the particle exceed its mean value (with, therefore, possible change of the sign of this net charge) the description of these fluctuations becomes of prime importance in order to describe the particle-particle interactions properly (e.g. the coagulation processes in the early step of dust formation).

2.2. Dusty dense plasmas

When the concentration of the particles is such that the elementary volume associated with each particle becomes of the order of the Debye shielding volume, the plasma properties cannot be considered independently and become connected with particle concentration. The transition from the isolated particles situation to the dusty dense plasma situation has been described [8] by using a capacitor model where the plasma parameters (T_e , T_i , n_e) are taken as given quantities. In this situation the mean negative charge concentration in the plasma becomes essentially represented by the negatively charged particles, the relative participation of the free electrons to the charge neutrality becomes very small and the charge on each particle in this situation is simply $Q_p \sim (n_i/N_p)e$.

This high dust concentration situation is relevant in extraterrestrial plasmas as planetary ring environments and high-concentration effects have been described [7, 9]. In these studies the free electrons and negatively charged dust concentrations are considered as given parameters.

A self-consistent description of the problem has been developed by Bocuf [11] with a particle-in-cell (PIC) Monte Carlo (MC) simulation where the only external parameter is the current density in the plasma. This has been done for situations (argon gas pressure 100 mTorr, particles with diameters and concentrations $0.1 \mu\text{m}$, 10^8 cm^{-3} respectively) relevant to those studied experimentally [13].

The results obtained in this self-consistent model of dusty dense plasmas show the following.

- (i) The charge and surface potential of the particles are severely reduced in comparison with isolated particles.

(ii) As a consequence, in 'dusty dense' plasmas, almost all electrons can reach the particle surface and surface induced recombination is a major effect, while in the situation of isolated particles, as clearly demonstrated in previous modelling work [14], the particle surface potential is such that only the high-energy tail of the EEDF is involved.

(iii) The lowering (by an order of magnitude) of the free electron concentration is more than compensated, in terms of ionization frequency, by a strong increase in

Table 1. Boeuf [9] model predictions for two situations of current density in the plasma and two particle sizes, the particle density being 10^8 cm^{-3} .

$J(\text{mA cm}^{-2})$	$d(\mu\text{m})$	$N_i(\text{cm}^{-3})$	$N_e(\text{cm}^{-3})$	$T_e(\text{eV})$	$\nu_i(10^7 \text{ s}^{-1})$	$Q_p(e)$
0.5	0.1	3×10^9	0.13×10^9	5.5	7	12
5.0	0.1	12×10^9	0.10×10^9	≈ 5.5	8	50
0.5	0.3	$\approx 3 \times 10^9$	0.045×10^9	7.7	35	≈ 12
5.0	0.3	$\approx 12 \times 10^9$	0.35×10^9	≈ 7.7	≈ 35	≈ 50

electron temperature induced by the electric field which penetrates in the plasma (at a given current density).

Typical parameters for this work are shown in table 1 for conditions close to those of the experiment (particle concentration $\approx 10^8 \text{ cm}^{-3}$, diameter $0.2 \mu\text{m}$, argon pressure 100 mTorr). In this table J is the current density through the plasma, d is the particle diameter, N_i and N_e are the argon ion and free electron concentrations respectively, T_e is the mean electronic energy, ν_i is the electron impact ionization frequency and Q_p is the charge of each particle expressed in number of electrons.

The above data have been obtained for DC plasma current densities as input parameters in the simulation, while in our experiment the plasma is excited in a RF (13.56 MHz) discharge. As the plasma appears as highly resistive for current transport this difference is not as drastic as might be expected in the pristine argon gas situation and the DC current density range selected in the table corresponds to the RF current amplitudes measured in the working conditions of our parallel plate discharge.

The data in table 1 show clearly that the influence of particle size on plasma properties concerns primarily the concentration and energy of the free electrons and this could be perhaps an interesting indication for diagnosis of particle size in a homogeneous dusty plasma.

For these dusty dense plasmas the electrostatic interaction between particles is not shielded, the mean interparticle distance being of the order of or less than the ionic Debye length. Even when taking into account the effect of reduction of particle charge, as seen in the above studies, this interaction energy is easily higher than the kinetic energy of the particles.

The thermodynamics of such plasmas are similar to the so called one component plasmas (OCPs) where one species of charged particles is considered in a slightly modulated neutralizing fluid. In his work on dusty dense plasmas Ikezi [15] points out that a liquid-solid transition in strongly interacting particle clouds could be obtained in laboratory discharges.

This phase transition is defined by the values of the two dimensionless parameters $K = a/\lambda_i$ and $\Gamma = V(a)/kT$ where a is the mean interparticle distance, λ_i is the ionic Debye length and $V(a)$ is the particle-particle interaction energy.

The critical value of the parameter Γ for which the free energy of the liquid and solid phases are equal is given as $\Gamma_c = 170$.

In a recent simulation of these systems [16], liquid-like behaviour was demonstrated through the pair correlation function of the particle positions when the Γ factor was significantly higher than one but below the threshold value of solidification. The present study by those workers of the particle-particle interaction potential as function of the mean distance between the particles seems to point out a net qualitative difference with the Yukawa monotonic repulsive potential: the short distance repulsive interaction is changed to an attractive one when the interparticle distance is higher than a critical value expressed as

$$r_c = (1 + \sqrt{3})L_D$$

where L_D is the characteristic Debye length for the background plasma. This, in addition of the particle polarizability effects, could be of importance when considering the natural propensity of particles to assemble in clouds, as observed experimentally in a number of situations.

Of course, for the same reasons as given above, if the particle diameter becomes small enough (in the 10 nm range for example) these results on dusty dense plasmas become questionable and statistical charging effects must be considered, which is out of the scope of the present paper.

3. Experimental characterization of dusty plasmas

The experimental data on RF discharge properties, plasma parameters and particle-particle interactions presented here have been obtained at Orléans in the same reactor where the growth processes of the particles have been characterized as reported in the companion paper [1].

3.1. RF argon discharge: a comparison of the pristine and dusty situations

The comparison between model predictions and the experimental behaviour of dusty discharges has been made in a situation as simple and well characterized as possible.

A dusty argon discharge is obtained in the following way. A transient flow (few sccm) of silane is added to the permanent (30 sccm) argon flow through the discharge box. After this transient addition of silane a given concentration of particles with well defined sizes is stored in the RF discharge while the pure argon gas

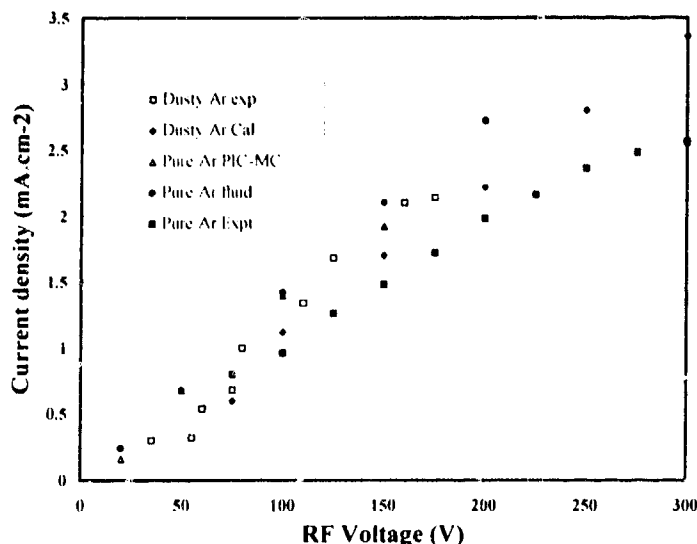


Figure 1. Current density in pure argon and dusty argon discharges as a function of the RF voltage. Comparison of the experimental results with a fluid and PIC-MC models.

situation (110 mTorr) is restored. The dusty situation obtained is a function of the silane transient flow, of the RF voltage applied during this transient flow and of the temperature of the reactor.

Typical transient conditions are 5 s at 1.2 sccm of silane flow and 200 V peak-peak, room temperature for the discharge. Under these conditions, a homogeneous distribution of monosized particles is obtained in the

argon plasma with a diameter of 84 nm and a concentration of 10^8 cm^{-3} .

A detailed comparison of experimental data with model predictions has been made in pristine and dusty discharge conditions and is already reported. Figures 1 and 2 (extracted from [13]) show that a good quantitative agreement is obtained over a rather wide range of discharge excitation voltages both for the discharge

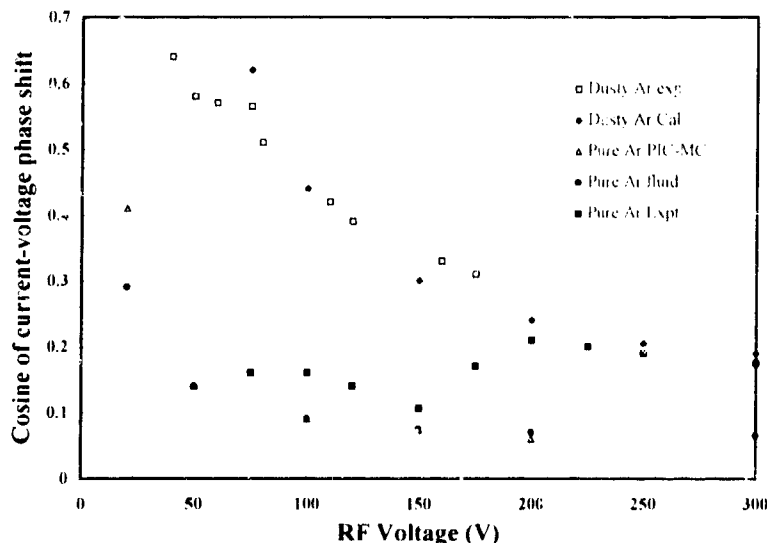


Figure 2. Cosine of the current-voltage phase shift, $\cos(\phi)$, in pure and dusty argon discharges as a function of the RF voltage. Comparison of the experimental results with fluid and PIC-MC models.

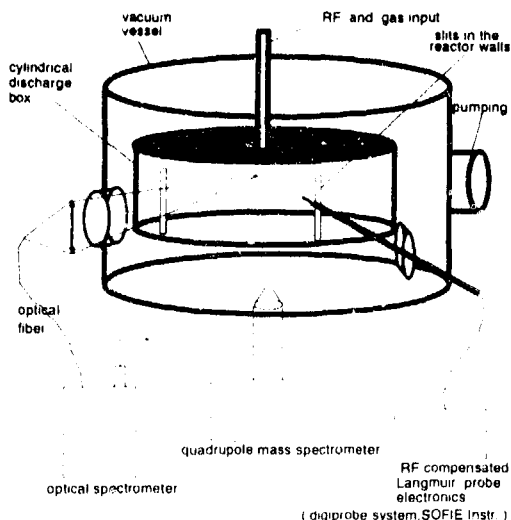


Figure 3. Schematic representation of the experimental set-up and diagnostics.

current and the current-voltage phase shift.

As shown in these figures, the presence of dust has a strong influence on the resistivity of the plasma but the RF current itself is not much affected, having mean absolute values comparable to those chosen in table 1.

More details on this argon dusty plasma study may be found in the literature.

The data of table 1 show that the EEDF must be strongly affected by the presence of the particles and our experimental studies reported in the following section confirm this theoretical prediction.

3.2. Evolution of the free electron population in a particle forming plasma

3.2.1. Diagnostics. Several diagnostics (shown schematically in figure 3) have been used in order to characterize the electron population in the same RF discharge where the particle formation kinetics have been studied.

The free electron density has been determined by using the whole reactor as a microwave resonant cavity. The frequency shift of this resonator, induced by the plasma, has been used for determination of the electron density. A network analyser (HP 8753 C), operating in the reflection mode, was used to measure this frequency shift.

As the plasma frequency remains an order of magnitude lower than the resonant frequency, a straightforward perturbation model gives the relation between the measured frequency shift Δf and the free electron density N (assumed to be homogeneous over the plasma):

$$\Delta f = f_0(N/N_0)(V_0/V)$$

where f_0 is the resonant frequency without plasma, N_0 is the electron density whose plasma frequency is f_0 , V_0

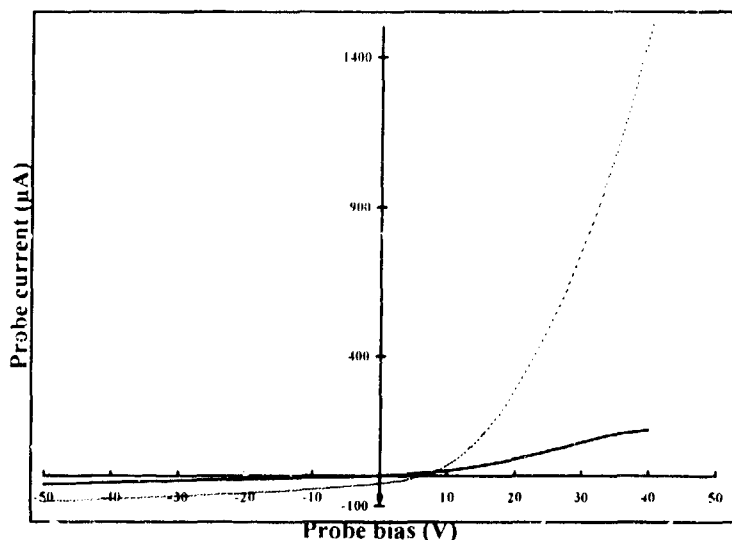


Figure 4. Electrostatic probe characteristic obtained in pristine and dusty argon plasmas. The external parameters are the same (RF voltage 300 Vpp, pressure 110 mTorr). The dusty situation is defined by particle size (66 nm) and concentration ($4.3 \times 10^7 \text{ cm}^{-3}$). The estimated electronic density and temperature are $n_e = 5.1 \times 10^8 \text{ cm}^{-3}$ and $T_e = 2.3 \text{ eV}$ for the pristine plasma and $3.5 \times 10^8 \text{ cm}^{-3}$ and 7.1 eV for the dusty plasma. The electronic temperatures as estimated by spectroscopy are 1.7 eV and 6.0 eV for pristine and dusty plasma respectively and the microwave measurements confirm the drastic drop in electron concentrations.

is the reactor volume and V is the volume occupied by the plasma between the sheaths.

We used also a RF compensated Langmuir probe (SOFIE digiprobe system) for the determination of ion and electron concentrations and also for electron mean energy evaluation. The probe current voltage characteristics are scanned following an initial procedure of cleaning, allowing stable and reproducible results. Examples of probe characteristics are given in figure 4 for pristine and dusty argon plasma situations. The evolution of the electronic concentration and energy obtained by Langmuir probe, microwaves, and spectroscopy are in good agreement, showing a strong decrease of concentration and a strong increase of energy of the free electrons in the dusty plasma.

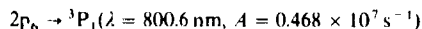
Optical emission spectroscopy has been used to obtain quantitative information on the population of the excited states of argon. Precise measurements of the intensities of several atomic spectral lines radiated per unit plasma volume have been performed by using a simple method developed in the laboratory and described elsewhere [17]. An optical fibre, equipped with a short focus lens, collects the light emitted by the plasma volume contained in a small diameter (2 mm) cylinder parallel to the discharge electrodes and aligned with the diameter of the reactor.

The end of the fibre is connected to the entrance slit of a monochromator and the calibration of the whole system, in terms of photomultiplier output for a given photon flux in the spectral range of interest, is performed in a standard way with a tungsten ribbon lamp.

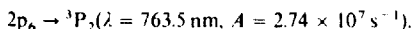
The absolute population of radiative excited states of argon is deduced from measurements of line intensities with the assumption of a homogeneous concentration along the plasma diameter.

For optical transitions whose lower level is a metastable state, the optical depth of the plasma is such that reabsorption phenomena are not negligible. This effect has been used in order to measure the concentration of the 3P_2 metastable state concentration by comparison of two argon line intensities in the following way [18].

Two transitions between the excited states ($4p \rightarrow 4s$) of the argon atom are selected:



and



They have the same $4p$ upper level but the first one is connected to a resonant state with a transition probability much lower than the second one which is connected to the lowest energy metastable 3P_2 state. In our conditions the plasma is optically thin for the first transition but reabsorption phenomena play a role in the plasma emission of the second line. The ratio of the line intensities measured for these two transitions is used for a determination of the metastable state concentration through a simple radiative transfer calculation assuming an homogeneous distribution of the excited states in the reactor [18].

The dissociation of silane in the reactor has been

measured by using a quadrupole mass spectrometer whose entrance hole is located 10 cm below the discharge box in the vacuum vessel. The characteristic time required to achieve a stationary situation in the vacuum chamber (in terms of chemical equilibrium) is of the order of 5–10 s. This prevents the observation of faster evolutions (1 s or less) of the plasma-induced dissociation factor of the silane flow in the reactor box itself.

3.2.2. EEDF evolution in a dust-forming argon-silane plasma. The modification of the EEDF due to the formation and storage of the particulates in the reactor is deduced from both spectroscopic and microwave measurements. Some examples of the time evolution of the intensities of argon spectral lines after starting an argon-silane RF discharge are shown in figures 5 to 7.

In figure 5 the two situations of pure argon and silane-argon discharges are compared. The same initial RF voltage is applied in both cases and the figure gives the time evolution of the intensity of the 750.3 nm argon

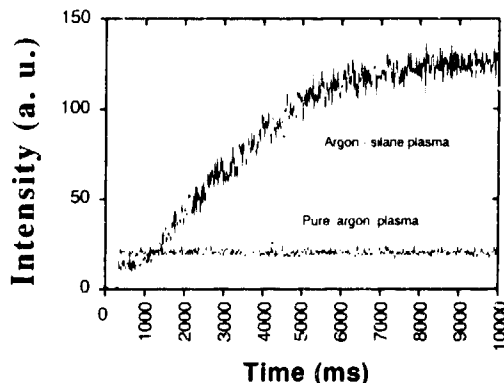


Figure 5. Time evolution of the 750.3 nm argon line in pure argon and argon-silane discharges.

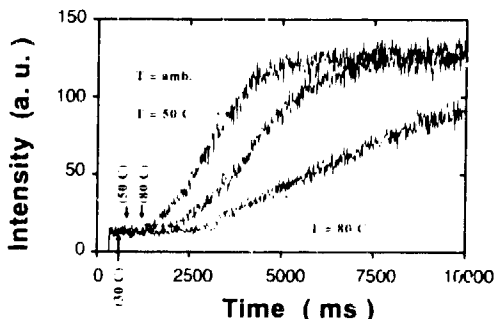


Figure 6. Temperature effect on the time evolution of the 750.3 nm argon line. The vertical thick arrows show the beginning of the coalescence of the crystallites.

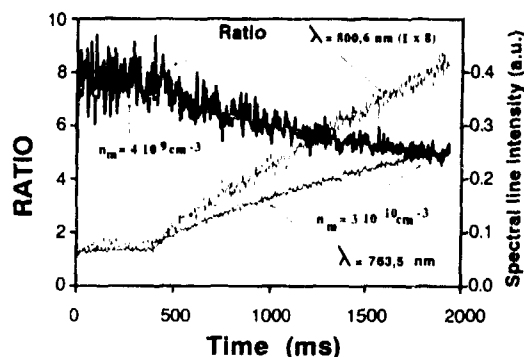


Figure 7. Time evolution of the 763.5 nm and 800.6 nm lines and their ratio. The ratio gives the 3P_2 metastable concentration.

line. In the situation of an argon silane plasma the particle appearance time, as viewed by laser scattering, is indicated by an arrow. A strong increase of the population of the argon excited level ($2p_1$) is clearly induced when a dusty plasma situation is created in the reactor.

The fact that such an enhancement of the excitation rate of the argon atoms is induced by the presence of particulates is confirmed by an analysis of the reactor temperature effects on this time evolution. As reported elsewhere [19] and in the companion paper the kinetics of the particle growth in the discharge are characterized by a sensitive delay effect when increasing the temperature of the reactor. Figure 6 shows that this delay effect for particle growth is observed also for the enhancement of the excitation rate of the argon upper levels.

Figure 7 shows the time evolution of the intensities of the two emissions (800.6 and 763.5 nm) used for the determination of the 3P_2 metastable state concentration. The ratio of the intensities $I(763.5)/I(800.6)$ decreases with a delay of the order of 0.5 s. This is a clear qualitative indication of an increase of the metastable state concentration.

This effect is indeed an important one as the quantitative analysis of the ratio of these line intensities leads to an increase of the metastable state concentration from $4 \times 10^9 \text{ cm}^{-3}$ at early time ($< 0.4 \text{ s}$) to $3 \times 10^{10} \text{ cm}^{-3}$ for a plasma duration of 10 s. The interpretation of this enhancement is straightforward: as shown below the electron concentration decreases strongly while the electron energy increases when the particles are formed and the net rate of excitation of the argon excited levels is increased; it is expected that the metastable concentration equilibrium is moved towards higher values because its quenching rate by electron

collisions is drastically reduced. The quenching effect due to the metastable-particulate collisions is considered as a negligible effect in our experimental conditions: the total surface developed in the volume of the reactor remains negligible (2%) as compared with the surface of the walls.

The absolute concentrations of argon excited ($4p$) levels have been determined by OES in pure argon gas and in argon-silane discharges. These excited states are:

$$2p_1(\lambda = 750.3 \text{ nm}), \quad 2p_6(\lambda = 800.6 \text{ nm})$$

and

$$2p_8(\lambda = 801.5 \text{ nm}).$$

By using microwave and OES data the evolution of the electron and argon excited states concentrations have been determined in an argon-silane discharge as a function of time.

Table 2 shows the data obtained before ($t = 0.4 \text{ s}$) and after ($t = 10 \text{ s}$) the formation of dust particles in the reactor. The operating conditions were: $V_{\text{rf}} = 600 \text{ Vpp}$, $d_{\text{Ar}} = 30 \text{ sccm}$, $d_{\text{SiH}_4} = 1.2 \text{ sccm}$, $T = 30^\circ \text{C}$. In Table 2 N_e , N_m , N_1 are the concentrations of the electrons, metastable (3P_2) and radiative ($2p_1$) argon levels respectively. N_6 and N_8 are the concentrations of the $2p_6$ and $2p_8$ argon levels respectively.

R_6 and R_8 are the estimated contributions of step-wise processes (involving electron-metastable state collisions) for the excitation rate of the $2p_6$ and $2p_8$ levels. These values are deduced from a detailed collisional radiative model of equilibrium of these two levels developed previously [20]. The strong difference between the cross sections for the excitation of these two ($4p$) levels by electron-metastable collisions together with the

Table 2.

	N_e (cm^{-3})	N_m (cm^{-3})	N_1 (cm^{-3})	N_6/N_8 (%)	R_6 (%)	R_8 (%)	T_e (eV)
$t < 0.4 \text{ s}$	4×10^9	3.2×10^9	1.5×10^6	0.44	29	9	2
$t = 10 \text{ s}$	3×10^8	1.1×10^{10}	9.6×10^6	1.07	20	6	8

measurements of their concentration in the same wavelength region (~ 801 nm) is a key point in the precision and usefulness of this model.

As the modelling of a dusty dense plasma [11] suggests that the EEDF is close to Maxwellian the above data can be used for an estimation of the electron temperature in the two situations. In what follows we assume that the population rate of the $2p_1$ excited level is equal to its radiative de-excitation rate (coronal equilibrium). This hypothesis is reasonable in our situation: the radiative lifetime of that level is $\tau_1 = 21$ ns and the collisional de-excitations by electron or neutral collisions remain comparatively negligible in our situation of gas pressure and electron density.

The equilibrium condition of the $2p_1$ level concentration N_1 is defined by the relation

$$k_{exc} \times N_e \times N_0 = N_1/\tau_1 \times (1 - R_1)$$

where N_e is the electron concentration, N_0 the argon atom concentration, k_{exc} is the excitation rate per electron averaged on the energy distribution function and corresponds to excitation of ground state atoms by electron impact. R_1 represents the possible contribution of a two-step process to the population of the $2p_1$ state. This contribution, smaller than the corresponding values for $2p_0$ and $2p_8$ states, is in fact negligible in our conditions.

The value of k_{exc} as a function of the electron temperature has been determined in previous work [20] and is used here for the determination of the electron temperature. In the two situations of table 2 the values of k_{exc} are 2×10^{-12} and 2.5×10^{-10} ($\text{cm}^3 \text{s}^{-1}$). The corresponding electron temperatures are 2 eV for pristine argon discharge and 8 eV for the dusty situation.

These determinations, obtained through spectroscopic data are in agreement with Langmuir probe measurements: by the RF compensated probe method the estimation of electron temperature in the two situations of pristine and dusty argon are respectively 2.3 eV and 7.1 eV. These probe measurements also show that the positive ion density in the plasma is only slightly increased, by a few ten %, when particles are formed in the reactor, while its initial value is close to the initial value of $4 \times 10^9 \text{ cm}^{-3}$ obtained for the electron density by the microwave method.

The dusty situation achieved in the reactor at the time (10 s) of the EEDF determination is well characterized: the particle diameter is 86 ± 4 nm and the concentration is 10^8 cm^{-3} . These data lead to a precise determination of the particle mean charge in these conditions which is of the order of 40 electrons and that value remains constant as a function of the particle size as soon as the particle charge density is much higher than the free electron density.

The particle-induced plasma modification clearly requires a minimum particle size to be effective. When only small crystallites are present the plasma appears as unperturbed through these spectroscopic measurements (figures 5–7). The time where the coagulation of these crystallites starts is indicated by an arrow, and it can be

seen that the plasma parameters remain unaltered. The critical size for which the particles induce a strong modification of the plasma appears to be of the order of few tens of nanometres. A more precise time-resolved study of the plasma evolution when the particles grow from the crystallite size (2 nm) to 50 nm diameter is now underway.

The experimental results obtained when the particles are of much larger size (≥ 100 nm) are in rather good agreement with the modelling studies reported above.

In our situation the mean absolute current density installed in the gas is of the order of 1 mA cm^{-2} , as deduced from the RF current in the discharge. The predicted charge per particle is close to the above experimental determination and the ratio of electron and positive ion concentrations is 1.3/30 while the experiment leads to a value of 3/40.

Nevertheless, a difference appears concerning the electron temperature. The model developed by Boeuf shows that this parameter is very sensitive to the particle size for otherwise given conditions. In the above conditions the expected value for the electron temperature is of 5.5 eV (table 1) while the experiment reveals a significantly higher value of 8 eV.

A detailed study is now underway, both experimentally and in modelling the RF discharge, in order to obtain a more precise insight on the evolution of the EEDF as a function of the particle size in the reactor. The strong enhancement of the electron energy in the dusty plasma situation is of prime importance for the chemical equilibrium in the reactor. The dissociation of the silane in the discharge is indeed drastically enhanced when particles are formed in the reactor. Figure 8 shows the time evolution of the peak 30 amu as recorded when the silane flow is added to the argon flow. The RF excitation of the discharge is started with a delay of few seconds, a delay which is required to achieve stationary chemical equilibrium in the whole pumping volume. This experi-

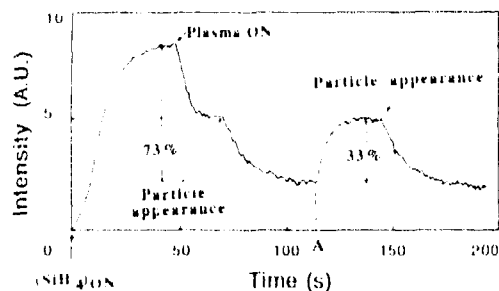


Figure 8. Time evolution of the 30 amu peak corresponding to the SiH_3 radical coming from the dissociation of silane molecules in the ionization source of a mass spectrometer (experimental conditions: $Q_{\text{Ar}} = 30 \text{ sccm}$, $Q_{\text{SiH}_4} = 1.2 \text{ sccm}$, $V_{\text{RF}} = 600 \text{ V}_{\text{eff}}$, $PT = 117 \text{ mT}$, $T = 393 \text{ K}$). At the time A the discharge is turned off for 1 s. During this lapse of time all the particles are swept out from the discharge box by the gas flow.

ment has been performed for a reactor temperature of 120 °C. The delay of the formation of the particles in these conditions is long enough to obtain a clear observation of the effect of the particle formation on the dissociation level of the silane molecules in the reactor. As expected from the above data the appearance of the particles leads to a strong enhancement (from 30% to 70%) of the silane molecule dissociation in the reactor, in spite of the drastically reduced concentration of the free electron population. When the same experiment is performed at room temperature the particle formation time is short in comparison with the measurement time constant and the dissociation as measured by the mass spectrometer reaches (in one apparently immediate step) a high (80%) value. When the temperature is high enough (200 °C) to prevent the formation of particles for plasma durations as long as 100 s the measured dissociation level remains at a lower level of 22%.

The clear conclusion of these studies is that the presence of dust in a discharge leads to a drastic modification of the EEDF with drastic consequences for the chemical equilibrium in the reactor. In that sense dusty dense plasmas appear as a very efficient way in order to achieve high efficiencies for electronic excitation and dissociation in plasma reactors.

Besides these 'chemical' considerations, a complementary attractive aspect concerns the physics of such dusty dense plasmas. The electrostatic interaction between the particles can play a major role for the physics of the dusty cloud. As already reported [21] a 'Coulomb liquid' situation has been clearly evidenced in our conditions. The following paragraph is devoted to a short review of this aspect of our work.

3.3. Particle cloud as a 'Coulomb liquid'

In order to compare the situation achieved in our reactor with the theoretical predictions in terms of the thermodynamic state of the dusty plasma, the important relevant parameters have to be determined. As shown in the brief survey of the theoretical works, the determination of the value of the Γ factor is critical in that respect. Such a determination has been obtained for a dusty plasma situation created in our reactor in the following way.

By using a laser Doppler anemometer (Dantec LDA04) the distribution function of the vertical speed of the particles is determined. Optical access to the plasma is limited by the small vertical slits in the cylindrical discharge box and even by using an argon ion laser (514 nm) the minimum particle diameter required for LDA speed measurements is found to be 80 nm. The corresponding particle growth time is 20 s in the typical conditions of our argon-silane discharge. The particle speeds have been measured for a dusty situation where the particles have grown to a diameter of 230 nm. The silane flow is stopped when this diameter is obtained and the particles remain trapped in an argon plasma with a concentration of 10^8 cm^{-3} . The results obtained

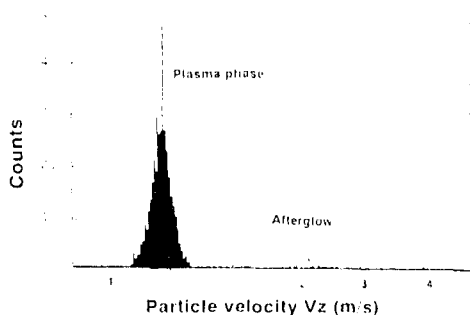


Figure 9. Histogram of the particle velocities in the plasma phase and when RF is turned off.

in the particle speed determinations are shown in figure 9. On the same figure are shown the particle speeds measured immediately after the extinction of the argon plasma. Before the extinction the speed distribution of the particles is characterized by a mean thermal velocity of 0.019 cm s^{-1} . Immediately after the plasma extinction, particle velocities can be measured in spite of the short time allowed for that determination and it is clear that the particles acquire the vertical speed of the gas flow in the reactor (0.21 cm s^{-1}) as soon as the plasma is stopped.

When the plasma is on, as the mean quadratic velocity of the particles is known, an estimation of the specific mass of the particle material can be deduced if thermal equilibrium of the dust cloud with the gas in the reactor is assumed. In the measurement conditions the reactor temperature was room temperature and the specific mass as obtained for the particle material is 1.9 g cm^{-3} , a value close to the specific mass of deposited layers of amorphous silicon. This result is in agreement with the description of particle growth as given in the companion paper where it is shown that the growth of particles is achieved through a deposition process as soon as the particle diameter is larger than a few tens of nanometres.

Under the same conditions the density of the positive ion (Ar^+) concentration has been measured by an electrostatic probe and is $5.6 \times 10^9 \text{ cm}^{-3}$. As shown above the free electron concentration is less than 10% of this value and the mean particle charge required for charge balance in the plasma is 43 electrons.

In these conditions the ionic Debye length has a value of $40 \mu\text{m}$ and is larger than the mean diameter of the volume affected to each particle ($26 \mu\text{m}$). The electrostatic interaction energy between the particles can be estimated from the OCP model and is found to be 0.3 eV per particle [21].

A good estimation of the Γ factor is defined from the above determinations and is found to be close to ten under our conditions. In this range of Γ values the cloud of charged particles in the plasma is to be described as a 'Coulomb liquid'. The theoretical estimations for a liquid-solid transition show that this transition requires much higher values ($\Gamma \sim 170$). This liquid (and rather

incompressible) behaviour is also consistent with the observation of an almost homogeneous distribution of the dust cloud in the reactor volume as observed under the experimental conditions of the previous study. The particles acquire the gas flow velocity as soon as the electrostatic confinement by the plasma sheaths is removed (when the RF excitation is stopped). The gas drag force on the particles, which is clearly evidenced by this observation, is also estimated to be the dominant one when the plasma is present (thermophoresis forces have also to be taken into account as suggested by recent temperature gradients measured by Perrin in a similar reactor). The drag force exerted by the gas flow is pushing the particles of the cloud towards the bottom grounded electrode and the homogeneous distribution observed is directly connected to the electrostatic repulsive forces leading to the 'Coulomb liquid' situation demonstrated above.

A recent (to be published) experiment has been performed [22] where a cloud of 10 μm diameter particles has been trapped in an argon RF discharge. This experiment demonstrates clearly that a 'Coulomb solid' situation is obtained with very high estimated values of the Γ factor, of the order of few 1000. Together with our results this observation confirms that dusty plasmas represent a very attractive way to study experimentally the behaviour of the so called one component plasmas, in particular to test the theoretical predictions for the liquid-solid transition of such systems.

4. Conclusion

In our experimental studies of dust-forming argon-silane plasmas the theoretical predictions of the behaviour of a RF dusty discharge and the main parameters of a dusty dense plasma have been tested quantitatively. In terms of discharge behaviour the agreement is found to be good and the main features of a dusty plasma are also in good agreement with the data obtained through a Monte Carlo PIC simulation developed by Boeuf. The EEDF as obtained experimentally reveals, however, that the mean electron energy is significantly higher than predicted by this simulation and this point has to be clarified. Nevertheless it is clear that dusty plasmas are highly energetic media and could be attractive to achieve very reactive plasma situations.

The basic physics of dusty plasmas also appears very attractive. Besides their collective behaviour in terms of fluctuations and wave propagation which is treated in the contribution of Tsytovich [10], an interesting way is clearly to use these media as a convenient support for basic research relevant to the thermodynamics of OCPs and dense plasmas.

Acknowledgments

This work has been performed with the active participation of J Ph Blondeau, C Laure and A Plain and with the support of contracts from CEC (BREU-CT91-0411) and CNET. The collaboration with J P Boeuf and his group at Toulouse as well as many stimulating discussions with J Perrin from Ecole Polytechnique (Palaiseau), Ch Hollenstein and his group at EPFL (Lausanne), G Kroesen and his group at UTE (Eindhoven) and J Schmitt (Balzers) are also to be mentioned as participating in our collective improvement of the knowledge of dusty plasmas.

References

- [1] Boufendi L and Bouchoule A 1994 *Plasma Sources Sci. Technol.* **3** 262-7
- [2] Spears K G, Kampf R P and Robinson T J 1988 *J. Chem. Phys.* **92** 5297
- [3] Jellum G M and Graves D B 1990 *Appl. Phys. Lett.* **57** 2077
- [4] Ganguly B, Garscadden A, Williams J and Haaland P 1993 *J. Vac. Sci. Technol. A* **11** 1119
- [5] Daugherty J E, Porteous R K, Kilgore M D and Graves D B 1992 *J. Appl. Phys.* **72** 3934
- [6] Goree J 1992 *Phys. Rev. Lett.* **69** 277
- [7] Goertz C K 1989 *Rev. Geophys.* **27** 271
- [8] Wipple E C 1981 *Rep. Prog. Phys.* **44** 1197
- [9] Haynes O, Goertz C K, Morfill G E, Grün E and Ip W 1987 *J. Geophys. Res.* **92** 2281
- [10] Tsytovich V N 1993 *NATO Advanced Research Workshop* unpublished
- [11] Boeuf J P 1992 *Phys. Rev. A* **46** 7910
- [12] Daugherty J E, Porteous R K, Kilgore M D and Graves D B 1992 *J. Appl. Phys.* **72** 3834
- [13] Belenger P, Blondeau J Ph, Boufendi L, Toogood M, Plain A, Bouchoule A, Laure C and Boeuf J P 1992 *Phys. Rev. A* **46** 7923
- [14] McCaughey M J and Kushner M J 1989 *Appl. Phys. Lett.* **55** 951
- [15] Ikezi H 1986 *Phys. Fluids* **29** 1764
- [16] Farouki R T and Hamaguchi S 1992 *Appl. Phys. Lett.* **61** 2973
- [17] Ranson P and Elyaakoubi M 1991 *Proc. XXth ICPIG (Pugnochiso, Italy)* ed V Pallechi p 265
- [18] Ranson P, Elyaakoubi M, Brault P and Bouchoule A 1991 *Proc. ISPC IX (Pugnochiso, Italy)* (Pisa: IFAM)
- [19] Bouchoule A and Boufendi L 1993 *Plasma Sources Sci. Technol.* **2** 204-13
- [20] Elyaakoubi M 1991 *Thesis* Orléans
- [21] Boufendi L, Bouchoule A, Porteous R K, Blondeau J Ph, Plain A and Laure C 1993 *J. Appl. Phys.* **73** 2160
- [22] Morfill G 1991 *NATO Advanced Research Workshop* unpublished

Particulates in C_2F_6 - CHF_3 and CF_4 - CHF_3 etching plasmas

Harold M Anderson†, Svetlana Radovanov†‡, Joseph L Mock† and Paul J Resnick§

†Department of Chemical & Nuclear Engineering, University of New Mexico, Albuquerque, New Mexico 87131, USA

§Sandia National Laboratories, Silicon Technologies Department, Albuquerque, New Mexico 87185-5800, USA

Received 7 January 1994, in final form 8 February 1994

Abstract. Particulate generation has been studied during reactive-ion etching of oxide wafers in C_2F_6 - CHF_3 and CF_4 - CHF_3 plasmas using both a commercial etch tool and the GEC reference cell modified to resemble the commercial tool. Under certain discharge process conditions, copious amounts of submicrometre-sized particles are shown to form due to plasma interactions with the oxide substrate. In the commercial tool, particles were detected only by a downstream particle flux monitor, whereas in the reference cell, particles were observed by both *in situ* laser light scattering and downstream monitoring. In the commercial tool, wafers etched to end-point were shown by post-process surface analysis to be contaminated by submicrometre-sized columnar structures. Previous reports of similar such columnar structures formed during reactive-ion etching of oxide films have attributed the phenomenon to polymer micromasking. However, the results of this study clearly contradict this conclusion and suggest that the presence of columnar oxide etch residues is linked to process-induced particulate contamination. Laser light scattering measurements were made in the reference cell during reactive-ion etching of blanket oxide wafers and used to help clarify the complex processes of particulate nucleation, growth and deposition during oxide etching. Polarization coagulation of spherical particles formed in the reference cell is shown to occur, presumably in the high-field regions of the sheath, forming filamentous rod-like particle aggregates. The implications of this observation for wafer contamination are explored.

1. Introduction

Wafer particle contamination resulting from 'dusty' plasma processes during IC fabrication is now recognized as a major threat to integrated circuit manufacturing yields, as well as the reliability and performance of completed devices [1-4]. Unfortunately, most commercial tools for plasma processing do not provide adequate optical access for diagnostics necessary for fundamental dusty plasma studies. As a consequence, a considerable amount of effort has been expended to study particles in laboratory apparatus, while only a limited amount of work has been performed in production line equipment with production processes. This work is a report on efforts to bridge that gap, through comparative particle studies in the reference cell and a representative parallel plate commercial etch tool, the Drytek Quad Model 480 single-wafer etcher.

In this work, detailed investigation is made of the process conditions in the Drytek tool that lead to particulate generation in fluorocarbon discharges used for selective oxide etching. Under a variety of processing conditions, massive amounts of particles were detected downstream of the chamber during etching, while post-process wafer analysis revealed that the wafer surface became severely contaminated with columnar residues. The residues observed on the wafer surface in this study appear in SEM photos to be nearly identical to columnar structures first observed by Ozaki and Hirata [5] during reactive-ion etching (RIE) of oxide wafers. Ozaki and Hirata reasoned in their study that an erodable polymer micromask was formed from a minuscule amount of photoresist scum contamination of the wafer surface and that the subsequent micromasking was responsible for columnar residues. In this study, the fact that unmistakably similar columnar residues were generated on blanket, unpatterned oxide wafers, throws this explanation into grave doubt. An alternative explanation for this type of wafer contamination must be found.

‡Visiting Scientist at UNM from the National Institute of Standards and Technology, Electronics and Electrical Engineering Laboratory, Gaithersburg, Maryland 20899, USA

Jellum and Graves [6] were the first to observe the formation of rod-like structures in dusty (sputtered aluminium particulates) helium plasmas. These macroscopic rods were aligned with the sheath fields and located at the plasma-sheath boundary. The mechanism suggested as being responsible for rod formation in plasmas was polarized, field-aligned particle coagulation, a well-known phenomenon in aerosol science [7]. Both Selwyn *et al* [1] studying O_2 - CF_4 etching plasmas and Jarrath *et al* [8] studying BCl_3 - CH_4 depositor plasmas have since observed macroscopic filamentous structures forming in a plasma, presumably due to the same field effect. Graves [9] observed that, occasionally, one of the macroscopic rod-like aggregates of his plasma would mysteriously slip through the plasma-sheath boundary and impact on the electrode surface. No explanation for this phenomenon could be found at the time. However, the possible implication of these findings for the problem of microscopic columnar etch residues resulting from plasma processing is worth exploring in much greater detail.

2. Experimental

2.1 Commercial etch tool studies

The effects of RF power, reactor pressure and feed gas composition on particle production rates were studied in a 13.56 MHz Drytek Quad Model 480 RIE single-wafer etcher using 150 mm, n-type monocrystalline wafers with a blanket 6300 Å thermally grown oxide film. The wafers rested on the powered, water-cooled, aluminium lower electrode. The C_2F_6 , CHF_3 feed gas mixture is introduced to the chamber through a grounded shower head electrode. Particles produced during discharge operation were detected with a High-Yield Technology (HYT) Model 20 particle flux monitor installed in one of two symmetrically located pump lines downstream of the etch chamber (figure 1). Limited optical access into the process chamber prevented meaningful efforts at detecting particles by *in situ* laser light scattering (LLS) at this stage of the research.

The HYT particle flux monitor measures diode laser light (780 nm) scattered from particles transiting the focus point of the laser in the detector plane of the pump

line. The laser-based particle detector operates on the Mie light scattering principle, with a lower detection limit of 0.35 µm. Particles are sized into five different bins, based on the intensity of scattered light. Detector particle counts were integrated over a 10 s time period. By operating the particle detector with and without a discharge present and with and without wafers being processed, it was determined that the downstream technique does in fact provide quantitative information on plasma process-induced particle generation under typical processing conditions.

A response surface methodology (RSM) experimental strategy was adopted for characterizing regions of the operational parameter space where the potential for generating particles was pronounced. To this end, a series of screening and central composite inscribed (CCI) factorially designed experiments were selected and performed. In the screening experiments, C_2F_6 alone was used as the etchant gas, the total gas flow was fixed at 50 sccm and only power and pressure varied. Following the screening experiments, a series of two CCI-designed experiments were performed to identify the influence of hydrogen-bearing gases in the feed. Power, pressure and percentage CHF_3 in a C_2F_6 , CHF_3 gas mixture were varied while maintaining total flow at 100 sccm.

In addition to measuring particle flux downstream of the etch chamber, particles deposited on the wafer after etching were analysed by a variety of *ex situ* characterization techniques. A Tencor Surfscan 4500 laser wafer scanner was used to map particle distributions over each wafer surface. Selected wafers were also analysed by SEM, TEM, Auger and XRF techniques for particle morphology and composition. In the case of TEM analysis, the wafer was back-side-milled to reveal thin layers of the silicon wafer surface heavily contaminated with particles at the end of the etch. Several partial etches of the oxide substrate were also conducted so that the oxide surface could be examined at intermediate points in the etch process. Focused Auger analysis (beam size about 2 µm) and XRF were performed over heavily contaminated regions of the wafer surface. A large aggregate sample of particles suitable for further chemical analysis was also collected from etched wafer samples by rinsing the wafer with methanol, drying and compacting the residue. An FTIR analysis was performed on these aggregate samples.

2.2 Reference cell studies

The reference cell used in this study has been described elsewhere [10]. The configuration of the cell was such that the lower electrode was powered, the showerhead gas inlet was on the upper electrode, and the insulator was Teflon. In this configuration, the reference cell is nearly identical in scale to a Drytek parallel plate reactor, except for the gap spacing, the presence of a quartz guard ring around the powered electrode and the optical access windows. To approximate more closely the Drytek tool, an electrode extension was machined for the reference cell to close the gap space to about 1 cm. A quartz guard ring, 0.5 inch thick, was machined

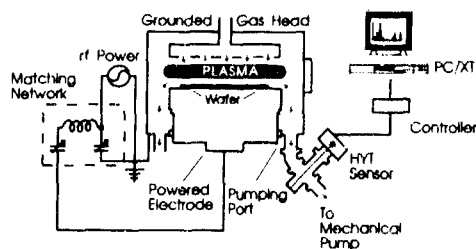


Figure 1. Schematic diagram of the Drytek Quad reactor.

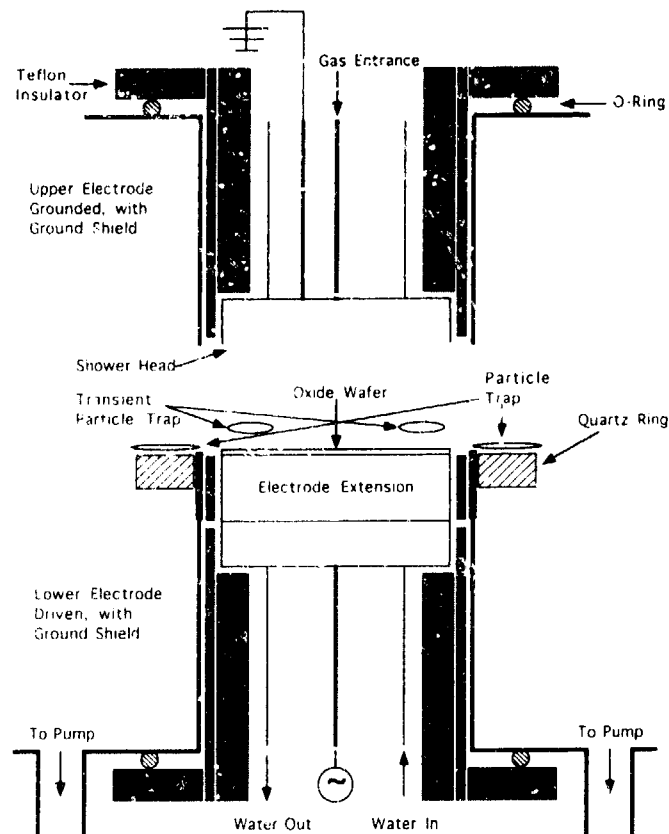


Figure 2. Schematic of the GEC reference cell, showing modifications and particle traps.

to slip around the powered electrode, level with the plane of the electrode surface. Miller and Greenberg [11] examined the electrical characteristics of the Drytek tool, and found by RF probe analysis that the actual power experienced by the electrode in this tool was approximately 50% of that indicated by the Drytek RF power supply meter over the range of conditions relevant to this study. Typical peak-to-peak RF applied voltages for peak particle production under these conditions in the reference cell corresponded to about 1250 V, or about 325 W. In the reference cell, 100 mm blanket, n-type thermal oxide wafers (10000 Å thick) were used as substrates. Etching gas mixtures used in the reference cell were CF_4 , CHF_3 .

To observe particles *in situ* in the reference cell, we employed a dynamic laser light technique based on homodyne photon correlation spectroscopy in the manner previously described by Hurd and Ho [12]. A Coherent DPSS 532 series solid-state, diode-pumped Nd:YAG frequency-doubled laser was used to produce light at 532 nm wavelengths, while a Brookhaven model BI 2030 AT digital, high-speed photomultiplier signal processor was used to perform photon correlation

spectroscopy on the scattered light signal. In homodyne photon correlation spectroscopy, fluctuations in laser light scattering due to Brownian motion of particles in the scattering field are correlated with the mean speed or diffusion coefficient for particle transport. Under certain conditions (a spherical particle assumption and *a priori* knowledge of the local temperature), the diffusion coefficient can in turn be related to a particle diameter [13]. The same HYT Model 20 particle flux monitor used in the Drytek tool studies was fitted to one of the four symmetric pump ports of the reference cell exhaust manifold for downstream particle flux monitoring.

3. Results and discussion

The results of this study show that, at least in the case of oxide substrate etching in fluorocarbon discharges, there is an underlying similarity between process-induced plasma particle generation in the Drytek and reference cell reactors. Figure 2 illustrates the modified reference cell configuration and the location of particle

traps in the cell. Addition of the 0.5 inch quartz guard ring to the reactor design had a pronounced effect on particle trapping. Previous studies of this cell showed that, in the conventional design (no guard ring), no particle clouds were observed in the plane of the electrode or in the gap space. Particle trapping was noted several centimetres below the plane of the electrode, adjacent to the metal ground shield. The simple addition of the quartz guard ring elevated the trapping region to the plane of the electrode, and a ring of particles was observed around the edge of the wafer, as has been reported previously [1]. No dome of particles was observed for any of the process conditions examined to date, but a noticeable sensitivity to total flow was observed in the intensity of LLS from the ring particle region of the discharge.

The intensity of the LLS signal was also very sensitive to the presence of the thermal oxide wafer substrate and the conditioning of the chamber walls. Routine chamber cleans (a CF_4 - O_2 discharge) were performed on the cell after wafer etching. If the cell was allowed to go through several etch cycles without a chamber clean, faint particle LLS signals could be detected under a variety of process conditions, and sometimes even without the presence of a wafer. However, if an oxide wafer was present and being etched, the intensity of the LLS signal was noticeably enhanced in the ring region, until the wafer was etched to end-point. These *in situ* observations provided clear evidence of the importance of oxygen in the SiO_2 layer for particle production in a CF_4 - CHF_3 discharge. As the etch process approached its end-point, such that only the underlying silicon remained, the intensity of the LLS signal faded rapidly in most instances to zero. Quartz in the chamber did not appear to be a factor. Once again, some variability in decay is observed, dependent on chamber wall conditions.

This same dependence was clearly noted in the commercial Drytek tool with use of the downstream particle counter, as shown in figure 3, which compares particle counts to the progress of the oxide etch by monitoring CO emission. As can be seen, no particle counts are detected downstream of the processing cham-

ber until a few seconds after oxide breakthrough. In the commercial tool, the indication is that the particles are totally trapped in the discharge until end-point of the oxide etch, at which point the trap breaks down and the particles are flushed from the chamber. Running the discharge with either no wafer or only a bare Si wafer under the same process conditions produced no noticeable particle counts above a random background signal. By comparison, the sharpness of the breakdown in the electrostatic trapping of particles coincident with oxide breakthrough was absent in the reference cell experiments, presumably due to the generally poor etch uniformity of the tool. Under most process conditions with the reference cell, the wafer edge etches much faster than the centre and no sharp breakthrough in the oxide layer occurs. This may be due in part to the presence of large optical access windows on the reference cell.

Figures 4 and 5 illustrate the variation in the rate of downstream HYT particle counts on the Drytek tool, as a function of the power, pressure and gas composition in a response surface model. Although a complete experimental mapping of the parameter space was not performed on the reference cell, the same general trends were observed by both *in situ* LLS and downstream detection. Particle generation appears to be sensitive to a threshold power level and CHF_3 concentration in the feed gas, while certain intermediate pressures may not be conducive to particle production. However, the critical variable underlying both of these plots was presence of the SiO_2 substrate. Also, in the reference cell operation, particle generation appeared to slow or stop altogether at the very highest power levels at which we could operate the etch process. Therefore, the trend depicted in the response surface plots for the Drytek tool of increasing particles with increasing power may have limits.

In the dynamic LLS experiments in the reference cell, vertically polarized light ($\lambda = 532 \text{ nm}$) was focused 1 mm out from the edge of the powered electrode and 1 mm above the quartz guard ring. The light scattered from the particles was collected with a 50 cm focal length lens in individual runs at horizontal scattering angles from $\Theta = 3^\circ$ to $\Theta = 20^\circ$. The scattering wavevector was parallel to the electrodes such that rf-driven particle motion should not affect the measurements. The scattered light was focused in an $800 \mu\text{m}$ masking pin-hole to reject flare light and then passed to a PMT. By autocorrelating the photocurrent we obtained the intensity correlation function. We observed a Gaussian-like decay of the light scattering correlation function. This suggests the particle motion is ballistic in nature, but the velocities were very small, typically of the order of $3 \times 10^{-3} \text{ cm s}^{-1}$. The initial average particle size (average radius of gyration) was $440 \pm 0.5 \text{ nm}$. However, as the etch progressed beyond the halfway point of the etch cycle, noticeable agglomeration of particles was observed, with particle sizes appearing to grow to in excess of $3 \mu\text{m}$. One should note that, even with the initial particle size measurement, the size is indicative of an agglomerated particle mass composed of many smaller

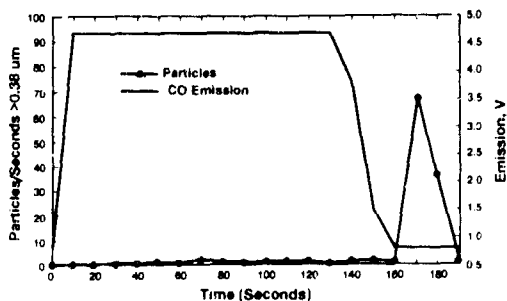


Figure 3. Downstream particle counts versus CO emission ($\lambda = 486 \text{ nm}$) end-point trace in the Drytek reactor.

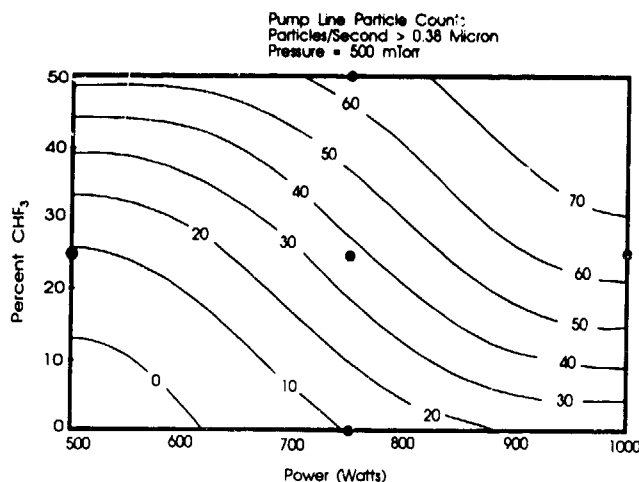


Figure 4. Contour plot of downstream particle flux (particles $s^{-1} > 0.38 \mu m$) at constant pressure (500 mTorr) in the Drytek reactor as a function of CHF_3 and power.

primary particles, as will be shown below. Light scattering from the individual primary particles was insufficient for the homodyne techniques to be applicable, under current experimental conditions.

Figure 6 illustrates a SEM photo of a typical particle contaminate found on the wafer at the end of the etch cycle in the reference cell reactor, when etching was performed under low-power conditions (about 500 V peak-to-peak). It can be readily seen that the particle is an agglomerate of perhaps 50 or so primary spherical

particles of 200 nm diameter, such that the effective diameter is in excess of $1 \mu m$. Such an agglomerated particle is consistent with the dynamic LLS measurements. The agglomeration appears to be quite random. Figure 7 illustrates a similar agglomerated particle wafer contaminant found on a substrate etched in the reference cell, but in this case under high-power conditions (about 1250 V peak-to-peak). Although the remnants of spherical primary particles are still visible in the agglomerate, significant fusion of the individual primary par-

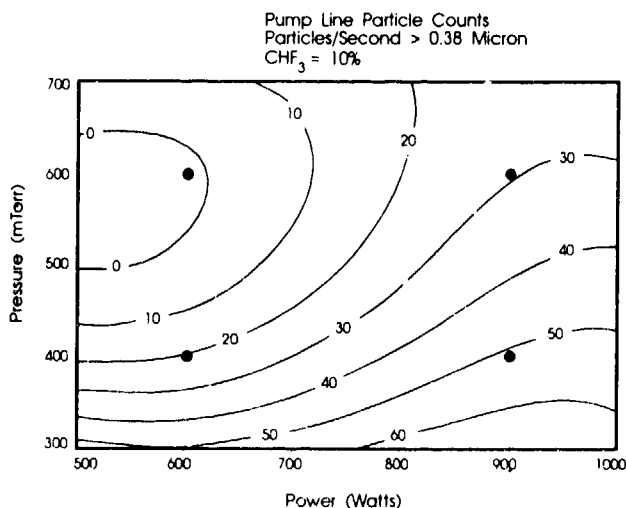


Figure 5. Contour plot of downstream particle flux (particles $s^{-1} > 0.38 \mu m$) at constant feed gas composition (10% CHF_3) in the Drytek reactor as a function of pressure and power.



Figure 6. A scanning electron microscopy micrograph of an agglomerated particle wafer contaminate produced at low power in the GEC reference cell.

ties has occurred and segments of the agglomerate have a more distinctive single-strand, filamentous appearance. This change in appearance of the particle agglomerates is directly related to increased power levels and hence applied electric fields in the reference cell discharge, as all other conditions were constant.

Figure 8 illustrates the contaminants observed on the wafer after etching in the Drytek tool under conditions for which significant particle production was observed by the downstream particle flux monitor. The surface of the wafer is contaminated heavily in spots with small columnar structures about 200 nm in height



Figure 7. A scanning electron microscopy micrograph of an agglomerated particle wafer contaminate produced at high power in the GEC reference cell.



Figure 8. A scanning electron microscopy micrograph of columnar residues on wafer etched in the Drytek reactor.

and 50 nm in width. Although most of the defects appear to be perpendicular to the surface, close examination of the structures in a number of TEM micrographs revealed that there is a distribution in the angular orientation of these structures to the surface ranging from a few degrees from normal to as much as 45° off normal.

A closer examination of the columnar structures is shown in figure 9, a TEM micrograph obtained by back-side-milling the wafer with an Ar ion beam until the surface is visible. Most of the columns in the TEM are oriented vertically and therefore appear as a dark, annular feature. In handling the wafer, several of the columns were knocked over, providing the cylindrical images.



Figure 9. A transmission electron microscopy micrograph of columnar residues on wafer etched in the Drytek reactor.

The much greater contrast in the outer annular ring of the vertically oriented columns is probably due to both material thickness and material properties. Based on these contrasts and other reports of columnar residues [5], it is most probable that the dark outer ring represents a thick polymeric coating or skin and the inner circle constitutes the structural core of the column. Detailed examination of the surface contrast of standing structures reveals that the inner regions of all the columns are either partially or completely hollow. The structural core therefore appears to be only either a partial plug or a cylindrical skeleton inside the outer annular polymeric skin. The polymeric outer wall thickness appears to be of the order of 20 nm and the inner core diameter is about 20 nm.

Since it was not possible to perform *in situ* LLS measurements in the commercial Drytek tool, it is difficult, if not impossible, to prove with certainty at this time that these wafer contaminants have a particle origin or a wafer origin due to micromasking. However, there is much circumstantial evidence to suggest that these rod-like structures are deposited, or redeposited, particles. Figure 10 illustrates that a near-linear correlation exists between particles detected downstream of the chamber and defect counts on the wafer due to these rod-like deposits. Figure 11 illustrates that the location of these particles on the wafer surface is not random, but is consistently oriented around the major flat of the wafer. Selwyn *et al* [1] have shown that electrostatic particle traps arise in processing plasmas due to discontinuities in material properties, such as one gets by having a silicon wafer occupying only a portion of the electrode surface or by placing metal strips adjacent to a silicon wafer. In the Drytek tool, the major flat on the wafer exposes a small portion of the underlying aluminium electrode to the discharge and sets up just such a material discontinuity between conducting and insulating surfaces, which is known to result in electrostatic trapping. The time-dependence of particle bursts detected from the chamber, as shown in figure 3, strongly

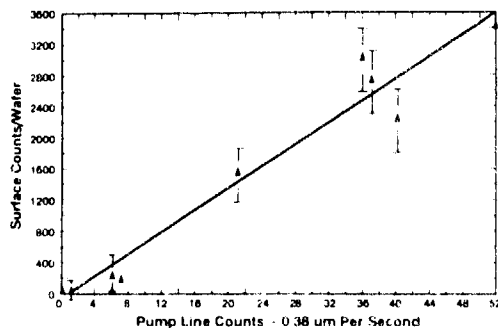


Figure 10. Tencor Surfscan columnar residue counts on wafer versus High Yield Technology downstream particle flux measurements for several etching cycles in the Drytek reactor.

PARTICLES TOT: 4027
PARTICLES/cm²: 29.67
AREA: 2.80 mm²

HISTOGRAM:

0.24 - 0.72:	3894
0.72 - 1.20:	243
1.20 - 1.68:	40
1.68 - 2.16:	12
2.16 - 2.64:	4
2.64 - 3.13:	4
3.12 - 3.60:	0
3.60 - 4.08:	3
4.08 - 4.56:	1
4.56 - 5.04:	3
5.04 - UP:	3

MEAN: 0.4421
STD. DEV.: 69.96%

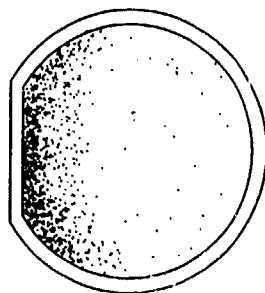


Figure 11. Tencor Surfscan wafer defect map showing the location of columnar residue concentrations.

suggests that electrostatic trapping is occurring in this tool.

Detailed Auger, XRF and EDX analyses of regions of the wafer heavily contaminated with these columnar residues failed to detect any other trace contaminants that could lead to micromasking, such as non-volatile aluminium fluoride. Since the wafers were blanket oxide coated without any exposure to photoresist, photoresist scum, as suggested by Ozaki and Hirata [5], cannot be a micromasking factor either. The XRD, XRF and EDX analyses showed that the columnar residues were either amorphous or very weakly crystalline, and composed of Si, C, O and F. The FTIR spectra of columnar residues extracted from the wafer by methanol wash showed a strong peak around 1200-1250 cm⁻¹ associated with C-F stretching vibrations and a weak mode at 760 cm⁻¹ associated with C-C or Si-C bonds [14]. Certain samples had a sharper peak at 760 cm⁻¹, which is more characteristic of Si-C bonding with some crystallinity [15]. These spectra suggest that the inner structural core of the column is composed of Si-C or C-C units, but the sample repeatability of these measurements was poor, leaving that interpretation open to question.

4. Conclusions

The combined observations by *in situ* LLS and downstream particle flux measurement on the reference cell and the Drytek tool clearly indicate that the etch product species from oxide etching play a critical role in generation of particulates in the etch process. These studies also show that the primary particles rapidly agglomerate in the plasma to form long chains. Under conditions of high power and high applied electric fields, some degree of polarized, field-aligned particle coagulation has been shown to occur in the reference cell, and the particles exhibit a more filamentous rod-like structure.

What has not been unequivocally shown is the impact that these particles have on wafer contamination. The regularity in size, shape and angular orientation of the columnar particles observed on the wafer after

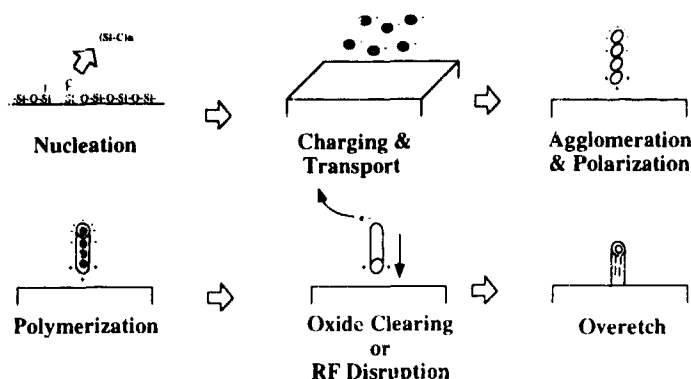


Figure 12. Possible mechanistic pathway for polarized, field-aligned particle coagulants to contaminate wafer surfaces with rod-shaped particles.

etching in the Drytek tool is difficult to attribute to particle contamination, at first sight. However, if polarization and field alignment of coagulated particles is occurring, then the collection of particles at 90° to the surface of the wafer would not be unlike Coulombic attraction/collection as used in electric precipitators for smoke and dust control. This leads to the possible sequence of events shown in figure 12, which may explain the connection between process-induced particles in oxide etching and columnar residues. The lack of such columnar residues in the reference cell experiments may simply be due to the different flow characteristics of the two tools and the disruption of field-aligned rod formation by molecular drag forces, as shown by the location of particle agglomerates by LLS.

If the above-suggested connection between particle generation and columnar residues in oxide etching is incorrect, then one is still faced with the dilemma that the original hypothesis of Ozaki and Hirata [5] of polymer micromasking is inconsistent with these results. It is possible that other micromasking contaminants were present and escaped our detection, but this puts into question the nature of the mechanism that would lead to such a direct correlation between particles and columnar etch residues as that observed in this study.

We can be sure that there is an important contribution to the particle confinement problem from seemingly benign aspects of plasma reactor tool construction, such as quartz guard rings around RF electrodes. The addition of a quartz guard ring, in combination with the gap size and gas flow, has been shown to have a dramatic concentrating effect on particles formed in the reference cell, in a location with serious ramifications for wafer contamination.

Acknowledgments

The authors would like to acknowledge gratefully the assistance and contributions of Richard Buss and Dan Rader of Sandia National Laboratories to this work. We also wish to thank Coherent Laser Group for providing the new DPSS 532 diode-pumped Nd:YAG laser used in this study. This work was partially performed at Sandia National Laboratories with support by USA Department of Energy under contract number DE-AC04-76DP00789.

References

- [1] Selwyn G S, Heidenreich J E and Haller K L 1991 *J. Vac. Sci. Technol. A* **9** 2817
- [2] Selwyn G S 1991 *J. Vac. Sci. Technol. B* **9** 3487
- [3] Selwyn G S, Singh J and Bennett R S 1989 *J. Vac. Sci. Technol. A* **7** 2758
- [4] Anderson H M, Jarrath R and Mock J L 1990 *J. Appl. Phys.* **67** 3999
- [5] Ozaki Y and Hirata K 1982 *J. Vac. Sci. Technol.* **21** 61
- [6] Jellum G M and Graves D B 1990 *Appl. Phys. Lett.* **57** 2077
- [7] Fuchs N A 1964 *The Mechanics of Aerosols* (New York: Dover)
- [8] Jarrath R, Anderson H M and Wong R 1991 *Microcontamination* **9** 17
- [9] Graves D B private communication
- [10] Miller P A, Anderson H M and Spilchal M P 1992 *J. Appl. Phys.* **71** 1171
- [11] Miller P A and Greenberg K E private communication
- [12] Hurd A J and Ho P 1989 *Phys. Rev. Lett.* **62** 3034
- [13] Zachariah M R, Chin D, Semerjian H G and Katz J L 1989 *Appl. Opt.* **28** 530
- [14] Catherine Y and Turban G 1980 *Thin Solid Films* **70** 101
- [15] Ganguly G, De S C, Ray S and Barua A K 1991 *J. Appl. Phys.* **69** 3915

A correlation between particle growth and spatiotemporal RF plasma structure

T Kamata†, S Kakuta†, Y Yamaguchi‡ and T Makabe†

†Department of Electrical Engineering, Faculty of Science and Technology, Keio University, 3-14-1 Hiyoshi, Yokohama 223, Japan

‡Research Centre, Mitsubishi Kasei Corporation, 1000 Kamoshida, Yokohama 227, Japan

Received 3 January 1994, in final form 14 February 1994

Abstract. Particle growth and subsequent extinction in plasma reactors for surface processing has been investigated in a parallel-plate radiofrequency discharge at 13.56 MHz in Ar with $(\text{CF}_2\text{CF}_2)_n$ and its fragments as an impurity. The space- and time-variation of the radiofrequency plasma structure is mainly studied simultaneously with the particle size and density by both spatiotemporally resolved optical emission spectroscopy and Mie scattering of laser light. A correlation is demonstrated between the particle size density and the radiofrequency plasma structure.

1. Introduction

There have been many experimental investigations of particle growth and migration in etching, deposition and sputtering reactors, driven by a radiofrequency (RF) discharge [1-7]. The size and density of particles have been extensively studied by laser light scattering in plasma reactors for surface processing. Particles were mostly found near the plasma/sheath boundary in previous studies. Particles of sizes larger than several tens of nanometres are observable by the Mie scattering technique [8], and electron microscopy is applicable to measurement of the size distribution in the range 10-100 nm [9]. Very few investigations of the spatiotemporal variation of the RF plasma structure have been performed simultaneously with particle detection [10].

The characteristics of the RF discharge between parallel-plate electrodes in pure Ar at 13.56 MHz are known to be capacitive. That is, the total current leads the sustaining voltage. This is a property of electropositive gases. The space- and time-structure of the Ar RF discharge has been elaborately studied as have the external electrical characteristics [11-13]. Thus, the RF Ar discharge plasma will be appropriate for investigation of the subsequent behaviour of dust initiated as an impurity in the plasma reactor. Another reason for the choice of Ar is its chemical non-reactiveness.

It will be possible to diagnose particle growth and extinction under circumstances of periodic steady state RF discharge, if it occurs from spatiotemporally resolved optical emission spectroscopy (STROES) and Mie scatter-

ing. The STROES will give information on the space- and time-variation of the plasma structure when we select the appropriate emission line with short lifetime and free of cascade from the upper levels. Emission from $\text{Ar}(3p_4)$ is employed for this purpose [11]. Mie scattering signals of an Ar^+ ion laser incident on the particle provide information about the particle radius and density, when the particle has a monodisperse distribution.

Two types of measurements have been performed in the present work to investigate the influence of particles on the parallel-plate RF plasma reactor. One is Mie scattering using an Ar^+ ion laser, the other is the indirect way, through observation of the spatiotemporal net production rate of $\text{Ar}(3p_4)$.

2. Experimental

Figure 1 is a schematic diagram of the experimental apparatus and the system, which has been described in detail in previous papers [11, 13, 14], except the channel of the Ar^+ ion laser scattering experiments. Parallel-plate aluminium electrodes of 8 cm diameter are positioned with 2 cm spacing in the centre of the stainless steel chamber 20 cm in diameter. The time and axial space resolutions are, respectively, 0.2 ns and 1 mm. Photons within 20 mm around the central axis of the discharge are detected [14]. The absolute net excitation rate by electron impact is derived by a deconvolution procedure from STROES in the calibrated detection system [11, 14]. That is, the emission intensity $\Phi_A(z, t)$

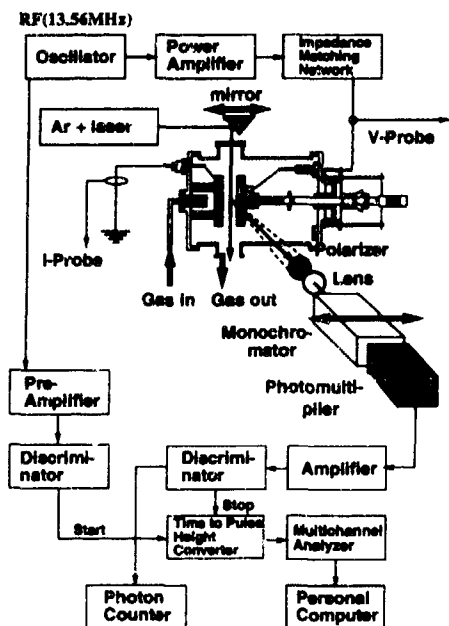


Figure 1. Schematic illustration of the experimental apparatus and the detector system.

($\text{cm}^{-3}\text{s}^{-1}$) from state j to k is expressed by the convolution integral for the condition that the radiative lifetime τ_{rad} is much shorter than the time constant of diffusion, τ_D , as

$$\Phi_{jk}(z, t) = k_0 \int_{-\infty}^t \frac{\Lambda_j(z, t')}{\tau_{\text{rad}}} \exp\left(-\frac{t-t'}{\tau_{\text{eff}}}\right) dt' \quad (1)$$

where $\Lambda_j(z, t)$ ($\text{cm}^{-3}\text{s}^{-1}$) is the net excitation rate to state j , and τ_{eff} is the effective lifetime considering self-quenching. k_0 is a constant showing the instrumental function. We can estimate τ_{eff} under the condition that the overall profile of the net excitation rate has a non-negative value. τ_{eff} of excited $\text{Ar}(3p_3)$ is estimated to be 50 ns.

An unpolarized Ar^+ ion laser ($\lambda = 488 \text{ nm}$) of beam diameter 0.62 mm is used as a coherent light source and is directed to the mirror mounted on the movable stage controlled by computer, which allows us to execute spatially resolved scattering measurements. Laser light enters the discharge parallel to the electrodes from the top window. Measurement by a photon counting technique is employed for detection of the laser beam scattered by 90° as well as the emission of excited species in the discharge. The scattered laser intensities parallel and perpendicular to the scattered plane, I_{\parallel} and I_{\perp} , can be observed individually by inserting a polarizer between the scattered beam and the lens system in front of the monochromator in figure 1.

Thus, we employ a technique based on Mie scattering by an unpolarized laser in order to measure particles *in situ* [8]. It is assumed that the particle is made from

$(-\text{CF}_2\text{CF}_2-)_n$ with monodispersion in size and refractive index 1.35. The experimental scattering intensities $I_{\perp, \parallel}$ are influenced by both the instrumental function of the detector system and the scattering angular distribution. The calibration of $I_{\perp, \parallel}$ is also performed beforehand in a manner similar to that in [14].

The particle size with monodispersion is estimated from the ratio of I_{\perp} to I_{\parallel} by using Mie scattering theory [8, 15]. In particular, particle radius r_p larger than 250 nm is estimated by comparing the theoretical $I_{\perp, \parallel} - r_p$ characteristics with the experimental $I_{\perp, \parallel}$ peaks against time from onset of discharge. Then, the particle number density is given from the absolute scattering intensity using the particle radius mentioned above.

3. Results and discussion

The RF glow discharge is sustained in pure Ar at 13.56 MHz, 1 Torr and 10 sccm under peak-to-peak voltage 120 V with the form

$$V(t) = V_0 \sin \omega t + V_{\text{DC}} \quad (2)$$

between both electrodes. Here, V_0 and V_{DC} are, respectively, the amplitude of the RF voltage and the DC self-bias voltage.

The net production rate of $\text{Ar}(3p_3)$ in pure Ar without any impurity is shown in figure 2 in the form of a spatiotemporal distribution under the same external discharge conditions. The net excitation rate, locally limited in front of both electrodes, leads the waveform of the applied voltage and almost corresponds to the maximum of the total current. The capacitive characteristics are a property of electropositive gases.

$(-\text{CF}_2\text{CF}_2-)_n$ and its fragments are prepared by Ar RF sputtering from the Teflon plate surrounding the Al electrodes before the measurement. The RF sputtering voltage is carefully chosen so that the Al electrode surface is not influenced by sputtering. After preparation of $(-\text{CF}_2\text{CF}_2-)_n$ and its fragments on the bottom of the reactor between both electrodes, the gas is renewed. Under these initial arrangements, the laser light scattering onset time and the succeeding temporal behaviour of the signal are reproducible within a scatter of 10% up to

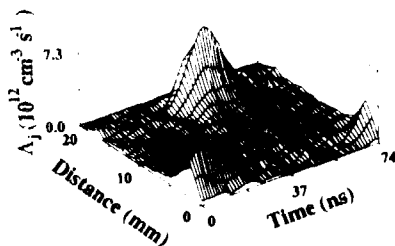


Figure 2. Spatiotemporal net excitation rate of $\text{Ar}(3p_3)$ in pure Ar at $V(t) = 60 \sin \omega t - 18 \text{ V}$ at 1 Torr, 10 sccm and 13.56 MHz.

600 s after initiation of discharge. Mie scattering intensity changes with time, initially increasing sharply and subsequently spreading into the bulk plasma, and finally decreasing gradually. Figure 3(a) shows the external electrical characteristics from onset of the RF discharge. That is, $t = 0$ corresponds to the circumstances in pure Ar with $(-\text{CF}_2\text{CF}_2-)_n$ and its fragments as an impurity. The impurity has no influence on the electrical characteristics nor on the inner discharge structure (figure 2). Successive long-term variation of the external characteristics will reflect the influence of particle growth and extinction originating from $(-\text{CF}_2\text{CF}_2-)_n$ in the RF glow plasma. The series of variations continues for 1000 s. The long-term evolution of particles in this work has been also observed in halocarbon-containing RF plasmas for dry etching [16].

The maximum phase for the influence occurs 200 s after the onset. That is, the phase shift ϕ between the sustaining voltage and the total current rapidly decreases, and has the minimum at 200 s as well as the lowest value of the DC self-bias voltage V_{DC} as shown in

figure 3(a). These facts mean the exhaustion of electron supply and the formation of massive negative ions, judging from the characteristics in the previously studied electronegative gases, SF_6 [17, 18], HCl [19] and SiH_4 [20]. This speculation is supported by the spatiotemporal profile of the net excitation rate of $\text{Ar}(3p_x)$, with two strong maxima in phase with the peaks of the sustaining voltage during one RF period over the whole space in the bulk plasma, as shown in figure 3(c I). Since it takes 165 s to measure a set of spatiotemporal distributions, figure 3(c I) illustrates the averaged profile between 110 and 290 s. The high net rate in the bulk plasma results from the high field penetration required to carry the negatively charged massive particles as well as minority electrons [18]. Insufficient evidence is observed for formation of a double layer in front of the instantaneous anode. This implies plasma density of the order of 10^9 cm^{-3} [18]. At $t = 600$ s, the production in front of the instantaneous anode begins to decline although the signals in the vicinity of the instantaneous cathode and in the bulk plasma still remain as shown in

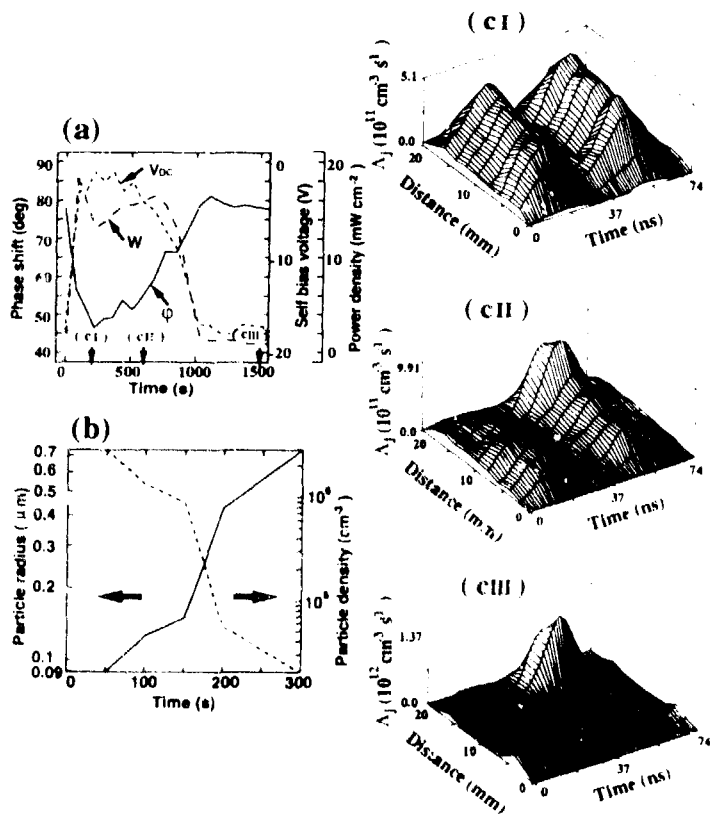


Figure 3. Influence of particles as a function of time after initiation of radiofrequency discharges in Ar with $(-\text{CF}_2\text{CF}_2-)_n$ and its fragments at 1 Torr, 10 sccm and $V = 60$ V at 13.56 MHz: (a) external electrical characteristics; (b) particle size and density at bulk plasma centre; (c I), (c II) and (c III) respectively the net production rate of $\text{Ar}(3p_x)$ at around 200, 600 and 1500 s.

figure 3(c-II). The external electrical characteristics almost recover at about 1000 s. No appreciable change of sheath width due to particle growth and extinction is detected during operation. As mentioned above, the external electrical property is sensitive to the evolution/decay of the particle.

Particle growth in the early stage of variation in the bulk plasma at 8 mm from the earthed electrode is exhibited in terms of the particle radius and density in figure 3(b), which is analysed in terms of the results of Mie scattering intensities, I_{\perp} and I_{\parallel} . The radius r_p grows almost linearly in time up to 700 nm for 300 s after initiation. As for the number density of the particle, it changes from 10^7 to $2 \times 10^4 \text{ cm}^{-3}$. In order to understand the highly electronegative profile at the phase of figure 3(c-I) with particle density 10^6 cm^{-3} , we have to estimate the number of electrons captured by one massive particle. It is deduced from the orbital motion-limited probe theory [15] that the number of captured electrons is $300\text{--}1000 \text{ cm}^{-3}$ in the bulk plasma under the condition of electron temperatures 1–5 eV at room temperature. At the final stage, the massive particles agglomerated in the RF discharge terminate in disappearance from the active plasma region due to gravity. In fact, it is found by SEM that the particles collected at the bottom of the reactor show spherical and monodisperse properties with diameter of 700 nm. Also EPMA and FTIR analyses of the particle show the presence of C and F and CF_2 bonds. We have no evidence for Al in the particle.

The effect of CH_4 on the present RF plasma has been preliminarily studied. It is noted that the presence of CH_4 (5%) in Ar under the same external condition drastically enhances the Mie scattering intensity, that is, particle growth. The details will be reported elsewhere.

Acknowledgments

This work was supported in part by Grant-in-Aid for

Scientific Research B05452106 from the Ministry of Education, Science and Culture of Japan.

References

- [1] Jellum G M, Daugherty J E and Graves D B 1991 *J. Appl. Phys.* **69** 6923–34
- [2] Selwyn G S, Heidenreich J E and Haller K L 1991 *J. Vac. Sci. Technol. A* **9** 2817–24
- [3] Selwyn G S, Singh J and Bennett R S 1989 *J. Vac. Sci. Technol. A* **7** 2758–65
- [4] Yoo W J and Steinbruehl Ch 1992 *Appl. Phys. Lett.* **60** 1073–5
- [5] Roth R M, Spears K G, Stein G D and Wong G 1985 *Appl. Phys. Lett.* **46** 253–5
- [6] Bouchoule A, Plain A, Boufendi L, Blondeau J Ph and Laure C 1991 *J. Appl. Phys.* **70** 1991–2000
- [7] Watanabe Y, Shiratani M and Yamashita M 1992 *Appl. Phys. Lett.* **61** 1510–2
- [8] Bohren C F and Huffman D R 1983 *Absorption and Scattering of Light by Small Particles* (New York: Wiley)
- [9] Boufendi L, Plain A, Blondeau J Ph, Bouchoule A, Laure C and Toogood M 1992 *Appl. Phys. Lett.* **60** 169–71
- [10] Jellum G M, Daugherty J E and Graves D B 1991 *J. Appl. Phys.* **69** 6923–34
- [11] Tochikubo F, Kakuta S, Suzuki A and Makabe T 1990 *J. Phys. D: Appl. Phys.* **23** 1184–92
- [12] Makabe T, Nakano N and Yamaguchi Y 1992 *Phys. Rev. A* **45** 2520–31
- [13] Kakuta S, Makabe T and Tochikubo F 1993 *J. Appl. Phys.* **74** 4907–14
- [14] Tochikubo F and Makabe T 1991 *Meas. Sci. Technol.* **2** 1133–7
- [15] Watanabe Y, Shiratani M and Yamashita M 1993 *Plasma Sources Sci. Technol.* **2** 35–9
- [16] O'Neill J A, Singh J and Gifford G G 1990 *J. Vac. Sci. Technol. A* **8** 1716–21
- [17] Gogohdes E and Sawin H H 1992 *J. Appl. Phys.* **72** 3971–87, 3988–4002
- [18] Nakano N, Shimura S, Petrovic Z I J and Makabe T 1994 *Phys. Rev.* to be published
- [19] Nakano N and Makabe T 1991 unpublished
- [20] Makabe T, Tochikubo F and Nishimura S 1990 *Phys. Rev. A* **42** 3674–7

Spectroscopic and probe measurements of structures in a parallel-plates RF discharge with particles

Kunihide Tachibana†, Yasuaki Hayashi†, Takuya Okuno† and Toshiaki Tatsuta†

† Department of Electronics and Information Science, Kyoto Institute of Technology, Matsugasaki, Sakyo-ku, Kyoto 606, Japan

† SAMCO International Inc Takeda, Fushimi-ku, Kyoto 612, Japan

Received 10 January 1994, in final form 1 February 1994

Abstract. The characteristics of plasma parameters and their spatial structures in a parallel-plates RF discharge in argon modified by the injection of small carbon particles have been investigated. A larger peak-to-peak fluctuation of space potential in the bulk plasma region was observed by an emissive probe measurement together with a decrease in the self-bias voltage. The electron energy distribution function in the plasma bulk as measured by an energy analyser also showed the presence of a higher energy tail. The enhancement of an argon atomic line emission in the midgap was consistent with the above results, showing the transition of the discharge mode from the gamma to alpha regimes. Spatial and temporal behaviours of particle density and size were measured by a newly proposed ellipsometric detection method of the laser Mie scattered light. Slow shift of the peak position of density and size distributions towards the sheath edge of the powered electrode was observed.

1. Introduction

Recently interest has been stimulated in a better understanding of the behaviour of particle growth and distribution in processing plasmas used in thin film deposition and etching. In addition to the importance of getting rid of production and accumulation of particles in industrial applications, the problem is interesting by its physical nature, because the presence of the particles strongly influences the discharge structure and the plasma parameters. Therefore, many theoretical (see e.g. [1–4]) and experimental (e.g. [5–8]) approaches have been performed up to now.

In this work, in order to see the effect of particles in a simplified system, we try to inject small carbon particles into a parallel plates RF discharge sustained in argon which itself shows electropositive characteristics. We use two different types of electric probe; one is an emissive probe by which the peak to peak (p-p) variation of space potential fluctuation between the electrode gap is measured, and the other is an electrostatic energy analyser by which the electron energy distribution function (EEDF) is measured. Optical emission spectroscopy is also used as a cross check of the changes in the plasma parameters.

The evolution of the density and size of particles in the plasma has been previously determined by polarization sensitive Mie scattering measurement [5]. In this method the diameter is deduced from the scattered light intensity ratio of horizontal-to-vertical polarization components based on the assumption of monodisperse size distribution, circular shapes and known optical index of particles. We propose here a new method using ellipsometrical analysis. In this method another independent parameter, which comes from the phase difference between the two polarization components, is obtained in addition to the intensity ratio. This gives useful information for the reduction of the assumptions compared with conventional methods. In this work we try to accurately determine the optical index of injected particles from the two ellipsometric parameters, and the value is used for quantitative analysis of spatial and temporal behaviours of the size and the density of particles.

2. Probe measurements

Our experimental set-up for the probe measurements is shown schematically in figure 1. The reactor of

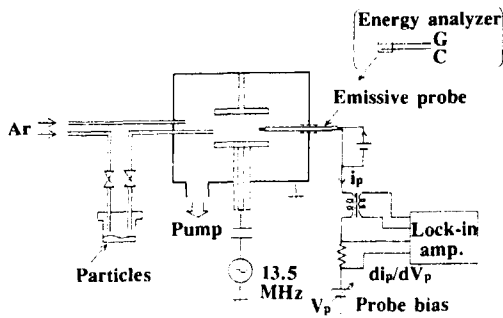


Figure 1. Schematic diagram of the experimental set-up for probe measurements.

30 cm inner diameter and 50 cm height was equipped with parallel electrodes of 10 cm in diameter at a separation of 3 cm. The input RF power was kept constant at 10 W. The gas pressure and flow rate of Ar were 40 Pa and 5 standard $\text{cm}^3 \text{min}^{-1}$ (sccm) respectively. Particles employed were carbon soots of nominal size 0.03–0.2 μm . They were puffed into the plasma instantaneously with carrier Ar gas through a bypass line at the beginning of each run.

Figure 2(a) shows that a time variation of the self-bias voltage appeared at the RF supplied electrode. Although the electrode configuration was symmetric (as seen in figure 1) a voltage of about -30 V appeared in pure Ar plasma because the metal chamber was grounded and its walls were partly taken into the area of grounded electrode. After the injection of particles the self-bias voltage decreased to a small value due to the change in discharge characteristics (see arguments below). The emission of an Ar line at the midgap of the electrodes increased dramatically as shown in figure 2(b) after the injection of particles. These facts suggest that a fairly large number of particles were trapped for a certain time, but only a small number can remain after about 200 s. The probe measurements described below were carried out within the early 100 s period after the injection, while the particle density was kept sufficiently high.

For the measurement of p-p fluctuations of space potential we used an ohmically heated emissive probe (0.1 mm diameter and 20 mm 1 turn length). The method was originally proposed by Hershkovitz [9] and used in the measurement of the RF plasma in He [10]. In this method two inflection points of probe characteristic give the lower and upper peaks of the fluctuation. These peaks were sensitively detected in the signal proportional to the first derivative of the characteristics through a lock-in amplifier by giving small AC (1 kHz) modulation to the probe bias voltage. The effect of probe heating on the gas temperature and the behaviour of particles (e.g. through thermophoretic force) could be negligible because the heating temperature was relatively low (500 C) and the surface area was small. Figure 3 shows the measured p-p values in pure Ar and in Ar mixed with carbon particles. It can be seen that the width of fluctuation increases dramatically with an injection

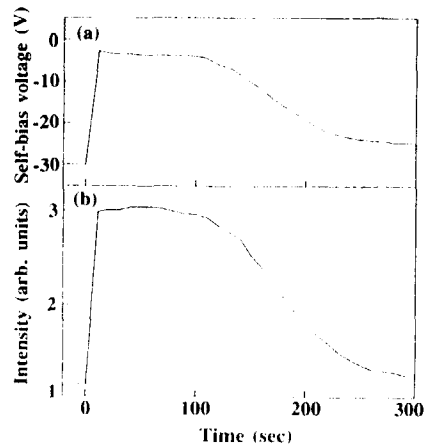


Figure 2. Time evolution of (a) self-bias voltage and (b) emission intensity of an Ar 419.8 nm line after injection of particles.

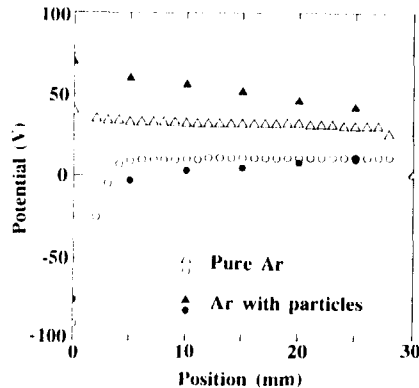


Figure 3. The spatial distribution of a peak-to-peak fluctuation in space potential measured by an emissive probe in pure Ar plasma and Ar plasma with particles.

of particles together with a decrease in the self-bias voltage. It is suggested that by the trapping of particles, the plasma self-organizes the potential distribution by reducing part of the sheath voltage and enhancing the bulk electric field so as to compensate for the electron attachment loss. Thus, the discharge feature tends to shift from the gamma regime in which the secondary electron emission from the self-biased RF electrode predominates the sustenance of the discharge to the alpha regime in which body ionization process becomes more important.

The structure of the energy analyser used in our experiment is shown in the inset of figure 1, and is similar to the one used by Okuno *et al* [11]. It was composed of a retarding grid, an insulating spacer and a collector, the outer and effective inner diameters of which were 10 and 7 mm respectively. Filters for compensating the first and second harmonics of RF space

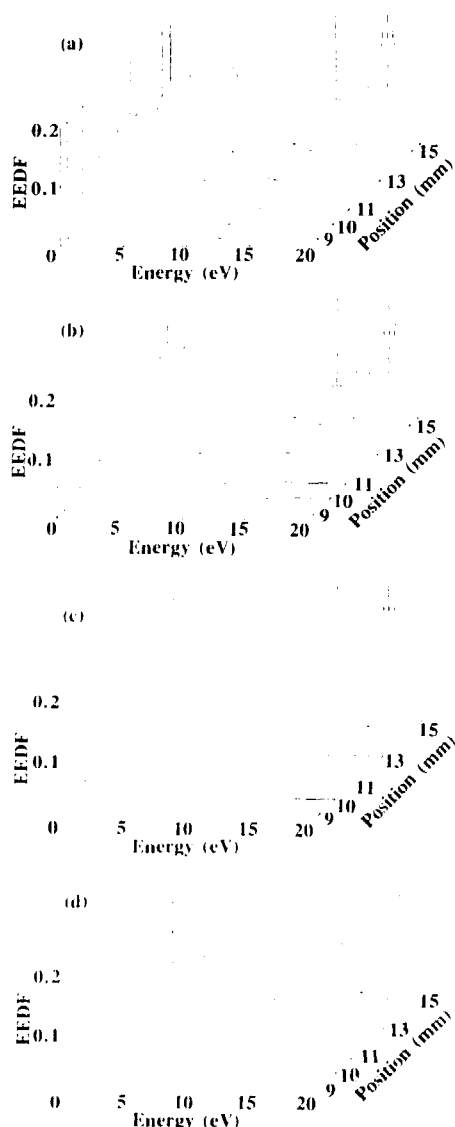


Figure 4. EEDF measured in pure Ar plasma ((a) and (b)) and in Ar plasma with particles ((c) and (d)) at several positions within the electrode gap (probe position is the distance from RF electrode). The arrangement of the probe is as shown as an inset in each figure.

potential fluctuation were connected independently to the grid and to the collector. In this measurement the probe could have given some disturbance to the plasma, especially near the sheath, because of its relatively large size, but the characteristic features can still give qualitative results.

Typical EEDFs measured by this method in Ar plasmas with and without particles are shown in figure 4 at two different arrangements of the analyser: faced

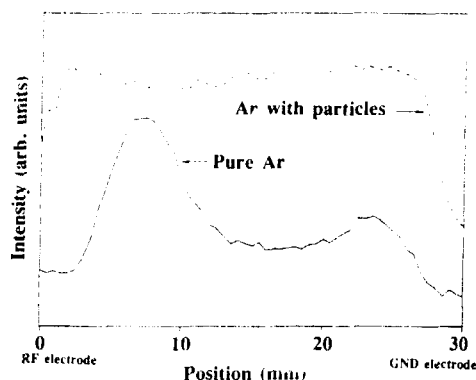


Figure 5. Spatial distribution of the emission intensity of an Ar 419.8 nm line between the two electrodes measured in pure Ar plasma and Ar with particles.

to the grounded electrode ((a) and (c)) and to the powered electrode ((b) and (d)). The EEDFs in the bulk plasma shown in (a) (e.g. at positions 11–15) are smaller for higher energy electrons than the Maxwellian distribution. In the latter arrangement the probe receives the directional beam component of high energy electrons accelerated in the sheath toward the plasma bulk. Therefore, in a pure Ar discharge the measured EEDFs shown in (b) have larger high energy tails than those in (a). In the case of a dusty Ar plasma, the high energy tail was observed even in the former arrangement as shown in (c) and became closer to the Maxwellian, which suggests that there exists a higher electric field, even in the plasma bulk, to heat up electrons. The detected electron saturation current, however, decreased to about 20% in the dusty plasma. This shows a large number of electrons were lost by attachment to particles.

Observed profiles of the emission intensity of a neutral Ar line are shown in figure 5 with and without dust particles. A double-peaked shape in pure Ar which typically appears at relatively high pressure has changed to have a higher intensity over all the bulk region in the presence of particles. This indicates that the EEDF in the bulk plasma tends to have a higher energy component, which gives an effect that more than compensates for the decrease in the electron density. This feature is quite similar to the one previously observed, e.g., in electronegative silane plasma which contains a large number of negative ions [12].

3. Mie scattering measurement

For the ellipsometric Mie-scattering measurement of the particles another set-up was used, as shown in figure 6. The chamber of 8×8 cm inner cross section and 30 cm length was equipped with a circular RF electrode of 5 cm diameter and a rectangular grounded electrode of 22×6.5 cm. The electrode separation was 2.6 cm. Gas inlet and outlet ports were arranged to be close to each other and set far from the plasma region so that

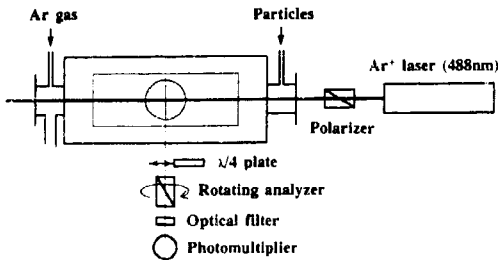


Figure 6. Schematic diagram of the experimental set-up for ellipsometric Mie-scattering measurements (top view).

the introduced gas flow might not blow away particles trapped in the plasma. An argon ion laser operating at a wavelength of 488 nm and an output power of 0.5 W was used as a light source for the measurement. Laser light was linearly polarized with an azimuth of 45° from the scattering plane through a Glan-Taylor prism polarizer. The light scattered by the particles at 90° from the incident laser beam was ellipsometrically analysed using a rotating analyser system.

In the ellipsometric measurement, two angle parameters, Ψ and Δ , are obtained. They are related to the amplitude functions, $S_1(\theta)$ and $S_2(\theta)$, as

$$\tan \Psi e^{i\Delta} = S_2(\theta)/S_1(\theta)$$

where θ is the scattering angle. The amplitude functions are defined as [13]

$$S_1(\theta) = \sum_{n=1}^{\infty} [(2n+1)/n(n+1)] \\ \times [a_n \pi_n(\cos \theta) + b_n \tau_n(\cos \theta)]$$

$$S_2(\theta) = \sum_{n=1}^{\infty} [(2n+1)/n(n+1)] \\ \times [b_n \pi_n(\cos \theta) + a_n \tau_n(\cos \theta)]$$

where

$$a_n = [(S_n'(y)S_n(x) - mS_n(x)S_n'(x)) \\ / [S_n'(x)I_n(x) - mI_n'(x)S_n(x)]]$$

$$b_n = [(mS_n'(x)S_n(x) - S_n'(x)S_n(x)) \\ / [mS_n'(x)I_n(x) - I_n'(x)S_n(x)]]$$

Functions π_n and τ_n are expressed with Legendre polynomials as

$$\pi_n(\cos \theta) = 1/\sin \theta [P_n^1(\cos \theta)]$$

$$\tau_n(\cos \theta) = (d/d\theta)[P_n^1(\cos \theta)]$$

$S_n(x)$ and $I_n(x)$ are expressed with Bessel functions as

$$S_n(x) = (\pi x/2)^{1/2} J_{n+1/2}(x)$$

$$T_n(x) = S_n(x) + i(-1)^n (\pi x/2)^{1/2} J_{-n-1/2}(x)$$

and x and y are defined as

$$x = \pi D/\lambda$$

$$y = mx$$

where λ is the wavelength of the scattered light, D is the diameter of particle and m is the complex optical index. Thus, the ellipsometric parameters can be calculated from Mie scattering theory if the particle diameter and its optical index are given.

The ellipsometric parameters on angles Ψ and Δ were determined by two-mode measurement; with and without a quarter-wave plate. By this mode the angle Δ is uniquely obtained in the full range of 360° , because Δ is derived from the Fourier coefficients, which are determined from the scattered intensity data measured as a function of analyser azimuth in the form of $\cos \Delta$ without a quarter-wave plate and in $\sin \Delta$ with the plate. The ellipsometric parameters were obtained at 8 s intervals from the average of 5 time measurements. The rotating analyser system was mounted on an x - z stage so as to acquire position dependent information on the particle behaviour.

Before the measurement, the discharge was sustained in pure Ar gas under the following conditions: gas pressure of 40 Pa, RF power of 2 W and gas flow rate of 14 sccm, and the carbon particles were injected instantaneously into the plasma through another gas inlet port.

The evolution of ellipsometric parameters during the trap of particles measured in the plasma bulk are shown in figure 7(a). The parameter Ψ increased with time. Comparing the trajectory in Ψ - Δ coordinates with the theoretical calculation with some different values of the optical index m , the best fit value is determined to be $2.5 \pm 0.5i$ for the carbon particles used in this experiment. The extinction coefficient becomes smaller than the value of evaporated carbon foil ($m = 2.5 \pm 0.8i$) [14]. The further evolution of ellipsometric parameters has been calculated with this value of optical index as shown in figure 7(b).

Figure 8 shows schematically the bright region of Mie scattering observed by the naked eye at the initial stage of particle trapping in the plasma. It can be seen from the figure that the particles were trapped around the sheath-plasma boundary near the RF electrode and at the dome region in the bottom of plasma bulk near the grounded electrode. The light intensity at each point changed with time as shown in figures 9(a) and (b). It is understood from the figures that the dome region slowly approaches the RF-electrode during the first 200 s.

The time evolution of the ellipsometric parameter Ψ is shown in figure 10 for each point on the centre axis of the plasma. As Ψ positively correlates with particle diameter as long as it is smaller than 280 nm (λ is larger than 220 nm, see figure 7(b)), the increase of particle diameter was larger in the plasma bulk than near the sheath plasma boundary in the indicated time range.

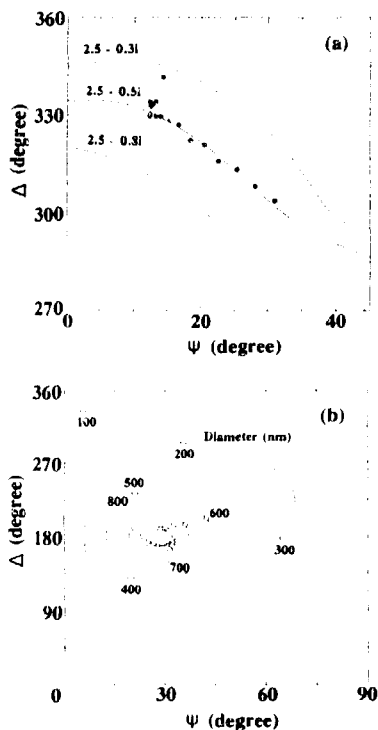


Figure 7. Evolution of the ellipsometric angles. (a) Experimental data superimposed on the theoretical curves for several values of the optical index. (b) Further evolution of ellipsometric angles calculated for larger diameter particles using the optical index of $2.5 - 0.5i$. Lozenge is marked at every 100 nm increment of diameter.

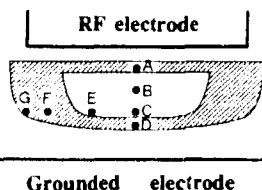


Figure 8. Scheme of bright region of Mie scattering from particles (indicated by hatching). Closed circles indicate measuring positions. A, B, C, and D are on the centre axis of plasma and 5, 10, 15, and 18 mm downward from the RF electrode respectively; E, F, and G are 15 mm downward from the RF electrode and 10, 20, and 25 mm outward from the centre axis respectively.

For the quantitative analysis of the diameter and density of the particles, the theoretical calculation of Mie scattering was performed using the data given in figure 9(a) and figure 10 and the optical index of the particles determined in figure 7(a). As seen from the results shown in figure 11, it is suggested that the particles trapped in the bulk plasma move slowly to the RF electrode, and that the diameter increases after the density reaches a peak (at positions C and B). This

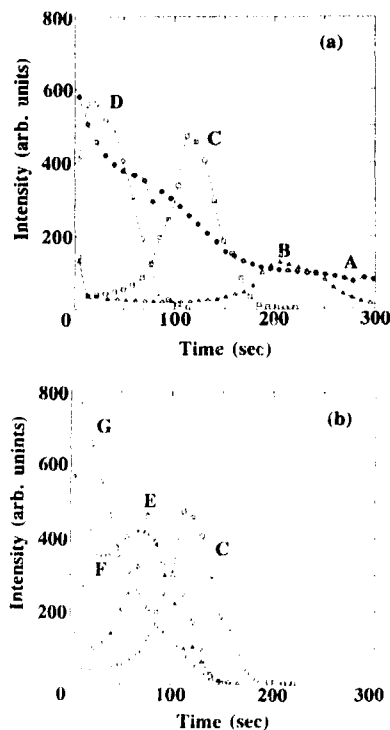


Figure 9. Time evolution of the scattered light intensity. A–G indicate the measuring positions shown in figure 8.

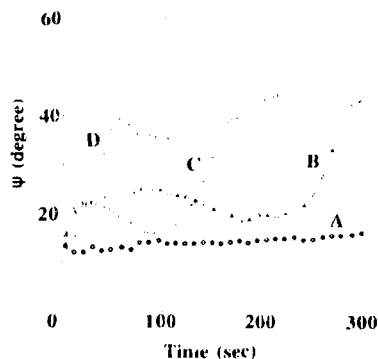


Figure 10. Time evolution of ellipsometric angle Ψ . A–D indicate the measuring positions shown in figure 8.

implies that the particles coalesce by collisions into larger diameter ones, and they are transferred towards the RF electrode predominantly by ion drag force [3]. The size of particles existing near the sheath plasma boundary (at position A) from the beginning is small as can be seen in figure 10, so that they can stay there for a longer time as a result of balance between electrostatic and ion drag forces.

The obtained density of particles is of the order of 10^6 cm^{-3} as shown in figure 11. If the electronegative

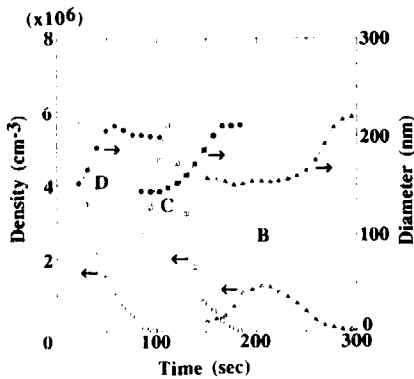


Figure 11. Time evolution of the density and diameter of particles. B–D indicate the measuring positions shown in figure 8.

nature is attributed to the presence of particles the net charge on a particle is estimated to be 10^3 in order to be balanced with the positive ion density. This is consistent with the results derived in [3, 5] from a probe theory.

4. Discussion

From the results of probe and ellipsometric measurements, the behaviour of particles in the plasma can be imaged as follows. For the first 200 s after injection, the particles are trapped mainly within the dome region in the bulk plasma, where the time-averaged plasma potential is most positive, as well as in the sheath-plasma boundary. The negatively charged particles enhance the electric field in the bulk plasma region by reducing the sheath voltage slightly through the change in the self-bias voltage at the RF supplied electrode. This bulk field then stimulates the body ionization process for sustenance of the discharge so as to compensate the electron loss by attachment.

During this stage particles increase their diameter by mutual coalescence and move towards the RF electrode by ion drag force. After about 200 s the particles in the bulk plasma are lost, because the force balance on weighted particles changes: they might fall onto the grounded electrode by gravity or be pumped out of the plasma region with the gas flow, and the few remainder reach the sheath-plasma boundary. Particles trapped in the boundary region at the beginning are smaller in size and the density decreases slowly. It is expected that particles of larger size are distributed towards the RF electrode because the ion drag force becomes larger but the density tends to decrease. Unfortunately, our measurement was impossible near the RF electrode due to the limiting size of the viewing window

After grown-up particles of larger size are lost and the total number becomes smaller in the bulk plasma, the potential (electric field) distribution in the plasma goes back to the gamma regime, in which the secondary electron emission at the cathode becomes more important for the discharge sustenance as in a plasma of electropositive gas.

To summarize, the changes in space potential and the electron energy distribution function in the presence of particles have been measured by using electric probes. The conclusions drawn from the measurements are consistent with the previously reported theoretical prediction [1], showing that the transition from gamma to alpha regimes occurs as the density of injected particles increases in order to compensate for the electron attachment loss onto the particles.

From the long term observation of trapped particles, the growth and the slow movement of particles towards the RF electrode has been analysed. It is also shown that the ellipsometric detection method of Mie scattering proposed for the first time in this paper has an advantage over a previously used conventional method. This will be demonstrated more clearly, e.g., in the measurement of particles growth with size dispersion. It is evident from figure 7(b) that the parameter Ψ corresponding to the polarization ratio in a conventional method becomes a multiple-valued function of the diameter. The other parameter Δ given by our method dissolves the multiplicity in the trajectory on the Ψ – Δ plane.

References

- [1] Belenguer Ph, Blondeau J Ph, Boufendi L, Toogood M, Plain A, Bouchoule A, Laure C and Boeuf J P 1992 *Phys. Rev. A* **46** 7923
- [2] Boeuf J P 1992 *Phys. Rev. A* **46** 7910
- [3] Sommerer T J, Barnes M S, Keller J H, McCaughey M J and Kushner M J 1991 *Appl. Phys. Lett.* **59** 638
- [4] McCaughey M J, Kushner M J 1991 *J. Appl. Phys.* **69** 6952
- [5] Watanabe Y, Shiratani M and Yamashita M 1992 *Appl. Phys. Lett.* **61** 1510
- [6] Bouchoule A, Plain A, Boufendi L, Blondeau J Ph and Laure C 1991 *J. Appl. Phys.* **70** 1991
- [7] Jellum G M, Daugherty J E and Graves D B 1991 *J. Appl. Phys.* **69** 6923
- [8] Selwyn G S, Heidenreich J E and Haller K L 1990 *Appl. Phys. Lett.* **57** 1876
- [9] Hershkovitz N 1989 *Plasma Diagnostics* vol 8 (San Diego: Academic) p 130
- [10] Okuno Y and Fujita H 1991 *J. Appl. Phys.* **70** 642
- [11] Okuno Y, Ohtsu Y, Komatsu and Fujita H 1993 *J. Appl. Phys.* **73** 1612
- [12] Makabe T, Tochikubo F and Nishimura M 1990 *Phys. Rev. A* **42** 3674
- [13] van de Hulst H C 1981 *Light Scattering by Small Particles* (New York: Dover) pp 114–30
- [14] Wolfe W L 1978 *Handbook of Optics* ed W G Driscoll and W Vaughan (New York: McGraw-Hill) pp 7–17

Infrared spectroscopy of a dusty RF plasma

W W Stoffels, E Stoffels, G M W Kroesen, M Haverlag,
J H W G den Boer and F J de Hoog

Department of Physics, Eindhoven University of Technology,
PO Box 513, 5600 MB Eindhoven, The Netherlands

Received 7 January 1994, in final form 20 January 1994

Abstract. *In situ* Fourier transform infrared spectroscopy has been used to study particulate formation in a $\text{CCl}_4/\text{F}_2/\text{Ar}$ RF discharge. Strong absorption bands at $1000-1100\text{ cm}^{-1}$ have been found and attributed to C-F and Si-F absorption. Furthermore continuous extinction due to Rayleigh and Mie scattering has been observed. The relative intensities of C-F, Si-F and scattering signals vary with plasma conditions. There are several experimental indications that the clusters are formed on the surface and ejected into the plasma. An SEM study of the substrate surface has allowed us to establish the mechanism for the particulate production in this discharge.

1. Introduction

Much effort has recently been made to clarify the formation mechanism of macroscopic particulates in an RF plasma due to their destructive role in surface processing like deposition, etching or sputtering. A full understanding of the formation process would not only help to prevent surface contamination but might also result in a means of synthesizing powders with some desired physical properties. The variety of gas mixtures and plasma conditions in which the particulate formation takes place makes it difficult to find one general mechanism for the formation process. At least two major particulate production channels can be distinguished. On one hand cluster formation can occur in the plasma due to radical and ion induced polymerization reactions, e.g. in SiH_4/Ar deposition plasmas [1-3]. In other discharges it has been shown that the surface plays an important role in the formation process, either by supplying directly large clusters [4-5] or by providing the reactive species [6]. In order to elucidate the actual formation process in a given gas mixture and configuration it is necessary to monitor the particulate composition during the growth process. If the clusters contain infrared active bonds, this analysis can be easily performed using Fourier transform infrared absorption spectroscopy.

In this work we apply this technique to particulates formed in an $\text{Ar}/\text{CCl}_4/\text{F}_2$ RF discharge with varying active gas content. In this kind of plasma, clusters are formed readily with typical time constants of 1 min to 1 h, depending on the plasma conditions.

2. Experimental

The experiments were performed in a 13.56 MHz capacitively coupled plasma in a planar 12.4 cm diameter parallel plate configuration. The distance between the aluminum electrodes was 5 cm. On top of the lower water-cooled RF electrode a 10 cm silicon wafer was placed. The input power could be varied between 0 and 150 W. The gases were fed through mass flow controllers and introduced homogeneously through a slit around the RF electrode. The gas pressure and flow could be varied independently from 5 to 500 mTorr and from 0 to 100 sccm respectively, using a throttle valve in the pumping line of a roots blower or a turbo molecular pump. Typical conditions in this work were: power input 100 W, pressure 200 mTorr, total gas flow 30 sccm. We studied particulate formation in a plasma containing 10% CCl_4 in Ar. Afterwards a pure argon plasma was applied to the same wafer and a rapid formation of a particle 'dome' above the wafer was observed.

A schematic diagram of the experimental set-up is shown in figure 1. For the infrared measurements BaF_2 windows were mounted. The spectra were collected using a Bruker IFS-66 Fourier transform infrared interferometer (FTIR) with a glow bar as a continuous light source. The FTIR is basically a Michelson interferometer, supplied with a fixed and a moving mirror. This provides a time-varying interference signal for all wavelengths. The parallel beam exiting the spectrometer was directed through the plasma (single pass) and a 1 mm diaphragm. Finally it was focused with a BaF_2 lens onto a mercury-cadmium-telluride (MCT) detector.

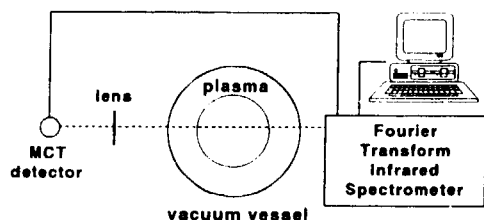


Figure 1. A schematic diagram of the experimental set-up.

A Fourier transform of the detector signal yields a spectrum in the wavelength range of $800\text{--}5000\text{ cm}^{-1}$ with a spectral resolution of 4 cm^{-1} . Spectra were taken at a rate of 15 Hz . A typical measurement was an average of a few hundred spectra. The plasma reactor has been translated vertically in order to obtain axially resolved absorption spectra. In order to eliminate the plasma absorption reference scans were taken immediately after the plasma had been switched on. In this period no dust could be detected, even by means of visible light scattering or the laser ablation method (see [7,8]). These reference scans in a dust free plasma were collected before and after each measurement to avoid a possible influence of the deposition layer on the windows, and variations in the intensity of the glow bar and the sensitivity of the detector.

3. Results and discussion

The size and density of the clusters formed in our discharge were strongly dependent on plasma conditions [7,8]. Typically, the particulates appear at high RF power input ($\geq 80\text{ W}$) and at relatively high pressures ($\geq 100\text{ mTorr}$). The particulate density decreases with increasing gas flow and decreasing plasma volume, most likely due to a limitation of the residence time of active species in the plasma. The presence of an Si wafer on the electrode is essential for particulate formation, which suggests that the surface chemistry is at least partially responsible for this process. The particulates were formed in a discharge containing up to 20% CCl_2F_2 . Their density decreases and their size increases with increasing CCl_2F_2 partial pressure.

In a plasma containing 10% CCl_2F_2 or more mainly large clusters ($\sim 1\text{ }\mu\text{m}$) were present, the largest ones reaching millimeter size. The clusters formed relatively slowly (time constant $\sim 30\text{ min}$) and they were strictly confined in a thin ($\leq 1\text{ mm}$) dome, localized at the glow-sheath boundary above the wafer. Typical absorption spectra of these clusters for several times of plasma operation are shown in figure 2. The 'continuum absorption' is in fact due to light scattering on these particulates, and it has a typical dependence on the photon energy. In the low photon energy region the extinction shows approximately the Rayleigh fourth power dependence on the wavenumber, as shown in figure 3. At higher wavenumbers the absorption deviates from the

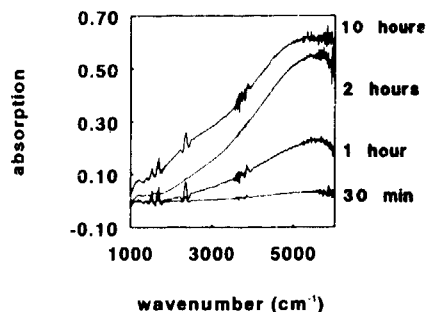


Figure 2. Infrared absorption spectra of particulates formed in a plasma of 10% CCl_2F_2 in Ar for various times of plasma operation. The spectra have been averaged over 500 scans. The continuous band in which intensity is increasing with wavenumber is due to scattering on particulates. A weak C-F absorption band around 1200 cm^{-1} is visible. The other absorption bands are due to water and CO_2 .

Rayleigh law as the scattering enters the Mie regime. The specific band absorption for these particulates is weak in comparison with scattering. Figure 4 displays a broad band around 1200 cm^{-1} , superposed on the tail of the scattering signal. Based on the infrared absorption of C-F containing molecules this band is likely to be due to C-F absorption. O'Neill *et al* reported an intense C-Cl absorption at 700 cm^{-1} and a very weak C-F band in an *ex situ* infrared spectrum for particulates produced in comparable conditions [9]. In order to clarify the origin of these particulates and their relation to surface processes the Si wafer after plasma operation was studied by means of scanning electron microscopy (SEM). A typical SEM photograph of the sample (figure 5) shows curious 'sea polyps', standing vertically on the surface. These structures seem to be hollow and their material is probably different from the crystalline wafer material. Such structures can be obtained by micromasking, followed by almost anisotropic etching of Si. As the side-walls are not subject to the ion bombardment a layer can be deposited on them. This process is known as

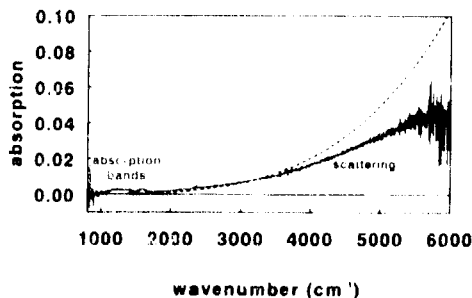


Figure 3. A typical absorption spectrum of particulates formed in a 10% CCl_2F_2 plasma. The broken curve is a fourth power fit, expected for Rayleigh scattering, for particulates much smaller than the wavelength. The deviation at high wavenumber shows that the scattering enters the Mie regime.

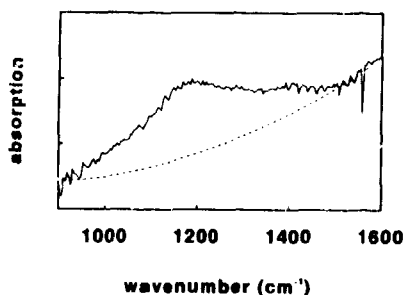


Figure 4. A part of the absorption spectrum of particulates in a 10% CCl_2F_2 plasma, showing a broad, weak absorption band superposed on the scattering signal (broken curve). This band can be attributed to C-F absorption.



Figure 5. An SEM of the surface of a Si wafer, treated by $\text{Ar}/\text{CCl}_2\text{F}_2$ plasma. The photograph is taken under 45° . The structures on the surface with a typical height of $1\text{ }\mu\text{m}$ are probably the result of micromasking and anisotropic etching of the substrate. If these structures break, they are ejected into the plasma.

sidewall passivation. Finally the micromask is removed and the inner silicon is etched away, while the relatively inert external coating stays intact. This mechanism can lead to the formation of the hollow 'sea polyps'. However, the origin of the masking agent is still not clear. The SEM pictures show that the structures become narrower towards their base, indicating that after some time they break and possibly enter the discharge. As both the surface and the structures are negatively charged, they will be accelerated through the sheath into the positive glow. Therefore we suppose that at least a part of the clusters in a $\text{CCl}_2\text{F}_2/\text{Ar}$ discharge comes directly from the surface. From the above consideration it is clear that a silicon wafer is needed for the particulate production.

However, it is not necessary that the clusters contain only Si. In fact their major component can be the halocarbon deposition layer. This mechanism is supported by the experimental observation that the particulates appear sooner if the wafer has previously been treated with an $\text{Ar}/\text{CCl}_2\text{F}_2$ plasma. As a processed wafer already has a developed surface structure, particulate production can start immediately after the plasma is switched on.

The efficiency of the described process is strongly dependent on the ion bombardment on the surface. It has been shown [10] that both positive ion flux and ion energy to the surface decrease with increasing CCl_2F_2 fraction in Ar plasma. Therefore it can be understood that the clusters are formed more readily at low CCl_2F_2 densities. Moreover, the most efficient cluster production can be expected in a pure Ar plasma with a wafer, which has been processed in an $\text{Ar}/\text{CCl}_2\text{F}_2$ mixture.

In order to verify this hypothesis a 'dusty' argon plasma was prepared as follows: first a 10% CCl_2F_2 in Ar plasma was operated for about 2 h. Subsequently the chamber was evacuated and a pure Ar plasma was started. In these conditions a 5 mm thick dome of relatively small clusters was formed above the wafer. The clusters appeared within a few minutes and they were more abundant than in a CCl_2F_2 containing plasma. As there was no active gas in the plasma the particulates must come from the surface. They are most likely sputtered from the Si wafer, in agreement with our previous considerations.

Infrared absorption spectra of these particulates at several times of plasma operation are shown in figure 6. Indeed, the formation time is shorter than in the CCl_2F_2 containing plasma (figure 2). Besides, the shape of the scattering curve indicates that the particulates are smaller. Most striking, however, is an intense absorption band around 1100 cm^{-1} . In figure 7 the absorption bands at different positions in the plasma are shown. They clearly consist of two overlapping bands around 1100 cm^{-1} and 1000 cm^{-1} . Based on the gas absorptions we attribute the former to C-F and the latter to Si-F absorptions in accordance with Ganguly *et al* [11].

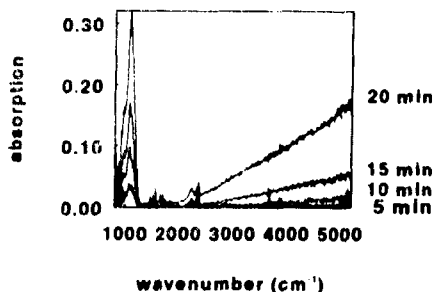


Figure 6. Absorption spectra of particulates in a 'dusty' argon plasma for various times of plasma operation. A wafer treated for 2 h in an $\text{Ar}/\text{CCl}_2\text{F}_2$ plasma has been used. Note the strong absorption around 1100 cm^{-1} and lower continuous extinction due to scattering.

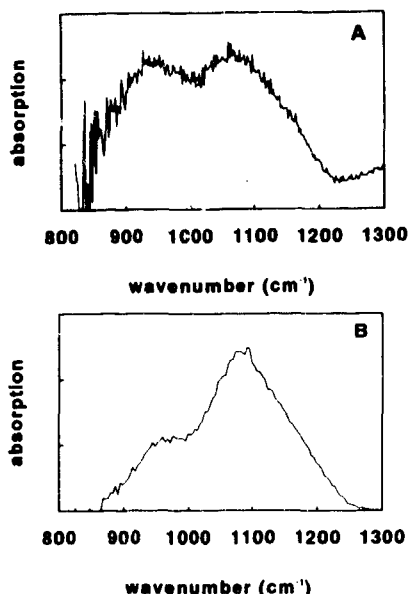


Figure 7. Absorption spectra of particulates in a 'dusty' argon plasma. (A) at 5 mm and (B) at 8 mm above the RF electrode. The absorption consists of two overlapping bands, which can be attributed to Si-F (1000 cm^{-1}) and C-F (1100 cm^{-1}). Their ratio depends on the position in the plasma.

The absorptions of these two bands as a function of height are shown in figure 8. From this vertical scan it follows that the particulate dome in this plasma is very structured. Namely, the silicon rich clusters accumulate mainly close to the RF electrode. The maximum C-F absorption can be found higher, while the scattering signal reaches a maximum even higher, at the top of the dome. It is not clear whether this is due to a gradual change in the chemical composition and size of the cluster, or the presence of several essentially different kinds of clusters having different spatial distributions.

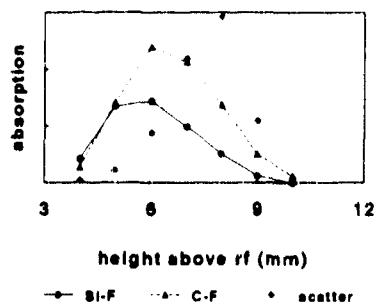


Figure 8. Absorption signals due to C-F, Si-F and scaled scattering as a function of height above the RF electrode in a 'dusty' argon plasma after one hour of plasma operation. It is clear that the three signals reach their maximum in intensity at different heights, which displays the structure of the particulate 'dome'.

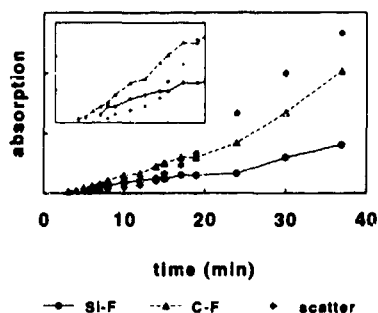


Figure 9. Absorption signals due to C-F, Si-F and scaled scattering as a function of time of plasma operation in a 'dusty' argon plasma 8 mm above the RF electrode. The ratio of C-F and Si-F absorptions remains constant with time, while the relative scattered intensity increases. In the upper left corner the signals during the first 20 min are exhibited.

Finally in figure 9 the time development of the three signals at one position is presented. It can be seen that the ratio of C-F to Si-F is constant with time, while the ratio of scattering to band absorption increases with time. This indicates that the particulate size increases, whereas their composition remains the same.

These measurements show that infrared absorption spectroscopy not only gives information about particulate composition, but also it can be a sensitive technique to study the early phase of particulate formation.

4. Conclusions

The major source of particulates in an $\text{Ar}/\text{CCl}_2\text{F}_2$ RF discharge is the silicon substrate surface. Based on an SEM study of the wafer surface a mechanism for cluster production is proposed. Under etching conditions (10% CCl_2F_2) elongated vertical structures on the Si surface are formed, probably due to micromasking and subsequent anisotropic etching. The structures break as a result of slight underetching and appear in the plasma as macroscopic particulates. Intensive ion bombardment accelerates the particulate production. Surface structures formed in the etching plasma can be therefore very efficiently sputtered in pure argon. The clusters observed in a pure Ar plasma exhibit intense infrared absorption at $1000\text{--}1100\text{ cm}^{-1}$, which indicates the presence of C-F and Si-F bonds in the sputtered material. In contrast, particulates formed in 10% CCl_2F_2 show only a weak absorption in this region. In both cases large scattering signals have been observed.

Acknowledgments

We would like to thank Pete Haaland and Danny Taminiau for their help with the SIMS. This work was supported by the commission of the European Community under BRITE-EURAM contract no. BRFU-CT91-0411.

References

- [1] Boufendi L, Plain A, Blondeau J Ph, Bouchoule A, Laure C and Toogood M 1992 *Appl. Phys. Lett.* **60** 169
- [2] Howling A A, Hollenstein Ch and Paris P-J 1991 *Appl. Phys. Lett.* **59** 1409
- [3] Shiratani M and Watanabe Y 1992 *Mat. Res. Soc. Symp. Proc.* **236** 301
- [4] Selwyn G S, Singh J and Bennett R S 1988 *J. Vac. Sci. Technol.* **A7** 2758
- [5] Selwyn G S, McKillop J S, Haller K L and Wu J J 1990 *J. Vac. Sci. Technol.* **A8** 1726
- [6] Garscadden A 1993 *Proc. 11th Int. Symp. Plasma Chemistry* (Loughborough: UK) p 785
- [7] Stoffels W W, Stoffels E, Kroesen G M W and de Hoog F J 1993 *J. Appl. Phys.* **74** 2959
- [8] Stoffels E, Stoffels W W, Vender D, Kroesen G M W and de Hoog F J 1994 *IEEE Trans. Plasma Sci.* at press.
- [9] O'Neill J A, Singh J and Gifford G G 1990 *J. Vac. Sci. Technol.* **A8** 1716
- [10] Stoffels E, Stoffels W W, Vender D, Kroesen G M W and de Hoog F J 1993 *Proc. 11th Int. Symp. Plasma Chemistry* (Loughborough: UK) p 1587
- [11] Ganguly G, De S C, Ray S and Barua A K 1991 *J. Appl. Phys.* **69** 3915

Particle behaviour in an electron cyclotron resonance plasma etch tool

M G Blain†, G D Tipton†, W M Holbert‡, G S Selwyn‡,
P L Westerfield[§] and K L Maxwell^{||}

†Sandia National Laboratories, Albuquerque, New Mexico, USA

‡IBM Research Division, Yorktown Heights, New York, USA

§SEMATECH, Austin, Texas, USA

Received 29 December 1993, in final form 1 February 1994

Abstract. Sources of particles in a closed-coupled electron cyclotron resonance plasma source used for polysilicon etch included flaking of a residual film deposited on chamber surfaces and shedding of material from the electrostatic wafer chuck. A large, episodic increase in the number of particles added to a wafer in a clean system is observed more frequently for a plasma-on than for a gas-only source condition. For film-forming process conditions, particles were added to wafers by a residual film, which was observed to fracture and flake away from chamber surfaces. The presence of a plasma, especially when radiofrequency bias is applied to the wafer, caused more particles to be ejected from the walls and added to wafers than the gas-only condition; however, no significant influence was observed with different microwave powers. A study of the effect of electrode temperatures on particles added showed that thermophoretic and gravitational forces are not significant for this electron cyclotron resonance operating configuration. Particles originating from the electrostatic chuck were observed to be deposited on wafers in much larger numbers in the presence of the plasma as compared with gas-only conditions, implying the existence of a large ion drag force.

1. Introduction

The sources and behaviour of particles in processing plasmas are of critical interest in the field of semiconductor wafer fabrication. Although particle generation in a plasma system was first reported in 1985 [1], the presence of particulate contamination and particle deposition on wafer surfaces has been observed for over a decade by users of plasma processes in the semiconductor industry. Only in the last few years have modelling studies as well as systematic and real-time experimental studies been performed on plasma systems as a means of understanding and, it is hoped, controlling particle generation [2–9]. The motivation, well known and appreciated in the high-density integrated circuit manufacturing industry, is to reduce yield loss due to wafer level particulate contamination.

With the advent of high-density, low pressure plasma sources, such as electron cyclotron resonance (ECR), radio-frequency induction (RFI) and helicon systems as promising candidates for critical layer etching, there is great interest in the particle generation modes and transport characteristics for these tools. For example, recent modelling work by Graves *et al* has demonstrated that, for an ECR source, particle trapping

is less likely than for parallel-plate electrode plasma sources [10]. A recent report by Selwyn [11] reporting laser light scattering results from an ECR tool is cited as evidence confirming this prediction.

In this paper we report post-processing wafer-level particle count results (using a laser-based surface particle detector) from a close-coupled ECR etch tool. The influence of the plasma, its characteristics and the reactor conditions on particles from two principal sources is investigated. The two sources are particles generated by cracking and delamination of a residual film deposited on chamber walls during ECR etching of polysilicon and particles from the electrostatic wafer chuck transported onto the wafer by a burst of He from the back side of the wafer.

2. Experiment

The configuration of the etching tool is shown in figure 1. 2.45 GHz microwave power (0–1400 W) is introduced through rectangular and circular waveguides into the quartz bell jar. The magnetic field are produced by two coils concentric with the process chamber with current ranges of 15–35 A (upper coil) and 3–25 A (lower coil). The resonance zone (nominally 87° G) was measured experimentally to occur at 85 mm above the wafer at coil current settings of 30 A (upper) and 4 A (lower) for the

^{||}Present address: Applied Science and Technology, Inc., Woburn, Massachusetts, USA

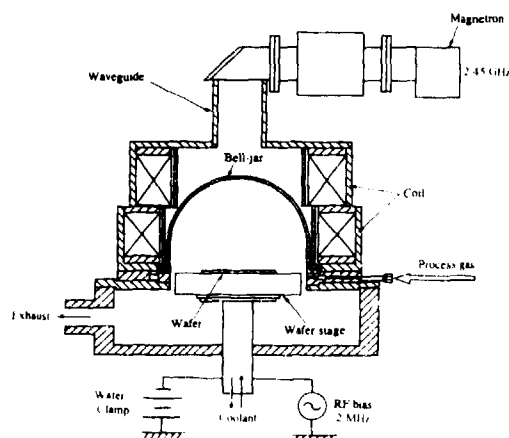


Figure 1. Configuration of the close-coupled electron cyclotron resonance plasma reactor.

process conditions in this work. The chamber is evacuated by a 2000 l s^{-1} turbomolecular pump through a large exhaust port below and to the side of the wafer chuck. The base pressure of the chamber is 1×10^{-6} Torr. Process gases are introduced through a gas-distribution grounding ring around the base of the bell jar. The system can be configured for 150 or 200 mm wafers, which are introduced into the chamber through a separately pumped load lock and clamped onto the chuck electrostatically with $\sim 500 \text{ V}$ clamping voltage. The electrostatic chuck is assisted by a mechanical clamp ring with 16 contact points around the wafer. For particle studies under gas-only (no plasma) conditions, no electrostatic clamping occurs. Radiofrequency power

(2 MHz) in the range 0–140 W is applied to the chuck for substrate bias control. Wafer temperature control is achieved by circulating coolant (from -50 to $+80^\circ\text{C}$) on the back side of the chuck and applying helium to the back side of the wafer. Electrode temperature, taken to be the coolant temperature exiting the electrode, was maintained at 20°C for all studies except where noted.

Wafer-level particle count data were obtained using a 488 nm Ar ion laser surface particle detector (Tencor Surfscan 6200). 3 mm edge exclusion was employed to eliminate observation of surface damage caused by the mechanical clamp fingers. All experiments were performed in a state-of-the-art, class 1 clean room using proper clean room practice. Particle test wafers were 150 or 200 mm diameter bare silicon substrates of prime grade (virgin) for studies during etch processing in a clean chamber; monitor grade wafers were used for studies of a heavily particle-contaminated chamber. Only wafers with 15 or fewer starting particles greater than $0.3 \mu\text{m}$ in size were used in the testing, and most had fewer than ten. All particle measurement data were obtained using the following procedure. Test wafers were flat, notch oriented and then pre-measured just prior to loading into the etch tool; then the wafers were post-measured just after exiting the plasma system. No manual wafer handling was performed between the pre- and post-measurements. Wafers are transferred from a load cassette to an unload cassette as a consequence of the etch tool wafer process sequence. Control wafers were run at regular intervals and consistently showed less than two particles added to wafers as a result of manual cassette handling during transfer between the measurement tool and the etch tool (separated by about 5 m). Consequently, all data reported as particles added are simply the difference between the pre- and post-etch tool measurements.

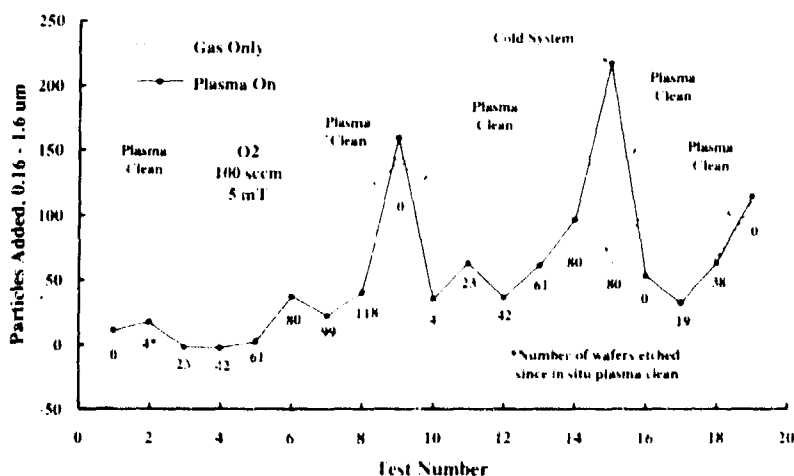


Figure 2. Comparison of particles ($0.16 - 1.6 \mu\text{m}$) added to wafers for plasma on and gas-only particle tests (using the conditions shown) during a stability test of an optimized, 200 mm etching process.

3. Particle addition to wafers in a clean ECR system

As part of a study of doped polysilicon gate etching processes using HBr and Cl_2 , a process stability experiment was performed on an optimized etch process. In the stability experiment, several hundred wafers were etched and etch process metrics (etch rates, selectivities and so on) were obtained at regular intervals. One of the metrics was particles added to wafers (Si substrates with native oxide) for gas-only (no plasma) and plasma-on (500 W) conditions, using 100 sccm O_2 at 5 mTorr. Figure 2 shows a plot of particles of size $0.16 \cdot 1.6 \mu\text{m}$ added to wafers at various points throughout the process stability experiment. The experiment was performed in a nominally clean system, namely all internal chamber parts were cleaned and a clean bell jar was installed prior to the optimization study. A 15 min *in situ* plasma cleaning of the reaction chamber was performed at the beginning of each day and at the end of the experiment. The cumulative number of wafers etched after each plasma clean is indicated for each particle test. All particle tests consisted of one wafer each for the conditions of plasma-on and no plasma (gas-only). Figure 2 illustrates five interesting points: (i) there is a slight upward trend in the data, indicating that the system is becoming dirtier; (ii) *in situ* plasma cleaning had no consistent effect on the particle counts; (iii) except for three points, the plasma-on particle test resulted in lower particle counts than the gas-only test; (iv) two of the plasma-on tests (numbers 9 and 15) show significant positive deviation from the rest of the plasma-on data (it will be shown that these excursions are common for plasma-on testing and are evidence of plasma-induced particle ejection from chamber surfaces); and (v) one of

the plasma-on tests with a large positive deviation (number 15) occurred in a cold system (the test was the first plasma in the system for that day) and this 'cold system' effect is repeatable.

To quantify whether there is a statistical difference between the plasma-on and the gas-only data in figure 2, a Wilcoxon test was performed to test the means and an *F*-test was performed to test the variances [12]. The Wilcoxon test assumes no particular type of distribution. The tests indicated that both the mean and the variance of the plasma-on data are statistically different from those of the gas-only data, the plasma-on mean being smaller but the variance larger due to the outliers (excursions). This is graphically illustrated in figure 3 by comparing the box plot for each data set [13].

4. Particle addition to wafers during a polymer forming etch process

A small amount of oxygen added to a doped polysilicon etch process using HBr greatly improves the ECR polysilicon etch selectivity to oxide [14]. If the amount of oxygen is greater than about 1% of the total flow, however, a deposition mode is entered during the etch reaction [14]. A residue is deposited as a film on the chamber surfaces, including the quartz bell jar. The film is observed to deposit preferentially in a ring half-way up the bell jar and at the top of the bell jar where there are microwave 'cold spots,' areas that are aligned with and close to physical nodes in the waveguide. Table 1 shows results of plasma-on and gas-only particle tests performed on the clean system just prior to running this etch process and after every ten resist-patterned, poly-

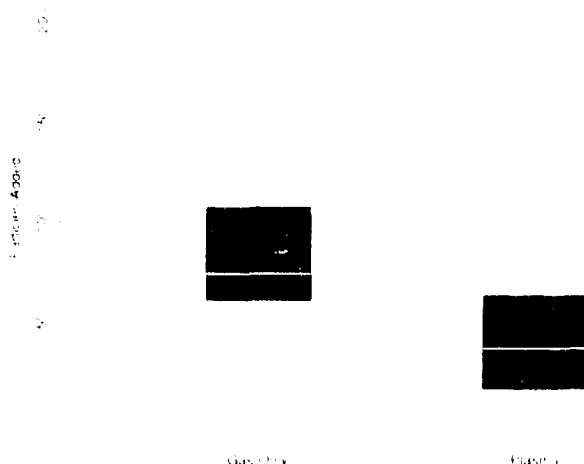


Figure 3. Box plot of the plasma-on and gas-only particle test data shown in figure 2. The white bar indicates the median value. The shaded area represents the inner quartile range (25th–75th percentile). Enclosures (connected by dotted lines) indicate the 2.5 and the 97.5 percentiles. Horizontal lines indicate outliers.

silicon wafers were etched. Two wafers were run for each of the gas-only and the plasma-on particle tests and both tests were performed using the etching process parameters 120 sccm HBr, 2 sccm O₂, 5 mTorr, and for the plasma-on test, 750 W incident microwave power, an ECR point of 85 mm, and 20 W RF bias. Except for the cold system tests in which both gas-only wafers were run first, the tests were performed in the following order: gas-only, plasma-on, gas-only and plasma-on. It should be observed that the gas-only and plasma-on particle tests do not etch the silicon substrate due to the high selectivity of HBr to native oxide; a breakthrough step, using Cl₂ for example, is required to initiate etching.

Table 1. Gas-only and plasma-on particle tests during the etching of polysilicon wafers using an etching process known to deposit a residual film on chamber surfaces

Number of wafers etched	Number of particles (0.32–28 µm)	
	Gas-only	Plasma-on
0	2, 13	8, 13
10	11, 15	36, 15
10*	600, 31*	678, 10*
20	44, 37	50, 151
30	213, 80	222, 115
40	339, 157	404, 215
50	369, 214	577, 263

*Cold system test results.

Several points are noted from these data: (i) the nominal, clean system background particle count is exceeded, indicating failure of the film, when 10–20 wafers are etched, but the film is evident after only a few wafers have been etched; (ii) the cold system effect is again realized, for both plasma-on and gas-only measurements; (iii) except for the second plasma-on test after 20 wafers (151 adders), and not including the cold

system results, the number of particle adders monotonically increases; (iv) the second plasma-on test after 20 wafers (151 adders) is a positive excursion and is probably a plasma-induced, episodic event; and (v) except for the clean system and the positive excursion just noted, the first plasma-on test places a larger number of particles on the wafer than the second test (this is also true of the gas-only tests when the system becomes very dirty).

5. Plasma effects on particle addition to wafers in a dirty ECR system

After the study described in section 4, 25 more wafers were etched using the residual depositing etching process. The bell jar was then removed and the system was thoroughly cleaned and converted to process 150 mm wafers. The dirty bell jar was reserved and the system was tested for particles with a clean bell jar in place. Plasma-on and gas-only tests using Ar proved that the system was clean, with mean particle additions of less than 15 particles (0.32–28 µm). The dirty bell jar was then placed in the system and used as a known source of particles to study plasma effects on particle behaviour. All regions of the bell jar coated with the residual film were cracked and delaminating to varying degrees. The following studies were performed with 100 sccm Ar at 5 mTorr pressure.

5.1. The effect of microwave power on particle addition to wafers

The effect of microwave power on particles added to wafers was evaluated by sequentially processing a cassette of wafers for each of three conditions in the following order: gas-only, plasma-on at 1100 W incident microwave power (300 W reflected) and plasma-on at

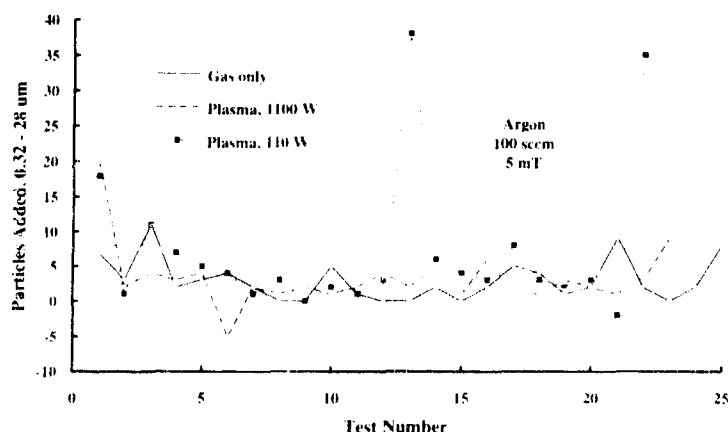


Figure 4. Comparison of particles added to 150 mm wafers (0.32–28 µm) for wafer runs with gas only, 1100 W plasma, and 110 W plasma for the conditions shown. The order of the runs was the same as the order in the legend.

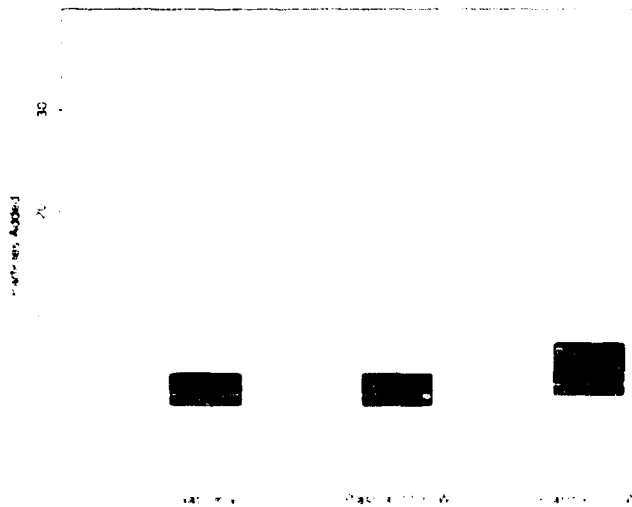


Figure 5. Box plot of the gas only, 1100 W plasma, and 110 W plasma data shown in figure 4. The symbols are described in the caption of figure 2.

110 W incident microwave power. No RF bias was applied for the plasma-on tests. For the condition of plasma-on at 110 W incident power, the microwave power was partially transmitted to the wafer since the reflected power was near zero (< 5 W) and a potential difference was induced in the RF bias circuit with RF bias off. The results for each wafer cycled under each condition are shown in figure 4. Two observations are noted: both plasma-on conditions show high first wafer counts and in addition to the first wafer tested, the 110 W plasma-on test had two large, positive excursions. To test for statistical difference in these results, a Wilcoxon test was performed on the means and an F -test was

performed on the variances. The test for the means showed no statistical difference for the three conditions. The test on the variances showed no difference between gas only and plasma-on at 1100 W. The variance of the 110 W plasma-on condition is different from that of the other two conditions, due to the two outliers of tests 13 and 22. The results are illustrated using box plots in figure 5. An important conclusion from these plots is that the presence of a plasma (at 110 or 1100 W incident power) in the system seems to increase the number and extremity of the outliers (excursions). This effect is observed consistently and appears to be characteristic of a plasma-on condition.

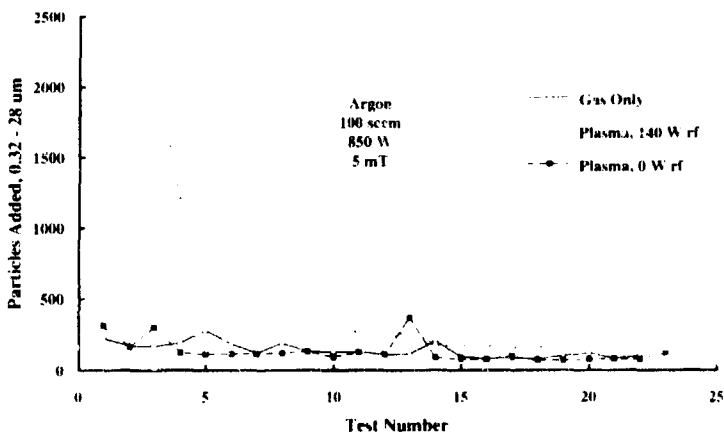


Figure 6. Comparison of particles added to 150mm wafers (0.32-28 μm) for wafer runs with gas only, 140 W radiofrequency bias plasma, and 0 W radiofrequency bias plasma for the conditions shown. The order of the runs was as indicated in the legend.

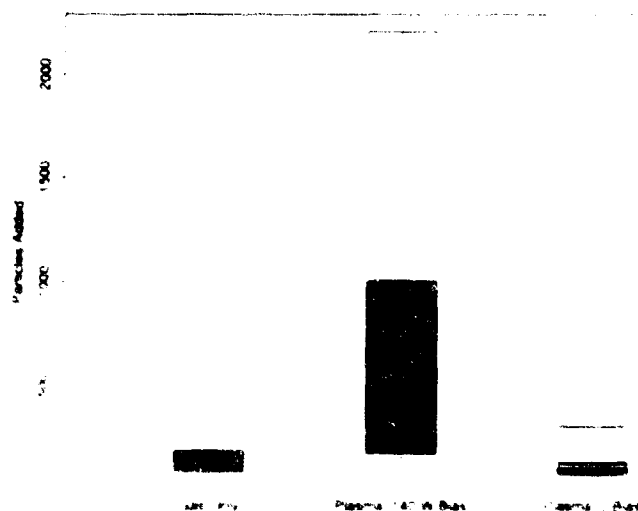


Figure 7. Bar plot of the gas only, 140 W radiofrequency bias plasma, and 0 W radiofrequency bias plasma data shown in figure 6. The symbols are as described in the caption of figure 2.

5.2. The effect of rf bias on particle addition to wafers

The effect of wafer rf bias on particle behaviour was studied for the conditions of gas only, 140 W rf bias, and 0 W rf bias. Incident microwave power was 800 W and reflected power was 160 W for the plasma on tests. 140 W rf bias resulted in an average peak to peak rf voltage of 260 V. The results for each wafer cycled under each condition are shown in figure 6. The results show a dramatic increase in the number of particles added to the wafers for the condition of plasma on with rf bias. A time dependent effect, possibly due to chamber heating, is also evident for this condition with the first

several wafers adding a factor of 20 more particles to wafers than for the gas only or zero bias conditions. Although the particle counts stabilize for the 140 W condition after about 13 wafers, note that this level is still a factor of two higher than that for the other conditions. One explanation for the higher level after 13 wafers may be that there is increased bombardment of the anodized gas grounding ring surrounding the wafer when the wafer is rf biased. For these tests, the external bell jar temperature at the beginning of each test sequence was 21, 22 and 25 °C for the conditions gas only, 140 W bias and 0 W bias, respectively.

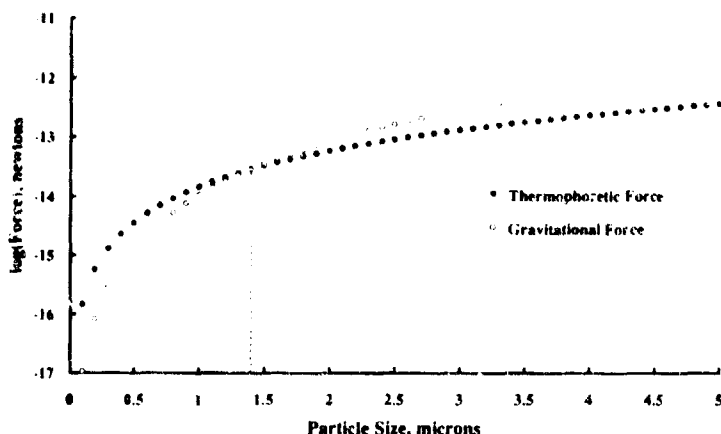


Figure 8. Calculated thermophoretic [13] and gravitational forces as a function of particle size for an Ar plasma at 5 mTorr, $\nabla T = -6 \text{ K cm}^{-1}$, a particle density of 2 g cm^{-3} and particle temperature less than 500 K.

Statistical tests of the means and variances showed no difference in the gas-only and 0 W bias conditions. The result for the test on the means is consistent with the results of the microwave power study (section 5.1). The box plots for these results, figure 7, show the impact of the 140 W RF bias condition. Although there is no statistical difference in the means or variances of gas-only and 0 W RF bias, note the presence of outliers for the plasma-on condition and the lack of any outliers for the gas-only condition. This is consistent with the results of the microwave power study.

5.3. The effect of electrode temperature on particle addition to wafers

Among the forces influencing particle behaviour in plasmas is drag due to collisions of particles with neutral gas molecules [9]. One way in which neutral drag can influence particles is by imparting a thermophoretic force due to thermal gradients (see [6] and references therein). Graves *et al.* [6] demonstrated that gradients of the order of 3 K cm^{-1} are sufficient to balance the gravitational force on $0.5 \mu\text{m}$ carbon particles at 50 mTorr in a parallel plate source, and the authors suggest that thermophoretic forces may be important in low temperature etching applications.

For the tool source used here, previous experiments showed that wafer surface temperatures when exposed to plasma are of the order of $10\text{--}20^\circ\text{C}$ higher than the electrode temperature at 20°C . If we assume that the same is true at electrode temperatures of -80°C and $+80^\circ\text{C}$, then wafer temperatures would be about -60°C and $+100^\circ\text{C}$, respectively, in the presence of plasma. For an average internal wall temperature of 40°C (corrected from average external wall temperature measurements) and an average wafer to wall distance of 10 cm, wafer to wall temperature gradients ∇T of the order of $+7$ and -6 K cm^{-1} are possible under these conditions. Since thermophoretic force varies with the

square of the particle diameter [13] $F_{th} = f(d_p^2)$, and gravitational force varies with the cube of the particle diameter, $F_g = f(d_p^3)$, the effect of thermal gradients becomes larger with smaller particles. Assuming a particle density of 2 g cm^{-3} and a particle temperature less than 500 K, calculations of the thermophoretic [13] and gravitational forces in Ar at 5 mTorr and $\nabla T = -6 \text{ K cm}^{-1}$ reveal a cross over in the two forces at a particle size of about $1.5 \mu\text{m}$ (figure 8). Particles smaller than this experience a thermophoretic force away from the wafer, which is larger than that due to gravity under these conditions. Consequently, if thermophoretic and gravitational forces represent a significant share of the total force experienced by the particles, then curves of wafer level particle counts versus size should be very different for the cases $\nabla T = -6$ and $+7 \text{ K cm}^{-1}$, that is, a step function decrease in added particles of size $< 1.5 \mu\text{m}$ is expected for the case $\nabla T = -6 \text{ K cm}^{-1}$ while no such decrease is expected for the case $\nabla T = +7 \text{ K cm}^{-1}$.

Experimental results showing the effect of electrode temperature on particle addition to wafers for particle sizes from 0.32–28 μm in size are shown in figure 9. No significant change in the mean number of particles added is observed for particle sizes $> 1.5 \mu\text{m}$ for either hot or cold electrode conditions. This suggests that both thermophoretic and gravitational forces are small components of the total force experienced by particles under these conditions.

6. Particles added by the electrostatic wafer chuck

Electrostatic wafer chucks can shed large numbers of particles because brittle ceramic materials are used to coat the chuck. Although particles may be added to the back side of a wafer, most are subsequently removed in a wet cleaning. When the wafer is electrostatically clamped, the back side is pressurized with up to 10 Torr of He to promote heat transfer from the wafer to the chuck.

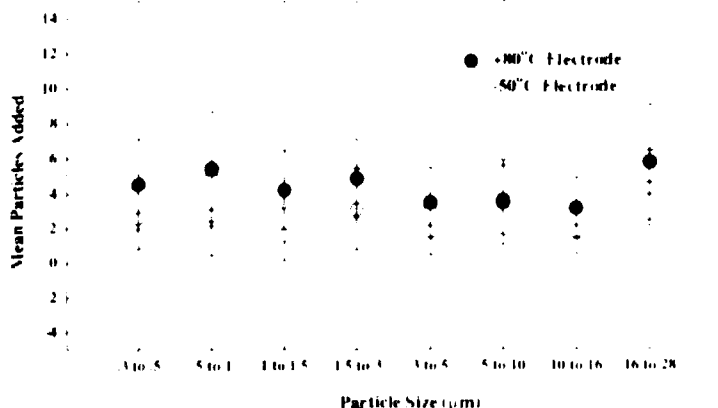


Figure 9. Average number of particles added to wafers as a function of particle size for 850 W Ar plasma runs at electrode temperatures of $+80^\circ\text{C}$ and -50°C .

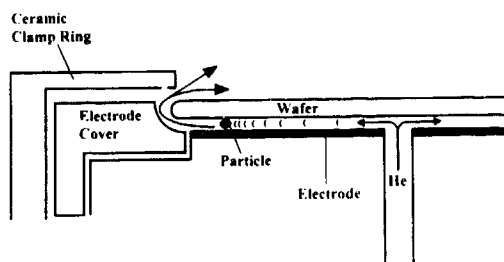


Figure 10. Schematic diagram of the electrostatic wafer electrode and the mechanical clamp.

The resulting pressure differential from the wafer back side to the source region causes some He to leak into the chamber. The He flow is pulse-width modulated at 1 secm, giving a time-averaged leak rate of about 0.1 secm, to maintain the correct back side pressure. This gives rise to the possibility that particles are blown from the back side and land on the front side of the wafer. This phenomenon has been investigated and no added particles were observed in a clean system under normal operation. If the back side He is pulsed instantaneously with 10 secm or if the clamping voltage is suddenly removed, however, particles can be added to the wafer under a variety of source conditions due to a shock-wave, which carries the particles around the edge of the wafer and into the chamber (figure 10). These two non-standard modes of operation of the chuck were used to test mechanisms of particle transport in this system. The geometry of the electrode cover and mechanical clamping ring are such that He flow is directed over and along the wafer, rather than away from it. The He burst (release point) originates at a fixed point around the circumference of the wafer. Larger particles land closer to the release point and smaller particles are carried farther away.

The finding relevant to particle behaviour in an ECR source is that there is a consistent order of magnitude increase in particles (0.32–25 amu) added to wafers for any given plasma-on condition (several thousand particles added) compared to a gas-only condition (several hundred particles added). This is strong evidence that ion drag is the dominant force influencing particle transport in this source. Under these particle injection conditions, the presence of the plasma provides a vertical force (in the form of ions) which drags the emitted particles down to the wafer surface. With no plasma present, most of the injected particles have enough radial kinetic energy to get clear of the wafer.

7. Discussion

The presence of plasma clearly can cause the ejection of particles from a chamber surface, validating earlier observations in an SiO_2 plasma deposition system [4]. This behaviour is seen most dramatically in the RF bias

study described in section 5.2. Thermal stress of the residual film on the bell jar and increased bombardment of the gas/grounding ring in the presence of RF bias are reasonable explanations for this phenomenon. The consistent observation of high plasma-on particle counts in a cold (room temperature) ECR system, even when gas-only counts are low, is evidence that thermal stress plays an important role. Even a short idle period for the system will cool the bell jar to a point at which subsequent exposure to plasma will eject particles.

Why are high plasma-on particle counts also observed in a hot system? Under standard processing conditions, external bell jar temperatures can reach a peak of 110°C during plasma-on periods of processing and cool by 15–20°C between wafers. (For the experimental results presented here, external bell jar temperatures were typically in the range 25–30°C.) Assuming that the interior bell jar temperatures are a minimum of 10–20°C hotter than the external temperature, this represents a reduction by more than 100°C of the temperature drop across the residual film relative to a cold system. Since this implies that thermal stress would be lower, a direct plasma-wall interaction may then explain particle ejection from a hot wall. Alternatively, if the residual film is not in good mechanical thermal contact with the bell jar, it may get much hotter than the bell jar itself, increasing the chance of the film failing under stress. Also, the film may get hotter due to greater photon absorption relative to the quartz. Thermal stress along the film may also be important, since the inside of the bell jar does not uniformly get heated (as revealed by increased residual deposition on microwave 'cold spots', as well as temperature measurements).

The effect of system-induced mechanical stress on particle ejection from walls is less clear. The fact that no mechanical perturbation of the system occurred during the particle test indicates that the plasma alone causes ejection of particles. This does not imply, however, that system-induced mechanical stress (such as gate valves opening/closing) has no effect: mechanical stress may condition the film such that it is more likely to eject particles upon exposure to a plasma, as suggested in [4].

In the light of the results with large neutral thermal gradients and the observation that particles ejected from the back side are driven to the wafer in the presence of a plasma, ion drag appears to dominate thermophoretic and gravity forces in this ECR source. The role of electrostatic force remains unclear. *In situ* laser light scattering results revealed no particle trapping during HBr etching of polysilicon in this tool in the regions over the clamping ring or several millimetres above the wafer surface. The plasma sheath boundary region above the wafer could not be observed because it was obscured by the clamping ring.

Acknowledgments

The authors gratefully acknowledge the excellent technical assistance provided by G. Roth and P. Chavez. Statistical analysis was provided by U. E. Halbleib. This

work was supported by SEMATECH and DOE contract DE-AC04-76DP00789.

References

- [1] Roth P M, Spears K G, Stein G D and Wong G 1985 *Appl. Phys. Lett.* **46** 253
- [2] Selwyn G S, Singh J and Bennett R S 1989 *J. Vac. Sci. Technol. A* **7** 2758
- [3] Jellum G M and Graves D B 1990 *J. Appl. Phys.* **67** 6490
- [4] Selwyn G S, McKillop J S, Haller K L and Wu J J 1990 *J. Vac. Sci. Technol. A* **8** 1726
- [5] Selwyn G S, Heidenreich J W and Haller K L 1991 *J. Vac. Sci. Technol. A* **9** 2817
- [6] Jellum G M, Daugherty J E and Graves D B 1991 *J. Appl. Phys.* **69** 6923
- [7] Selwyn G S 1991 *J. Vac. Sci. Technol. A* **9** 3487
- [8] Logan J S and McGill J J 1992 *J. Vac. Sci. Technol. A* **10** 1875
- [9] Barnes M S, Keller J H, Forster J C, O'Neill J A and Coultas D K 1992 *Phys. Rev. Lett.* **68** 313
- [10] Kilgore M D, Daugherty J E, Porteous R K and Graves D B 1994 *J. Vac. Sci. Technol. B* **9** 486
- [11] Selwyn G S 1992 *Proc. 1992 Dry Process Symposium* (Tokyo: Institute of Electrical Engineers of Japan) p 123;
Selwyn G S, Haller K L and Patterson E F 1992 *Proc. 9th Symp. on Plasma Processing* ed G S Mathad and D W Hess (Pennington, New Jersey: Electrochemical Society) p 236
- [12] Box G E P, Hunter W G and Hunter J S 1978 *Statistics for Experimenters* (New York: Wiley)
- [13] A description of the box plot is given by Tukey J W 1977 *Exploratory Data Analysis* (Reading, Massachusetts: Addison-Wesley). Statistical analyses and graphics were generated using *S-Plus* (1991) Statistical Sciences, Inc. Seattle
- [14] Tipton G D, Blum M G, Westerheld P L, Frutna L S and Maxwell K L 1994 *J. Vac. Sci. Technol. B* **9** 416

Contamination particle traps due to a cone, cube and disc

Robert N Carlile, John F O'Hanlon, Lazaro M Hong,
Mary P Garrity† and Sean M Collins

Department of Electrical and Computer Engineering and Department of Chemical Engineering, University of Arizona, Tucson, AZ 85721, USA

Received 11 January 1994, in final form 3 February 1994

Abstract. This paper studies asymmetric particle clouds confined within electrostatic particle traps in the presence of a molecular drag force. The drag force, due to flow of neutral Ar gas around a particle, is proportional to the gas flow, which can be controlled by a mass flow controller. Our system has a component of the drag force parallel to the water electrode surface. The particle clouds associated with a cube and a disc are seen to be highly asymmetric in the direction of the drag force, as would be expected. The asymmetry increases as gas flow increases. In order to visualize the clouds quantitatively, we have introduced a technique called *spot scanning* in which we move the laser beam slowly with a serpentine path through the particle cloud. The forward scattered light is recorded by a charge-coupled device camera onto videotape. The image of the scattered light on a frame of the videotape is a nearly circular red spot. Using commercially available computer software, the red spots can be used to determine the boundary of the cloud as well as to find contours of constant power density scattered from the cloud.

1. Introduction

Several workers have observed particle clouds in traps in a parallel plate plasma processing system, using laser light scattered from the particles [1-6]. For a He-Ne laser, the laser beam can be rastered in a plane parallel to the water, and the forward scattered light is recorded on videotape via a CCD camera. Impressive real time displays of the dynamics of particle clouds and sometimes discrete particles have been observed. These observations, while giving much intuitive insight into particle cloud behaviour, are nevertheless qualitative.

The drag force on a particle, due to the flow of the neutral gas around a particle, has recently been shown to be comparable to the electrostatic force that confines a particle within a trap for typical gas flows into a chamber [7]. This suggests that if the drag force is azimuthally asymmetric with a component tangential to the water electrode surface, then a particle cloud within a trap, which would usually be expected to exhibit azimuthal symmetry about an axis normal to the electrode (such as a ring cloud over the circumference of a disc perturbed on the water electrode) would instead be asymmetric (for example, only a partial ring). This tangential component of the drag force would occur if the gas is not admitted or pumped out azimuthally symmetrically about the water electrode.

We therefore chose trap creating perturbations on the

water electrode which, in our geometrically azimuthally symmetric chamber, would be expected to produce clouds with azimuthal symmetry, namely a cone, cube and disc. Since our experimental etch system has both an azimuthal asymmetry in gas admittance and pump-out, the tangential component of drag force naturally occurs. One purpose of this work is therefore to observe the asymmetry that the drag force creates in the particle cloud.

However, to do this effectively, we needed to find quantitatively the boundaries of the cloud and to be able to plot this boundary for cases of increasing tangential component of drag force. A second purpose of this paper, therefore, is to describe a simple technique that we developed for using He-Ne laser light scattering not only to find these boundaries quantitatively but also to plot contours of constant scattered light power density within the cloud region. We call this technique *spot scanning*.

2. The experimental system

We have used the modified Legal MCR Etch system described elsewhere [1-6]. All experiments were done using Ar gas and therefore an Ar plasma. In this system, Ar is admitted through a thin annular gap via six orifices, however, because of the configuration of the gas supply manifold, the gas flow is asymmetric. Argon flow is highest through the annular gap located closest to the manifold inlet, and lowest through the gap diametrically

† On leave from IBM, El Segundo, California, USA.

opposite to the inlet. Furthermore, the gas is pumped out through a port located diametrically opposite the manifold gas supply inlet. Thus, the Ar gas molecules will have an asymmetric distribution of average velocity $U(x, y, z)$, a vector. Here, let y be normal to the electrode surface; the laser beam axis, discussed below, is parallel to the z axis; let positive x point from the point in the annular gap where gas flow is lowest to the point where it is highest. Then, $U_x(x, y_0, z_0) < 0$ for constant y_0, z_0 and all x , indicating that U_x is positive in the $-x$ direction so that there is a positive component of velocity U_x directed from the highest to lowest gas flow inputs. This system is ideally suited to our experiments.

The gate valve between the plasma chamber and the turbo pump was set for a fixed aperture, thus causing the pumping speed S to be fixed. We have confirmed this by experimentally showing that the chamber pressure P is a linear function of Ar gas flow Q (sccm), which is controlled by an MFC. For all experiments discussed here, $S = 18.9 \text{ l s}^{-1}$. Also, $3.0 < Q < 60 \text{ sccm}$ so that at 300 K, $0.29 < P < 5.9 \text{ Pa}$. Since S is a constant, $U(x, y, z)$ stays approximately constant and is independent of Q and P .

O'Hanlon *et al* [7] have shown that, for this range of pressure, one should use the vector molecular drag force F_D :

$$F_D = 135.1 \pi \eta d^2 P (U - v) \quad (1)$$

where SI units are used throughout, the constant 135.1 has the units of $\text{Pa}^{-1} \text{ m}^{-1}$, η is the viscosity (Pa-s), d is the particle diameter (m) and v is the particle velocity (m s^{-1}). The drag force F_D is in the same direction as U (for $v = 0$) so that F_D has a component $F_{Dx} < 0$ directed in the $-x$ direction, and is tangential to the water electrode.

Alternately, F_D can be expressed in terms of a normalized flow Q/Q_m , where Q_m is chosen to be the minimum flow used in this work (3.3 sccm). Thus, Q/Q_m varies from 1 to about 18. Since U is independent of P and Q/Q_m , while P is proportional to Q/Q_m , equation (1) tells us that F_D is proportional to Q/Q_m . Thus, as we vary Q/Q_m via a MFC, the drag force on every particle must vary proportionately.

On the driven electrode (100 mm in diameter) we have placed a 100 mm disc of graphite. At the centre of the graphite disc, we place either an aluminium cone, cube or disc. The cone has a base diameter of 12.5 mm and an altitude of 12.5 mm. The cube is 12.5 mm on a side. The disc has a diameter of 23.8 mm and a height of 1.6 mm.

We have observed the particle clouds associated with these objects using forward scattered HeNe laser light. The scattered light is detected by a colour sensitive CCD camera (Sony DXC-750) and can be recorded on super 8 video tape using a VCR (Panasonic PV-N4564). The entire system is colour sensitive. The axis of the laser beam is parallel to the z axis of the coordinate system set up above. The laser and camera system have been described elsewhere [5].

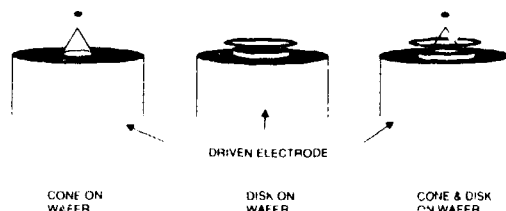


Figure 1. Superposition of particle traps. Left: dot cloud above peak of cone on graphite; middle: ring cloud above disc on graphite; right: dot and ring traps above cone on disc on graphite.

3. Raster scanning

Initially, we placed the cone on the graphite disc. Then, using the conventional raster technique [1-3], we observed a small 'dot' particle cloud over the tip of the cone, as shown in the left-hand drawing in figure 1. We then varied the gas flow and found that the appearance of the trap was independent of gas flow within our ability to observe changes qualitatively.

Next, we replaced the cone with the disc. A ring cloud was observed, as shown in the middle drawing in figure 1. However, the distribution of particles in the ring was a sensitive function of gas flow. As gas flow increased, the particles of the cloud seemed to be 'blown' to the left side of the ring, in the direction of F_{Dx} , and U_x , both of which are positively directed from right to left in figure 1. For even moderate values of Q/Q_m , such as 5.2, the ring became a partial ring in which particles could only be seen on the left-hand side of the ring in figure 1. We assume that the drag force is moving particles to the left-hand side of the ring.

Finally, we placed the cone on the disc as shown in the right-hand drawing in figure 1, and found that the dot and ring clouds associated with the two objects individually were also both present. It is as if the clouds were observing superposition.

4. Spot scanning

4.1. Technique

We have found a simple technique, using the HeNe laser system that would give us quantitative information about the particle clouds. Rather than rastering the laser beam, we moved it manually and very slowly through the cloud, at a rate low relative to the videotape frame speed (about 30 frames per second). We followed a serpentine path with the beam, so that the entire cross section of the cloud perpendicular to the beam was traversed (the xy plane). By examining quantitatively the beam image on the videotape, we were able to find the cloud boundary as well as contours of constant scattered power density within the cloud. This process is analogous to the tomography x-ray technique used in

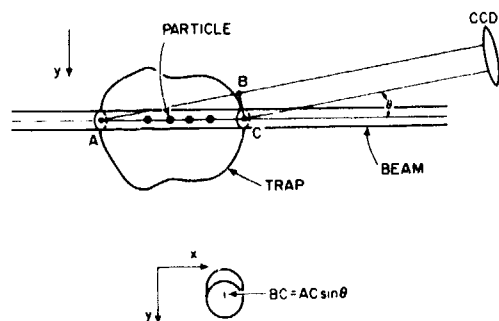


Figure 2. Light from a particle cloud scattered into a charge-coupled device camera. Inset: cylindrical intersection of laser beam and particle cloud as seen by the camera.

medical CAT scans, in which a cross section of the human body can be imaged.

The laser beam penetrating the particle cloud is shown in figure 2. The CCD camera is positioned so that it receives forward scattered light from the particles at a small angle θ with respect to the beam axis. Typically, $\theta \approx 2.5^\circ$. If light were scattered uniformly from the cylindrical section of the beam that intersects the cloud, that scattered light would appear as shown in the inset. For small θ , the scattered light is nearly circular, being slightly elongated by an amount BC in the vertical or y direction. Thus, on a colour-sensitive videotape frame, the scattered light will be nearly circular at the colour red corresponding to the wavelength of the HeNe laser. In fact, we cannot visually see any deviation from a circular red spot on the frame. We thus call this technique *spot scanning*.

After a cloud has been established over an object for a specified Ar flow, the laser beam is spot scanned through the cloud, and the scattered spot of light, received by the CCD camera, is recorded on videotape using a VCR. Typically, the time to spot scan is about 2 min. Next, selected frames from this section of videotape are digitized and stored on the hard disc of a PC. This is accomplished by inputting the analogue signal of the VCR from a single frame through an A/D converter card in the PC. The entire procedure is controlled by appropriate software such as FRAMEGRABBER (Raster Ops Corp). Digitization consists of subdividing the area of the frame into a large number of discrete points or pixels. The intensities of the three fundamental colour components, red, green and blue, at each point on the frame are each assigned 1 byte of information, or 0–255 on base 10. Thus one pixel contains 3 bytes and its location is inferred.

Next, a second application program such as PHOTOSHOP (Adobe Corp), is used to analyse a frame. The PHOTOSHOP program will retrieve any frame from memory, and re-display the frame on the computer monitor screen. The red spot of scattered light is easily recognizable, even when reflections are present. This is clearly one of the strengths of this process. It allows

movement of an arrow, via a mouse, from pixel to pixel with the red, green and blue intensities displayed in an inset box on the screen. Also, the x and y locations of the pixel are displayed, where x and y are the same coordinates set up above (see figure 2); we now choose y to be downward, that is, into and normal to the wafer electrode. Within the red spot, blue and green intensities are usually 0–5 and are ignored. There is always a small cluster of pixels near the centre of the spot that have much larger red intensities than others. We have plotted the red intensity across a typical diameter of a red spot. Based on this result, we can conclude that we can locate the centre of the spot to $x, y \pm 0.35$ mm. We select a pixel at the centre, and note its location and red intensity. Since this process must be done by eye, we ignore spots with maximum red intensities less than 20 since they are difficult to distinguish from the dark blue background. Typically, maximum red intensities vary from 20 to over 200.

We have manually recorded x, y and the maximum R_{\max} red intensity for those frames that contain a red spot. Finally, and most important, since the object producing the cloud is always in view on a frame, we record the x, y location of two points on the object, such as the upper left- and right-hand corners of the cube.

These data are now used with a graphics program, such as GRAPH TOOL (3-D Visions, Inc), to construct contours of constant red intensity in the $x-y$ plane. The measured two points on the object, which are a known distance apart, allow an absolute scaling for the x, y coordinate system, and the contours can thus be located with respect to the object.

As an example, the cloud created by the cube for Ar at 7 sccm is shown in figure 3, where the contours have been labelled. As in all other contour plots in this paper, the contours are 20 intensity units apart with a contour of intensity of 40 always being the contour of minimum intensity. We estimate that the accuracy of determining

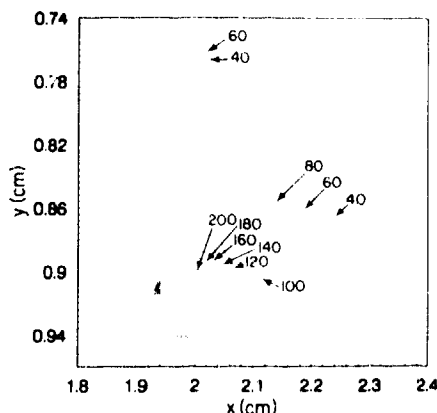


Figure 3. Contours of constant intensity of scattered light for a particle cloud above a cube with multi-dipoles removed. 7.0 sccm, 350 W radiofrequency power. The cube is not shown.

the intensity value of a point on a contour of constant intensity is ± 10 .

Using the known distance between the two reference points on the object, the x, y coordinates are measured in centimetres with respect to an origin in the upper right-hand corner of the frame; positive x extends to the right and positive y extends downward, as shown in figure 2. The cube is not shown in figure 3, but the cloud is distorted to the left-hand side of the cloud, the same direction as F_{Dx} , the tangential component of the drag force.

The red intensity numbers shown labelling the contours in figure 3 are proportional to the power density of the scattered light arriving at the light-sensitive element in the CCD camera at corresponding points. We can therefore calibrate the CCD camera/VCR/computer system such that the contours can be labelled with power density (Poynting vector) of the scattered HeNe light in W m^{-2} . We have not done this.

In order to obtain closed contours as shown in figure 3, a closed contour of points of zero red intensity (zeros) must enclose the measured points. This contour should correspond to the boundary of the cloud such that outside the boundary the red intensity is below 20. Since there is no scattered light from a zero, one must approximate their location. There are two ways to do this. The first, which is what was done here, is to watch the red spot drift off the cloud; then 'grab' several sequential frames, and find the frame in which the spot is just visible as it slides off the cloud. Then use the x, y location of that spot as a zero. Alternatively, a statistical method can be used in which pixel number N in all 36 000 frames (2 min at 30 frames per second) is examined to see whether it has a red intensity that exceeds some threshold, 10 for example. With some added summing and statistical processing, if the answer is 'no', the pixel is outside the cloud, while for 'yes', it would be inside the cloud, and a boundary can be established.

4.2. Results

For the disc on the graphite plate, a complete ring-shaped particle cloud is observed for $Q/Q_0 < 5.2$; for $Q/Q_0 > 5.2$, only a partial ring is observed. To demonstrate this, we set the Ar flow at 20 sccm, or $Q/Q_0 = 6.1$, and used the spot scanning technique to image the partial ring, which is shown in figure 4. The tangential component of the drag force F_{Dx} points toward the left in figure 4, and has caused the particles to move to the left-hand side of the ring. The line connecting the two dots in figure 4 is the top of the disc. To see both the front and the back of the ring, the laser beam was tipped slightly out of the plane of the ring. The quantity R_{max} is the largest intensity contour, 40 is the minimum intensity contour.

Next, we investigated clouds associated with the cube. The MCR-1 etch chamber normally contains a set of permanent magnets of alternate polarity around the side wall of the chamber, constituting multi-dipoles; however, these were removed for this experiment (they

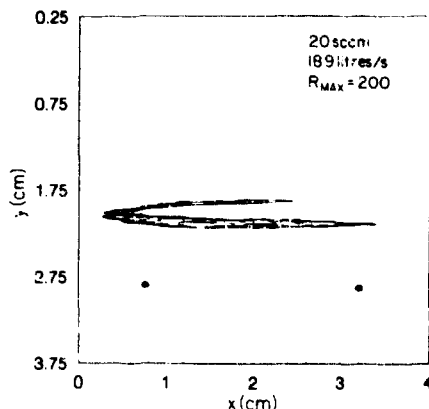


Figure 4. Partial ring above the disc, with multi-dipoles in place. The axis of the laser beam is tipped slightly out of the plane of the ring so that both front and back can be seen: 20 sccm, 200 W. The horizontal line is the diameter of the upper surface of the disc.

were present for the disc and ring cloud shown in figure 4). The spot scanning images of the traps for 3.3, 31 and 55 sccm Ar flow, or Q/Q_0 of 1, 9.4 and 16.7 are shown in figures 5(a)–(c). The horizontal lines represent the top side of the face of the cube normal to the incoming laser beam. In figure 5(a), the cloud has about the same width as the cube side, but is displaced to the left, in the direction of F_{Dx} . In figure 5(b), for $Q/Q_0 = 9.4$ the cloud is much reduced in size in the plane normal to the laser beam, and is displaced considerably to the left. Note that the drag force has increased in strength by a factor of about nine from the case in figure 5(a). Finally, in figure 5(c), the distortion continues, for this case, the drag force is 16.7 times larger than is the case for figure 5(a). For larger Ar flows than Q/Q_0 of 16.7, the cloud disappeared; we theorize that the drag is large enough to free the particles from the trap. The cloud in figure 3 is another image for this case, corresponding to $Q/Q_0 = 2.1$.

5. Discussion

The spot scanning technique described here is probably not optimum, since videotape is inherently a noisy medium. If the light could be focused on a photodiode and the system moved about to discrete points simulating pixels, then the errors reported above could be reduced. Selwyn *et al* have taken a first step toward doing this [8].

We theorize that F_{Dx} plays an important role in the distribution of trapped particles and in the shape of the particle cloud. Now, F_{Dx} , the tangential component of the drag force on any particle is proportional to Q/Q_0 . One would expect that particle distributions would be displaced in the direction of F_{Dx} , which is what we have observed for the two cases shown in figures 4 and 5; we

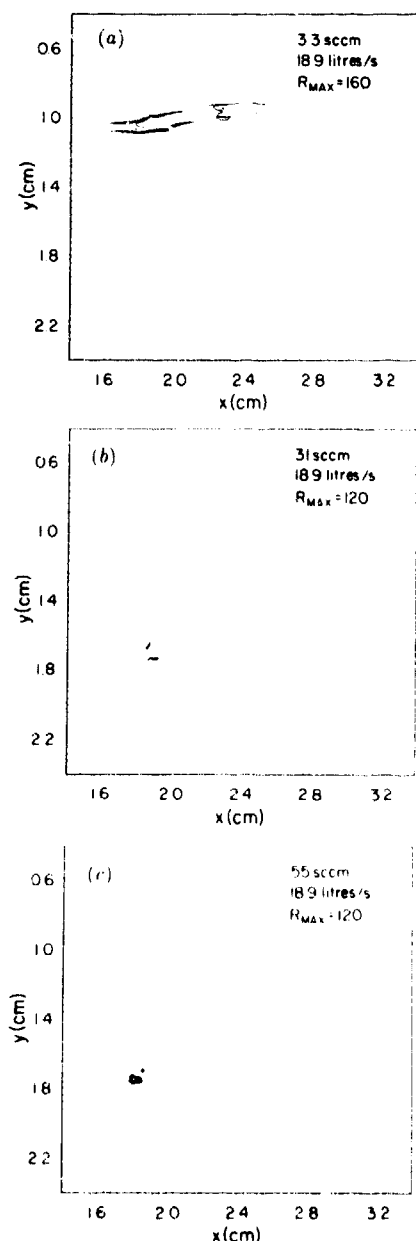


Figure 5. Clouds above the cube, with multi-dipoles removed. The horizontal line is the top side of the face of the cube normal to the laser beam axis: 350 W (a) 3.3 sccm, (b) 31 sccm, (c) 55 sccm

have also observed displacement of clouds in the F_D direction for other cases not reported here

In figure 5, the x, y plane cross section of the trap decreases significantly from figure 5(a) to figure 5(c), as Q/Q_0 increases from 1 to 16.7, while R_{MAX} does not

change much for the three cases. If we assume that the dimension of the cloud (which we cannot measure) into the page in the z direction is at least not increasing, and that the particle size is constant, then the particle density remains nearly constant. If all this were true, then particles are not conserved. They would be leaking out of the cloud and trap as Q/Q_0 increases. This is consistent with the concept that the drag force becomes large enough that some particles may escape the trap. For $Q/Q_0 > 16.7$ sccm, no cloud is seen, so that the drag force must be large enough that all particles escape the trap.

A separate issue is the behaviour of the electrostatic trap containing the particles. Our view is that a trap is created at the instant the RF power is turned on by the system itself in some manner as yet to be determined, and its existence does not depend on particles [5, 6]. The negatively charged particles then flow into the trap. Subsequently they may change its boundaries.

We theorize that the drag force influences the position of particles *within the trap*. The final position of a particle is determined by balance of the drag force with the electrostatic force associated with the trap boundaries [5] and the gravitational force. A particle with thermal energy may move about some equilibrium position. Thus a strong transverse drag force can cause the cloud of particles to move to one side of a trap, and if it is large enough, the particle will escape the trap.

Charged particles certainly can alter the boundaries of the trap [5]. As the trap fills with particles, the trap may expand like a balloon filling with water. If particles are moved to one side of a trap by the drag force, then the trap may be badly distorted on that side. All of these suppositions are consistent with the results shown here.

The details of the electrostatic boundaries of a trap need to be investigated as a function of Ar flow, using, for example, a Langmuir probe [4, 6]. We have seen that the cloud of a dot trap over the cone was unaffected by Ar flow or, apparently, by the drag force. One explanation is that the incremental change in the plasma potential at the trap boundary between the interior of the trap and the surrounding ambient plasma is very large, leading to a large electric field, so that the drag force would have small influence.

From figure 2, it is clear that we are creating an image of a three-dimensional cloud on a two-dimensional plane normal to the laser beam, such as is shown in figure 3. While the location and intensity values of a contour of constant intensity are certainly accurate to within error values stated above, the interpretation in terms of particle size and particle density distribution within the particle cloud cannot be deduced from this single two-dimensional plot. Thus the intensity values of figure 3 have little meaning at present; the most valuable information obtainable is the boundaries of the cloud as projected on this plane. However, as in medical tomography, if, in addition to the plot of figure 3, two-dimensional images can be obtained in planes perpendicular to that of figure 3, then information about particle size density may be forthcoming.

Acknowledgment

This work was sponsored by the University of Arizona Sematech Center of Excellence for Contamination/Defect Assessment and Control, SRC Contract 91-MC-501.

References

- [1] Selwyn G S, Heidenreich J E and Haller K L 1990 *Appl. Phys. Lett.* **57** 1876
- [2] Selwyn G S, Heidenreich J E and Haller K L 1991 *J. Vac. Sci. Technol. A* **9** 2817
- [3] Selwyn G S and Patterson E F 1992 *J. Vac. Sci. Technol. A* **10** 1053
- [4] Carlile R N, Geha S G, O'Hanlon J F and Stewart J C 1991 *Appl. Phys. Lett.* **59** 1167
- [5] Geha S G, Carlile R N, O'Hanlon J F and Selwyn G S 1992 *J. Appl. Phys.* **72** 374
- [6] Carlile R N and Geha S G 1993 *J. Appl. Phys.* **73** 4785
- [7] O'Hanlon J F, Kang J, Russell L K and Hong L M 1994 *IEEE Trans. Plasma Sci.* **22** 122
- [8] Selwyn G S, Singh J and Bennett R S 1989 *J. Vac. Sci. Technol. A* **7** 2758
- [9] Collins S M, O'Hanlon J F and Carlile R N 1994 *J. Vac. Sci. Technol. A* at press

Optical characterization of particle traps

Gary S Selwyn

IBM Research Division, PO Box 218, Yorktown Heights, New York 10598, USA

Received 11 January 1994, in final form 18 January 1994

Abstract. Particles or 'dust' in etching or deposition plasmas are an important cause of product yield loss and equipment down-time. Traditional methods of particle control are only partially effective in plasma processing. This is because formation and transport of particles are strongly influenced by plasma electrical and chemical properties. Particle control in plasma processing requires understanding of these effects and their relation to aspects of tool and process design. Laser light scattering has been used to monitor the behaviour of particles for a wide range of plasma tools. This method provides information on location and transport of particles. In some variations, light scattering may also be used for particle size determination. Results have been obtained in sputter, etch and deposition tools of planar diode and magnetron-enhanced designs. Some results have also been obtained in electron cyclotron resonance tools and radio-frequency inductive tools. From this database, differences and common elements are observed for the behaviour of particles. The *particle trapping* phenomenon is often observed. Particle traps have an important bearing on wafer contamination. Traps cause particles to accumulate into localized regions during plasma operation, only to be suddenly released at the end of the process, thereby contaminating the wafer. Spatially resolved optical emission may be used to map the location and intensity of particle traps. This method also provides a semi-quantitative comparison with two-dimensional modelling studies. It may also be used to optimize grooved electrode design for particle contamination control.

1. Introduction

Particle contamination is a key concern amongst manufacturers of semiconductor and magnetic storage technologies as well as makers of flat panel displays and thin film coatings. Plasma processes are used for etching, deposition, sputtering and surface modification. Despite the low operating pressure and improvements in automated wafer handling systems in these tools, particle contamination is still a major cause of yield loss and down-time in many plasma processes. Further, improvements in contamination control for plasma processes have lagged behind that of other fabrication tools. As a result, plasma tools are now identified as a major contributor to product contamination in many semiconductor processes [1-4].

One reason for this undesirable distinction is that particles behave differently in plasmas than in neutral environments, such as clean rooms, inspection stations and steppers. Particulates in neutral environments are primarily influenced by thermal gradients, turbulence, gravity and gas drag. These effects have been extensively studied and are well recognized. Controlling contamination in neutral environments requires evaluation of the forces acting upon particles, engineering means to divert particles from sensitive surfaces and control of particles sources. Hence, the evolution of the clean room.

The same approach may be used for control of

particles in plasmas, provided there is proper recognition and understanding of the plasma environment. In addition to any external sources, plasmas *generate* particles by reactive, homogeneous chemistry [1, 5-7] and by fracture of deposited wall films [8, 9]. The presence of free electrons causes accumulation of negative charge on particles [10-12]. As many as 10^5 negative charges may accumulate on a $10\text{ }\mu\text{m}$ particle in a typical plasma [8]. In addition to the forces present in neutral environments, particles in plasmas are influenced by electrical field gradients and inhomogeneities [13-16]. The role of these forces and of particle generation must be evaluated in an effective control strategy.

Being complicated environments, plasmas are often modelled only along the spatial dimension between the electrodes, with the radial dimension considered infinite. In reality, the radial dimension is bounded by tool walls, clamp rings, view ports, pump exhausts and even the edges of a wafer. One-dimensional models and related experimental studies often overlook these effects, which have much bearing on particle behaviour.

This work focuses upon optical methods of characterizing particles and the plasma inhomogeneities that influence particle transport. Study of these effects is essential for effective contamination control. As an added benefit, it is seen that particles delineate certain properties not previously noted in experimental or modelling studies. Characterization of these 'new'

plasma properties provides clues not only for contamination control, but also for solution of other processing problems.

2. Particle measurement and detection

2.1. Light scattering

Laser light scattering (LLS) has been the primary means of detecting particles. In this technique, a laser (often one operating in the visible region) is directed into the plasma parallel to the electrode at the plasma/sheath interface [8]. For particles $> 0.5 \mu\text{m}$ and for visible light, elastic scattering (sometimes called Mie scattering) occurs primarily along the forward direction within an about 15° cone [17]. Particles smaller than $0.5 \mu\text{m}$ typically scatter light in a more isotropic manner (commonly called Rayleigh scattering). The forward scattered light is collected with a camera or lens assembly and is detected with a photomultiplier or CCD video camera.

Some studies *raster* the incident laser light using a rapidly scanning mirror [15,18]. In this approach a plane is mapped and particles may be detected within the raster limits. Because particles in plasmas concentrate within a few millimetres of the sheath, aligning the raster plane with the sheath plane provides an efficient means of detecting and monitoring particle motion. This capability is further enhanced by use of a video camera to detect the moving points of scattered light. The technique can also be used to monitor the wafer surface during processing. This is especially useful in high-density plasma tools with very thin sheaths.

The video framing frequency used in LLS also provides a convenient timing mark. This may be used with known distances (such as the diameter of silicon wafers) to infer particle transport velocities. The 'snapshot' pro-

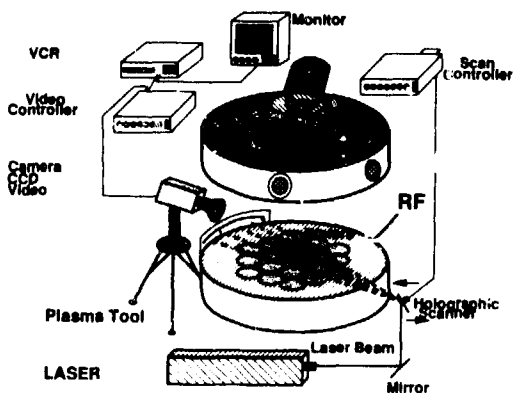


Figure 1. The rastered laser light scattering experimental set-up, showing the position of the laser, video detection system and the plasma tool.

vided by a single video frame is highly useful in identifying transient events that are easily missed by the human eye and photomultipliers. For example, frame-by-frame comparison can reveal the exact timing and source of particles in the plasma or on the wafer surface. The background imagery of the plasma is helpful in inferring causes and possible corrections to troublesome particle sources.

Figure 1 shows a rastered LLS set-up. Clouds of particles can be viewed by moving the raster plane along the interelectrode axis and by expanding the rastered laser beam. A photograph of a trapped cloud of particles over three silicon wafers in a sputtering plasma is shown in figure 2 [14]. Particle trapping is clearly evident. More will be said later about particle traps.

Rastered LLS requires careful optical alignment and consideration of laser power density as the expanded



Figure 2. A photograph of the rastered laser light scattering image showing trapped particle clouds over three closely packed Si wafers on a graphite electrode.

laser plane has much lower power density than an unexpanded beam. Multiple reflection from tool walls, windows and silicon wafers can cause misleading measurements. Similarly, an excessively dirty or clouded window can complicate detection. LLS typically requires two windows in opposing directions and in view of the plasma sheath boundary. Wafer clamp rings or deep wafer wells can obscure detection of particle traps. A single window has been used for both entering the laser light and scattered light detection [19]. This is most feasible for detection of metal particles as these have preferential back scattering [20]. The use of two windows on the same side of the plasma tool has been described [21]. Intense incoherent light has been used for volume particle detection [22], but it should be noted that this approach is generally less sensitive (but often more convenient and with much fewer safety concerns) than the use of coherent laser light because of the ability of lasers to deliver greater brightness with better monochromaticity and polarization purity than incoherent light sources.

The use of LLS combined with electric probe measurements provides a convincing argument for the coincidence of particles with localized plasma disturbances [15,16]. Optical emission spectroscopy may also be used to detect particle traps, as described below, and these results may be compared with particle imaging provided by LLS.

Particle sizing is usually done by angular measurement of light scattering. Clearly, this is inconvenient for plasma tools. Instead, other techniques are necessary. Light scattering intensity from particles $>0.2\mu\text{m}$ depends on the particle size, index of refraction and shape; and the wavelength and detection angle for the scattered light [17,23]. By measuring the light intensity scattered from multiple incident wavelengths at various

wavelengths, particle size may be inferred from a fixed detection orientation, provided that assumptions about particle shape and index of refraction are valid. This method is simplified by the recent commercial availability of 'white' light lasers. These continuous wave lasers operate with a Kr-Ar-He gas mixture that provides multiple, coherent wavelength emission at several discrete wavelengths throughout the visible region.

Figure 3 shows a calculation of light scattering intensity for 5° detection orientation as a function of particle size for three laser wavelengths: 488 (blue), 514 (green) and 632 nm (red). From figure 3 it is also seen that, as a particle grows in size, its apparent scattering colour will cycle between blue, green and red. This phenomenon has been observed for plasma nucleated particles [14]. However, for a particle cloud containing a distribution of particle sizes, white light scattering is observed. This limits the sizing ability of the technique. Monodisperse particle distributions are typically observed for short duration plasmas, which are prone to particle nucleation [6]. A broader particle distribution is often seen in plasmas after prolonged operation or in plasmas contaminated by wall flaking.

Dynamic light scattering, which measures the fluctuations of scattered light intensity, has also been used to determine particle size in plasmas [24,25]. This method is especially useful for measurement of particles $\leq 0.2\mu\text{m}$ in size. Results using dynamic light scattering often show a uniform particle size for very small, growing particles. This result is in agreement with TEM measurements of particles in pulsed plasmas [26]. Particle size has also been deduced from particle mass measurements. Particle mass was measured by a Doppler anemometry technique, which measures the axial velocity of particles when the plasma is briefly interrupted [6,27].

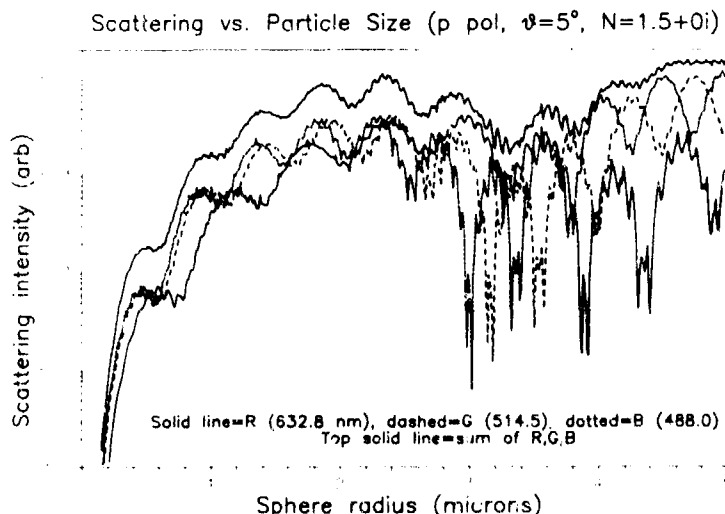


Figure 3. Calculated scattering power for three laser wavelengths (488, 514 and 632 nm) for a fixed detection angle of 10° as a function of particle size.

2.2 Influence of tool design

Using this experimental database of particle locations and behaviour has been obtained for a broad range of laboratory and manufacturing plasma tools. With this database it is seen that much commonality exists regarding the trapping and transport of particles in these tools. Differences also exist in the location and density of particles and the timing of entry of these particles into the process. These results have been discussed in detail elsewhere [19-21]; the major conclusions of some of these studies are briefly summarized below to demonstrate these commonalities and differences.

2.2.1. The single wafer plasma etching tool This planar diode etching tool showed two distinct clouds of particle trapping structures: a ring surrounding the edge of the wafer and a dome or disc above the centre of the wafer. The bottom edge of each trap also coincided with the sheath-plasma boundary and the top of the structures extended up to several millimetres into the plasma [15,16].

2.2.2. The batch wafer plasma etching tool Multiple, separated wafers showed trapping effects similar for each individual wafer [14]. Decreasing the separation between wafers on the RF electrode caused differences in the shape and intensity of the particle clouds. Nearly touching wafers caused very strong traps to form above the interstitial regions between the wafers. These traps were affected by wafer positional changes as small as 1 mm. Particles were found to accumulate first in the stronger locations, then spread out to other traps.

2.2.3. The batch wafer plasma deposition tool Ten 125 mm diameter wafers were rotated slowly on the lower, grounded electrode during the deposition process [21]. The wafers were mounted on pedestals grouped along the perimeter of the electrode. Thus, the central electrode region was shadowed from the laser beam and could not be monitored. However, in this tool, clouds of submicrometre size particles were trapped in the tubes mounting the viewports. This region acted as a particle 'cannon' by trapping particles during the process and then expelling the particles onto the wafers at the process completion. Time-resolved video measurements and wafer spot counts were used to confirm this mechanism.

2.2.4. The magnetron plasma etching tool The wafer clamp ring was found to be an important contributor to wafer contamination in this tool, due to the intense traps formed along the inside edge of the clamp ring and near the 'fingers', or clamp ring contact points [28]. Magnetron operation caused the particles to drop closer to the wafer as the sheath grew thinner. Rotation of the magnetron field similarly caused rotation of particle clouds about the interior of the clamp ring and the tool walls. Low-pressure operation (20-50 mTorr) of this tool did

not reduce particle density, evidently because the particles were formed from heterogeneous sources.

2.2.5. The magnetron sputter deposition tool This compact tool used for magnetic storage disc fabrication showed significant numbers of large particles along the inside section of the magnetron track on the negatively biased electrodes [19]. Because the tool is operated continuously, no formation of huge particles was observed. In some cases, particles could be observed simply with a powerful camera lens. The trapping, growth and eventual deposition of these huge particles may be related to the problem of wart formation in sputter targets [29].

2.2.6. The electron cyclotron resonance plasma deposition tool Use of a vertically oriented electrostatic wafer chuck in this SiH_4 - $\text{N}_2\text{O}/\text{SiO}_2$ deposition tool had little apparent bearing on the transport of particles onto the wafer. Instead, particles ejected into the plasma from the tool walls due to thermal or electrical stresses were carried about 1 m by the ion current to the wafer. These particles were buried by the deposition film [21]. Naturally, these buried particles were impossible to remove in subsequent steps. Some large particles actually bounced off the wafer. Aside from transport in the ion current, no similarity with other trapping effects was noted.

2.2.7. The electron cyclotron resonance plasma etching tool This compact ICR tool used an upward facing wafer located close to the resonance region and typically operated at pressures <10 mTorr [30]. As in the previous tool, some particles were seen moving with the ion current, but appeared to deviate around the wafer in agreement with model predictions [31]. However, the upward facing wafer was susceptible to particle deposition from the upper regions of the tool and was augmented by other particles created during the process.

2.2.8. The RF-inductive plasma tool Topographic structures designed into the RF-biased electrode of this inductive tool showed clear evidence of trapped particle clouds, even for sheaths smaller than 0.07 mm. Operation of the inductive coupling source showed little change in particle trap behaviour, with the exception of a curious striation observed in the trapped particle clouds. A silicon wafer was also found to trap particles. In addition, particles were also seen in tool view ports and along the outside edges of the RF-biased electrode.

3. Measurements of sheaths and particle traps

3.1. Nature of particle traps

As described above, experimental studies have shown that topographic and material discontinuities on the electrode and other parts of plasma tools induce disturbances in the plasma that attract or trap particles. Particle traps are three-dimensional inhomogeneities,

bounded by the plasma sheath interface on one side and the perimeter of the electrode disturbance along the horizontal dimension. The trap often projects up into the plasma in a dome or conical shape [18, 32]. Despite the repulsive force upon like charged particles, particles are confined within these localized regions. Inside the traps, particles often display collective behaviour, resembling 'Coulombic liquids' [6, 27].

Probe measurements have shown that particle traps have a higher plasma potential than the surrounding plasma regions, possibly explaining the drift of particles to these localized regions [15]. Alternatively, ion drag force, also influenced by plasma inhomogeneities, can impart momentum and cause particle transport [33, 34]. Particle traps have been identified in a wide range of etching and deposition planar diode plasma tools, as well as magnetron etching and sputtering tools and high-density inductive plasma tools. In each case, electrode topography and/or changes in surface material composition have been related to the presence of the traps.

How might the presence of topographic changes and/or material discontinuities affect the plasma and thereby affect particles? Clearly, the sheath has significant influence on particles because of the flux of ions to the electrode and the electrostatic influence it has on charged particles. Intuitively, topographic changes on the electrode must in some way alter the spatial profile of the sheath, causing localized changes in the sheath thickness. Material changes on the electrode influence secondary electron emission and thereby cause changes in the localized plasma density.

Clearly, this explanation is overly simplified. To understand how electrode topographic and material changes influence particles, it is first necessary to understand how these factors influence the sheath. Two-dimensional and perhaps even three-dimensional modelling is needed. More experimental studies are needed to test the models. Probes may be used for this analysis. However, the use of probes in and near the sheath can be tricky, especially in situations of varied sheath thickness. As indicated below, optical emission may be used to map the location and intensity of particle traps and the sheath. This has added benefit in studying chemically reactive plasmas which attack or coat probes.

3.2. Spatially resolved optical emission detection

Analysis of optical emission intensity variations provides a non-intrusive means for detection of particle traps. Optical emission intensity is a convolution of the density of ground state species and the probability of electron-induced excitation, to high electronic states. Because particle traps are, in fact, localized plasma disturbances, the rate of electron-induced excitation is also altered in these regions. Accordingly, the intensity of optical emission spectroscopy (OES) will vary spatially due to the presence of traps. This approach may be used

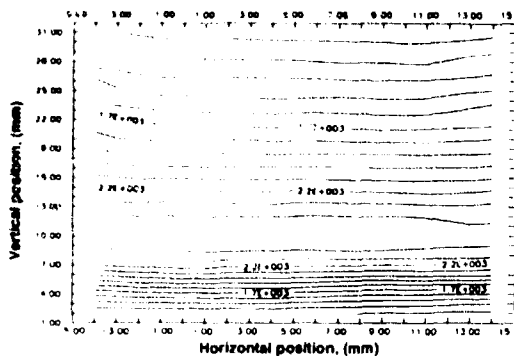


Figure 4. Optical emission spectroscopy isophotal map of Ar neutral emission signal (420.1 nm line) over a flat, uniform electrode cover.

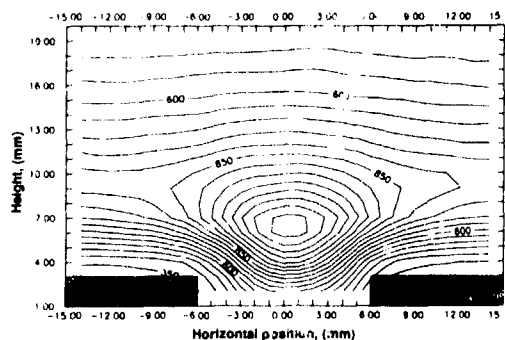


Figure 5. Optical emission spectroscopy isophotal map of Ar neutral emission signal (420.1 nm line) over a grooved electrode (type 1). The dimensions of the groove are 3 mm deep \times 12 mm wide. The groove extends the entire length of the 120 mm square electrode.

to map quantitatively the presence and intensity of particle traps and to correlate these formations with features on the tool electrode [35, 36].

The experimental apparatus for spatially resolved OES detection of particle traps is described elsewhere [35]. Briefly, a series of lenses and apertures is used to define a cylindrical volume element, aligned with a groove in the RF-biased electrode of a planar diode plasma tool. The detection volume is continuously varied as a function of time in a controlled, serpentine manner with respect to the RF electrode by moving the entire optical system and the tool. A 50 mm \times 30 mm region directly above the RF electrode is mapped using this approach. To avoid errors arising from path length differences, a square electrode is used, with good results [36].

The 420.1 nm Ar neutral emission line is monitored with spectral resolution of about 0.2 nm. The time-dependent OES signal is converted to a map of intensity of the 420.1 nm neutral Ar emission line versus horizontal and height coordinates above the electrode. This, we call an *isophotal map* because the contours denote lines of equal emission intensity in this phase space. As shown

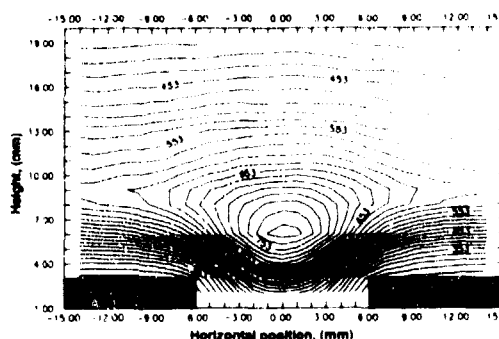


Figure 6. Optical emission spectroscopy isophotal map of Ar neutral emission signal (420.1 nm line) over a grooved electrode (type 2). The groove is of the same dimension as that of type 1 but stops 12 mm from both sides of the electrode. Results were obtained in a clean plasma, before particle injection.

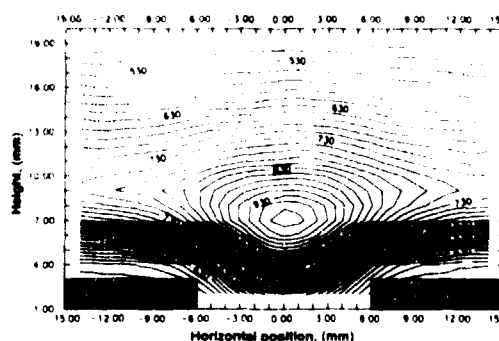


Figure 8. Optical emission spectroscopy isophotal map of Ar neutral emission signal (420.1 nm line) over a grooved electrode (type 2). The plasma was cleaned immediately after results of figure 7 by pulsing the plasma. Laser light scattering showed no particles. Note that the trap is more tightly focused, similar to that in figure 6.

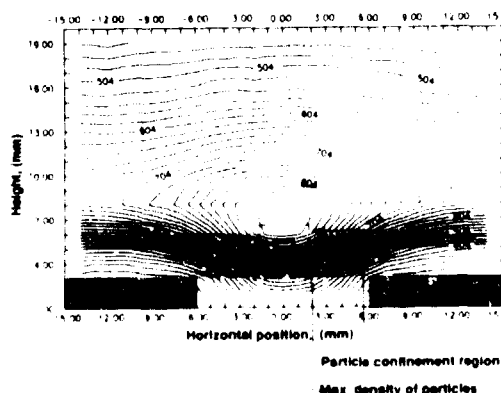


Figure 7. Optical emission spectroscopy isophotal map of Ar neutral emission signal (420.1 nm line) over a grooved electrode (type 2). This plasma was heavily contaminated by particles using an injector. The particles collected over the groove in the regions indicated by the broken line. The centre rectangle shows the greatest density of particles.

in figure 4, results obtained with a perfectly flat and uniform electrode show consistently level contours with no observed spatial variations. The sheath region is indicated by an increase in emission intensity due to the increasing, time-averaged excitation by electrons. Above the sheath, in the plasma, the emission intensity gradually decreases with height.

In contrast, figure 5 shows an isophotic map over an Al electrode with a 12 mm \times 3 mm deep groove. The length of the groove is aligned with the axis of the optical detection cylinder. As indicated by the emission contours, the sheath dips closer to the electrode directly over the groove, centred at 0 mm. A bright region is seen above the centre of the groove. The location and intensity of the bright spots were seen to vary with pressure, groove design, RF power and chemical composition of the plasma [36].

Properly designed, grooved electrodes have been shown to be an effective means of controlling particle contamination in plasma tools [37]. Particles are attracted to well-defined, localized regions in the grooves and tend to collect preferentially in or above the grooves, thereby reducing the density of particles trapped over wafers. By connecting the grooves and channelling them to the pump port, particles may be purged from the plasma.

To help correlate the position of trapped particles with the electrostatic traps quantified by spatially resolved ion mapping, a particle injector was mounted on the top flange of a GFC plasma tool [38] fitted with a grooved electrode. The particle injector consists of a Macor cylinder connected to a ferrofluidic rotary vacuum feed-through. Argon feed gas for the plasma entered upstream and above the Macor cylinder. Two stainless steel fine mesh 'brake pads' were spring-loaded to press continuously against the Macor cylinder, which was rotated using a controllable electric motor mounted outside the plasma tool. By pulsing the motor, it was possible to pulse the flux of particles entering the plasma without disturbing the gas flow or otherwise altering plasma conditions. Below the cylinder and pad assembly, a series of fine mesh screens were placed to control the size of particles entering the plasma. In this work, particles smaller than about $3\text{ }\mu\text{m}$ could pass through the screens. However, most particles were $1\text{ }\mu\text{m}$ or smaller. Two grooved electrodes were tested: one with a groove extending across the entire electrode (electrode 1, figure 5) and one with a central groove that does not extend to the edges of the square electrode (electrode 2, figures 6–8). Laser light scattering and spatially resolved optical emission maps were used to monitor results obtained with both electrodes.

Particles injected into the plasma powered by electrode 4 showered down onto the electrode. Some particles collected in the centre of the groove. These particles were grouped into a narrow line, then channel-

led across the groove and drifted out along the electrode edge into the pump port. The particles were continuously purged out of the plasma along the electrode groove. A few particles lingered momentarily in some sections of the groove where a minor surface imperfection was found; however, these particles were eventually purged out of the plasma. Results obtained with electrode 2 were dramatically different. Particles collected into a line above the groove. Over time, the density of these trapped particles increased.

Isophotic emission maps were obtained for identical plasma conditions using electrode 2 first without, then with particle injection, and again in a relatively clean plasma. In this last case, the plasma was slowly pulsed to release particles. No particles were seen by LLS after this procedure. The results are shown in figures 6-8. The location of the trapped particles in figure 7 was measured by LLS using a He-Ne laser aligned with the optical detection axis.

As indicated by the closed contours in the isophotal maps, the trap seen in figure 6 is strong and focused whereas the trap seen in figure 7, in the presence of particles, is significantly larger and displaced slightly upward into the plasma. The presence of particles has weakened this trap and dislocated its location. In figure 8, for the 'cleaned' plasma, the trap has again been focused tighter, but remains dislocated higher into the plasma. The trapped particles in figure 7 are aligned with the trap, but are lower into the sheath by a few millimetres, probably the result of other force balances such as gravity, ion drag and gas flow, which is downward in this case. It is important to recognize that the isophotal maps indicate the position and intensity of the *electrostatic* trap in the plasma resulting from the interaction of the plasma and sheath with the electrode surface, whereas the particles are localized at the point of net force balance, the spot at which electrostatic, neutral drag, ion drag and gravitational forces are equalized. The optical emission method demonstrated above is especially useful for designing grooved or self-cleaning electrodes because it provides a quantitative yet non-intrusive measurement of the strength and position of the resultant electrostatic traps in the plasma. These have significant influence on the location of trapped particles and on the capacity of the traps to confine particles.

The presence of particles appears to *weaken* and *defocus* trap formation. This may be due to localized loss of free electrons. Owing to charge balance in the plasma, negative charge from particles can only result in locally reduced electron density. This might also explain the 'leakage' of particles from densely filled traps [13]. To summarize, traps are seen (i) *without* concurrent detection of particles by LLS, (ii) over electrodes shown to purge particles continuously, (iii) in regions *other than* the regions in which particles are detected (especially in a *balance between* two traps [35]) and (iv) the intentional addition of particles to traps causes a weakening and 'defocusing' of the optically detected traps. The combination of these observations suggests that traps

can exist *without the presence of particles*.

What might be the significance of particle traps without particles? Traps are a consequence of plasma inhomogeneity, caused by localized changes in electron density or temperature. In high-density tools, traps may also be caused by source non-uniformities. Ions must also respond to these disturbances. Process uniformity effects may be expected in regions near particle traps due to this influence [16]. In some cases traps may reduce process uniformity, but traps may also improve uniformity by compensating for chemical nonuniformities. It is also interesting to note that plasma uniformity problems often accompany plasma contamination problems. However, contamination is sporadic in nature, due to variations in particle sources, whereas the uniformity problems are consistent. Clearly, this is a fertile area for future study and modelling.

4. Conclusions

Particles are readily observed in plasma processes using laser and incoherent light scattering. Typically, the particle density observed in plasma tools far exceeds the clean room background and is often the single major contributor to wafer contamination in manufacturing processes.

Particles in plasma processes behave differently from those in other vacuum processes because of the ionized ambient of plasmas. Particles acquire negative charge and are attracted to, or pushed towards localized *traps*. The exact physical location of particles is determined by the force balance point between the electrostatic trap delineated in this study and other vector forces acting upon particles: ion drag, gravity, neutral drag and thermophoresis. Particle traps of different forms and locations have been observed in a wide range of plasma tools. Material and/or topographic discontinuities on the electrode coincide with the location of particle traps. One reason for this is the influence electrode topographic and material discontinuities have on the sheath structure and profile. Recent two-dimensional models have successfully predicted the location of particle traps.

Spatially resolved optical emission spectroscopy may be used to map the location and intensity of particle traps. This is possible because optical emission intensity is sensitive to the density and temperature of electrons. Maps of emission intensity show a close coincidence of bright spots and location of trapped particles. Using this technique, LLS and measurements for various grooved electrodes, it is shown that particle traps are an inherent aspect of plasma processing. Traps may be formed in the absence of particles, but are changed by the accumulation of particles. Finally, it is suggested that particle traps also influence etching, deposition or sputter uniformity. This may result from changes in ion bombardment below a trap. However, in some cases, this may compensate for chemical non-uniformities, which also influence process uniformity.

Acknowledgments

I thank M Dalvie, M Surendra, H Grabarz, W H Holber, J E Heidenreich, J McGill and C R Guarnieri of IBM Yorktown Heights, E F Patterson of IBM, E Fishkill and K L Haller of IBM Burlington, M Blain and G Tipton of Sandia National Laboratories and R Carlile and J O'Hanlon of the University of Arizona for their help in various portions of this work.

References

- [1] Selwyn G S, Singh J and Bennett R S 1989 *J. Vac. Sci. Technol.* **A7** 2758
- [2] Braithwaite N and Graham B 1993 *New Scientist* **140** November 27, 34
- [3] Bouchoule A 1993 *Phys. World* **6** August 47
- [4] Selwyn G S 1993 *Semicond. Int.* **16** March 72
- [5] Spears K, Robinson T J and Roth R M 1986 *IEEE Trans. Plasma Sci.* **14** 179
- [6] Bouchoule A, Plain A, Boufendi L, Blondeau J P and Laure C 1991 *J. Appl. Phys.* **70** 1991
- [7] Jellum G M and Graves D B 1990 *J. Appl. Phys.* **67** 6490
- [8] Selwyn G S, McKillop J S, Haller K L and Wu J J 1990 *J. Vac. Sci. Technol.* **A8** 1726
- [9] Logan J S and McGill J J 1992 *J. Vac. Sci. Technol.* **A10** 1875
- [10] McCaughey M J and Kushner M J 1989 *Appl. Phys. Lett.* **55** 951
- [11] Nowlin R N and Carlile R N 1990 *J. Vac. Sci. Technol.* **A9** 2824
- [12] Belenguer P, Blondeau J P, Boufendi L, Toogood M, Plain A, Bouchoule A, Laure C and Boeuf J P 1992 *Phys. Rev.* **A46** 7923
- [13] Selwyn G S 1991 *J. Vac. Sci. Technol.* **B9** 3487
- [14] Selwyn G S, Haller K L and Heidenreich J E 1991 *J. Vac. Sci. Technol.* **A9** 2817
- [15] Carlile R N, Geha S G, O'Hanlon J F and Stewart J C 1991 *Appl. Phys. Lett.* **67** 1167
- [16] Geha S G, Carlile R N, O'Hanlon J F and Selwyn G S 1992 *J. Appl. Phys.* **72** 374
- [17] Bohren C F and Huffman D R 1983 *Absorption and Scattering of Light by Small Particles* (New York: Wiley)
- [18] Selwyn G S, Haller K L and Heidenreich J E 1990 *Appl. Phys. Lett.* **57** 1876
- [19] Selwyn G S 1993 *Japan. J. Appl. Phys.* **32** 21
- [20] Asano S and Yamamoto G 1975 *Appl. Opt.* **14** 29
- [21] Selwyn G S, Haller K L and Patterson E F 1992 *Proc. 9th Symp. Plasma Proc.* ed G S Mathad and D W Hess (Pennington, New Jersey: Electrochemical Society) p 236
- [22] Howling A A, Hollenstein C and Pais P J 1991 *Appl. Phys. Lett.* **59** 1409
- [23] Bayvel L P and Jones A R 1981 *Electromagnetic Scattering and its Applications* (Englewood, New Jersey: Applied Science) pp 16–54
- [24] Spears K G, Kampf R P and Robinson T J 1988 *J. Phys. Chem.* **92** 5297
- [25] Hurd A J and Ho P 1989 *Phys. Rev. Lett.* **62** 3034
- [26] Boufendi L, Plain A, Blondeau J P, Bouchoule A, Laure C and Toogood M 1992 *Appl. Phys. Lett.* **68** 169
- [27] Boufendi L, Bouchoule A, Porteous R K, Blondeau J P, Plain A and Laure C 1993 *J. Appl. Phys.* **73** 2160
- [28] Selwyn G S, Haller K L and Patterson E F 1993 *J. Vac. Sci. Technol.* **A11** 1132
- [29] Chen C W, Makowiecki D M, Alford C S, McKernan M A and Ramsey P B 1990 *J. Vac. Sci. Technol.* **A8** 3157
- [30] Blain M G, Tipton G D, Westerfield P L, Holber W B, Selwyn G S and Maxwell K L 1994 *Plasma Sources Sci. Technol.* **3** 325–33
- [31] Kilgore M D, Daugherty J E, Porteous R K and Graves D B 1994 *J. Vac. Sci. Technol.* **B12** 486
- [32] Durham J 1989 *Masters Thesis Rensselaer Polytechnic Institute, Troy, New York*
- [33] Sommerer T J, Barnes M S, Keller J H, McCaughey M J and Kushner M J 1991 *Appl. Phys. Lett.* **59** 638
- [34] Barnes M S, Keller J H, Forster J C, O'Neill J and Coultas D K 1992 *Phys. Rev. Lett.* **68** 313
- [35] Dalvie M, Surendra M, Selwyn G S and Guarnieri C R 1994 *Plasma Sources Sci. Technol.* **3** 442–7
- [36] Dalvie M, Selwyn G S, Surendra M, Guarnieri C R and McGill J J 1993 *Appl. Phys. Lett.* **63** 3279
- [37] Selwyn G S and Patterson E F 1992 *J. Vac. Sci. Technol.* **A10** 1053
- [38] Hargis P J Jr, et al 1994 *Rev. Sci. Instrum.* **65** 140

Effects of plasma processing on the microstructural properties of silicon powders

E Bertran, J Costa, G Sardin, J Campmany, J L Andújar and A Canillas

Departament de Física Aplicada i Electrònica, Universitat de Barcelona,
Av. Diagonal 647, E08028 Barcelona, Spain

Received 7 January 1994, in final form 14 January 1994

Abstract. The effects of plasma processing conditions on the microstructural properties of silicon powders are presented. Hydrogenated nanophase silicon powders were prepared using low-pressure and low-temperature square wave modulated RF plasma (13.56 MHz) using pure silane gas. Plasma parameters such as pressure, RF power, plasma modulation frequency, and gas flow rate were varied. *In situ* analysis by quadrupole mass spectroscopy and *ex situ* analysis of the silicon powders by Fourier transform infrared spectroscopy (FTIR) and thermal desorption spectrometry of hydrogen were performed. The thermal desorption spectrometry results show the fundamental differences between the concentrations of hydrogen weakly and strongly bonded in silicon powders as compared to amorphous silicon films. The FTIR analysis also determined the microstructural characteristics of powders and hence their volume surface ratio. This parameter was determined from the balance of P probabilities of having one of the H , Si , Si_2 bond arrangements in the powder particles. These results reveal an increase in hydrogen content and a reduction in volume surface ratio as the modulation frequency of RF power increases. In consequence, higher compactness of silicon powders is associated with long particle residence times inside the plasma as a result of ion bombardment. TEM analysis indicated a considerable dispersion of particle size and some degree of structure of the silicon powder characterized by intergrain linkage. We point out the dominant presence of hydrogen on the particle surfaces (external voids), which may cause the high reactivity of grains, increasing the degree of intergrain linkage.

1. Introduction

The generation of powder in plasmas is interesting due to its involvement as a contaminant in surface processes, e.g. plasma etching, and in deposition processes such as reactive sputtering, chemical vapour deposition (CVD) and other techniques [1-5]. The contamination from particles originating in the plasma itself is an important limitation to enlarging the scale of integration in microelectronics and a handicap for the microelectronic industry (production of photovoltaic cells, displays, flat panels, large area detectors and sensors, etc).

Silicon powder formation in silane plasma enhanced chemical vapour deposition (PECVD) processes is also interesting because of its possible use as a raw material for new ceramics, for nanoscale filters or as a support of catalytic surfaces.

Special characteristics associated with powder prepared by PECVD are nanometric size, the high purity (electronic grade), which results in an increase in both

structural and compositional homogeneity, the possibility of preparing alloys by mixing precursor gases, the chemical reactivity that depends on the degree of compactness and the surface hydrogen coverage. The possibility of controlling the size, the compactness and the morphological characteristics of powder produced by low-pressure and low-temperature plasmas mainly depends on the process conditions: pressure, gas flow rate, temperature, power density, and modulation frequency of the excitation power.

Other more fundamental characteristics of the powder, such as hydrogen content, $Si-H$ bond distribution, oxygen reactivity and microstructure have not yet been studied in detail, although these may also be expected to have considerable dependence on the process parameters: preparation and annealing.

Previous reports dealing with the influence of the technological parameters on both film structure and powder formation dynamics [6-10] reveal the square wave modulation (SQWM) of the RF power to be an easy way to control powder formation and film microstruc-

ture. The increase of the microstructure when the SQWM frequency decreases is due to the incorporation into the growing film of large particles coming from the plasma, the size of which depends on the SQWM time period [6]. These negatively charged particles are electrostatically confined by the plasma sheath during the 'plasma on' periods and deposit or leave the plasma chamber as soon as the sheath disappears [6, 9–11]. An analysis of the evolution of discharge electrical properties, powder volumetric density and size distribution [2], and the effects of different initial discharge parameters, shows that powder formation takes place in successive phases after plasma ignition [12]. An initial phase ($\Delta t \approx$ milliseconds) of generation of radicals and ions during which electron attachment occurs on the SiH_4 radicals [9] is followed by other phases characterized by the growth of negative ions limited by a gas residence time (Δt of several seconds, depending on the experimental conditions). Experiments of SQWM RF plasma, at suitably low frequencies depending on the plasma conditions, allow control of the degree of polymerization of powders measured by *ex situ* characterization. This can also be performed by controlling the residence time of powders inside the plasma through the gas flow rate [13].

This paper is focused on the microstructural characterization of silicon powder obtained from SQWM plasma silane processes. In particular, we study the dependence of the silicon powder microstructure firstly on the silane flow rate (experiment A) and secondly on the SQWM frequency (experiment B). The silicon powder was analysed by Fourier transform infrared spectroscopy (FTIR), thermal desorption spectrometry of hydrogen (TDS), and transmission electron microscopy (TEM).

2. Experimental procedure

Amorphous silicon thin films and silicon powder were obtained by plasma enhanced chemical vapour deposition (PECVD) of SiH_4 in a capacitively coupled RF reactor [14]. The reaction chamber had a rectangular parallel-epipedic shape, which enabled a vertical laminar flow to be piped between the RF electrode and the grounded plate. Figure 1 is a schematic diagram of the plasma confinement chamber. The RF electrode was connected to a RF power generator by an automatic matching network, which guaranteed maximum transmitted RF power to the plasma. The RF power generator could be modulated by a square-wave signal with different frequencies and periods of duty cycle.

Experiment A studied gas flow rate effects. Silicon powder was synthesised inside the reactor at 30 °C, and the silane flow rate was varied from 5 to 90 sccm at 0.1 Hz modulation frequency of RF power. The other plasma conditions for these experiments were kept constant: 65 Pa pressure, and 200 mW cm^{-2} RF power density.

Experiment B studied SQWM frequency effects. In this experiment the silane plasma was modulated at frequencies ranging from 0.05 to 100 Hz, using a 50% duty cycle

of SQWM RF power at 15 sccm SiH_4 gas flow rate. As in experiment A, the other plasma conditions for these experiments were kept constant: 30 °C temperature, 65 Pa pressure, and 200 mW cm^{-2} RF power density.

The total time for discharge processes (considering only the plasma on periods) was 15 min. Powder samples were collected using glass slides placed horizontally on the reactor chamber.

The reactor chamber was provided with a quadrupole mass spectrometer (QMS) (Hiden HAL PMS300) to identify the neutral and ionized species of the plasma from 0 to 300 amu. The micrographs obtained by TEM provide an estimate of particle size of the silicon powder [13]. To perform the thermal desorption spectrometry (TDS) of hydrogen we used an experimental set-up [15] composed of a vacuum chamber (10^{-6} hPa pressure), a mass spectrometer to quantify the desorbed hydrogen flow, and a furnace with a thermocouple monitored by a computer generating a linear temperature ramp of 20 °C min^{-1} in a temperature range from room temperature to 1000 °C. The infrared spectroscopic analysis of powders was carried out by a fast Fourier infrared spectrophotometer Nicolet 5ZDX FTIR, which provides the characteristic absorption peaks corresponding to the different bands present in the silicon powder.

3. Results and discussion

In recent years we have studied the effect of pressure on amorphous silicon thin films [16], and have seen that their compactness (related to the maximum of the imaginary part of the effective dielectric function $\epsilon_{2\text{max}}$, determined by ellipsometry) [17] decreases as pressure increases, as shown in figure 2. We also studied the effects of RF power on the compactness of a-Si:H thin films [18] and observed an increase in porosity with RF power. This effect is more significant at very low SQWM frequencies, as shown in figure 3. Furthermore, the highly porous material deposited at high RF power and high pressure, in the PECVD range, becomes silicon powder when we perform the deposition process at room temperature.

Figures 4(a) and 4(b) show an example of the mass spectra corresponding to neutral and positive ions from a pure silane RF plasma. In order to optimize the detection, the conditions of the plasma were set to 80 W RF power modulated by a square signal of 1000 Hz frequency and 50% duty cycle, 10 Pa total pressure, 15 sccm pure silane flow rate and room temperature. The neutral fragmentation spectrum (figure 4(a)) shows the peaks corresponding to silane, disilane and trisilane present in the plasma. Figure 4(b) shows the positive ion spectrum characterized by the presence of Si_nH_m^+ ions, from monosilane to hexasilane ($n = 1$ to 6). The other mass signals located between silane peaks are probably due to the presence of hydrocarbon contaminants and other minor species, the heights of which are always lower than 1% of main peaks.

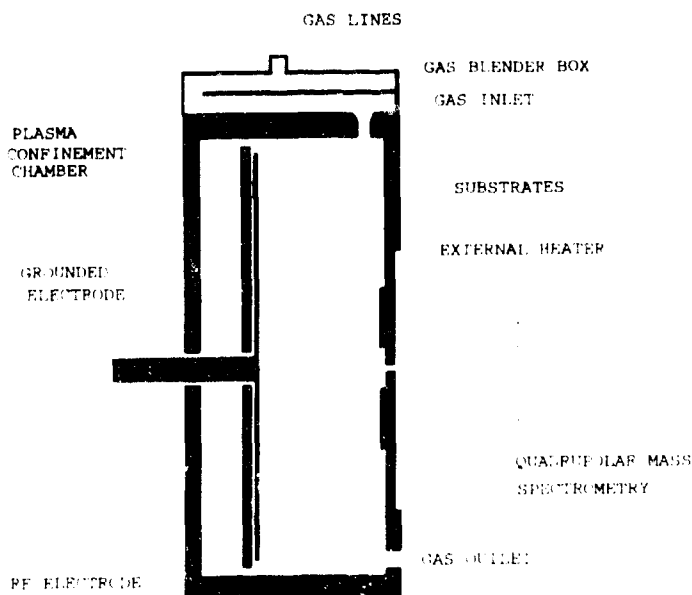


Figure 1. Schematic diagram of the plasma confinement chamber, which has a parallel-epipedic geometry. The mass spectrometer head that analyses the species present in the plasma is also shown.

TDS results for both experiments A and B show fundamental differences between a-Si:H films [15] and powders: in a-Si:H films the strongly bonded hydrogen is dominant and the main peak is at 600 °C, whereas in a-Si:H powders the maximum desorption is centred at 290–330 °C, indicating that the weakly bonded hydrogen prevails against the strongly bonded hydrogen.

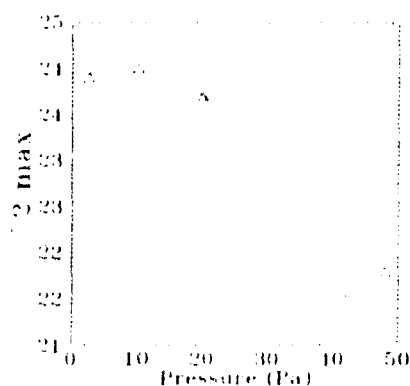


Figure 2. Dependence on gas pressure of the maximum of the effective dielectric function (determined by ellipsometry) of a-Si:H thin films deposited from silane plasma. The deposition conditions were: 20 W RF power, 300 °C substrate temperature, 30 sccm silane flow rate.

Another cause of this predominance could be that the hydrogen diffusion process delaying hydrogen effusion in films is practically insignificant in Si powders due to their larger surface bulk ratio. We proposed a value of 30% hydrogen content, corresponding to films with very high hydrogen content, as the low limit for total hydrogen content (bonded and molecular hydrogen) for hydrogenated silicon powders [19]. In figure 5 we show the normalized hydrogen TDS results for several samples of silicon powders prepared at sqwm frequencies in the range 0.05 to 40 Hz. We attribute the weak dependence of TDS characteristics on sqwm frequency to the insignificant variation of diffusion of hydrogen between different powders, as compared to that of films, and furthermore, to the similar wide particle size distribution, from 10 to 200 nm, that powder shows at different process conditions [13]. This is shown by TEM micrographs, from which two predominant size distributions appeared (the smaller one about 30 nm in diameter and the larger between 80 and 150 nm) irrespective of the process parameters.

We performed the measurements of particle size by evaluating the diameter of the largest and the smallest particle in every micrograph. In figure 6 we show the diameter of the smallest particles against flow rate. In spite of the dispersion of the measurements, particle size increases linearly with gas flow rate. In contrast, the size of the largest particles (80 nm to 150 nm) appears to be independent of the gas flow rate except for the lowest gas flow rate, at which the larger powder particles are practically non-existent.

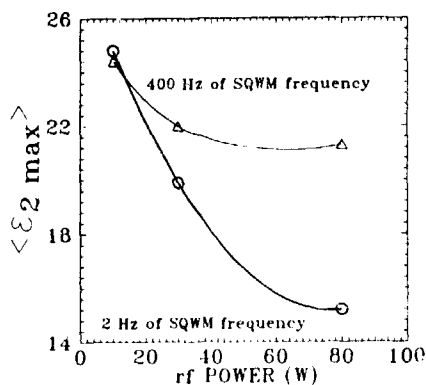


Figure 3. RF power effects on $\varepsilon_{2 \text{ max}}$ for a-Si:H thin films deposited from silane plasma at a substrate temperature of 300 °C, at two sqwm frequencies (2 Hz and 400 Hz) and using a duty cycle of 75%. The silane flow rate and the pressure were kept at 30 sccm and at 30 Pa respectively.

Figure 6 also shows the continuous decrease in the density of powder particles when the gas flow rate increases. This phenomenon may be attributed either to the reduction of powder particle yield as a consequence of the decrease in residence time of the particles inside the plasma, or to an increase in the dragging effect of the flowing gas which reduces the number of powder particles deposited on the TEM grid.

We studied the microstructure of silicon powders using FTIR spectroscopy on two series obtained at different gas flow rates and at different sqwm frequencies (experiments A and B). In outline, IR spectra revealed extensive hydrogenation of the silicon powder and the dominant absorption corresponding to hydrogen bonded to polymeric chains or to silicon on the particle surface [20].

We focused the analysis on the evolution of the stretching IR absorption band (2000–2150 cm^{-1}). We divided this band into three Gaussian peaks corresponding to the following. (i) SiH bonds inside the bulk of the

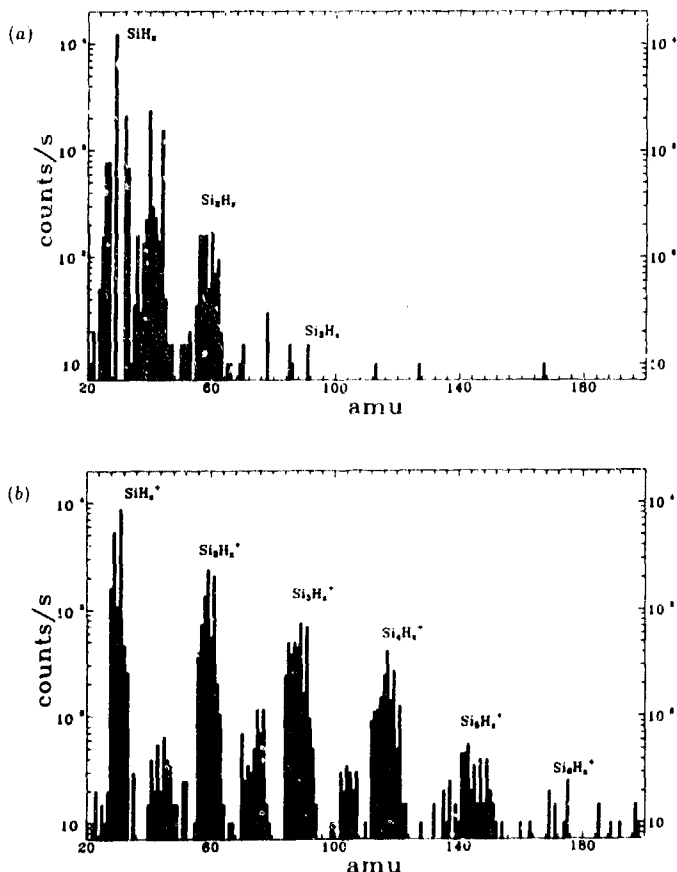


Figure 4. Fragmentation OMS spectra of (a) neutrals and (b) ions of a pure silane RF plasma. The conditions of the process were: 80 W RF power modulated by a 1000 Hz sqwm frequency at 50% duty cycle, 10 Pa total pressure, 15 sccm pure silane flow rate, and room temperature.

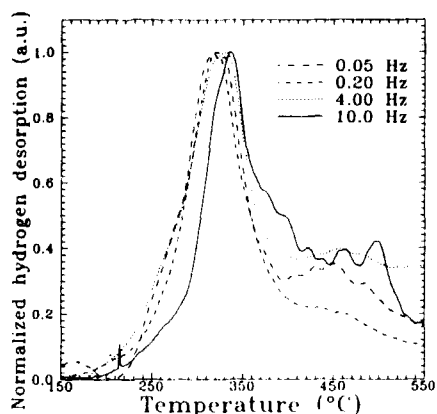


Figure 5. Normalized hydrogen thermal desorption spectra corresponding to silicon powders grown at different sqwm frequencies. The deposition conditions were 50% duty cycle, 15 sccm silane flow rate, 65 Pa pressure and 80 W RF power.

particle (located between 2020 and 2060 cm^{-1}). The variation of peak position is due to the different density of the material surrounding the SiH bond, which produces a shift from 2000 cm^{-1} for a-Si:H films to 2186 cm^{-1} for a pure silane gas [21]. (ii) Absorption of SiH bonds on the particle surface, SiH_2 , and $(\text{SiH}_2)_n$ (at 2090–2100 cm^{-1}). (iii) The peak generally attributed to the SiH_3 group (centred at 2140 cm^{-1}). The Gaussian areas, A_1 , A_2 and A_3 respectively, were normalized to the total area of the stretching band.

For experiment A, figure 7 displays the relative concentration of the three different stretching contributions to the absorption against the residence time in the range from 1 to 15 s. When the residence time increases, the 2030 cm^{-1} peak is enhanced while 2090 and 2140 cm^{-1} peaks decrease.

For experiment B, figure 8 shows the relative concen-

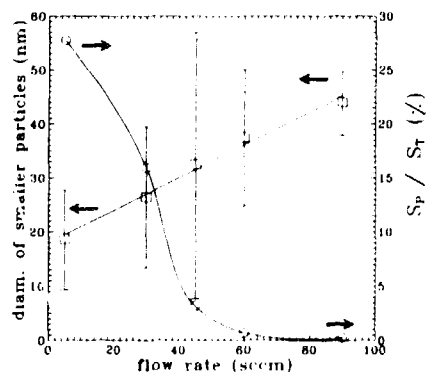


Figure 6. Effect of the gas flow rate on the particle diameters and their dispersion: corresponding to the population of the smallest particles determined by TEM analysis. Dependence of the ratio between the surface covered by powder (S_p) and the total micrograph surface (S_t) against gas flow rate.

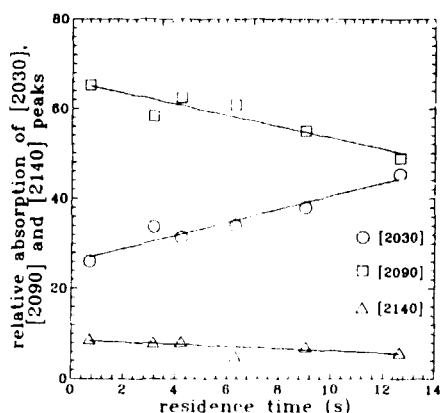


Figure 7. Relative absorption of [2030], [2090] and [2140] peaks, corresponding to Si-H stretching modes, against the residence time.

tration of the SiH, SiH_2 and SiH_3 bonds against the sqwm time period T_{sqwm} in the range from 1.0 to 20.0 s. The evolution of the three contributions has a strong correlation to those shown in figure 7. This result confirms that the main effect of sqwm for low frequencies is due to the control on the residence time (the sqwm semi-period $T_{\text{sqwm}}/2$ determines the time the particles are confined within the 'plasma on' events).

Therefore, the effect on the microstructural characteristics of power square wave modulation at low frequencies comes from the control of residence time. This microstructural dependence denotes that short residence times cause highly polymeric powders, with a rich microstructure, while with longer residence times the particles become more compact. This phenomenon suggests the following growth mechanism of siliceous powder inside the plasma: initially, small particles appear as a

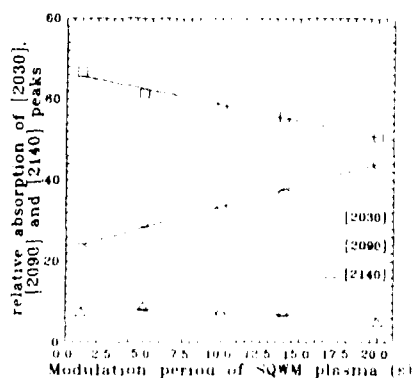


Figure 8. Representation of the relative concentration of different Si-H bonds, calculated from the IR absorption band, and corresponding to the stretching vibration modes, against the RF power sqwm period T_{sqwm} for silicon powder.

consequence of polymerization; as the residence time of the particles inside the plasma increases, crosslinking between polymeric chains is favoured and consequently the powder particles become more compact.

In order to obtain further microstructural information of FTIR spectra, a random bonding theory [22] was used to model the silicon-hydrogen bonding arrangement (Si_4 , H-Si_3 , $\text{H}_2\text{-Si}_2$, $\text{H}_3\text{-Si}$) statistics. If s is the probability of a Si atom filling one of the four available Si sites, and h the same probability for a H atom, the probability of the four sites being occupied by either H or Si atoms is:

$$P = (s + h)^4 \quad (1)$$

which must equal one by definition, because $h = 1 - s$ (assuming a small number of dangling bonds). This probability function is affected by the fact that the possibility of hydrogen occupying the four possible sites cannot be considered. Then, developing:

$$P(s, h) = s^4 + 4s^3h + 6s^2h^2 + 4sh^3 + P_0 + P_1 + P_2 + P_3 = 1 \quad (2)$$

where P_j is the probability of the $\text{H}_j\text{-Si}_{4-j}$ bond arrangements, and $P(s, h) = 1$. We can express these terms as a function of the hydrogen percentage of the sample C_H defined by:

$$h = C_H(h + s) \quad (3)$$

If the absorptions of SiH , SiH_2 , and SiH_3 were directly assigned to the absorption areas A_1 , A_2 , A_3 defined above, one might have expected these A_j to be proportional to the values $P_j^* = P_j(1 - P_0)$. However, from equation (2), the maximum value corresponding to $P_2(1 - P_0)$ is 0.4, and the corresponding area A_2 in all experimental cases is 0.6. This confirms the existence of an additional absorption in the peak centred at 2100 cm^{-1} , attributed to Si-H_2 owing to other oscillators such as Si-H oscillators [23-25] localized on the surface. We have considered that a fraction α of Si-H oscillators contributes to the 2100 cm^{-1} peak. Under these considerations, the application of the above statistical model to the series of samples obtained at different SQWM frequencies leads to the determination of the dependences of α and $C_H = [\text{H}] / ([\text{Si}] + [\text{H}])$ shown in figure 9.

One of the most important structural characteristics of powders could be expressed through the volume-surface ratio, which can be estimated from the balance of P_j probabilities and the α factor. If we consider the addition $P_1 + P_2 + \alpha P_3$ corresponding to Si-H_1 , Si-H_2 and Si-H bonds localized on the surface, and the addition $P_0 + (1 - \alpha)P_3$ associated with volume, the resulting volume-surface ratio diminishes with increasing SQWM frequency, which corroborates previous results of major compactness of silicon powders associated with long residential times as a consequence of plasma ion bombardment [13].

Finally, TEM micrographs show some degree of structure of the silicon powder characterized by intergranular

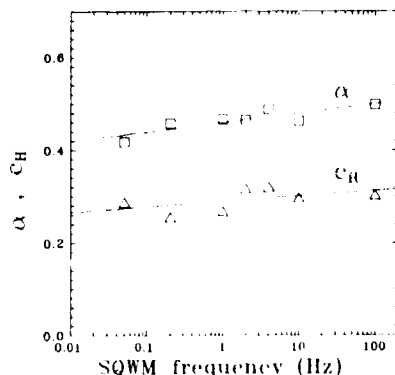


Figure 9. Dependences of hydrogen content C_H and α factor determined by FTIR analysis against SQWM frequency.

linkage. We have pointed out the dominant presence of hydrogen on the grain surfaces (external and voids). This circumstance emphasises the probable high reactivity of the grain surface, and hence the degree of inter-grain linkage.

4. Conclusions

Hydrogenated silicon powder has been obtained by means of square-wave modulated RF pure silane plasma. qms analysis of SQWM plasma (1000 Hz) of silane reveals the dominant presence of SiH^+ and SiH_2^+ and the existence of polysilane positive ions Si_nH_n^+ up to $n = 5$ ($Q = 0.001$). TEM analysis of the microstructure of the powder indicates a dispersion of particle size characterized by two different populations of particles (80-150 nm and 10-50 nm particle size), showing dependence on the silane flow rate and hence, on the residence time. The results of thermal desorption spectrometry of hydrogen show the fundamental differences between the concentrations of hydrogen weakly and strongly bonded in silicon powders as compared to amorphous silicon films, demonstrating the insignificant hydrogen diffusion process as compared with the surface hydrogen desorption process on silicon powders (due to a larger surface volume ratio). The infrared absorption peaks have been identified, indicating the polymeric character of the powder and its large hydrogenation. FTIR analysis also shows the microstructural characteristics of powders through their surface-volume ratio. The application of a random bonding model to the IR results agrees with the interpretation of the additional contribution of SiH bonds to the absorption peak centered at $2090-2100\text{ cm}^{-1}$. This model allows us to define a factor α directly related to the volume-surface ratio. Finally, the results of studying the influence of the residence time of particles inside the plasma (through both flow rate and plasma modulation) on the microstructure of the silicon powder suggest its growth mechanism, which consists of a polymeric step and a later compaction due to ion bombardment inside the plasma.

Acknowledgments

This work was partially supported by the CEC BRITE-EURAM program, under contract no. BREU-CT91 0411 (DSCN).

References

- [1] Howling, A A, Hollenstein Ch and Paris P J 1991 *Appl. Phys. Lett.* **59** 1409
- [2] Boufendi L, Plain A, Blondeau J P, Bouchoule A, Laure C and Toogood M 1991 *Appl. Phys. Lett.* **60** 169
- [3] Watanabe Y, Shiratani M, Makino H 1990 *Appl. Phys. Lett.* **57** 1616
- [4] Watanabe Y, Shiratani M and Yamashita M 1992 *Appl. Phys. Lett.* **61** 1510
- [5] Jellum J M, Daughert J E and Graves D B 1991 *J. Appl. Phys.* **69** 6925
- [6] *Proc. 39th National Symp. of the American Vacuum Society* 1993 *J. Vac. Sci. Technol. A* **11** 1119-41, 1258-67
- [7] Lloret A, Bertran E, Andújar J L, Canillas A and Morenza J L 1991 *J. Appl. Phys.* **69** 632
- [8] Andújar J L, Bertran E, Canillas A, Campmany J, Serra J, Roch C and Lloret A 1991 *J. Appl. Phys.* **71** 1546
- [9] Watanabe Y, Shiratani M, Kubo Y, Ogawa I and Ogi S 1988 *Appl. Phys. Lett.* **53** 1263
- [10] Verdeyen J T, Beberman J and Overzet L J 1990 *J. Vac. Sci. Technol. A* **8** 1851
- [11] Howling A A, Sansonnens L, Dorier J-L and Hollenstein Ch 1993 *J. Phys. D: Appl. Phys.* **26** 1003
- [12] Overzet L J, Beberman J H and Verdeyen T J 1989 *J. Appl. Phys.* **66** 1622
- [13] Perrin J 1993 Private communication
- [14] Costa J, Sardin G, Campmany J, Andújar J L, Canillas A and Bertran E 1993 *MRS Symp. Proc.* **286** 155
- [15] Andújar J L, Bertran E, Canillas A, Esteve J, Andreu J and Morenza J L 1989 *Vacuum* **39** 795
- [16] Sardin G, Kasaneva J, Bertran E, Andújar J L, Roch C, Andreu J, Morenza J L 1989 *9th EC Photovoltaic Solar Energy Conf.* 1021
- [17] Andújar J L, Bertran E, Canillas A, Roch C and Morenza J L 1991 *J. Vac. Sci. Technol. A* **9** 2216
- [18] Aspnes D E 1982 *Thin Solid Films* **89** 249
- [19] Andújar J L 1990 *PhD Thesis* Barcelona University
- [20] Costa J, Sardin G, Campmany J and Bertran E 1994 *Vacuum* at press
- [21] Costa J, Sardin G, Campmany J, Andújar J L, Canillas A and Bertran E 1993 *MRS Symp. Proc.* **297** 1031
- [22] Hadni A 1967 *Essentials of Modern Physics Applied to the Study of the Infrared* (New York: Pergamon)
- [23] Tsu D V, Lucovsky G and Davidson B N 1989 *Phys. Rev. B* **40** 1795
- [24] Paul W 1980 *Solid State Commun.* **34** 283
- [25] Wagner H and Beyer W 1983 *Solid State Commun.* **48** 585
- [26] Lucovsky G 1985 *J. Non-Cryst. Solids* **76** 173

Effects of particles on He-SiH₄ modulated RF discharges

Yukio Watanabe, Masaharu Shiratani, Tsuyoshi Fukuzawa and Hiroharu Kawasaki

Department of Electrical Engineering, Faculty of Engineering, Kyushu University, Hakozaki, Fukuoka 812, Japan

Received 10 January 1994, in final form 31 January 1994

Abstract. The effects of particles on helium-diluted silane RF discharge are studied using a power modulation method for various values of relevant parameters. Compared with cw discharge cases, close correlation is clearly found between the particle growth, the self-bias voltage and the phase shift between the current and voltage of the RF discharge. Total particle number and optical emission intensity in the bulk plasma region increase monotonically after RF power-on. With these increases, the magnitude of self-bias voltage and the current-voltage phase shift decrease considerably to their minimum values and then slightly increase to their quasi-steady values. The decreases can be explained by the fact that particles in plasmas behave as very heavy negative ions. The increases may be related to the increase in the diffusion rate of electrons. It is also confirmed through this study that the modulation is very effective in the suppression of particle growth. In particular, for a duty cycle of 20%, the discharge parameters are close to those for a pure He discharge. This tendency is consistent with the result that no particles can be observed for this duty cycle.

1. Introduction

Recently, there has been intense interest in plasmas which contain particles. Particles in a size range from nanometers to micrometers become electrically charged in plasmas and may alter discharge properties. Up to now, some studies have been carried out concerning the effects of particles on the discharge properties. Jellum *et al* [1] have shown, using steady state CW RF discharges, that for a constant RF power discharge with particles, the current, the voltage and their phase shift decrease, and the optical emission intensity increases. These discharge properties are similar to those associated with discharges in electronegative gases. Bouchoule *et al* and Howling *et al* [2, 3] have measured time evolutions of current-voltage phase shift and reflected power in RF discharges and have shown that the presence of particles makes a discharge impedance more resistive. In their cases, the change in such impedances arises before particles begin to be observed by light scattering methods, and hence the latter group suggests that the change is due to invisibly small particles. Boeuf and Belenguer and Belenguer *et al* [4, 5] have analysed a transition from a capacitive to a resistive regime in an RF discharge using self-consistent fluid and particle-in-cell simulation models and have suggested a possible relation between the transition and particle formation.

We have studied the growth kinetics and behaviour of particles in power-modulated RF silane (SiH₄) discharges

using two kinds of laser light scattering (LLS), a Langmuir probe, an emissive probe and an absorption method [6–14]. Such studies have revealed many features, including that the modulation brings about a drastic decrease in the particle amount. This drastic decrease is expected to lead to discharge properties similar to those associated with pristine discharges of electropositive gases.

Despite previous studies, the relationships between the particle growth and the discharge parameters have not been fully understood. To understand these better, the relationships between particle growth and both the self-bias voltage and the current-voltage phase shift in the RF discharges must be investigated for various values of parameters such as pressure (SiH₄ concentration), RF power and duty cycle of the modulation. In this paper, we present these experimental results, and based on these, mechanisms by which particles affect the discharge parameters are discussed.

2. Experimental

The experiments were performed in a conventional parallel plate reactor [9]. Plane electrodes of 10 cm diameter were placed at a separation of 4.3 cm. The particle growth was observed using the LLS method, which gives the time evolution of a two-dimensional LLS intensity profile described in detail elsewhere [9].

Optical emission profiles were detected using an image intensified CCD camera equipped with an interference filter. The RF voltage and current were measured using a high voltage probe (Tektronix P6015) and an AC current probe (Iwatsu CP-502) respectively. Their phase shift θ is defined by $\cos \theta = 2\langle P \rangle / V_{\text{RF}} I_{\text{RF}}$, where $\langle P \rangle$, V_{RF} and I_{RF} are the averaged power dissipated and amplitudes of the voltage and current respectively. In these experiments, an RF power of 20–40 W was applied during an RF power-on period $T_{\text{on}} = 4$ s at intervals of an RF power-off period $T_{\text{off}} > 60$ s. The gas used was 0–5% SiH_4 diluted with He.

3. Results

Since the electric field is closely correlated with the behaviour of negatively charged particles in an RF discharge containing particles, the spatial profile of the number of particles should be greatly affected by the self-bias voltage and vice versa. From this viewpoint, the magnitude of self-bias voltage V_{DC} in a quasi-steady state was measured for various SiH_4 concentrations. With increasing the concentration from 0 to 5%, V_{DC} decreased from 110 to 25 V for an RF power of 20 W (not shown here). These results suggest that V_{DC} changes with time after RF power-on in power-modulated RF SiH_4 discharges for which the particle amount evolves considerably with time.

To confirm this suggestion, time evolutions of particle amount and electrical discharge parameter values were measured. Figures 1(a) and (b) show time evolutions of RF discharge voltage V_{RF} , current I_{RF} , RF power P and power factor $\cos \theta$ for pure He and He+ SiH_4 (5%) discharges respectively. For the pure He discharge, all these electrical discharge parameters keep up constant values during T_{on} . Conversely, for the He+ SiH_4 (5%) discharge, they change with time until about 1.5 s after RF power-on, and after that they attain their quasi-steady values.

Since the number of particles depends on parameters such as RF power, pressure and duty cycle, correlations were investigated varying these parameters. Figures 2 and 3 show time evolutions of LLS intensities integrated over the discharge space (total particle amount), V_{DC} and $\cos \theta$ as functions of RF power and pressure. For all RF power and pressure cases, total number of particles monotonically increases with time during T_{on} . With this increase, θ and V_{DC} at first tend to decrease considerably to their minimum values and then tend to increase slightly to their quasi-steady values. One can see that, with the increases in RF power and pressure, the particle amount increases rapidly with time and, corresponding to this increase, $\cos \theta$ and V_{DC} change quickly with time.

Figure 4 shows the dependence of time evolutions of the total particle amount, V_{DC} and $\cos \theta$ on the duty cycle D . In the figure, time evolutions of V_{DC} and $\cos \theta$ for pure He CW discharges are also shown. It can be seen that V_{DC} decreases and $\cos \theta$ increases with time after RF power-on for $D > 60\%$, in which cases the

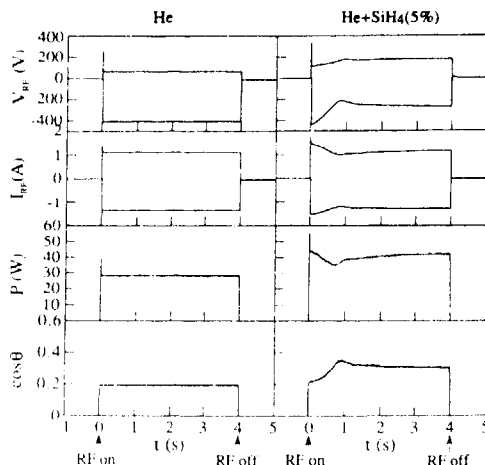


Figure 1. Time evolutions of RF discharge voltage V_{RF} , RF discharge current I_{RF} , RF power P and power factor $\cos \theta$ for pure He and He+ SiH_4 (5%) discharges. $D = 100\%$, $T_{\text{on}} = 4$ s, 40 W, 30 sccm, 80 Pa.

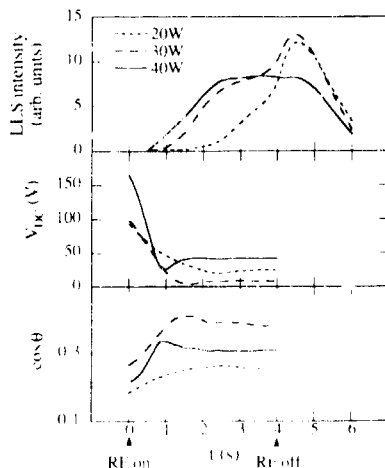


Figure 2. Time evolutions of LLS intensity integrated over discharge space, magnitude of self-bias voltage V_{DC} and power factor $\cos \theta$ as a parameter of RF power. $D = 100\%$, $T_{\text{on}} = 4$ s, He+ SiH_4 (5%), 30 sccm, 80 Pa.

number of particles is large. These general tendencies are similar to those in figures 2 and 3. On the other hand they keep almost constant values for $D < 40\%$. From figures 2–4 one can see that V_{DC} and θ after RF power-on decreases with the increase in the particle amount. The characteristic time of decrease in V_{DC} and θ is of the order of a second. This very long characteristic time corresponds to the appearance time of particles. Features shown in figures 2–4 indicate that the presence of particles firstly reduces V_{DC} and θ , and then increases them to quasi-steady values. These results are consistent with those reported before [2]. On the other hand, the discharge parameters for $D = 20\%$ are close to those for

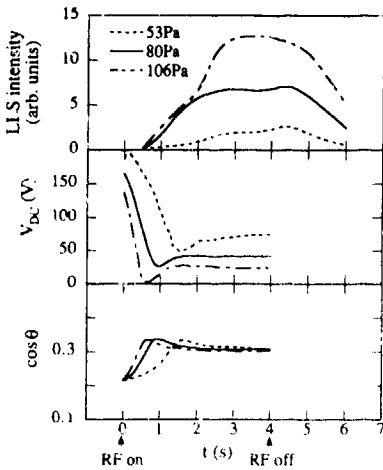


Figure 3. Time evolutions of LLS intensity integrated over discharge space, magnitude of self-bias voltage V_{DC} and power factor $\cos \theta$ as a parameter of pressure. $D = 100\%$, $T_{on} = 4$ s, 40 W, He+SiH₄ (5%), 30 sccm.

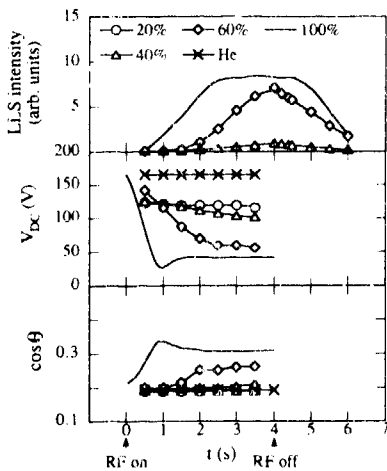


Figure 4. Time evolutions of LLS intensity integrated over discharge space, magnitude of self-bias voltage V_{DC} and power factor $\cos \theta$ as a parameter of duty cycle D . $T_{on} = 4$ s, 40 W, He+SiH₄ (5%), 30 sccm, 80 Pa. No particles were observed for $D = 20\%$ and pure He $D = 100\%$ discharges.

a pure He discharge. This tendency is consistent with the result that no particles can be observed for this case.

The optical emission intensity in the bulk plasma region is considered to be higher for a more resistive discharge. To confirm this tendency, spatial resolved intensity profiles of SiH 413.5 nm optical emission were measured. The typical results are shown in figure 5. As expected, the intensities increase especially in the bulk plasma region with time, that is, with the increase in the total particle amount.

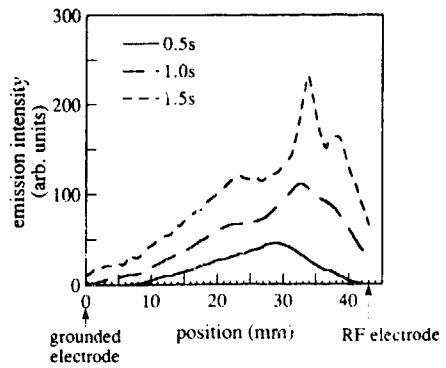


Figure 5. Intensity profiles of SiH 413.5 nm optical emission for $t = 0.5, 1.0, 1.5$ s. $D = 100\%$, $T_{on} = 4$ s, 40 W, He+SiH₄ (5%), 30 sccm, 80 Pa.

4. Discussion

Firstly, we shall discuss that the particle species responsible for the changes in electrical discharge parameters shown in the last section are negatively charged particles grown in the plasma. Main charged species in SiH₄ RF discharges are considered to be electrons, positive ions such as SiH₄⁺ and negative ions such as SiH₃⁻ and negatively charged particles. In general, the parameters θ and V_{DC} are expected to decrease for electronegative gas plasmas containing negative ions for the following reasons: negative ions act as loss centres of electrons and their momentum, inducing a large increase in the electric field in the bulk plasma region and the presence of negative ions brings about a decrease in the electron current flowing into electrodes. This trend can be seen in the early phase until about 1 s after RF power-on in figures 2–4. Further, all our results described in this paper show that the time evolutions of the electrical parameters always correlate well with that of particle amount. Hence one can conclude that particles grown in the plasma dominantly affect the time evolutions of the electrical parameters. This conclusion is consistent with those of previous reports [1–5].

Next we shall discuss the mechanisms by which particles of interest affect $\cos \theta$ and V_{DC} . With the increase in particle amount, the optical emission intensity in the bulk plasma region increases considerably, as shown in figure 5. This increase in the intensity indicates that the power dissipated in the bulk plasma increases with the particle amount, because the charged particles act as loss centres of electrons and their momentum in the plasma. We have measured the plasma potential profile with an emissive probe and shown that the electric field in the bulk plasma increases considerably with the particle amount [14]. All these facts show that the presence of particles brings about a more resistive discharge, leading to an increase in $\cos \theta$. Further, the increase in density of negatively charged particles brings about a decrease in electron density which causes a decrease in V_{DC} .

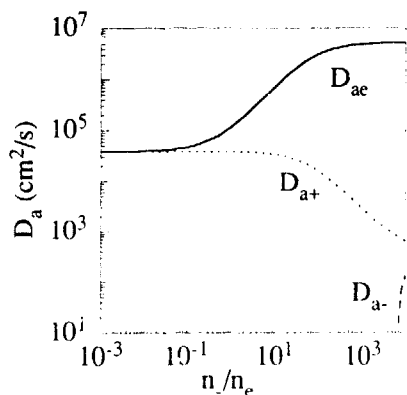


Figure 6. Dependence of ambipolar diffusion coefficients of electrons D_{ae} , positive D_{a+} and negative ions D_{a-} on ratio of negative ion to electron density n_-/n_e for $T_e = 3$ eV, $T_+ = T_- = 0.03$ eV, $M_+ = M_- = 31$ (theory).

Finally, we shall suggest a possible mechanism which brings about an increase in V_{DC} and θ after about 1 s as shown in figure 1(b). During the RF power-on period, the particle amount and the optical emission intensity keep increasing and concomitant optical sheath width decreases to a quasi-steady value. In spite of monotonical changes in these parameters, V_{DC} and θ firstly decrease until about 1 s after the RF power-on and then increase slightly. As one possible mechanism of interest, we point out the enhancement of electron diffusion from the periphery of the discharge column due to the increase in negative ion density. It is known that ambipolar diffusion coefficients of electrons, positive ions and negative ions depend on a ratio between negative ion and electron densities n_-/n_e . These values were estimated using Rogoff's formulation [15] for electron temperature $T_e = 3$ eV, positive ion temperature $T_+ = 0.03$ eV, negative ion temperature $T_- = 0.03$ eV, mass number of positive ions $M_+ = 31$ and mass number of negative ions $M_- = 31$. In the formula, the spatial density distributions of all charged species are assumed to have the same shape. Although particle growth may bring about some differences among their shapes, the formula was used for simplicity. The result is shown in figure 6. One can see that the diffusion of electrons increases dramatically for $n_-/n_e \geq 0.1$, while negative ions are hard to diffuse. Because negatively charged particle density increases with time after RF power-on, n_-/n_e continues to increase and, in our case, can get to more than 0.1. As a result, the electrons tend to diffuse more freely from positive and negative ions. This diffusion enhancement can bring about the increase in the effective surface area of the grounded electrode, which causes an increase in V_{DC} and also in the equivalent capacitance leading to a decrease in $\cos \theta$.

5. Conclusions

Close correlation is clearly found between the particle growth, the self-bias voltage and the phase shift between

the current and voltage of the RF discharge using the power modulation method for various values of parameters such as duty cycle of the modulation, RF power and pressure. With the increase in the particle amount, the optical emission intensity in the bulk plasma region is monotonically enhanced, and, on the other hand, both the self-bias voltage and the current-voltage phase shift first decrease to their minimum values, and then increase slightly to their quasi-steady values. The mechanism by which the particles decrease V_{DC} and θ can be explained by the fact that negatively charged particles in plasmas behave as heavy negative ions. The slight increases in V_{DC} and θ subsequent to such decreases may be due to the enhancement of electron diffusion caused by the increase in the density ratio between negative ions and electrons. It is also confirmed through this study that the modulation is very effective in suppressing the particle growth. In particular, for a duty cycle of 20%, the discharge parameters are very close to those for a pure He discharge. This tendency is consistent with our experimental result that no particles can be observed for this duty cycle.

Acknowledgments

This work was supported principally by a Grant-in-Aid for Scientific Research on Priority Areas and a Grant-in-Aid for Cooperative Research (A) from the Ministry of Education, Science and Culture and also supported partly by the Casio Science Promotion Foundation. The authors would like to acknowledge the assistance of Messrs T Kinoshita and H Matsuzaki who contributed greatly to preparing the experimental set-up.

References

- [1] Jellum G M, Daughty J E and Graves D B 1991 *J. Appl. Phys.* **69** 6923
- [2] Bouchoule A, Plain A, Boufendi L, Blondeau J Ph and Laure C 1991 *J. Appl. Phys.* **70** 1991
- [3] Howling A A, Hollenstein Ch and Paris P-J 1991 *Appl. Phys. Lett.* **59** 1409
- [4] Boeuf J P and Belenguer Ph 1992 *J. Appl. Phys.* **71** 4751
- [5] Belenguer Ph, Blondeau J Ph, Boufendi L, Toogood M, Plain A, Bouchoule A, Laure C and Boeuf J P 1992 *J. Appl. Phys.* **71** 4751
- [6] Watanabe Y, Shiratani M, Kubo Y, Ogawa I and Ogi S 1988 *Appl. Phys. Lett.* **53** 1263
- [7] Shiratani M, Matsuo S and Watanabe Y 1991 *Japan. J. Appl. Phys.* **30** 1887
- [8] Watanabe Y, Shiratani M and Yamashita M 1992 *Appl. Phys. Lett.* **61** 1510
- [9] Watanabe Y and Shiratani M 1993 *Plasma Sources Sci. Technol.* **2** 35
- [10] Watanabe Y and Shiratani M 1993 *Japan. J. Appl. Phys.* **32** 63
- [11] Shiratani M, Fukuzawa T, Eto K and Watanabe Y 1992 *Japan. J. Appl. Phys.* **31** L1791
- [12] Shiratani M, Fukuzawa T and Watanabe Y 1994 *IEEE Trans. Plasma Sci.* **22** 103
- [13] Fukuzawa T, Shiratani M and Watanabe Y 1994 *Appl. Phys. Lett.* **64** at press
- [14] Okuno Y, Fujita H, Shiratani M and Watanabe Y 1994 *Appl. Phys. Lett.* **63** 1748
- [15] Rogoff G L 1985 *J. Phys. D: Appl. Phys.* **18** 1533

The dynamics of dust particles in silane glow discharges between parallel plates

R J Seeböck†, W Böhme††, W E Köhler†, M Römheld† and S Vepřek‡

† Siemens Research Laboratories, PO Box 3220, D-91050 Erlangen, Germany

†† Institute for Chemistry of Information Recording, Technical University of Munich, Lichtenbergstrasse 4, D-85748 Garching, Germany

Received 3 January 1994, in final form 5 April 1994

Abstract. In order to avoid particle contamination of substrates during the plasma-enhanced chemical vapour deposition of amorphous silicon, we have investigated the dependence on temperature and gas flow conditions of the dynamics of submicrometre particles in discharges in silane. We report on light scattering experiments in an RF-powered plasma reactor with heatable parallel electrodes. The motion and trapping of particles was found to be strongly influenced by the gas flow conditions and the temperature gradient in the discharge.

To understand this behaviour the equation of motion of a particle was solved in one dimension including gravitation, electric force on a 'dressed' particle, friction force and thermophoresis. The validity of the friction force is verified by observing experimentally the sinking of particles without electric force after switching off the discharge. Results for calculated particle positions and velocities as a function of time are presented for the cases of particles with radii of 0.1 and 0.15 μm . When the discharge is on, the light particle is trapped at the sheath boundary. In the case of a temperature gradient (heating the lower electrode to 80 °C) the lighter particles are driven upward by thermophoresis and may be trapped at the sheath edge. Finally, a strong downward-directed gas flow (feeding gas through the upper electrode) of 30 cm s^{-1} prohibits the trapping of particles at the lower sheath boundary in agreement with the experimental observation. Electrode heating, together with proper gas flow, is found in our experiments to completely avoid the trapping of particles in the interelectrode space.

1. Introduction

The deposition rate of thin films of amorphous silicon (a-Si:H) by plasma-enhanced chemical vapour deposition (PECVD) from SiH_4 discharges is a limiting factor in solar cell production. Many attempts have been made to increase the deposition rate by higher RF power densities or higher pressures. In those experiments the formation of fine powders in the discharge by plasma-induced gas-phase reactions has frequently been observed [1–5]. Particles have also been reported to occur in discharges in argon and nitrogen [6]. Mechanisms for the initial stages of cluster formation have recently been suggested [7,8]. The aim of the present work is to study experimentally how gas flow conditions and temperature gradient govern the trapping and fallout of such particles in RF discharges between parallel plates and to understand this behaviour by simplified theoretical modelling.

The paper is organized as follows: in section 2 we give a brief description of the experimental set-up used for plasma generation and the detection of particles in the gas and plasma phase. Then we discuss the forces acting

on charged particles in a parallel-plate discharge and the equation of motion that has to be solved numerically. In section 4 we describe the observed spatial structure of discharge regions with high particle density and discuss the influence of electrode temperatures and gas flow conditions on their formation. For each experiment we discuss the theoretical results that were obtained under similar conditions and the way they may explain the experimental observations. We also briefly report on the fallout of particle clouds after switching off the discharge. These experiments were reported more extensively in a recent paper [9]. Finally we summarize and draw conclusions.

2. Experimental techniques

2.1. Plasma reactor

The experiments were carried out in a parallel-plate plasma reactor, a schematic view of which is shown in figure 1. Substrates consisting of Corning glass of an area of 25.4 \times 25.4 mm^2 and a thickness of

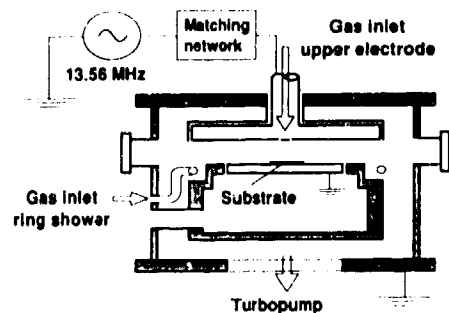


Figure 1. Schematic view of the parallel-plate plasma reactor used for the investigations. The gas inlet was either through the ring shower surrounding the lower electrode or through five holes in the centre of the upper electrode. Both electrodes were electrically heatable and temperature controlled.

0.7 mm were located on the grounded lower electrode with a diameter of 153 mm. The upper electrode, with a diameter of 250 mm was 40 mm above the lower one. It was connected to a 13.56 MHz generator via an impedance matching network. The output power of the generator was varied between 15 and 80 W in the forward direction, while the reflected power was matched to approximately zero. Both electrodes were heatable to 400 °C by heater windings incorporated in the electrodes. The temperatures were measured by thermocouples and controlled by a PID controller to an accuracy of ± 10 °C.

During all the investigations the process gas used was pure SiH_4 with a standard flow rate of 10 ml min^{-1} at a pressure of 20 Pa. The reactor was equipped with two alternative gas inlets: one consisted of five holes in the central part of the upper electrode, the other of a ring shower surrounding the lower electrode (see figure 1). Only one inlet was used at a time.

2.2. Detection of scattered light from particles

The optical set-up used to observe the light of an HeNe laser, scattered from particles between the electrodes, is schematically shown in figure 2. The beam of the laser is shaped into a light sheet and directed into the interelectrode region of the reactor. The scattered light is observed by a video camera. With the help of the mirror shown in figure 2, particles in various regions of the reactor, particularly off-axis regions at the edge, can be visualized. Printouts from video tapes were made on a video printer. For the observation of particles sinking to the lower electrode on the reactor axis, the light band was directed through the reactor centre. The scattered light was detected under an angle of 90° by imaging the reactor axis onto the entrance slit of a monochromator, at the exit slit of which a diode array camera was vertically mounted.

The light intensities measured by this scattering method are only approximately proportional to the particle densities. Consider, for example, the particle

density $N(0, z)$ on the reactor axis. Laser light travelling through the reactor to the axis at different axial heights z experiences on its way different particle densities as a function of distance x from the axis and hence different values of the extinction coefficient $\sigma_e(x, z)$ which is proportional to the particle density $N(x, z)$ [10]. According to the Lambert-Beer law the total extinction on this passage in height z is given by

$$\exp\left(-\int_{R_i}^0 \sigma_e(x, z) dx\right) = \exp\left(-A \int_{R_i}^0 N(x, z) dx\right)$$

where A is a constant independent of position that contains the single-particle extinction coefficient and R_i is the distance of the entrance window from the axis. The light scattered from particles on the axis experiences a similar extinction on its way to detection with the difference that light rays tilted somewhat against the electrode surfaces also contribute to the image. The net effect is that the measured light intensity is a product of the particle density on the axis and a factor depending itself on the axial particle density and hence on z . Therefore, those axial regions with high particle densities are under-represented in the scattered light intensity. Nevertheless, as long as particle densities are not too high, the main features of the axial particle density are represented by the detected light. Two other possible reasons for the disproportionality between intensity and particle density, namely distribution of particle sizes and/or change of particle size during sinking of particles can be excluded [9].

The monochromator was tuned to the red HeNe laser wavelength, to suppress plasma-induced emission. The spatial resolution on the reactor axis was about 0.1 mm, which was checked by the imaging of black and white line patterns. The readout speed of the camera for its 1024 pixels was 60 scans/s. It could be increased up to 250 scans/s with reduced scan width.

3. Modelling of the particle dynamics

3.1. Forces acting on the particles

We consider spherical aerosol particles of radius R , mass m and a negative charge $-Nq$ ($N \gg 1$), where q is the elementary charge, in a horizontal parallel-plate plasma reactor operating in the continuous-flow mode. In the following, for simplicity, DC discharges are treated. This is equivalent to the case of AC discharges if the frequency is high enough so that the particles will only experience the averaged electric field. We assume that the electric field E in the plasma points in the (axial) z direction, the cathode plane being located at $z = 0$. This geometry is schematically shown in figure 3. Both electrode sheaths are plotted equally wide, because the powered upper electrode is by a factor 2.67 larger than the lower one. On the other hand, part of the grounded wall area has to be added to the lower electrode, so that its effective area is similar to that of the upper electrode leading to similar sheath potentials and sheath thicknesses. A stationary flow field v_i exists and a temperature field $T(z)$ may be present. Then the forces described in the following act on the particles.

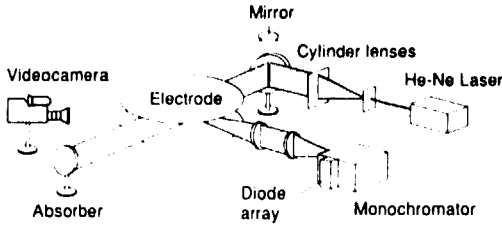


Figure 2. Set-up used for optical detection of particles in the gas phase. Red light from an HeNe laser is shaped into a sheet and directed into the plasma. The scattered light from particles in the plasma is observed by means of either a video camera or a diode array camera.

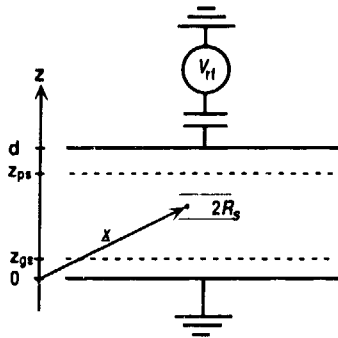


Figure 3. Schematic diagram showing a dressed particle between the electrodes of an RF-excited parallel-plate reactor and the coordinate axis used in the calculations.

3.1.1. Gravitation.

$$F_g = -m_g e_z. \quad (1)$$

For a particle homogeneous in mass density $F_g \propto R^3$ holds.

3.1.2. Friction. In the pressure regime used for PECVD of a-Si:H ranging from 5 to 50 Pa, the mean free path of the SiH_4 molecules, given by $\lambda_f = (N_g \sigma_s)^{-1}$, where N_g is the silane density and σ_s the total cross section for molecular collisions, lies in the range between 0.7 and 0.07 cm. Therefore, for those particles of practical interest with diameters less than $5 \mu\text{m}$, the free molecular case ($\lambda_f \gg R$) has to be considered. (For this estimation we use a hard sphere molecular radius of 1.91×10^{-8} cm and neglect that the measured pressure is only partly due to the density N_g of gas molecules and partly to that of dissociation and ionization products present in the discharge.) We assume the friction force on a particle immersed in polyatomic SiH_4 to be identical to that acting in a monatomic gas, given in [11]

$$F_f = -\frac{32}{3} R^2 \frac{p}{v_{th}} \left(1 + \frac{\pi}{8}\right) (\mathbf{v} - \mathbf{v}_f) \quad (2)$$

where $p = N_g kT$ is the gas pressure, $v_{th} = \sqrt{8kT/\pi m_g}$ is the mean thermal velocity of the gas molecules with

mass m_g and \mathbf{v} is the particle velocity. For a particle with $R = 0.1 \mu\text{m}$ at rest in SiH_4 (pressure 20 Pa, gas temperature 300 K) a force $F_f = 5.6 \times 10^{-17}$ ($\text{v}_f \text{ cm s}^{-1}$) N results. With the gas inlet through the upper electrode the force may thus range up to 10^{-14} N close to the inlet holes.

Comparison with Stokes' friction force $F_s = -6\pi\eta R(\mathbf{v} - \mathbf{v}_f)$, valid for the hydrodynamic case $\lambda_f \ll R$, where η is the dynamic viscosity of the gas, shows that for low gas pressure an effective viscosity η_{eff} may be introduced by

$$\eta_{eff} = \frac{16(1 + \pi/8)}{9\pi v_{th}} R p = 0.79 R p / v_{th}. \quad (3)$$

3.1.3. Thermophoresis. Experimental evidence for the importance of the thermophoretic force has already been given in [6]. Again for the limiting case $\lambda_f \gg R$, in the simplest approximation the thermal force on a spherical particle is given by [12]

$$F_t = -\kappa \nabla T \quad \kappa = \frac{32 R^2 \lambda_f^t}{15 v_{th}} \quad (4)$$

where λ_f^t is the translational part of the heat conductivity of the gas. In a hard sphere model with molecular radius r_0 , κ is given by

$$\kappa = \frac{5\sqrt{2}}{32} k \left(\frac{R}{r_0}\right)^2 \quad (5)$$

and the thermophoretic force is thus proportional to R^2 . For a particle with $R = 0.1 \mu\text{m}$ in SiH_4 ($r_0 = 1.91 \times 10^{-8}$ cm) the factor κ is given by $5.3 \times 10^{-19} \text{ J K}^{-1}$. More general formulae for the thermal force may be found in [13, 14].

3.1.4. Electric force. In the following, we apply as an example for the electric force the model of a 'dressed' particle proposed in [1]. It assumes that negatively charged dust particles are surrounded by a positive charge cloud with radius R_s (see figure 3). For the calculation of this force, we consider a negative point charge $-Nq$ surrounded by a positive space charge homogeneously distributed over a sphere of radius R_s of some Debye lengths centred at the particle midpoint position \mathbf{x} . The negative and positive charge densities at a space point \mathbf{x}' are

$$\rho_-(\mathbf{x}, \mathbf{x}') = -Nq \delta(\mathbf{x} - \mathbf{x}'), \quad \rho_+ = \frac{3N|q|}{4\pi R_s^3} \cdot |\mathbf{x} - \mathbf{x}'| \leq R_s. \quad (6)$$

Such a particle has practically the same mass as the undressed dust particle and is uncharged as a total. It does not experience a force in a homogeneous electric field. The charge Nq is given in the electrostatic approximation of a conducting sphere by [15]

$$-Nq = (\Phi_p - V_p) 4\pi \epsilon_0 R (1 + R/\lambda_D) \quad (7)$$

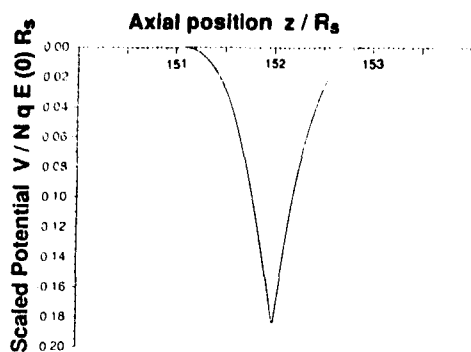


Figure 4. Scaled potential $V / -NqE(0)R_s$ for a linear sheath electric field as functions of the scaled coordinate z/R_s with $R_s = 33 \mu\text{m}$ and $z_{gs} = 5 \text{ mm}$.

where Φ_p , V_{pl} , λ_D are the potential of the sphere, the plasma potential and the Debye length respectively. For the limiting case $R \ll \lambda_D$, which is always met for the particles under consideration, and the assumption $V_{pl} - \Phi_p = 10 \text{ V}$, which corresponds to $kT_{el} \approx 2 \text{ eV}$, equation (7) reduces to

$$N = 6.94(R \text{ nm}). \quad (8)$$

The charge of the real particle is lower than this value and not fully screened by trapped positive ions [16]. Nevertheless we use this model to qualitatively understand our experimental observations.

The force on the screened particle in an arbitrary electric field can be calculated according to

$$F_{el}(x) = \int_{\text{sphere}} (\rho_-(x, x') + \rho_+(x, x')) E(x') d^3x'. \quad (9)$$

A non-zero force can be exerted on a dressed particle in regions where one-half of the charge cloud experiences a different mean electric field from the other in such a way that their average is different from the field at the position of the core. This means that the second derivative of the field with respect to position must be non-vanishing. Therefore the particle will experience a relatively strong force in the transition regions between the bulk plasma with $E_z \approx 0$ and the electrode sheaths. The force contribution resulting from a possible distortion of the spherical positive charge cloud due to polarization is disregarded. For the calculations the rather realistic model of a linear electric field in the sheath region above the lower electrode of the form $E(z) = E(0)(1 - z/z_{gs})$ with $E(0) < 0$ is considered. The evaluation of the integral, equation (9), for the one-dimensional case yields

$$F_{el} = \frac{-Nq|E(0)|}{4R_s^3} \left(\pm \frac{3R_s^4}{4z_{gs}} - \frac{2R_s^3}{z_{gs}}(z - z_{gs}) \pm \frac{3R_s^2}{2z_{gs}}(z - z_{gs})^2 \mp \frac{1}{4z_{gs}}(z - z_{gs})^4 \right) \quad (10)$$

where the upper sign holds for $z_{gs} < z < R_s + z_{gs}$ and the lower sign for $z_{gs} - R_s < z < z_{gs}$. In figure 4, the z/R_s dependence of the scaled potential ($V / -NqE(0)R_s$) is displayed for $R_s = 33 \mu\text{m}$ and $z_{gs} = 5 \text{ mm}$.

3.1.5. Ion drag force. The ion drag force exerted on particles due to the directed motion of ions in the discharge has been treated in [15]. To obtain an upper limit for this force we use the simple model that a directed ion beam with current density j_i , as present in the sheath, is hitting the particle and that no ions are reflected by the particle. The momentum change per incident ion is then equal to the momentum $m_i v_i$ of the ion. The drag force exerted on the particle is thus equal to $F_i = \pi R^2 j_i m_i v_i / q$. We assume an ion current density of 0.1 mA cm^{-2} and a sheath voltage of 100 V . We further take into account that at the pressure of interest, 20 Pa , the sheath is collision dominated and the average ion energy will be of the order of 10% of the full sheath potential. The force exerted on a particle with a diameter of $1 \mu\text{m}$ is then equal to $2.03 \times 10^{-15} \text{ N}$. We have to compare this value to the gravitational force acting on the same particle, which is equal to $1.03 \times 10^{-14} \text{ N}$ where we have assumed a mass density of 2 g cm^{-3} . Therefore the ion drag force is a correction of 20% in the sheath region. In the presheath, where ion velocities are only of the order of a few kT_e , the contribution is even less. We therefore neglect the ion drag force for silane discharges at 20 Pa and discharge power levels of much less than 100 W in our further considerations. It will become important at lower pressures around 1 Pa and higher power levels as are found in reactive ion etching. It is also mentioned that due to the R^2 dependence of the ion drag force and the R^3 dependence of the gravitational force the ion drag force becomes more important for small particles.

3.2. Particle motion with thermal and electric force and gas flow in the z direction

For the calculations we will only consider the simplified case where the gas flow, the electrical and the thermal forces have only a z component. With the forces discussed in the last section, the components of the equation of motion read

$$m\dot{v}_x = -6\pi R\eta_{\text{eff}}v_x \quad (11)$$

$$m\dot{v}_y = -6\pi R\eta_{\text{eff}}v_y \quad (12)$$

$$m\dot{v}_z = -mg - \kappa \nabla_z T - 6\pi R\eta_{\text{eff}}(v_z - v_f) + F_{el}(z). \quad (13)$$

In general, the flow velocity is a function of x, y, z and κ is a function of the spatially dependent temperature $T(z)$. Thus one has a system of three coupled second-order differential equations which have to be solved numerically. In case of constant flow velocity in the z direction and constant thermophoretic force, equations (11), (12) and (13) are decoupled. Outside the sheath region (where $F_{el} = 0$) they can be solved analytically. The solution of equation (13) is then

$$v_z = v_{0z}[1 - \exp(-t/\tau)] + v_{0z} \exp(-t/\tau) \quad (14)$$

where $\tau = m/6\pi R\eta_{\text{eff}}$ and v_{0z} is the z component of the initial velocity, and where

$$v_z = v_i - g\tau - \frac{\kappa}{6\pi R\eta_{\text{eff}}} \nabla_z T \quad (15)$$

is the asymptotic velocity for $t \rightarrow \infty$. The solutions of equations (11) and (12) are exponentials.



Figure 5. Two bands of trapped particles between the electrodes of the reactor. Both electrodes are kept at 26 °C. The forward power was 70 W.

4. Results and discussion

4.1. Gas inlet through the ring shower

In the first set of experiments the process gas was injected through the ring shower surrounding the lower electrode. A simulation of the gas flow under these conditions shows that there is practically no flow in the centre of the interelectrode region. Silane is transported there mainly by diffusion.

4.1.1. Both electrodes at room temperature (case 1).

Observation of particle clouds. In the first investigated case both electrodes were at room temperature (26 °C). The forward power was 80 W. After short plasma burning times many particles can be observed between the electrodes. The accumulation of the particles in two bands between the electrodes indicates their trapping at the plasma sheath boundaries by the sum of gravitation, friction drag forces and electric forces [1, 15]. The width of the particle bands fluctuates in a chaotic way. These bands can be seen in figure 5, where between the bands two brighter zones are reflections from windows on the opposite side of the reactor. The bright lines below the lower band are reflections from two edges of a substrate lying on the lower electrode. The arrangement of figure 5 is schematically reproduced in figure 6 to clarify the position of the different elements. Particle trapping of a similar type was also observed by other groups; see for example [1, 4, 6]. Gravitation and drag forces then may lead to the fallout of particles that exceed a critical size.

Particle fall out without plasma. The aim of these experiments was to verify the friction force equation (2) to be used in the calculations. We report on results of the measurements of light scattering from sinking particles after switching off the discharge. The conditions of these experiments were those of case 1. The plasma burning time before turning off was varied between 0 and 160 s. In figure 7 a typical diagram of the intensity of scattered light from the reactor axis versus axial position z and time t is shown for a burning time of 70 s. The two

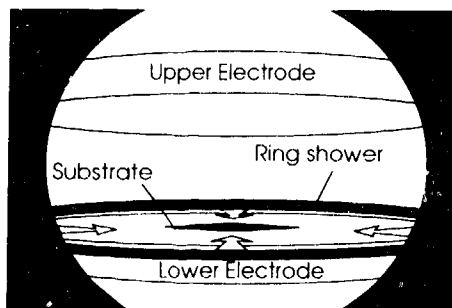


Figure 6. Schematic view of the situation with gas inlet through the ring shower corresponding to figure 5.

peaks at $z = 0$ and $z = 40$ mm result from reflections from the electrodes and were used to calibrate the z axis. The time intervals between subsequent scans are 33 ms. The instant of switching off the discharge is clearly identified as $t = 70$ ms by the change in the scattered light distribution.

While the discharge is on ($t = 65$ ms) two stable particle bands, as discussed in the previous section, are observed at positions $z = 10$, 20 mm and $z = 30$ mm. After turning off the discharge, both bands start to sink towards the lower electrode. They reach a nearly equal stable sinking speed in a relaxation time τ less than the time difference between subsequent camera scans. The measured sinking speeds are plotted versus the discharge burning time in figure 8. The increase of the sinking speed with burning time is due to particle growth, as was shown in [9].

If there is no temperature gradient and no electric force, as in this sinking experiment, the z component of the velocity of a particle, according to equation (15), relaxes to $v_z = gr$. In the case of gas inlet through the ring shower, the flow velocity on the reactor axis is practically zero, and the speed relaxes to gr . With the values $\rho = 2 \text{ g cm}^{-3}$, $R = 0.1 \text{ }\mu\text{m}$, $T = 300 \text{ K}$, $p = 20 \text{ Pa}$ for SiH_4 , we find $v_z = 1.23 \text{ cm s}^{-1}$. This has to be compared with the experimental value of 3 cm s^{-1} found for the burning time of 20 s which corresponds to the particle radius $R = 0.1 \text{ }\mu\text{m}$. The fact that the result is of the right order of magnitude strongly supports the validity of equation (2). The deviations are most probably due to a difference in particle radius between experiment and calculation, because particle radii were not determined in the same experiment where the sinking speed was determined but under identical conditions in a different experiment. Part of the deviation may also be due to incomplete accommodation of the temperature of the molecules as they are reflected from the particle surface, which modifies equation (3) to decrease η_{en} , for a detailed discussion see [17]. The calculated relaxation time is $\tau = 1.26 \text{ ms}$ which explains the fast relaxation to stationary sinking.

Modelling of the trapping at the sheath boundary. In this section we show that particles of the experimentally observed size moving towards the lower electrode ($z =$

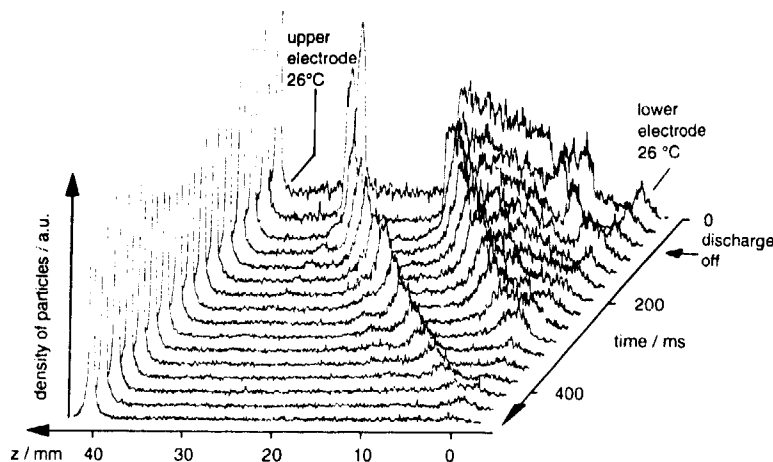


Figure 7. Intensity of scattered light from particles versus z position and time as measured by the diode array camera. Different traces belong to subsequent scans. The forward power was 70 W. The on-time of the discharge was 70 s before it was turned off to measure the sinking speed of particle clouds. Both electrodes were at 26 °C. The peaks at $z = 0$ and $z = 40$ mm are reflections from the lower and upper electrodes respectively. Between the electrodes the scattered light from two particle clouds is visible. They start to sink towards the lower electrode (substrate) when the discharge is turned off. Note that time proceeds from back to front!

0) are trapped near the sheath boundary ($z = z_{gs}$). It is clear from energy conservation that particle trapping cannot occur without a friction force. Particle motion is studied in this work only for the case of a DC discharge. For particles with their space charge cloud crossing the boundary of the sheath, the electric force, equation (10), was taken into account and equation (13) was numerically solved using a fourth-order Runge-Kutta method. The time step was chosen to be not smaller than τ . In the neighbourhood of the discontinuity at $z = z_{gs}$ the electric force was approximated by a cubic parabola. The following parameters were used: $z_{gs} = 5$ mm, $R_s = 33 \mu\text{m}$, N according to equation (8), $v_i = 0$, uniform temperature ($\nabla_z T = 0$), $E(0) = 100 \text{ V cm}^{-1}$, mass density $\rho = 2 \text{ g cm}^{-3}$. The particle starts at rest and is accelerated by gravitation. It has already reached its stationary sinking speed when it enters the range of action of the electric force at $z = z_{gs} + R_s$.

Heavier particles ($R > 0.15 \mu\text{m}$) traverse the range of the electric force and move on without drastic change in their states of motion because the gravitational force ($\propto R^3$) dominates. In figure 9 the z position and the z velocity of such a particle ($R = 0.15 \mu\text{m}$, $N = 1.04 \times 10^3$) are shown. The particle is first accelerated in the force field (conversion of potential into kinetic energy) and then slowed down again. This leads to a dip in the velocity curve. The speed after passage is somewhat smaller in magnitude because of the energy loss due to friction.

A smaller particle with $R = 0.1 \mu\text{m}$ ($N = 0.69 \times 10^3$) is trapped at the sheath boundary, as is seen in figure 10. The excess energy is then converted into

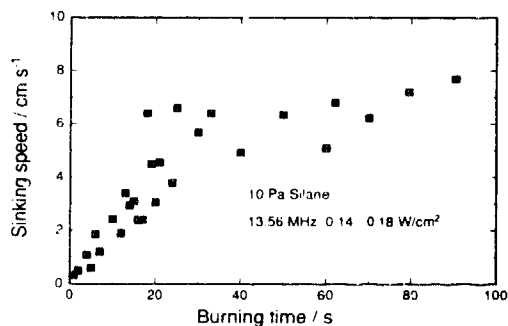


Figure 8. Sinking speed of particles of different size that grew in an SiH_4 plasma in different burning times versus burning time.

gas heating in a damped oscillation around the sheath edge. This result is in agreement with the experiments where the observed particles of radius up to $0.1 \mu\text{m}$ are found to fall out only after switching off the discharge [9]. The boundaries between trapping and fallout will be investigated in a forthcoming paper [18]. The width of the bands found in the experiment may be due to the very smooth plasma sheath transition and to Brownian motion together with fluctuations in gas flow patterns.

4.1.2. Lower electrode heated (case 2). *Particle trapping in pockets above the substrate.* In the second case the lower electrode was heated to a temperature of 88 °C while the upper electrode was kept at 40 °C.

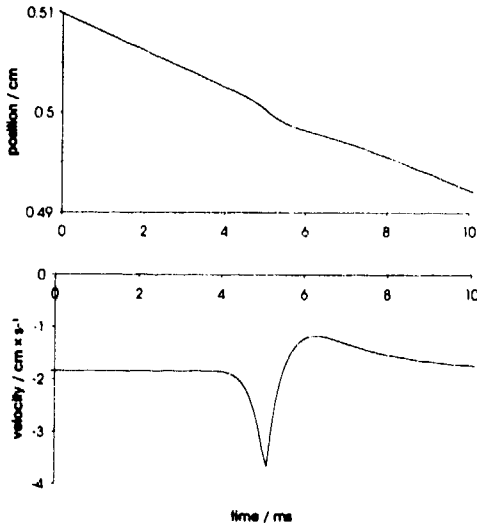


Figure 9. Calculated z position and z velocity of a particle penetrating into the plasma electrode sheath. Parameters: $R = 0.15 \mu\text{m}$, $z_{gs} = 5 \text{ mm}$, $R_s = 33 \mu\text{m}$, $E(0) = 100 \text{ V cm}^{-1}$, $v = 0$, $\nabla_z T = 0$, $z(0) = 0.51 \text{ cm}$. At time $t = 0$ the particle has already reached its stationary sinking speed. It is not trapped.

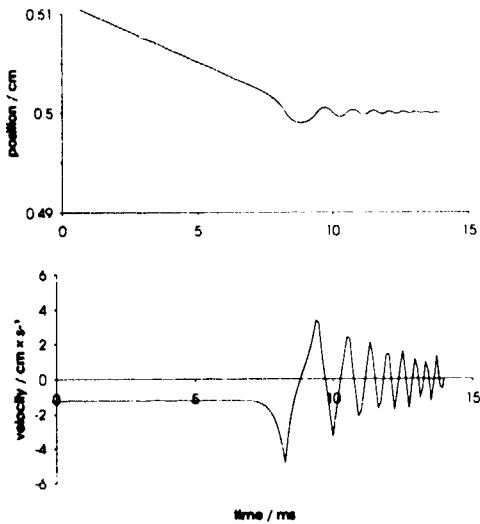


Figure 10. Calculated z position and z velocity of a particle with $R = 0.1 \mu\text{m}$; the other parameters are chosen as in figure 9. The particle is trapped at the sheath edge.

Figure 11 shows the influence of thermophoresis on the two broad bands of case 1 (figure 5). The view is somewhat enlarged as compared with figure 6. The dark regions are the electrodes, the sharp bright lines are reflections of the laser sheet from the electrodes and the substrate. The grey background between the electrodes is due to the plasma-induced emission whereas the bright

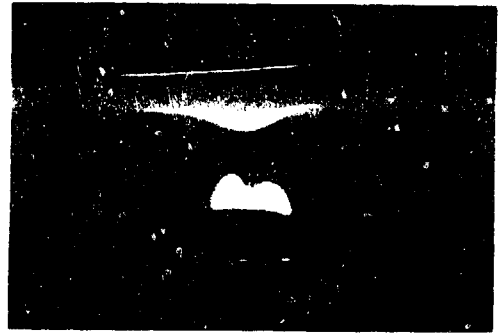


Figure 11. Particle traps above the substrate with gas inlet through ring shower, forward power 20 Watt, $T_e = 40^\circ\text{C}$, $T_{\text{sub}} = 88^\circ\text{C}$.

areas are two-dimensional cuts of the light sheet through the regions with high particle density. There are far fewer particles between the electrodes than in the first case. The remaining particles accumulate in two clouds above the substrate. At greater distances from the substrate no particles are detected. It is observed that a stream of particles leaves the lower cloud and moves upward to enter the upper cloud.

We assume that thermal effects are responsible for the observed trapping of the particles in a small region above the substrate. Figure 12 shows calculated isotherms in the space between the electrodes for electrode temperatures of 40°C and 88°C . The temperature of the upper substrate surface is assumed to be 76°C . Large temperature gradients between electrode and substrate surfaces must be present when the substrate is not clamped to the electrode and thermal coupling is accomplished mostly by radiation, which is not very effective for glass in this temperature range. From figure 12 it can be seen that thermal gradients in the x and y direction are induced above the substrate edge which lead to a radial inward force component. This acts on the particles and tends to accumulate them above the substrate. These forces could be the reason for the shape of particle accumulations in figure 11. The axial component of the thermal force is directed from the hot lower to the cooler upper electrode. A comparison of equations (1) and (4) shows that the thermal force is balanced by gravitation for

$$|\nabla_z T| K \text{ nm}^{-1} \approx R \mu\text{m}. \quad (16)$$

Therefore, above the substrate, where temperature gradients may be very close to zero (see figure 12), very small particles may float or sink to the substrate immediately after their creation. Therefore the probability of trapping at the sheath boundary is very high for these small particles and pockets are formed. In regions with higher thermal gradient, particles are moving upward. This explains the upward-directed particle movement between the two clouds. The particles may be trapped at a pocket near the upper electrode

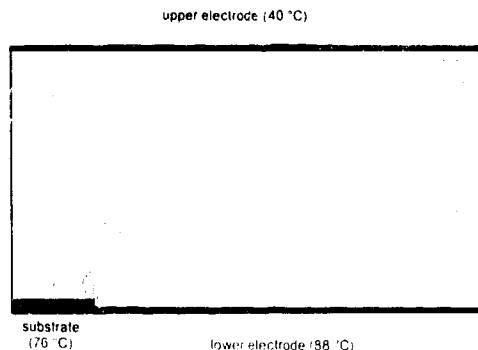


Figure 12. Calculated isotherms between a heated lower electrode with substrate and the opposite cold electrode. The temperatures of the lower and the upper electrodes are 88 °C and 40 °C, while the temperature of the substrate surface is assumed to be 76 °C. Notice the axial and radial components of the temperature gradient above the substrate.

sheath edge. Very large particles may also sink down again and fall out, as is sometimes observed.

In the vicinity of the substrate there may also be an electric force due to different surface charge densities on the electrode and the substrate. This behaviour has already been described for the case of large substrates in semiconductor processing [19]. The axial component of this force together with the very small axial flow velocity leads to a bending of the pocket surface above the substrate (dome) while the radial components contribute to particle collection above the substrate.

Particle motion in off-axis regions. Off the axis the thermal gradient is rather large all over the discharge gap so that the thermal force drives particles upward (see figure 12). Small particles may be trapped at both sheaths. On the other hand, as the thermal force is much stronger than gravitation for particles with $R \ll 0.5 \mu\text{m}$ (see equation (16)), these particles are rapidly moving upward and trapping is rare. In figure 13 the calculated upward z motion of a particle with $R = 0.1 \mu\text{m}$ starting closely below the lower sheath is shown. It is not trapped due to the much larger resulting force compared with the case of figure 10. The small particles that are trapped at the electrode edges are either moving radially inward because of the radial forces induced by the substrate or outward because of the influence of the cold wall. Therefore the case of figure 11 is qualitatively understood.

4.2. Gas inlet through the upper electrode shower

The influence of a pronounced gas flow between the electrodes on the behaviour of particles was studied in the third and fourth cases. In both experiments the gas was led through the centre of the upper electrode. It had to flow through the interelectrode space to reach the pumping port (see figure 1). A flow simulation shows that flow velocities of up to 10 m s^{-1} may appear at the inlet. The gas drags the particles to the outer regions by

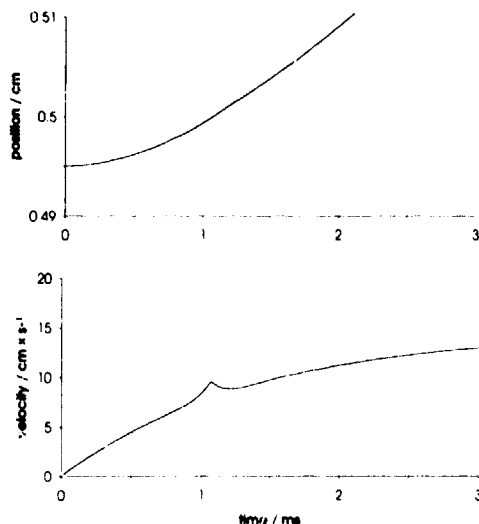


Figure 13. Position and velocity of a particle with $R = 0.1 \mu\text{m}$ travelling through the sheath edge of the lower electrode in a temperature gradient of $\nabla_z T = -1.2 \text{ K mm}^{-1}$; the parameters were $T_{\text{le}} = 88 \text{ °C}$, $T_{\text{ue}} = 40 \text{ °C}$, other parameters are chosen as in figure 10. The particle is not trapped at the sheath edge due to the driving thermal force, the absolute value of which is much larger than that of gravitation.

the friction force equation (2). Eddies may appear at the inlet holes.

4.2.1. Both electrodes at room temperature (case 3).

Observation of eddies and trapped particles. In the third experiment both electrodes were at 26 °C as in the first case. Figure 14 serves to illustrate the geometry of figures 15 and 17. Figure 15 shows the effect of the gas flow on the two bands of the first case. The lower particle band nearly disappears in the centre of the electrode and stays narrow at its peripheral zone. The upper band is reduced to particles rotating in the predicted whirl near the gas inlet holes and thus serves for visualization of the flow. The reduction of particle density in the central region in figure 15, is due to two effects. Firstly, there is a large flow velocity component in the centre, directed radially outward, dragging out the particles. Secondly, particles may be driven through the sheath edge by the friction drag force. An example for this behaviour is shown in figure 16. Here a particle with $R = 0.1 \mu\text{m}$ is moving downward under the combined action of gravitation, a gas flow of 30 cm s^{-1} in the z direction and the frictional drag force. The particle has already reached its stationary speed $v_s = v_t - g\tau$ (see equation (15)) when it enters the force field. The speed is so high that no trapping takes place. There is a very small change in velocity, but the particle falls through the sheath edge.

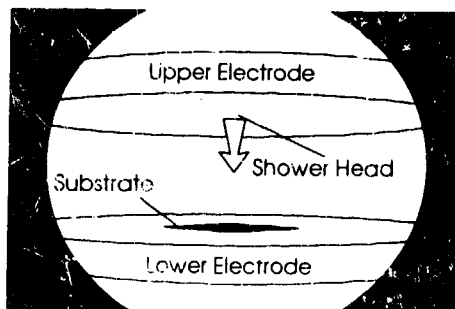


Figure 14. Schematic view of the situation with gas inlet through the shower in the upper electrode. This view corresponds to figures 15 and 17.



Figure 15. View of the remaining particle clouds when the gas is fed through the upper electrode (see figure 14). Note the eddy around the inlet and the narrow band at the lower sheath edge. The circular structure behind the eddy is a window on the opposite side of the vessel. Both electrodes are at temperatures of 26 °C.

4.2.2. Lower electrode heated (case 4). In the final case, heating of the lower electrode and gas injection through the upper one led to an interelectrode space totally free of particles within our detection limits. This result is shown in figure 17. The combined action of upward-directed thermophoresis and outward-directed drag force leads to the transport of the particles away from the substrate and out of the interelectrode space. Notice, however, that the increase of temperature not only induces thermal forces but also reduces particle creation [5].

5. Conclusions

For long plasma burning times particles may form large clouds in plasma reactors. We have shown that the gas flow conditions and temperature gradient in the reactor have reduced the number of particles present during the experiments to levels not detectable with light scattering. Therefore we conclude that the proper use of thermal and drag forces in the design of PECVD reactors can solve the problem of particle contamination.

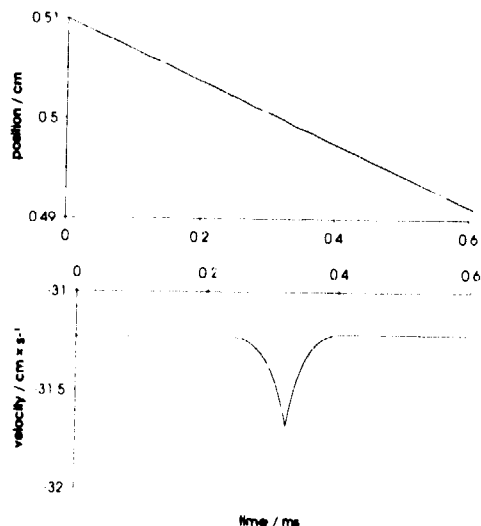


Figure 16. Calculated z position and z velocity of a particle with $R = 0.1 \mu\text{m}$ penetrating into the lower electrode sheath in the presence of a downward-directed gas flow. The following parameters were chosen: $v_i = -30 \text{ cm s}^{-1}$, $z_{gs} = 5 \text{ mm}$, $R_s = 33 \mu\text{m}$, $E(0) = 100 \text{ V cm}^{-1}$, $z(0) = 0.51 \text{ cm}$. At time $t = 0$ the particle has reached its stationary speed, the absolute value of which is larger than v_i because of gravitation. The particle is not trapped due to the large drag force.

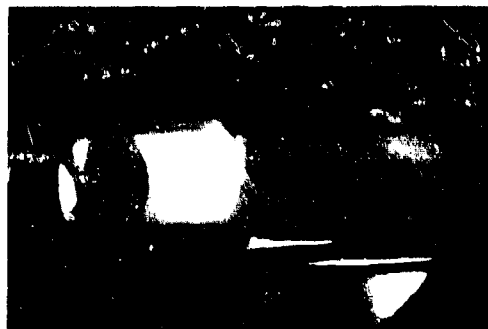


Figure 17. View of the reactor space with gas inlet through the upper electrode and heated lower electrode ($T_{he} = 68 \text{ °C}$, $T_{le} = 40 \text{ °C}$). The particle contamination is below the detection limit.

By numerical analysis of the particle dynamics it was shown that particle trapping may be understood on the basis of the 'dressed' particle model. As soon as particles grow heavier they are no longer trapped and may fall to the substrate during the process. Therefore it is necessary to keep the contamination during the process at a low level. The experimentally determined sinking speeds of particles to the substrate after turning off agree well with those calculated using Epstein's friction law for low pressures.

Acknowledgments

The authors want to thank R Einzinger, H Kausche and R Plättner for many discussions, and R Birckigt, D Falkenberg and S Korbei for assistance in the experiments and the calculations.

References

- [1] Bouchoule A, Plain A, Boufendi L, Blondeau J Ph and Laure C 1991 *J. Appl. Phys.* **70** 1991
- [2] Howling A A, Hollenstein Ch and Paris P-J 1991 *Appl. Phys. Lett.* **59** 1409
- [3] Hundhausen M and Ley L 1991 *J. Non-Cryst. Solids* **137&138** 795
- [4] Kausche H and Plättner R D 1992 *Proc. 11th E C Photovoltaic Solar Energy Conf. (Montreux)* p 195
- [5] Perrin J 1991 *J. Non-Cryst. Solids* **137&138** 639
- [6] Jellum G M, Daugherty J E and Graves D B 1991 *J. Appl. Phys.* **69** 6923
- [7] Anderson H M, Jairath R and Mock J L 1990 *J. Appl. Phys.* **67** 3999
- [8] Vepřek S, Schopper K, Ambacher O, Rieger W and Vepřek-Heijman M G J 1993 *J. Electrochem. Soc.* **140** 1935
- [9] Böhme W, Köhler W E, Römhild M, Vepřek S and Seeböck R J 1994 *IEEE Trans. Plasma Sci.* **22** at press
- [10] Hinds W C 1982 *Aerosol Technology* (New York: Wiley)
- [11] Epstein P E 1924 *Phys. Rev.* **23** 710
- [12] McCourt F R W, Beeuacker J J M, Köhler W E and Kušćer I 1991 *Nonequilibrium Phenomena in Polyatomic Gases* vol 2 (Oxford: Clarendon)
- [13] Fotiadis D I and Jensen K F 1990 *J. Crystal growth* **102** 743
- [14] Chen X and Tao X 1992 *Plasma Chem. Plasma Process.* **12** 345
- [15] Barnes M S, Keller J H, Forster J C, O'Neill J A and Coultas D 1992 *Phys. Rev. Lett.* **68** 313
- [16] Daugherty J E, Porteous R K and Graves D B 1993 *J. Appl. Phys.* **73** 1617
- [17] Vestner H and Halbritter J 1981 *Z. Naturf.* **36a** 559
- [18] Böhme W, Köhler W E and Seeböck R J 1994 to be published
- [19] Selwyn G S 1991 *J. Vac. Sci. Technol. B* **9** 3487

Real-time compositional analysis of submicrometre particles

W D Reents Jr, S W Downey, A B Emerson, A M Majsce, A J Muller, D J Siconolfi, J D Sinclair and A G Swanson

AT&T Bell Laboratories, 600 Mountain Avenue, Murray Hill, NJ 07974, USA

Abstract. A particle analyser is described that simultaneously detects and characterizes < 0.02 to $> 10 \mu\text{m}$ diameter particles independent of particle composition in real time. No previous instrument has been able to perform these functions simultaneously. Our design uses pulsed laser ablation of particles followed by time-of-flight mass spectrometric analysis of the resulting ions. The ion intensity is related to particle size at least for small particles. Thus particle size information is obtained concurrently with the other information.

1. Introduction

Particles continue to haunt semiconductor processing. Particles in plasma processes are particularly challenging. Knowing the physical and chemical properties of these particles is an important step towards preventing their formation.

Particle counting is the simplest and most widely used method of particle characterization. Light scattering, the technique of choice in plasma processing tools, is used to monitor particle position and movement but the relationship between the scattered light and the size and density of particles is not easily interpreted. Additional information, such as particle composition, is unavailable.

Several types of instruments have been described in the literature for real-time compositional analysis of particles. One type, using surface ionization, detects particles continuously [1-9]. However, only a single ion mass can be monitored and only easily ionized materials can be detected. The second type, using pulsed laser ablation, can detect a wide range of particle compositions [10, 11]. A CW laser is used to 'sense' a particle and fire the pulsed laser. A complete mass spectrum of the resulting ions from a single particle is detected with a time-of-flight mass spectrometer. The disadvantage is the CW laser: only particles $> 0.2 \mu\text{m}$ scatter sufficient light. Smaller particles are not detected.

We have built a prototype instrument for characterization of individual particles. The characterization provides both chemical composition from the complete mass spectrum of a single particle and some size information for particles at least as small as $0.02 \mu\text{m}$. This is accomplished by laser ablation of a single particle followed by time-of-flight mass spectrometric analysis of the ions characteristic of the particle's composition. The CW laser to 'sense' the particles is omitted to allow detection of particles too small to scatter sufficient light.

At present, particles have been characterized in air at atmospheric pressure. Characterization in other gases and at lower gas pressures is also possible.

2. Experimental

Several particle sources are used to calibrate and evaluate our particle analyser. A TSI model 3076 Constant Output Atomizer produces aerosols from 0.02 M aqueous solutions of CsNO_3 , RbNO_3 , and $(\text{NH}_4)_2\text{SO}_4$ with a wide particle size distribution. Two synthetic dust mixtures of particles, one containing 13% CsCl , 13% CsNO_3 , 13% RbCl , 13% NaCl , 13% KCl and 33% talc (silica and magnesium silicate) and the other containing talc and $(\text{NH}_4)_2\text{SO}_4$, are also used as particle sources. These dry sources are dispersed as powders from polyethylene bottles with stainless steel ball bearings to grind the particles. Shaking produces particle-laden air which is then drawn into the particle analyser through a capillary inlet.

Particle size distributions for the aqueous salt solutions are measured using a TSI model 3071 Electrostatic Classifier. Higher salt concentrations produce a wider size distribution and higher concentration of particles. The particles are introduced into our prototype particle analyser either directly from the atomizer or as a narrow size distribution that is isolated by passing through the TSI Electrostatic Classifier. Particle concentrations for each size are determined using a TSI model 3022 Condensation Particle Counter.

All water in these experiments is purified using a Millipore Milli-Q Plus Water system. Tap water is treated by reverse osmosis, dissolved organics removed with activated charcoal, inorganic ions further reduced to $18 \text{ M}\Omega$ resistivity with ion exchange resins, and organic material further removed with a final scavenger [12].

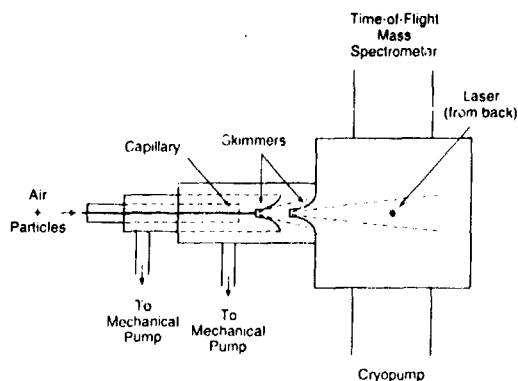


Figure 1. Schematic diagram of prototype particle analyser.

In addition, the water is irradiated with UV to destroy bacteria and decompose organic compounds.

The prototype particle analyser contains a capillary tube for particle introduction, a pulsed laser for particle ablation and ionization, and a commercially available time-of-flight mass spectrometer (Jordan Associates, CA, USA) for identification of the particle's composition. A schematic diagram of the instrument is shown in figure 1. Particles are introduced via the 0.053 cm ID fused silica capillary. The particles pass through two stages of differential pumping consisting of two skimmers (Beam Dynamics, MN, USA) with 0.1 cm ID holes. Two 30 cfm mechanical pumps provide the vacuum at each stage with a CTI Cryotorr 8 cryopump providing the $1-3 \times 10^{-5}$ Torr vacuum in the ionization region. The particles travel 15 cm from the capillary to the ion source of the time-of-flight mass spectrometer. The particles are struck with a pulse from a Lambda-Physik model EMG 202 excimer laser. The laser is operated at 10–30 Hz with 130–300 mJ of energy/pulse at 308 nm and a pulse width of 40 ns. The laser is focused with a 30 cm focal length lens to a rectangle 0.08 cm high and 0.3 cm wide. A laser power density of 1.7×10^8 W cm⁻² is achieved. The resulting ions are accelerated to 4 kV with mass separation occurring over a 1 m flight path. A secondary electron multiplier with a gain of 10^6 is used as a detector. The signal goes to a Tektronix 2440 digital oscilloscope with a 50 Ω termination. The laser trigger is used to initiate recording of mass spectra, but the background fluorescence resulting from the UV laser light is used as the time zero point. The 2048 data points are collected over the entire time range (0–25 μ s, 1–145 Daltons) or, for increased mass resolution, over a narrower time range of interest (e.g. 20–22 μ s). The time-of-flight for Cs⁺ is 21 μ s.

3. Results and discussion

We have characterized our prototype particle analyser in terms of particle size detection limit, particle detection

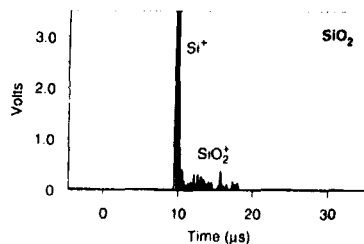


Figure 2. Mass spectrum of single silica particle from talc.

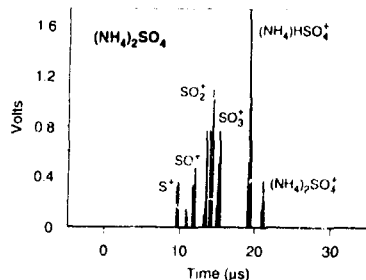


Figure 3. Mass spectrum of single ammonium sulphate particle. Particle introduced from solid mixture with talc.

efficiency, and dependence upon particle composition. We are able to detect particles having a variety of compositions and with diameters as small as 0.02 μ m. Currently, high particle densities are required for high rates of particle detection. Improvements will be made to reduce this limitation.

We have mass spectra from a variety of particle compositions. Our aim is to demonstrate the ability to detect particles regardless of composition and obtain mass spectra that are characteristic of the particle's composition. Figures 2–4 illustrate mass spectra for particles composed of SiO₂, (NH₄)₂SO₄, and RbNO₃, respectively. These spectra can be easily distinguished. Both SiO₂ and (NH₄)₂SO₄ give molecular ions whereas RbNO₃ gives only Rb⁺ (likewise CsNO₃ gives only Cs⁺). At present we have no way of distinguishing the various rubidium or caesium salts (e.g. RbCl versus RbNO₃). Note that strong ion signals can be obtained for both easily ionized material (e.g. RbNO₃) and difficult to ionize material (SiO₂). This method should be suitable for particles of any composition.

Particles over a wide size range (0.02–10 μ m diameter) have been detected. Micrometre-sized particles give intense ion signals that represent ablation of only a fraction of the particle. Small (0.02–0.1 μ m diameter) particles give weaker signals that may represent destruction of the whole particle. For small particles, there is a linear relation between particle size and ion intensity (see figure 5). The intensity for Rb⁺ is greater since only one ion is produced: there are several ions produced by (NH₄)₂SO₄ over which the total ion intensity is distributed.

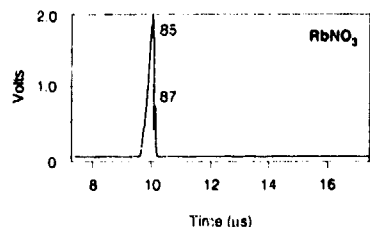


Figure 4. Expanded scale mass spectrum of RbNO_3 showing resolved $^{85}\text{Rb}^+$ and $^{87}\text{Rb}^+$ isotopes. Only Rb^+ is observed

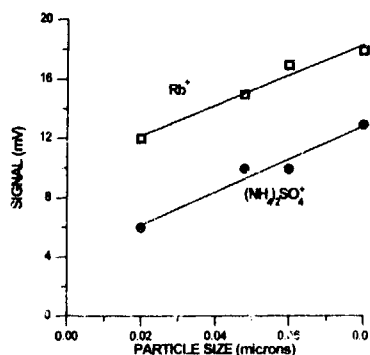


Figure 5. Dependence of ion signal on particle size for both RbNO_3 and $(\text{NH}_4)_2\text{SO}_4$ particles. The particles are size selected with a TSI electrostatic classifier and introduced into the particle analyser via the capillary tube.

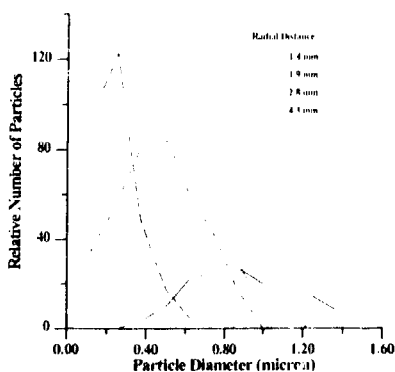


Figure 6. Size-dependent dispersion for CsNO_3 particles exiting a 0.053 cm id, 50 cm long capillary column and passing through two 0.1 cm id skimmer cones. The measurement is at a distance of 3 cm from the end of the capillary.

Particle transport into the vacuum chamber is less than optimum. Transmission through the capillary and two skimmers is evaluated by exposing a silicon wafer to our source of RbNO_3 particles. The rubidium content on two wafers, one exposed directly to the particle output and the other exposed to the output after the second

skimmer (in a vacuum chamber) is measured with an ion chromatograph. A comparison shows that only 9% of the particles are transmitted through the system.

Size-dependent particle dispersion significantly reduces particle detection and causes size discrimination. We have measured the dispersion after the particles have passed through the second skimmer at a distance of 3 cm from the skimmer. Figure 6 clearly shows a significant size-dependent dispersion. Any compositional analysis of unknown aerosols will be size selective. The centre of the particle beam will be enriched in larger particles, whereas the smaller particles will predominate at some distance from the centre dependent upon the distance travelled. Clearly, the distance between the capillary and the laser focal point is important to particle detection efficiency.

Presently, particle concentrations of $\sim 1 \times 10^8$ per ft^3 are required for reasonable detection rates. Decreasing the distance between the capillary and the laser focal point will greatly enhance the particle count rate. A larger laser spot size and faster repetition rate laser will also improve the count rate.

4. Plasma particles

The current system is amenable to sampling high pressure plasmas. For low pressure plasmas, the skimmer cone should be placed in the plasma chamber so as to directly sample plasma particles. We have not interfaced our instrument to a plasma reactor yet, since we are still optimizing the design.

The current method, without presensing particles with a continuous laser, provides the ability to detect and analyse individual particles as small as $0.02 \mu\text{m}$. We feel that even smaller particles can be detected, although this has not been attempted as yet. This technique should be useful for particle diagnosis in plasma reactors. The high concentration of particles within plasmas is ideal for a system without CW laser 'sensing' of particles.

5. Conclusions

We have demonstrated the ability to simultaneously detect and analyse individual particles at least as small as $0.02 \mu\text{m}$. The ability to evaluate particle size allows further characterization of the ensemble of particles to be analysed. Although this technique has not been applied to plasma particle analysis, it should nevertheless work with only minor modifications.

References

- [1] Sinha M P 1990 *Particles in Gases and Liquids* vol 2 ed K L Mittal (New York: Plenum) p 210
- [2] Davis W D 1973 *J. Vac. Sci. Technol.* **10** 278
- [3] Davis W D 1977 *Environ. Sci. Technol.* **11** 587-92
- [4] Davis W D 1977 *Environ. Sci. Technol.* **11** 593-6
- [5] Stoffers J J 1981 *Int. J. Mass Spectrom. Ion Phys.* **40** 217-22

- [6] Stoffels J J 1981 *Int. J. Mass Spectrom. Ion Phys.* **40** 223-4
- [7] Stoffels J J and Lagergren C R 1981 *Int. J. Mass Spectrom. Ion Phys.* **40** 243-54
- [8] Wacker J F 1989 *Proc. American Association for Aerosol Research* p 276
- [9] Myers R L and Fite W L 1975 *Environ. Sci. Technol.* **9** 334-6
- [10] Ramsey J M 1992 private communications
- [11] McKeown P J, Johnston M V and Murphy D M 1991 *Anal. Chem.* **63** 2069-73
- [12] Siconolfi D J, Frankenthal R P and Sinclair J D 1992 *Proc. 2nd Int. Symp. on Cleaning Technology in Semiconductor Device Manufacturing* ed J Ruzyllo and R E Novak (Pennington, NJ: The Electrochemical Society) pp 34-40

Water induced particle formation in the ion chemistry of silane

W D Reents, Jr and M L Mandich

AT&T Bell Laboratories, Murray Hill, New Jersey 07974, USA

Received 28 December 1993; in final form 3 February 1994

Abstract. Potential particle-forming reactions of hydrogenated silicon cations with silane and disilane, in the presence and absence of water, are summarized. The reactions are studied in the ion trap of a Fourier transform mass spectrometer at 10^{-7} – 10^{-5} Torr. Cations react sequentially with silane to produce larger silicon-containing ions. In general, reaction rates decrease with increasing number of silicon atoms in the ion; no ions containing more than six silicon atoms are formed in reactions with pure silane. Reaction with disilane produces larger silicon-containing ions; reaction rates decrease with increasing number of silicon atoms in the cation. The largest ion produced is larger than for the silane system but still contains less than nine silicon atoms. There is insufficient reactivity for hydrogenated silicon cations in pure silane or disilane to produce macroscopic particles. Mixtures of silane or disilane containing 7% water, however, significantly enhance the growth of ions. In the limit of our measurements, the reactions in both silane and disilane do not terminate.

1. Introduction

Silicon-containing ions are readily formed in silane plasmas under conditions used to deposit silicon films. Since some ion/molecule reactions go much faster than neutral reactions, ions may be responsible for rapid gas-phase particle formation within the plasma [1–6]. Veprek *et al* [7] have evidence for clustering via neutral species. Perrin *et al* [8] and Howling *et al* [9] determined that negative ion chemistry leads to particle formation under some conditions. Kushner [10] has modelled positive ion chemistry in plasmas to understand their effect on particle formation, but the kinetic data required for modelling was sparse prior to our studies. We have examined the positive ion chemistry of silane, starting with the monosilicon ions through to the final reaction, to determine whether (1) positive ions are the initiators of particle growth and (2) they provide detailed kinetic information for modelling studies. In agreement with Howling *et al*, we found that cations terminate their growth at small cluster sizes.

Disilane is formed in silane plasmas and, depending on plasma conditions, may represent several per cent of the neutral species present [7–10]. Since disilane has a silicon-silicon bond that is weaker than the silicon-hydrogen bond [11], more extensive ion/molecule chemistry than that observed for silane occurs. We have also examined the ion chemistry of disilane through to the terminating reactions.

We have also examined the ion chemistry of silane and disilane in the presence of water. Water is the most common background constituent in vacuum chambers and its concentration increases during heating, such as

when a plasma is ignited. We have found that water has a profound effect on the ion chemistry; it must be seriously considered in all plasma reactions.

2. Experimental

The ion chemistry of silane and disilane is examined in the ion trap of a modified Extrel FTMS-1000 Fourier transform mass spectrometer (FTMS) with an Ionspec[®] Omega data system (for more information on FTICR see [12–14]). The FTMS ion trap is an electromagnetic bottle that stores ions in the presence of neutral reagents. Storage times can be varied from 0.002 to >99 s which allows considerable ion chemistry to occur. Ion-molecule chemistry is monitored by the mass spectrometer capabilities inherent in the ion trap technique as described below. Ions are confined in the *X-Y* directions by the magnetic field and in the *Z* direction by the electrostatic potential on the trapping plates. Figure 1 is a schematic diagram of the trapped ion cell. Ion motion within the cell is circular in the *X-Y* direction (perpendicular to the magnetic field) with a cyclotron frequency related to mass:

$$m/z = A/f + c \quad (1)$$

where m/z is the mass-to-charge ratio, f is the cyclotron frequency, A is a constant proportional to the magnetic field strength and c is a constant related to the ion density and trapping plate voltage. There is also ion motion in the *Z* direction (parallel to the magnetic field) at a lower frequency than the cyclotron frequency. The ions are formed, trapped and detected within the trap-

FTMS TRAPPED ION CELL

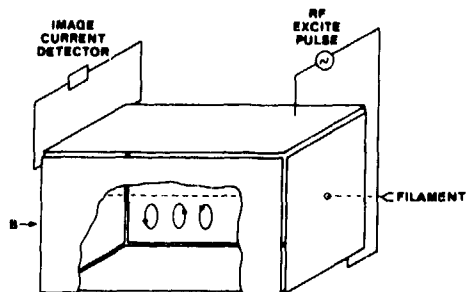


Figure 1. Schematic diagram of a cubic trapped ion cell in a Fourier transform mass spectrometer. The trapped ion cell is located in a 2.97 T magnetic field designated by B. The plates perpendicular to the magnetic field electrostatically confine the ions along the magnetic field axis with a potential of 1–3 V. Two opposite plates are used for the RF excitation to coherently excite the ion cyclotron motion for detection. The remaining two plates are detection plates for receiving the induced charge from the coherent ion motion.

ped ion cell. During the ion trapping time the ions collide, and possibly react, with molecules in the vacuum chamber. Both the reactant ions and the product ions remain trapped in the cell, allowing further reaction if desired, until the reaction is quenched by taking a mass spectrum of the entire ion ensemble in the cell. This is accomplished by coherent excitation of the cyclotron motion of the ions by a swept RF frequency pulse (applied to the transmitter plates) that covers the entire frequency range of the trapped ions in the cell. This is typically from 3 MHz ($m/z = 15$) to 150 kHz ($m/z = 300$). After this excitation pulse, the current induced in the detect plates by the coherent motion is digitized, Fourier transformed, and then the resulting frequency spectrum calibrated in terms of mass-to-charge ratios. By this technique, the intensity of every ion in the cell is determined simultaneously. If a sufficiently long detection time is used, high mass resolution is obtained ($> 10,000$). Mass resolution is defined as $m/\Delta m$ where m is the measured mass of the ion and Δm is the width of the peak at half height. An additional feature is the ability to accurately measure the ion's mass and thereby assign elemental composition. Since there are few elements present in the system, this might seem unnecessary. However, a reaction with background moisture occurs to form products containing an oxygen atom. This will cause overlap of two ions with different elemental compositions, e.g., D_8 versus ^{16}O ($\Delta m = 0.117$ amu) or $^{16}O_2$ versus SiD_2 ($\Delta m = 0.015$ amu). High mass resolution coupled with accurate mass measurement is used to confirm the elemental composition of each ion detected.

Double resonance ejection is a technique for the removal of an ion from the trapped ion cell. Ejection is accomplished by applying to the excitation plates an RF signal whose frequency matches the cyclotron frequency

of the ion. In this manner, either removal of ions of a single mass or of all ions except for a single mass is possible. The reaction chemistry of the remaining ions in the trap is easily followed by increasing the time between ion ejection and ion detection (trapping time). To evaluate the reaction sequence for ions of a particular mass, these ions are ejected and the resulting mass spectrum (double resonance spectrum) is compared to a mass spectrum without ion ejection. Product ions of the ejected ions will be absent in the double resonance spectrum. Alternatively, all ions except those of the mass to be monitored are ejected. Although this can be more difficult to accomplish, the mass spectra only show product ions for the reactant ions of a single mass.

Silane- d_4 (MSD Isotope Co, 99.7 at.%), disilane- d_6 (Cambridge Isotope Laboratories, 98 at.%), and D_2O (MSD Isotope Co, 99.7 at.%) are used without further purification. Isotopic purity is confirmed by mass spectrometric analysis. Introduction of D_2O required a delay (1–2 h) until background protiated water had been replaced with deuterated water. The effective isotopic purity of D_2O in the trapped ion cell is 95–98 at.% for most experiments.

When spectra are obtained at different reaction times, the pseudo first-order reaction kinetics can be monitored. Figure 2 presents ion intensity plotted as a function of time for the reaction of SiD^+ and its product ions with SiD_4 . Since the total number of ions contained in the ion trap is limited (less than 10^6), the reactant gas is in relatively infinite supply since there is a constant flow through the cell of new gas from an external reservoir via a variable leak valve. Thus, the ion/molecule reaction kinetics may be evaluated easily; the pseudo first order rate constant may be converted to an absolute rate constant by incorporating the absolute

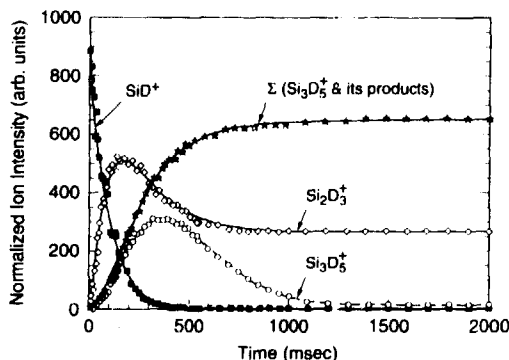


Figure 2. The time evolution for the intensity of SiD^+ and its product ions in the presence of SiD_4 . SiD^+ is formed by electron impact on SiD_4 in less than 5 ms. The population of SiD^+ is contained in the ion trap allowing it to collide and react with the ambient SiD_4 . All product ions are retained within the trap, undergoing their own collisions with SiD_4 . The time evolution is sampled at discrete times and plotted. The full curves through the data points represent kinetic fits to the data with the product ion fits constrained by the rate constant for the decay of the reactant ion.

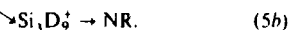
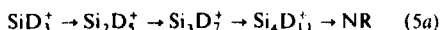
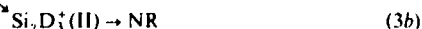
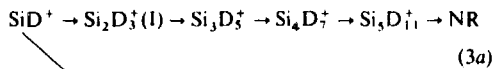
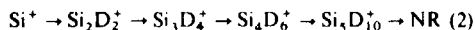
concentration (pressure) of the reactant gas [15]. In this manner the reaction rates for all the ions may be obtained. The FTMS is operated at 2.97 T with typical conditions as follows: trapping plates voltage, 1–3.5 V; RF chirp rate, $6000 \text{ Hz } \mu\text{s}^{-1}$; RF chirp intensity, 120–240 $\text{V}_{\text{p-p}}$; reactant gas pressures, $1-100 \times 10^{-7}$ Torr; electron ionization energy, 12–80 eV. The initial ion kinetic energy is limited by the trapping potential (3.5 V maximum), but is quickly thermalized to the gas temperature (300 K) by non-reactive collisions with silane.

Phase space theory (PST) is used to compare critical transition state energies from *ab initio* calculations by Raghavachari [16–19] to values derived from the reaction kinetics measured in the FTMS trapped ion cell. The excellent agreement (typically within 3 kcal mol^{-1}) gives strong support to the accuracy of the calculated transition state energies as well as the proposed reaction mechanism. The details of the calculations will not be described; they may be found elsewhere [16–19]. However, the energetics of the microscopic reaction pathways derived from experiment and PST calculations permit extrapolation of the experimental data for the pure silane and pure disilane systems to higher pressures so as to compare with plasma reactor pressures.

3. Results and discussion

3.1. Silane reactions

Reactions of Si_xD_y^+ with silane proceed to terminal (unreactive) cations containing less than 7 silicon atoms. Sequential ion/molecule reactions with silane are shown in equations (2)–(5). For conciseness, the explicit neutral reagent, SiD_4 , and neutral products are not shown; only the ionic reactants and products are given. The reaction rates are illustrated in figure 3 and listed in table 1 [20–25]. Although the initial reactions proceed near the collision rate (except for SiD_2^+), the reaction rates decrease with increasing number of silicon atoms until a non-reactive species terminates the reaction sequence. This decrease in reaction rate with number of silicon atoms in the reacting ion is apparent in figure 3. The largest ion produced from each initial reactant ion is shown in table 2. Clearly, positive ion chemistry is not responsible for gas phase particle growth in pure silane plasmas, in agreement with the findings of Howling *et al* [9]:



Raghavachari has used accurate *ab initio* calculations to elucidate the structures of all of the ions and reaction

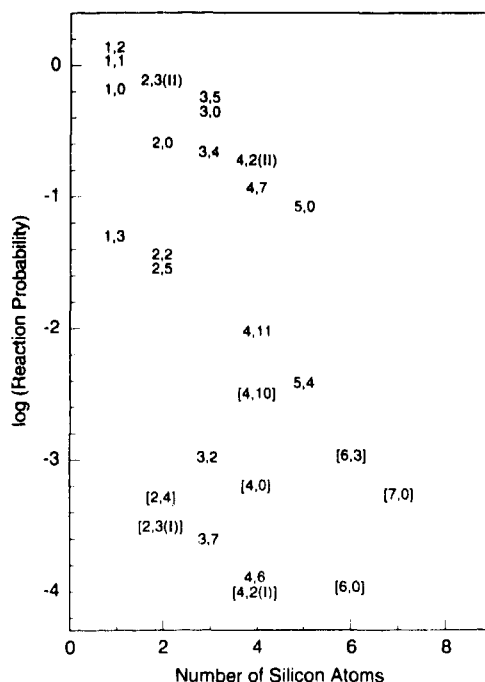
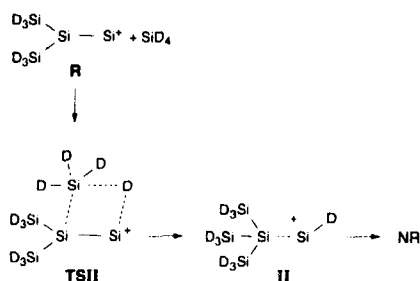
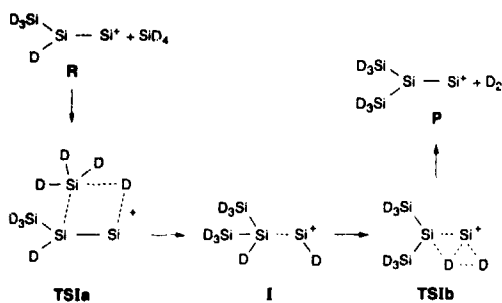


Figure 3. Plot of the absolute pseudo first-order reaction rates for Si_xD_y^+ with SiD_4 . The paired numbers x, y represent number of silicon atoms and deuterium atoms, respectively, in the reactant ion. Paired numbers in brackets represent unreactive ions whose position indicates the upper limit of reaction rate. This graph illustrates the decreasing reactivity of Si_xD_y^+ with increasing x .

intermediates involved in equations (2)–(5). From his calculations, we can understand in detail why reaction of unsaturated silicon cations with silane leads to unreactive ions. One reason, typified by $\text{Si}_5\text{D}_{10}^+$, is that the reactive centres become saturated, resulting in a large energetic barrier to further reaction. The reactions leading to $\text{Si}_5\text{D}_{10}^+$ involve three sequential additions of silane to Si^+ (equation (1)), with each addition followed by 1,2 elimination of D_2 , to produce Si_4D_6^+ (see scheme 1 for final reaction step). Subsequent reaction of Si_4D_6^+ with silane produces the intermediate $\text{Si}_5\text{D}_{10}^+$ (structure II, scheme 2) which, lacking deuteriums on neighbouring silicon atoms, cannot undergo 1,2 elimination of D_2 . This $\text{Si}_5\text{D}_{10}^+$ intermediate is observed, however, because it can be collisionally stabilized. The second reason, typified by Si_3D_7^+ , is the formation of internal hydrogen (deuterium) bonds. The internal hydrogen bonding in Si_3D_7^+ is sufficient to stabilize it from further reaction, except for simple silane attachment to produce $\text{Si}_4\text{D}_{11}^+$. The calculated transition state energies for reaction of Si_3D_7^+ with and without hydrogen bonding reveal the effects of that stabilization (figure 4); further reaction would be exothermic only if hydrogen bonding did not occur.



3.2. Disilane reactions

The reactions of $\text{Si}_{1-2}\text{D}_0^+$ in pure disilane lead to unsaturated ions containing less than nine silicon atoms. The reaction rates are illustrated in figure 5 and listed in table 1 [15]. As for the silane system, reaction rates decrease with increasing number of silicon atoms until a

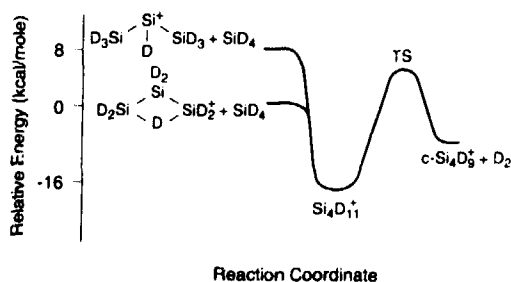


Figure 4. Schematic energy profile for reaction of Si_3D_7^+ with SiD_4 . Both the higher energy open form and the lower energy cyclic form of Si_3D_7^+ are depicted on the left. The transition state to form products lies 2 kcal mol⁻¹ below the high energy form but 6 kcal mol⁻¹ above the low energy form actually present in the reaction. The 8 kcal mol⁻¹ of hydrogen bonding stabilization is sufficient to prevent further reaction (except collisional stabilization of $\text{Si}_4\text{D}_{11}^+$, an unreactive product). Taken from [19]. Note that substitution of deuterium for protium has an insignificant effect on relative energies.

Table 1. Rate constants for reaction of Si_nD_m^+ with SiD_4 and Si_2D_6 .

Reactant ion	Rate constant ($\times 10^{10}$) (cm ³ mol ⁻¹ s ⁻¹) ^a	
	with SiD_4	with Si_2D_6
Si^+	6.9 ± 0.3	20 ± 2
SiD^+	12 ± 2	19 ± 4
SiD_2^+	21 ± 3	40 ± 6
SiD_3^+	0.6 ± 0.1	6 ± 1
Si_2^+	2.5 ± 0.4	14 ± 2
Si_2D^+	—	10 ± 2
Si_2D_2^+	0.32 ± 0.04	4.6 ± 0.5
Si_2D_3^+ (I)	7.5 ± 1.5	5.8 ± 1.7
Si_2D_3^+ (II)	< 0.003	< 0.004
Si_2D_4^+	< 0.005	3.6 ± 0.4
Si_2D_5^+	0.28 ± 0.10^b	7 ± 1
Si_2D_6^+	—	9.5 ± 1.5
Si_3^+	4.8 ± 0.7	—
Si_3D^+	—	14 ± 2
Si_3D_2^+	0.010 ± 0.003	0.02 ± 0.01
Si_3D_3^+	—	2.7 ± 0.3
Si_3D_4^+	1.7 ± 0.3	9.4 ± 0.2
Si_3D_5^+	5 ± 1	8 ± 4
Si_3D_6^+	—	3.9 ± 0.4
Si_3D_7^+	0.0023 ± 0.0004^a	0.34 ± 0.03
Si_3D_8^+	—	0.64 ± 0.21
Si_3D_9^+	—	3.5 ± 1.5
Si_4^+	< 0.006	—
Si_4D_2^+	1.8 ± 0.3	—
Si_4D_3^+	—	< 0.05
Si_4D_4^+	—	2.2 ± 0.8
Si_4D_5^+ (I)	—	0.13 ± 0.02
Si_4D_5^+ (II)	—	13 ± 4
Si_4D_6^+	0.0010 ± 0.0003^b	0.55 ± 0.11
Si_4D_7^+	1.1 ± 0.8^c	2.7 ± 0.7
Si_4D_8^+	—	0.84 ± 0.14
Si_4D_9^+	—	< 0.002
$\text{Si}_4\text{D}_{10}^+$	—	< 0.03
$\text{Si}_4\text{D}_{11}^+$	—	0.07 ± 0.02
Si_5^+	0.8 ± 0.1	—
Si_5D_4^+	0.036 ± 0.009	—
Si_5D_6^+	—	0.19 ± 0.04
Si_5D_7^+ (I)	—	< 0.005
Si_5D_7^+ (II)	—	0.04 ± 0.01
Si_5D_8^+	—	0.90 ± 0.27
Si_5D_9^+	—	1.5 ± 0.5
$\text{Si}_5\text{D}_{10}^+$	—	0.054 ± 0.001
$\text{Si}_5\text{D}_{11}^+$	—	< 0.005
$\text{Si}_5\text{D}_{13}^+$	—	< 0.005
Si_6^+	< 0.001	—
Si_6D_2^+	< 0.01	—
Si_6D_3^+	< 0.01	—
Si_6D_6^+	—	0.04 ± 0.03
Si_6D_8^+	—	0.8 ± 0.3
$\text{Si}_6\text{D}_{10}^+$	—	0.10 ± 0.05
$\text{Si}_6\text{D}_{11}^+$	—	< 0.004
$\text{Si}_6\text{D}_{12}^+$	—	< 0.004
Si_7^+	< 0.005	—
$\text{Si}_7\text{D}_{11}^+$ (I)	—	< 0.009
$\text{Si}_7\text{D}_{11}^+$ (II)	—	0.02 ± 0.01
$\text{Si}_7\text{D}_{12}^+$	—	< 0.002
$\text{Si}_8\text{D}_{13}^+$	—	< 0.1

^a Rates exclude isotope exchange reactions.

^b Measured at silane-d₄ pressure of 2.0×10^{-7} Torr.

^c Measured at silane-d₄ pressure of 1.0×10^{-6} Torr.

^d Measured at silane-d₄ pressure of 2.0×10^{-6} Torr.

^e Measured at silane-d₄ pressure of 5.6×10^{-6} Torr.

Table 2. Terminal ions in the silane and disilane system.

Neutral reactant	Initial reactant ion						
	Si ⁺	SiD ⁺	SiD ₂ ⁺	SiD ₃ ⁺	Si ₂ ⁺	Si ₂ D ⁺	Si ₂ D ₆ ⁺
SiD ₄	Si ₅ D ₁₀ ⁺	Si ₅ D ₁₁ ⁺	Si ₂ D ₄ ⁺	Si ₃ D ₉ ⁺	Si ₄ D ₆ ⁺	—	—
Si ₂ D ₆	Si ₇ D ₁₂ ⁺	Si ₈ D ₁₃ ⁺	Si ₇ D ₁₂ ⁺	Si ₅ D ₁₃ ⁺	Si ₇ D ₁₀ ⁺	(Si ₄ D ₅ ⁺) ^a	Si ₅ D ₁₃ ⁺

^a Poor signal-to-noise prohibited evaluation of this reaction sequence beyond Si₄D₅⁺.

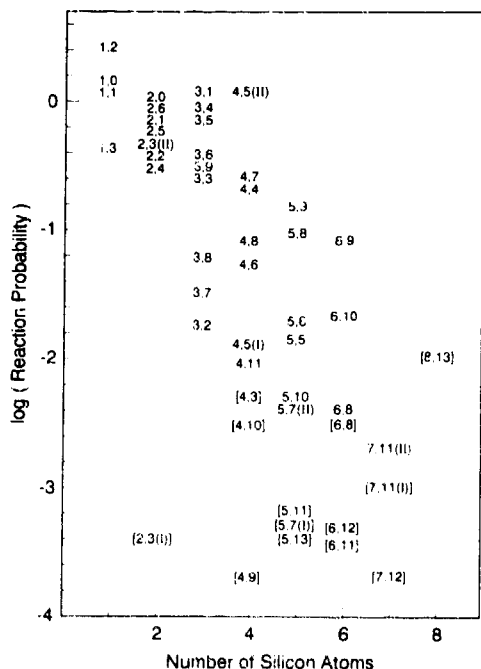


Figure 5. Plot of the absolute pseudo first-order reaction rates for Si_xD_y⁺ with Si₂D₆. The paired numbers *x*, *y* represent number of silicon atoms and deuterium atoms, respectively, in the reactant ion. Paired numbers in brackets represent unreactive ions whose position indicates the upper limit of reaction rate. This graph illustrates the decreasing reactivity of Si_xD_y⁺ with increasing *x*.

terminal structure is reached. The reactions terminate for similar reasons as the silane system. As shown in table 2, the reactions proceed to larger terminal ions than for the silane system.

A comparison of the energetics for the reactions of Si₂D₅⁺ with silane and disilane demonstrates the reason for further reaction in the disilane system. Figures 6 and 7 illustrate the transition state energies for reaction of Si₂D₅⁺ with silane and disilane, respectively. The energy of the transition state, *TS*, is nearly endoergic with the reactant energy for the silane system. Reaction of Si₂D₅⁺ with disilane, in contrast, involves no transition state energy higher than the product energy. The energy barrier for the silane system is 0.7 kcal mol⁻¹ lower than

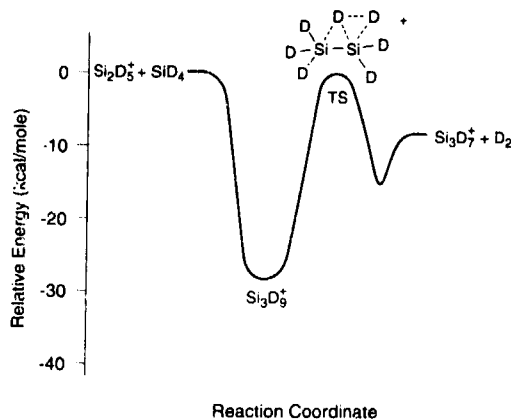


Figure 6. Schematic energy profile for reaction of Si₂D₅⁺ with SiD₄. Note that the energy of the transition state leading to product formation, *TS*, is 0.7 kcal mol⁻¹ lower than the energy of the reactants. Taken from [19]. Note that substitution of deuterium for protium has an insignificant effect on relative energies.

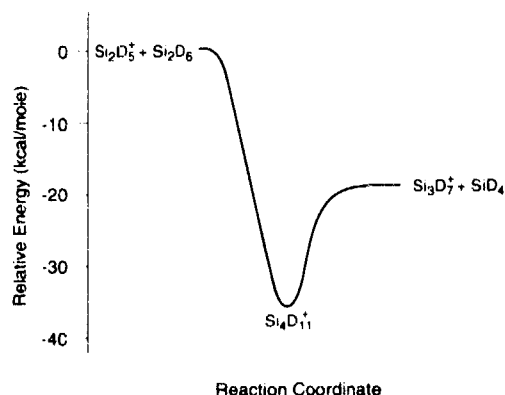


Figure 7. Schematic energy profile for reaction of Si₂D₅⁺ with Si₂D₆. The transition states (not depicted) have not been calculated but are believed to lie well below the energy of the reactants. This belief is supported by the high measured reaction efficiency (60%): Taken from [19, 26]. Note that substitution of deuterium for protium has an insignificant effect on relative energies.

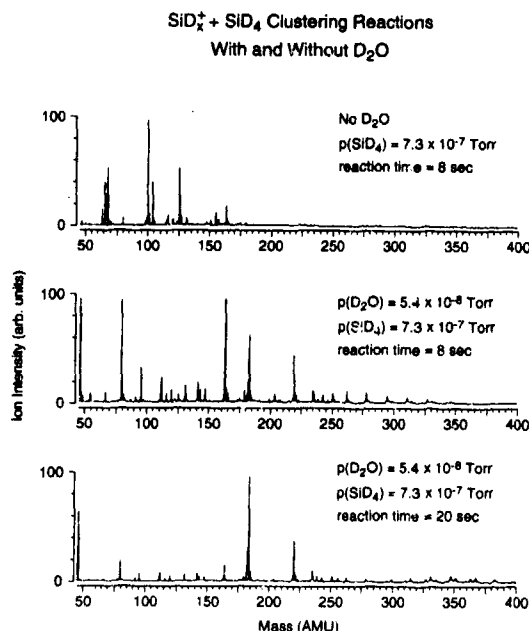


Figure 8. The upper mass spectrum illustrates the extent of ion/molecule reactions in pure silane. Additional reaction time does not alter the mass spectrum. The middle mass spectrum illustrates the extent of reaction under the same conditions as the upper figure plus addition of 7% water. The lower mass spectrum illustrates that additional reaction time in the presence of water results in formation of larger ions. There is no evidence for growth to cease. Note, however, that some ions in the lower two figures do not react further.

the reactant energy whereas the energy barrier for the disilane system is 19 kcal mol⁻¹ lower than the reactants. This difference in energy barriers is reflected in the reaction rates; reaction with silane is 5% efficient whereas reaction with disilane is 60% efficient.

Lower reaction barriers for the disilane system, compared with the silane system, explain why the disilane reaction sequences proceed several more steps before terminating. They do terminate, however, at sizes far smaller than observable particles, preventing particle growth via positive ion chemistry in a pure disilane plasma.

3.3. Water-enhanced reactivity of silane and disilane

Addition of water to either silane or disilane sufficiently alters the positive ion chemistry so as to allow unrestrained growth of positive ions containing both silicon and oxygen [26]. The chemistry is of Si_xD₃⁺ with neutral silane or disilane and with neutral water. No ions from water are involved. Figure 8 compares a mass spectrum for pure silane ion chemistry with a mass spectrum of 7% water in silane. Whereas pure silane chemistry terminates at *m/z* = 162, the silane/water mixture con-

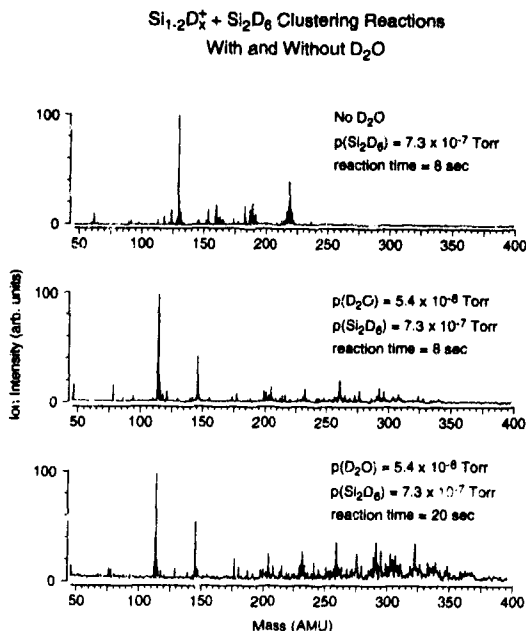
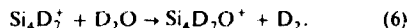


Figure 9. The upper mass spectrum illustrates the extent of ion/molecule reactions in pure disilane. Additional reaction time only shows the slow appearance of an Si₆D₃⁺ at mass 250. The middle mass spectrum illustrates the extent of reaction under the same conditions as the upper figure plus addition of 7% water. The lower mass spectrum illustrates that additional reaction time in the presence of water results in formation of larger ions. There is no evidence for growth to cease. Note, however, that some ions in the lower two figures do not react further. A comparison of this lower figure with that of figure 8 shows that a greater variety of masses are present.

tinues unabated beyond *m/z* = 400. This additional reactivity is even more pronounced for disilane (figure 9) for conditions similar to those for silane. This additional reactivity in silane can be traced to one key ion, Si₄D₃⁺. The intensity of all the high mass ions are reduced due to ejection of Si₄D₃⁺ from the trapped ion cell (see figure 10). The high mass ions do not completely disappear since, in this experiment, only the ²⁸SiD₃⁺ isotope has been ejected; the Si₄D₃⁺ containing one ²⁹Si or ³⁰Si atom, representing roughly 30% of the Si₄D₃⁺ ion population, remain. The critical change in the chemistry involves reaction with D₂O:



In subsequent reactions, the cations react with either silane or water to continue the ion growth. Without the presence of water, the sequence would terminate on the next reaction with silane:



These competing pathways produce larger ions with a range of oxygen content. Due to the similarity in mass between SiD₂ and O₂ (both nominally 32 amu), there

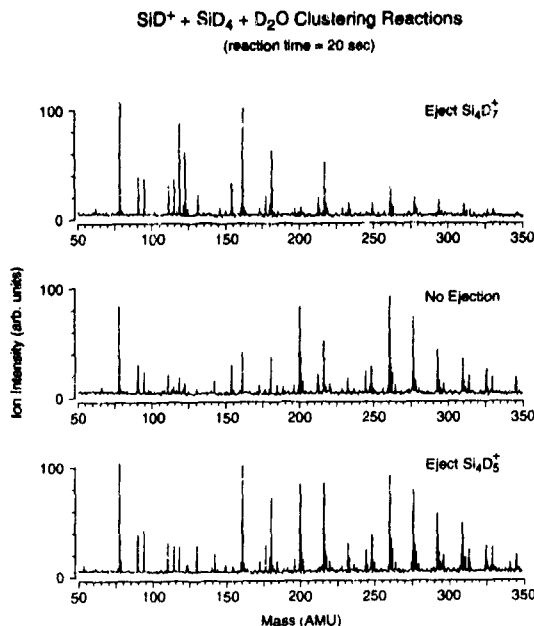


Figure 10. These mass spectra illustrate the effects of removing selected ions from the trapped ion cell prior to reaction. The middle mass spectrum is indicative of the ion population prior to selected ion ejection. The upper mass spectrum illustrates the loss of intensity for all high mass ions due to ejection of $^{28}\text{Si}_4\text{D}_7^+$. The lower mass spectrum illustrates that the higher mass ion intensities are unaffected by removal of $^{28}\text{Si}_4\text{D}_5^+$. Only the ions leading to the formation of $^{28}\text{Si}_4\text{D}_7^+$, starting with SiD^+ , and its product ions, are responsible for all of the high mass ions. Note that in the upper mass spectrum, a fraction of the high mass ion intensity remains. This results from the unejected Si_4D_7^+ with one ^{28}Si or ^{30}Si present. Subsequent isotope exchange with $^{28}\text{SiD}_4$ results in typical silicon isotope distributions.

are ions with different elemental compositions for the same mass. For example, $m/z = 218$ consists of both $\text{Si}_4\text{D}_5\text{O}_2^+$ and $\text{Si}_2\text{D}_7\text{O}_2^+$.

The ubiquitous presence of moisture in vacuum chambers makes its involvement in gas phase chemistry plausible. When it is considered that igniting the plasma also heats the vacuum chamber, a sudden evolution of copious amounts of water is to be expected. These events coupled with the ion chemistry described above make moisture's involvement in the formation of particles quite credible.

3.4. Effect of high pressure on ion/molecule reactions

The ion chemistry in silane plasmas at approximately 1 Torr pressure may be deduced in part from our low pressure (10^{-7} – 10^{-5} Torr) studies. Reaction at low pressure involves competition between two reaction pathways; addition of silane (or disilane) followed by loss of a neutral molecule (typically D_2 or SiD_4 , respectively) versus simple attachment of silane (or disilane).

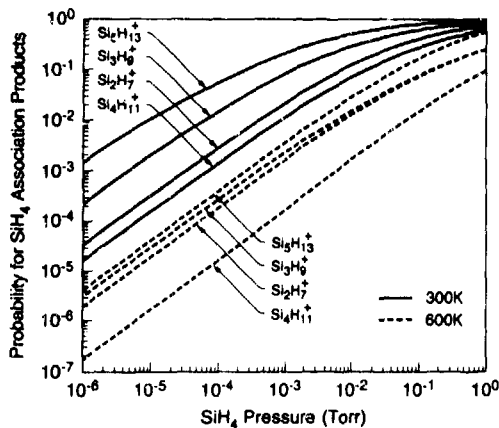


Figure 11. Formation probabilities of all of the silane attachment products for SiH_4^+ and its product ions as a function of silane pressure at reaction temperatures of 300 K and 600 K. Values are based upon phase space calculations [24] using *ab initio* calculated structures and bonding energies [19].

The attachment reaction requires collisional stabilization to remove excess energy; thus there is a strong pressure and temperature dependence for this reaction. Formation of attachment products at 1 Torr occurs with greater efficiency and for smaller ions than under our low pressure conditions. Figure 11 illustrates this effect for the attachment products of SiH_4^+ and its product ions. At room temperature, the attachment approaches 100% efficiency at a Torr whereas at 600 K it is approximately 10–50% efficient. Attachment of a second silane (or disilane) molecule is far less efficient; its binding energy is significantly reduced relative to the binding energy of the first molecule. The reactions will still terminate at small sizes.

3.5. Extrapolation to actual plasma conditions

Can cation/molecule chemistry produce a particle of sufficient size that it will spontaneously grow within a silane plasma? Competing against the growth is loss of the cation by ambipolar diffusion or charge neutralization. However, as pointed out by Perrin *et al* [8], although trapped particles have a negative charge, a positively charged particle could be neutralized and then capture an electron. As a negatively charged particle, it would be trapped in the plasma, allowing sufficient time for growth to observable sizes. To what size can a particle grow prior to removal from the plasma and is this of sufficient size to allow rapid neutralization and reionization? We can answer this question by using typical plasma conditions and extrapolating the ion chemistry we have observed. The relevant plasma conditions are: 0.1 Torr silane, E/P of 100 V Torr $^{-1}$ cm $^{-1}$, electron flux density of 10^{15} electron cm $^{-2}$ s $^{-1}$, ambipolar diffusion of 2000 cm s $^{-1}$ for SiH^+ , and a maximum diffusive travel distance of 1 cm [6, 10]. Note that the

ambipolar diffusion is inversely proportional to ion mass; the diffusion will slow as the particle growth proceeds. The relevant ion chemistry considerations are: reaction efficiency with silane of 1%, reaction efficiency with water of 100%, water concentration of 10^{-3} Torr. Assuming these reaction efficiencies continue beyond our observation range, there will be 10^5 reactive collisions per second. Under these conditions, it will take 10 ms to produce an ion of mass $\sim 23\,000$ (average of 23 amu for either SiH_2^+ and O attachment). This ion will have moved 0.15 cm due to ambipolar diffusion. If reaction ceases, electron recombination will occur in 11 ms with an additional 11 ms required for electron capture. With a diffusion velocity of 2.4 cm s^{-1} , there is insufficient time for loss from the plasma. A water pressure of 10^{-3} Torr lasting $< 1 \text{ s}$ is not unreasonable; the heat from the plasma will rapidly desorb water from the wafer and surrounding chamber. As to whether the ion/molecule reactions will proceed to 23 000 amu with equal reaction efficiency is unknown. However, we do observe an increase in reaction efficiency upon increasing the gas pressure from 10^{-6} to 10^{-5} Torr. The reaction may be even more efficient than stated at 0.1 Torr. Note that although our studies have involved primarily perdeuterated systems, the perprotiated systems have similar reaction rates and identical reaction products. Thus, the scenario described here is plausible under silane plasma conditions.

The presence of vibrationally excited silane in the plasma will alter the chemistry to some extent. We have examined reactions of ions in various excited states [21]. The low energy present in vibrational states ($< 6 \text{ kcal mol}^{-1}$) will be effective in making an unreactive ground state ion reactive only if there is a great excess of energy compared with the reaction barrier; otherwise the reaction is inefficient and is not competitive with efficient cooling by the silane. This, in fact will not aid the particle formation process as demonstrated by the reaction of Si_2D_2^+ with disilane. Having disilane as a reaction partner lowers the reactant barrier, just as if the ion had excess vibrational energy for reaction with silane. Although the disilane reaction proceeds further than the silane system, it is still halted at small ion sizes. Thus vibrationally excited ions will not significantly extend the ion growth.

4. Conclusions

The gas phase ion chemistry of either pure silane or pure disilane terminate at small ions containing less than 7

silicon atoms and nine silicon atoms respectively. Positive ion chemistry in silane plasmas cannot lead to particles. Addition of water overcomes the kinetic barrier for certain larger ions, allowing unabated ion chemistry. The ubiquitous presence of water in vacuum chambers makes it a plausible initiator for particle formation in silane plasmas.

References

- [1] Eversteijn F C 1971 *Phillips Res. Rep.* **26** 134
- [2] Murthy T U M S, Miyamoto N, Shimbo M and Nishizawa J 1976 *J. Crystal Growth* **33** 1
- [3] Spears K G, Robinson T J and Roth R M 1986 *IEEE Trans. Plasma Sci.* **14** 179
- [4] Ho P and Breiland W G 1984 *Appl. Phys. Lett.* **44** 51
- [5] DeJoseph, Jr C A, Haaland P D and Garscadden A 1986 *IEEE Trans. Plasma Sci.* **14** 165
- [6] Chatham H and Gallagher A 1985 *J. Appl. Phys.* **58** 159
- [7] Veprek S, Schopper K, Ambacher O, Rieger W and Veprek-Heijman M G J 1994 *J. Electrochem. Soc.* at press
- [8] Perrin J, Lloret A, de Rosny G and Schmitt J P M 1984 *Int. J. Mass Spectrom. Ion Processes* **57** 249
- [9] Howling A A, Saisonens L, Dorier J-L and Hollenstein Ch 1993 *J. Phys. D: Appl. Phys.* **6** 1003
- [10] Kushner M J 1991 *J. Appl. Phys.* **63** 2532
- [11] Curtiss L A, Raghavachari K, Deutsch P W and Pople J A 1991 *J. Chem. Phys.* **95** 2433
- [12] Buchanan M V and Hettich R L 1993 *Anal. Chem.* **65** 245A
- [13] Dunbar R C 1992 *Mass Spectrom. Rev.* **11** 309
- [14] Marshall A G and Schweikhard L 1992 *Int. J. Mass Spectrom. Ion Processes* **118/119** 37
- [15] Reents, Jr W D, Mandich M L and Wang C R C 1992 *J. Chem. Phys.* **97** 7226
- [16] Raghavachari K 1988 *J. Chem. Phys.* **88** 1688
- [17] Raghavachari K 1991 *J. Chem. Phys.* **95** 7373
- [18] Raghavachari K 1992 *J. Chem. Phys.* **96** 4440
- [19] Raghavachari K 1990 *J. Chem. Phys.* **92** 452
- [20] Mandich M L, Reents, Jr W D and Jarrold M F 1988 *J. Chem. Phys.* **88** 1703
- [21] Reents, Jr W D and Mandich M L 1988 *J. Phys. Chem.* **92** 2908
- [22] Mandich M L and Reents, Jr W D 1991 *J. Chem. Phys.* **95** 7360
- [23] Reents, Jr W D and Mandich M L 1992 *J. Chem. Phys.* **96** 4429
- [24] Mandich M L, Reents, Jr W D and Kolenbrander K D 1990 *J. Chem. Phys.* **92** 437
- [25] Reents, Jr W D and Mandich M L 1990 *J. Chem. Phys.* **93** 3270
- [26] Reents, Jr W D, Mandich M L and Wang C R C 1992 *J. Chem. Phys.* **97** 7226

On form and flow in dusty plasmas

P D Haaland†‡, A Garscadden†, B Ganguly†, S Ibrani‡ and J Williams§

† Wright Laboratory, Wright-Patterson AFB, OH 45433, USA

‡ Analatom Inc, 1183 Bordeaux Drive, Suite 1, Sunnyvale, CA 94089, USA

§ Lawrence Associates Inc, 5100 Springfield Pike Suite 509, Dayton, OH 45431, USA

Received 29 December 1993, in final form 25 January 1994

Abstract. Microscopic cauliflowers have been observed in a suprisingly diverse range of dusty plasmas. Their microstructure, as analysed by electron microscopy, is consistent with growth by ballistic deposition rather than diffusion limited aggregation. The morphology of the grains supports the inference from dust growth kinetics that they form by accretion of positive ions rather than neutral radicals. The dense, amorphous structure is capped by a fractal surface whose texture is concisely described by a recursion based on the modified midpoint method. The surface texture may be reconstructed by ion bombardment, providing a quantitative link between growth kinetics and roughness through a Mullins-Sekerka stability analysis of Laplacian growth.

1. Introduction

Micrometer-sized particles have been observed in many plasma sources. Their presence fundamentally alters the plasma's properties and can seriously contaminate industrial processes, most notably in semiconductor manufacturing [1]. While the role of dust in optical coating operations has received less attention, the presence of optical inhomogeneity caused by dust incorporation might prove critical in, for example, high quality mirror or waveguide fabrication [2]. As information processing technology moves from electrical through electrooptical to optical logic, dust contamination in plasma reactors will continue to impact process conditions and device yields.

Particles may arise either from surfaces or by homogeneous growth in the plasma. Homogeneous growth is characterized by spherical or spheroidal symmetry, and it is with these spherical grains that the present article is concerned. The simplest recipe for growing carbon cauliflowers uses a 1 Torr helium or argon plasma with graphite electrodes (figure 1) [3, 4]. In a symmetric geometry, excitation of tens of kilohertz rapidly provides ample dust particles which are trapped by electrostatic forces and can be studied *in situ* by Mie scattering. Similar particles of other materials have been reported in a 13 MHz argon plasma with a variety of substrates including silicon [5, 6] and aluminum [7].

A variety of dust sizes and shapes have been reported in deposits from a 5 kW cascaded arc deposition reactor, where dust grains several hundred micrometres in diameter have been observed (figure 2) [8]. The striking feature of these carbon-containing grains is their similarity, on a larger scale, to 400 nm grains grown in



Figure 1. Scanning electron micrograph of dust obtained from a 15 kHz 1 Torr helium plasma with 5 cm graphite electrodes separated by 2 cm. The dust sample was collected with a swab after several hours of discharge operation. Most of the grains are 900 nm in diameter with eight per cent having twice this diameter and about two percent having a diameter of 450 nm.

the 5 W, 15 kHz helium plasma. Another source of textured spheroids is the flowing afterglow deposition reactor in which nonlinear optical organic polymer films are synthesized (figure 3) [9].

Many dusty plasmas have in common the presence of reactive chemical precursors and steadily flowing gas. The observed particle sizes and structures imply

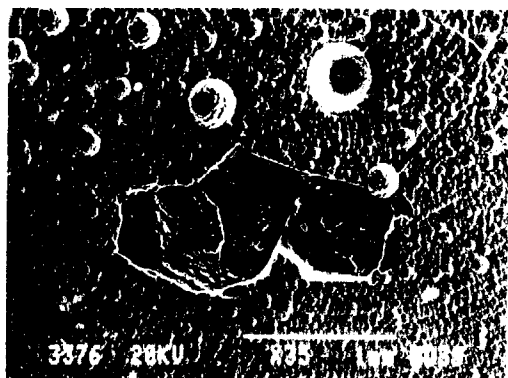


Figure 2. SEM image of large dust particles grown in the cascaded arc reactor at Technische Universiteit Eindhoven using C_2H_2 added to a 5 kW cascaded argon arc plasma. Directly above the scale bar and shoe-shaped outline is a depression (proven by the orientation of the shadows), showing the spheroidal shape of the particles which have been implanted into the growing carbon film. This image is courtesy of Ad Bijeron, TUE. Further details are to be found in reference [11].

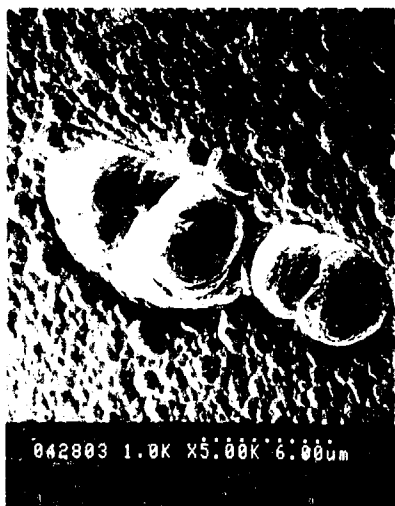


Figure 3. Benzene polymer dust particle collected from the flowing afterglow synthesis reactor described in references [9] and [12].

residence times in plasma regions which substantially exceed the normal gas residence times. As an illustration of the interplay between drag forces and particle structure we briefly present some results on fluid dynamics in the flowing afterglow as they relate to particle shape.

Our principal goal was to analyse the microstructure of various dust particles, primarily using high resolution, field emission, low energy scanning electron microscopy. The morphologies, surface textures, and their variation constrain aspects of the grains' growth mechanisms.

Their internal structures are consistent with ballistic deposition, while their surface textures appear to have been reconstructed by ion bombardment. As an indicator of a more quantitative approach we also present a simple fractal recursion for describing the observed surface textures.

2. Dust structure

Electron microscopy of dust collected from laboratory plasmas involves some subtleties not required for examination of standard metallurgical samples. We use a high resolution, low energy, field emission scanning electron microscope [10] to minimize charging of uncoated samples and to resolve surface texture of low atomic number material such as carbon. Probe current densities are kept low to avoid beam damage to individual grains or differential charging which can cause uncoated clusters to explode like popcorn in the microscope.

As we have reported previously [3], the distribution of grain sizes in the 15 kHz helium plasma with graphite electrodes is nearly monodisperse, as shown in figure 1. At the higher magnification of figures 4 and 5 the surface texture and internal structure of individual grains are succinctly described as corresponding to submicrometre cauliflower. The radial or columnar symmetry of these graphite grains is also evident in transmission electron micrographs (figure 6). Electron diffraction in the TEM shows no crystallinity in the dense centres of these grains for domains larger than 20 nm across.

The silicon grains grown in a 13 MHz sputtering diode by Stenbruchel presented in this issue [6] have similar structure and texture. Grains on a larger scale but with analogous structure and texture are also to be found in figure 2, figure 11 of reference [8] and in a recent thesis [11]. These 'organic flora', some with diameters greater than 100 μm , were formed in a cascaded arc deposition reactor. Finally, in figure 3, we show a dust particle collected from a low power, flowing afterglow plasma [9, 12].

3. Growth mechanisms

It is probable that dust with spherical or spheroidal symmetry grows by homogeneous processes. Given that grains are growing in the gas phase at very low partial pressures of plausible neutral precursors, one must invoke positive ion collection by the Debye sheaths, which surrounds the electrically floating particles, to account for observed growth rates [3, 4]. What, if anything, do the structure and texture of the grains reveal about the growth mechanisms?

Starting with the work of Witten and Sander [13] the process of growth by diffusion limited aggregation (DLA) has been extensively studied [14, 15]. The result of diffusion limited aggregation is a fractal geometry whose dimension is linked to the short range interaction



Figure 4. SEM images of dust from the 15 kHz helium plasma at higher magnification illustrate columnar internal structure and surface roughness on scales of tens of nm.

between a cluster and the precursors which diffuse to its surface [16]. A simpler growth mechanism, for which particles arrive along straight line trajectories, is called ballistic deposition (BD). Early work on BD suggested that fractal structures would result, but more recently this has been shown not to be the case [17, 18]. Ballistic deposition leads to dense, amorphous solids with surface roughness that has fractal scaling properties. DLA materials are, by contrast, fractal throughout.

A $1\text{ }\mu\text{m}$ grain at room temperature rotates, by energy equipartition, at a frequency in the kilohertz range. The transit time across this particle for a neutral radical precursor is about 10^{-5} s . Therefore neutral fluxes to the grain are isotropic within the solid angle subtended by the surface. Positive ion fluxes, by contrast, must respond to local electric fields at the grain surface. The electric field arises from the negative charge which maintains the particle at the plasma's floating potential and generates an ion sheath. For a perfect sphere the surface charge would lead to a radial electric field and cause ballistic, inward trajectories for the depositing ions. The actual electric field at the surface of a charged cauliflower is more complex, but the essential differences between ionic and neutral fluxes come from their isotropy, or lack of it, and their collection radii.

Ballistic deposition leads to conical deposits similar to those we find in dusty plasmas. Their cone angle is, for small angles, approximately proportional to the angle with which the ballistic flux approaches the growth surface [19]. The density of the resulting compact

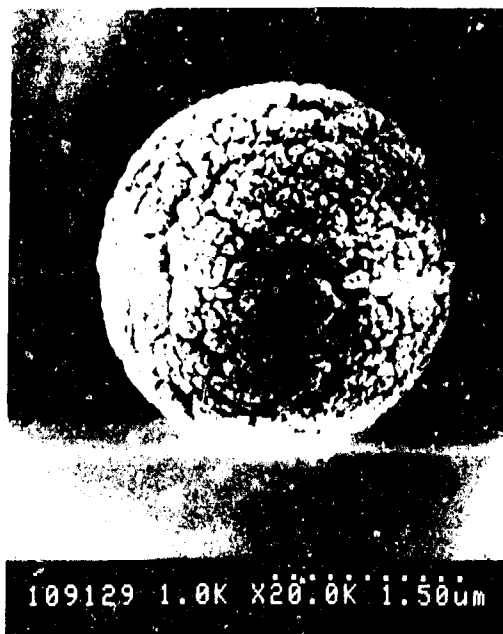


Figure 5. SEM image of dust from a 15 kHz argon plasma with graphite electrodes showing similar texture and structure to the grains grown in helium.

structures, the constant of proportionality relating impact and growth angles, and the roughness of the growth surface vary with model details, but the overall structure and surface texture provide an apt description of our plasma dust. By contrast, the loosely packed structure of DLA clusters, which have a tree-like morphology, is qualitatively incompatible with our SEM and TEM images. We conclude that the microstructure of the dust results from ballistic deposition rather than diffusion-limited aggregation. The regular conical segments of the grains further imputes ionic precursors since cation fluxes, incident on the sheath and then accelerated by the electrostatic sheath field which surrounds the grain, are anisotropic.

4. Fractal surfaces

While the interior of the dust is dense and amorphous the surface has a very interesting, intuitively fractal texture. One can parsimoniously summarize this texture using a simple fractal algorithm that is described for structures embedded in two dimensions in reference [4]. The approach is based on the modified midpoint method [20]. Extension to objects embedded in three dimensions is accomplished with a recursion outlined in figure 7. Proceeding from a point A construct a tetrahedron. Next draw a line from one vertex through the centre M of the opposing face BCD. Proceed for some distance MX to a point X, which now defines three new triangles



Figure 6. New image of dust showing surface texture and internal radial symmetry. No evidence of crystallinity was observed in the electron diffraction from thin sections or regions as small as 20 nm.

XBC, XBD, and XCD. Repeat the construction for each of these triangles while scaling MX by some fraction F . The fraction F is tied to the fractal dimension of the resulting surface, so that small variation of F leads to dramatic changes in the surface texture (figure 8). One also finds that small, random fluctuations in F give textures which, by disrupting the rigorous symmetry of the idealized fractal construction, closely approximate the surfaces of plasma-generated dust.

5. Dust transport

A detailed discussion of dust transport in plasmas is beyond the scope of this article [21]. However some aspects of dust motion in the plasma bear directly on the observed morphology. The gas residence time in typical reactors is many orders of magnitude less than the time required to form micrometer grains at plausible growth rates. The particles are clearly trapped by the several forces which act on them in a plasma environment so that they can remain in regions where growth can proceed. Forces due to gravity, electrostatic interactions, ion drag, thermophoresis, pressure gradients and neutral collisions must all be considered.

Table 1 summarizes the forces on a stationary 1 μm grain in the 1 Torr flowing afterglow from which the benzene polymer particle in figure 3 was produced. We have solved the Navier-Stokes equations for gas

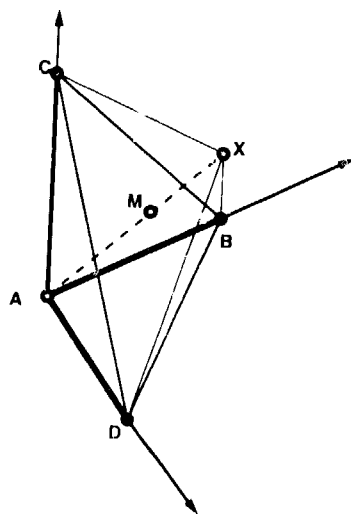


Figure 7. Modified midpoint fractal recursion for bodies embedded in three dimensions.

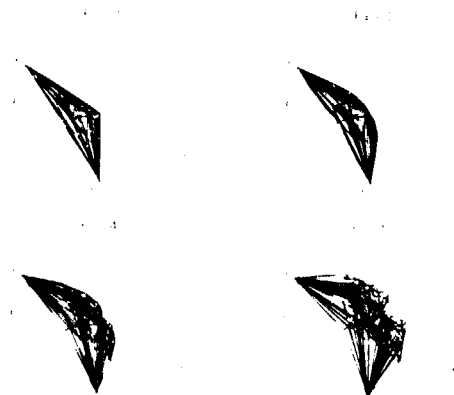


Figure 8. Typical surfaces computed using the fractal recursion on one face of a square pyramid. Scaling by the fraction F causes dramatically different surface textures in the four cases shown here, where $F = 0.2, 0.3, 0.4$ and 0.5 .

flow in an axisymmetric model of the afterglow reactor and computed the thermophoretic, pressure gradient, and neutral drag forces. Details of these calculations can be found in reference [12]. In figure 9 we show the geometry for the flow calculations, while in figure 10 the fluid drag and thermophoretic forces on a 1 μm grain are summarized. The scaling of these forces with grain size is also illustrated in table 1. The dominant force on micrometric particles in the afterglow reactor is neutral drag, which encourages the growing grains to recirculate in a toroidal region in front of the substrate where the ionic precursor concentration is high (figure 11). Thermophoretic forces, though smaller, further aid the trapping of particles between the injector and

substrate. Forces due to pressure gradients are, for the case considered here, four orders of magnitude smaller than the neutral drag or thermophoretic forces. The irregular shape of the particle in figure 3, combined with the fluid dynamic results, suggests sporadic periods of growth as seen by macroscopic analogy to hailstones.

Roughly spherical symmetry is the dominant motif observed for homogeneously grown grains. Plasmas are usually run for many hours or through several on-off cycles before dust is collected. Thus there is the possibility that early particles which collect on the wall are reintroduced to the plasma and experience renewed growth, resulting in an oblate or distorted structure such as is seen in figure 12. We have previously described the self-limiting nature of ionic growth due to reduction of electron density in dusty volumes [4]. A micrometre-scale spherical grain at a wall will be charged negatively when a new plasma is initiated. The combined electrostatic repulsion between the wall and grain and the electric field of the ion sheath may overcome the force binding the dust to the wall. The grain is then injected into the plasma and, due to its size, competes for the ions from which smaller particles would grow. The fact that grain sizes in figure 1 are multiples of 450 nm supports this hypothesis, as do the two sets of grains shown in figure 13. The two smaller grains have a common texture which differs from the common texture of the two larger particles. We infer that the larger particles either grew under different plasma conditions or resulted from accretion of more material on dust which reentered the plasma region during an off-on cycle.

Particles clearly collect on reactor walls as the plasma is cycled on and off. Whether these particles return to the plasma depends on myriad details for specific reactors. The morphology of irregular grains gives an indication of the role played by dust recycling, whether by flowing gas or ejection from walls, as plasma conditions are changed.

6. Surface modification

In noble gas plasmas most of the ions which impinge on the surface of a growing grain will be chemically unreactive. They may still play a role in texturing the cauliflower surface. However there are fundamental limits to the surface roughness which can be attained. Whether by diffusive or ballistic fluxes the growth of small perturbations is coupled to the solid angle subtended by the growing surface. In either case one must consider the stability with which growth at various spatial frequencies may occur.

Mullins and Sekerka presented, using harmonic analysis in an important and elegant paper, the stability criteria for growth on a sphere [22]. In the absence of an equivalent surface tension, smooth surface growth is exponentially unstable; whiskers grow without restraint. A restoring force, whether by true surface tension or an electrostatic constraint, is crucial to the stability of self-affine or Laplacian growth. Mullins and Sekerka derived

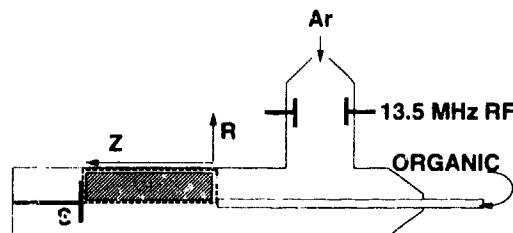


Figure 9. Schematic outline of the flowing afterglow reactor. The cylindrical glass reactor is 10 cm in diameter. Axisymmetric modelling of the gas flows is bounded by the hatched region with the origin $(H, Z) = (0, 0)$ located where about 1 sccm of organic is injected through a glass tube. Argon carrier gas (200 sccm, 1 Torr) is capacitively excited by 5 W of RF power at 13.6 MHz. An organic precursor such as benzene or thiophene is introduced downstream, where electron-ion recombination leaves only metastable argon atoms in the flow. Mixing of the organic and metastable Ar leads to Penning ionization, with the resulting organic cations producing dense, uniform polymer film on the 5 cm diameter substrate S. The distance between substrate and injector along Z is 12.5 cm.

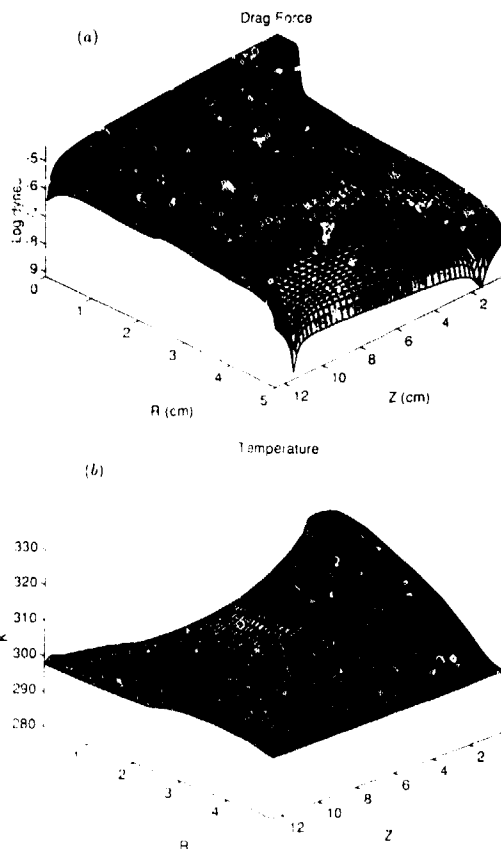


Figure 10. (a) Common logarithm of the neutral drag force (Dynes) acting on a stationary $1 \mu\text{m}$ particle and (b) temperature field from which thermophoretic forces are inferred for conditions described in figure 9.

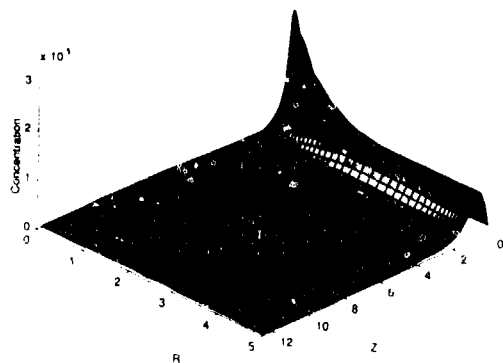


Figure 11. Concentration of ionic precursor computed using the published kinetics for reaction of thiophene with metastable argon [9] and the concentration and flow fields from the Navier-Stokes solutions. The precursor concentration is predicted to be high in precisely the region where the forces from figure 10 would trap and recycle growing particles.

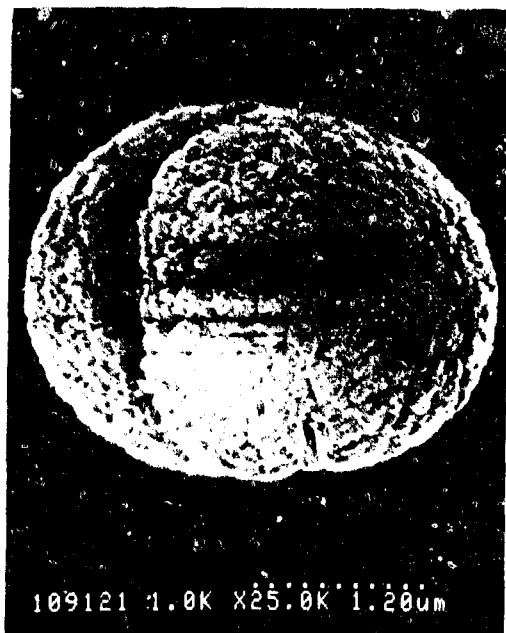


Figure 12. Oblate particles whose growth has been interrupted and renewed in the 15 kHz helium plasma from reference [3].

the dispersion relation for growth of instabilities as a function of spatial frequency and found a wavelength above which growth was critically damped. The fastest growth occurs for a spatial wavelength $\lambda_c = \sqrt{3ld_0}$ where l and d_0 are the capillary and diffusion lengths for the system. Solids such as graphite or silicon have capillary lengths of nanometer order. While the surface

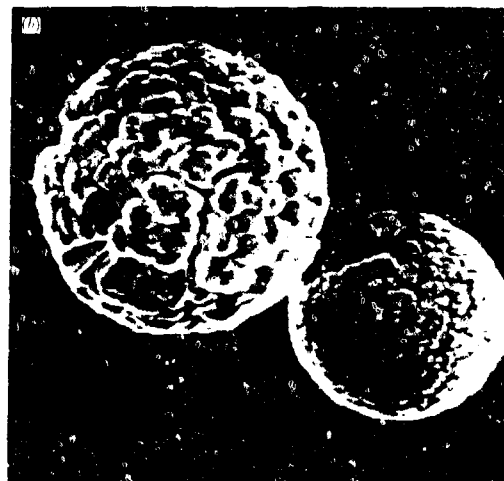
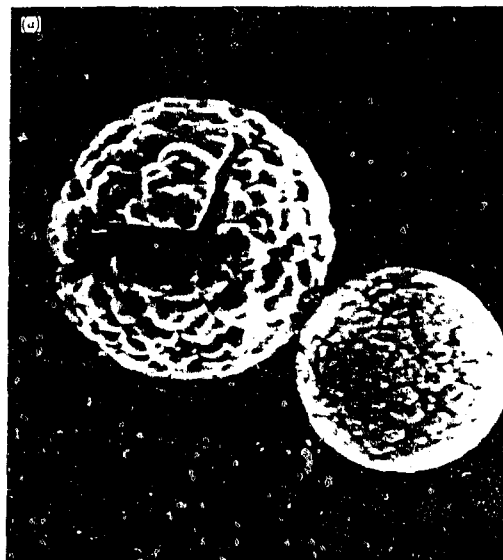


Figure 13. Two pairs of particles from the same sample. Note the common texture for the two small and two large particles at the same time that the small and large grains differ. We infer that the larger grains either grew under different plasma conditions or resulted from accretion of material on smaller particles which were recycled by the plasma after switching off and on.

diffusion length for impinging species is not known, it seems unlikely that ions would wander far after colliding with several eV of kinetic energy. Typical scales for both l and d_0 combined with the analysis of Mullins and Sekerka suggest quantitative links between surface roughness and the mechanism of grain growth. This connection appears worthy of further study.

Table 1. Summary of forces (dynes) on a stationary dust grain in a 1 Torr Ar plasma.

F_{nd}	Neutral drag	$5 \times 10^{-9} r^2 v_f$ $0.00213 \rho_g r^2 v_f$	r in μm v_f = flow velocity (cm s^{-1}) ρ_g = gas density (g cc^{-1})
F_g	Gravitational	$3.82 \times 10^{-9} r^2 \rho$	ρ = grain density (g cc^{-1})
F_{th}	Thermophoretic	$1.2 \times 10^{-7} r^2 \nabla T$	∇T in K cm^{-1}
F_{es}	Electrostatic	$1.6 \times 10^{-12} qE$	q in electronic charges E in V cm^{-1}
F_{id}	Ion drag	$0.137 JQ$	J current density in mA cm^{-2} Q cross section in cm^2
F_{pg}	Pressure gradient	$5.5 \times 10^{-10} r^3 \nabla P$	∇P in Torr cm^{-1}

7. Conclusions

The microstructures of diverse grains which arise from homogeneous processes in plasmas are clearly consistent with a growth mechanism by ballistic deposition rather than by diffusion limited aggregation. The combination of a dense, compact morphology with fractal surface textures and rapid initial growth rates is consistent with accretion of positively charged precursors through the electrostatic sheath which envelopes floating grains. The microstructure of irregular grains imputes fluid dynamics and injection of accumulated dust from walls as important processes in dusty plasmas. There is hope that a more quantitative connection between the surface texture and growth mechanisms will result from application of Mullins' and Sekerka's Laplacian growth analysis to the inorganic, mesoscopic garden of dusty plasmas.

References

- [1] Selwyn G S, Singh J and Bennett R S 1989 *J. Vac. Sci. Technol. A* **7** 2758
- [2] Pulker H 1988 *Coatings on Glass* (New York: Springer)
- [3] Ganguly B, Garscadden A, Williams J and Haaland P 1993 *J. Vac. Sci. Technol. A* **11** 1119
- [4] Garscadden A, Ganguly B, Haaland P, and Williams J 1994 *Plasma Sources Sci. Technol.* **3**
- [5] Yoo W J and Steinbruchel Ch 1993 *J. Vac. Sci. Technol. A* **11** 1258
- [6] Steinbruchel Ch 1994 *Plasma Sources Sci. Technol.* **3**
- [7] Jellum G M and Graves D B 1990 *J. Appl. Phys.* **67** 6490
- [8] Beulens J J, Buuron A J M, de Graaf M J, Meeusen G J, van de Sanden M C M, Wilburs A T M and Schröter D C 1992 *High Temp. Chem. Processes* **1** 105
- [9] Haaland P and Targove I 1992 *Appl. Phys. Lett.* **61** 34
- [10] Hitachi S-900 High resolution, low energy, field emission scanning electron microscope (Japan: Hitachi Inc)
- [11] Buuron A J M 1993 *Plasma Deposition of Carbon Materials Dissertation* Eindhoven Technical University, The Netherlands
- [12] Haaland P, Ibrani S and Jiang H 1994 *Appl. Phys. Lett.* **64** 1629
- [13] Witten T A and Sander L M 1981 *Phys. Rev. Lett.* **47** 1400
- [14] Vicsek T 1993 *Fractal Growth Phenomena* (Singapore: World Scientific)
- [15] Weitz D A and Oliveria M 1984 *Phys. Rev. Lett.* **52** 1433
- [16] Nakagawa M and Kobayashi K 1991 *Chaos, Solitons, and Fractals* **6** 535
- [17] Meakin P 1983 *Phys. Rev. B* **28** 5221
- [18] Ball R C, and Witten T A 1984 *Phys. Rev. A* **29** 2966
- [19] Meakin P 1988 *Phys. Rev. A* **38** 994
- [20] Mandelbrot B 1982 *The Fractal Geometry of Nature* (New York: Freeman)
- [21] Barnes M S, Keller J H, Forster J C, O'Neill J A and Coultas D K 1992 *Phys. Rev. Lett.* **68** 313
- [22] Mullins W W and Sekerka R F 1963 *J. Appl. Phys.* **34** 323

Particle nucleation and growth in thermal plasmas

Steven L Girshick

Department of Mechanical Engineering, University of Minnesota,
Minneapolis, MN 55455, USA

Received 29 December 1993, in final form 10 January 1994

Abstract. Particle nucleation in a thermal plasma reactor occurs as a high-temperature gas undergoes a cooling trajectory. Cooling leads to formation of supersaturated vapours, which causes either homogeneous or ion-induced nucleation. Detailed models have been developed for homogeneous nucleation in a plasma reactor, including discrete-sectional models and moment-type models. The discrete-sectional models are capable of incorporating size-dependent cluster property data as these become available. Calculations in which a one-dimensional cooling trajectory was assumed in a discrete-sectional code indicate that cooling rates play a key role in determining the final particle size. Moment-type models are more computationally efficient, and have been coupled to two-dimensional reactor transport models. A two-dimensional model was compared with experimental results for synthesis of iron particles over a range of conditions in which the volume-mean particle size ranged from roughly 20 nm to 70 nm, with reasonable quantitative agreement for particle size versus reactant feed rate. The major weakness of current models for particle formation in thermal plasmas is the lack of an adequate understanding of ion-induced nucleation. Additionally, there is considerable need for well-characterized experiments in which particle sizes are determined by probe sampling or light scattering.

1. Introduction

Particle formation in thermal plasma reactors is of interest in the context of powder synthesis. A wide variety of ceramic and metallic powders have been synthesized in thermal plasma reactors [1]. The size of these powders is virtually always submicrometre, and often smaller than 0.1 μm . There is increasing interest in methods for producing powders with average particle sizes smaller than 0.1 μm , which can be consolidated and sintered to create nanophase materials [2]. Thermal plasma reactors are well suited to high-rate generation of such ultra-fine powders.

Reactants may be injected into a thermal plasma reactor in powder form, as a liquid spray, or in gaseous form. If the reactants are injected as solids or liquids then the process is usually designed to accomplish their complete vapourization in the hot plasma. Gaseous species in the hot plasma are substantially dissociated. The gas cools after flowing past the high-temperature core. Finally, particles nucleate and grow.

2. Nucleation mechanisms

A complete model of particle formation in a thermal plasma reactor would include both a model for the plasma and a model for particle nucleation and growth.

The nucleation process itself is both a crucial and a poorly understood aspect of this problem. By nucleation we mean the growth of clusters to critical size, the size at which they are as likely to grow as to decay.

Particle nucleation in a thermal plasma reactor may be driven either by physical condensation of a supersaturated vapour or by chemical reactions where no supersaturated vapour exists. In the former case (which we term *physical nucleation*) the growth of clusters to critical size can occur with or without the presence of ions as nucleation sites. These two cases are referred to respectively as *homogeneous nucleation* and *ion-induced nucleation*. We use the term *chemical nucleation* to denote the case in which subcritical clusters grow to critical size by a sequence of chemical reactions rather than by physical condensation [3].

Chemical nucleation under thermal plasma conditions has received scant attention. Even for the simplest of systems a proper treatment would require data on chemical rate constants for a number of clustering reactions at high temperatures, which data are sparse to say the least. However, chemical nucleation is perhaps a less common route to particle formation in thermal plasmas than one might suppose. As the plasma cools chemical clustering can occur, but it is also likely that a specific vapour becomes supersaturated. Because condensation of a monomer to a cluster involves attachment by a relatively weak van der Waals bond, rate constants for physical clustering are likely to be several

orders of magnitude higher than for clustering involving formation of chemical bonds. The nucleation process itself can be physical while subsequent growth is chemical and/or physical. For example, as a hot plasma cools a material such as silicon carbide (SiC) can be formed by chemical nucleation, or it can be formed by physical nucleation of supersaturated silicon vapour, followed by heterogeneous reactions at the surfaces of stable clusters, diffusion and chemical reactions within the condensed phase.

An assessment of whether homogeneous or ion-induced nucleation dominates is difficult, though such an assessment has appeared in other contexts [4, 5]. A first estimate for electron concentrations under thermal plasma conditions is that they are given by their equilibrium value, namely by the Saha equation. Typical nucleation temperatures for refractory materials are roughly 2000 K, and in most systems at atmospheric pressure the equilibrium degree of ionization at that temperature is extremely small. However, the primary mechanism for electron recombination in this regime (if particles are not present) is likely to be three-body electron-catalysed recombination, which is slow at low electron concentrations. Therefore the electron concentration is likely to be frozen at a value characteristic of equilibrium at some higher temperature, the value of which depends on the temperature-time trajectory followed by the plasma.

Smirnov and Tishchenko [6] considered ion-induced nucleation of titanium particles in a thermal plasma by following a one-dimensional cooling trajectory. They modelled nucleation by estimating the fractional ionization of titanium vapour at the instant it became saturated, and assumed that all titanium atoms condensed instantaneously at that point onto all the titanium ions. However, this calculation neglects the experimental evidence and theoretical arguments for an energy barrier to ion-induced nucleation. That is, a vapour must be supersaturated for either homogeneous or ion-induced nucleation to occur [7]. Also, recent experiments [8] suggest that during ion-induced nucleation only a small fraction (about 0.1%) of ions may be effective as nucleation sites.

The theory of ion-induced nucleation [7, 9-11] is less well developed than for homogeneous nucleation, and is presently incapable of predicting the observed dependence of ion-induced nucleation rates on the particular ion species involved and on whether the ion is positively or negatively charged. A further complication is that growth of an ion cluster can be terminated before it reaches critical size by capture of an electron. Ion clusters may be more effective at scavenging electrons than are atomic ions, particularly via dissociative recombination.

Thus our current understanding of ion-induced nucleation is unsatisfactory, making the development of detailed models for thermal plasma reactors a difficult undertaking. The remainder of this discussion considers models that have been developed for homogeneous nucleation in thermal plasma reactors.

3. Modelling approaches

We have pursued two different approaches to computational modelling of particle nucleation and growth under conditions appropriate to the thermal plasma regime.

(i) 'Discrete' models, in which separate rate equations are written for the populations of monomers, dimers, trimers and so on, up to some specified size, with larger sizes treated either in terms of a continuous distribution [12] or by grouping sizes into sections, these sections typically being spaced logarithmically by particle volume [13, 14].

(ii) 'Moment-type' models, in which an analytical expression for the nucleation rate serves as a source term to equations that describe evolution of the stable aerosol in terms of the first few moments of the size distribution [15].

Discrete models are more rigorous than moment-type models. Unlike moment-type models they can treat coagulation among subcritical clusters, and they require no *a priori* assumptions concerning the form (for example, log-normal) of the size distribution. They are capable of simulating evolution of the entire size distribution, including subcritical clusters, thereby resolving the behaviour of the size distribution during the nucleation burst.

The major advantage of moment-type models is computational economy. Thermal plasma reactors have steep temperature gradients. As nucleation rates are extraordinarily sensitive to the vapour saturation ratio, acceptable accuracy in modelling nucleation by either approach requires extremely small time steps (equivalently, an extremely fine numerical grid). Discrete models require solution of a large set of coupled equations at each point, as a result of which their use is presently restricted to one-dimensional simulations. (The one-dimensional calculations discussed below each required approximately 300 s CPU time on a Cray-2 or Cray X-MP supercomputer.) In contrast, moment-type models require solution of only a few equations at each point, and thus can realistically be coupled to a two-dimensional plasma reactor model. Although moment-type models calculate only the first few moments of the size distribution (for example, the number of particles, a measure of their mean diameter, and the width of the size distribution), this information is adequate for most purposes.

Results obtained using a discrete-sectional model and a moment-type model have been compared for simple test cases [16]. If the classical Becker-Döring-Zel'dovich expression for the rate of homogeneous nucleation is used as a source term to a moment model, and the usual physical assumptions of classical theory are utilized in writing the coagulation and evaporation coefficients in the rate equations of the discrete-sectional model, then the results obtained by the two methods are remarkably different. However, excellent agreement between the two approaches is obtained if a modified

expression for the nucleation rate is assumed in the moment model. This modification is derived [17, 18] by enforcing self-consistency in the expression for the equilibrium cluster distribution, which is required for evaluation of cluster evaporation rates (see equation (10) below). The proposed modification multiplies the expression for the classical nucleation rate by a factor e^{Θ}/S , where S is saturation ratio and $\Theta = \sigma s_1/(k_B T)$ is a dimensionless surface tension. Here σ is surface tension, s_1 is monomer surface area, k_B is Boltzmann's constant and T is temperature. Typical values of Θ for refractory materials undergoing high-temperature nucleation are in the range 10–30.

4. One-dimensional modelling; discrete representations of the cluster size spectrum

Consider a dilute condensable vapour following a specified temperature time trajectory along a fluid stream line. Accounting for the fact that the gas density ρ_g changes for non-isothermal conditions, one can write the population balance equation for monomers as

$$\frac{D\hat{n}_1}{Dt} = \frac{R}{\rho_g} - \rho_g \hat{n}_1 \sum_{j=1}^{\infty} \beta_{1j} \hat{n}_j + \sum_{i=2}^{\infty} (1 + \delta_{2i}) E_i \hat{n}_i \quad (1)$$

while for dimers and all larger j -mers (clusters containing j monomers) one can write

$$\begin{aligned} \frac{D\hat{n}_k}{Dt} = & \frac{1}{2} \rho_g \sum_{i+j=k} \beta_{ij} \hat{n}_i \hat{n}_j - \rho_g \hat{n}_k \sum_{i+j=k} \beta_{jk} \hat{n}_j \\ & + E_{k+1} \hat{n}_{k+1} - E_k \hat{n}_k \quad k \geq 2. \end{aligned} \quad (2)$$

In these equations \hat{n}_j denotes the number of j -mers per unit mass of gas, R is the rate of monomer generation by gas-phase chemical reactions, β_{ij} is the collision-frequency function for collisions between i -mers and j -mers, E_j is the j -mer evaporation coefficient, and the Kronecker delta function δ_{2j} accounts for the fact that two monomers are created by dissociation of a dimer.

The collision-frequency function is given from ideal gas kinetic theory for the free-molecule regime by [19]

$$\beta_{ij} = r_i^2 \left[\frac{8\pi k_B T}{m_i} \left(\frac{1}{i} + \frac{1}{j} \right) \right]^{1/2} (i^{1/3} + j^{1/3})^2 \quad (3)$$

where r_i and m_i are respectively the radius and mass of a monomer. Under the capillarity approximation (which assigns to the cluster a surface tension equal to that of a flat liquid surface in equilibrium with its vapour) the evaporation coefficient can be written [20]

$$E_j = \beta_{1,j-1} n_s \exp\{\Theta[j^{2/3} - (j-1)^{2/3}]\} \quad (4)$$

where $n_s(T)$ is the equilibrium monomer concentration for the saturated vapour.

We have used equations of the form of equations (1) and (2) in a discrete-sectional approach to model nucleation and growth of iron [21], magnesium oxide [22] and silicon [23] under high-temperature conditions at total pressure 1 atm. In the case of iron the initial vapour concentration and cooling rate were treated as free parameters. In the case of MgO the chemical generation rate R in equation (1) was obtained by coupling to a set of chemical rate equations describing formation of MgO monomers in a Mg–O–Ar mixture. For calculations involving silicon the temperature trajectory was obtained by solving the one-dimensional continuity, momentum and energy equations for isentropic flow through a nozzle having a specified geometry, correcting the temperature profile to account for wall heat losses and for the rapid heat release accompanying particle formation. The motivation for these last calculations is that we are currently conducting experiments in which silicon and silicon carbide are synthesized in a converging nozzle through which a thermal plasma expands.

A typical solution for time evolution of the particle size distribution is shown in figure 1, from the silicon calculations, for conditions corresponding to the experiments. We assumed that the gases (Ar, H₂ and SiCl₄) had adequate time to reach thermochemical equilibrium

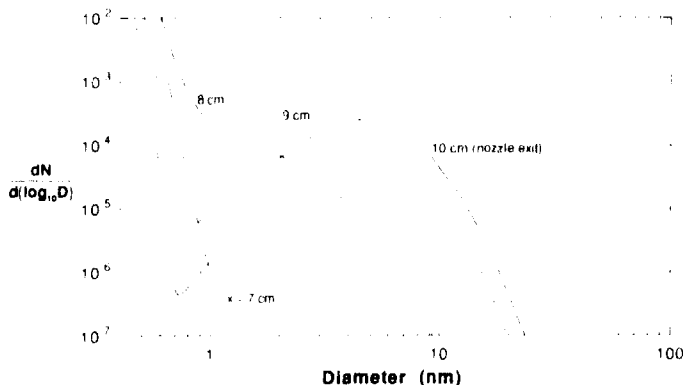


Figure 1. Calculated evolution of the silicon particle size distribution, for flow through a converging nozzle [22]. Nozzle inlet temperature 3000 K. Typical experimental flow rates are assumed. x is the distance from the nozzle inlet.

at the nozzle inlet (in this case at 3000 K), but that the chemical composition was frozen at its nozzle inlet value, the nozzle flow time being less than 0.4 ms (this latter assumption was supported by kinetics calculations). As seen in figure 1, these calculations resolve the nucleation burst. As the temperature drops along the nozzle (from 3000 K to about 2350 K) the silicon vapour becomes supersaturated. At a location $x = 7$ cm from the inlet (and at all upstream locations) one finds a monotonically decreasing distribution of subcritical clusters. At $x = 8$ cm there has been a sudden shift to formation of larger clusters, the homogeneous nucleation burst is in progress. By $x = 9$ cm the distribution curve has developed a sharp minimum at particle diameter smaller than 1 nm. The shift in the size distribution from $x = 9$ cm to $x = 10$ cm is indicative of growth by coagulation, which will continue after the aerosol exits the nozzle.

These types of calculations have provided insights into the role of cooling rate and monomer concentration in affecting nucleation dynamics and thereby the final particle size. For example, figure 2 shows the calculated evolution of the mass-mean diameter for iron particles with three different cooling rates. The cooling rate is seen to have a pronounced effect on the size that particles attain during the brief nucleation burst: the higher the cooling rate, the smaller the particle that is produced. This phenomenon is caused by the fact that there is a characteristic time for clustering, given by $\tau_c \approx (\beta_{11} n_1)^{-1}$, and if the cooling rate is higher then the vapour shoots to a higher critical supersaturation before nucleation can occur. This is seen in figure 3, which shows the evolution of the iron vapour saturation ratio S for two different cooling rates. The higher the value of S , the smaller the critical cluster size. Therefore a higher critical supersaturation corresponds to many more clusters being made stable for growth (note the distribution of subcritical clusters in figure 1), which then occurs rapidly by condensation from the supersaturated vapour. However, the quantity of vapour available for condensation is finite, and therefore if there are more stable

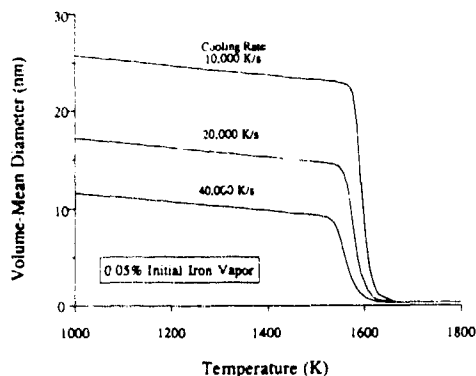


Figure 2. The effect of cooling rate on calculated evolution of volume-mean diameter of iron particles [20]. Initial iron vapour concentration was 0.05% by volume in an atmospheric pressure argon plasma.

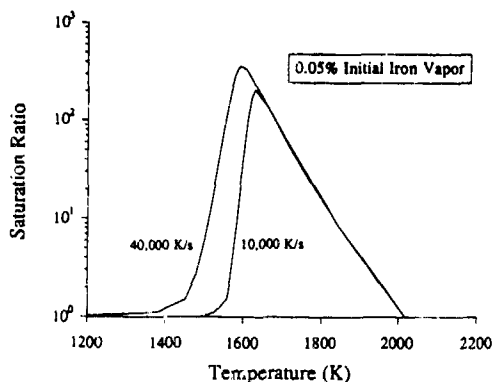


Figure 3. Effect of cooling rate on the calculated evolution of the iron vapour saturation ratio, for same conditions as in figure 2 [20].

clusters they will grow to a smaller size. As can be seen in figure 2, further growth by coagulation is relatively a second-order effect. The same arguments support the result that larger vapour concentrations produce larger particles rather than more particles. There is evidence from thermal plasma synthesis experiments to support qualitatively these predicted effects of cooling rate [24, 25] and reactant concentration [26, 27] on particle size.

5. Two-dimensional modelling; moment representations of the particle size spectrum

A limitation of one-dimensional models is that most real thermal plasma reactors are far from one-dimensional, because the walls must be cooled to avoid melting. Thus particles may nucleate in the cold boundary layer near the wall. A realistic model of this situation therefore requires a full two-dimensional solution of the equations that describe the plasma, coupled to equations describing the vapour and aerosol dynamics. As discussed in section 3 above, computational economy then dictates use of a moment-type model for the aerosol dynamics, although this situation will presumably change as computational costs decrease.

The k th moment of the particle size distribution is defined by

$$M_k \equiv \int_0^\infty v_p^k n(v_p) dv_p \quad (5)$$

where v_p is particle volume and $n(v_p)$ is the size distribution function. The balance equation for the k th moment, accounting for various effects expected in a thermal plasma reactor, can be written in general form as

$$\rho_k \mathbf{u} \cdot \nabla \left(\frac{M_k}{\rho_k} \right) = (\dot{M}_k)_{\text{nucleation}} + (\dot{M}_k)_{\text{coagulation}} + (\dot{M}_k)_{\text{condensation}} + (\dot{M}_k)_{\text{diffusion}} + (\dot{M}_k)_{\text{thermophoresis}} \quad (6)$$

where \mathbf{u} is the fluid velocity vector and appropriate expressions are required for each of the terms on the right-hand side [28, 29].

The first term on the right-hand side is non-zero only for $k = 0$, in which case it equals the nucleation rate. The modified expression for the nucleation rate discussed in section 3 is given by

$$J = v_1 n_1^2 S \left(\frac{2\sigma}{\pi m_1} \right)^{1/2} \exp \left(\Theta - \frac{4\Theta^3}{27(\ln S)^2} \right) \quad (7)$$

where v_1 is the monomer volume.

We used the modified nucleation rate, together with equations for the first three moments of the particle size distribution, to model particle nucleation and growth in a thermal plasma reactor used for experiments in our laboratory involving synthesis of iron powder [27]. A detailed discussion of the expressions used to model coagulation, condensation, diffusion and thermophoresis is provided elsewhere [27, 29]. In the experiments relatively coarse (5–9 μm) iron powder was coaxially injected into an atmospheric pressure, 2.9 MHz inductively coupled RF plasma. The powder evaporated in the plasma to form iron vapour, which then nucleated to form ultra-fine particles.

The plasma velocity and temperature profiles were calculated by solving the fluid continuity, momentum and energy equations, together with an appropriate form of Maxwell's equations in which the RF current in the induction coils was used as a boundary condition [30]. A model for heating and evaporation of the feed powder, together with iron vapour diffusion, was coupled to the flow equations. 'Base case' results for the reactor temperature distribution are shown in figure 4. Calculations were run for a range of powder feed rates

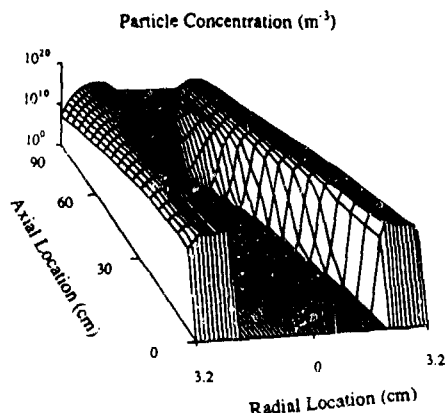


Figure 5. Calculated particle distribution in downstream tube (bottom tube of figure 4) [26].

corresponding to the experimental conditions. Nucleation of iron particles is predicted to occur around the 1600 K isotherm, giving rise to the distribution of particles shown in figure 5. (In these experiments argon was transpired through the permeable wall of the tube downstream of the plasma, so as to suppress wall deposition; this was included in the model.)

A description of the experimental apparatus and results is presented in [27]. Aerosol measurements were obtained by sampling through a capillary probe inserted into the flow near the downstream end of the reactor. The sampled aerosol was rapidly diluted by a venturi

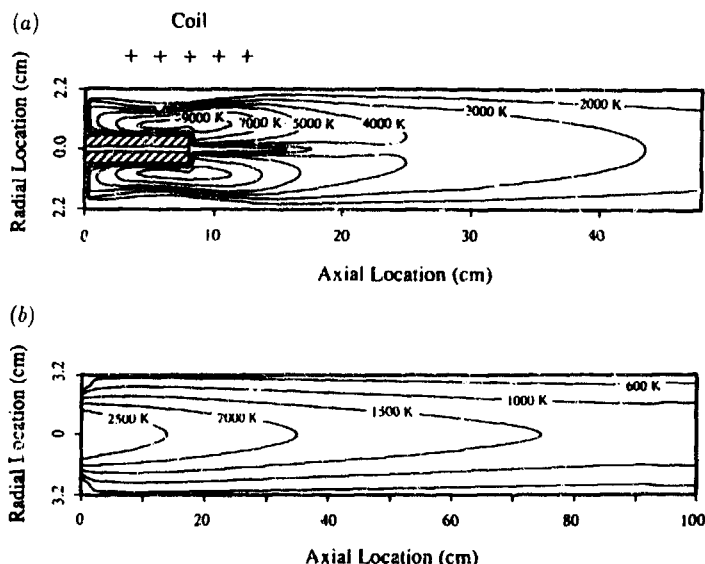


Figure 4. Calculated temperature distribution in the plasma reactor for synthesis of iron particles under typical experimental conditions [26]. (a) Iron powder is injected into the induction coil region in the plasma tube. (b) The plasma tube is followed by a 1 m long tube with permeable wall through which argon is transpired.

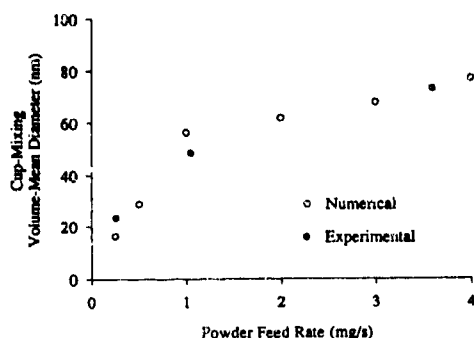


Figure 6. Comparison of volume-mean diameter calculated by numerical model (○) with experimental results (●), for a range of iron feed rates [26]. The 'cup-mixing' diameter is obtained by averaging the results over a flow cross section.

diluter [31], and the diluted sample was directed to several instruments, including an electrical aerosol analyser (TSI 3030), which provided particle size distribution histograms for particles down to 10 nm in diameter. A comparison of these results with the model predictions is shown in figure 6, which gives the results in terms of an average over the entire flow cross section where the measurements were made. Presented in this way the agreement between model and experiment appears excellent, although the data obtained at specific radial locations indicated that there was more cross stream mixing than predicted by the model. Considering uncertainties in both the model and the experiment, the excellent quantitative agreement seen in figure 6 is considered fortuitous. Nevertheless, the results clearly reproduce the experimental trends and the right magnitudes of particle size, which is impressive considering that a 30 nm iron particle contains about 10^6 iron atoms.

6. How to use cluster property data in a dynamic nucleation model

The capillarity approximation may be reasonably valid for high-temperature nucleation. There is considerable evidence for a sharp decrease in melting temperature with decreasing cluster size [32, 33]; that is, at sufficiently high temperatures (but well below the bulk melting point), clusters may be effectively liquid-like, structureless spheres. Furthermore, there is evidence from electronic structure calculations, at least for sodium clusters, that the main contribution to lowering of binding energy with decreasing cluster size is a surface effect, indicating the validity of surface-energy-based arguments down to surprisingly small sizes [34].

Consider the condensation/evaporation 'reaction'



where A_j represents a j -mer. At equilibrium the forward and backward rates must balance, hence

$$\beta_{j,j-1} n_j^e n_{j-1}^e = E_j n_j^e \quad (9)$$

where the superscript 'e' denotes an equilibrium state. The most convenient choice of equilibrium state is that of a saturated vapour at the same temperature as the system in question [17, 35]. It is conventionally assumed that clusters at equilibrium follow a Boltzmann-type distribution, which can be written

$$n_j^e = n_1^e \exp\left(-\frac{\Delta G(j)}{RT}\right) \quad (10)$$

where R is the universal gas constant. It can be shown [36] that this form of the distribution is correct provided that $\Delta G(j)$ denotes the standard free energy change associated with the 'reaction' in which one mole of monomer vapour plus $(j-1)$ moles of liquid equals one mole of j -mer. Combining equations (9) and (10), one obtains

$$E_j = \beta_{j,j-1} n_1 \exp\left(\frac{\Delta G_{j-1,j}}{RT}\right) \quad (11)$$

where $\Delta G_{j-1,j} = \Delta G(j) - \Delta G(j-1)$.

Equation (11) is a general expression for the evaporation coefficient which can be used in equations (1) and (2). To specify $\Delta G_{j-1,j}$ lacking better information, the conventional approach is to adopt the capillarity approximation, which produces equation (4). However, if data on cluster free energies are available, these can readily be incorporated. For example, low-temperature binding energies have been calculated for silicon clusters up to size 30 [37], and efforts are presently underway to extend the approaches of local-density theory and molecular dynamics to calculate these properties at the high temperatures pertinent to thermal plasma systems.

This approach can further be extended to ion-induced nucleation. Briefly (a more detailed development is the subject of current work), one would first need to estimate the frozen ion concentration by means of an analysis for electron recombination under prescribed conditions pertinent to a thermal plasma reactor. Then, discrete equations of the form of equations (1) and (2) could be used, except that coagulation among subcritical ion clusters can safely be neglected in comparison with condensation. The ideal gas expression for collision rates, equation (3), should be replaced with a more accurate expression from ion-neutral capture collision theory [38]. Finally, a growing body of data exists on the thermodynamic properties of small ion clusters, for example from Castleman's group [39]. When these are available they can be used in equation (11) in preference to the classical Thomson expression for the free energy of an ion cluster [40], which treats the cluster as a dielectric droplet surrounding an ionic core.

7. Conclusions

The modelling of particle nucleation and growth in thermal plasma systems has advanced to the point at which a model can be implemented, which describes

homogeneous nucleation, condensation, coagulation, vapour diffusion and thermophoretic transport in a two-dimensional reactor space. The next major tasks for modelling are to generate and incorporate data on size-dependent cluster free energies, and to investigate ion-induced nucleation.

Results from two-dimensional modelling to date, for a simple substance such as iron, appear to be in reasonable agreement with experimental data. It must be emphasized, however, that the experiments cited [27] are the only known case in which aerosol was sampled from the gas stream in a thermal plasma reactor rather than being scraped from walls or filters. Wall deposits may have a poorly characterized flow history, may be non-representative and may be significantly modified subsequent to deposition. Therefore there are few experimental data with which particle formation models (which treat only phenomena preceding wall deposition) can meaningfully be compared, and there is a great need for more experiments based on probe sampling or light scattering.

Acknowledgments

This work was partially supported by the National Science Foundation (grant ECS-9118100) and by the Minnesota Supercomputer Institute.

References

- [1] Young R M and Pfender E 1985 *Plasma Chem. Plasma Process.* **5** 1-37
- [2] Siegel R W 1991 *Processing of Metals and Alloys* ed R W Cahn (Weinheim: VCH) pp 583-614
- [3] Katz J L and Donohue M D 1982 *J. Colloid Interface Sci.* **85** 267-77
- [4] Hamill P, Turco R P, Kiang C S, Toon O B and Whitten R C 1982 *J. Aerosol Sci.* **13** 561-85
- [5] Moses J I, Allen M and Yung Y L 1992 *Icarus* **99** 318-46
- [6] Smirnov B M and Tishchenko N P 1991 *Plasma Chem. Plasma Process.* **11** 561-77
- [7] Castleman A W 1979 *Adv. Colloid Interface Sci.* **10** 73-128
- [8] Adachi M, Okuyama K and Seinfeld J H 1992 *J. Aerosol Sci.* **23** 327-37
- [9] Volmer M 1939 *Kinetik der Phasenbildung* (Dresden: Theodor Steinkopff)
- [10] Russell K C 1969 *J. Chem. Phys.* **50** 1809-16
- [11] Keesee R G 1989 *J. Geophys. Res.* **94** 14643-92
- [12] Gelbard F and Seinfeld J H 1978 *J. Comput. Phys.* **28** 357-75
- [13] Wu J J and Flagan R C 1988 *J. Colloid Interface Sci.* **123** 339-52
- [14] Rao N P and McMurry P H 1989 *Aerosol Sci. Tech.* **11** 120-32
- [15] Friedlander S K 1983 *Ann. N.Y. Acad. Sci.* **404** 354-64
- [16] Girshick S L, Chiu C-P and McMurry P H 1990 *Aerosol Sci. Technol.* **13** 465-77
- [17] Girshick S L and Chiu C-P 1990 *J. Chem. Phys.* **93** 1273-7
- [18] Girshick S L 1991 *J. Chem. Phys.* **94** 826-7
- [19] Friedlander S K 1977 *Smoke, Dust and Haze, Fundamentals of Aerosol Behavior* (New York: Wiley)
- [20] Seinfeld J H 1986 *Atmospheric Chemistry and Physics of Air Pollution* (New York: Wiley)
- [21] Girshick S L and Chiu C-P 1989 *Plasma Chem. Plasma Process.* **9** 355-69
- [22] Girshick S L and Chiu C-P 1990 *J. Aerosol Sci.* **21** 641-50
- [23] Hatch M, Wei Q, Yang L, Stachowicz L, Chiu C-P, McMurry P H, Heberlein J H and Girshick S L 1993 *11th Int. Symp. on Plasma Chemistry, Loughborough, August 22-27, 1993*
- [24] Kong P, Huang T T and Pfender E 1986 *IEEE Trans. Plasma Sci.* **14** 357-69
- [25] Yoshida T 1990 *Combustion and Plasma Synthesis of High-Temperature Materials* ed Z A Munir and J B Holt (New York: VCH) pp 328-39
- [26] Wassenaar P, Young R M and McPherson R 1989 *9th Int. Symp. on Plasma Chemistry, Pugnuchiuso, Italy, 1989* pp 919-24
- [27] Girshick S L, Chiu C-P, Muno R, Wu C Y, Yang L, Singh S K and McMurry P H 1993 *J. Aerosol Sci.* **24** 367-82
- [28] Pratsinis S E and Kim K-S 1989 *J. Aerosol Sci.* **20** 101-11
- [29] Chiu C-P 1992 *PhD Thesis* University of Minnesota
- [30] Yu B W and Girshick S L 1991 *J. Appl. Phys.* **69** 656-61
- [31] Brockmann J E, Liu B Y H and McMurry P H 1984 *Aerosol Sci. Technol.* **3** 441-51
- [32] Duncan M A and Rouvray D H 1989 *Scient. Am.* **261** December 110-115
- [33] Goldstein A N, Echer C M and Alivisatos A P 1992 *Science* **256** 1425-7
- [34] Martins J L 1989 *Z. Phys. D.* **12** 347-51
- [35] Katz J L and Wiedersich H 1977 *J. Colloid. Interface Sci.* **61** 351-5
- [36] Blander M and Katz J L 1972 *J. Statist. Phys.* **4** 55-9
- [37] Chelikowsky J R, Glassford K M and Phillips J C 1991 *Phys. Rev. B* **44** 1538
- [38] Ridge D P 1987 *Structure/Reactivity and Thermochemistry of Ions* ed P Ausloos and S G Lias (Dordrecht: Reidel) pp 1-13
- [39] Castleman A W 1982 *J. Aerosol Sci.* **13** 73-85
- [40] Holland P M and Castleman A W 1982 *J. Phys. Chem.* **86** 4181-8

Production of negative ion plasmas in a Q machine

Noriyoshi Sato

Department of Electronic Engineering, Tohoku University, Sendai 980, Japan

Received 4 January 1994; in final form 31 January 1994

Abstract. A negative ion plasma is produced by introducing a small amount of SF_6 gas into a low-temperature (≈ 0.2 eV) potassium plasma produced in a Q machine. The density ratio of negative to positive ions is continuously varied in the range up to more than 0.9999, where there appears a remarkable decrease in electron shielding for potential variations, yielding a clear effect on plasma collective phenomena. By introducing fullerene (C_{60}) particles into the Q-machine plasma, we can produce a plasma including large negative C_{60} ions. This ultrafine particle plasma might prove very attractive in fields of materials science.

1. Introduction

When large neutral particles are introduced into a plasma they are often charged negatively. Especially, in the case of electronegative particles with large electron attachment cross sections, there appears a drastic decrease in electron density, accompanied by the production of many negative ions. In work to produce plasmas including large negative ions, we have chosen 'soft' interaction between neutral and charged particles, where there is no direct electron impact ionization. To realize this condition, neutral electropilic particles are introduced into a low-temperature (≈ 0.2 eV) potassium plasma produced in a Q machine [1].

As a first step, a small amount of sulphurhexafluoride (SF_6 , mass number ≈ 146) gas was introduced into the Q machine plasma [2], a technique also employed by other groups [3, 4]. In our experiment the density ratio of negative to positive ions is varied in the range up to more than 0.9999 (almost positive ion negative ion plasma), yielding a remarkable decrease in electron shielding for potential variations. An effect of this decrease in electron shielding on plasma collective phenomena is clearly demonstrated for low-frequency plasma waves and instabilities.

By introducing so called 'fullerene' (C_{60} , mass number ≈ 720) particles [5] into the Q-machine plasma, we can produce a magnetized plasma consisting of electrons, positive K ions, and negative C_{60} ions. This ultrafine particle plasma might be very attractive in fields of materials science because it could inspire many possibilities of developing new materials based on C_{60} . In this experiment, an oven for sublimation of C_{60} is situated in the Q machine. Up to more than 90% of the electrons are observed to be attached to C_{60} particles, producing negative C_{60} ions. In the present phase of our research, we are interested in basic features of the

interaction between C_{60} particles and charged particles in a low-temperature plasma.

2. Negative ion plasma

The experiment is carried out using a single-ended Q machine [1] with a vacuum chamber, 208 mm in diameter and 1670 mm long, with pumping systems at both ends, as shown schematically in figure 1. A potassium plasma is produced by contact ionization of K atoms at a hot 52 mm diameter W plate heated up to about 2300 K under a background gas pressure of $\leq 1 \times 10^{-6}$ Torr. The plasma, with density $n_p \leq 1 \times 10^{10} \text{ cm}^{-3}$ and electron temperature $T_e \approx 0.2 \text{ eV} \approx T_i$ (ion temperature), flows along a uniform magnetic field $B \leq 2.8 \text{ kG}$ and is terminated by a metal endplate kept at a floating potential.

SF_6 gas is introduced into the machine through a

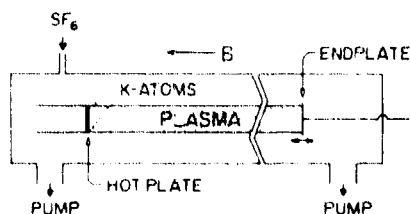


Figure 1. Schematic diagram of experimental apparatus for the production of negative ion plasmas in the case of SF_6 introduction. $P(\text{SF}_6)$ (SF_6 pressure) is estimated from an increment of the total gas pressure with an increase in SF_6 introduction. The SF_6 gas, the temperature of which is much smaller than the hot plate temperature, has no appreciable effect on the electron emission from the hot plate under our conditions.

leak valve, as shown in figure 1. The pressure of the SF_6 gas, $P(\text{SF}_6)$, is varied in the range 1×10^{-7} – 1×10^{-3} Torr. Since the SF_6 molecules have a large electron attachment cross section ($\approx 2 \times 10^{-14} \text{ cm}^2$) for $\text{SF}_6 + e \rightarrow \text{SF}_6^-$ at $T_e \approx 0.2 \text{ eV}$, a drastic decrease in electron density n_e should appear with an increase in $P(\text{SF}_6)$. For an electron fraction $1-\epsilon > 10^{-3}$, a value of $1-\epsilon$ can be determined by the Langmuir probe, where $1-\epsilon = n_e/n_+ \approx 1 - n_-/n_+ (n_+ (=n_p) \text{ and } n_- \text{ are positive and negative ion densities respectively})$. For $1-\epsilon \leq 1 \times 10^{-3}$, it is difficult to obtain a correct value of $1-\epsilon$ from the probe measurements. However, even in such a case, $1-\epsilon$ can be estimated from propagation of ion waves excited externally [2]. In our experiment, ion wave propagation measurements are used to obtain values of $1-\epsilon$ over a wide range.

Typical examples of the probe characteristics are presented in figure 2, where a drastic decrease in the negative saturation current is found in the presence of SF_6 gas. Roughly speaking, $1-\epsilon \approx 2 \times 10^{-1}$ is obtained at $P(\text{SF}_6) \approx 1 \times 10^{-6}$ Torr. With an increase in $P(\text{SF}_6)$, $1-\epsilon$ is found to decrease, yielding $1-\epsilon \approx 5 \times 10^{-2}$ and 5×10^{-3} at $P(\text{SF}_6) \approx 1 \times 10^{-5}$ and 1×10^{-4} Torr respectively. It is possible to estimate $1-\epsilon \approx 1 \times 10^{-4}$ at $P(\text{SF}_6) \approx 5 \times 10^{-4}$ Torr from ion wave propagation. At $P(\text{SF}_6) \approx 1 \times 10^{-3}$ Torr, $1-\epsilon$ is supposed to be around 1×10^{-5} , i.e. $\epsilon \approx 0.99999$, although it is almost impossible to measure such an extremely small value of $1-\epsilon$. The theoretical dependence of $1-\epsilon$ on $P(\text{SF}_6)$ will be discussed elsewhere.

With a decrease in $1-\epsilon$, there appears a decrease in electron shielding for potential variations, yielding a large effect on plasma collective phenomena. Here, typical examples of such an effect are presented for low-frequency plasma waves and instabilities.

Ion waves are typical low-frequency electrostatic plasma waves for which electron shielding is quite important. In a plasma consisting of electrons, positive ions of mass m_+ and temperature T_+ , and negative ions of mass m_- and temperature T_- , there are two branches, fast and slow modes, corresponding to the two ion species [6]. Here, for simplicity, we assume $m_- \gg m_+$, $T_+ \gg T_- \gg T_e$, and plane waves propagating along a

strong magnetic field. The dispersion relation of the fast mode is then given by

$$\omega^2 \approx \omega_p^2 / (1 + k_e^2/k^2) + 3(T_+/m_+)k^2 \quad (1)$$

where $\omega/2\pi$ and $2\pi/k$ are wave frequency and wavelength respectively, $\omega_p/2\pi (= (n_+ e^2/\epsilon_0 m_+)^{1/2}/2\pi)$ is the positive ion plasma frequency, and $1/k_e (= (\epsilon_0 T_e/n_e e^2)^{1/2})$ is the electron Debye shielding length. In this equation, k_e^2/k^2 shows a contribution of the electron shielding for potential variations provided by ion motions. For $k_e^2/k^2 \gg 1$, equation (1) is reduced to $\omega^2/k^2 \approx [T_e/(1-\epsilon) + 3T_+]/m_+$ which yields the phase velocity $v_p (= \omega/k)$ of ion sound waves. For $k_e^2/k^2 \ll 1$, however, the potential variations are not shielded by electrons and $\omega^2 \approx \omega_p^2 + 3(T_+/m_+)k^2$ which yields ion plasma waves as an extension of ion plasma oscillations ($\omega^2 \approx \omega_p^2$). The relation (1) can also be applied to a plasma consisting of electrons and positive ions. In this case, $v_p \approx (T_e + 3T_+)/m_+$ for ion sound waves. In the presence of negative ions, $k_e^2 = k_e^{*2}(1-\epsilon)/k^{*2} = n_e e^2/\epsilon_0 T_e$ and, with a decrease in $1-\epsilon$ for a fixed plasma density $n_p (=n_+)$, k_e^2 decreases, showing a decrease in electron shielding. Thus, $T_e(1-\epsilon)$ appears instead of T_e and provides a drastic increase in v_p of ion sound waves as $1-\epsilon \rightarrow 0$, although $k_e^2/k^2 \gg 1$ is satisfied in the frequency range much lower than that in a plasma without negative ions.

On the other hand, the slow mode appears only in the presence of negative ions and has the dispersion relation:

$$\omega^2 \approx \omega_p^2 / (1 + k_e^2/k^2 + k_-^2/k^2) + 3(T_-/m_-)k^2 \quad (2)$$

where $\omega_p/2\pi (= (n_- e^2/\epsilon_0 m_-)^{1/2}/2\pi)$ is the negative ion plasma frequency and $1/k_- (= (\epsilon_0 T_-/n_- e^2)^{1/2})$ is the positive ion Debye shielding length. In this relation, k_-^2/k^2 shows a positive ion shielding for potential variations provided by negative ions. Under our assumptions, $k_-^2 \ll k_e^2$ and equation (2) is reduced to $\omega^2 \approx \omega_p^2 / (1 + k_e^2/k^2) + 3(T_-/m_-)k^2$ which does not yield such a drastic dependence on $1-\epsilon$ as the fast mode.

Here we are interested in the fast mode because this mode is very sensitive to $1-\epsilon$. In our experiment, the assumption $T_+ \gg T_-$ is not satisfied and there is an ion flow with speed $v_{i0} \lesssim (T_+/m_+)^{1/2}$. But, when $1-\epsilon$ is so small that the conditions $T_e(1-\epsilon) \gg T_+$ and $[T_+(1-\epsilon)]^{1/2} \gg v_{i0}$ are satisfied, relation (1) can be applied to the results of the fast mode in our experiment.

In the experiment, a grid is used to generate small-amplitude ion waves propagating toward the endplate along a magnetic field [7]. Typical examples of the wave patterns obtained from an interferometer detection system are presented in figures 3 and 4. In the presence of a small amount of SF_6 gas, there appears a clear increase in the wavelength, as shown in figure 3 where the patterns of the fast mode with $\omega/2\pi = 250 \text{ kHz}$ are demonstrated at $P(\text{SF}_6) = 0, 1.5 \times 10^{-6}$, and 4.5×10^{-6} Torr. It is also found that the spatial wave damping at $P(\text{SF}_6) = 1.5 \times 10^{-6}$ Torr is small in comparison with that at $P(\text{SF}_6) = 0$ Torr. This is because the Landau

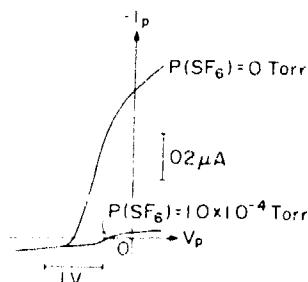


Figure 2. Typical probe characteristics at $P(\text{SF}_6) = 0$ and 1.0×10^{-4} Torr. Probe is a tantalum wire of 0.125 mm in diameter and 1.5 mm long.

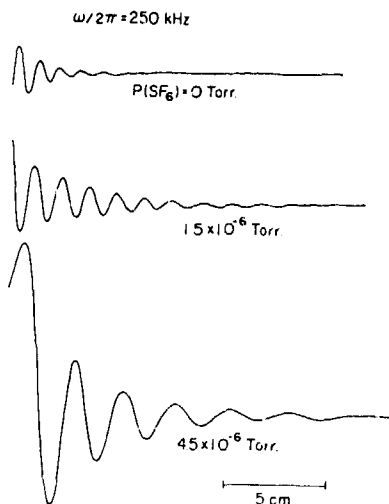


Figure 3. Wave patterns of ion waves (fast mode) with $\omega/2\pi = 250$ kHz.

damping due to positive ions decreases with an increase in v_p . For a further increase in v_p , however, the damping again becomes large because the Landau damping due to electrons increases, as shown by the wave pattern at $P(\text{SF}_6) = 4.5 \times 10^{-6}$ Torr. If $\omega/2\pi$ is decreased, we can observe the slow mode in addition to the fast mode in the presence of negative ions, as shown at $\omega/2\pi = 5$ kHz in figure 4. The dispersion relations of the fast mode are shown with $P(\text{SF}_6)$ as a parameter in figure 5. At $P(\text{SF}_6) = 0$ Torr, there is a linear relation between $\omega/2\pi$ and k [7]. At $P(\text{SF}_6) \geq 5.0 \times 10^{-5}$ Torr, where $1 - \epsilon \leq 5 \times 10^{-2}$, the ion waves are found to become dispersive, although v_p is almost constant in the low-frequency range. We can estimate $1 - \epsilon$ by measuring v_p in this range of $\omega/2\pi$. For example, at $P(\text{SF}_6) \approx 5 \times 10^{-4}$ Torr, v_p is larger by two orders of magnitude than $(T_e/m_e)^{1/2} (\approx 7.0 \times 10^4 \text{ cm s}^{-1})$, yielding $1 - \epsilon \approx 10^{-4}$. A further increase in $P(\text{SF}_6)$ yields a much smaller value of $1 - \epsilon$. For such a small value of $1 - \epsilon$, however, the

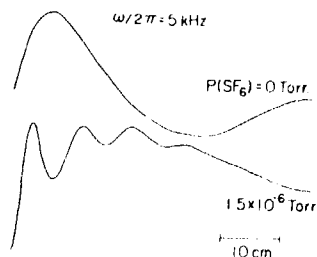


Figure 4. Wave patterns of ion waves with $\omega/2\pi = 5$ kHz. Upper trace: the fast mode in the absence of SF_6 . Lower trace: the slow mode in addition to the fast mode in the presence of SF_6 .

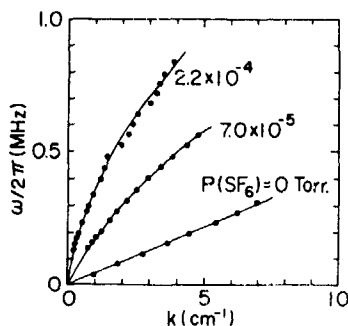


Figure 5. Dispersion relations of ion waves (fast mode) observed with $P(\text{SF}_6)$ as a parameter.

wavelength of the fast mode in the low frequency region is much longer than the plasma column length in our machine. Besides, the wave damping is strong because the Landau damping due to electrons becomes extremely large as v_p approaches the electron thermal speed although the electron fraction is quite small. Thus, ion wave propagations do not give a correct value of $1 - \epsilon$ for $1 - \epsilon < 10^{-4}$. However, $1 - \epsilon$ is supposed to be around 10^{-3} at $P(\text{SF}_6) \approx 1 \times 10^{-3}$ Torr as an extrapolation of our measurements of ion sound waves.

Similar phenomena have also been observed on low-frequency electrostatic plasma instabilities. In the case of an ion cyclotron wave instability [2, 4], two modes appear corresponding to the ion species in the presence of negative ions. Both of them show an increase in $\omega/2\pi$ as $1 - \epsilon$ is increased. The effect on drift wave instability is quite remarkable [2]. With an increase in $1 - \epsilon$, there appears a drastic increase in the amplitude which has a maximum value around $P(\text{SF}_6) \approx 8 \times 10^{-5}$ Torr; this is accompanied by a decrease in $\omega/2\pi$. But, at $P(\text{SF}_6) \geq 5 \times 10^{-3}$, no coherent signal of drift waves is observed.

3. C_{60} plasma

Since a simple method for producing Buckminster fullerene (C_{60}) particles was established [8], a number of works have been performed on C_{60} because this new form of carbon is of crucial importance for the development of new materials. C_{60} particles have a large electron affinity (≈ 2.65 eV), although this value is smaller than that of SF_6 molecules (≈ 3.39 eV). Thus, as a result of their interaction with a low-temperature plasma, electrons are expected to be attached to C_{60} particles, yielding large negative C_{60} ions in the plasma. Because of their stability and well defined mass and size (diameter ≈ 0.7 nm), the ultrafine particle plasma including large negative C_{60} ions is rather simple and might be easy to treat in comparison with plasmas including unstable fine particles (or dusts) of variable mass and size.

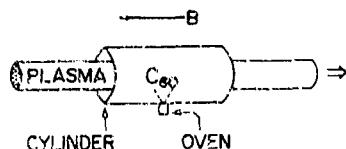


Figure 8. An oven for C_{60} sublimation, together with a cylinder surrounding a plasma column produced in the Q machine. Oven: copper pot, 18 mm in diameter and 20 mm long, with a 3 mm diameter hole for C_{60} injection. Cylinder: copper cylinder with open ends, 76 mm in diameter and 200 mm long.

In our experiment, a plasma consisting of electrons, positive K ions, and negative C_{60} ions is produced by sublimating C_{60} , which is placed in a special oven, into the Q machine described in section 2. Temperature for the sublimation is in the range 350–400 °C. As shown schematically in figure 6, the Q-machine plasma passes through a cylinder (76 mm in diameter and 200 mm long) which is situated at a position around the machine centre. The cylinder has a 20 mm diameter hole on the side wall, where the oven is set with a small hole to inject C_{60} particles in the direction toward the Q-machine plasma. In the oven, C_{60} is kept as a soft film on the inner surface. The oven temperature T_o , which is measured at its base, is carefully changed in the range 200 (no oven heating)–500 °C while the cylinder is kept at a constant temperature around 400 °C. In the axial region surrounded by the cylinder, the C_{60} density is estimated to be, depending on T_o , in the range $\lesssim 10^{13} \text{ cm}^{-3}$ which corresponds to the pressure range of C_{60} particles, $P(C_{60}) \lesssim 10^{-6} \text{ Torr}$. In the region outside the cylinder, these values are smaller than those inside the cylinder by one to two orders of magnitude.

An 'omegatron' analyser [9], situated behind a small hole in the endplate, is used for detection of negative C_{60} ions. This analyser gives signals due to the cyclotron resonance of ion species when the frequency of an applied RF electric field is equal to the corresponding ion cyclotron frequencies.

C_{60} particle control is monitored by a negative saturation current of the Langmuir probe I_{s-} , which depends on T_o , as shown schematically in figure 7. With an increase in T_o , I_{s-} decreases, implying a decrease in n_e . The probe characteristics at $T_o = 480$ °C, together with the curve at $T_o = 200$ °C, are presented in figure 8, where the probe is set at the radial centre. It can be

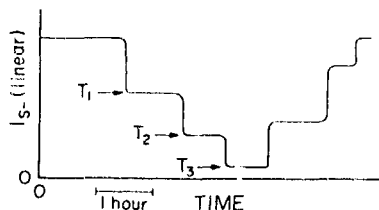


Figure 7. Variation of negative saturation current I_{s-} of the Langmuir probe against the oven temperature T_o , which is increased to T_1 (≈ 350 °C), T_2 (≈ 400 °C), and T_3 (≈ 450 °C).

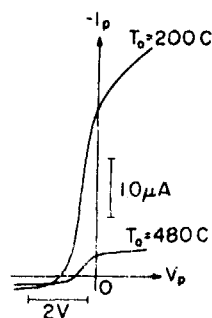


Figure 8. Typical probe characteristics at $T_o = 200$ and 480 °C.

found that a decrease in the positive saturation current I_{s+} also appears as T_o is increased. However, I_{s+} decreases more drastically than I_{s-} , meaning that a decrease in n_e is accompanied by an increase in n_- [10, 11]. According to the measurements using the omegatron analyser, a signal appears when the applied frequency $\omega/2\pi$ is equal to $\omega_{C_{60}}/2\pi$ (ion cyclotron frequency of C_{60}), as shown in figure 9 (proving that negative ions produced are exactly C_{60}). In this experiment $1 - \epsilon \gtrsim 1 \times 10^{-1}$. With an increase in n_- , the radial plasma profile becomes broad. This is due to the large Larmor radius of C_{60} ions, which gives rise to a profile broadening of K⁺ ions, yielding the decrease in I_{s+} at the radial centre in figure 8.

Wave patterns of ion waves are presented in figure 10. The same effects of negative ions on ion wave propagation as in the case of the introduction of SF_6 into the Q machine are observed. We observe an increase in the phase velocity v_p of the fast mode when T_o is increased. As mentioned above, $1 - \epsilon \gtrsim 1 \times 10^{-1}$ in our experiment and we cannot neglect the flow speed of K⁺ ions, which is due to acceleration by the electron sheath of a potential drop $\gtrsim 0.5$ V in front of the hot plate. Thus, the increase in v_p is not so drastic as in the case of SF_6 . The lower trace in this figure, however, clearly demonstrates the propagation of the slow mode in addition to the fast mode in the presence of C_{60} ions. The observed phase velocities of the fast and slow modes are almost consistent with predicted values although we cannot apply the simple dispersion relations given by equations (1) and (2) to the results in the experiment.

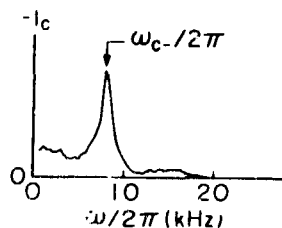


Figure 9. Collector current I_c of 'omegatron' analyser as a function of frequency $\omega/2\pi$ of applied RF electric field. $\omega_c/2\pi$ is the ion cyclotron frequency of C_{60} . $B = 3.98 \text{ kG}$.

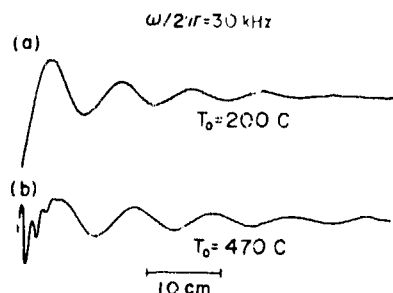


Figure 10. Wave patterns of ion waves with $\omega/2\pi = 30$ kHz. Upper trace: the fast mode in the absence of C_{60} ($T_0 = 200^\circ\text{C}$). Lower trace: the slow mode in addition to the fast mode in the presence of C_{60} ($T_0 = 470^\circ\text{C}$).

The electrostatic ion cyclotron instability is also observed to be generated in the frequency ranges above the ion cyclotron frequencies of K^+ and SF_6^- ions as in the measurements on the plasma including K^+ and SF_6^- ions. These results also confirm the existence of C_{60}^- ions.

4. Conclusions

In this work we have produced two kinds of magnetized plasmas with negative ions which are much larger than positive ions. One of them is a plasma consisting of electrons, K^+ ions, and SF_6^- ions, produced by introducing SF_6 gas into a low-temperature potassium plasma in a Q machine. The SF_6^- fraction is increased up to a value more than 0.9999. A decrease in electron shielding causes a large effect on plasma collective phenomena, as demonstrated by ion wave propagations. This plasma is useful for investigating characteristic features of negative ion plasmas.

By introducing C_{60} particles into the Q machine, an ultrafine particle plasma consisting of electrons, K^+ ions, and C_{60}^- ions has been produced. In this case, the C_{60}^- fraction is ≥ 0.9 , smaller than that in the case of SF_6^- . This is partly due to the electron affinity being smaller than that of SF_6 . However, the C_{60}^- fraction could be increased

by increasing the C_{60} flux introduced into the machine. Because of its simplicity the plasma produced would be useful for investigating the basic features of various ultrafine particle plasmas. This particular plasma might also be attractive in fields of materials science. Since C_{60} particles are charged, it is easy to control them electrically and/or magnetically, providing a new approach for producing C_{60}^- based materials.

Acknowledgments

The author would like to thank many colleagues, especially R Hatakeyama, S Iizuka, I Ishikawa, T Mieno and T Hirata, who have participated in the experiments on production of negative ion plasmas at Tohoku University. He also thanks H Ishida for his technical assistance.

References

- [1] Motley R W 1975 *Q Machines* (New York: Academic)
- [2] Sato N 1989 *A Variety of Plasmas* ed A Sen and P K Kaw (Bangalore: Indian Academy of Sciences) p 79
- [3] Sheehan D R and Rynn N 1988 *Rev. Sci. Instrum.* **59** 1661
- [4] Song B, Suszczyński B, D'Angelo N and Merlino R L 1989 *Phys. Fluids* **B1** 2316
- [5] Kroto H W, Heath J K, O'Brien S C, Curl R E and Smalley R E 1985 *Nature* **318** 162
- [6] D'Angelo N, Geeler S V and Ohe T 1966 *Phys. Fluids* **9** 1605
- [7] Sato N, Sugai H, Sasaki A and Hatakeyama R 1973 *Phys. Rev. Lett.* **30** 685
- [8] Krätschmer W, Lamb L D, Fortovopoulos E. and Huffman D R 1990 *Nature* **347** 754
- [9] Sommer H, Thomas H A and Hipple J A 1951 *Phys. Rev.* **82** 697
- [10] Sato N, Mieno T, Hirata T, Hatakeyama R and Iizuka S 1992 *Proc. 9th Autumn Meeting of the Japan Society of Plasma Science and Nuclear Fusion Research (Sendai, Japan)* p 201
- [11] Hirata T, Yagi Y, Mieno T, Iizuka S, Hatakeyama R and Sato N 1993 *Proc. 48th Annual Meeting of the Physical Society of Japan (Sendai, Japan)* p 184

Charging of particles in a plasma

J Goree

Department of Physics and Astronomy, The University of Iowa, Iowa City, IA 52242, USA

Received 28 December 1993, in final form 30 December 1993

Abstract. Several models that predict the charge of particles in a plasma are reviewed. The simplest is based on orbit-limited probe theory. This basic model can be improved by adding several effects: charge reduction at high dust densities, electron emission, ion trapping and fluctuations. The charge is reduced at high dust densities, when a significant fraction of the charge in the plasma resides on the particles, depleting the plasma. Electron emission due to electron impact or ultraviolet exposure can cause a particle to have a positive charge, which has useful implications for plasma processing, since particles are confined in a discharge only if they have a negative charge. Ion trapping occurs due to ion-neutral collisions within the attractive Debye sphere of a negatively charged particle. Trapped ions reduce the net electric force on a particle. A particle's charge fluctuates because the currents collected from the plasma consist of discrete charges arriving at the particle at random intervals. The root mean square fractional fluctuation level varies as $0.5\langle N \rangle^{-1/2}$ where $\langle N \rangle = \langle Q \rangle/e$ is the mean number of electron charges on the particle.

1. Introduction

A dust particle in a plasma gains an electric charge and responds to electric forces. The charge can range from zero to hundreds of thousands of electron charges, depending on the particle size and the plasma conditions. It arises from collecting electrons and ions from the plasma and sometimes from emitting electrons. In a plasma in which emission processes are unimportant, the equilibrium charge is negative because the flux of electrons to an uncharged surface is high relative to that of ions. On the other hand, when electron emission is significant, the equilibrium charge is positive.

A calculation of the charge on a particle is the starting point of every theory of dusty plasmas. Here I review the common 'orbit-limited' theory of charge collection, and then I present some effects that are often neglected in this model, but may have a significant impact on the particle's transport. These effects are: a reduction in charge due to high dust density, positive charging by electron emission, a reduction in electric forces due to ion trapping and charge fluctuations. These effects have been presented already in the literature; the purpose of this paper is to review them and to give practical formulae with illustrative examples.

2. The basic model: orbit-limited theory

Most dusty plasma charging theories are based on theories of electrostatic probes in plasmas. These theories

predict the electron and ion currents to the probe. The currents are termed 'orbit-limited' when the condition $a \ll \lambda \ll \lambda_{\text{mfp}}$ applies, where a is the particle radius, λ is the Debye length and λ_{mfp} is a collisional mean free path between neutral gas atoms and either electrons or ions [1, 2]. In that case, the currents are calculated by assuming that the electrons and ions are collected if their collisionless orbits intersect the probe's surface. It is assumed that the currents are infinitely divisible; that is, the discrete nature of the electronic charge is ignored. The latter assumption must be reversed to account for the fluctuations of the particle, as shown later.

For the collection of Maxwellian electrons and ions, characterized by temperatures T_e and T_i , the orbit-limited currents for an isolated spherical particle are [3]

$$\begin{aligned} I_e &= I_{0e} \exp(e\phi_s/kT_e) & \phi_s < 0 \\ I_e &= I_{0e}(1 + e\phi_s/kT_e) & \phi_s > 0 \\ I_i &= I_{0i} \exp(-z_i e\phi_s/kT_i) & \phi_s > 0 \\ I_i &= I_{0i}(1 - z_i e\phi_s/kT_i) & \phi_s < 0. \end{aligned} \quad (1)$$

Here ϕ_s is the surface potential of the particle relative to the plasma and z_i is the electronic charge of the ions. The coefficients I_{0e} and I_{0i} represent the current that is collected for $\phi_s = 0$, and are given by $I_{0\alpha} = n_\alpha q_\alpha (kT_\alpha/m_\alpha)^{1/2} \pi a^2 f_\alpha(w, v_{th})$, where n_α is the number density of plasma species α . Here $f_\alpha(w, v_{th})$ is a complicated function of the thermal velocity $v_{th} = (2kT_\alpha/m_\alpha)^{1/2}$ and the drift velocity w between the plasma and the particle. [3]. Simple expressions are available in the limiting cases of

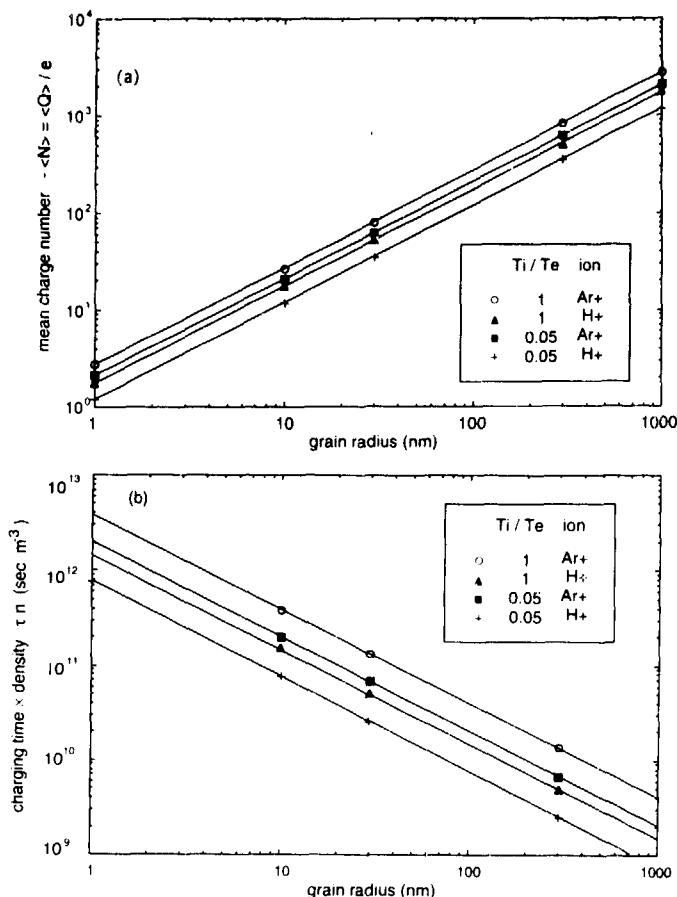


Figure 1. (a) Mean charge number $\langle N \rangle = \langle Q \rangle / e$ and (b) charging time τn (sec m^{-3}) as a function of particle radius for four combinations of temperature ratios and ion masses. These values are for the basic orbit-limited charging model, assuming non-drifting Maxwellians and no electron emission.

small and large drift velocities:

$$I_{0z} = 4\pi a^2 n_i q_i (kT_i / 2\pi m_i)^{1/2} \quad w/v_{th} \ll 1 \quad (2a)$$

$$I_z = \pi a^2 n_i q_i w [1 - 2q_i \phi_s / (m_i w^2)] \quad w/v_{th} \gg 1. \quad (2b)$$

In some laboratory discharges, the ions or electrons may drift at a significant speed. For example, the ions enter the electrode sheath at the ion acoustic speed, which is much faster than the ion thermal speed.

The charge Q is related to the particle's surface potential ϕ_s , with respect to a plasma potential of zero, by

$$Q = C\phi_s \quad (3)$$

where C is the capacitance of the particle in the plasma. For a spherical particle satisfying $a \ll \lambda$, the capacitance is [3]

$$C = 4\pi\epsilon_0 a. \quad (4)$$

The standard 'continuous charging model' of particle charging in a plasma neglects the discrete nature of the electron's charge. The particle's charge is assumed to vary smoothly, rather than in integer increments. A particle with zero charge that is immersed in a plasma will gradually charge up, by collecting electron and ion currents, according to

$$dQ/dt = \sum I_s \quad (5)$$

To find the equilibrium, one can set $dQ/dt = 0$ in equation (5). This yields the steady-state potential ϕ_s and steady-state charge $\langle Q \rangle$.

Table 1. Coefficients for ϕ_i , Q and τ appearing in equations (6) and (7). These values were found by a numerical solution of the continuous charging model, assuming non-drifting Maxwellians and no electron emission. From [5].

m_i (amu)	T_i/T_e	K_ϕ (V eV ⁻¹)	K_Q ($\mu\text{m}^{-1}\text{eV}^{-1}$)	K_τ (s $\mu\text{m cm}^{-3}\text{eV}^{-1/2}$)
1	0.65	-1.698	-1179	7.66×10^2
1	1	-2.501	-1737	1.51×10^3
40	0.05	-2.989	-2073	2.05×10^3
40	1	-3.952	-2631	3.29×10^3

$$\phi_i = \langle \phi_i \rangle = K_\phi T_e$$

$$\langle Q \rangle / e = K_Q a k T_e \quad (6)$$

where the coefficients K_ϕ and K_Q are functions of T_i/T_e and m_i/m_e , and they must be determined numerically. Useful values for these coefficients are listed in table 1, and illustrative values of the charge are shown in figure 1(a). When electron emission is neglected, the floating potential and K_ϕ are both negative, since the electrons have higher thermal velocity than ions.

Note that ϕ_i is independent of the particle's size, but it depends on the plasma temperatures. On the other hand, the charge $\langle Q \rangle$ is proportional to the particle's radius, $\langle Q \rangle \propto a$. For example, a sphere in a hydrogen plasma with $T_e = T_i$ has the Spitzer [4] potential $\phi_i = -2.50 k T_e / e$.

The charging time τ is inversely proportional to the plasma density. It depends on the particle size, temperature and ion mass according to [5]

$$\tau = K_\tau \frac{(k T_e)^{1/2}}{an} \quad (7)$$

where K_τ is a function of T_i/T_e and m_i/m_e . The fact that τ is inversely proportional to both a and n means that the fastest charging occurs for large particles and high plasma densities. One can define τ as the time required for a particle's charge to reach a fraction $(1 - e^{-1})$ of its equilibrium value, when it is initially uncharged. [5] Using this definition, the constant K_τ has the values summarized in table 1. Illustrative values of the charging time are shown in figure 1(b).

No dust particle is perfectly spherical, and so one should ask how much the sphericity assumption limits the theory's validity. This assumption appears twice in the model: the capacitance in equation (4) and the currents in equation (1). For the capacitance, the shape does not matter greatly as long as one chooses for a the typical size of the particle. The electron and ion currents are dominated by the shape of the electrostatic equipotential surfaces around the particle. The electric perturbation caused by the particle extends into the plasma a distance characterized by the shielding length, λ . Since the case treated here is $a \ll \lambda$, the equipotentials are distorted from a spherical shape only in a small central part of a spherical region of radius λ . Consequently, the

sphericity assumption will introduce only a small error, as long as $a \ll \lambda$, as it is in most dusty plasmas.

3. Reduction of the charge due to high particle density

So far, I have considered the case of a single isolated particle, but this assumption is often unsuitable for modelling dusty laboratory plasmas, since they can have high particle concentrations. Several theorists have demonstrated that, as the dust number density is increased, the particle's floating potential and charge are reduced, due to electron depletion on the particles. [9] This electron depletion also modifies the plasma potential. The crucial parameter is Havnes's value P , which is basically the ratio of the charge density of the particles to that of the electrons. When $P > 1$, the charge and floating potential are significantly diminished, while for $P \ll 1$ the charge and floating potentials approach the values for an isolated particle (see section 2). In practical units, P is given by [6]

$$P = 695 T_e v_{Te} a_{\mu\text{m}} N_{\text{cm}^{-3}} / n_{\text{cm}^{-3}} \quad (8)$$

where N and n are the dust and electron number densities, respectively. This expression is written in a form for a mono-dispersive size distribution; a more general expression accounting for size dispersion is offered by Havnes *et al* [6].

Havnes *et al* [6] solved the charge balance equations, and reported useful analytic expressions for the particle's floating potential ϕ_i (referenced to the plasma potential) and the plasma potential ϕ_p (referenced to a dust-free plasma). These are functions of the parameter, P ,

$$e\phi_i/kT = (K_\phi + a_1 P) / (1 + b_1 P + b_2 P^2)$$

$$e\phi_p/kT = (c_1 P + c_2 P^2) / (1 + d_1 P + d_2 P^2) \quad (9)$$

where the coefficients K_ϕ , b , c and d are listed in table 2.

Table 2. Coefficients for charge and plasma potential, assuming non-drifting Maxwellians with $T_e = T_i$, singly charged ions, and no electron emission. From [6].

Coefficient	Ion mass (amu)	
	1	32
K_ϕ	2.5	3.9
a_1	0.764	1.14
b_1	1.09	1.1
b_2	0.12	0.0754
c_1	1.21	1.98
c_2	0.21	0.252
d_1	1.04	1.17
d_2	0.112	0.0917

A representative plot of equation (9) is shown in figure 2.

In a RF discharge, the dust density is often high enough to attain $P \gg 1$. Consider for example the dust density measurements of Boufendi *et al* [7]. In a silane RF discharge, particles grew to a radius $a = 115$ nm, as determined by electron microscopy. Mie scattering indicated a particle density of $1 \times 10^9 \text{ cm}^{-3}$, while the ion density was $5 \times 10^9 \text{ cm}^{-3}$, based on ion saturation current measurements using a Langmuir probe. I assume $T_e = 2 \text{ eV}$, which is probably accurate to within a factor of three. This yields $P = 3.2$ (accurate to within the same factor of three), corresponding to a 60% reduction in the particle's charge (according to equation (9) and figure 2).

4. Electron emission

Electrons can be emitted by the particle due to electron impact, UV exposure, thermionic emission and field emission. The first two are probably the most important for laboratory dusty plasmas. Electron emission constitutes a positive current with respect to the particle, and, if it is large enough, it can cause the particle to be positively charged. Even if the particle is not always positive, it might sometimes fluctuate to a positive level, as described in sections 6 and 7.

4.1. Secondary electron emission

The secondary emission yield δ depends on both the impact energy E and particle material. The yield is generally much larger for electron impact than for ion impact. For bulk materials, the energy-dependence of the electron-impact yield is [8,9]

$$\delta(E) = 7.4\delta_m(E/E_m)\exp[-2(E/E_m)^{1/2}]. \quad (10)$$

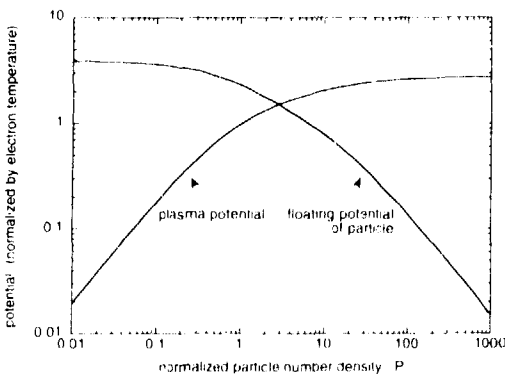


Figure 2. Dependence of floating potential ϕ_f/kT and plasma potential ϕ_p/kT on particle number density. These data are from equation (9) and table 2, for singly charged ions of mass 32 amu, with non-drifting Maxwellians and $T_e = T_i$. The normalized particle density is $P = 695 T_{av} a_{min} N_{cm} / n_{cm}$.

The peak yield δ_m is at energy E_m , and both of these are material constants. Graphite, for example, has $\delta_m = 1$ and $E_m = 250 \text{ eV}$, while for quartz $\delta_m = 2.1-4$ and $E_m = 400 \text{ eV}$ [8].

Secondary emission from small particles is significantly enhanced above the value for bulk materials. This was shown by Chow *et al* [10], whose theory included geometric effects. Scattered electrons escape more easily from a small particle than from a semi-infinite slab of material, and so δ is enhanced.

Expression (10) is for mono-energetic electrons of energy E . It must be remembered that electrons in a plasma have a distribution function. Assuming a Maxwellian primary electron distribution with temperature T_e , Meyer-Vernet [8] found the secondary currents I_{sec} due to an impinging electron current I_e ,

$$\begin{aligned} I_{sec}/I_e &= 3.7\delta_m F_3(E_m/4kT_e) & \phi_s < 0 \\ I_{sec}/I_e &= 3.7\delta_m \exp[(-e\phi_s/k)(T_e^{-1} - T_e^{-1})] & (11) \\ & \times F_{3B}(E_m/4kT_e) & \phi_s < 0 \end{aligned}$$

where

$$\begin{aligned} F_3(x) &= x^2 \int_0^x t^5 \exp[-(xt^2 + t)] dt \\ F_{3B}(x) &= x^2 \int_B^x t^5 \exp[-xt^2 + t] dt \\ B &= [(e\phi_s/kT_e)(4kT_e/E_m)]^{1/2} \end{aligned}$$

and T_e is the temperature of the emitted electrons, typically $1 < T_e < 5 \text{ eV}$.

By including these currents into the charging balance the particle potential can become positive [8,9]. For Maxwellian electrons, a switch in polarity occurs at an electron temperature of 1–10 eV, depending on δ_m . The reason this happens at temperatures well below the energy for peak emission E_m is the contribution of electrons in the tail of the distribution.

4.2. Photoelectric emission

Absorption of UV radiation releases photoelectrons and hence causes a positive charging current. Just like secondary electron emission, it can make the particle positively charged [9].

Electron emission depends on the material properties of the particle (its photoemission efficiency). It also depends on the particle's surface potential, because a positively charged particle can recapture a fraction of its photoelectrons. Taking this into account, the photoemission current is [9]

$$\begin{aligned} I_p &= 4\pi a^2 I_\nu \mu & \phi_s < 0 \\ I_p &= 4\pi a^2 I_\nu \mu \exp(-e\phi_s/kT_p) & \phi_s > 0 \end{aligned} \quad (12)$$

Here I_ν is the UV flux and μ is the photoemission efficiency ($\mu \approx 1$ for metals and $\mu \approx 0.1$ for dielectrics). Equation (12) assumes an isotropic source of UV and

that the photoelectrons have a Maxwellian energy spectrum with a temperature T_p .

A laboratory plasma is a source of UV, due to electron-impact excitation of neutrals. However, there has been no analysis known to the author of whether this UV radiation can be strong enough to alter the charge significantly. In space plasmas, it is well known that dust and other objects often charge to positive polarity due to UV exposure.

5. Ion trapping

A particle's negative charge creates a Debye sheath, which is an attractive potential well for positive ions. A passing ion can become trapped in this well when it suffers a collision within the particle's Debye sphere, simultaneously losing energy and changing its orbital angular momentum. It remains trapped there, in an orbit bound to the particle, until it is detrapped by another collision [11].

Trapped ions are important because they shield the charged particle from external electric fields. Since these fields provide the particle's levitation and confinement in the discharge, shielding must be modelled in order to understand confinement. This shielding works the same way as in an atom, where orbital electrons screen the charge of the nucleus. The effectiveness will vary with the number of trapped ions.

Untrapped ions do nothing to screen the particle's charge from an electric field. The author believes there has been some confusion in the literature over how Debye shielding works. Untrapped ions do contribute to reducing the force applied by the particle on other distant charges, but they do not reduce the force applied to the particle by an electric field. Only trapped ions can do that.

Ion trapping has been ignored often in dusty plasma theories, probably because it is not easy to deal with analytically. At least two numerical methods [11,12] have been reported recently. The methods are useful for estimating the number of trapped ions, N_{trap} . However, this value has been reported for only a limited number of conditions, to date.

Both methods involve simulating ion motion in the field of the charged particle by integrating the equation of motion. They also both include collisions. In a code with a fixed time step that is short compared with the mean time between collisions, this is done typically by using a Monte Carlo method. The collision probability $1 - \exp(-\Delta t/\tau_{ion,p})$ is evaluated at each time step and compared with a random number between 0 and 1 to determine whether a collision took place during that time step.

Choi and Kushner [12] developed a three-dimensional particle-in-cell (PIC) code, where all the ion orbits were tracked in a simulation box. Electrons and ions are absorbed by the particle, allowing dynamic simulation of the particle's charge and the surrounding electrostatic potential. Ions are subject to collisions, and those that

are trapped are counted. This number of trapped ions fluctuates in time, as individual ions became trapped and then lost.

Goree [11] handled the incoming flux of incoming ions, one at a time, as individual test particles. The number of trapped ions at steady state is computed by assuming a balance between collisional trapping and detrapping. Assuming that ion neutral collisions are dominant, this theory predicts that N_{trap} is independent of the mean free path, and increases with the plasma ion density. The model was implemented as a Monte Carlo code for many test ions selected from the incoming ion flux. If an ion becomes trapped, its orbit is followed until it is eventually scattered into an untrapped trajectory by further collisions. This code showed that $N_{trap} \gg 1$ when the ion density is $\gg 10^6 \text{ cm}^{-3}$, which it always is in plasma processing discharges, indicating that ion trapping will cause significant electrical screening. These results were for $a = 10 \mu\text{m}$ and a plasma with $\lambda_D = 100 \mu\text{m}$ and an ion-neutral mean free path much shorter than λ_D . A limitation of this theory is that it uses a prescribed electrostatic potential. This makes the simulation valid only when the number of trapped ions is small, $N_{trap} \ll Q/e$. In principle it could be extended to compute the potential self-consistently for the actual electron and ion densities, as is done in the simulation by Choi and Kushner [12].

6. Charge fluctuations

The standard continuous charging model described in section 2 neglects the fact that the electron and ion currents collected by the particle actually consist of individual electrons and ions. The charge on the particle is an integer multiple of the electron charge, $Q = Ne$, where N changes by -1 when an electron is collected and by $+1$ when an ion is absorbed. Electrons and ions arrive at the particle's surface at random times, like shot noise. The charge on a particle will fluctuate in discrete steps (and at random times) about the steady-state value $\langle Q \rangle$.

Several models have been reported recently to predict the fluctuation level. Choi and Kushner's PIC simulation [12] yielded a time series for the charge of an isolated particle, for a particular set of parameters. The charge clearly fluctuated about a mean value. Tsyrovitch [13] developed an analytic theory that is unique because it was not for an isolated particle, but rather for a cloud of particles in the plasma. Taking into account how the fluctuation of the charge on one particle affects the charge on a neighbour, he found that the fluctuation level increases with particle number density.

Cui and Goree [8] used a numerical method, where the problem for an isolated particle was cast in terms of a probability per unit time of collecting an electron or ion from the plasma. To do this, they first converted the current I_s of the continuous charging model into a probability per unit time (dP/dt) of collecting an ion or electron, by $(dP/dt) = I_s/q_i$. This probability depends

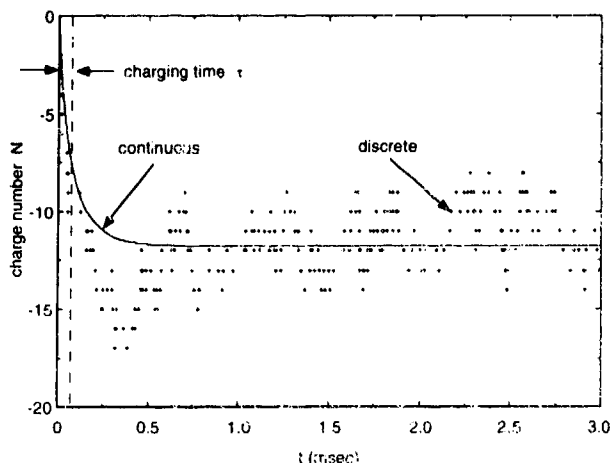


Figure 3. Temporal evolution of charge number $N = Q/e$, for a small particle ($a = 10$ nm) in an H^+ plasma with $T_e/T_i = 0.05$ and $n = 10^{15} \text{ m}^{-3}$. When discrete electronic charges are taken into account, fluctuations of the particle's charge are apparent, due to electrons and ions arriving at random times. From [5].

in a realistic way on the particle's potential; when the particle becomes more negative, it becomes less likely to collect an electron, for example. This probability is used with a random number generator to determine the times when an individual electron or ion is collected, and to charge is advanced by -1 or $+1$, accordingly.

Cui and Goree's simulation [5] begins with a particle that is initially uncharged, and it is allowed to continue for a long time after reaching a steady state. Figure 3 shows the early part of the time series for the particle's charge. The charge builds up from zero toward an equilibrium charge $\langle Q(t) \rangle = \langle N \rangle$. The continuous model gives a smooth curve for $Q(t)$, while the discrete model reveals the discrete nature of Q , with random time steps and fluctuations about the smooth curve from the continuous model.

The fractional fluctuation is strongest for smallest particles. It obeys $\Delta Q / \langle Q \rangle = 0.5 \langle Q / e \rangle^{-1/2}$, for a wide range of plasma and particle parameters. The square-root scaling is the same as in counting statistics, where the fractional uncertainty of a count N is $N^{-1/2}$. The power spectrum of the fluctuations is dominated by very low frequencies, with half the spectral power lying at frequencies below $0.024 \tau^{-1}$. Here τ is the charging time, as defined in equation (7). At higher frequencies, the spectral power diminishes as the second power of frequency, f^{-2} .

7. Contamination control

Here I suggest a speculative idea for contamination control during plasma processing, based on an understanding of the charging processes described in this paper.

Contamination might be controlled by inducing a

positive charge on the particles. A positive charge is important because it is believed that only negatively charged particles are confined in a laboratory discharge. A discharge (in the absence of significant negative ion density) has a natural electric potential that tends to confine negatively charged particles. By promoting electron emission, the particles will charge positively and be expelled from the plasma. They will either strike the electrode or escape radially from the discharge.

In the case of secondary emission, electron emission can be promoted by heating the electrons, perhaps by operating with a low gas pressure or using an electron-heating source such as microwave power. For photoemission, one could deliberately illuminate the plasma with a UV source. It may be useful to know that the particle's charge can fluctuate to a positive value even if it is not possible to charge it positively all of the time.

To be effective, a contamination control method must either prevent growth of particles to a harmful size or transport them away from the substrate. The technique proposed here could serve the first purpose, and perhaps the second. Some particles might be forced to land on the substrate by promoting a positive charge. This would be acceptable if it happens while they are still nano-particles, which are too small to cause a defect. Provided that the source of UV or electron heating is applied constantly, or pulsed rapidly, any particle that begins growing will be expelled from the plasma before it has time to grow to a harmful size.

Acknowledgments

Figures 2 and 3 were prepared by C Cui. The author thanks O Havnes and G Morfill for helpful discussions.

This work was supported by NSF ECS-92-15882, NASA Origins of the Solar System Program NAGW-3126 and NASA Microgravity Science and Applications Division NAG8-292.

References

- [1] Bernstein I B and Rabinowitz I N 1959 Theory of electrostatic probes in a low-density plasma *Phys. Fluids* **2** 112-21
- [2] Chen F F 1965 Numerical computations for ion probe characteristics in a collisionless plasma *Plasma Phys.* **7** 47-67
- [3] Whipple E C 1981 Potentials of surfaces in space *Rep. Prog. Phys.* **44** 1198-250
- [4] Spitzer L 1978 *Physical Process in the Interstellar Medium* (New York: Wiley)
- [5] Cui Chunshi and Goree J 1994 Fluctuations of the charge on a dust grain in a plasma *IEEE Trans. Plasma Sci.* **22** 151-8
- [6] Havnes O, Aanesen T K and Melandso F 1990 On dust charges and plasma potentials in a dusty plasma with dust size distribution *J. Geophys. Res.* **95** 6581-5
- [7] Boufendi L, Plain A, Blondeau J Ph, Bouchoule A, Laure C and Toogood M 1992 Measurements of particle size kinetics from nanometer to micrometer scale in a low-pressure argon-silane radio-frequency discharge *Appl. Phys. Lett.* **60** 169-71
- [8] Meyer-Vernet M 1982 *Astron. Astrophys.* **105** 98
- [9] Goertz C K 1989 Dusty plasmas in the solar system *Rev. Geophys.* **27** 271-92
- [10] Chow V W, Mendis D A and Rosenberg M 1994 Secondary emission from small dust grains at high electron energies *IEEE Trans. Plasma Sci.* **22** 179-86
- [11] Goree J 1992 Ion trapping by a charged dust grain in a plasma *Phys. Rev. Lett.* **69** 277-80
- [12] Choi S J and Kushner M J 1994 A particle-in-cell simulation of dust charging and shielding in low pressure glow discharges *IEEE Trans. Plasma Sci.* **22** 138-50
- [13] Tsytovich V N 1993 Dispersion properties of dusty plasma, fluctuations, anomalous transport and dust-wall interaction *Nato Advanced Research Workshop* unpublished

Plasma particle interactions

J P Boeuf, Ph Belenger and T Hbid

Centre de Physique Atomique de Toulouse (CNRS URA 277), Université Paul Sabatier, 118, route de Narbonne, 31062 Toulouse Cedex, France

Received 28 December 1993, in final form 19 January 1994

Abstract. We present some results from numerical, fluid and particle models of non-thermal low pressure RF discharges contaminated by dust particles. These models have been used (1) to show the effect of the presence of dust particles on the electrical characteristics of an RF discharge, (2) to study the charge and floating potential of dust particles in a low pressure plasma from situations where the particles can be considered isolated to situations where they interact electrostatically and (3) to study the effect of the electrode geometry on the spatial distribution of dust particles in an RF discharge. The results confirm the existence of electrostatic traps close to the plasma-sheath boundary whose shape is very sensitive to the electrode configuration.

1. Introduction

The formation of dust particles has been observed in a number of plasma applications such as gas discharge lasers, arc discharges for surface processing and low pressure radio frequency plasmas [1-8] used in the microelectronics industry. These particles are typically tens of nm to tens of μm in size and their density can be as high as 10^8 cm^{-3} in low pressure RF plasmas [3,8]. The presence of dust particles in etching or deposition plasmas is problematic due to the contamination of the substrates to be processed. The mechanisms of generation of the particles are system dependant. They can be produced by plasma surface interaction or created in the volume by polymerization of the gas or its dissociation products. It has been observed that dust particles are more easily formed in discharges in electronegative gases. This suggests that particle formation and growth is often linked to the presence of negative ions which have long residence times in RF glow discharges and can initiate clustering. Particles can also be present in discharges in inert gases where their presence probably results from the discharge-electrode interaction.

A number of modelling studies of dusty laboratory plasmas have been published recently, where attempts have been made to understand the charging of dust particles and plasma-particle interactions [9-12] and transport phenomena of dust particles in low pressure RF plasmas [13-16]. These studies have benefited from the important literature published in the field of dusty plasmas in space (see, e.g., [17-19] which presents many similarities with dusty laboratory plasmas).

In this paper we shall concentrate on the consequences of the presence of dust particles in a low pressure plasma and on the plasma-particle electrical

interactions, without considering the mechanisms of the formation of these particles.

The main consequences of the plasma-particle electrical interactions can be summarized as follows. (1) Particles immersed in a plasma acquire a negative charge and negative potential with respect to the plasma, due to the large mobility of electrons compared with that of positive ions. The role of this negative charge and potential is to ensure, at steady state, equality of electron and positive ion fluxes to the particle (the particle behaves as a probe). The charge and floating potential of a dust particle depend on its size, on the electron to ion mass ratio, and on the local plasma properties (electron and ion temperature). Note that the charge and floating potential of a particle may also depend on the concentration of dust particles, since electrostatic interaction between dust particles is possible at large concentrations. (2) Due to the continuous electron and ion fluxes to the particles, the presence of a large concentration of dust particles can have a strong influence on the creation/loss balance of charged particles in the plasma [9-11]. These losses must be compensated by an increase in the ionization rate and therefore in the plasma electric field. (3) Dust particles are subjected to various forces: electrostatic (due to the field in the discharge), ion drag (momentum exchange with ions), force due to the gas flow, thermophoretic force, gravity, etc. The competition between these different forces may result in the trapping of the dust particles in some well defined regions of the discharge as suggested in [13-16].

Experiments by Bohm and Perna [20] have shown a good example of the effect of the presence of charged particles on the electrical characteristics of a silane RF discharge. Their measurements of the power dissipated in the discharge as a function of RF voltage (at constant pressure) exhibit an abrupt transition in the discharge

impedance, from capacitive to resistive, above a critical RF voltage. This transition is accompanied by a complete spatial redistribution of the light emitted by the discharge. The transition has been attributed to the appearance of large concentrations of dust particles in the discharge. We shall discuss in section 2 some of the experimental results, and the numerical, fluid and particle models [21] which have been developed to analyse this transition.

In order to better understand plasma particles interactions, Boufendi *et al* [8,11] have designed an experiment where dust particles created in a silane-argon plasma are subsequently trapped in a pure argon plasma. Such a plasma is easier to study and to model since the formation and growth processes are expected to stop when silane is removed. We have developed, under the conditions of the experiments of Boufendi *et al* where the particle concentration and size as well as the discharge electrical characteristics had been measured, a particle-in-cell Monte Carlo simulation able to provide the charge and floating potential of the dust particles, and the plasma electric field [10]. These parameters have then been used to calculate the electrical characteristics of the discharge in contaminated argon, and to compare these results with experiments [11]. This work will be described in section 3.

A number of optical measurements have shown that particulates tend to accumulate in some well defined regions close to the plasma-sheath boundaries [1-6]. Seiwyn *et al* [2] have observed by laser light scattering some spectacular distributions of dust particles (rings around semiconductor wafers and dome above the wafers) in RF etching reactors and have shown that these distributions are very sensitive to the electrode configuration. Measurements of the spatial distribution of potential in pristine and contaminated RF plasmas by Geha *et al* [22] and Carlile and Geha [23] tend to prove that, depending on the electrode configuration, on-axis or off-axis electrostatic traps for dust particles (regions of local maximum of the potential) can exist in an RF discharge near the plasma-sheath boundaries. We have developed 2D fluid models of RF discharges to study the influence of the electrode geometry, gas pressure and other parameters on the electrical properties of the discharges. We present in section 4 some results from these 2D models in contaminated and pristine plasmas. The results show, in qualitative agreement with the experiments, the presence of local maxima of the potential in the plasma-sheath region, and the accumulation of dust particles in these regions.

2. Influence of dust particles on the characteristics of a silane discharge

We discuss here the influence of the presence of dust particles on the electrical characteristics of an RF discharge in silane on the basis of experiments by Böhm and Perrin [20], and numerical models by Boeuf and Belenguer [21].

The experiments of Böhm and Perrin [20] were performed in a symmetric discharge chamber with a 3.6 cm gap, at 13.56 MHz in pure silane and for two values of pressure: 55 mTorr and 185 mTorr (at 220 °C). Current and power dissipated in the discharge have been carefully measured as a function of applied RF voltage.

Two different self-consistent models [21] have been used to calculate the same parameters under the same conditions as in the experiments. The models are based on solutions of electron and ion transport equations in silane, coupled with Poisson equation. In the first model (fluid model), electron and ion transport is described by macroscopic, fluid equations, while in the second model, a particle-in-cell Monte Carlo (PIC MC) simulation [24-26] is used (the PIC MC model is more accurate, especially at low pressure, but considerably more time consuming than the fluid model).

Figure 1 shows a comparison between experimental and numerical results for the power deposition versus the RF voltage for the two pressures considered. At low pressure (55 mTorr, figure 1(a)), the PIC MC model is in good agreement with the experiments while the fluid model, as expected, does not compare very well with the experiments. At higher pressure (185 mTorr, figure 1(b)), fluid and PIC MC models give similar results, but both models predict a power deposition much lower than the experimental one, when the RF voltage amplitude is above 100 V. The measured and calculated phase shift between current and voltage is displayed in figure 2 as a function of RF voltage, for 55 and 185 mTorr. Again, reasonable agreement between experiments and calculations is obtained at 55 mTorr, while the phase shift predicted by both models is considerably lower than the measured one at 185 mTorr. The measured phase shift at 185 mTorr shows that the discharge impedance becomes strongly resistive above 100 V.

The abrupt transition observed experimentally, from a capacitive impedance to a resistive impedance at 185 mTorr, has been attributed [20,21] to the presence of dust particles in the discharge. These particles may be either produced in larger quantities or more easily trapped when the RF voltage is increased above 100 V (note also the existence of a hysteresis effect around 100 V). This interpretation of the experimental results is supported by some numerical calculations also displayed in figures 1 and 2, which have been performed assuming that the attachment cross section is about ten times larger than in pure silane (no other fitting parameter has been used). Under this assumption, the power dissipated and the phase shift predicted by the models are in excellent agreement with the experiments in a large range of RF voltages (see the square symbols in figures 1 and 2). Increasing the attachment cross section of silane in the calculations is equivalent to increasing the electron losses in the plasma volume. The results therefore show that the transition observed experimentally is associated with an abrupt increase of the electron losses in the plasma volume. This increase of charged particles losses can be associated with the presence of particulates in the

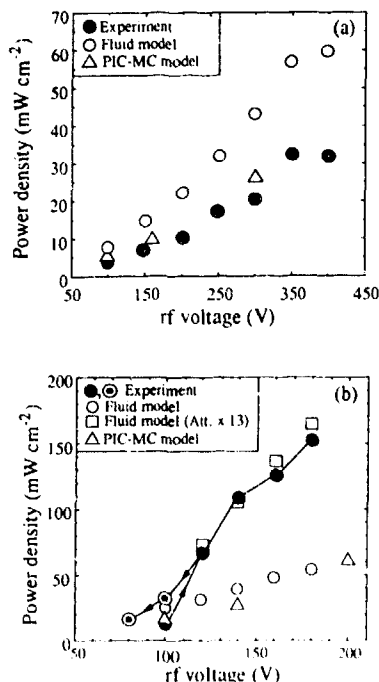


Figure 1. Measured and calculated power dissipation in a 13.56 MHz discharge in silane (gap length 3.6 cm, gas temperature 220 °C) as a function of the peak rf voltage: (a) 55 mTorr, (b) 185 mTorr; after [21] (measurements are by Böhm and Perrin [20]).

discharge (particulates behave as microscopic probes and can be considered as a distributed sink of electrons and positive ions, see below).

Finally, we mention that measurements of the spatial, time averaged distribution of the optical emission of the discharge in the 185 mTorr case show that, during the transition, the emission profile changes from the well known two-peaks (maxima of the emission at the sheath edge, lower emission in the plasma) profile, to a profile with a much more intense emission in the plasma volume [20]. The nature of the emission also changes during the transition. These changes are due to the fact that the distribution of the electric field in the discharge is strongly affected by the presence of dust particles. The plasma electric field has to increase substantially in order for electron impact ionization to balance the electron losses to the particulates in the plasma volume.

3. Charge, floating potential and plasma electric field in a contaminated plasma

In order to better understand and quantify the charging of dust particles in a laboratory plasma, we have developed a self-consistent PIC-MC simulation [10] which can provide the charge and floating potential of a dust particle as well as the electric field which

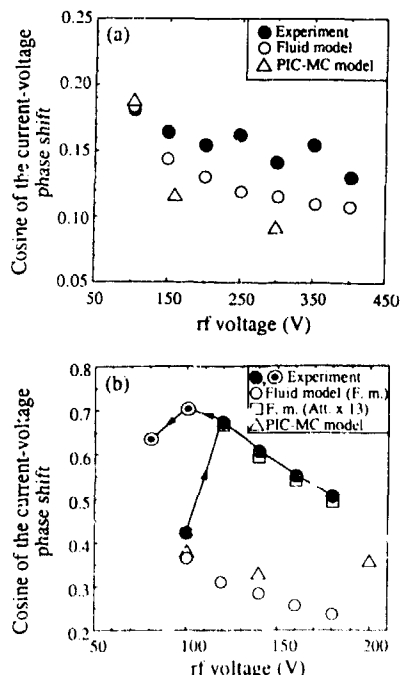


Figure 2. Measured and calculated cosine of the current-voltage phase shift in a silane discharge as a function of the peak rf voltage (same conditions as figure 1): (a) 55 mTorr, (b) 185 mTorr; after [21] (measurements are from [20]).

is required to sustain the plasma. This model allows the determination of these parameters from situations where the particulates can be considered to be isolated to situations where they interact electrostatically. It assumes a uniform, steady state, DC plasma. For a given density and size of particulates, the charge and floating potential are obtained by simulating the trajectories of a large number of electrons and ions in a volume element around the particulate (with proper boundary conditions) subjected to acceleration by the self-consistent electric field (particle-in-cell) and collisions with neutrals (Monte Carlo). The average electric field is obtained by requiring that the plasma be self-sustained, i.e. that electron and ion losses to the particulates must be exactly balanced by ionization. The simulations have been performed under conditions close to the experiments of Boufendi *et al.* [8, 11] where dust particles created in an argon-silane discharge are subsequently trapped in a pure argon discharge. These conditions correspond to 0.1 Torr (300 K) argon with a dust particle density of 10^8 cm^{-3} and size in the 0.1–1 μm range. Calculations for smaller particle densities and larger size have also been performed.

Figure 3 shows the sustaining electric field and electron temperature as a function of current density flowing through the plasma, predicted by the simulation for a dust particle density of 10^8 cm^{-3} and various sizes

of the dust radius. The electric field can reach quite large values (E/p is in the $100 \text{ V cm}^{-1} \text{ Torr}^{-1}$ range) and does not depend on the current density in the considered range. The average electron temperature and electron energy distribution function (EEDF) (see [10]) are very close to the temperature and the EEDF which would be calculated in a pristine plasma, under the same reduced electric field. This is due to the fact that under these conditions of large dust particle density, the floating potential of the dust particles is relatively small, as shown in figure 4(a). The shape of the electron distribution function is therefore not affected much by the presence of the dust particle. For lower dust particle concentrations, the floating potential is larger and the EEDF is shifted to lower energies [9]. The low values of the floating potential and charge of the dust particles (figures 4(a) and (b)) under our conditions of large particle concentrations, are due to the fact that the dust particles cannot be considered to be isolated, and that the distance between them is much smaller than the electron Debye length and is not large with respect to the ion Debye length (which is closer to the actual shielding length for small particle radii [12]). This situation corresponds to the case where the dust particles interact electrostatically. The plasma behaves as a strongly electronegative plasma, and the electron number density is between one and two orders of magnitude lower than the ion density (see figure 5 of reference [10]). For example, for a current density of 0.1 mA cm^{-2} , the calculations give (for dust particle density and radius of 10^8 cm^{-3} and $0.1 \mu\text{m}$) values of the electron and ion number densities around 2×10^7 and 10^9 cm^{-3} respectively. This is consistent with figure 4(b) which shows that each particulate carries about ten negative charges under these conditions (plasma neutrality). The effect of large particle concentrations has two consequences which have opposite effects, as discussed by Whipple *et al* [17]. The first consequence is a decrease in the floating potential due to electron depletion. The second consequence is an increase in the dust particle capacitance which leads to an increase in the number of charges carried by the particles for a given floating potential (the number of charges Z_d carried by each particle is related to the floating potential ϕ_d by $eZ_d = C_d|\phi_d|$, where C_d is the dust particle capacitance [17]). However this increase is not important for conditions where the dust particle radius is small with respect to the distance between particles (which is the case here) and the dust particle capacitance is well approximated by the isolated particle capacitance, $C_d = 4\pi\epsilon_0 r_d$ (r_d is the particle radius), as can be checked in the numerical results of figure 3. The overall effect of large particle concentrations is therefore a decrease in the floating potential and in the number of charges carried by the particles.

For smaller dust particle densities, the electric field in the plasma is no longer independent of the current density and the floating potential can reach higher values, as can be seen in figure 5. This corresponds to a transition from a situation where the distance between

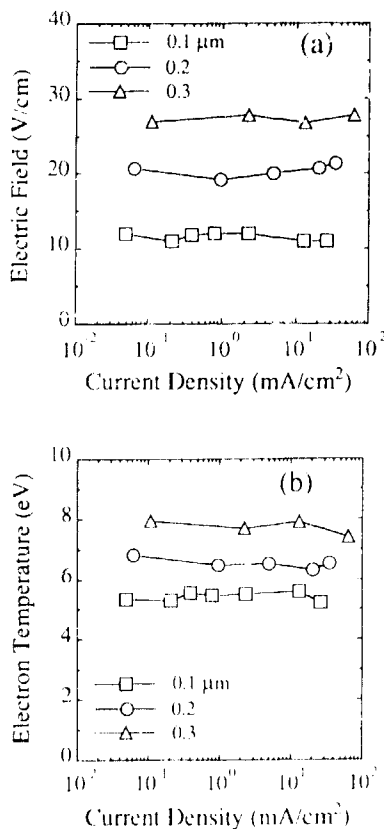


Figure 3. Variations of (a) sustaining electric field and (b) electron temperature with current density in a dusty argon plasma at 0.1 Torr (300 K), concentration of dust particles 10^8 cm^{-3} , for three values of the dust particle radius; after [11].

particulates is small with respect to the Debye length (dust particles interact electrostatically), to a situation closer to the case of isolated particulates. Figures 5(a) and (b) show that when the electron Debye length becomes small enough, the floating potential of the dust particles tends to a constant value corresponding to the isolated case (the ion Debye length, not represented on figure 5, is closer to the actual shielding distance and is less than ten times smaller than the electron Debye length).

A 1D model of the complete RF discharge in contaminated argon, including a given particulate concentration and size corresponding to the experiments of Boutendi *et al* [8], and electron and ion losses terms derived from the above PIC-MC simulation has been developed and is described in [11]. The current-voltage characteristics derived from this model are in good agreement with the measurements [11]. Measurements of the positive ion density in the plasma [8] also confirm the values of the dust particles' charge predicted by the PIC-MC simulation (of the order of a few tens).

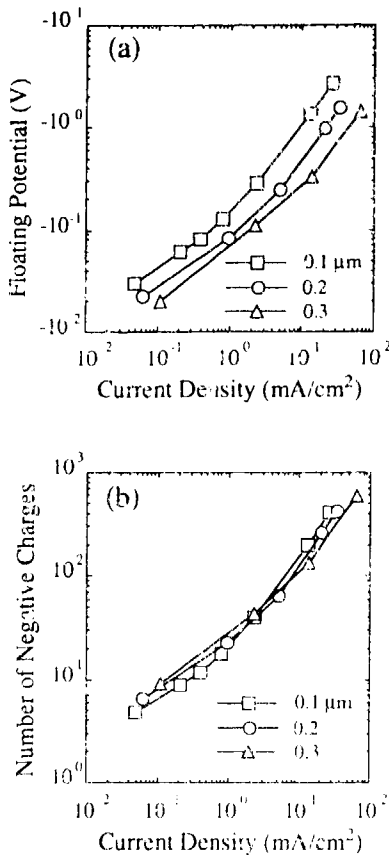


Figure 4. Variations of (a) floating potential (the potential reference is the average plasma potential), and (b) number of negative charges with current density in a dusty argon plasma at 0.1 Torr (300 K) (same conditions as in figure 3); after [11].

4. Particle traps in an RF discharge

Under the experimental conditions of Boufendi *et al* (i.e. very large particle concentrations, up to 10^8 cm^{-3}), laser light scattering measurements of the dust particle concentration showed that the particulates were roughly uniformly distributed spatially in the plasma volume. This is the reason why the PIC MC model described above assumed a uniform plasma.

However, as already mentioned, a number of experiments have shown that dust particles often accumulate in some very localized regions of the discharge, generally close to the plasma sheath boundaries. Measurements of the spatial distribution of the potential in the plasma by Geha *et al* [22] and Carlile and Geha [23] have suggested that the particulates may be confined by electrostatic traps whose structure and location is very sensitive to the electrode configuration and nature.

In order to study the questions of electrostatic traps in the discharge and of their influence on the confinement

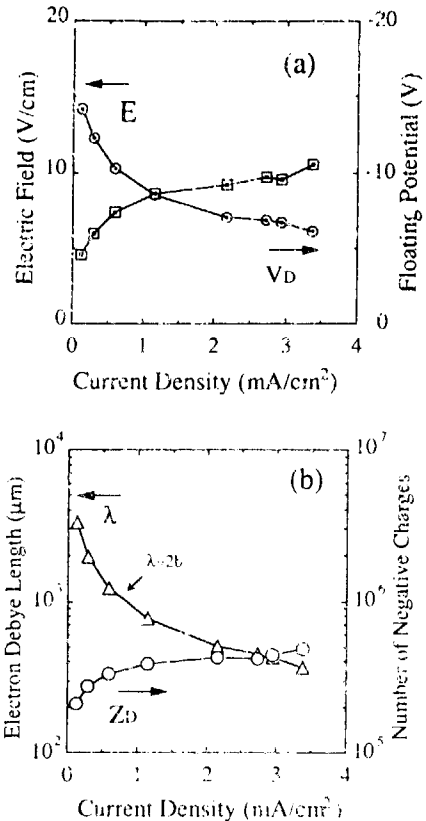


Figure 5. Variations of (a) sustaining electric field and dust floating potential (the potential reference is the average plasma potential) and (b) electron Debye length and number of charges with current density in a dusty argon plasma at 0.1 Torr (300 K), concentration of particulates 10^3 cm^{-3} , radius of particulates $100 \mu\text{m}$; after [11].

of dust particles, we have developed a 2D self-consistent fluid model of RF discharges which can deal with various electrode and chamber geometries. In this model electron transport is described by continuity, momentum and energy equations. The model is more accurate than the discharge models described in [27] since it does not use the local equilibrium approximation to calculate the ionization rate and other electron transport parameters. Frequencies for ionization, momentum exchange and energy exchange as well as the diffusion coefficient and mobility at a given location and time, are assumed to depend on the value of the electron mean energy (obtained from the energy equation) at the same position and time. The corresponding functionals of the mean energy are determined in such a way that they would give the usual equilibrium swarm data under a constant and uniform electric field (see, for example, [28] for a discussion on this point). Inertia terms are neglected in the momentum transfer equation which reduces to the classical drift-diffusion representation of the electron flux. The transport

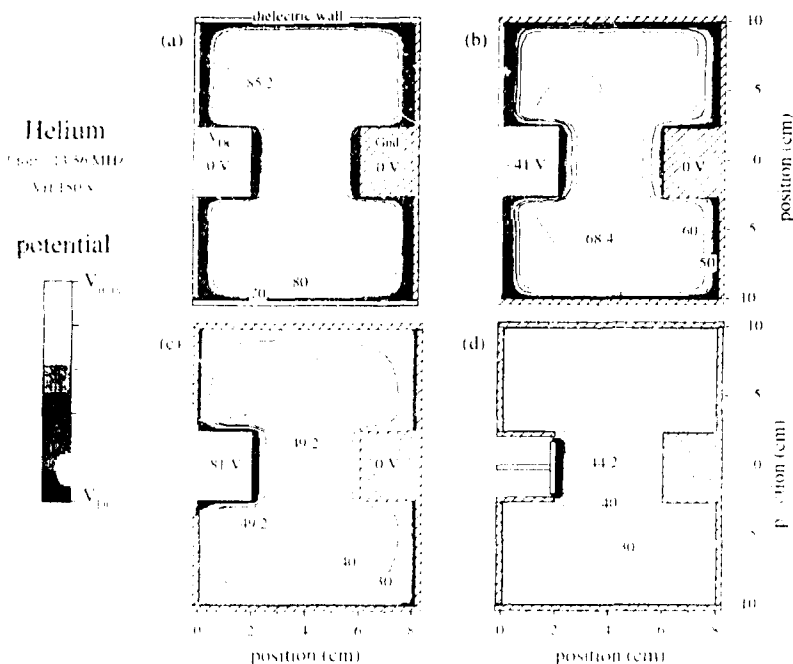


Figure 6. Contours of constant (time averaged) potential in a helium discharge (1 Torr, 13.56 MHz, 150 V peak generator voltage), for four different electrode configurations, from a 2D fluid model. The left (white) electrode is powered through a capacitor. The (calculated) DC bias on this electrode is indicated in each case. The other electrode is grounded. The highest equipotential contours shown correspond to a value of the potential 0.5 V below the maximum. Cases (a)–(d) correspond to situations of increasing asymmetry of the electrode configuration: (a) the walls of the chamber are dielectric, and the discharge is symmetric, (b) the walls of the chamber are grounded, (c) the left wall surrounding the cathode is also grounded, (d) the cylindrical wall around the cathode is also grounded.

terms of the energy equation are approximated in the usual way, including the thermal flux term (see for example [28–31]). Ion transport is described with a continuity and momentum equation in the drift-diffusion approximation. The numerical method used for electron and ion transport equations is based on an implicit finite-difference technique using the Scharfetter-Gummel scheme [27, 32]. The Poisson equation is solved with an SOR (successive over relaxation) method. The model can deal with various electrode and chamber configurations with different kinds of boundary condition (cylindrical or rectangular geometry, metallic walls, dielectric walls, floating potential conducting walls, or periodic transverse boundary conditions in the rectangular case). The DC bias is calculated self-consistently so that no DC current flows through the discharge.

The calculations described below correspond to discharges in pure helium and contaminated helium (secondly electron emission from the electrodes or walls is not included).

4.1. Results in pure helium

Figure 6 presents the contours of a constant (time averaged) potential in a 13.56 MHz discharge in 1 Torr pure helium, 150 V peak generator voltage, for four different electrode configurations. The small (left) electrode is powered through a capacitor and the large electrode is grounded. The calculated DC bias in each case is indicated on the figure. We see that the averaged potential presents local maxima at different locations of the chamber, depending on the electrode geometry. The region of maximum potential forms a ring around the discharge gap in figure 6(a) where the walls of the chamber are dielectric (symmetric configuration, no DC bias). In figure 6(b) (conducting, grounded walls) the region of potential maximum forms a ring around the smaller electrode. In the configuration of figure 6(c) where the walls of the chamber on the small electrode side are also grounded, one can see two regions of maximum potential, one in the form of a ring around the small electrode, and the other one in the form of an ellipsoid on the discharge axis, close to the powered electrode. In figure 6(d), where the cylinder

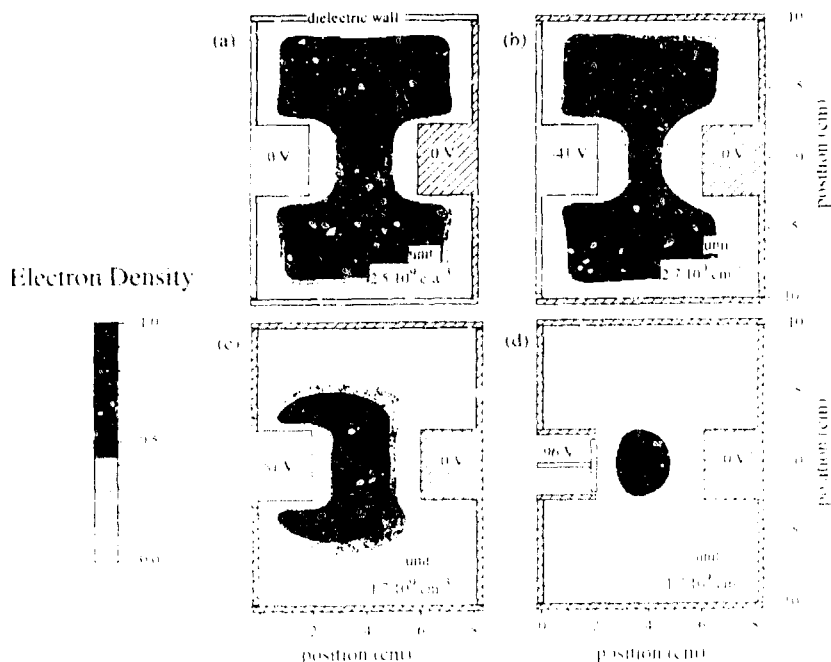


Figure 7. Contours of constant time averaged electron density under the conditions of figure 6.

surrounding the powered electrode is grounded, the ellipsoid is still present, but the ring has disappeared. These results are in qualitative agreement with the light scattering observations of Selwyn *et al.* [2] and with the potential distribution measurements of Geha *et al.* [22]. Note that the highest equipotential contours displayed in figures 6(a)–(d) correspond to a value of the potential 0.5 V below the maximum potential (different for each of the four cases). This means that most of the dust particles present in the discharge would be located in the region delimited by these contours, if forces other than the electrostatic force were negligible (the thermal energy of the particulates is a fraction of an eV).

The potential maxima are, as expected, associated with maxima of the plasma density, as seen in figure 7, which are themselves related to the spatial distribution of the ionization rate in the discharge (displayed in figure 8). Note that in a 1D parallel plate geometry the maximum of potential is necessarily located in the mid gap if electron losses, such as recombination, are negligible, even though the ionization rate presents strong maxima near each electrode. In a 2D geometry, potential maxima can be located on the discharge axis and closer to one electrode due to the asymmetry of the configuration (figures 6(b), (d)), but can also be off axis (figures 6(a), (c)). This is because radial ambipolar losses of ions are possible in a 2D geometry, and maxima of plasma density can be closer to maxima of ionization rate. Figure 8 shows clearly the effect of the electrode

geometry on the ionization rate, and comparisons between figure 3 and figure 7 help understanding the locations of maximum plasma density and potential (note, however, that the relation between the spatial distributions of electron density and ionization rate is rather complex and that maxima of plasma density do not correspond to maxima of ionization rate).

The position of the maximum potential is extremely sensitive to various parameters such as electrode geometry (figure 6) and also gas pressure, as seen in figure 9 (helium, 13.56 MHz, 150 V peak generator voltage, DC bias indicated on the figure). In the geometry of figure 9, the powered electrode forms a cavity. We see that, when the pressure increases from 0.3 Torr to 2 Torr, the region of maximum plasma density (and potential) moves closer to the inside of the powered electrode, while its shape changes from an 'ellipsoid' to a 'ring'. Note also that the calculated DC bias increases when the pressure decreases, in agreement with experimental observations.

4.2. Results in contaminated helium

We have included in the 2D model above, dust particles of given size, with self-consistent calculations of their charge and transport due to the electrostatic and ion drag force. The space charge induced by the dust particles is also taken into account. We have added to the set of equations of the fluid model, a continuity equation for the

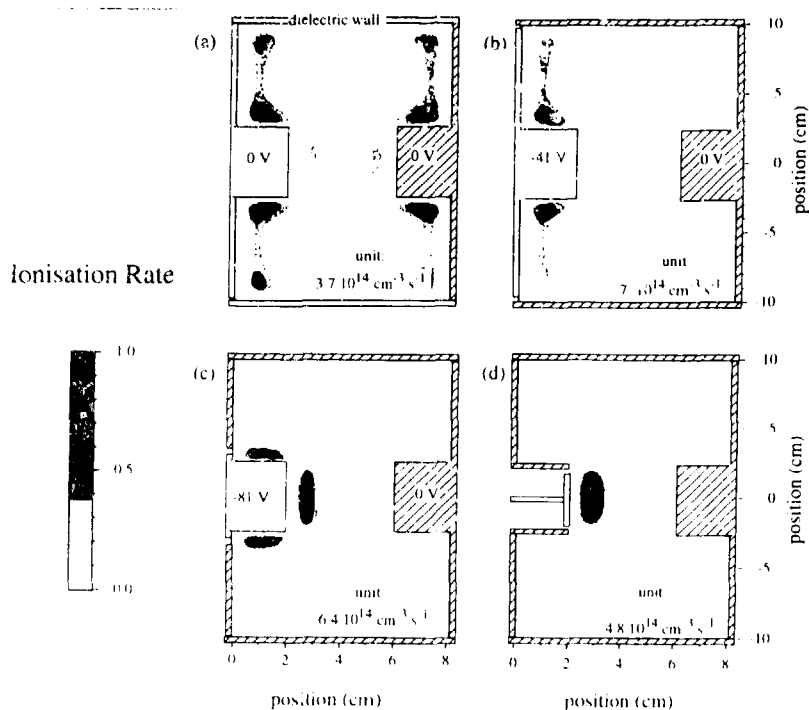


Figure 8. Contours of constant time averaged ionization rate under the conditions of figure 6.

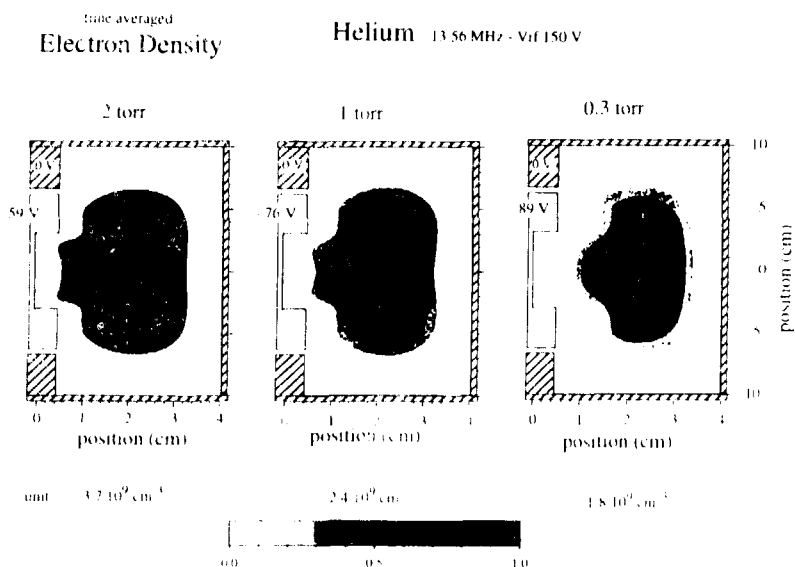


Figure 9. Contours of constant time averaged electron density for a geometry with a cavity in the cathode, in a helium discharge (13.56 MHz, 150 V peak generator voltage) for three values of the gas pressure: (a) 2 Torr, (b) 1 Torr, (c) 0.3 Torr.

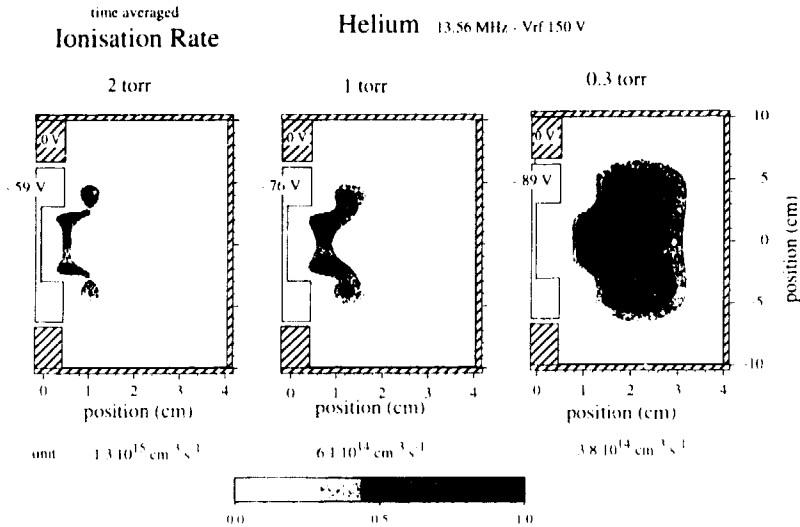


Figure 10. Contours of constant time averaged ionization rate in the conditions of figure 9.

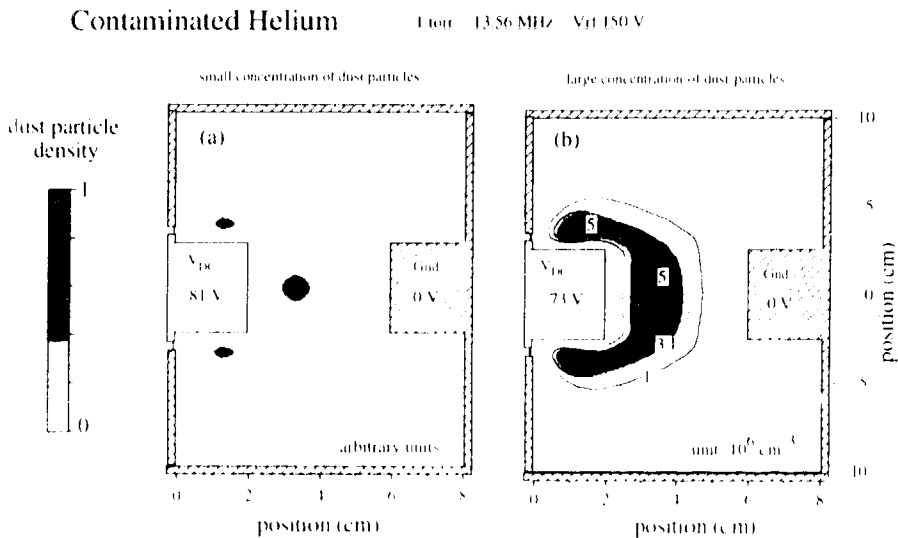


Figure 11. Contours of constant dust particle concentration in the conditions of figure 6(c); (a) small dust particle concentration, (b) large dust particle concentration (the electric field is affected by the presence of dust particles).

dust particles which has the following form (subscripts d, e, and p refer to dust particles, electrons, and positive ions, respectively):

$$\frac{\partial n_d}{\partial t} + \nabla \cdot (n_d \mathbf{v}_d) = 0$$

$$n_d \mathbf{v}_d = n_d k_d (-e Z_d \mathbf{E} - \mathbf{F}_{\text{drag}}) - D_d \nabla n_d$$

where n_d and \mathbf{v}_d are the density and velocity of dust particles, Z_d is the number of negative charges carried by each particle, $(ek_d Z_d)$ and D_d their mobility and diffusion coefficient. All these quantities depend on space and time. The ion drag force \mathbf{F}_{drag} is taken from the analytical expression given by Daugherty *et al* [15].

The number of negative charges Z_d on the particles

is obtained, (at each location) by

$$\frac{\partial Z_d}{\partial t} = \nu_{d,e} - \nu_{d,p}$$

where $\nu_{d,e}$ and $\nu_{d,p}$ are respectively the number of electrons and ions collected by the particle per unit time and are given by classical orbit theory [14]

$$\nu_{d,e} = \pi r_d^2 n_e \left(\frac{8kT_e}{\pi m_e} \right)^{1/2} \exp\left(\frac{e\phi_d}{kT_e}\right)$$

$$\nu_{d,p} = \pi r_d^2 n_p \left(\frac{8kT_p}{\pi m_p} \right)^{1/2} \left(1 - \frac{e\phi_d}{kT_p} \right)$$

where m_e and m_p are the electron and positive ion mass, T_e and T_p the electron and ion temperature. ϕ_d is the floating potential of the dust particle at each location and is related to the number of charges Z_d by (r_d is the radius of the particles)

$$eZ_d = |\phi_d| 4\pi\epsilon_0 r_d.$$

Loss terms of the form $n_d \nu_{d,e}$ and $n_d \nu_{d,p}$ were subtracted from the source terms of the electron and ion continuity equations.

The set of transport equations of electrons, positive ions, and dust particles coupled with Poisson equation (including the dust particle charge density, $-Z_d n_d$) is integrated in space and time until a harmonic steady state is reached. In order to make the calculation tractable in a reasonable time, the dust particle mobility $\mu_d (= ek_d Z_d)$ was supposed to be much larger than its real value and of the order of the positive ion mobility. The value of the diffusion coefficient was chosen so that D_d/μ_d was a fraction of kT_e/e where T_e is the neutral gas temperature. For low values of the dust particle density (when the dust particle space charge can be neglected) the discharge calculations and the dust particle transport calculations were uncoupled and much bigger time steps could be used for the transport of dust particles. Note that if the ion drag force is neglected, in the case of small concentrations of dust particles, the transport equation above gives a Boltzmann distribution for the dust particles.

The approximations above on the dust particle transport are quite crude, but our goal is only qualitative. The purpose of the calculations was (1) to estimate the influence of ion drag on the transport and spatial distribution of dust particles and (2) to study how this distribution is modified when collective effects are present (large concentrations of dust particles).

The results, for dust particles of 0.2 μm radius and under the discharge conditions of section 4.1, show that the electrostatic force is always larger than the ion drag force. For low particle concentrations (figure 10(a)), particles are therefore confined in the electrostatic traps described above. For large concentrations of dust particles (typically above 10^5 cm^{-3} for 0.2 μm radius particulates) the distribution of dust particles is modified (figure 10(b), due to the changes in the

potential distribution induced by their space charge, and to the increase in electron and ion losses which leads to an increase in the plasma field. The distribution of dust particles tends to be more uniform for larger concentrations. For dust particles concentrations above 10^7 cm^{-3} , strong (probably numerical) oscillations of the plasma potential appear. When the initial concentration of particles was increased from a few 10^4 to a few 10^7 cm^{-3} the number of charges Z_d on the particles dropped from a few thousands to a few hundreds, in qualitative agreement with the results of section 3 (transition from the isolated particles case to the case of electrostatic interaction between particles).

5. Conclusion

The results presented in this paper can be briefly summarized in two points.

(1) The presence of large concentrations of dust particles in an RF plasma strongly affects the distribution of electric field in the discharge. A substantial increase in the plasma electric field is necessary to ensure that electron and ion losses to the dust particles are balanced by ionization. This increase in the plasma field completely modifies the electron temperature and distribution function. This certainly affects the chemical kinetics of the plasma and may lead to a more efficient production of radicals or active species (due to the increase in electron temperature). One can therefore think of using dust particles to increase the process efficiency, although this would need a complete control of the transport of dust particles in the reactor (in order to avoid substrate contamination.)

(2) The 2D discharge models have shown that potential traps for dust particles exist in an RF discharge, their localization depending strongly on the electrode and chamber configuration. The positions of the calculated potential traps have been found to present strong similarities with the locations of maximum dust particle concentrations observed experimentally and with those deduced from probe measurements. Although it is clear that other forces (ion drag, gas flow, gravity, thermophoretic force) affect the transport of dust particles under some conditions, our results strongly suggest that the electrostatic force related to potential traps plays a central role in the spatial distribution of dust particles. We think that 2D models could be used to help designing reactor configurations allowing a better control of dust particle distribution and transport.

Acknowledgments

This work has been supported by CNRS-PIRSEM under contract No 89N80/0095, and by the CNRS GRECO 57 'Interactions Plasmas Froids-Matériaux'. The authors would like to thank A Bouchoule, I. Boufendi, J Ph Blondeau, C Böhm, J P Couderc, B Despax, J Ferrin,

L C Pitchford and J Schmitt, for a number of stimulating discussions.

References

- [1] Roth R M, Spears K G, Stein G D and Wong G 1985 *Appl. Phys. Lett.* **46** 235
- [2] Selwyn G S, Singh J and Bennet R S 1989 *J. Vac. Sci. Technol. A* **7** 2758
- [3] Selwyn G S, Heidenreich J E and Haller K L 1990 *Appl. Phys. Lett.* **57** 1876
- [4] Jellum G M and Graves D B 1990 *J. Appl. Phys.* **67** 6490
- [5] Watanabe Y, Shiratani M and Yamashita M 1993 *Plasma Sources Sci. Technol.* **2** 35
- [6] Garscadden A 1992 *Proc. of the XXth ICPIG, (Invited paper)*, ed V Palleschi *et al* (Pisa Istituto de Fisica Atomica e Molecolare) p 147
- [7] Bouchoule A, Plain A, Boufendi L, Blondeau J Ph and Laure C 1991 *J. Appl. Phys.* **70** 1991
- [8] Boufendi L, Bouchoule A, Porteous R K, Blondeau J P, Plain A and Laure C 1993 *J. Appl. Phys.* **73** 2160
- [9] McCaughey M J and Kushner M J 1989 *Appl. Phys. Lett.* **55** 951; 1991 *J. Appl. Phys.* **69** 6952
- [10] Boeuf J P 1992 *Phys. Rev. A* **46** 7910
- [11] Belenguer Ph, Blondeau J Ph, Boufendi L, Toogood M, Plain A, Bouchoule A, Laure C and Boeuf J P 1992 *Phys. Rev. A* **46** 7923
- [12] Daugherty J E, Porteous R K, Kilgore M D and Graves D B 1992 *J. Appl. Phys.* **72** 3
- [13] Sommerer T J, Barnes M S, Keller J H, McCaughey M J and Kushner M J 1991 *Appl. Phys. Lett.* **59** 638
- [14] Barnes M S, Keller J H, Forster J C, O'Neil J A and Coultas D K 1992 *Phys. Rev. Lett.* **68** 313
- [15] Daugherty J E, Porteous R K and Graves D B 1993 *J. Appl. Phys.* **73** 1617
- [16] Kilgore M D, Daugherty J E, Porteous R K and Graves D B 1993 *J. Appl. Phys.* **73** 7195
- [17] Whipple E C 1981 *Rev. Prog. Phys.* **44** 1197
- [18] Whipple E C, Northrop T G and Mendis D A 1985 *J. Geophys. Res.* **90** 7405
- [19] Havnes O, Morfill G E and Goertz C K 1984 *J. Geophys. Res.* **89** 10999
- [20] Goertz C K 1989 *Rev. Astrophys.* **27** 271
- [21] Böhm C and Perrin J 1991 *J. Phys. D: Appl. Phys.* **24** 865
- [22] Boeuf J P and Belenguer Ph 1992 *J. Appl. Phys.* **71** 4751
- [23] Geha S, Carlile R N, O'Hanlon J F and Selwyn G S 1992 *J. Appl. Phys.* **72** 374
- [24] Carlile R N and Geha S 1993 *J. Appl. Phys.* **73** 4785
- [25] Birdsall C K 1991 *IEEE Trans. Plasma Sci.* **PS-19** 65
- [26] Surrendera M and Graves D B 1991 *IEEE Trans. Plasma Sci.* **PS-19** 144
- [27] Pitchford L C, Belenguer Ph and Boeuf J P 1993 *Microwave Discharges: Fundamental and Applications* NATO ASI, ed C M Ferreira and M Moisan (New York: Plenum)
- [28] Boeuf J P 1988 *J. Appl. Phys.* **63** 1342; 1987 *Phys. Rev. A* **36** 2782
- [29] Gogolides E and Sawin H 1992 *J. Appl. Phys.* **9** 3971
- [30] Graves D B 1987 *J. Appl. Phys.* **62** 88
- [31] Richards A D, Thompson B E and Sawin H H 1987 *Appl. Phys. Lett.* **50** 492
- [32] Meyappan M and Govindan T R 1991 *IEEE Trans. Plasma Sci.* **19** 122
- [33] Scharfetter D L and Gummel H K 1969 *IEEE Trans. Electron Devices* **16** 64

Spatial distributions of dust particles in plasmas generated by capacitively coupled radiofrequency discharges

Seung J Choi†, Peter L G Ventzek‡, Robert J Hoekstra and Mark J Kushner§

Department of Electrical and Computer Engineering, University of Illinois, 1406 W. Green St. Urbana, IL 61801, USA

Abstract. The transport of particles ('dust') in low-pressure electrical glow discharges is of interest with respect to contamination of semiconductor wafers during plasma etching and deposition. The distribution of dust particles in these reactors is determined by a variety of forces, the most important being electrostatic, viscous ion drag, gravitational, thermophoretic and neutral fluid drag. In this paper we present results from a series of computer models to predict the spatial distribution of dust particles in capacitively coupled electrical glow discharges considering these forces. The results are parametrized over power deposition, gas flow and particle size. We find that the spatial distribution of dust depends on the spatial dependence of the sheaths and plasma potential in bulk plasma which in turn depend upon the electrical topography of the surfaces. Experimentally observed 'dome' and 'ring' distributions of dust particles are computationally reproduced for specific combinations of discharge power, particle size and substrate topography.

1. Introduction

Particulates ('dust' particles) are common contaminants in low-pressure (< 100 mTorr), partially ionized (electron density 10^9 – 10^{11} cm $^{-3}$) plasma processing electrical glow discharges for semiconductor etching and deposition [1–10]. The dust particles negatively charge, and particles of a few micrometres in size have hundreds to thousands of elementary charges [11,12]. Dust particles generally accumulate in specific regions of the radio frequency (rf) discharges which are commonly used in plasma processing. Roth *et al* first used laser light scattering to observe that particles accumulate near the bulk plasma sheath boundary in these discharges [1], as was later confirmed by Selwyn *et al* [2–4], Jellum *et al* [5–7], and Watanabe *et al* [8,9]. Large particles (> 0.1 μ m) accumulate near the sheath edge, while small particles accumulate in the centre of the discharge at the location of the maximum in the plasma potential. Selwyn *et al* [3] and Carlie *et al* [10] also observed that particles accumulated in rings around and domes above the semiconductor wafers in reactive ion etching (RIE) discharges.

Sommerer *et al* [13] and Barnes *et al* [14] proposed that transport of small particles (when gravity is not important) is dominated by two forces, electrostatic and viscous ion drag. The former force accelerates negatively charged particles towards the centre of electropositive

plasmas or towards local maxima in the plasma potential. The latter force accelerates particles in the direction of net ion flux, which is generally towards the boundaries of the plasma. (The ion drag force results from orbits of positive ions around the dust particle which transfer momentum to the particle in the direction of the net ion flux [11,12]. These forces have also been theoretically addressed by Graves *et al* [15,16] and computationally addressed by Choi and Kushner [11,12].

The details of the geometry of the reactor are important in determining the location at which particles accumulate in RIE discharges. For example, for large particles, the electrostatic and ion drag forces balance near the edge of the sheath. The electrical topography of the substrate, which determines the shape of the sheath, is therefore important in determining the distribution of dust particles. Viscous fluid forces accelerate particles in the direction of the gas flow. The flow field through nozzles and around obstacles is therefore important with respect to dust distributions. The geometry of the reactor can also determine the temperature field, which generates thermophoretic forces [17].

The importance of the electrical topography of the substrates in determining the distribution of dust has been noted by the experimental observations that dust often accumulates in rings and domes above semiconductor wafers [18]. Selwyn *et al* [3] also observed that particles accumulate in the centre of metallic washers placed on the electrode and in grooves surrounding the wafers in RIE discharges. These observations are presumably explained by the perturbing effects of the electrotopographies on the potential profile and ion fluxes. Further

† Present address: Sandia National Laboratory, Albuquerque, NM 87185, USA.

‡ Present address: Hokkaido University, Department of Electrical Engineering, Sapporo, Japan.

§ Author to whom correspondence should be addressed.

evidence for the importance of the electrical topography in determining dust distributions can be found with recent electric probe measurements of the plasma potential in RF discharges. These measurements showed that particles are commonly found in the vicinity of positive potential traps (perhaps as large as 7 V) at the edges of wafers [10,18].

To predict the accumulation of particles in RF discharges one must therefore self-consistently account for the shielding and charging of particles in the plasma, the ion flux which provides the ion drag forces, the electric field which generates the electrostatic force, the fluid flow field which provides the viscous drag force and the temperature field which generates thermophoretic forces. A series of computer models has been developed to predict the dynamics of the motion of dust particles in capacitively coupled RF discharges considering these forces. The models are described in section 2 followed by a discussion of our results in section 3. Our concluding remarks are presented in section 4.

2. Description of the model

The model we have used in this study is a series of five linked simulations, schematically shown in figure 1. The first model is a pseudoparticle in cell simulation (pics) which provides the electrical charges on the dust particle and ion dust momentum transfer cross sections [11,12]. The second is a two-dimensional Monte Carlo fluid hybrid (MCH) model for plasma properties of RF discharges [19]. The third is a two-dimensional plasma chemistry Monte Carlo simulation (PCMS) which provides ion velocity distributions [19]. The fourth is an advective flow field model. The fifth is the dust particle transport (DPT) model which is the module in which the dust particle trajectories are actually computed. (To avoid confusion computational particles in a pics or MCS will be called pseudoparticles; contaminating particulates in the plasma will be called dust particles.)

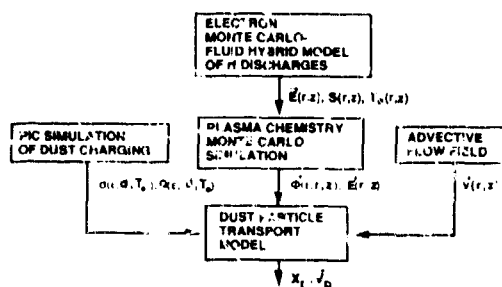


Figure 1. Schematic of the model for particle trapping. Results from a Monte Carlo fluid hybrid model for RF discharges provide ion sources, electron temperature and electric potential. A pics simulation provides ion-dust momentum transfer cross sections and charges on the dust. A plasma chemistry Monte Carlo simulation provides ion fluxes. A separate model provides the fluid flow field. These results are combined in the dust particle transport model.

The modelling process begins by computing the electrical charges on the dust and the ion-dust momentum transfer cross sections as a function of ion energy and plasma parameters (such as electron density and temperature). These cross sections are obtained from the pics which follows electron and ion trajectories in the vicinity of a dust particle while solving Poisson's equation for the electric field. Before executing the pics, Monte Carlo simulations (MCS) of both the electron and ion swarms are performed using a specified and spatially uniform E/N (electric field/gas number density). The purpose of performing the MCS is to obtain the quasi-steady state electron energy distribution and ion energy distribution for use as initial conditions in the pics. The details of the MCS are described by Weng and Kushner [20]. All pertinent elastic and inelastic collisions of electrons with the neutral gas and ions are included in the MCS. After the electron and ion energy distributions are obtained, a spherical dust particle is introduced into the centre of the computational volume having a specified charge Q . The pics is then performed while including all the collision processes. This portion of the model differs from the MCS in that now the self-consistent electric field in the vicinity of the dust particle is obtained by solving Poisson's equation while the equations of motion of the pseudoparticles are advanced. When solving Poisson's equation, the net charge density in the plasma and on the surface of the dust particle are accounted for. The surface charge density provides a boundary condition in the form of the electric field at the surface. Pseudoparticles striking the dust particle are assumed to be collected with unity efficiency. The collected charge density was averaged over the surface of the dust particle. The pics is executed to obtain dQ/dt . Based on the sign of dQ/dt , the pics is repeated with different values of Q to search for the value of Q which yields $dQ/dt = 0$ which signals an equilibrium of electron and ion fluxes to the dust particle.

At the end of the pics, cross sections for electron and ion momentum transfer to the dust particle, and for collection by the dust particle are calculated using molecular dynamics (MD) techniques. Given the electric field around the dust particle obtained from the pics, electron and ion pseudoparticles are launched into the computational volume with varying impact parameters. By gathering statistics on the change in momentum and number of pseudoparticles as they leave the volume, one can calculate the momentum transfer and capture cross sections.

A two-dimensional MCH model of RF discharges is then used to obtain electric fields as a function of position and source functions for ions and radicals [19]. The two-dimensional (r, z) model is a hybrid simulation consisting of an electron Monte Carlo simulation (MCS), a fluid-chemical kinetics simulation (FCKS), and an off-line plasma chemistry Monte Carlo simulation. The model is conceptually a 2D analogue of the 1D MCH model for RF discharges described previously [21]. The hybrid model begins by estimating electric fields in the plasma as a function of position and phase $E(r, z, \phi)$.

These fields are used in the EMCs to advance electron trajectories to calculate the time averaged electron energy distribution, $f(\mathbf{r}, \mathbf{v}, z)$. This is obtained by averaging electron trajectories over ≈ 50 RF cycles while including all pertinent elastic, inelastic, and Coulomb collisions [21]. $f(\mathbf{r}, \mathbf{v}, z)$ is then used to calculate source functions for electron impact processes, transport coefficients, and average electron energies as a function of (\mathbf{r}, z) . These quantities are then passed to the FKS. The FKS integrates the continuity equations for the densities of all charged and neutral species and solves Poisson's equation for the electrostatic plasma potential using the method of successive-over-relaxation. A semi-implicit solution of Poisson's equation allows us to take time steps tens to hundreds of times larger than the dielectric relaxation time if necessary. An acceleration technique is used to speed the convergence of the FKS by predicting future species densities based on recent time histories of those densities [22].

We account for the different effective areas of the electrodes by using a simple circuit having a blocking capacitor, and calculate the DC bias generated on the substrate. The surfaces of the chamber are specified as being either metal or dielectric. We can also include on the substrate topography such as wafers, discs and grooves of specified dielectric constant. After the FKS, $E(\mathbf{r}, z, \phi)$ and species densities are cycled back to the EMCs to iterate through the model until the plasma density converges.

In the MCFH model, electrons are treated kinetically while ions are treated as a fluid. We therefore do not generate the information on the ion energy distributions that is required to compute the forces on the dust particles. To obtain these distributions, the electric field and source functions from the MCFH model are imported into the PCMCs. In the PCMCs, source functions and electric fields from the MCFH are used to launch and follow trajectories of pseudoparticles representing ions and radicals. All pertinent elastic and inelastic collisions for both ions and radicals are included. An iterative particle-mesh algorithm incorporating a modified null cross section technique is used to account for ion-ion (such as negative ion-positive ion neutralization) and radical-radical collisions [23]. Statistics are collected on the velocity and spatially resolved ion momentum flux distribution, $\phi_i(\mathbf{r}, z, \mathbf{v}_i)[\text{g}(\text{cm}^2\text{s}^{-1})(\text{cm}^{-1}\text{s}^{-1})]$.

The fluid flow field in the reactor is obtained by solving the perturbative pressure form of the continuity and momentum equations.

$$\frac{\partial \mathbf{u}}{\partial t} = -\nabla \cdot \mathbf{u}\mathbf{u} - \frac{\nabla p}{\rho_0} - D\nabla^2 \mathbf{u} \quad (1a)$$

$$\frac{\partial p}{\partial t} = -\rho_0 \nabla \cdot \mathbf{u} \quad (1b)$$

In equation (1) \mathbf{u} is the advective fluid velocity, p is the perturbative pressure, ρ_0 is the gas density, v_0 is the sound speed and D is the velocity diffusion coefficient. This flow field is also used in the PCMCs to account

for momentum transfer between the pseudoparticles and buffer gases during elastic collisions.

The motions of the dust particles are calculated in the DPR model where we compute the spatially dependent ($\mathbf{r} = (r, z)$) forces on the dust particles. To obtain these forces we import the ion-momentum transfer cross sections and dust charges (from the PICS), electric fields (from the MCFH model), ion momentum distributions (from the PCMCs model) and the fluid flow field. For this work we have simply specified a temperature gradient. The force on a dust particle i having a specified radius r_i and mass M_i is

$$\begin{aligned} \mathbf{F}_i(\mathbf{r}) = & M_i \mathbf{g} + q_i \mathbf{E} + \int \sigma(|\mathbf{v}_i|) \phi(\mathbf{r}, \mathbf{v}_i) |\mathbf{v}_i| d\mathbf{v}_i \\ & - \frac{6\pi\mu r}{C(Kn)} (\mathbf{v}_i - \mathbf{u}) \cdot \mathbf{C}_D(Re_p) \frac{Re_p}{24} - 6\pi\mu r_i v_i K_T \frac{\nabla T}{T}. \end{aligned} \quad (2)$$

The terms on the right-hand side of equation (2) are for gravitational, electrostatic forces, ion drag, viscous fluid drag and thermophoretic forces respectively. \mathbf{E} is the electric field (obtained from the MCFH model), q_i is the charge on the dust particle (obtained from the PICS), σ is the ion momentum transfer cross section (obtained from the PICS) and ϕ is the ion momentum flux distribution (obtained from the PCMC model). The last two terms, viscous fluid drag and thermophoretic forces, are derived from classical thermodynamics based on the hard sphere particle assumption [17, 24]. The constants are

$$C(Kn) = 1 + Kn(\alpha + \beta) \cdot \exp\left(-\frac{\gamma}{Kn}\right) \quad (3a)$$

$$C_D(Re_p) \frac{Re_p}{24} = 1 + 0.1/3 \cdot Re_p^{0.657} + \frac{0.01721 \cdot Re_p}{1 + 16.300 \cdot Re_p^{1.09}} \quad (3b)$$

$$Re_p = \frac{2\mu r_i |\mathbf{v}_i - \mathbf{u}|}{\mu} \quad (3c)$$

$$K_T = \frac{2C_\infty [(k_g/k_p) + C_m Kn]}{(1 + 3C_m Kn)[1 + 2 \cdot (k_g/k_p) + 2C_m Kn]} \quad (3d)$$

\mathbf{v}_i is the velocity of the dust particle, Kn is the Knudsen number (λ/r_i), Re_p is the Reynolds number, μ is the fluid viscosity, $v = \mu/\rho$ (ρ is the gas density), and T is the mean gas temperature. In equation (3) α , β and γ are experimental constants which depend on the nature of the gas-particle interaction at the particle surface and so are affected by both gas composition and particle surface roughness. k_g and k_p are the gas and particle thermal conductivities respectively, and C_∞ , C_m and C_m are the thermal creep coefficient, temperature jump coefficient, and velocity jump coefficient respectively. All values of the constants in equation (3) are listed in table 1.

To begin the DPR model, we specify a volumetric rate of generation of dust particles of a given radius. We then launch pseudoparticles representing the dust particles from those locations, and simply integrate the equations of motion of those pseudoparticles while continuously

Table 1. Values of constants used in force calculations

Constant	Value	Reference
α	1.227	[24]
β	0.42	[24]
γ	0.85	[24]
k_0	$0.1799 \text{ mW cm}^{-1} \text{ K}^{-1}$	[28]
k_0	$1240 \text{ mW cm}^{-1} \text{ K}^{-1}$	[28]
C_0	2.2	[24]
C_0	1.147	[24]
C_m	1.146	[24]

launching additional pseudoparticles until the dust distribution achieves a steady state.

3. Distribution of dust particles

In this work we investigated dust particle distributions in a capacitively coupled RF (13.56 MHz) discharge sustained in 100 mTorr of argon with a nominal power deposition of $\approx 20-200 \text{ W}$ (see figure 2). The electrodes are separated by 3 cm and the plasma zone is 10 cm in diameter. The gas flows through a showerhead nozzle and out radially to a pump port (figure 3). A wafer (dielectric constant $\epsilon/\epsilon_0 = 11.8$, thickness 3 mm) sits on the lower powered electrode. The top electrode is grounded. The radial boundary condition is approximated as a ground plane (at $r = 10 \text{ cm}$) which allows the advective flow to pass. For these results we have assumed a constant thermal gradient of 15 K cm^{-1} as

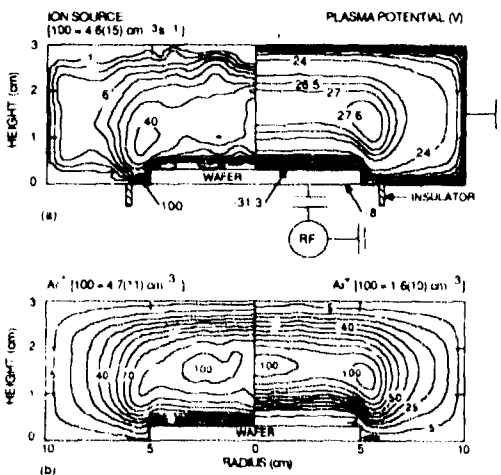


Figure 2. Plasma parameters from the MCF model for a capacitively coupled RF discharge (13.56 MHz) in 100 mTorr Ar^+ . (a) ion source and plasma potential. (b) $\text{Ar}(4s)$ and Ar^+ densities. The contour labels for ion source and densities are a percentage of the maximum value, noted at the top of the figure. A 3 mm thick wafer (10 cm diameter) is on the lower powered electrode. The electrode topography produces a local maximum in the plasma potential and the ion source.

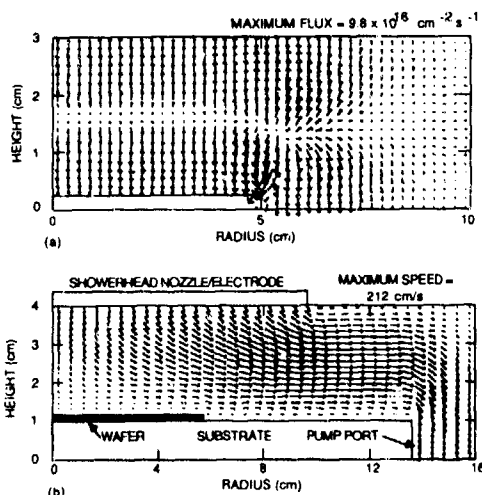


Figure 3. Flow fields for the condition of figure 2. (a) ion flux and (b) advective fluid velocity. The size of the arrow denotes the magnitude of the ion flux or fluid velocity. The maximum value is shown at top. The ion flux moves away from the local maxima in ion source and plasma potential to the boundaries. The fluid velocity is most negative at the showerhead nozzle and is almost totally radial near the edge of the wafer.

could occur when actively cooling the wafer. We observe that the calculated thermophoretic force is smaller than the electrostatic or ion drag forces, and therefore is not a major consideration under our operating conditions.

Typical results from the MCF models are given in figure 2 where the time averaged plasma potential, ion source, ion density and argon metastable density are shown. A 10 cm diameter wafer is placed on the powered electrode. The powered diameter of the lower surface is $\approx 12 \text{ cm}$ and is separated from the annular ground plane by a dielectric spacer. The metal surface of the powered electrode generates a dc bias of -8 V , while the surface of the wafer acquires a dc bias of -31 V . Note that there are local maxima in the plasma potential, electron sources and ion density in the form of a toroidal ring $1-1.5 \text{ cm}$ from the edge of the wafer.

The positive potential well has a depth of $\approx 1-1.5 \text{ V}$. These local maxima, perhaps similar to those observed by Gehe *et al* [18], result from a discontinuity in the electrical topography produced by the sharp edge of the wafer, and by the transition between the dielectric wafer and the metal. In this regard, the discontinuity in electrode topography resembles the metal-gas-dielectric triple point at which electric field enhancement occurs in high-voltage switches [25]. The ion density shows a small maximum in the toroidal region as well as at the centre of the plasma. The $\text{Ar}(4s)$ density also shows a weak off-axis peak. Note that, although the ion source has a local maximum near the edge of the wafer, its absolute maximum value is near the exposed

powered electrode. This results from the fact that the full capacitive voltage drop is across the sheath as opposed to sharing the voltage between the wafer and the sheath.

The ion flux (obtained from the PCMCs) and fluid flow fields for these conditions are shown in figure 3. The ion flux typically flows from maxima in the plasma potential and ion sources to the peripheries of the reactor. The local maxima in the plasma potential and ion source at the edge of the wafer produces a vertex in the ion flux with ions flowing from that location. The fluid flow starts from the showerhead and gains speed in the radial direction as the edge of the showerhead is approached.

Predictions of dust particle locations for dust diameters of 0.5 to 4 μm are shown in figure 4 for the geometry just discussed. These results are an instantaneous 'snapshot' of the dust particle locations 0.15 s after beginning to generate particles. The dust particles are generated at a constant rate of $2.6 \times 10^4 \text{ s}^{-1}$ in the plasma region of the reactor weighted by a cosine (maximum in the centre) in both the axial and radial

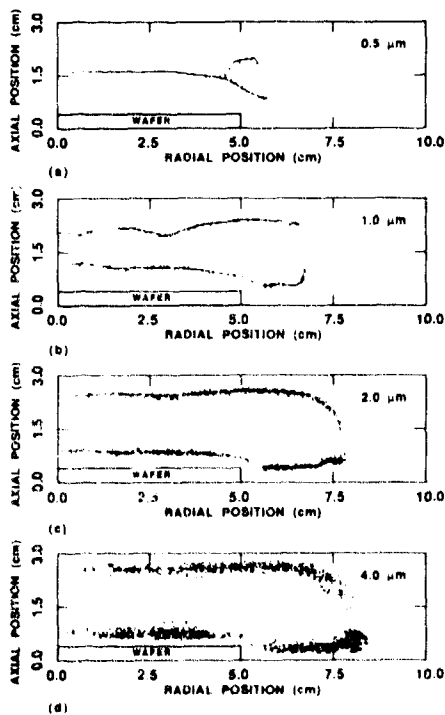


Figure 4. Dust particle locations with a 10 cm diameter wafer on the powered electrode. Locations are shown for (a) 0.5, (b) 1.0, (c) 2.0 and (d) 4.0 μm particles. Small particles are more sensitive to the electric potential and may form domes and rings around local maxima in the potential caused by ion drag away from these locations. Large particles have larger ion drag forces, which push them towards the boundaries. Inertial effects cause oscillation about the equilibrium locations.

directions. The power is 80 W and the gas flow is turned off. The smaller sized particles are trapped near the centre plane of the reactor at the maximum in the plasma potential. The dust particles are also trapped around, but not in, the positive potential well. Ion flux flowing out of the well is fairly efficient at removing particles from that region and holding them at the periphery. We also observe that the plasma optical emission and particle locations do not necessarily coincide. Trapped particles follow a contour on which ion drag and electrostatic forces balance. This contour moves down towards the edge of the wafer around both sides of the local maximum in potential on both sides. These loci of points forming the trapping locations give the appearance of a 'dome' above the wafer and 'ring' around the wafer as observed experimentally by others [2, 26, 27] at a similar power deposition value (240 mW cm^{-2}).

As the particle size increases, the trapping location moves toward the electrodes and a flatter dome and a wider ring form. The ion drag force increases at a faster rate with increasing particle size than does the electrostatic force, and so the large particles are pushed by the ions towards the periphery. The ion drag forces are sufficiently large for particles $\geq 2.4 \mu\text{m}$ that inertial effects are important. That is, the dust particles are accelerated to high velocities which overshoot the equilibrium location at which ion drag and electrostatic forces are balanced. The particles therefore oscillate about those locations as their velocities are slowly damped by fluid drag force. The oscillation is shown by the 'blurring' of the particle locations in the snapshot of figure 4(d). Although we collect all particles striking the electrodes, many of the larger particles strike the electrodes and could conceivably bounce off the surface.

Particle locations are shown in figure 5 (1 μm diameter) for similar conditions as in figure 4 except for a 15 cm diameter wafer on the powered electrode and power deposition of 20–240 W. The largest difference which occurs with increasing power deposition is an increase in the ion flux while the potential profile does not change appreciably. As with the smaller wafer, there is a local maximum in the plasma potential and ion flux near the edge of the wafer as shown in figure 6. But now with the larger wafer, there is also a maximum in the plasma potential at the centre of the wafer. At low-power deposition, the electrostatic forces dominate, and the particles accumulate at the ridge the maximum in the plasma potential. As the power increases and ion drag forces increase, the particles are pushed away from the maximum in the plasma potential, and form ring- and dome-like structures. These locations are on opposite sides of the maximum in the plasma potential where the ion drag caused by ions flowing away from the maximum is balanced by electrostatic forces. As the power continues to increase, the ion drag forces dominate and push the particles to the sheaths at the edge of the wafer. At high powers, the ion drag forces accelerate the dust particles to sufficiently high velocities that they overshoot the equilibrium location. Evidence of oscillation

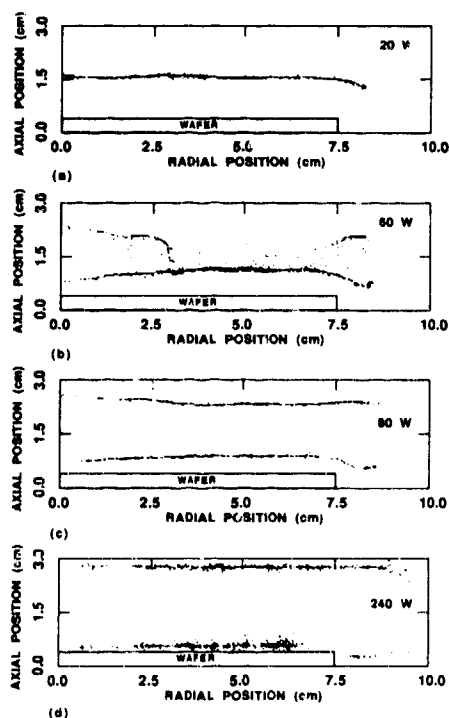


Figure 5. Dust particle ($1\text{ }\mu\text{m}$) locations with a 15 cm diameter wafer on the powered electrode. Locations are shown for power depositions of (a) 20, (b) 60, (c) 80 and (d) 240 W. Increasing power increases the ion drag force, pushing particles towards the electrodes. The dome and ring structures result from local maxima in the plasma potential.

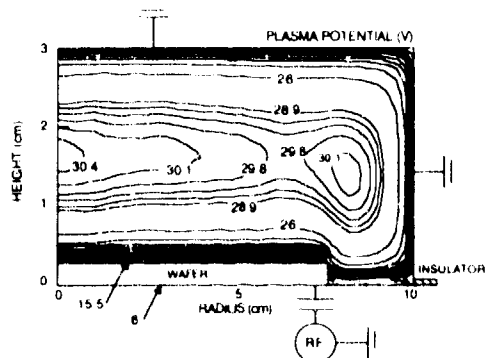


Figure 6. Plasma potential for the conditions of figure 5 (20 W). The dots denote regions of negative potential. Maxima in plasma potential occur near the edge of the wafer and in the centre of the reactor.

power deposition, an effect we attribute to an increased component of ion drag.

The effects of gas flow on trapping are shown in figure 7 for $1\text{ }\mu\text{m}$ particles and a power deposition of 80 W. Note that no wafer is used in this sequence where we varied the gas flow from zero to 500 sccm. Without gas flow, the particles are trapped at the sheath edges where electrostatic and ion drag forces balance. As the gas flow increases the particle trap near the top grounded electrode is eliminated by the fluid forces. At this location the fluid drag force is negative (towards the lower electrode) and opposes the ion drag which forces the particles towards the upper electrode (see figure 3). With increasing gas flow particles are swept in the radial direction where they are lost out of the gas outlet and accumulate to some degree at the radial sheath. This accumulation may be exaggerated by our electrical radial boundary condition. At very high gas flow, the inertia imparted to the particles by the high axial gas flow near the showerhead causes particles to oscillate about equilibrium trapping points.

The disposition of $1\text{ }\mu\text{m}$ particles is shown in figure 8 where the normalized rates of loss of particles to traps,

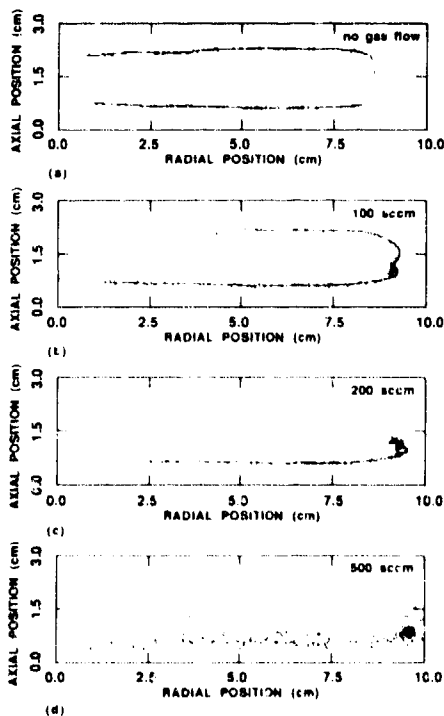


Figure 7. Dust particle locations with a bare powered electrode. Locations are shown for (a) 0, (b) 100, (c) 200 and (d) 500 sccm of gas flow. The gas flow detraps particles at the upper boundary where the fluid velocity is negative and opposes the ion drag forces. Particles are lost via the radial pump port at high gas flow.

tion in the location of the particles can be seen by the 'blurred' line of particles. These predictions agree with the experimental observations of Selwyn *et al* [26] who noted that particle traps can be emptied by increasing

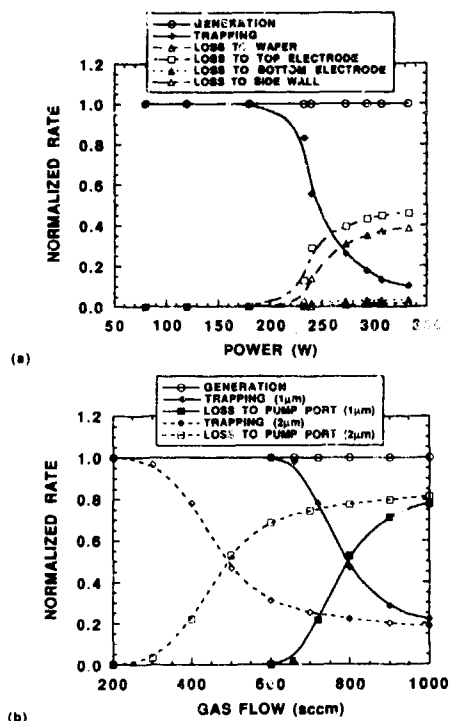


Figure 8. Disposition of particles as a function of (a) power deposition ($1\ \mu\text{m}$ diameter) and (b) gas flow (1 and $2\ \mu\text{m}$ diameter). Rates of trapping and loss to the wafer, bottom electrode (but not the wafer), top electrode and to the side wall or gas outlet are shown.

the top electrode, the bottom electrode (but not the wafer), the wafer and to the side wall (or out the pump port) are shown. Results are presented as a function of power deposition (without gas flow) and gas flow (at 80 W). In the low-power regime and without gas flow, most particles are trapped in the plasma. As the power increases the trapping rate decreases and the particle loss to the reactor boundaries increases. This results from ion drag forcing particles over the potential hill at the boundaries. At 300 W (without gas flow), only 10% of the particles are trapped. Note that the rate of loss of particles to the wafer is smaller than to the top electrode because of its more negative sheath (and smaller size). The particle dispositions as a function of gas flow show that at sufficiently high gas flows, the particles can be blown out of the pump port. Larger particles are more easily blown out of the reactor because both the fluid drag and ion drag forces increase with radius of the dust particle. These results are sensitive to the starting locations of the dust particles.

The interplay between electrostatic, ion drag and fluid forces ultimately determines the disposition of the particles. This interplay is illustrated in figure 9 where particle locations are shown when a metal washer is placed on the lower electrode. The gas flow is 200 sccm

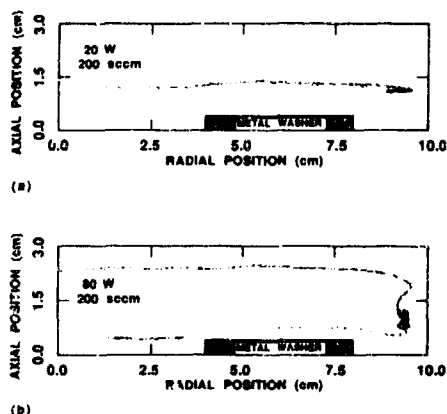


Figure 9. Particle traps are shown when a metal washer is placed on the powered electrode for a gas flow of 200 sccm with (a) 20 W and (b) 80 W of power deposition. With the higher power particles are trapped on the inside of the wafer where an axial potential well exists.

and results are shown for 20 and 80 W power deposition. The sheath follows the contours of the washer, thereby creating a potential well with respect to axial location in the centre of the washer. At the lower powers, $1\ \mu\text{m}$ particles are trapped in a flat dome above the wafer and are blown towards the radial boundary. When the power is increased to 80 W, the particles are pushed by ion drag to the electrodes. Some particles, which are generated in the centre of the reactor, are trapped inside the washer. The particles inside the washer do not have enough energy to climb the electrostatic potential barrier over the washer and exit through the gas outlet. The gas flow inside the washer has no appreciable radial component to push the particles out of the centre of the ring.

4. Concluding remarks

A series of linked computer models has been developed and used to investigate the trapping of dust particles in capacitively coupled RF discharges with various electrode topographies. Lower rates of wafer contamination are obtained at low-power deposition where particles are allowed to be trapped in the gas phase, and high gas flow where the particles are blown towards the pump ports. At higher power deposition, ion drag forces dominate and particles are pushed through the sheaths to the boundaries. Various shapes of particle trapping locations are formed under different operating conditions. At low powers, we observed both 'dome' and 'ring' types of particle traps as seen experimentally [3, 26, 27] which result from a balance of ion drag and electrostatic forces generated by perturbations in these quantities caused by local extrema in the ion generation and potential, ultimately caused by electrode topography. At high power or high gas flow, the dust particles can gain sufficient

inertia that they will oscillate about the equilibrium trapping locations, or climb potential hills of tens of volts to reach the substrate.

5. Acknowledgments

We thank D Rader, A Geller, M Barnes, G Selwyn, J Goree, J Keller and D Graves for their advice and discussions on dusty plasmas. This work was supported by the National Science Foundation (CTS 91-13215 and ECS 91-09326), Sandia National Laboratory, the Semiconductor Research Corporation and the University of Wisconsin-ERC for Plasma Aided Manufacturing.

References

- [1] Roth R M, Spears K, Gr Stein G D and Wong C 1985 *Appl. Phys. Lett.* **46** 235
- [2] Selwyn G S, Hendenreich E E and Haller K J 1990 *Appl. Phys. Lett.* **57** 1876
- [3] Selwyn G S, Singh J and Bernier R S 1989 *J. Vac. Sci. Technol. A* **7** 2758
- [4] Selwyn G S, McKillop J S, Haller K J and Wong C 1990 *J. Vac. Sci. Technol. A* **8** 2726
- [5] Jellum G M and Graves D B 1990 *Appl. Phys. Lett.* **57** 2077
- [6] Jellum G M and Graves D B 1990 *J. Appl. Phys.* **67** 6490
- [7] Jellum G M, Daugherty J J and Graves D B 1991 *J. Appl. Phys.* **69** 6923
- [8] Watanabe Y, Shiratani M and Makino H 1990 *Appl. Phys. Lett.* **57** 1616
- [9] Watanabe Y, Shiratani M and Yamashita M 1992 *Appl. Phys. Lett.* **61** 1510
- [10] Carlile R N, Geha S G, O'Hanlon J and Stewart J 1991 *Appl. Phys. Lett.* **59** 1167
- [11] Choi S J and Kushner M J 1995 *Appl. Phys. Lett.* **62** 2197
- [12] Choi S J and Kushner M J 1994 *IEEE Trans. Plasma Sci.* to be published
- [13] Sommerer T J, Barnes M S, Keller J H, McCaughey M J and Kushner M J 1991 *Appl. Phys. Lett.* **59** 638
- [14] Barnes M S, Keller J H, Forster J C, O'Neill J A and Coutas D K 1992 *Phys. Rev. Lett.* **68** 313
- [15] Daugherty J J, Porteous R K and Graves D B 1993 *J. Appl. Phys.* **73** 1617
- [16] Kilgore M D, Daugherty J J, Porteous R K and Graves D B 1993 *J. Appl. Phys.* **73** 5995
- [17] Edson T, Cheng R K, Scheler R W and Willis D R 1980 *J. Fluid Mech.* **102** 737
- [18] Cichy S G, Carlile R N, O'Hanlon J E and Selwyn G S 1992 *J. Appl. Phys.* **72** 374
- [19] Ventrak G E, Sommerer T J, Hoekstra R J and Kushner M J 1993 *Appl. Phys. Lett.* **63** 995
- [20] Wong Y, Cho K and Kushner M J 1992 *Phys. Rev. A* **42** 6092
- [21] Sommerer T J and Kushner M J 1992 *J. Appl. Phys.* **71** 3684
- [22] Pak H and Rhee M 1992 *Phys. and Geophys. Experiments* (ed. by R. Heide) (Boca Raton, FL: CRC Press) in press
- [23] Hwang M J and Kushner M J 1993 *Appl. Phys. Lett.* **62** 1844
- [24] Rader D J 1994 *Plasma Sources Sci. Technol.* **A4** 26
- [25] Gendron G and Sudrajat I S 1993 *J. Appl. Phys.* **73** 7643
- [26] Selwyn G S, Hendenreich E E and Haller K J 1991 *J. Vac. Sci. Technol. A* **9** 2817
- [27] Selwyn G S 1991 *J. Vac. Sci. Technol. B* **9** 3487
- [28] Weast R C, Lide D R, Astle M J and Beyer W H (eds) 1989 *CRC Handbook of Chemistry and Physics* (Boca Raton, FL: CRC)

Particle transport modelling in semiconductor process environments

Daniel J Rader and Anthony S Geiler

Engineering Sciences Center, Sandia National Laboratories, Albuquerque,
New Mexico 87185-0834, USA

Received 6 January 1994, in final form 12 February 1994

Abstract. We review current efforts in developing and applying computational models that can predict fluid, thermal, and particle transport in semiconductor process environments such as that used for chemical vapor deposition in plasma etching. The purpose of this work is to supply equipment designers and operators with models that allow them to optimize process parameters, troubleshoot problems, and design reactors that reduce particle contamination levels. The algorithms for solving the fluid, thermal, and particle transport problems are briefly described. A diagram and appendix are used in this work where the particle transport and deposition are the important variables. An appendix is included to illustrate the use of a simple geometry representation of a single-wafer process chamber. The geometry is axisymmetric, but the fluid and thermal transport equations are solved in a three-dimensional geometry. The particle transport equations are solved in a two-dimensional geometry. The transport equations are solved using a finite difference method. The results are presented in a series of plots. The plots show the particle transport and deposition rates as a function of position. The plots also show the fluid and thermal transport results. The plots are used to illustrate the importance of the particle transport and deposition rates in the design of a reactor. The plots are also used to illustrate the importance of the fluid and thermal transport results in the design of a reactor. The plots are also used to illustrate the importance of the particle transport and deposition rates in the design of a reactor.

1. Introduction

A programme is underway at Sandia National Laboratories to apply analytic and computational techniques to predict formation and transport of contaminants in semiconductor manufacturing processes and thereby reduce defect production. One of the main goals of this SEMATECH-sponsored effort is to supply equipment designers with models to allow them to identify process conditions and to develop tool designs that reduce defect formation by preventing contaminant generation or by isolating the wafer from contamination. General purpose models are needed that accept geometry, flow rates, chemistry, RF power and environmental conditions as input, and provide local contaminant concentration, formation rates, deposition rates and size distribution as output. The strategy is to apply existing codes (from commercial, university or national laboratory sources), to modify existing codes, or to develop new computational techniques, as needed. Modeling of both generic and commercial process reactors is currently under way.

Here, results for particle transport in a simple generic reactor geometry will be presented as a demonstra-

tion of current capabilities. The geometry consists of uniform flow through a showerhead separated by a finite gap from a parallel substrate, as shown in figure 1. In unpublished work, we have found that calculations of fluid, thermal and particle transport in this simple geometry are representative of the results to be expected from calculations in more complicated parallel-plate, single-wafer, commercial process chambers. Particle concentrations are assumed to be low enough to allow a dilute approximation, for which the coupling between fluid and particle phases is one way. In this case, the fluid/thermal transport equations can be solved neglecting the particle phase; the resulting velocity and temperature fields are then used as input for the particle transport calculations. The results presented here assume steady, laminar, incompressible, isothermal flow (constant fluid properties) in the absence of a plasma; although subsonic compressible flows, transient flows and non-isothermal flows can also be readily handled.

Plasma effects on fluid, thermal and particle transport are not considered here. Despite this considerable simplification, the present results are still pertinent to defect reduction in plasma systems, as a significant fraction of a wafer's time in a plasma reactor is spent

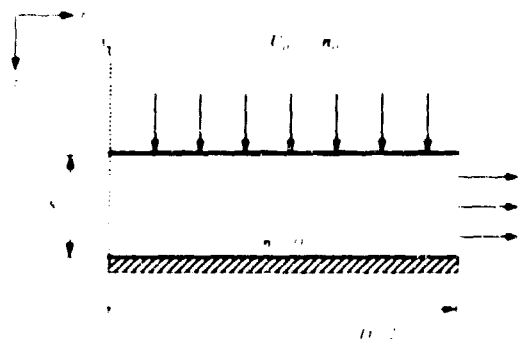


Figure 1. Schematic diagram of axisymmetric flow between two parallel plates.

with the plasma turned off (venting, purging, wafer handling and chamber preparation). Also, while the formation of plasma-induced particle traps may isolate the wafer from contamination while the plasma is on, when the plasma is turned off the particles are released from the traps and are free to be deposited on the wafer. This post-plasma transport is governed by the non-plasma forces described here if particle charge loss times are short relative to particle transport times (which is assumed here). If the traps are robust enough, the majority of particle deposition on a wafer probably occurs when the plasma is off. Finally, the particle transport formulations presented here provide a general framework within which models for plasma-induced forces (such as electrostatic and ion drag) can be included as they become available (Choi *et al.* 1994). All of the forces described here continue to act on a particle when a plasma is present, although the magnitude of the forces may change as a result of plasma effects on process conditions (such as temperature) and fluid properties (such as species distribution and viscosity).

The solution of the parallel-plate flow field is discussed next, followed by a description of the basic modelling techniques for particle transport. Both Lagrangian (in which individual particle trajectories are calculated) and Eulerian (in which particles are modelled as a continuum) approaches are considered. Results for the simple parallel-plate geometry follow, together with additional discussion and conclusions.

2. Fluid transport theory

Calculations of fluid velocity and temperature are made using the most recent version of the commercial fluid dynamics analysis code FIDAP (Version 7, Fluid Dynamics International, Evanston, Illinois, USA). This general purpose finite-element code allows steady-state or transient simulations of fluid and thermal transport in two or three dimensions and axisymmetric geometries. Although FIDAP is capable of analysing a wide range of problems, the code is used here to model laminar, isothermal, incompressible flow and subsequently, ad-

vection and diffusion of a dispersed particle phase in the flow. Under these simplifications, the equations used to calculate the velocity field are mass conservation:

$$\nabla \cdot \mathbf{U} = 0 \quad (1)$$

and momentum conservation:

$$\rho \left(\frac{\partial \mathbf{U}}{\partial t} + \mathbf{U} \cdot \nabla \mathbf{U} \right) = -\nabla P + \mu \nabla^2 \mathbf{U} \quad (2)$$

where \mathbf{U} is the fluid velocity vector, P is the pressure, and ρ and μ are the constant values of the fluid density and viscosity, respectively.

3. Particle transport theory

This section provides a brief review of the theoretical models available to describe particle transport in typical semiconductor processing environments. In the light of the brevity of the discussion, references have been provided wherever possible for additional background. Both the Lagrangian approach (in which individual particle trajectories are calculated) and the Eulerian approach (in which particles are modelled as a continuum) are considered. In all discussion that follows, particle concentrations are assumed to be low enough that particle-particle interactions and particle effects on the flow field can be neglected.

3.1. The Lagrangian formulation

In the Lagrangian approach to particle transport, individual particle trajectories (position and velocity as a function of time) are determined by integrating the following system of ordinary differential vector equations:

$$\frac{d\mathbf{x}_p}{dt} = \mathbf{V}_p \quad (3)$$

$$m_p \frac{d\mathbf{V}_p}{dt} = \mathbf{F}_D + \mathbf{F}_G + \mathbf{F}_T + \sum_i \mathbf{F}_i \quad (4)$$

where \mathbf{x}_p is the particle position vector, \mathbf{V}_p is the particle velocity vector, m_p is the particle mass, and \mathbf{F}_D , \mathbf{F}_G , \mathbf{F}_T and \mathbf{F}_i are the fluid-drag, gravitational, thermophoretic and any additional forces (including plasma-induced electrostatic and ion drag forces) acting on the particle. Equation (3) relates the change in a particle's position to its velocity, while equation (4) equates particle acceleration to the forces acting on it. In this work the chaotic effect of particle Brownian motion (particle diffusion) on particle trajectories is neglected.

3.1.1. Non-continuum considerations. In the following discussion, frequent mention will be made of the continuum or free molecular regimes. These terms are used here to distinguish between the two limiting cases characterizing the nature of the particle-gas interaction. In the continuum limit (large particles or high gas pressures), the gas surrounding the particle appears as a

continuous fluid and the Navier-Stokes equations apply. In the free molecular limit (small particles or low gas pressures), however, the discrete nature of the gas becomes important and individual molecule/particle collisions must be considered. Discrimination between these two regimes is made by comparing the particle diameter with the gas mean free path (the average distance a molecule travels between collisions with other gas molecules); the Knudsen number is commonly used for these comparisons:*

$$Kn = \frac{2\lambda}{d_p} \quad (5)$$

where λ is the gas mean free path (cm) = $\mu/(\phi\rho\bar{c})$, d_p is the particle diameter (cm), \bar{c} is the mean velocity of the gas molecules (cm s^{-1}) = $(8RT/\pi M)^{1/2}$, R is the universal gas constant ($8.31448 \times 10^7 \text{ g cm}^2 \text{ s}^{-2} \text{ K}^{-1} \text{ mol}^{-1}$), M is the gas molecular weight (g mol^{-1}) and T is the absolute temperature (K).

Also, ϕ is a dimensionless parameter that depends on the kinetic-theory model used to define the gas mean free path in this work the value $\phi = 0.491$ has been adopted (Allen and Raabe 1982). A large Knudsen number (say >10) corresponds to the free-molecular regime, while a small Knudsen number (say <0.1) corresponds to the continuum regime. At atmospheric pressures, the mean free path for most gases is typically of order $0.1 \mu\text{m}$. Gas mean free path is inversely proportional to pressure at constant temperature, for example, the mean free path in air is $0.674 \mu\text{m}$ at 76 Torr, $6.74 \mu\text{m}$ at 7.6 Torr, and $67.4 \mu\text{m}$ at 76 mTorr at 296 K. Thus, for low-pressure applications, the Knudsen number for sub-micrometre size particles can be large.

3.1.2. The fluid-particle drag force. A particle moving at a different velocity than the surrounding gas will experience a gas resistance or fluid-drag force. A great deal of research has been devoted to describing this fluid drag; only a brief review of this body of literature is reported here. For a rigid sphere of diameter d_p moving at constant velocity, V_p (relative to the local fluid velocity U), and low particle Reynolds number (through a fluid of viscosity μ), the drag force is given by the slip-corrected form of Stokes' law (Hinds 1982, p.45)

$$F_D = \frac{3\pi\mu d_p(U_p - U)}{C(Kn)} \quad (6)$$

where the slip correction factor first proposed by Cunningham (1910) is given by

$$C(Kn) = 1 + Kn \left[\alpha + \beta \exp\left(-\frac{\gamma}{Kn}\right) \right] \quad (7)$$

*The flow field entraining the particle can also be either molecular or continuum in nature. In this case, discrimination between the two flow regimes is made by comparing some characteristic length associated with the reactor geometry with the gas mean free path; a Knudsen number for the flow field could be defined by replacing the particle diameter in equation (5) with a characteristic reactor length scale. For small particles, it is frequently the case that the flow regime can be considered continuum while the fluid-particle interaction is characterized as free molecular.

In equation (7), α , β and γ are parameters that depend on the nature of the gas-particle interaction at the particle surface, and so are affected by both gas composition and particle surface roughness (see Rader (1990) for a recent review). In general, only small errors result if the slip factor is calculated using the fitted constants for oil droplets in air ($\alpha = 1.207$, $\beta = 0.440$ and $\gamma = 0.78$) for different gases or for particles of different surface roughness. Note that $C(Kn)$ approaches unity in the continuum limit, and approaches $(\alpha + \beta)Kn$ in the free-molecule limit.

The requirement of low particle Reynolds number is met practically for $Re_p = \rho d_p |V_p - U|/\mu \leq 0.3$, where ρ is the gas density. At higher values of particle Reynolds number (called the non-Stokesian regime), the linear relationship between drag and velocity represented in equation (6) breaks down and calculation of fluid drag must be done using empirically based correlations (Turton and Levenspiel 1986). Note that low particle Reynolds numbers are expected for most semiconductor process applications, so the Stokes drag law itself (equation (6)) can generally be used with negligible error.

Strictly speaking, equation (6) applies to the uniform (non-accelerating), straight-line motion of a sphere in a constant-velocity fluid. In the present application, however, the drag on an accelerating particle in a non-uniform flow field is needed. Fuchs (1964, ch.3) and Clift *et al.* (1978, ch.11) review the issues related to non-uniform rectilinear motion of aerosol particles. Although it will introduce some inaccuracy, the instantaneous drag acting on an accelerating particle is approximated here with the above constant-velocity drag expressions, with the fluid and particle velocities taken as their local, instantaneous velocities.

3.1.3. Terminal velocity. Dimensional analysis of equation (4) using the drag law given by equation (6) reveals a characteristic particle response time, $\tau = \rho_p d_p^2 C(Kn)/18\mu$, which is a measure of the particle's ability to respond to changes in the flow field. For typical semiconductor applications in which small particles are of interest, the response time τ becomes small and the acceleration term on the left hand side of equation (4) can be neglected. This approximation corresponds to the physical situation in which the particle instantaneously achieves its terminal velocity and external forces acting to move the particle balance the drag force retarding the motion. For Stokes drag the net terminal velocity of a particle relative to the local fluid velocity is

$$V_p = \frac{C(Kn)}{3\pi\mu d_p} \left(F_G + F_I + \sum_i F_i \right) = V_{pG} + V_{pI} + \sum_i V_{pi} \quad (8)$$

It is the linear nature of the problem resulting from the Stokes-drag assumption that allows the final equality in equation (8), namely that the net terminal velocity equals the sum of the terminal velocities, arising from each force acting independently against the resistance of the fluid. The absolute velocity of the particle would be

the vector sum of the local fluid velocity and the net terminal velocity.

3.1.4. Gravitational force. The gravitational force acting on a particle is given by (Hinds 1982)

$$F_G = m_p g = v_p (\rho_p - \rho) g \quad (9)$$

where m_p , v_p and ρ_p are the particle mass, volume and density, respectively, and g is the gravitational acceleration vector. Considering only the gravitational and fluid drag forces and neglecting buoyancy, the terminal velocity for a particle settling under gravity is

$$v_{pG} = \frac{\rho_p d_p^2 g C(Kn)}{18\mu} \quad (10)$$

3.1.5. Thermophoretic force. Because of the thermophoretic force, particles suspended in a gas with a temperature gradient will migrate in the direction opposite to the gradient, namely away from hot regions and towards cold regions. This phenomenon results in preferential deposition of particles on a cold wall, and explains the appearance of a particle-free zone near a hot wall. The currently accepted formulation for the thermophoretic force on a spherical particle (spanning the free-molecular to the continuum regime) was developed by Talbot *et al* (1980)

$$F_T = -3\pi\mu d_p K_T \frac{\nabla T}{T} \quad (11)$$

where

$$K_T = \frac{2C_1[(k_g/k_p) + C_2(Kn)]}{(1 + 3C_3(Kn)[1 + 2(k_g/k_p) + 2C_2(Kn)])} \quad (12)$$

and where ∇T is the temperature gradient in the gas, T is the mean gas temperature about the particle, $\mu = \mu_p$, k_g and k_p are the gas and particle thermal conductivities, and C_1 , C_2 and C_3 are the thermal creep, temperature jump and velocity jump coefficients, respectively. For non-atomic gases, Talbot *et al* recommend the use of the 'translational' thermal conductivity, which is given by simple kinetic theory as $k_g = (15/4)\mu R/M$. Talbot *et al* (1980) compared their correlation with other experimenters' data over a wide range of Knudsen numbers, and found that it agrees with available experimental data within 20% or less. The currently accepted values of the coefficients are $C_1 = 1.147$, $C_2 = 2.20$ and $C_3 = 1.146$ (Batchelor and Shen 1985).

The thermophoretic terminal velocity resulting from the balance of thermophoretic and drag forces alone can be found by equating equations (6) and (11)

$$v_{pT} = K_T C(Kn) \frac{\mu \nabla T}{\rho I} = K_T C(Kn) \frac{\mu R \nabla T}{PM} \quad (13)$$

Interestingly, the terminal velocity given by equation (13) depends on particle diameter only implicitly through the slip correction factor and K_T , specifically, in both large and small particle limits the thermophoretic velocity becomes independent of particle size

3.1.6. Plasma-induced forces. In addition to the forces described above, Sommerer *et al* (1991) and Barnes *et al* (1992) have proposed that the transport of small particles in a plasma reactor is dominated by two forces: electrostatic and ion drag. The electrostatic force accelerates negatively charged particles towards the centre of electropositive plasmas or towards local maxima in the plasma potential. The ion drag force accelerates particles in the direction of net ion flux, which is generally towards the boundaries of the plasma (the ion drag force results from open orbits of positive ions around the dust particle, which transfer momentum to the particle in the direction of the net ion flux (Choi and Kushner 1993)). In the Lagrangian framework, these plasma-induced forces are added to equation (4) as for each of the forces above. When particle inertia can be neglected, both an electrostatic and an ion-drag-induced terminal velocity can also be defined. Models for the force acting on dust particles in a plasma are complicated, as the forces can depend on the local electric field, the ion momentum flux, particle size, the gas flow rate, the plasma density, and the electron temperature, T_e . Numerical models that can predict these forces are now becoming available (Choi *et al* 1994).

3.2. The Eulerian formulation

While the Lagrangian (particle-tracking) method predicts particle transport by considering single particle motion, the Eulerian formulation predicts particle transport by viewing the particle concentration and velocity fields as a continuum. In this case, the solution of the particle transport problem becomes very much like that posed by the flow field; there is one continuous equation for particle mass (concentration) conservation and one continuous equation for particle momentum (velocity) conservation. Particle transport by diffusion (Brownian motion) is naturally included in this formulation. A great simplification is obtained if particle inertia is neglected, that is, if it is assumed that the particle instantaneously reaches the terminal velocity at which drag and imposed forces are in balance. In this case, the particle momentum equation is no longer needed, and only the particle continuity equation for particle concentration n (particles cm^{-3}) remains (Fuchs 1964, p 190)

$$\frac{dn}{dt} + \mathbf{U} \cdot \nabla n - \nabla^2 n = \nabla \cdot (\mathbf{U}_p n) \quad (14)$$

where \mathcal{D} ($\text{cm}^2 \text{s}^{-1}$) is the particle diffusion coefficient

$$\mathcal{D} = \frac{kT/(K_n)}{3\pi\mu d_p} \quad (15)$$

and k is Boltzmann's constant. Equation (14) has the form of an advection-diffusion equation (similar to that for species mass transport that can be solved by (10a)) with a source equal to the second term on the right hand side. Before solving this advection-diffusion equation, the fluid velocity field \mathbf{U} is calculated neglecting the particle phase. Note that the net terminal velocity \mathbf{U}_p

appearing in equation (14) can include contributions from plasma-induced forces in addition to gravitational and thermophoretic forces; in this case the net terminal velocity would clearly vary spatially. In this work, however, the particle diffusivity and terminal velocity are assumed constant (the latter implies $\mathbf{V} \cdot \nabla_p n = \nabla_p \cdot \nabla n$); also, only steady state solutions are sought.

4. Problem description

To demonstrate the relative capabilities of the Lagrangian and Eulerian schemes, we consider axisymmetric flow (no plasma) between two plates as discussed above and as shown in figure 1. The flow entering through the top plate (showerhead) is assumed to be uniform and steady in velocity and concentration. For all calculations, both plates are assigned a diameter $D_p = 24$ cm; we assume a fluid density $\rho = 1 \text{ g cm}^{-3}$ and a fluid viscosity $\mu = 1 \text{ g cm}^{-1} \text{ s}^{-1}$, and an inlet concentration $n_c = 1 \text{ particle cm}^{-3}$. Two gap spacings ($S = 4$ or 8 cm) and two inlet velocities ($U_0 = 1$ or 4 cm s^{-1}) are used in the calculations to explore the sensitivity of the solution to these parameters. Boundary conditions at the wall are taken as zero for both velocity components and for particle concentration. In this example the particle terminal velocity is taken as constant and is directed toward and normal to the lower plate (so as to enhance deposition). Following grid refinement studies, a graded grid of 45 elements in the axial and 30 elements in the radial direction was chosen for all calculations; all elements are nine-node, biquadratic quadrilaterals. A mixed pressure scheme was applied.

Since all calculations are made with dimensional parameters, the utility of the results can be increased by expressing the results in dimensionless terms. For this purpose, equation (14) is non-dimensionalized by choosing S as a characteristic length, U_0 as a characteristic velocity and n_c as a characteristic concentration. Under the present assumptions, equation (14) becomes

$$\hat{\mathbf{U}} \cdot \hat{\nabla} \hat{n} - \frac{1}{\text{Pe}} \hat{\nabla}^2 \hat{n} - \hat{\mathbf{U}}_p \cdot \hat{\nabla} \hat{n} = 0 \quad (16)$$

where the Peclet number is defined as $\text{Pe} = SU_0/\nu$. In standard problems of species mass transfer, the Peclet number would be sufficient to characterize completely the problem for a given geometry and flow field. For particles, however, the presence of a terminal velocity term (the second term on the right hand side) means that the Peclet number no longer uniquely specifies the solution. For our example, in which the terminal velocity is constant and normal to the plate, a dimensionless velocity ratio must also be considered: U_p/U_0

5. Results and discussion

5.1. Flow field calculations

Streamlines from the solution of the flow between the two plates are shown in figure 2 for $S = 4$ and $U_0 = 1$

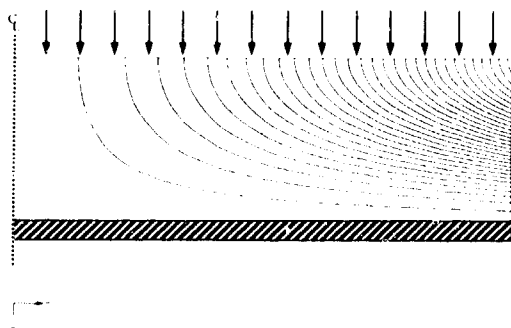


Figure 2. Streamlines for $S = 4$ cm, $U_0 = 1 \text{ cm s}^{-1}$ and $\text{Re} = 4$.

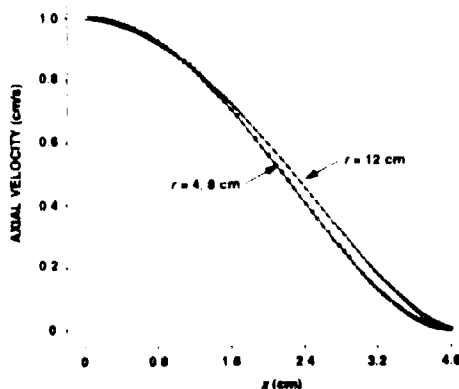


Figure 3. Axial velocity as a function of axial position (z) at radial positions $r = 4.8$ and 12 cm ($S = 4$ cm, $U_0 = 1 \text{ cm s}^{-1}$ and $\text{Re} = 4$).

which corresponds to a fluid Reynolds number of $\text{Re} = \rho U_0 S / \mu = 4$. As expected for such a low Reynolds number, viscous effects dominate and a strongly parabolic radial velocity profile is found. In the central core the flow is pseudo one dimensional; by this we mean that the axial velocity depends only on axial position (z), while the ratio of the radial velocity divided by radius depends only on z . Thus if the radial velocity is scaled by the radius, then the radial velocity profiles will collapse to one curve (the radial velocities must increase with radius to conserve mass). Figure 3 shows profiles of axial velocity as a function of axial position (z) for several radial positions. The one dimensional character of the axial velocity is strongly evident except very near the exit.

5.2. Lagrangian particle transport

An example of a Lagrangian transport calculation is shown in figure 4, which shows trajectories for 11

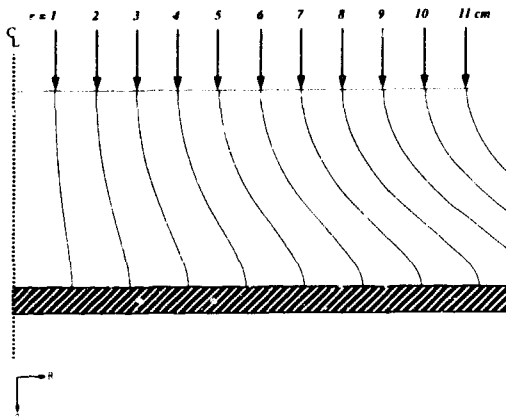


Figure 4. Particle tracks for particle response time $\tau = 0.0025$ s with terminal velocity $V_p = 1$ cm s $^{-1}$ ($S = 4$ cm, $U_0 = 1$ cm s $^{-1}$ and $Re = 4$).

particles, which started from the upper plate at 1 cm radial intervals. Particles with a very small response time ($\tau = 0.0025$ s) were chosen for this calculation, so that the particles are always moving at close to their net terminal velocity. Here, a gravitational acceleration was used, which gave a gravitational terminal velocity of 1 cm s $^{-1}$. The particles were started in equilibrium, with an initial velocity of 2 cm s $^{-1}$ (the vector sum of the 1 cm s $^{-1}$ fluid velocity plus the 1 cm s $^{-1}$ gravitational terminal velocity). In this calculation, eight of the 11 particles were deposited on the lower plate. Additional trajectory calculations were made to identify the initial location of a particle being deposited on the very outer edge of the lower plate; this critical trajectory was found to start at $r = 8.50$ cm. For a uniform influx of particles at the top plate, these calculations show that 50% of particles entering the domain would be collected on the lower plate. Increasing the particle response time increases this collection efficiency; in the limit of large particle response time, particles continue to travel with their initial velocity normal to the lower plate and the collection efficiency becomes unity.

5.3. Eulerian particle transport

A series of calculations were also made in which particle transport was characterized using the Eulerian formulation. The calculations show that the particle concentration field is one-dimensional (depending only on axial position) except very near the exit. This result holds for all combinations of parameters, for example the concentration field is one-dimensional in both diffusion-dominated and terminal-velocity-dominated regimes for both gap spacings ($S = 4$ or 8 cm) and both Reynolds number ($Re = 4$ and 16). An implication of this result is that the particle flux to the lower plate is uniform; figure 5 shows a calculation of particle flux to the lower plate as a function of radial position for the case $S = 4$ cm, $U_0 = 1$ cm s $^{-1}$, $\tau = 2$ cm 2 s $^{-1}$, $Pe = 2$, $V_p/U_0 = 1$ and

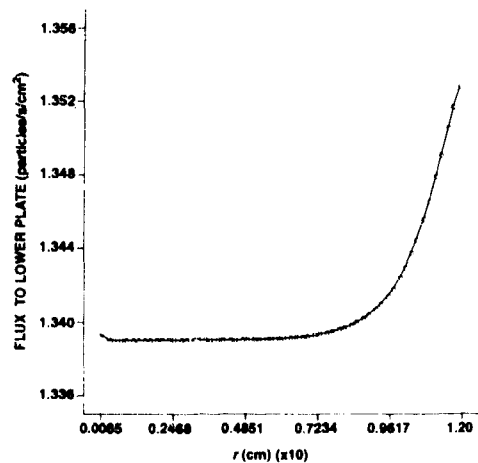


Figure 5. Local flux to the lower plate as a function of radial position ($S = 4$ cm, $U_0 = 1$ cm s $^{-1}$, $\tau = 2$ cm 2 s $^{-1}$, $Pe = 2$, $V_p/U_0 = 1$ and $Re = 4$).

$Re = 4$. Although there is a distinct increase in deposition rate near the outer radius of the domain, the edge-to-centre variation is less than about 2%. The average flux to the lower plate is calculated to be 1.34 particles cm $^{-2}$ s $^{-1}$, as compared with an inlet flux of 2.06 particles cm $^{-2}$ s $^{-1}$, which gives a collection efficiency of 65% (where collection efficiency is defined as the fraction of particles entering the reactor that end up being deposited on the lower plate).

Collection efficiencies as a function of Pe are plotted in figure 6 for the same flow conditions ($S = 4$ cm, $U_0 = 1$ cm s $^{-1}$ and $Re = 4$) for three values of V_p/U_0 . Two interesting qualitative observations should be noted: first, in the limit of small Pe (diffusion-dominated transport), the collection efficiency tends to unity. Second, in the limit of large Pe (terminal-velocity-dominated transport), the collection efficiency tends to

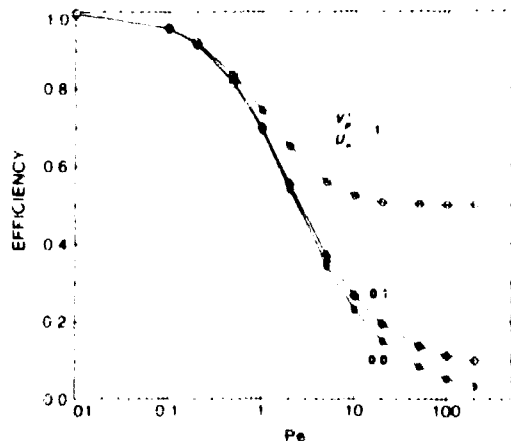


Figure 6. Collection efficiencies as a function of Pe for three particle terminal velocities ($S = 4$ cm, $U_0 = 1$ cm s $^{-1}$ and $Re = 4$).

$V_p/(U_o + V_p)$. For example, for $V_p = U_o = 1$ the collection efficiency tends to 50%. As expected, this result agrees with the calculations of the same physical problem using the Lagrangian formulation presented in section 5.2.

6. Conclusions

The algorithms underlying both Lagrangian and Eulerian formulations for particle transport have been briefly described. Using a commercial finite-element code, these two approaches have been demonstrated on a generic parallel-plate reactor geometry. Both techniques provide information on particle motion within the fluid domain and give deposition rates to the lower plate. The Lagrangian approach is used in this work when both particle inertia and applied forces are important, while the Eulerian approach is used when both particle Brownian motion and applied forces are important. In the overlap region of negligible particle Brownian motion and inertia, both techniques give the same particle collection efficiency for terminal-velocity-dominated transport. Although plasma-induced forces on the particles are not treated in detail, we have shown how models for these forces can be incorporated into the Lagrangian or Eulerian framework as they become available.

Acknowledgments

This work was performed at Sandia National Laboratories under USA Department of Energy contract DE-AC04-94AL85000, and supported by the Contamination

Free Manufacturing Research Center jointly operated by Sandia National Laboratories and Sematech.

References

- Allen M D and Raabe O G 1982 Re-evaluation of Millikan's oil drop data for the motion of small particles in air *J. Aerosol Sci.* **6** 537-47
- Barnes M S, Keller J A, Forster J C, O'Neill A and Coultas D K 1992 Transport of dust particles in glow-discharge plasmas *Phys. Rev. Lett.* **68** 313-6
- Batchelor G K and Shen C 1985 Thermophoretic deposition of particles in gas flowing over cold surfaces *J. Colloid Interface Sci.* **107** 21-37
- Choi S J, Bentzek P L G, Hoekstra R J and Kushner M J 1994 Spatial distributions of dust particles in plasmas generated by capacitively coupled radio frequency discharges *Plasma Sources Sci. Technol.* **3** 418
- Choi S J and Kushner M J 1993 Simulation of the shielding of dust particles in low pressure glow discharges *Appl. Phys. Lett.* **62** 2197-9
- Clift R, Grace J R and Weber M E 1978 *Bubbles, Drops, and Particles* (New York: Academic)
- Cunningham E 1910 On the velocity of steady fall of spherical particles through fluid medium *Proc. R. Soc. A* **83** 357-65
- Fuchs N A 1964 *The Mechanics of Aerosols* (New York: Dover)
- Hinds W C 1982 *Aerosol Technology* (New York: Wiley)
- Rader D J 1990 Momentum slip correction factor for small particles in nine common gases *J. Aerosol Sci.* **21** 161-8
- Sommerer T J, Barnes M S, Keller J H, McCaughey M J and Kushner M J 1991 Monte Carlo-fluid hybrid model of the accumulation of dust particles at sheath edges in radio-frequency discharges *Appl. Phys. Lett.* **59** 638-40
- Talbot L, Cheng R K, Schefer R W and Willis D R 1980 Thermophoresis of particles in a heated boundary layer *J. Fluid Mech.* **101** 737-58
- Vurton R and Levenspiel O 1986 A short note on the drag correlation for spheres *Powder Technol.* **47** 83-6

Charging, transport and heating of particles in radiofrequency and electron cyclotron resonance plasmas

D B Graves, J E Daugherty, M D Kilgore and R K Porteous

University of California at Berkeley, Department of Chemical Engineering, Berkeley, California 94720-1462, USA

Received 7 January 1994, in final form 18 January 1994

Abstract. Once particles are formed or injected into plasmas used for materials processing, such as in plasma etching, plasma-assisted chemical vapour deposition or sputtering plasma systems, the nature of particle transport will largely determine whether a processing surface will be contaminated. We investigate the situation in which the particle density is low enough to ignore particle–particle and particle–plasma interactions. Emphasis is placed on obtaining expressions for the forces experienced by particles. These expressions depend on the local plasma condition: plasma density, electron temperature, positive ion directed and random kinetic energies, electric field and ion mass. We apply a model of an electron cyclotron resonance discharge to prediction of the existence and nature of particle trapping. Model predictions indicate that a high-density source such as an electron cyclotron resonance discharge is unlikely to trap particles mainly because of the large ion drag force sweeping particles out of the discharge. Finally, we present a model of particle heating in discharges. Under typical radiofrequency discharge conditions, particles are generally predicted to be near the neutral gas temperature in the discharge. We have conducted experiments and found results in agreement with these predictions. However, under conditions typically encountered in high-density plasma sources such as an electron cyclotron resonance source, the model predicts that particles may be heated to temperatures of two to three times room temperature.

1. Introduction

The reduction of particulate contamination in plasma-assisted semiconductor processing is a matter of major economic importance [1]. It is essential, therefore, to understand the behaviour of particles in processing plasmas in order to minimize their effect on microelectronic device production. In this article we consider particles to be objects of larger than atomic dimensions, typically spheres or agglomerates of spheres ranging in size from nanometres to micrometres in diameter. We review the charging and transport behaviour of such particles in plasmas, and apply this knowledge to understanding how particles reach surfaces. In addition, we investigate the temperature of particles. This is of interest for understanding particle growth and morphology.

The main thrust of this paper is to outline a theory of the forces on particles in processing plasmas given a model of the plasma. The first requirement is a model of the sheath around the particle and the particle charge. These require a model for the particle capacitance and the ion and electron currents to the particle. We summarize results from a model based on theories first

applied to the analysis of electrostatic probes. Once we have the form of the sheath profile, expressions for the particle capacitance and the monopolar and dipolar forces on the particle can be obtained. The potential profile and particle charge are used to obtain expressions for the momentum transfer cross section due to ion drag.

The expressions for the forces on particles are used to predict particle trajectories in a high-density electron cyclotron resonance (ECR) plasma. Model predictions suggest that particles in high-density plasmas are not trapped by the plasma potential, unlike in RF discharges. The ion drag force is much stronger in high-density plasmas, and the neutral drag and plasma potential are relatively small. Particles become entrained in the ion flux, and can often scale the retarding sheath potentials and leave the discharge. Inertia plays an important role in particle transport. We explore particle trajectories that originate at the chamber walls, following evidence presented by Logan and McGill that stressed film deposits eject micrometre-scale particles with considerable velocity [2].

Finally, we present a model to predict particle tem-

perature. Particle surfaces are heated by ion-electron recombination and are cooled by radiation and conduction from the neutral gas. Under RF discharge conditions, particles are predicted to remain at or slightly above room temperature. Experimental measurements confirm this prediction. However, relative to RF discharge conditions, the higher plasma density and lower neutral gas density in the high-density sources greatly increases the heating of particles and reduces conductive cooling. Since small particles tend to be relatively inefficient radiators at infrared wavelengths, particles are predicted to reach temperatures of the order of 1000 K.

2. Particle charging and sheath structure

In this section we summarize our model for particle charging and the associated issue of the structure of the sheath that forms around a small particle immersed in the plasma. The results that we present are based on the solution of the coupled Poisson-Vlasov equations. This theory was first formulated and applied to the problem of current collection by a spherical electrostatic probe by Bernstein and Rabinowitz [3]. In this theory, ions and electrons are assumed to move without collisions in the vicinity of the particle, although collisions must establish some distribution function far from the particle. Electron and ion densities can therefore be obtained, in principle, by the solution of the Vlasov equation. Ions are assumed to be monoenergetic and electrons are assumed to have a Maxwell-Boltzmann distribution in the Bernstein and Rabinowitz theory. Laframboise [4] extended the Bernstein and Rabinowitz approach by generalizing to non-monoenergetic ion velocity distribution functions. In general, the space charge in the particle sheath influences the ion and electron trajectories, so expressions must be obtained for the net charge density as a function of radial position from the particle. These expressions, obtained from orbit theory, are inserted into Poisson's equation to solve for the potential profile. The result is the spherically symmetric solution of the coupled Poisson-Vlasov equations. The major complications in this theory have to do with the existence of the absorption radius and associated extrema in the curves of effective potential [5]. Additional complications that we do not deal with include non-monoenergetic ion energy distributions in computing the sheath potential (although this is accounted for in the charging and force calculations that follow), fluctuations in particle surface potential due to finite-charge effects, collisions in the sheath, the effects of ions in trapped orbits and deviations from a central force field, due to streaming plasma [5].

Figures 1(a) and (b) summarize the results of the sheath structure predicted by solving the Poisson-Vlasov equations for a typical set of conditions of interest for particles in high-density plasma systems [5]. Table 1 lists the conditions assumed for the plasma far from the particle surface. We assume that the particle has a $0.05\text{ }\mu\text{m}$ radius and that no negative ions are

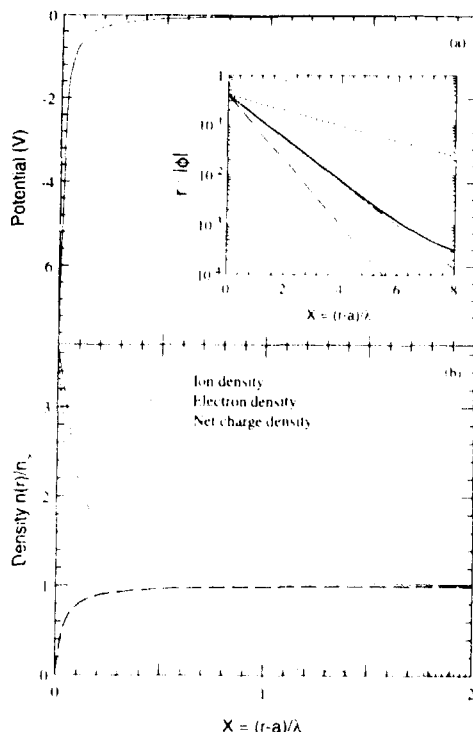


Figure 1. (a) Plot of potential as a function of position for a particle of radius $0.05\text{ }\mu\text{m}$. The full curve in the inset shows the same result plotted to display the similarity to Debye-Hückel solutions with the following screening lengths: (---) electron Debye length, (----) linearized Debye length (equation (1)), and (---) ion Debye length. (b) Ion, electron and net charge density profiles near the particle.

present. Figure 1(a) is a plot of the potential profile in the vicinity of the particle. The inset in figure 1(a) indicates that the Poisson-Vlasov solution is well approximated (except far from the particle, where the potential varies as r^{-2}) by a Debye-Hückel or screened Coulomb potential, $\phi(r) = (\phi_p/a)r \exp[-(r-a)/\lambda]$, with the characteristic screening length

$$\lambda = \left[\frac{e^2 n_e}{\epsilon_0 \left(\frac{1}{kT_e} + \frac{1}{2E_i} \right)} \right]^{1/2} \quad (1)$$

where a is the particle radius, $\phi_p = \phi(a)$ is the particle surface potential, n_e is the plasma density far from the particle, e is the elementary unit of charge, ϵ_0 is the vacuum permittivity, k is Boltzmann's constant, T_e is the electron temperature and E_i is the ion energy far from the particle. Equation (1) results from the linearization of the full set of Poisson-Vlasov equations, and for this reason we call λ the linearized Debye length. We note that in the Poisson-Vlasov equations, the ion density depends on the square root of $\phi(r)/E_i$; the factor 2 multiplying E_i in equation (1) results from the linearization of this square-root term [5]. For the conditions in

Table 1. Conditions assumed for plasma for example of figure 1.

Gas	Argon (ion mass 6.634×10^{-26} kg)
Plasma density	$5 \times 10^{17} \text{ m}^{-3}$
Electron temperature	2.5 eV (electron Debye length $17 \mu\text{m}$)
Positive ion energy	0.15 eV (positive ion Debye length $4 \mu\text{m}$)

table 1, λ is $6 \mu\text{m}$, which is smaller than the electron Debye length ($17 \mu\text{m}$) because $kT_e \gg E_i$.

Figure 1(b) is a plot of the charge density profile corresponding to the potential profile in figure 1(a). The most striking aspect is that the ion density increases rapidly near the particle surface. It turns out that the local rise in the ion density around small particles results from the spherical geometry and the corresponding importance of ion angular momentum.

Examination of figure 1(a) shows that near the particle, the Poisson Vlasov potential profile differs little from a purely Coulomb potential profile. Even though the ion density n_i increases in the vicinity of the particle, the number of positive charges corresponding to this density is relatively small in such a small volume. This is illustrated more clearly in figures 2(a) and (b) [5].

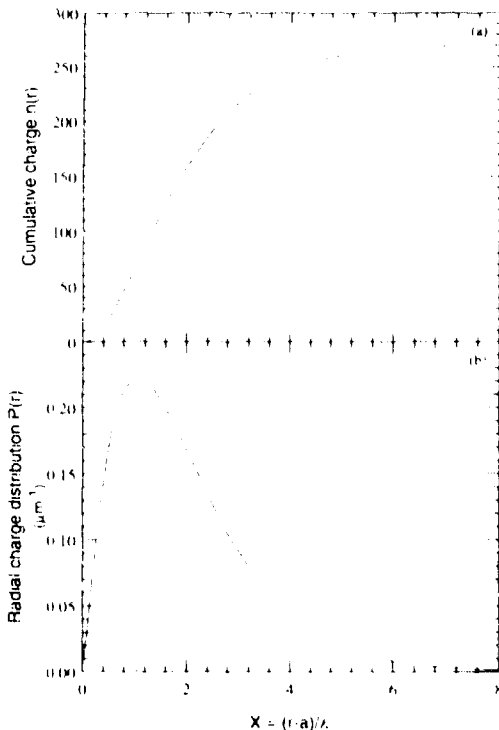


Figure 2. (a) Cumulative charge $n(r)$. This function gives the net positive charge as a function of the radial position from the particle surface. (b) Radial charge distribution function $P(r) = (1/n_i)(dn_i/dr)$. This function gives the probability of finding net charge in a spherical shell between the radii r and $r + dr$.

Figure 2(a) is a plot of the net positive charge as a function of radial position from the particle surface. The quantity $P(r) dr$ that is plotted in figure 2(b) is the probability of finding charge in a spherical shell between the radial positions r and $r + dr$. The peak in this curve is about one linearized Debye length from the particle surface. Figure 2(b) indicates that most of the charge shielding the plasma from the particle resides at least one Debye length from the particle. We expect that, very near the particle, the instantaneous charge density will show significant fluctuations since the average number of ions in a sphere of radius about $0.5 \mu\text{m}$ (for the conditions of figure 1) is on the order of one [6]. However, within a linearized Debye sphere (radius about $6 \mu\text{m}$), there are hundreds of charges. We conclude that the predictions of ion density break down for radial positions much less than about one Debye length, but they are appropriate for radii of the order of λ . Particles with radii greater than one linearized Debye length have screening lengths that approach or exceed the electron Debye length [5].

We have shown previously that when $a/\lambda \ll 1$, orbital motion limit (oml) theory can be used to provide an estimate of the ion and electron currents to the particle [5]. In this theory, only the surface potential affects current collection; the profile of potential surrounding the particle is unimportant in this limit. Obviously, this simplifies the analysis considerably. This theory breaks down when extrema in the curves of effective potential arise, but it turns out that the effect of these complications is minimal under most conditions of interest in this application. The oml theory was originally derived for electrostatic probes by Mott-Smith and Langmuir [7]. These authors derived the charging currents for both Maxwellian and ion-beam velocity distribution functions. However, under the conditions of interest in processing plasmas, the ion velocity distribution function more closely resembles a drifting Maxwellian than either a pure Maxwellian or a beam [8-10]. Consequently, we have re-derived the oml charging equation for a drifting Maxwellian ion distribution function. Uglyov and Gnedovets [11] and Chen and Chen [12] derive similar expressions for the charging currents. Using oml theory, the ion current is

$$I_i = \frac{e}{4} (4\pi a^2) n_i \left(\frac{1}{\sqrt{\pi}} \int_0^\infty \left(1 + \frac{2u^2}{\pi} \right) \exp(-u^2) du \right) \quad (2)$$

where

$$u = \frac{2}{\sqrt{\pi}} \left(\frac{r-a}{\lambda} \right) \left(\frac{8kT_i}{\pi m_i} \right)^{1/2} - \frac{e\phi}{kT_i}$$

In equation (2), $v_{+p} = v_{D+} - v_p$ is the ion drift velocity relative to the particle velocity v_p , v_{D+} is the ion drift velocity relative to stationary coordinates, $v_{+p} = |v_{+p}|$ is the relative ion drift speed, \bar{c}_+ is a measure of the ion thermal speed, m_+ is the ion mass, \bar{n}_+ is the average ion density in the vicinity of the particle, ϕ_p is the particle surface potential with respect to the local plasma potential and T_+ is the ion temperature. We note that equation (2) reduces to Mott-Smith and Langmuir's current expression for Maxwellian ions when $v_{+p} \ll \bar{c}_+$, and it reduces to their expression for beaming ions when $v_{+p} \gg \bar{c}_+$ [7].

Since the electron drift velocity is much smaller than the electron random thermal velocity, we use Mott-Smith and Langmuir's original expressions for the electron charging current [7]

$$I_e = \frac{-e}{4} (4\pi a^2) \left(\frac{8kT_e}{\pi m_e} \right)^{1/2} \bar{n}_e \exp\left(\frac{e\phi_p}{kT_e}\right). \quad (3)$$

In equation (3) m_e is the electron mass, \bar{n}_e is the local electron density and T_e is the electron temperature. The total charge on the particle, Q_p , may be found by requiring charge conservation at the surface of the particle

$$\frac{dQ_p}{dt} = I_+ + I_e. \quad (4)$$

Under the conditions of interest, it can be shown that the screened Coulomb potential profile determines the capacitance relation $C = Q_p/\phi_p = 4\pi\epsilon_0 a(1 + a/\lambda)$ [13]. The charge in equation (4) may therefore be expressed as $Q_p = 4\pi\epsilon_0 a\phi_p(1 + a/\lambda) \approx 4\pi\epsilon_0 a\phi_p$, since usually $a/\lambda < 1$.

An initial condition is needed for equation (4). We have assumed that the particle comes off the wall with no charge. In fact, since dielectric surface films could be charged, a particle could come off the wall with a considerable amount of charge. We have found that the particle charging time is very rapid ($\tau_{\text{charge}} \approx 1 \mu\text{s}$ or less) for particles with sizes $a \approx 0.05 \mu\text{m}$ and larger in high-plasma-density systems [23]. Consequently, the particle trajectory is not sensitive to the assumption made about the initial particle charge.

3. Forces on particles

Once we obtain the form of the sheath potential profile and we have an expression for the charge on the particle, we can calculate forces on the particle due to an applied, external electric field and field gradient. The monopole force, F_m , on a particle due to the applied field E_0 can be shown to be [13]

$$F_m = \frac{4}{3} \pi \epsilon_0 a \phi_p E_0 \left[\left(\frac{a}{\lambda} \right)^2 + 3 \left(\frac{a}{\lambda} \right) + 3 \right]. \quad (5)$$

This result may be simplified by using the Debye-Hückel capacitance (C) of the sphere, $C = 4\pi\epsilon_0 a(1 + a/\lambda)$, to give the final result [13]

$$F_m = Q_p E_0 \left(1 + \frac{(a/\lambda)^2}{3(1 + a/\lambda)} \right). \quad (6)$$

Equation (6) indicates that the electrostatic force on a particle immersed in a plasma is at least $Q_p E_0$. In the majority of cases in which the Debye-Hückel theory is applicable [5] $a/\lambda \ll 1$ and the force is almost identically $Q_p E_0$.

A similar calculation for the dipole moment p gives the expression $p = 4\pi\epsilon_0 a^3 E_0$. (In this expression, we have dropped terms of order of a/λ and smaller [13].) Note that this result is identical to the dipole moment of a charged sphere in vacuum. Since the dipole moment p is proportional to a^3 , the resulting dipole force on the particle from a gradient in the electric field is generally much smaller than the monopole force.

A very important force on particles in discharges is the ion drag or ion wind force [14-18]. When positive ions drift towards walls, they interact with the sheath of the particulate, transferring momentum in what are essentially Coulomb collisions. In order to compute the magnitude of this force, we use the following expression:

$$F_{\text{ion drag}} = K_{mi} \bar{n}_+ m_+ v_{+p} \quad (7)$$

where K_{mi} is the momentum transfer rate coefficient. The momentum transfer rate coefficient can be calculated from

$$K_{mi} = \int_0^\infty \sigma(v_+) v_+ f(v_+) dv_+, \quad (8)$$

if the cross section $\sigma(v_+)$ and the ion speed distribution $f(v_+)$ are known.

In order to evaluate equation (8), we need an estimate for the cross section, and this can be obtained from classical scattering theory and knowledge of the potential around the particle. Details can be found elsewhere [14, 15], but a result predicted from a screened Coulomb potential profile and classical scattering theory is shown in figure 3.

In order to evaluate the integral in equation (8), we generally use a screened Coulomb form for the cross section, and a shifted Maxwellian for the ion speed distribution function $f(v_+)$. An example is provided in figure 4, where the rate coefficient is plotted as a function of ion density with the ratio of ion drift speed to random thermal speed as a parameter. The other discharge conditions are listed in figure 4. The general trend is that the rate coefficient declines with increasing plasma density. This is because the size of the sheath decreases as plasma density goes up. The dependency of K_{mi} on \bar{n}_+ and ion drift speed can change as other discharge parameters (and particle size) change. This illustrates the complex parameter dependencies that are often observed in modelling particles in plasmas.

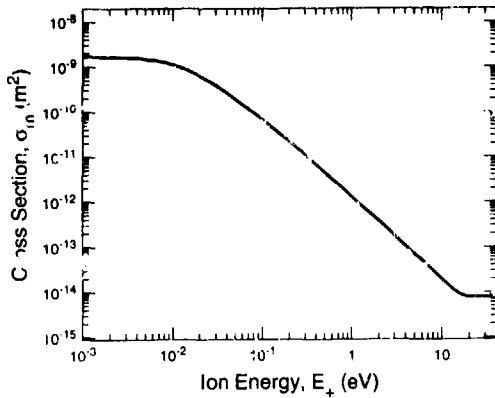


Figure 3. Ion-particle momentum transfer cross section as a function of ion energy for the following conditions: electron temperature 2.5 eV, ion temperature 0.15 eV, plasma density $5 \times 10^{17} \text{ m}^{-3}$ and particle diameter $0.1 \mu\text{m}$. At high ion energies, the cross section approaches the hard sphere cross section, which is $7.85 \times 10^{-15} \text{ m}^2$.

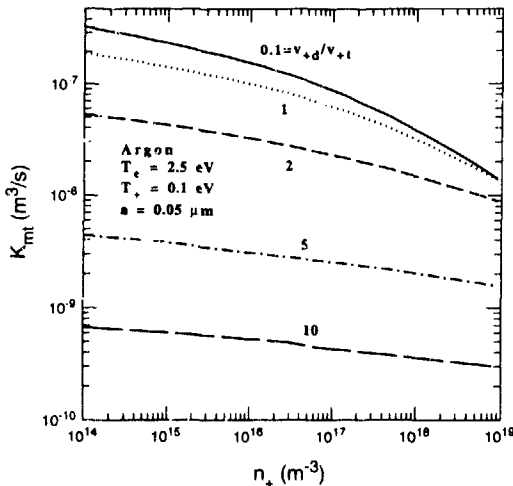


Figure 4. A plot of momentum transfer rate coefficient versus positive ion density for various ratios of ion drift speed to random thermal speed, for the conditions shown.

Figure 5 is a plot of the ion drag force for the same conditions and parameters. Note that, while the rate coefficient declines with density, the force increases with density. Note that the ion drift speed will greatly exceed the ion random thermal speed by the time ions attain the Bohm velocity near the sheath edge. For the conditions of this example, the ion drag force is predicted to drop when the drift speed exceeds the thermal speed by a factor of two.

Additional forces on the particulates include thermophoresis [19], gravity and drag due to the relative velocity between the particle and the neutral gas. Only the last force is significant for the conditions of interest in the following section, so we limit the discussion to it.

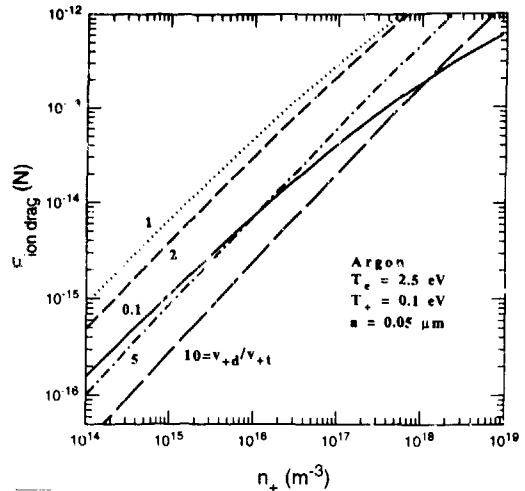


Figure 5. A plot of ion drag force versus positive ion density for various ratios of ion drift speed to random thermal speed, for the conditions shown.

From gas kinetic theory the neutral drag force can be written as [20]

$$F_{ND} = 2\sqrt{\pi} n_n k T_n a^2 \left[\left(s + \frac{1}{2s} \right) \text{erf}(s) + \sqrt{\pi} \left(1 + s^2 - \frac{1}{4s^2} \right) \text{erf}(s) \right] \quad (9)$$

where

$$s = \frac{2}{\sqrt{\pi}} \frac{|v_{np}|}{\bar{c}_n} \quad \bar{c}_n = \left(\frac{8kT_n}{\pi m_n} \right)^{1/2}$$

In equation (9), n_n is the neutral gas density, \bar{c}_n is the neutral thermal speed, $v_{np} = v_{Dn} - v_p$ is the average relative velocity between the neutral gas and the particle, T_n is the neutral temperature, and m_n is the mass of a neutral molecule. Note that when $s \ll 1$, equation (9) reduces to the more familiar Epstein expression for neutral drag in the kinetic regime [20, 21]:

$$F_{ND} = \frac{4}{3} \pi a^2 m_n n_n \bar{c}_n v_{np}$$

4. Particle trajectories in high-density plasmas

We now come to the point where the model for the forces on the particles can be combined with a plasma model to predict particle trajectories. In this illustration, we assume that particles are emitted from the chamber walls due to film stress, as has been reported by Logan and McGill [2]. We speculate that this is an important mechanism for the introduction of particles into a high-

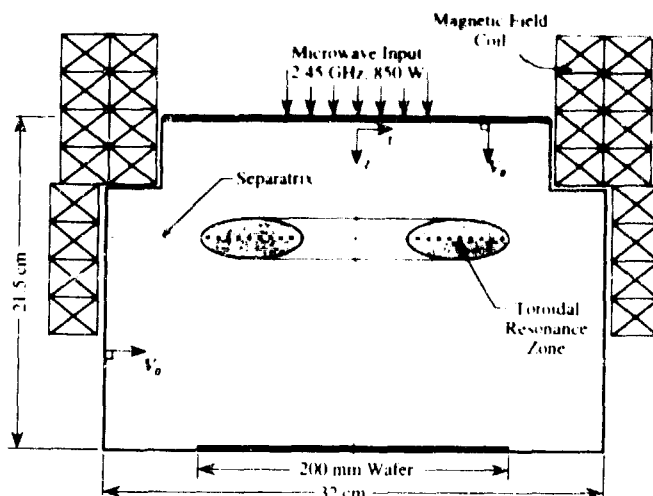


Figure 6. Schematic diagram of the electron cyclotron resonance chamber configuration. The arrows labelled V_0 represent the initial positions and velocities for the particle trajectories that are discussed in the text.

density plasma device. In the analysis that follows, we use our model of the forces that particles experience and a model of the plasma to predict particle trajectories. We assume that particles are emitted from walls at a given velocity, without attempting to model the actual ejection process. For the results presented, a particle diameter of $0.1 \mu\text{m}$ has been chosen.

We consider the ECR geometry shown schematically in figure 6 [8]. Discharge and plasma conditions are listed in tables 2 and 3. The plasma model has been discussed in detail elsewhere [8, 9]. The essential plasma features are that the peak plasma density is of the order of 10^{12}cm^{-3} , the ion current to the walls is of the order of 5 mA cm^{-2} , the electron temperature is about 2.5 eV , and the sheath potential is about 15 V . Ion velocity distribution functions are close to drifting Maxwellians with random energies of the order of a few tenths of an electron-volt. The ion flux vectors are shown in figure 7. These conditions are typical of a variety of high-density plasma devices currently under investigation, including for example, RF inductive, helicon and helical resonator devices [22].

Illustrative trajectories for two different initial positions and ten different initial velocities of the particle are shown in figure 8 [2, 23]. First consider the five trajectories that originate on the left side wall. The three trajectories with initial velocities between

225 and 530 m s^{-1} intersect the 200 mm diameter wafer centred at the bottom of the chamber ($z = 21.5 \text{ cm}$, $-10 \text{ cm} < r < 10 \text{ cm}$ represents the wafer position). The trajectory on the far left has insufficient initial velocity (145 m s^{-1}) to make it to the wafer. The one on the far right has a very high initial velocity (620 m s^{-1}) and it overshoots the wafer and hits the opposite corner. If the particle were started from a different point on the wall, the range of initial velocities that result in the particle hitting the wafer would be different. For example, figure 8 also illustrates five trajectories that originate on the top surface of the reactor ($z = 0 \text{ cm}$, $r = 8 \text{ cm}$). For this starting location, particles with velocities greater than 485 m s^{-1} will hit the wafer. The trajectory labelled A has an initial velocity of 332 m s^{-1} . This trajectory is discussed in detail in the following paragraphs.

The particle z position and kinetic energy as a function of time are shown in figure 9 for the $0.1 \mu\text{m}$ diameter particle that follows trajectory A. Note that this trajectory is also shown in figure 8, and that it terminates near the bottom corner of the chamber at $r = 15.7 \text{ cm}$, $z = 21.5 \text{ cm}$. Initially the particle loses kin-

Table 2. Operating conditions for the electron cyclotron resonance simulation.

Gas	Argon
Neutral gas pressure	5 mTorr
Neutral gas temperature	420 K
Microwave power	850 W

Table 3. Typical parameter values in the electron cyclotron resonance discharge.

Plasma density, n	$5 \times 10^{11} \text{ m}^{-3}$
Plasma potential, ϕ_{plasma}	15 V
Electron temperature, kT_e	2.5 eV
Ion temperature, kT_i	0.1 eV
Wall ion flux, j_i	70 A m^{-2}
Ion drift velocity, v_{D_i}	10^3 m s^{-1}
Neutral thermal velocity	400 m s^{-1}
Particle diameter, $2a$	$0.1 \mu\text{m}$
Particle charge, Q_p	$270e$
Particle shielding length, λ	$6 \mu\text{m}$

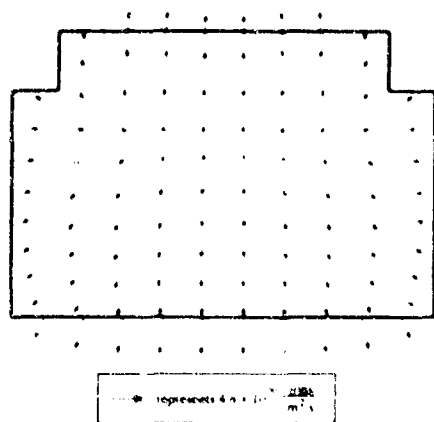


Figure 7. Ion flux vectors from the plasma simulation

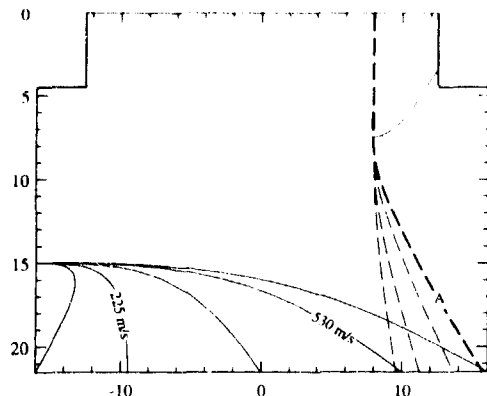


Figure 8. Particle trajectories for $0.1 \mu\text{m}$ diameter particle, emitted normal to the wall at the various velocities shown. For the particles emitted from the side wall, particles with initial velocities of at least 225 m s^{-1} and less than 530 m s^{-1} will hit the 200 mm diameter wafer, assumed to be positioned at $z = 21.5 \text{ cm}$ and $-10 \text{ cm} < r < 10 \text{ cm}$. Particles emitted from the top surface location will hit the wafer if their initial velocity is greater than 485 m s^{-1} . Properties of the trajectory labelled A (initial velocity 332 m s^{-1}) are shown in figures 9 and 10.

etic energy as it moves against the ion wind and the neutral gas. After about $500 \mu\text{s}$, the particle crosses the point where the z component of the ion flux changes sign (see figure 7) and its kinetic energy begins to increase as it accelerates downward towards the wafer. For this case, the particle hits the sheath edge about 1.2 ms after starting from its initial position, and the z component of the directed kinetic energy at the sheath edge, $(KE)_z$, is about three fifths of the total particle kinetic energy $(KE)_{\text{tot}}$. Since $(KE)_z \approx \frac{3}{5}(KE)_{\text{tot}} \approx 300 \text{ keV}$ in this case, the particle easily scales the sheath potential (about 15 V) and hits the wafer. Note that a sheath potential exceeding 800 V would be necessary to repel the particle since the particle charge is $270e$.

It is well known that particles are often trapped in RF capacitively coupled glow discharges [24–26]. Hence

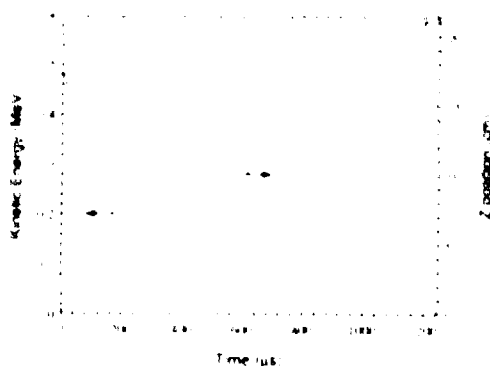


Figure 9. Plots of particle axial (z) position (broken line) and kinetic energy (full line) along trajectory A (see figure 8) as a function of time after being emitted from the wall. This particle remained in the discharge for about 1.2 ms , and hit the sheath edge with about 500 keV kinetic energy. This is more than enough kinetic energy to scale the sheath electrostatic potential.

the strong tendency to push particles through high-density plasma discharge sheaths predicted in this model may seem surprising. The relative lack of trapping in high-density plasmas can be understood qualitatively with the following argument. The ion drag force tends to drive particles to the sheath in both RF and high-density systems, but when the ion flux is lower and the sheath potential is higher (the RF case), particles tend to be trapped at the plasma sheath boundary. The momentum transfer cross section drops off when ion energies increase, so, as ions are accelerated into the sheath, the ion drag force decreases, and the increase in the electric field in the sheath can cause the particle to be trapped [14]. The lower neutral drag a particle encounters in a high-density plasma is also a factor in increasing particle momentum at the sheath edge. The lower neutral drag is simply a consequence of the lower neutral pressure in high-density discharges compared with that in RF systems. We emphasize that the inertia of the particle is often responsible for particles traversing sheaths since the ion drag force tends to become much smaller in the sheath. There has been some experimental evidence that particles are not trapped in high-density plasmas [26–28].

5. Particle temperature

As the particle moves through the plasma it is heated by ion–electron recombination on its surface. We anticipate that the high ECR plasma density will result in a large amount of particle heating, and the low neutral pressure will reduce conductive cooling of the particle compared with that in RF systems. To test this hypothesis, we couple a particle temperature model [23, 29] to the particle transport model to predict how the particle

heats along a trajectory. The model is based on the following energy balance [29]

$$4\pi a^2 \rho_p C_p \frac{dT_p}{dt} = Q_{in} - 4\pi a^2 (q_r + q_k) \quad (10)$$

where T_p is the particle temperature, ρ_p is its mass density, C_p is its heat capacity, Q_{in} is the heating rate due to ion-electron recombination and q_r and q_k are the heat fluxes from the particle due to radiative cooling and Knudsen conduction, respectively. Note that infrared wavelengths are larger than the diameter of a particle. Consequently, particles are generally inefficient radiators of thermal energy, and the emissivity and absorptivity are functions of particle radius and temperature.

Equation (10) was applied to particle heating in a RF parallel-plate electrode plasma system ($n_e \approx 0.6 \times 10^{16} \text{ m}^{-3}$, $T_e \approx 2.5 \text{ eV}$, $T_n \approx 335 \text{ K}$) [29]. The model predicts that particles in an argon glow under these conditions are slightly above the gas temperature. Experiments that measured particle temperature directly confirmed these predictions [29]. Under these more conventional plasma conditions, particle heating by electron-ion recombination is relatively mild, and conductive cooling to the neutral gas is relatively efficient.

Figure 10 shows the temperature along the same trajectory of the $0.1 \mu\text{m}$ diameter particle ($a = 0.05 \mu\text{m}$) that is shown in figure 9 (trajectory A). The initial temperature of the particle was taken as 300 K (the wall temperature), and the neutral gas temperature was assumed to be 420 K [30]. We assume that the particle has the density and optical properties of solid aluminium. The particle gets quite hot ($T_p \approx 1300 \text{ K}$) even though it is only in the plasma for about 1.2 ms . We point out that the prediction of high particle temperature is not restricted to aluminium particles. For example, a $0.1 \mu\text{m}$ quartz

particle on a similar trajectory also reaches an exit temperature in excess of 1000 K . Also shown in figure 10 is the temperature of a larger particle ($1 \mu\text{m}$ diameter or $a = 0.5 \mu\text{m}$). This particle also originated at $r = 8 \text{ cm}$, $z = 0 \text{ cm}$ (same as trajectory A) but its initial velocity was 180 m s^{-1} . This velocity was chosen so that the residence time of the larger particle would be similar to the residence time of the smaller particle on trajectory A. Of course, the larger particle follows a slightly different trajectory, but it samples roughly the same plasma conditions. Note that the larger particle reaches a temperature of only 400 K before leaving the plasma after 1.2 ms . The larger particle remains cold mainly because of thermal inertia. That is, because of its greater mass, the larger particle has a larger total heat capacity, and therefore it gets heated more slowly. If this particle were somehow trapped in the plasma, it would eventually reach a steady-state temperature of about 1000 K . We conclude that small particles can reach high temperatures, but larger particles (diameter $\geq 0.5 \mu\text{m}$) are swept from the discharge before they can get hot [23].

6. Conclusions

We reviewed a model of the particle sheath structure and the forces on isolated particles in plasma processing discharges. These expressions can be coupled to a plasma model to predict the particle trajectory, if information about how the particle enters the plasma is available.

The key result presented here is the prediction that particles that are emitted from the walls of high-density plasma sources can be carried to the wafer surface, or back to other walls, by the strong ion flux. Particles larger than a few nanometres in diameter can easily attain enough momentum to scale the sheath potential and escape the plasma. Although the instantaneous particle density in a high-density plasma tool may be low, particle contamination on the wafer might still be unacceptably high, depending on the rate at which particles are emitted from walls. The model results suggest that high-density tools might be intrinsically quite clean if walls are kept sufficiently clear of stressed film deposits.

We suggest that it might be possible to test the predictions of this model by deliberately depositing stressed films of different composition at different locations within the chamber. The model predicts that particles emitted at certain locations along the wall are most likely to reach the wafer surface. By collecting deposited particles and measuring their composition, the particle wall emission characteristics could be explored. It is conceivable that tool chamber design could be altered to minimize the probability that particles emitted from walls could impact the wafer surface.

The particle energy balance predicts that small particles get heated to high temperatures in high-density plasmas. Small particles that remain in the discharge for more than a few tens of milliseconds are likely to

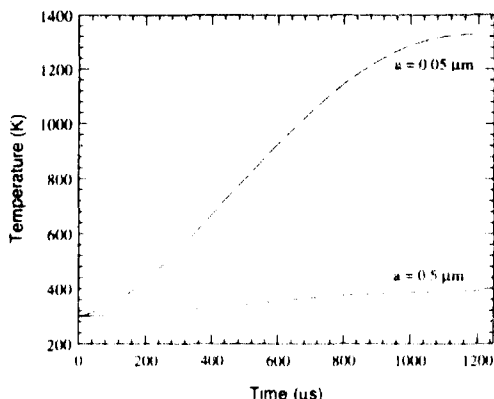


Figure 10. Plots of particle temperature as a function of time after being emitted from the wall. The dashed line is for a $0.1 \mu\text{m}$ diameter particle ($a = 0.05 \mu\text{m}$) travelling on trajectory A (see figure 9). The full line is for a $1 \mu\text{m}$ diameter particle ($a = 0.5 \mu\text{m}$) on a trajectory chosen so that the residence time in the plasma is the same as trajectory A.

become particularly hot ($T_p > 1000$ K). Larger particles (diameter $> 0.5 \mu\text{m}$) are swept from the discharge before they reach high temperatures.

Acknowledgments

We thank H-M Wu for assistance with the plasma results. We appreciate useful discussions with G S Selwyn, W M Holber and M Blain regarding particles in high-density plasmas. We also thank the authors of [15, 26, 28] for providing us with their manuscripts prior to publication. This work was supported in part by National Science Foundation Grant CTS-8957179. M D Kilgore was supported by a NSF Graduate Fellowship. J E Daugherty was supported by an IBM Manufacturing Fellowship.

References

- [1] Donovan R P 1990 *Particle Control for Semiconductor Manufacturing* (New York: Marcel Dekker)
- [2] Logan J S and McGill J J 1992 *J. Vac. Sci. Technol. A* **10** 1875
- [3] Bernstein I and Rabinowitz I 1959 *Phys. Fluids* **2** 112
- [4] Laframboise J G 1966 University of Toronto, Institute for Aerospace Studies, Report No 100
- [5] Daugherty J E, Porteous R K, Kilgore M D and Graves D B 1992 *J. Appl. Phys.* **72** 3934
- [6] Choi S J and Kushner M J 1994 *IEEE Trans. Plasma Sci.* **22** 138
- [7] Mott-Smith H M and Langmuir I 1926 *Phys. Rev.* **28** 727
- [8] Graves D B, Wu H-M and Porteous R K 1993 *Japan. J. Appl. Phys.* **32** 2999
- [9] Porteous R K, Wu H-M and Graves D B 1994 *Plasma Sources Sci. Technol.* **3** 25
- [10] Woods R C, McClain R L, Mahoney I J, Den Hartog E A, Pershing H and Hamers J S 1991 *SPIE Proc.* **1594** 366
- [11] Uglov A A and Gnedovets A G 1991 *Plasma Chem. Plasma Proc.* **11** 251
- [12] Chen X and Chen X 1989 *Plasma Chem. Plasma Proc.* **9** 387
- [13] Daugherty J E, Porteous R K and Graves D B 1993 *J. Appl. Phys.* **73** 1617
- [14] Kilgore M D, Daugherty J E, Porteous R K and Graves D B 1993 *J. Appl. Phys.* **73** 7195
- [15] Choi S J and Kushner M J 1993 *Appl. Phys. Lett.* **62** 2197
- [16] Barnes M S, Keller J H, Forster J C, O'Neill J A and Coultas D K 1992 *Phys. Rev. Lett.* **68** 313
- [17] Sommerer T J, Barnes M S, Keller J H, McCaughey M J and Kushner M J 1991 *Appl. Phys. Lett.* **59** 638
- [18] Boeuf J P 1992 *Phys. Rev. A* **46** 7910
- [19] Jellum G M, Daugherty J E and Graves D B 1991 *J. Appl. Phys.* **69** 6923
- [20] Baines M J, Williams I P and Asebiomo A S 1965 *Mon. Not. R. Astron. Soc.* **130** 63
- [21] Fuchs N A 1964 *Mechanics of Aerosols* (New York: Dover) p 21
- [22] Lieberman M A and Gottscho R A 1993 *Physics of Thin Films* ed M Francombe and J Vossen (Orlando, Florida: Academic)
- [23] Kilgore M D, Daugherty J E, Porteous R K and Graves D B 1994 *J. Vac. Sci. Technol. B* **12** 486
- [24] Spears K G, Robinson T J and Roth R M 1986 *IEEE Trans. Plasma Sci.* **14** 179
- [25] Selwyn G S 1991 *J. Vac. Sci. Technol. B* **9** 3487
- [26] Selwyn G S, Haller K L and Patterson F F 1992 *Proc. 9th Symp. on Plasma Processing* ed G S Mathad and D W Hess (Pennington, New Jersey: Electrochemical Society)
- [27] Selwyn G S 1992 *Proc. 1992 Dry Process Symposium* vol IV-1 (Tokyo: Institute of Electrical Engineers of Japan) p 123
- [28] Blain M 1993 personal communication
- [29] Daugherty J E and Graves D B 1993 *J. Vac. Sci. Technol. A* **11** 1126
- [30] King G, Sze F C, Mak P, Grotjohn T A and Asmussen J 1992 *J. Vac. Sci. Technol. A* **10** 1265

Detection and modelling of electrode topography effects on particle traps

M Dalvie, M Surendra, G S Selwyn and C R Guarnieri

IBM Research Division, Thomas J Watson Research Center, P.O. Box 218,
Yorktown Heights, NY 10598, USA

Received 7 January 1994, in final form 2 February 1994

Abstract. Spatially resolved optical emission from an argon discharge is used to detect regions of enhanced emission over a grooved electrode designed to trap and channel particles. A groove extends the entire length of the electrode and is aligned with the optical detection axis. Thus we measure the integrated line-of-sight emission inside, above and next to the groove. Enhanced emission is seen and shown to be pressure-dependent for a given groove design. At low pressure (< 100 mTorr) a single 'bright' spot is noted above the centre of the groove. This spot splits into two with increasing separation as the pressure increases. Laser light scattering detection of suspended particles shows correlated splitting of a single trapping region at low pressure into two traps at higher pressure. A two-dimensional radiofrequency discharge model is applied to the grooved electrode. The model consists of solving the electron, ion and continuity equations, the electron energy balance and Poisson's equation over the two-dimensional domain. The drift-diffusion approximation is used for electron and ion fluxes. Model results of the ionization rate are in reasonable agreement with experimental measurements. The resulting potential profiles from the model solution may be used to analyse particle trap locations.

1. Introduction

Plasma processing equipment has recently been shown to be especially susceptible to particulate contamination [1–3]. Particles formed, or introduced, during plasma processing acquire a net negative charge in the plasma [1]. Interaction between the negatively charged particle and the bounded plasma medium is very complex [4–9] and leads to unexpected and ill-understood particle behaviour. In particular, charged and suspended particles collect in well-defined localized regions (particle traps). Laser light scattering studies indicate that particle traps can be formed by various topographical features on the electrode. A step created by the edge of a wafer or clamp ring, for example, may result in a 'ring' trap around the periphery of the wafer and/or a 'dome' trap centred over the wafer. Similar effects have also been noted for material discontinuities on electrode surfaces [2]. If traps occur in the vicinity of substrates (as in the case of ring or dome traps over wafers), it is likely that some particles will land on the substrate at the end of the process when the plasma is turned off. Since substrate contamination is a major cause of product yield loss, it is important to understand the nature of particle trapping in plasma equipment.

While particle trapping has been observed in a variety of tool process conditions [1–3], the mechanisms behind it have not been clearly understood. An isolated particle in a plasma is negatively charged in order to equalize the electron and ion fluxes incident on the particle surface, and thus creates a positive space charge around the particle. This is analogous to sheath formation at a wall. The extent of the space charge cloud has been estimated to be of the order of the ion Debye length (about $50\text{ }\mu\text{m}$) [10]. In addition to the electric field forces (monopole and dipole), particles are also influenced by the streaming motion of the plasma (ion drag), and other forces including gravity, neutral drag and thermophoresis. Different combinations of these have been used to construct various force balance models to explain experimental observations of particles collecting at the plasma sheath edge [4–9]. To date, however, forces on particles have generally been analysed in only one spatial dimension.

Spatially resolved Langmuir probe measurements over electrode features (steps and material boundaries) indicate that these cause perturbations in the plasma potential that correspond in location to the trapping regions (electrostatic traps) [3]. However, interpretation of probe measurements is made difficult by the necessary

closeness of the measurement to the sheath edge, by the intrusive nature of the probe and by the uncertainty of probe behaviour in the presence of particles. Here, we show that non-intrusive, spatially resolved optical emission spectroscopy (OES) of the discharge yields valuable information regarding particle traps.

One scheme to counteract particle trapping that has been demonstrated involves *introducing* particle traps into plasma equipment, which serve the special function of directing particles away from other (weaker) traps, such as those *created* by the wafer. Thus a groove cut into the electrode, which traps particles, can be used to guide particles away from the wafer region towards a chamber pumping port [11]. In this paper, we present experimental measurements of spatially resolved optical emission over a grooved electrode at 50, 200 and 400 mTorr (low, intermediate and high pressure, respectively). These measurements are correlated with the location of observed particle traps in the groove at each pressure.

In addition to the experimental results, rf discharge simulation solutions over the grooved electrode are presented at intermediate and high pressure. Since we use a fluid model of the discharge, the low-pressure case is outside the range of the simulation. Simulation results are in reasonable agreement with optical emission measurement. Besides providing explanation for the optical emission behaviour, the simulation results may be used as a basis to study the accuracy of various particle force models [4–9] in describing the observed trap locations.

The following sections describe the experimental apparatus and the rf discharge simulation. The experimental and simulation results are presented together with the discussion. Particle force models are discussed in the conclusion.

2. Experimental

Details of the experiments have been described elsewhere [12]. Figure 1 is a schematic diagram of the apparatus. Briefly, the plasma chamber is a modified Gaseous Electronics Conference reference cell [13]. The upper electrode (including the earthing shield) has been removed. Nominally 30 W of rf power at 13.56 MHz is capacitively coupled to the lower electrode. Because of the asymmetric reactor configuration, a substantial dc self-bias develops on the electrode, measured to be ~ 310 V at 50 mTorr. The Ar flow rate is 50 sccm in all experiments.

A $10\text{ cm} \times 10\text{ cm}$ Al plate is placed on the lower electrode to 'square' the discharge in the vicinity of the electrode, thus minimizing any sampling length variation in the OES measurements [12]. The experiments are performed over a $22\text{ mm} \times 6\text{ mm}$ groove cut into the Al plate (the plate and the groove are also shown with the emission plots). The groove is centred laterally in the square plate and runs the entire length of the plate (10 cm).

Spatially resolved OES measurements are made using a collimated view of the discharge through two aligned apertures, which define a cylindrical line-of-sight volume element over which the measurement is averaged. The collimated light is focused on the slit of a monochromator, which is used to measure the spatial variation in the intensity of the 420.1 nm ($4p[3/2] (2) \rightarrow 5[5/2](3)$) neutral Ar line. Other neutral Ar emission lines (451.1 , 592.9 and 604.3 nm) show the same behaviour. The plasma region mapped is typically 5 cm wide \times 3 cm high. The measured spatial resolution of this apparatus is $\pm 1\text{ mm}$ horizontally and $\pm 2\text{ mm}$ vertically.

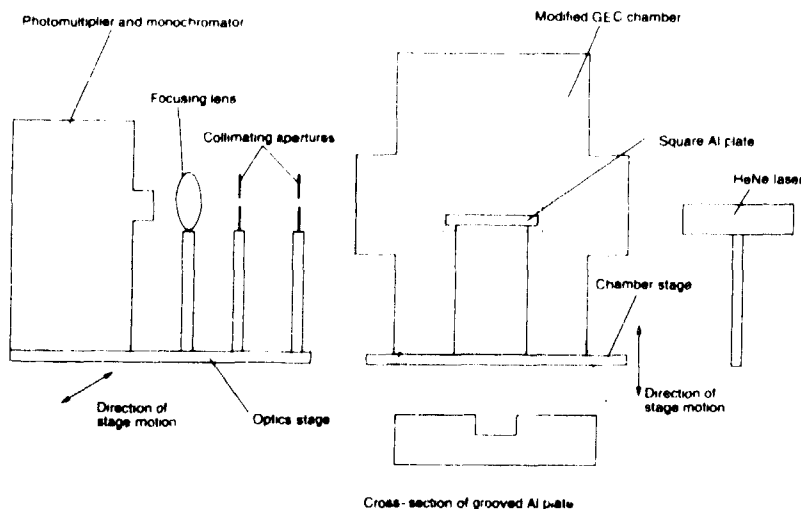


Figure 1. Schematic diagram of the experimental apparatus.

Particles are introduced in controlled sizes by means of a filtered particle generator mounted over the electrode. Light scattering off the particles from a He-Ne laser beam, aligned with the optical axis of the OES system, is used to locate the position of particles independently with respect to the groove.

3. Radiofrequency discharge simulation

Details of the RF simulation, including the transport parameters used to approximate Ar discharges, have been described elsewhere [14]. Briefly, the fluid model consists of the time-dependent electron and ion continuity equations, the time-dependent electron energy balance and Poisson's equation. The drift-diffusion approximation is used for the electron and ion fluxes. The equations are solved using the Galerkin finite-element method and integrated in time to a harmonic steady state.

Here we describe differences between the current simulation scheme and that in [14]. Since the plasma chamber is three-dimensional (a round chamber with a square electrode) it is not computationally feasible to simulate the entire chamber. Instead, we focus on the immediate vicinity of the groove, and construct a simulation domain as shown in figure 2. Since the discharge is 'square' near the electrode, we use Cartesian $x-z$ coordinates in the simulation with the y axis placed parallel to the groove length. The centre plane of the groove is assumed to be a plane of symmetry with zero-gradient boundary conditions. The distance between the other vertical boundary and the groove side

wall is slightly greater than the groove height, and zero-gradient boundary conditions are enforced there as well. The lower boundary is the grooved Al electrode, and we place an artificial earthed upper electrode 4 cm away from the bottom of the groove (the actual counter electrode in the experiment comprises the chamber wall and the top flange considerably further than 4 cm away). Only the lower half of the domain is displayed in the results.

The current boundary condition used for the cathode in [14] is replaced by an external circuit consisting of a resistor, capacitor and voltage source ($V_s \sin(2\pi t/T)$, where T is the RF period) in series, as shown in figure 2. The driving voltage amplitude is $V_s = 50$ V, C is the blocking capacitance (340 pF m^{-1}) and R is the series resistance ($0.006 \Omega \text{ m}$). The values of V_s , C and R are arbitrary (not those of the experimental system, see below). The secondary electron emission coefficient is set to 0.03.

Forward Euler in time is used to solve the ion continuity equation. In order to satisfy the CFL condition, the ion solver uses smaller time steps than the implicit time integrator for the electron equations. The number of ion time steps per electron time step ranges from 5–25. Explicit solution of the ion equation makes the acceleration scheme used in [14] prohibitively expensive; therefore, we rely only on direct time integration.

Given the difference between the simulation domain and the experimental system, the simulation is not expected to reproduce the actual relationship between the driving voltage, the gap length, and the plasma density (or sheath thickness). Rather, the gap length and voltage are chosen such that the sheath thickness at 200 mTorr approximates the experimental value for reasonable plasma density levels. Owing to the slightly larger area of the cathode, we obtain a small positive bias on the cathode.

4. Results and discussion

Figures 3–5 show contour maps of optical emission intensity at Ar pressures of 50, 200 and 400 mTorr respectively. Note the different ordinate scale in figure 3. Figures 3–5 also show the measured locations of particles (typically a line of particles along the length of the groove) trapped by this electrode structure. The groove-enhanced emission is clearly visible in figures 3–5. At 50 mTorr (figure 3) there is a single bright spot, centred over the groove, 10 mm from the groove bottom. Particles introduced at this pressure form a single line above the centre of the groove. The emission intensity at 200 mTorr (figure 4) shows two bright spots, symmetrically placed, closer to the groove bottom (concomitant with a reduction in the sheath thickness). Particles, however, still form a single line in the centre of the groove. At 400 mTorr (figure 5) the separation between the two bright spots increases as the sheath continues to shrink, and here the particles form two distinctly separated lines inside the groove. Separation between par-

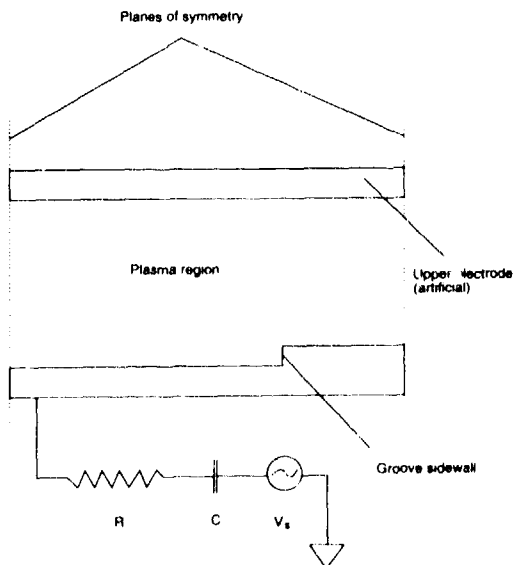


Figure 2. Schematic diagram of the simulation domain.

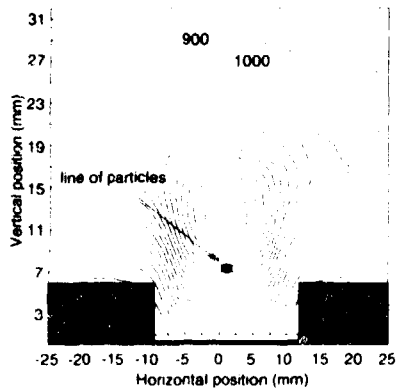


Figure 3. Contour map of spatially resolved optical emission intensity (420.1 nm line) over a 22 mm \times 6 mm groove, arbitrary units. Ar pressure 50 mTorr.

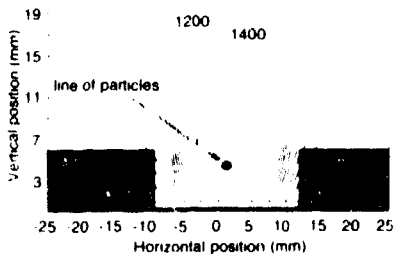


Figure 4. Contour map of spatially resolved optical emission intensity (420.1 nm line) over a 22 mm \times 6 mm groove, arbitrary units. Ar pressure 200 mTorr.

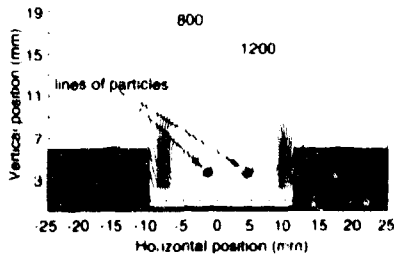


Figure 5. Contour map of spatially resolved optical emission intensity (420.1 nm line) over a 22 mm \times 6 mm groove, arbitrary units. Ar pressure 400 mTorr.

ticles is smaller than that between emission bright spots.

Next we show the ionization rate from the simulation at 200 mTorr (figure 6) and 400 mTorr (figure 7). The groove is assumed symmetric around the centre (see figures 4 and 5). The low-pressure case (50 mTorr) is considered outside the range of applicability of the fluid model. The ionization rate correlates well with the emission rate since the shapes of the inelastic collision

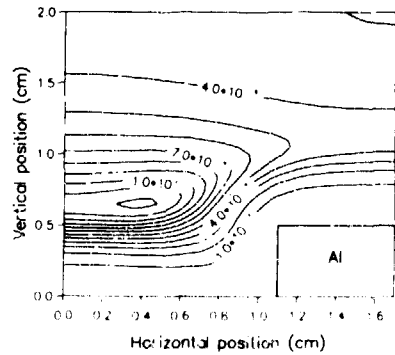


Figure 6. Contour map of the simulated ionization rate ($\text{m}^{-3} \text{s}^{-1}$). Ar pressure 200 mTorr.

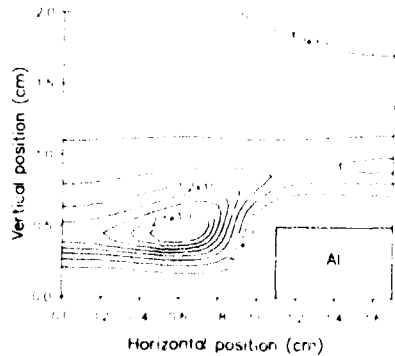


Figure 7. Contour map of the simulated ionization rate ($\text{m}^{-3} \text{s}^{-1}$). Ar pressure 400 mTorr.

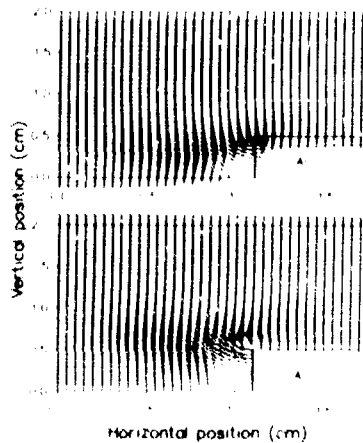


Figure 8. Vector plot of current flow to ($t = T/2$) and from ($t = T$) the grooved electrode. Ar pressure 400 mTorr.

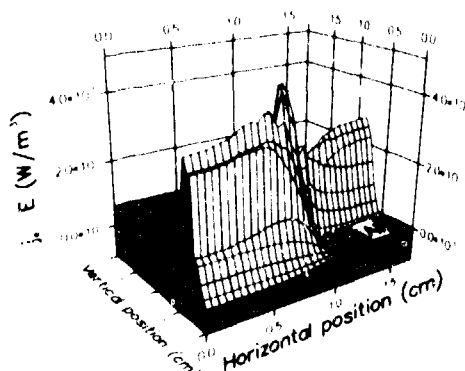


Figure 9. Electron heating rate ($J_e E$) as a function of position. Ar pressure 400 mTorr.

cross sections are similar. We show the ionization rate because it is more directly related to the plasma density and potential profiles. Once the simulation conditions are chosen to match the sheath height in figure 4, the simulated ionization and experimentally measured emission agree well (figure 6 with figure 4, figure 7 with figure 5).

The groove-induced enhancement of ionization rate is due to a focusing of the RF current near the side wall of the groove. Since the enhancement is stronger at 400 mTorr, the simulation at that pressure is used to analyse this effect. Figures 8 and 9 are drawn from the 400 mTorr case. Figure 8 shows the current flow to and from the grooved electrode at two different times in the RF period, $t = T/2$ and $t = T$. The physical step in the electrode causes the current to bend near the side wall, and creates a region of 'excess current'. This current focusing creates extra electron heating near the top of the side wall, shown in figure 9. The higher electron heating rate results in greater ionization and excitation rates near the side wall [14].

Figures 10 and 11 show the simulated potential profiles obtained at 200 and 400 mTorr, respectively. Considering the arbitrary choice of discharge conditions used in the simulation, the actual voltage values do not

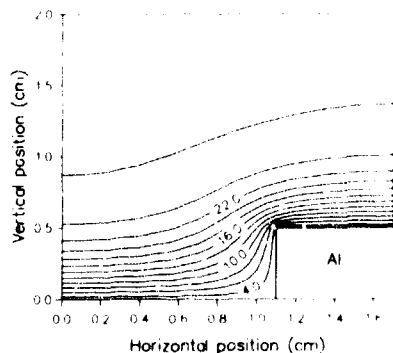


Figure 10. Contour map of simulated potential (V). Ar pressure 200 mTorr.

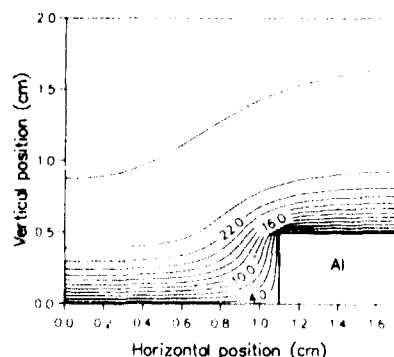


Figure 11. Contour map of simulated potential (V). Ar pressure 400 mTorr.

represent those in the experiment. Nevertheless, certain features of the potential profiles are useful to note. There is a high-field region at the top edge of the groove side wall, while the bottom edge of the groove is a low-field region. The results do not show any regions that may be identified as electrostatic traps for particles as measured in [3]. Rather, the potential increases monotonically with distance away from the cathode. This is confirmed by figure 12 a plot of the lateral electric field (E_y) versus horizontal position 3 mm above the bottom of the groove. The groove side wall is located at 1.1 cm. The electric field increases monotonically, with no sign change, towards the side wall. This suggests that trapping in this system occurs through a balance of different forces [4–9] rather than through a single, dominant trapping force. Differences between the simulation domain, the experimental system and the system used in [3] may explain the different results.

5. Discussion of particle trapping

In the absence of an isolated electrostatic trap for particles, that is, a local maximum in plasma potential

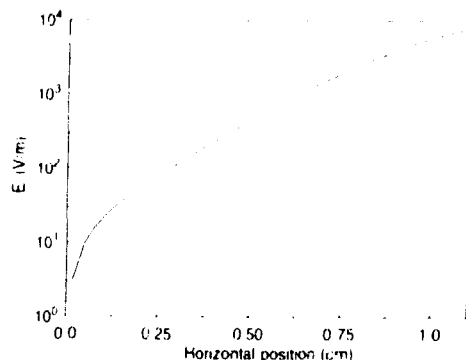


Figure 12. Plot of the lateral electric field (E_y) versus horizontal position at height $z = 3$ mm above the bottom of the groove. Ar pressure 400 mTorr.

[3], it is unclear whether there is a direct causal relationship between the enhanced emission (ionization) rate and particle trapping. Rather, both phenomena may be caused by sheath perturbation due to the groove. Nevertheless, optical emission is a sensitive and non-intrusive indicator of sheath non-uniformities, which are believed to trap particles in this system.

The trapping mechanism in the groove is believed to be a two-dimensional variation of the force balance discussed in the literature [4-9]. Before proceeding to analyse the applicability of various published models, it is necessary to have a more reliable prediction of the ion flux, since ion drag is believed to be one of the crucial forces affecting particle location [4]. With the drift-diffusion model used here, the ion drag is always anti-parallel to the electric field force on the particle if the small ion diffusion term is neglected. It is unclear what effect ion inertia may have on the ion drag force. While ion inertial effects are important in the sheath, they may be small in the presheath where the particles collect. Inclusion of ion inertial effects, to allow the ion drag force to deviate from the electric field direction, is currently under way.

It seems clear on comparing figures 10 and 11 that the high-pressure case in figure 11 shows a larger region inside the groove with relatively flat isopotential contours. The 200 mTorr case therefore shows stronger lateral fields inside the groove (which might cause particles to collect in the centre of the groove as observed) than at 400 mTorr. This is consistent with the thinner sheath thickness at 400 mTorr. The flatter contours imply that, based on considerations of electric field and gravity alone, the particles have a smaller tendency to collect in the centre at 400 mTorr than at 200 mTorr. Therefore, any force pushing the particles away from the centre (such as the dipole force $E \cdot \nabla E$ [9]) would encounter less resistance at 400 mTorr than at 200 mTorr. Prediction of the off-centre particle trap at 400 mTorr is expected to yield valuable insight into trapping forces.

Summary

Spatially resolved optical emission is shown to be a sensitive indicator of particle traps in RF discharges.

Sheath non-uniformities, which may be responsible for trapping particles in grooved electrodes, may be detected by non-uniformities in the emission profiles. A single region of enhanced emission at low pressure centred over the groove splits into two symmetric, off-centre bright regions at high pressure. A correlation is noted between the emission behaviour and the observed splitting of a single particle trap, centred over the groove at low pressure, into two traps as pressure is increased. A two-dimensional simulation of a grooved electrode indicates that emission enhancement occurs near the groove side wall because of RF current focusing effects, which create extra electron heating near the side wall. Particle trapping in the groove is believed to occur through a balance of axial and lateral forces.

References

- [1] Selwyn G S, McKillop J S and Haller K L 1990 *Proc. SPIE* **1185** 86
- [2] Selwyn G S, Heidenreich J E and Haller K L 1991 *J. Vac. Sci. Technol. A* **9** 2817
- [3] Geha S G, Carlile R N, O'Hanlon J F and Selwyn G S 1992 *J. Appl. Phys.* **72** 374
- [4] Barnes M S, Keller J H, Forster J C and O'Neill J A 1992 *Phys. Rev. Lett.* **68** 313
- [5] Daugherty J E, Porteous R K and Graves D B 1993 *J. Appl. Phys.* **73** 1617
- [6] Jellum G M, Daugherty J E and Graves D B 1991 *J. Appl. Phys.* **69** 6923
- [7] Goree J 1992 *Phys. Rev. Lett.* **69** 277
- [8] Choi S J and Kushner M J 1993 *Appl. Phys. Lett.* **62** 2197
- [9] Bouchoule A, Plain A, Boufendi L, Blondeau J Ph and Laure C 1991 *J. Appl. Phys.* **70** 1991
- [10] Daugherty J E, Porteous R K, Kilgore M D and Graves D B 1992 *J. Appl. Phys.* **72** 3934
- [11] Selwyn G S and Patterson E F 1992 *J. Vac. Sci. Technol. A* **10** 1053
- [12] Dalvie M, Selwyn G S, Surendra M, Guarnieri C R and McGill J J 1993 *Appl. Phys. Lett.* **63** 3279
- [13] Roberts J R, Olthoff J K, Van Brunt R J and Whetstone J R 1991 *Proc. SPIE* **1392** 428
- [14] Dalvie M, Surendra M and Selwyn G S 1993 *Appl. Phys. Lett.* **62** 3207

On the thermophoretic force close to walls in dusty plasma experiments

O Havnes[†], T Nitter[‡], V Tsytovich[‡], G E Morfill[§] and T Hartquist[§]

[†]Auroral Observatory, University of Tromsø, Tromsø, Norway

[‡]Institute of General Physics, Russian Academy of Science, 117924 Moscow, Russia

[§]Max-Planck-Institute for Extraterrestrial Physics, Garching bei München, Germany

Received 6 January 1994, in final form 13 January 1994

Abstract. One observes in radiofrequency-heated vacuum chambers that dust, if present or being produced within the chamber, may float in layers close to both the upper and lower electrodes. Important forces on the dust are the electric force, gravity, plasma drag and the thermophoretic force, which is caused by temperature gradients in the background neutral gas in the vacuum chamber. We here discuss the thermophoretic force and show that the normally adopted formula for this force, which is computed on the assumption of an infinite plasma in all directions from the dust, must be modified when close to the plasma chamber walls. Taking into account the closeness of the plasma walls, we find that the thermophoretic force will be reduced out to many neutral gas molecular collision lengths from the wall, compared with the results from the standard formula. This modification of the thermophoretic force should be of importance for the force equilibrium and stability of dust in the dust layers observed in so many dust levitation experiments.

1. Introduction

There has recently been increased interest in studying the suspension of dust in gases. The realization that dust is formed and suspended in the sheaths near plasma chamber walls and that it can cause severe contamination problems in, for example, plasma etching processes of microelectronic circuits (Selwyn *et al* 1989, 1990a, b) is one reason for this. The dust is suspended in layers near the chamber electrodes, with a topology that is dependent on the electrode structures, and it may fall down onto and contaminate the microchips. The dust particles are charged in the radiofrequency-heated plasmas and an electric force acts on the dust in the electric sheaths near the wall (Barnes *et al* 1992). Other major forces that act on the suspended dust particles are gravity, ion and neutral gas drags if these species are drifting and a thermophoretic force if a temperature gradient is present (Talbot *et al* 1980, Jellum *et al* 1991). Since dust particles are suspended in the plasma it follows that there must exist regions in which there is a stable equilibrium between the different forces. Nitter and Havnes (1992) show that, for dust suspended in the electric sheaths near moon, asteroidal and planetary satellite surfaces, one will normally find two equilibrium points. However, only one of these will be stable. The calculations of Nitter and Havnes (1992) did not include the thermophoretic force, which is of no importance in the rarefied gases in space.

Since the thermophoretic force may be one of the dominant forces in low-pressure RF-heated plasmas (Jel-

lum *et al* 1991), knowledge of its form near the walls where the particles are suspended will be of crucial importance not only to find positions with force equilibrium but also to determine if such equilibrium positions are stable or not.

We will in the following discuss the form of the thermophoretic force and demonstrate that it must be modified, compared with its conventional form for dust particles within a distance from the plasma walls corresponding to several collision lengths of the neutral gas.

2. The thermophoretic force distant from and close to plasma walls

Talbot *et al* (1980) have given a review of earlier works on thermophoresis. They show that a dust particle of radius R in a gas or liquid with a temperature gradient $\partial T / \partial x$ at the position of the dust, will be acted upon by a so-called thermophoretic force along the direction of x equal to

$$F_x = -8R^2nz\lambda k \left(\frac{\partial T}{\partial x} \right). \quad (1)$$

Here k is the Boltzmann constant, the neutral gas density is n while the average collision length in the neutral gas is λ . We neglect the effect of a dust surface temperature on the thermophoretic force since this is small for dust temperatures less than 500 K (Talbot *et al* 1980).

Talbot *et al* (1980) (see also Waldmann (1961)) compute the thermophoretic force F_x by using a velocity distribution function for gas molecules colliding with the dust of

$$f_{in} = f_x = f_0 \left[1 + D \left(c^2 - \frac{5}{2} \right) c_x \right] \quad c_n < 0. \quad (2)$$

We here use relative velocities, the molecular speed is v and

$$c = v/v_s \quad (3)$$

where the gas thermal velocity of particles of mass m and temperature T_0 is $v_s = (2kT_0/m)^{1/2}$. In equation (2) c_x and c_n are the components of c along the temperature gradient (x direction) and along the outward normal to the surface of the grain with the positive direction of c_n being out from the surface. The parameter $D = -6\lambda(\partial T/\partial x)/\sqrt{\pi}T_0$. The unperturbed velocity distribution function is taken to be Maxwellian:

$$f_0 = n_0 \left(\frac{m}{2\pi k T_0} \right)^{3/2} \exp(-c^2). \quad (4)$$

The distribution function given in (2) corresponds to that which is formed in a gas with a temperature gradient and where there is an 'infinite' amount of gas surrounding the dust. Infinite in this context means that there is gas present for many gas molecule momentum transfer collision lengths on both sides of x . This leads to, compared with f_0 , a surplus of slow ($c^2 < 5/2$) and a deficit of fast particles for that part of the distribution function that moves in the direction of ∇T ($c_x > 0$) (namely from lower to higher temperatures) and the opposite for that part that moves against ∇T ($c_x < 0$). An integration of the force due to the impact of particles with the velocity distribution given by equation (2) leads to equation (1) (Talbot *et al* 1980). However, these calculations do not take into account that very close to the wall the distribution function for particles moving away from the wall must be influenced by the manner in which particles are reflected from the wall. If we assume that the particles are reflected with a Maxwellian velocity distribution at wall temperature T_w then (2) is not correct very near to the wall. At the wall itself we will have

$$f_{in} = f_0(T_w) \quad c_x > 0 \quad (5)$$

while for $c_x < 0$ (2) might still hold since the deviation from f_0 for $c_x < 0$ is mainly formed due to particles streaming towards the wall. If we now follow Talbot *et al* (1980) and calculate the thermophoretic force at the wall by using (5) for $c_x > 0$ and (2) for $c_x < 0$ we find that

$$F_{x,w} = F_x/2 \quad (6)$$

where F_x is the thermophoretic force given by (1). The reason for this is simply that the force due to collisions by the dust with gas particles from the wall is now larger so that the net force towards the wall is decreased. This assumes that the temperature gradient points away from the wall as it normally does in RF plasma experiments (Jellum *et al* 1991) since energy is created in the gas and has to escape through the walls.

At intermediate distances from the wall (out to several collision lengths from the wall) we expect the thermophoretic force gradually to approach the one given by (1). The manner in which the thermophoretic force changes as we go away from the wall is dependent on how the velocity distribution for $c_x > 0$ changes from (5) at the wall to (2) distant from the wall. We will make an approximate estimate of this by solving the Boltzmann equation for neutral particles with a simple model for the collision term

$$\frac{\partial f}{\partial t} + \frac{P}{m} \nabla_x f = \frac{1}{\tau} (f_0 - f). \quad (7)$$

We consider a one-dimensional stationary case. In (7) τ is the neutral neutral collision time and we have assumed that f does not deviate much from the equilibrium distribution f_0 . In general we could have used

$$f = f_0(1 + g_+ + g_-) \quad (8)$$

where $f_0 g_+$ is the deviation from f_0 for particles moving away from the wall and $f_0 g_-$ the deviation from f_0 for particles moving towards the wall. We will assume that g_- is known and equal to the deviation for $c_x < 0$ given by equation (2). However, since $f_0 g_-$ is small relative to f_0 we neglect g_- when calculating the variation of g_+ from the wall and outwards. Using $\partial/\partial t = 0$ and inserting equation (8) in equation (7) and using equations (2)–(4) we find for the one-dimensional case

$$\frac{dg_+}{dx} + \frac{g_+}{c_x \tau} = \left(\frac{5}{2} - \frac{c^2}{2} \right) \frac{1}{T} \frac{dT}{dx} \quad (9)$$

where we have used the condition of pressure equilibrium ($d/dx(nT) = 0$). This can be integrated to give

$$g_+(x) = g_+(0) \exp\left(-\frac{x}{c_x \tau}\right) + \left(\frac{5}{2} - c^2\right) \frac{1}{T} \frac{dT}{dx} \times \tau \left[1 - \exp\left(-\frac{x}{c_x \tau}\right) \right] \quad (10)$$

when we neglect the variation of T relative to the exponential term. If the particles are reflected from the wall with the wall temperature then $g_+(0) = 0$ and we get

$$g_+ \approx -g_- \left[1 - \exp\left(-\frac{x}{c_x \tau}\right) \right] \quad (11)$$

We now calculate the correction to the thermophoretic force by using (11) for g_+ instead of the one used by Talbot *et al* (1980) where $g_+ = -g_-$. Following the method of Talbot *et al* we find that the corrected F_x becomes

$$F_x = F_{x,\infty} \left[1 - \int_0^x c^5 \left(c^2 - \frac{5}{2} \right) \exp(-c^2) \exp\left(-\frac{x}{\lambda c}\right) dc \right] \\ = F_{x,\infty} \left[1 - I\left(\frac{x}{\lambda}\right) \right] \quad (12)$$

when we use $\tau = \lambda/c_s$. We see that $I(x=0) = \frac{1}{2}$ but that the exponential term in x will, at large distances x from the wall, make the integral approach zero. However, if we, as here, use a collision or thermalization length that increases with velocity and since the force due to collisions with the gas molecules is mainly determined by the fast molecules at $c > \sqrt{5}$, the decrease of the integral in (12) with x is considerably slower than if we, for example, replaced $\exp(-x/\lambda c)$ with $\exp(-x/\lambda)$ that is, we put $c = 1$ or used $\langle \tau \rangle = c_s$. Computations of the collision cross section $Q^{(2)}$ (Hirschfelder *et al* 1967, figure 8.4-4) as a function of c show that our use of a constant collision time τ , namely a collision length $\lambda(\tau) = \tau c_s$, is a good approximation at our low temperatures. Figure 1 shows a comparison between the integral in (12) and $0.5 \exp(-x/\lambda)$. This indicates that the wall effect will be felt out to many average collision lengths from the wall and that the conventional expression for the thermophoretic force is not correct in this region.

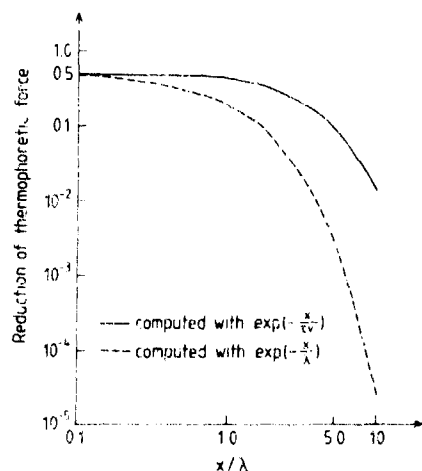


Figure 1. The factor by which the thermophoretic force is reduced due to the wall effect, as a function of the ratio of distance x from the wall and average collision length λ . The full line is for a velocity-dependent and the broken line for a constant, velocity-independent collision length.

3. Discussion

The action of the thermophoretic force in RF dusty plasma experiments is apparently one reason that a layer of dust can be found near the upper electrode (Selwyn *et al* 1989, Jellum *et al* 1991). Both gravity and the electric force on the dust point away from this electrode while ion drag and the thermophoretic force will normally point towards it (Jellum *et al* 1991). A stable equilibrium point for the dust requires that the forces pointing away from the wall dominate inside the equilibrium point and that, in this case, the thermophoretic force, which points towards the wall, dominates outside the equilibrium distance. If we assume a parabolic temperature profile near a wall then the uncorrected thermophoretic force will increase linearly towards the wall as shown schematically in figure 2. This shape of F_x may not allow stable equilibria of dust close to the wall. Such may much more easily be found if the thermophoretic force is corrected for the wall effect since it leads to a reduction of F_x close to the wall. We also show the corrected thermophoretic force $F_{x,w}$ in figure 2. The correction due to the wall is felt out to about five or six collision lengths λ from the wall.

If we consider the experiments by Selwyn *et al* (1989) and Jellum *et al* (1991), which both had Ar as a background gas, we find from Hirschfelder *et al* (1967)

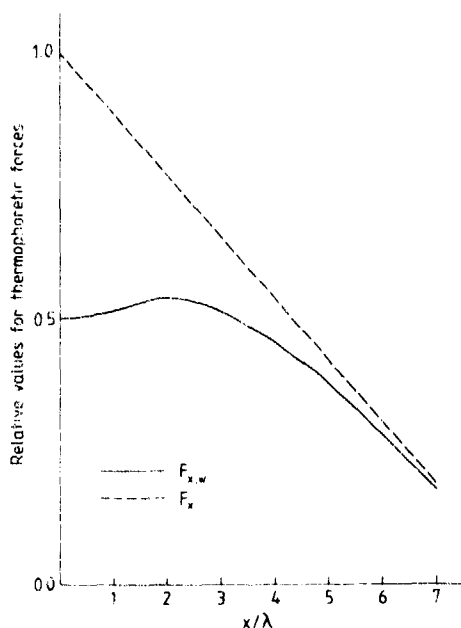


Figure 2. The relative curves for the unmodified (broken line) and modified (full line) thermophoretic force near the wall, for a temperature profile of second order in distance from the wall.

that, at the gas densities and temperatures in those experiments, the collision lengths should be $\lambda \approx 0.7$ and 0.1 mm respectively. This indicates that the thermophoretic force is affected out to about 4 mm in the experiment by Selwyn *et al* (1989) and out to about 0.6 mm in that by Jellum *et al* (1991). These distances are very similar to the distances from the upper electrode at which the maximum laser scattered signal is found for the respective experiments. This indicates that the correction to the thermophoretic force is of importance in understanding the force balance on dust near the upper electrode. At the lower electrode the equilibrium distances are much further from the wall, where the corrections to F_T are probably negligible.

Acknowledgments

We thank Liv Larssen for typing the manuscript and for drawing the figures. This work was supported by the Norwegian Research Council.

References

- Barnes M S, Keller J H, Forster J C, O'Neill J A and Coultas D K 1992 Transport of dust particles in glow-discharge plasmas *Phys. Rev. Lett.* **68** 313
- Hirschfelder J O, Curtiss C F and Bird R B 1967 *Molecular Theory of Gases and Liquids* (New York: Wiley)
- Jellum G M, Daugherty J E and Graves D B 1991 Particle thermophoresis in low pressure glow discharges *J. Appl. Phys.* **69** 6923
- Nitter T and Havnes O 1992 Dynamics of dust in a plasma sheath and injection of dust into the plasma sheath above moon and asteroidal surfaces *Earth Moon Planets* **56** 7–34
- Selwyn G S, Heidenreich J E and Haller K L 1990b Particle trapping phenomena in radio frequency plasmas *Appl. Phys.* **57** 1876
- Selwyn G S, McKillop J S, Haller K L and Wu J J 1990a *In situ* plasma contamination measurements of HeNe laser light scattering: a case study *J. Vac. Sci. Technol.* **A8** 1726
- Selwyn G S, Singh J and Bennett R S 1989 *In situ* laser diagnostic studies of plasma-generated particulate contamination *J. Vac. Sci. Technol.* **A7** 2758
- Talbot L, Cheng R K, Schefer R W and Willis D R 1980 Thermophoresis of particles in a heated boundary layer *J. Fluid Mech.* **101** 737–58
- Waldman L 1961 *Rarefied Gas Dynamics* ed L. Talbot (New York: Academic) p 327

- 355 Effects of particles on He-SiH₄ modulated RF discharges**
Y Watanabe, M Shiratani, T Fukuzawa and H Kawasaki
- 359 The dynamics of dust particles in silane glow discharges between parallel plates**
R J Seeböck, W Böhme, W E Köhler, Römheld and S Vepřek
- 369 Real-time compositional analysis of submicrometre particles**
W D Reents Jr, S W Downey, A B Emerson, A M Muijsce, A J Muller, D J Siconolfi, J D Sinclair and A G Swanson
- 373 Water induced particle formation in the ion chemistry of silane**
W D Reents Jr and M L Mandich
- 381 On form and flow in dusty plasmas**
P D Haaland, A Garscadden, B Ganguly, S Ibrani and J Williams
- 388 Particle nucleation and growth in thermal plasmas**
S L Girshick
- 395 Production of negative ion plasmas in a Q machine**
N Sato
- 400 Charging of particles in a plasma**
J Goree
- 407 Plasma particle interactions**
J P Boeuf, Ph Belenger and T Hbid
- 418 Spatial distributions of dust particles in plasmas generated by capacitively coupled radiofrequency discharges**
S J Choi, P L G Ventzek, R J Hoekstra and M J Kushner
- 426 Particle transport modelling in semiconductor process environments**
D J Rader and A S Geller
- 433 Charging, transport and heating of particles in radiofrequency and electron cyclotron resonance plasmas**
D B Graves, J E Daugherty, M D Kilgore and R K Porteous
- 442 Detection and modelling of electrode topography effects on particle traps**
M Dalvie, M Surendra, G S Selwyn and C R Guarnieri
- 448 On the thermophoretic force close to walls in dusty plasma experiments**
O Haynes, T Nitter, V Tsytoich, G F Morfill and T Hartquist

PLASMA SOURCES SCIENCE AND TECHNOLOGY

Volume 3

Number 3

August 1994

PAPERS

- 239 **Overview of growth and behaviour of clusters and particles in plasmas**
A Garscadden, B N Canguly, P D Haaland and J Williams
- 246 **Negative ions and particle formation in low-pressure halocarbon discharges**
G M W Kroesen, W W Stoffels, E Stoffels, M Haverlag, J H W G den Boer and F J de Hoog
- 252 **Possible routes for cluster growth and particle formation in RF silane discharges**
J Perrin, C Bohm, R Etemadi and A Lloret
- 262 **Particle nucleation and growth in a low-pressure argon-silane discharge**
L Boufendi and A Bouchoule
- 268 **Gas phase particulate formation in radiofrequency fluorocarbon plasmas**
R J Buss and W A Hareland
- 273 **Process-induced particle formation in the sputtering and reactive ion etching of silicon and silicon dioxide**
C Steinbrüchel and W J Yoo
- 278 **Diagnostics of particle genesis and growth in RF silane plasmas by ion mass spectrometry and light scattering**
Ch Holenstein, J-L Dorier, J Dutta, L Sansonnens and A A Howling
- 286 **Experimental investigation of particulate formation in He-SiH₄ modulated RF discharges**
Y Watanabe and M Shiratani
- 292 **High concentration effects in dusty plasmas**
A Bouchoule and L Boufendi
- 302 **Particles in C₂F₆-CHF₃ and CF₄-CHF₃ etching plasmas**
H M Anderson, S Radovanov, J L Mock and P L Resnick
- 310 **A correlation between particle growth and spatiotemporal RF plasma structure**
T Kamata, S Kakuta, Y Yamaguchi and T Makabe
- 314 **Spectroscopic and probe measurements of structures in a parallel-plates RF discharge with particles**
K Tachibana, Y Hayashi, T Okuno and T Tatsuta
- 320 **Infrared spectroscopy of a dusty RF plasma**
W W Stoffels, E Stoffels, G M W Kroesen, M Haverlag, J H W G den Boer and F J de Hoog
- 325 **Particle behaviour in an electron cyclotron resonance plasma etch tool**
M G Blain, G D Tipton, W M Holber, G S Selwyn, P L Westerfield and K L Maxwell
- 334 **Contamination particle traps due to a cone, cube and disk**
R N Carlile, J F O'Hanlon, L M Hong, M P Garrity and S M Collins
- 340 **Optical characterization of particle traps**
G S Selwyn
- 348 **Effects of plasma processing on the microstructural properties of silicon powders**
E Bertran, J Costa, G Sardin, J Campmany, J L Andújar and A Canillas

Continued on inside back cover